

β -LAPACHONE NANOTHERAPEUTICS FOR LUNG CANCER THERAPY

APPROVED BY SUPERVISORY COMMITTEE

Jinming Gao, Ph.D.

David A. Boothman, Ph.D.

Kytai Truong Nguyen, Ph.D.

Ohwofiemu E. Nwariaku, M.D., F.A.C.S.

Rolf Brekken, Ph.D.

To my mother Maria, my father Elvin, and my sister Maria

β -LAPACHONE NANOTHERAPEUTICS FOR LUNG CANCER THERAPY

by

ELVIN BLANCO

DISSERTATION

Presented to the Faculty of the Graduate School of Biomedical Sciences

The University of Texas Southwestern Medical Center at Dallas

In Partial Fulfillment of the Requirements

For the Degree of

DOCTOR OF PHILOSOPHY

The University of Texas Southwestern Medical Center at Dallas

Dallas, Texas

December, 2008

Copyright
by
ELVIN BLANCO, 2008
All Rights Reserved

ACKNOWLEDGEMENTS

I wish to thank first and foremost my graduate school and research advisor, Professor Jinming Gao, for taking me in and giving me the opportunity to conduct research in his laboratory. Not many would have taken the chance he took on me, and for this, I am forever grateful and indebted. Thank you Dr. Gao for challenging me to become a better scientist and for taking a vested interest in my success. I also wish to thank Dr. David A. Boothman, not only for his contributions and efforts in bringing β -lapachone to the clinics, but for insightful conversations and guidance throughout the second act of my graduate career. I would also like to thank my committee members, Drs. Kytai Nguyen, Rolf Brekken, and Ohwofiemu Nwariaku for serving on my committee and for their sound advice throughout.

A large part of the work presented herein would not have been possible without the help of my labmates, who I consider the best and brightest people in their respective fields. Chief among them are Dr. Erik Bey, who assisted in animal studies, as well as Dr. Chalermchai Khemtong, for help with the materials aspect of the project, and Chase Kessinger for help with graphics. I thank them, as well as all of my labmates, past and present, which assisted in my scientific endeavors. I will always cherish their contribution, but more importantly, I will cherish their friendship and comradery.

Last but certainly not least, I wish to thank those closest to my heart. I thank my parents, Maria and Elvin, as well as my sister, Maria, for their unconditional love and support throughout my graduate career.

β -LAPACHONE NANOTHERAPEUTICS FOR LUNG CANCER THERAPY

ELVIN BLANCO, M.S.

The University of Texas Southwestern Medical Center at Dallas, 2008

JINMING GAO, Ph.D.

A rising trend in lung cancer chemotherapy involves the development of agents that exploit molecular targets overexpressed in tumors, with hopes of increasing specificity, and in turn, efficacy. β -Lapachone (β -lap) is a novel anticancer drug whose mechanism of action relies on its bioactivation by the enzyme NAD(P)H:quinone oxidoreductase-1, NQO1, found overexpressed in NSCLC. While promising, its low water solubility limits its clinical translation. Moreover, a clinical formulation of the drug proves highly hemolytic and relatively ineffective. Our objective was to develop β -lapachone polymer micelles for lung cancer treatment, in hopes of targeting tumors: 1) pharmacokinetically, through the use of a platform that will ensure drug stability,

bioavailability, and targeted localized delivery; and 2) pharmacodynamically, through the use of an anticancer drug that is bioactivated by a tumor-specific enzyme. We hypothesize that β -lapachone polymer micelles will result in a highly specific and effective nanotherapeutic platform for the treatment of lung cancer.

Studies involving the clinical formulation of β -lap demonstrated that the vehicle, hydroxypropyl- β -cyclodextrin (HP β -CD), causes hemolysis. The rapid dissociation of β -lap with HP β -CD led to short blood circulation times and rapid distribution among all organs. By contrast, a micellar formulation of β -lap did not cause hemolysis, and displayed increased blood circulation times and relatively high and sustained accumulation in tumors.

β -Lap micelles were small in size (~30 nm), possessed core-shell morphology, and displayed favorable release kinetics. *In vitro* examination of β -lap micelle efficacy in cancer cell lines demonstrated an NQO1-dependent mechanism of cell death. Upon translation to *in vivo* models of lung cancer in mice, β -lap micelles hindered tumor growth in subcutaneous lung tumors. It is important to note at this time that the clinical formulation of β -lap displayed no antitumor effects when compared to control tumors. Upon examination in an orthotopic model of lung cancer in mice, β -lap micelles were shown to prolong animal survival. Results from this study point toward the therapeutic potential of β -lap micelles for lung cancer treatment. Future studies involve optimization of the basic platform, as well as adjuvant use with current therapeutic strategies, to help propel this technology to preclinical studies and eventual clinical use.

TABLE OF CONTENTS

DEDICATION	ii
ACKNOWLEDGEMENTS	v
ABSTRACT	vi-vii
PRIOR PUBLICATIONS	xiv-xvi
LIST OF FIGURES	xvii-xviii
LIST OF TABLES	xix
LIST OF APPENDICES	xx
LIST OF DEFINITIONS	xxi-xxv
CHAPTER 1-INTRODUCTION	1-66
1-1-BACKGROUND AND SIGNIFICANCE OF LUNG CANCER	1-2
1-1-1-CURRENTLY AVAILABLE THERAPIES AND LIMITATIONS	2
1-1-1-1-TISSUE DEBULKING STRATEGIES: SURGERY, RADIATION THERAPY, AND ABLATION	2
1-1-1-2-CHEMOTHERAPY	3-4
1-1-1-3-ADVANTAGES OF DRUG DELIVERY DEVICES FOR CHEMOTHERAPY	4-5
1-1-2-ADJUVANT, NEOADJUVANT STRATEGIES, AND THE FUTURE TREND OF LUNG CANCER CARE	6-7
1-2- β -LAPACHONE: A NATURAL, NOVEL ANTICANCER AGENT	7-19
1-2-1-HISTORY AND VARIED MEDICINAL USES	7
1-2-2-MECHANISM OF ACTION SPECIFIC TO TUMOR TOXICITY	7-13

1-2-3- β -LAP DELIVERY STRATEGIES EXPLORED THUS FAR.....	13-19
1-2-3-1- β -LAP COMPLEXATION WITH CYCLODEXTRINS	13-15
1-2-3-2- β -LAP-CONTAINING POLYMER MILLIRODS	16-19
1-3-POLYMER MICELLES AS EFFECTIVE NANOSCALE CANCER DRUG	
DELIVERY DEVICES	19-44
1-3-1-BACKGROUND ON POLYMER MICELLES	19-23
1-3-2-COMPARISON OF POLYMER MICELLES TO ALTERNATE	
NANOTHERAPEUTIC PLATFORMS	23-27
1-3-3-TARGETED MICELLAR SYSTEMS	27-31
1-3-4-STIMULUS-RESPONSIVE MICELLE SYSTEMS	31-36
1-3-5-MICELLES FOR CANCER IMAGING	36-41
1-3-6-MULTIFUNCTIONAL POLYMER MICELLES	41-44
1-4-OVERVIEW AND ORGANIZATION OF THE THESIS	44-45
1-5-REFERENCES.....	45-66
CHAPTER 2- PHARMACOLOGICAL STUDIES OF B-LAP•HPB-CD (ARQ 501): A	
CASE FOR MICELLAR ENCAPSULATION	67-100
2-1-INTRODUCTION	67-70
2-2-MATERIALS AND METHODS	70-76
2-2-1-MATERIALS	70
2-2-2-PREPARATION β -LAP•HP β -CD COMPLEXES	70-71
2-2-3- β -LAP MICELLE FABRICATION	71-72
2-2-4-HEMOLYSIS ASSAYS	72

2-2-5-PHARMACOKINETIC ANALYSIS OF β -LAP•HP β -CD	72-74
2-2-6-PHARMACOKINETIC ANALYSIS OF β -LAP MICELLES	75-76
2-3-RESULTS	76-84
2-3-1-HEMOLYSIS RESULTING FROM ARQ 501	76
2-3-2-INTERACTION OF β -LAP WITH RBCS	76-78
2-3-3-PHARMACOKINETIC ANALYSIS OF β -LAP•HP β -CD	78-81
2-3-4-PHARMACOKINETIC ANALYSIS OF β -LAP MICELLES.....	82-84
2-4-DISCUSSION	84-92
2-4-1-HP β -CD IS A HIGHLY HEMOLYTIC SOLUBILIZATION VEHICLE	84-85
2-4-2- β -LAP OXIDATION OF HEMOGLOBIN AND POTENTIAL ANEMIA	85-87
2-4-4- β -LAP•HPB-CD IS RAPIDLY CLEARED FROM BLOOD AND	
DISTRIBUTES EVENLY AMONG ORGANS.....	88-89
2-4-5- β -LAP MICELLES DISPLAY PROLONGED BLOOD RESIDENCE	
AND DISTRIBUTE TO SPECIFIC ORGANS	89-92
2-5-CONCLUSIONS	92-93
2-6-ACKNOWLEDGEMENTS	93
2-7-REFERENCES	93-100

CHAPTER 3- DEVELOPMENT AND CHARACTERIZATION OF β -LAPACHONE	
MICELLE NANOTHERAPEUTICS	100-135
3-1-INTRODUCTION	100-104
3-2-MATERIALS AND METHODS	104-111
3-2-1-MATERIALS	104

3-2-2-DIFFERENTIAL SCANNING CALORIMETRY (DSC) ANALYSIS	104-105
3-2-3- β -LAP MICELLE FABRICATION	105-106
3-2-4- β -LAP MICELLE CHARACTERIZATION	106-110
3-2-4-1-SIZE CHARACTERIZATION	106-107
3-2-4-2-CORE-SHELL MORPHOLOGY AND DRUG ENCAPSULATION	107-108
3-2-4-3-EXAMINATION OF β -LAP RELEASE FROM MICELLES.....	108
3-2-4-4-MODELING OF β -LAP RELEASE KINETICS FROM MICELLES	108-110
3-2-5-CYTOTOXICITY OF β -LAP MICELLES <i>IN VITRO</i>	110
3-2-6-DNA DAMAGE AND CELL DEATH ASSAYS	111
3-3-RESULTS	111-124
3-3-1-SOLUBILITY OF β -LAP IN PLA POLYMER	111-112
3-3-2-EFFECT OF DIFFERENT MICELLE FABRICATION METHODS ON DRUG LOADING	112-115
3-3-3-EXAMINATION OF β -LAP CRYSTAL FORMATION	113-117
3-3-4- β -LAP MICELLE CHARACTERIZATION	117-120
3-3-5-MECHANISM OF ACTION OF CELL DEATH INDUCED BY β -LAP MICELLES	120-124
3-4-DISCUSSION	124-129
3-5-CONCLUSIONS	129
3-6-ACKNOWLEDGEMENTS	129
3-7-REFERENCES	130-135

CHAPTER 4- <i>IN VIVO</i> EXAMINATION OF β -LAP MICELLE EFFICACY IN LUNG	
TUMOR MODELS.....	136-161
4-1-INTRODUCTION	136-139
4-2-MATERIALS AND METHODS	139-144
4-2-1-MATERIALS	139
4-2-2-PREPARATION β -LAP•HP β -CD COMPLEXES	139-140
4-2-3- β -LAP MICELLE FABRICATION	140
4-2-4-ESTABLISHMENT AND TREATMENT OF SUBCUTANEOUS A549	
LUNG TUMORS IN MICE	140-142
4-2-5-ESTABLISHMENT AND TREATMENT OF ORTHOTOPIC LUNG	
TUMORS IN MICE	142-144
4-3-RESULTS	144-150
4-3-1- β -LAP•HP β -CD TREATMENT OF SUBCUTANEOUS LUNG	
TUMORS	144-146
4-3-2- β -LAP MICELLE EFFICACY IN SUBCUTANEOUS A549 LUNG	
TUMORS	146-150
4-3-3- β -LAP MICELLE TREATMENT OF ORTHOTOPIC LUNG TUMORS	150
4-4-DISCUSSION	150-156
4-4-1- β -LAP•HP β -CD PROVED INEFFECTIVE AT INHIBITING TUMOR	
GROWTH	150-152
4-4-2- β -LAP MICELLES PROVE EFFECTIVE AT HINDERING TUMOR	
GROWTH AND PROLONGING SURVIVAL	152-156
4-5-CONCLUSIONS	156

4-6-ACKNOWLEDGEMENTS	156
4-7-REFERENCES	157-161
CHAPTER 5- SUMMARY AND FUTURE WORK.....	162-169
5-1- SUMMARY OF THE PROJECT	162-163
5-2- FUTURE DIRECTIONS	163-167
5-2-1-SYNERGY OF β -LAP MICELLES WITH IONIZING RADIATION (IR) AND DNA REPAIR INHIBITORS	164-165
5-2-2-EXPLORATION OF MICELLES CONTAINING PRODRUGS OF β - LAP	165-166
5-2-3-FUNCTIONALIZATION OF β -LAP MICELLES	166-167
5-3- REFERENCES	167-169

PRIOR PUBLICATIONS

Blanco, E.; Kessinger, C.W.; Sumer, B.D. Gao, J. Multifunctional Micellar Nanomedicine for Cancer Therapy. *Exp Biol Med*, In press.

Dong, Y.; Chin, S-F.; Blanco, E.; Kabbani, W.; Bey, E.A.; Boothman, D.A.; Gao, J. Efficacy of Intratumoral β -Lapachone Polymer Millirod Implants for Prostate Cancer Treatment. *Clin Can Res*, In press.

Yang, X.; Chen, Y.; Yuan, R.; Chen, G.; Blanco, E.; Gao, J.; Shuai, X. Folate-Encoded and Fe₃O₄-Loaded Polymeric Micelles for Dual Targeting of Cancer Cells. *Polymer* 2008, 49, 3477-3485.

Weinberg, B.D.; Patel, R.B.; Wu, H.; Blanco, E.; Barnett, C.C.; Exner, A.A.; Saidel, G.M.; Gao, J. Model Simulation and Experimental Validation of Intratumoral Chemotherapy Using Multiple Polymer Implants. *Med Biol Eng Comput* 2008, 46, 1039-1049.

Yang, X.; Deng, W.; Fu, L.; Blanco, E.; Gao, J.; Quan, D.; Shuai, X. Folate-Functionalized Polymeric Micelles for Tumor Targeted Delivery of a Potent Multidrug-resistance Modulator FG020326. *J Biomed Mat Res A* 2008, 86A, 48-60.

Blanco, E.; Bey, E.A.; Dong, Y.; Weinberg, B.D.; Sutton, D.M.; Boothman, D.A.; Gao, J. β -Lapachone-containing PEG-PLA Polymer Micelles as Novel Nanotherapeutics against NQO1-overexpressing Tumor Cells. *J Control Release* 2007, 122, 365-374.

Weinberg, B.D.; Blanco, E.; Gao, J. Polymer Implants for Intratumoral Drug Delivery and Cancer Therapy. *J Pharm Sci* 2007, 97, 1681-1702.

Sutton, D.; Nasongkla, N.; Blanco, E.; Gao, J. Functionalized Micellar Systems for Cancer Targeted Drug Delivery. *Pharm Res* 2007, 24, 1029-1046.

Weinberg, B.D.; Blanco, E.; Lempka, S.F.; Anderson, J.M.; Exner, A.; Gao, J. Combined Radiofrequency Ablation and Doxorubicin-Eluting Polymer Implants for Liver Cancer Treatment. *J Biomed Mat Res A* 2007, 81, 205-213.

Weinberg, B.D.; Ai, H.; Blanco, E.; Anderson, J.M.; Gao, J. Antitumor Efficacy and Local Pharmacokinetics of Doxorubicin via Intratumoral Delivery from Polymer Millirods. *J Biomed Mat Res A* 2007, 81, 161-170.

Wang, F.*; Blanco, E.*; Ai, H.; Boothman, D.A.; Gao, J. Modulating β -Lapachone Release from Polymer Millirods through Cyclodextrin Complexation. *J Pharm Sci* 2006, 95, 2309-2319.

*Contributed equally

Blanco, E.; Weinberg, B.D.; Stowe, N.T.; Anderson, J.M.; Gao, J. Local Release of Dexamethasone from Polymer Millirods Effectively Prevents Fibrosis following Radiofrequency Ablation. *J Biomed Mat Res A* 2006, 76A, 174-182.

Blanco, E.; Qian, F.; Weinberg, B.D.; Stowe, N.T.; Anderson, J.M.; Gao, J. Effect of Fibrous Capsule Formation on Doxorubicin Distribution in Radiofrequency Ablated Rat Livers. *J Biomed Mat Res A* 2004, 69, 398-406.

LIST OF FIGURES

FIGURE 1-1 CHEMICAL STRUCTURE OF β -LAP	8
FIGURE 1-2 SCHEMATIC OF THE MECHANISM OF ACTION OF β -LAP	10
FIGURE 1-3 SCHEMATIC OF β -LAP CYCLODEXTRIN COMPLEXATION	15
FIGURE 1-4 SCHEMATIC OF β -LAP MILLIROD FABRICATION	17
FIGURE 1-5 ANTITUMOR EFFICACY OF INTRATUMORAL IMPLANTATION OF β -LAP-LOADED MILLIRODS	18
FIGURE 1-6 SCHEMATIC OF POLYMER MICELLE	20
FIGURE 1-7 MULTIFUNCTIONAL DESIGN OF A MICELLE NANOMEDICINE PLATFORM.....	28
FIGURE 2-1 PERCENT (%) HEMOLYSIS AS A RESULT OF β -LAP	77
FIGURE 2-2 β -LAP INTERACTION WITH HEMOGLOBIN (HB).....	79
FIGURE 2-3 PHARMACOKINETIC ANALYSIS OF β -LAP•HP β -CD.....	81
FIGURE 2-4 PHARMACOKINETICS OF β -LAP MICELLES	83
FIGURE 3-1 STRUCTURE OF β -LAP AND SCHEMATIC OF β -LAP MICELLE..	102
FIGURE 3-2 SOLID STATE SOLUBILITY STUDIES OF β -LAP IN PLA.....	113
FIGURE 3-3 EXAMINATION OF CRYSTALLIZATION OF β -LAP.....	116
FIGURE 3-4 TEM IMAGE OF β -LAP MICELLES.....	118
FIGURE 3-5 ¹ H-NMR ANALYSIS OF β -LAP MICELLES	119
FIGURE 3-6 <i>IN VITRO</i> β -LAP RELEASE PROFILE.....	121
FIGURE 3-7 RELATIVE SURVIVAL ASSAYS OF CELLS TREATED WITH β -LAP MICELLES.....	123

FIGURE 3-8 CELL DEATH AND DNA DAMAGE ASSAYS RESULTING FROM β -LAP MICELLES	125
FIGURE 4-1 REPRESENTATIVE BLI IMAGE OF LEWIS LUNG CARCINOMA ORTHOTOPIC MODEL IN MOUSE.....	143
FIGURE 4-2 EFFICACY OF INTRAVENOUS INJECTION OF β -LAP•HP β -CD IN SUBCUTANEOUS A549 LUNG TUMORS.....	145
FIGURE 4-3 EFFICACY OF β -LAP MICELLES INJECTED INTRATUMORALLY IN SUBCUTANEOUS A549 LUNG TUMORS.....	147
FIGURE 4-4 EFFICACY AND TOLERABILITY OF β -LAP MICELLES INJECTED INTRAVENOUSLY IN SUBCUTANEOUS A549 LUNG TUMORS	149
FIGURE 4-5 KAPLAN-MEIER CURVE DISPLAYING % OF ANIMAL SURVIVAL OF MICE WITH ORTHOTOPIC LEWIS LUNG CARCINOMA TREATED WITH β -LAP MICELLES	151

LIST OF TABLES

TABLE 1-1 SUMMARY OF NANOTHERAPEUTIC TECHNOLOGIES	25
TABLE 3.1. β -LAPACHONE MICELLE PARAMETERS	114

LIST OF APPENDICES

APPENDIX A - QUANTUM DOT (QD) POLYMER MICELLES FOR *IN VITRO*
TRACKING..... 170-185

APPENDIX B - INTRATUMORAL DELIVERY OF β -LAPACHONE VIA POLYMER
IMPLANTS FOR PROSTATE CANCER THERAPY 186-216

APPENDIX C-PUBLISHED MANUSCRIPTS 217

LIST OF DEFINITIONS

SCLC - small cell lung carcinoma

NSCLC – non-small cell lung carcinoma

RF - radiofrequency

5-FU – 5-fluorouracil

EGFR - epidermal growth factor receptor

TK – tyrosine kinase

IV - intravenous

β -Lap - β -lapachone

NQO1 - NAD(P)H:quinone oxidoreductase-1

ROS – reactive oxygen species

NADPH - nicotinamide adenine dinucleotide phosphate

Dic – dicoumarol

SSBs – single stranded breaks

PARP-1 - poly(ADP-ribose)polymerase-1

PAR - poly(ADP-ribose)

3-AB - 3-aminobenzamide

BAPTA-AM - 1,2-bis-(2-aminophenoxy)ethane-N, N, N', N' -tetraacetic acid tetra-(acetoxymethylester))

IR – ionizing radiation

CDs – cyclodextrins

HP β -CD - hydroxypropyl- β -cyclodextrin

ARQ501 - β -lap•HP β -CD

PLGA - poly(D,L-lactide-co-glycolide)
PEG - polyethylene glycol
PPO - poly(propylene oxide)
PLA - poly(D,L-lactic acid)
PCL - poly(ϵ -caprolactone)
RES – reticuloendothelial system
CMC - critical micelle concentration
EPR - enhanced permeability and retention
DOX – doxorubicin
HSRs - hypersensitivity reactions
MTD - maximum tolerated dose
NCS – neocarzinostatin
SMA - poly(styrene-co-maleic acid)
TAT – transactivating transcriptional activator
PSD - poly (methacryloyl sulfadimethoxine)
cRGD - cyclic(Arg-Gly-Asp-D-Phe-Lys)
ASGPR - asialoglycoprotein receptor
PE-PEG - diacyllipid-PEG
PSMA - prostate specific membrane antigen
PEG-pAsp - polyethylene glycol-poly(aspartic acid)
DMA - (2-(dimethylamino) ethyl methacrylate)
DEA - poly(2-diethylamino)ethyl acrylate
pNIPAM - poly(N-isopropylacrylamide)

LCST - lower critical solution temperature

PBMA - poly(butyl methacrylate)

DMMAAm – dimethylacrylamide

PEG-PPO-PEG – pluronic

PEG-DSPE - PEG-phospholipid

MRI - magnetic resonance imaging

CT - computed tomography

SPECT - single photon emission computed tomography

PET - positron emission tomography

Gd – gadolinium

PAA - poly(allylamine)

PG-*b*-PLA - poly(L-glutamic acid)-*b*-polylactide

SPIO - superparamagnetic iron oxide

QDs – quantum dots

PFP – perfluoropentane

RBCs – red blood cells

Hb – hemoglobin

LOD – limit of detection

LLOQ - lower limit of quantitation

RT – room temperature

$t_{1/2,\alpha}$ - short phase (distribution) half-life

$t_{1/2,\beta}$ – long phase (elimination) half-life

MRT – mean residence time

ID – injected dose

DM- β -CyD - heptakis(2,6-di-*O*-methyl)- β -cyclodextrin

λ_{\max} – maximum wavelength

metHb – methemoglobin

DSC - differential scanning calorimetry

DLS – dynamic light scattering

TEM – transmission electron microscopy

PTA - phosphotungstic acid

CDCl₃ - deuterated chloroform

D₂O - deuterated water

DSBs – double stranded breaks

LLC – Lewis lung carcinoma

IT – intratumoral

e.o.d. – every other day

BLI – bioluminescent imaging

RLU – relative light intensity units

PEO-b-PBCL - poly(ethylene oxide)-block-poly(alpha-benzyl carboxylate epsilon-caprolactone

SN-38 - Ethyl-10-hydroxy-camptothecin

CPT-11 - irinotecan hydrochloride

PEG-PE - *n*-poly(ethylene glycol) phosphatidylethanolamine

IgG - immunoglobulin G

TOPO – tri-octylphosphine oxide

FRET - Förster resonance energy transfer

CHAPTER ONE

Introduction

1.1 Background and significance of lung cancer

With 1.44 million new cases and over 500,000 deaths estimated in 2008, cancer has currently surpassed heart disease as the leading cause of mortality in the population 85 years and younger.¹ While estimated new cases of prostate and breast cancers are highest in their respective genders, estimated deaths from lung cancer alone account for roughly one third of cancer-related deaths in both males and females, highlighting the severity of the disease. Fortunately, present-day incidence rates for lung cancer have reached a plateau for women and are on the decline for men, an encouraging result considering the recent increasing trend of the disease over the last several decades. And while major scientific advances have led to several breakthroughs in the area of lung cancer imaging and diagnosis, as well as in the understanding of underlying molecular mechanisms of tumorigenesis, the five-year relative survival rates for lung cancer are 49, 15, and 3% for localized, regional, and distant metastatic disease, respectively.¹ In light of this despairing outcome, adequate treatment regimens are still lacking, with the public warranting more effective strategies to combat this dreadful disease.

Lung cancer is divided histologically into two different types, with the difference ultimately determining the treatment regimen employed.² Small cell lung carcinoma (SCLC), which constitutes 20% frequency, arises from the large airways such as the bronchi and is highly metastatic.³ It is the type most associated with cigarette smoking.⁴ Non-small cell lung carcinoma (NSCLC) accounts for the remaining 80% frequency and

is further categorized into squamous cell lung carcinoma, adenocarcinoma, and large cell lung carcinoma.⁵ While all three have similar prognoses, their origins are different, with adenocarcinomas originating in peripheral lung tissue and squamous cell lung carcinoma originating from a central bronchus. While widely associated with smoking as well, adenocarcinomas are the predominant form of lung cancer in patients who have never smoked.

1.1.1 *Currently available therapies and limitations*

1.1.1.1 *Tissue debulking strategies: surgery, radiation therapy, and ablation*

Traditionally, NSCLC is more amenable to surgery, making resection the gold standard for treatment. However, surgery is limited in the majority of cases by the anatomical inaccessibility of the tumor, the overall poor state of health of the patient, the invasiveness of the procedure, and by local recurrence of the tumor, which in lung cancer has been shown to occur in up to 50% of the cases.⁶ Radiation therapy represents another mainstay in lung cancer treatment, with recent advances yielding image-guided radiation therapy, doses that can conform to the shape of the tumor, and compensation for target motion.⁷ In spite of these developments, there is still a fine line between curative doses and those that prove detrimental to surrounding tissue and can cause patient side effects.⁸ Ablative techniques such as radiofrequency (RF) ablation have garnered much attention recently as alternatives to surgery and radiotherapy because of their minimal invasiveness and highly localized mode of action.⁹ RF ablation, which involves the destruction of lung tumor tissue by heat, is very effective at eliminating the majority of the tumor within the

heat burst radius, but fails to eradicate viable malignant cells beyond the ablated boundary.¹⁰

1.1.1.2 *Chemotherapy*

There has been much focus on the discovery and development of anticancer drugs, to the extent that clinicians now possess a vast arsenal of potent cytotoxic agents ranging from those of microbial origin, such as doxorubicin, to plant-derived agents such as paclitaxel.¹¹ The mechanisms of action of anticancer drugs are widely diverse as well, spanning from alkylating agents such as cisplatin to topoisomerase inhibitors like etoposide.¹² Cisplatin has been shown to be an effective first line chemotherapeutic for the treatment of NSCLC,¹³ becoming a primary treatment option in combination used in third-generation drugs such as docetaxel, gemcitabine, paclitaxel, or irinotecan.¹⁴ If the patient proves non-responsive to platinum-based drug therapy, docetaxel is considered a therapeutically viable second-line treatment option.¹⁵ Presently, gemcitabine, a nucleoside analog that replaces cytidine during replication, is also being used as a second-line chemotherapeutic in conjunction with other drugs such as 5-FU, a pyrimidine analog.¹⁶ The synergistic effect of these two drugs have led to disease control rates of up to 66.7%. Recently, insights into the pathogenesis of tumors have revealed novel molecular targets for drugs. As an example, it was noted that mutations in epidermal growth factor receptor (EGFR), specifically its overexpression, were present in NSCLC.¹⁷ Therefore, drugs have been developed to inhibit EGFR signaling. As examples, gefitinib and erlotinib, two tyrosine kinase (TK) inhibitors, showing substantial patient improvement in terms of stable disease rates (50% and 35%, respectively), as well as

alleviation of symptoms.¹⁸ Cetuximab, a monoclonal antibody that prevents ligand binding to the extracellular domain of EGFR, proved extremely beneficial when combined with cisplatin, leading to 3-year survival rates of 57%.¹⁹

While the administration of anticancer drugs has developed into a potential option for the management of cancer, the strategy is not without its limitations. A major disadvantage of anticancer drugs is their non-specific drug distribution given their inability to target tumor tissue, resulting in low tumor concentrations. Consequently, the therapeutic window is very small, making drug toxicity an unavoidable factor.²⁰ Doxorubicin proves a perfect example to highlight this point, with high doses of the drug resulting in cardiac toxicity. Another severe limitation to the use of anticancer agents is the acquired drug resistance by the tumor, rendering even higher doses of the drug ineffective.²¹ Last but not least, the majority, if not all anticancer drugs, prove extremely water insoluble due to their polycyclic nature. While increased hydrophobicity is favorable for membrane permeation and efficacy, lipophilicity hinders the IV administration of these drugs. Undissolved drug, administered via IV injection can form aggregates which are filtered rapidly to the liver and undergo metabolic degradation.²²

1.1.1.3 *Advantages of drug delivery devices for chemotherapy*

Traditional drug administration routes (i.e. oral, intravenous) prove pharmacologically unsuitable for the majority of anticancer drugs. Once introduced orally, the agent must navigate through the stomach to reach the intestines before crossing the intestinal wall into the circulation, all the while resisting enzymatic degradation. Upon intravenous administration, the drug is rapidly filtered through the

kidney and other organs before it has time to exert its effects.²³ While it would be ideal to modify the drug with features that would guarantee increased stability, solubility, and targeting to the site of action, such alterations are not always feasible. This realization is the fundamental driving force behind the concept of polymeric drug delivery - to enhance drug function irrespective of poor innate pharmacokinetics.

Currently, drug delivery systems continue to enable the clinical use of existing anticancer agents, expanding new horizons for chemotherapy by significantly augmenting treatment and prolonging patient life expectancy. The advantages afforded by drug delivery in cancer therapy are numerous and easily appreciable: 1) therapeutic levels of drug are maintained within a desired range due to controlled release; 2) toxic side effects are minimized due to localized mode of treatment; 3) patient compliance increases due to less invasive treatment and less dosing frequency; 4) amount of drug needed for therapy is reduced; and 5) delivery of drugs with short *in vivo* half-lives can be facilitated.²⁴ Important considerations in the design of controlled delivery systems are the biocompatibility of the components that constitute the device and the possible toxicity spurred by byproducts of polymer degradation. An example of a drug delivery device on the macro-scale that is presently used in the clinics is Gliadel®, a device FDA approved for the treatment of glioblastoma multiformae. Following surgical excision of the tumor, polyanhydride polymer discs loaded with the anticancer drug carmustine are placed at the resection site, eliminating remnant malignant cells.²⁵ Drug delivery strategies like Gliadel® are currently being used by hundreds of thousands of patients worldwide, catapulting the highly interdisciplinary field of drug delivery into a \$20 billion a year enterprise.²⁶

1.1.2 *Adjuvant, neoadjuvant strategies, and the future trend of lung cancer care*

In light of the shortcomings demonstrated by current chemotherapeutic techniques, as well as with the major debulking strategies discussed above, the majority of these treatments are conducted in an adjuvant or neoadjuvant fashion. As an example, in the case of regional disease, surgery is performed, followed by chemotherapy and radiation therapy. In the case where surgery is not an option, radiation is used followed by chemotherapy. In low stage lung cancer, RF ablation has been used in combination with radiation in an adjuvant fashion, with local control and survival rates much improved over either treatment alone.²⁷ Hence, no one, single strategy is utilized as a potential cure-all, but rather used in complementary and safe-guard fashion. Neoadjuvant therapies, such as the administration of anticancer drugs in order to reduce the size of the tumor prior to surgery, have also yielded positive results in cancer therapy.²⁸

Despite advances in individual modalities and adjuvant and neoadjuvant therapies, complete treatment of the tumor is presently only achieved in a low percentage of patients undergoing a combination of therapies.²⁹ In response to these limitations stemming from current cancer treatment modalities, an intense amount of effort has been devoted to the development of nanotechnology platforms, including polymer-drug conjugates, liposomes, dendrimers, and polymer micelles, for the diagnosis and treatment of cancer.³⁰ This research initiative harkens back to the concept put forth by Paul Ehrlich in the early 20th century, in which a “magic bullet,” a chemical substances equipped with high affinity for a malignancy, would provide for ideal treatment.³¹ Currently, nanocomposite drug delivery devices are being developed that are small in size and able

to elude nonspecific uptake by the body. Moreover, several nanoplateforms are currently being functionalized with targeting ligands and controlled-release moieties that enable the site-specific release of drugs. While currently applied for stalwart agents such as doxorubicin and paclitaxel, nanoscale drug delivery platforms, such as polymer micelles, will no doubt play a major role in the clinical translation of novel chemotherapeutic agents, adding to an already heightened cell-killing specificity.

1.2 β -Lapachone: A Natural, Novel Anticancer Agent

1.2.1 *History and varied medicinal uses*

The ortho-naphthoquinone β -lapachone (β -lap, 3,4-dihydro-2,2-dimethyl-2Hnaphtho[1,2-b]pyran-5,6-dione, MW = 242 Da, Figure 1.1) was initially isolated from the bark of the Lapacho tree (*Tabebuia avellanedae*), indigenous to Central and South America.³² Traditional lore alleged that an herbal tea made from extracts of the bark possessed remedial effects against a broad spectrum of illnesses ranging from ulcers to diabetes to cancer. While this claim is widely unfounded, it is now well known that β -lap possesses anti-inflammatory, antifungal, antibacterial, and antiviral therapeutic effects.³³ In recent years, it has garnered much attention as a potent cytotoxic agent with proven antineoplastic activity in a variety of human tumors involved in cancers of the breast, colon, prostate, and lung.³⁴

1.2.2 *Mechanism of action specific to tumor toxicity*

Early studies involving β -lap cytotoxicity initially placed topoisomerase-I inhibition as the key factor responsible for β -lap-mediated cancer cell death.³⁵⁻³⁸ It was

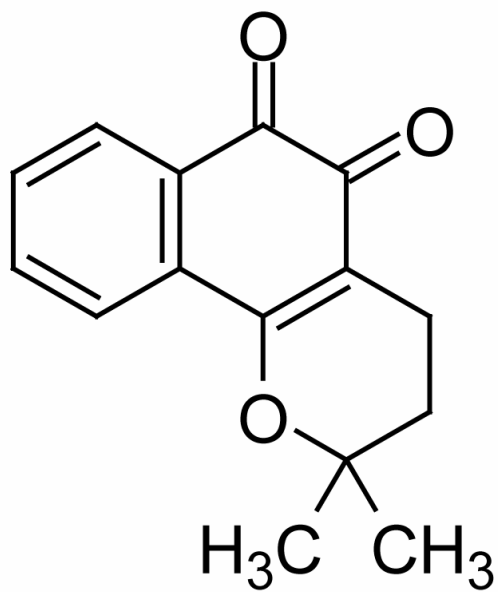


Figure 1.1. Chemical structure of β -lap.

also suggested that β -lap was cell-cycle specific, a characteristic found in the majority of approved anticancer drugs, inducing delays at the G₁ or S phase.³⁹ However, recent research by Boothman and coworkers strongly suggest that the elevated expression of the enzyme NAD(P)H:quinone oxidoreductase-1, NQO1, as the key determinant of β -lap cytotoxicity, negating previous findings regarding topoisomerase-I inhibition and cell-cycle dependence as determinant factors in β -lap-mediated cell death.^{34,40-46} NQO1 is an ubiquitous flavoprotein (30 kDa)⁴⁴ found in the majority of human tissues, whose main function is to detoxify reactive and toxic quinones and quinone epoxides via a two electron reduction,⁴⁷ as well as protect against reactive oxygen species (ROS).⁴⁸ More importantly, considerable research has shown that NQO1 is overexpressed (up to 20-fold) in a variety of human cancers, including those of the breast,⁴⁹ colon,⁴⁹ lung,⁵⁰ pancreas,⁴⁸ and prostate.⁵¹ As a result, NQO1 has been identified as a vital, exploitable target in the treatment of cancer cells with drugs that are bioactivated by the enzyme.

A detailed schematic of β -lap cytotoxicity in a tumor cell with elevated levels of NQO1 can be found in Figure 1.2A. Upon β -lap exposure, NQO1 catalyzes a two-electron reduction of the drug, using 1 molecule of NADPH per reaction as an electron donor, reducing β -lap to a hydroquinone form.⁴⁴ However, this hydroquinone is unstable, and is spontaneously autoxidized back to the quinone form, not without first going through a semiquinone intermediate. The latter process causes oxidative stress via the production of free radicals, which in turn initiate a redox cycle that generates superoxide. Superoxide then dismutate to hydrogen peroxide, ultimately generating hydroxyl radicals. All the while, the quinone form of the drug can undergo another round of reduction, resulting in a futile cycling of β -lap. This futile cycling exhausts the NADH and NADPH

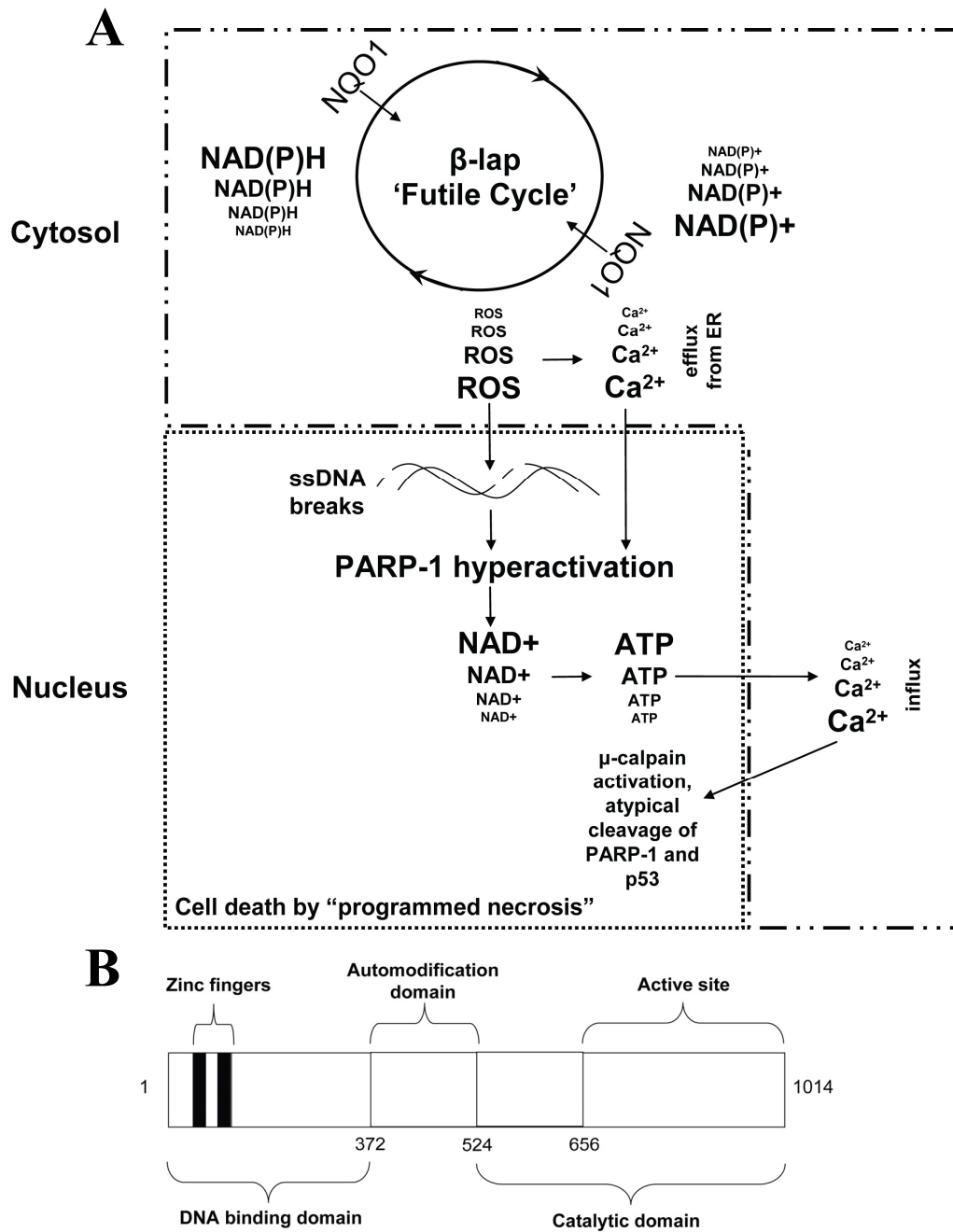


Figure 1.2. (A) Schematic of the mechanism of action of β -lap in a tumor cell with elevated levels of NQO1. (B) Modular schematic of PARP-1.

in the cell and results in a concomitant rise in NAD⁺ and NADP⁺.⁴⁴ It is important to note at this time that NQO1, the driving force behind the futile cycle, can be inhibited by such agents as dicoumarol (3–3'-methylene-bis(4-hydroxycoumarin) (Dic), which binds to the oxidized form of NQO1, therefore competing with NADH. As a result, cells pretreated with Dic are spared from cytotoxic effects of β -lap at low doses. It is only in the excess of drug that β -lap kills cells in the presence of dicoumarol, presumably via oxidative stress arising from the one electron reduction by cytochrome *b*₅ reductase and/or cytochrome P-450 reductase.⁴⁴

Downstream, the reactive oxygen species (ROS) generated from the futile cycling of the drug causes ER stress resulting in release of, and a cytoplasmic rise in Ca²⁺, and more importantly for cell cytotoxicity, extensive damage to DNA. The overwhelming single-stranded breaks (SSBs) that occur in DNA, in combination with nuclear Ca²⁺ accumulation, bring about poly(ADP-ribose)polymerase-1 (PARP-1) hyperactivation, a phenomenon observed in all NQO1+ cells to date.^{52,45} The main function of PARP-1 consists of sensing DNA damage by responding to single- and double-stranded breaks. Briefly, its mechanism involves facilitating DNA repair by binding to these breaks, stabilizing and protecting the lesions, and converting NAD⁺ into branched poly(ADP-ribose) (PAR) units via the protein's polymerase activity. These units, in turn, are attached to nuclear acceptor proteins such as histones, ligase IV, and PARP-1 itself.⁵² When damage to the DNA becomes massive and insurmountable, PARP-1 is hyperactivated, leading to a rapid loss of NAD⁺ and ATP. The loss of NAD⁺ and ATP causes an influx of Ca²⁺ from cytosolic and extracellular sources, leading to μ -calpain activation, as well as cleavage of p53 and PARP-1. The summation of the

aforementioned events, including NAD⁺ and ATP losses, result in a pattern of cell death dubbed “programmed necrosis” or “necroptosis,”⁵³ with cell death resulting only after a short 2 h “bolus” exposure to the drug. It is important to note at this time that inhibition of PARP-1 activity with either 3-aminobenzamide (3-AB) or 1,2-bis-(2-aminophenoxy)ethane-N, N, N', N'-tetraacetic acid tetra-(acetoxymethylester) (BAPTA-AM) spared NQO1+ lung and breast cancer cells, respectively, from β -lap-mediated cell death, highlighting the vital role that PARP-1 hyperactivation (which is dependent on ROS and Ca²⁺) plays in cytotoxicity.^{45,52}

In light of this unique mechanism of action, there are several interesting features of β -lap-mediated cytotoxicity worth emphasizing. β -Lap is non-cell cycle specific and irreversibly kills NQO1+ cancer cells regardless of both p53 status and loss of proapoptotic “caspase” factors.^{41,43,54,55} Additionally, its mechanism of action is carried out in spite of caspase activation, which taken together, bypass the traditional route of apoptosis brought about by exposure to clinically used anticancer drugs. Moreover, it is hypothesized that the antitumor efficacy of β -lap can be enhanced by manipulating key components and factors related to its mechanism of action. As an example, given that NQO1 expression is the principal determinant of β -lap-mediated cell death, methods to try to elevate the levels of this protein in tumors have been explored by Park and coworkers.^{32,56} After inducing mild hyperthermia (42°C) in FSall and A549 tumor cells *in vitro*, Park and coworkers noticed that the NQO1 levels increased after 1 h and remained elevated for more than 72 h.⁵⁶ They were then able to show that this increase in temperature correlated with reduced cell survival following exposure with β -lap. Upon heating of FSall tumors implanted in the hind leg of C3H mice, tumor suppression

resulting from an IP injection of β -lap resulted in tumor suppression. In another study, the same group used ionizing radiation (IR) in combination with β -lap for tumor treatment. They noticed that exposure of the cells to 2.5 Gy prior to β -lap addition resulted in a synergistic pattern of cell killing, a phenomenon previously observed by Boothman and coworkers.⁵⁷ Park and coworkers were able to demonstrate that IR exposure of the cells resulted in an increase in NQO1 levels, which *in vivo*, showed a growth delay of FSall tumors following a 20 Gy irradiation of the tumors and an IP injection of β -lap.³² However, recent research by Boothman and coworkers show that this elevation in NQO1 is not the only reason for the synergistic cell killing potential of β -lap and IR, with findings pointing towards the effect that β -lap has on inhibiting DNA repair as an additional factor in synergy.⁴⁶ This brings to light the possibility of using DNA break inhibitors that can synergize with β -lap as a novel avenue for therapy as well. And, as novel components related to the mechanism of action of β -lap become elucidated, several synergistic approaches may be examined in the future to enhance the therapeutic potential of the drug.

1.2.3 *β -Lap delivery strategies explored thus far*

1.2.3.1 *β -lap complexation with cyclodextrins*

In spite of the immense therapeutic potential of β -lap, its low aqueous solubility at 0.04 mg/mL⁵⁸ limits its clinical translation. While this increased hydrophobicity is favorable for membrane permeation and efficacy, lipophilicity hinders the IV administration of drugs. Undissolved β -lap administered IV can form aggregates, which in turn can form embolisms in capillaries. Furthermore, hydrophobic drugs are filtered to

the liver rapidly and undergo metabolic degradation. Research from many groups has shown that drug complexation with cyclodextrins (CDs) can effectively enhance the solubility and bioavailability of otherwise water insoluble drugs.^{59,60} CDs are cyclic oligosaccharides in the form of truncated cones consisting of a hydrophobic core and a hydrophilic outer surface.^{61,62} These oligosaccharides have the ability to form inclusion complexes with drug molecules (Figure 1.3), which subsequently increases the apparent water solubility of the drug. CDs are differentiated mainly in the number of glucopyranose units (6, 7, and 8 for α , β , and γ -CD, respectively).⁶¹⁻⁶³ Hydroxypropyl- β -cyclodextrin (HP β -CD) is obtained by treating a base-solubilized solution of β -CD with propylene oxide, resulting in a CD with greater solubility (~500 mg/mL vs 18.5 mg/mL for β -CD). Our laboratory recently utilized CDs to solubilize β -lap in aqueous solutions, and we were able to determine the binding affinities of the drug with the different CDs.⁵⁸ HP β -CD and β -CD had the highest binding affinity to β -lap ($K_c = 1.1 \times 10^3 \text{ M}^{-1}$), followed by γ -CD and α -CD (160 M^{-1} and 20 M^{-1} , respectively). In the case of β -lap complexed with HP β -CD, a 400-fold increase in drug solubility was observed (16.0 mg/ml compared to 0.04 mg/ml), with increased β -lap solubility also arising through complexation with γ -, β -, and α -CD.⁵⁸ Currently, a formulation of β -lap complexed with HP β -CD (β -lap•HP β -CD) is being explored in clinical trials under the name of ARQ 501. Findings and outcomes from these clinical trials, as well as *in vivo* results regarding pharmacokinetics, possible toxicity, and antitumor activity, will be discussed in a later chapter.

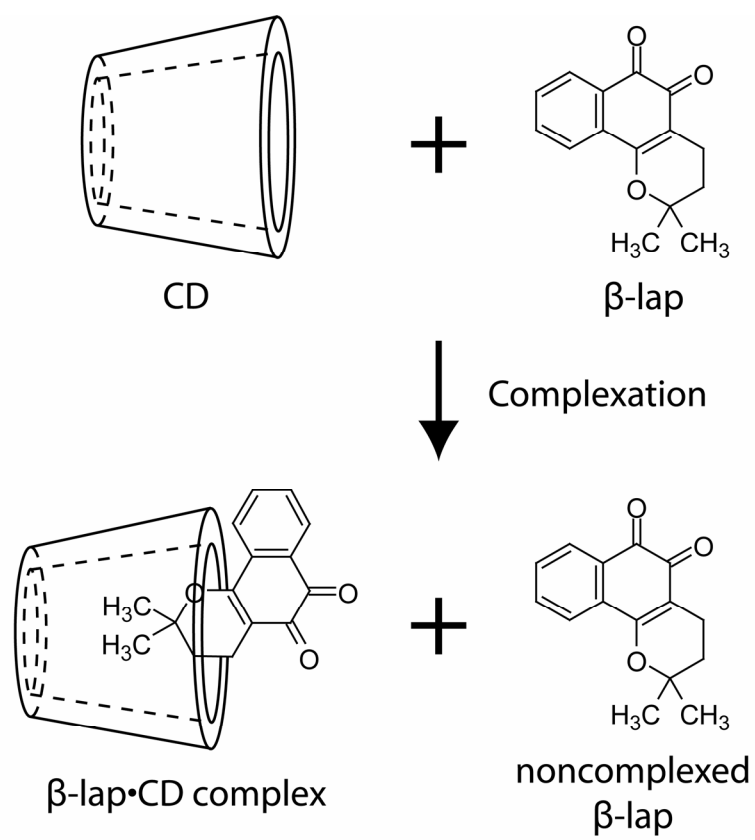


Figure 1.3. Schematic of β -lap complexation with cyclodextrins.

1.2.3.2 β -lap-containing polymer millirods

A rising trend in cancer chemotherapy involves site-specific, controlled release of cytotoxic agents from intratumorally-implanted biodegradable polymer depots, proving advantageous because tumors are exposed to therapeutic levels of the drug for a prolonged time periods, all the while reducing toxicity to healthy cells.⁶⁴ Our laboratory developed a polymeric drug depot in the form of a cylindrical millirod composed of poly(D,L-lactide-*co*-glycolide) (PLGA), designed specifically for intratumoral delivery of anticancer agents.⁶⁵⁻⁶⁷ Direct implantation of doxorubicin-millirods has shown successful antitumor efficacy in rabbit VX-2 liver tumors *in vivo*.⁶⁸

In light of the immense potential for cancer therapy afforded by polymer millirods, our laboratory set out to develop β -lap-eluting PLGA polymer millirods for site specific delivery (Figure 1.4). It was found that CDs with different complexation affinities toward β -lap provided for an effective strategy to modulate β -lap release kinetics from PLGA millirods, with β -lap complexed with HP β -CD proving to release drug faster than free drug and β -lap complexed with other CDs. β -Lap-containing polymer millirods with modulated release kinetics were then examined *in vivo* for antitumor efficacy against prostate tumors (subcutaneous) in mice.⁶⁹ Following direct implantation of the control and drug-containing millirods inside PC-3 tumor xenografts, control tumors were shown to measure $551 \pm 39 \text{ mm}^3$ after 3 days, nearly doubling treated tumors, which had regressed to an average size of $204 \pm 12 \text{ mm}^3$ (Figure 1.5A). As evident from the figure, treated tumors took nearly 11 days to reach its starting size of 300 mm^3 , whereas control tumors have already surpassed the 1000 mm^3 mark by this

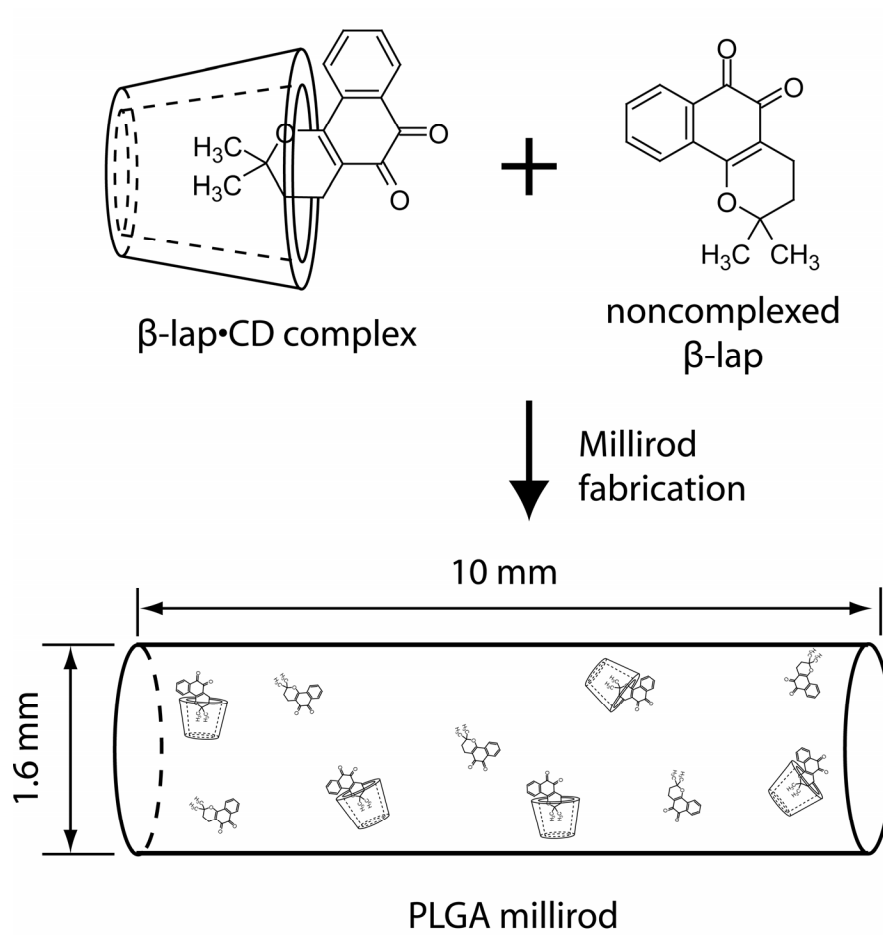


Figure 1.4. Schematic of β -lap millirod fabrication, and resulting millirod with free and cyclodextrin complexed β -lap.

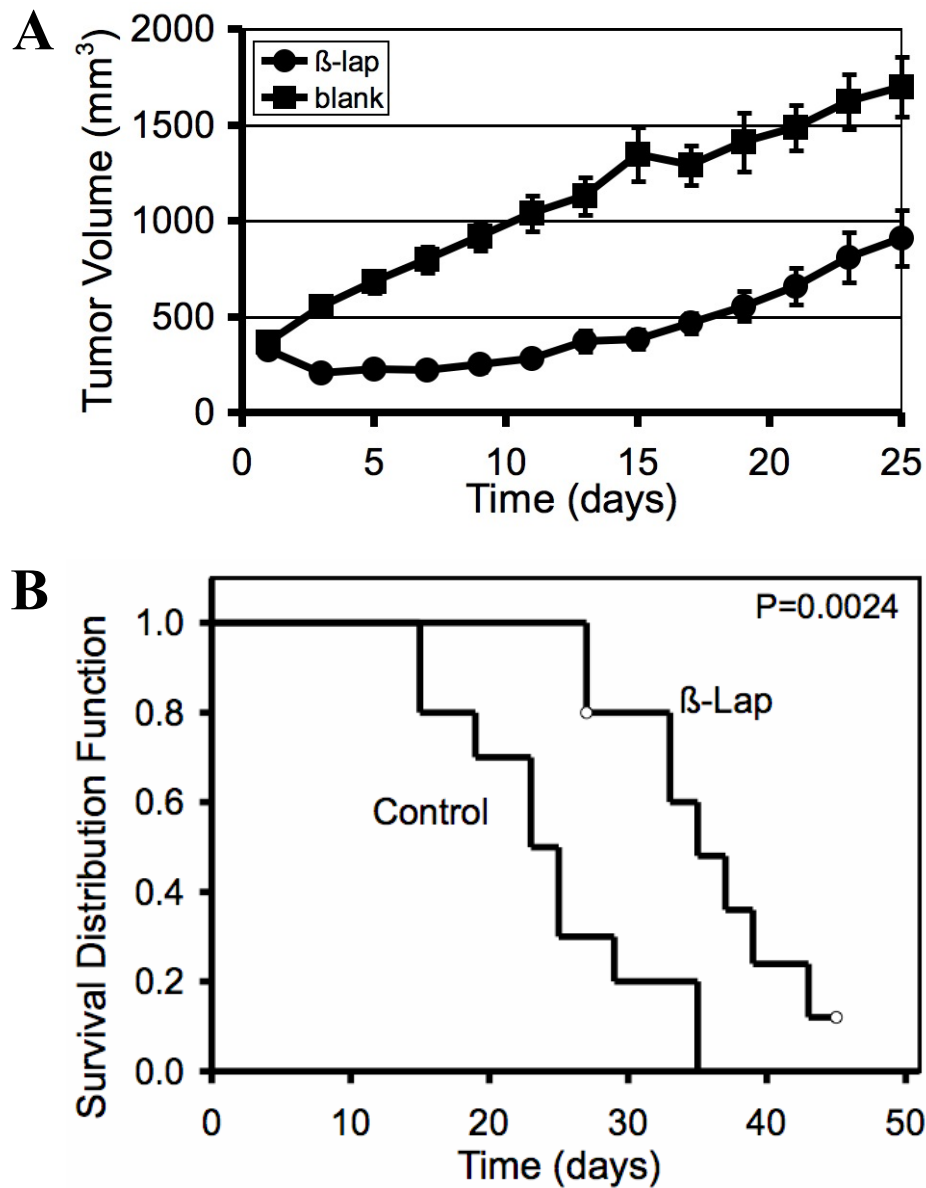


Figure 1.5. (A) Comparison of PC-3 tumor volume after intratumoral implantation of either β -lap-loaded millirods or control millirods containing HP β -CD alone. Values are means \pm SEM (n=10). (B) Kaplan-Meier curves comparing the antitumor efficacy of two different types of millirods as shown in (A). Open circles represent either accidental animal loss at day 27 or animal survival at the end of the experiment.

time. This delayed tumor growth achieved with the β -lap millirods translated into marked differences in animal survival (Figure 1.5B). By day 25, an approximate 50% loss of animals was observed in the control group. By comparison, all animals in the β -lap millirod treatment group survived at this timepoint. A 50% loss in survival did not occur in the β -lap treated group until after 35 days.⁶⁹

β -Lapachone proves a promising new anticancer drug whose unique mechanism of action allows for heightened tumor specificity. However, its low aqueous solubility limits its clinical translation. While polymer millirods have been utilized to enhance solubilization and site-specific delivery, their main use is limited to the treatment of primary tumors through direct implantation of the device inside tumors. Novel nanodelivery platforms can be established as injectable strategies for treating tumors that are not amenable to surgery or localized interventions. Therefore, nanotherapeutics such as polymer micelles are required to maximize the therapeutic potential of β -lap, all the while reducing toxicity and increasing patient compliance.

1.3 Polymer micelles as effective nanoscale cancer drug delivery devices

1.3.1 Background on polymer micelles

Polymer micelles represent a versatile platform whose potential to revolutionize chemotherapy was originally conceptualized in the 1970's by Gros, Ringsdorf, and Schupp.⁷⁰ These spherical, nanosized (~10-100 nm) supramolecular constructs are formed from the self-assembly of biocompatible amphiphilic block copolymers in aqueous environments.⁷¹ In water, the hydrophobic portion of the block copolymer self-associates into a core so as to escape contact with the surrounding water, all the while

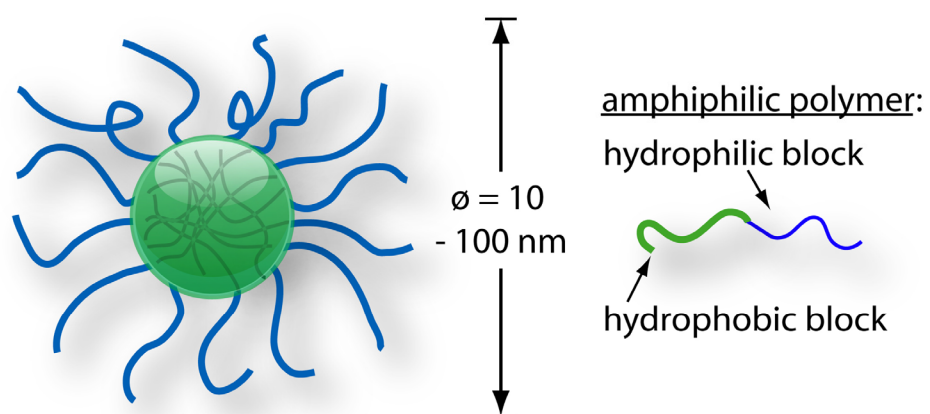


Figure 1.6. Schematic of the core-shell architecture of a polymer micelle and its dimensions.

pushing the hydrophilic region into a corona that surrounds the core (Figure 1.6). The resulting core-shell architecture is of paramount importance to drug delivery, because the hydrophobic core can act as a reservoir or cargo space for lipophilic drugs, while the outer shell shields the micelle from rapid clearance.⁷² The majority of research concerning micelles until now has focused on the development of novel block-forming polymers, and the arrangement of these into the customary di-block, tri-block, or grafted copolymer scheme. While several functional aspects from the constituent blocks have been desired and explored (e.g. temperature or pH sensitive blocks), the primordial criteria for core and corona forming blocks is biocompatibility and/or biodegradability, so as to ensure satisfactory patient response and proper device function. Presently, the prime corona-forming polymer is the water miscible and non-toxic polymer polyethylene glycol (PEG), usually with a molecular weight range from 2 to 15 kD. Core-forming blocks typically utilized are poly(propylene oxide) (PPO), poly(DL-lactic acid) (PDLLA), poly(ϵ -caprolactone) (PCL), or poly(β -amino ester).⁷³

Owing to their unique chemical composition, polymer micelles prove attractive modalities for drug delivery purposes. Given their polycyclic nature, many anticancer drugs are inherently water insoluble. As an example, paclitaxel, a highly effective anticancer agent that inhibits microtubule growth by binding to the β subunit of tubulin, has a water solubility of 0.0015 mg/mL. While this degree of hydrophobicity is favorable for membrane permeation, IV administration would result in aggregation and the formation of embolisms, in addition to rapid filtration by the liver.²² By entrapping and solubilizing the anticancer agent within the hydrophobic core of the micelle, the solubility of the drug can be increased several orders of magnitude. In the case of the

aforementioned paclitaxel, encapsulation of the hydrophobic drug within micelles increased the solubility from 0.0015 mg/mL to 2 mg/mL.⁷⁴ Additionally, encapsulating the drug within the hydrophobic core affords increased drug stability by hindering enzymatic degradation and inactivation, enabling effective transportation of therapeutic nucleic acids (e.g. siRNA) and imaging agents (e.g. SPIO). Hence, polymer micelles allow for the *in vivo* use of previously existing drugs otherwise deemed too hydrophobic or toxic, without having to manipulate the structure or chemical identity of the agent. In addition to the hydrophobic core, the hydrophilic micellar corona plays an important role in micellar *in vivo* applications by forming a hydrating layer on the surface of the micelle that hinders plasma protein interactions. In the absence of this protective brushlike coating that endows the micelle with 'stealth-like' properties, the micelle would fall victim to opsonization and would undergo rapid phagocytic clearance by the reticuloendothelial system (RES).⁷⁵ A distinguishing property of polymer micelles that make them attractive for *in vivo* therapeutic purposes is their small size, which prevents RES uptake and subsequent accumulation in the liver and spleen.⁷⁶ Additionally, the critical micelle concentration (CMC), or the concentration at which monomeric amphiphiles form micelles, is very low for amphiphilic polymers, typically on the order of 10^{-6} - 10^{-7} M, resulting in very stable constructs that do not easily dissociate *in vivo*.²² All of these characteristics contribute to longer circulation times, and this longevity results in an increase in the bioavailability of the drug. The long circulation times and small size of polymer micelles also aid in the preferential accumulation of micelles in tumor tissue, a result of the enhanced permeability and retention (EPR). The EPR effect, also known as passive targeting, arises from the fact that tumor blood vessels are

unusually 'leaky' compared to normal blood vessels because of their ongoing angiogenic state.^{77,78}

The main thrust behind ongoing research in polymer micelles has indeed been in their development as drug delivery vehicles for chemotherapy, with several first generation micelle platforms proving successful. Kataoka and co workers developed polymer micelles by conjugating doxorubicin (DOX) to a poly(ethylene glycol)–poly(aspartic acid) block copolymer, showing impressive preclinical antitumor efficacy.⁷⁹ Their micelle formulation, currently in clinical trials under the name NK911, nearly tripled the half-life of doxorubicin (from 48 minutes to 2.3-2.8 hours) and reduced the clearance of the drug by half (from 14.4 ± 5.6 ml/(min kg) to $(6.7 \pm 1.1$ ml/(min kg)).⁸⁰ A paclitaxel-containing polymer micelle formulation, consisting of PEG-PDLLA block copolymer, also showed impressive phase I clinical data when compared to a traditional paclitaxel formulation.⁸¹ While pharmacokinetically the two formulations proved similar in terms of half-lives and clearance rates, Genexol-PM demonstrated improved patient tolerance, with no patients suffering from hypersensitivity reactions (HSRs) and only a low degree of myelosuppression observed. As a result, the maximum tolerated dose (MTD) of the drug was increased, which may have resulted in the favorable tumor response observed in two patients.

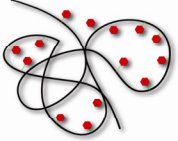
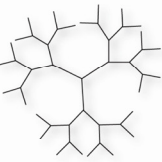
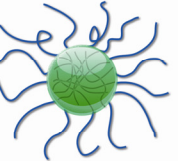
1.3.2 *Comparison of polymer micelles to alternate nanotherapeutic platforms*

Polymer-drug conjugates⁸², dendrimers⁸³ and liposomes⁸⁴ represent other major polymer-based nanotherapeutic systems, each with different chemical structures and biological properties. Among these systems, polymer-drug conjugates and liposomes

have a longer history of development and to this date have found the most success in the clinics. For example, SMANCS, a conjugate of neocarzinostatin (NCS) and poly(styrene-co-maleic acid) (SMA), was developed by Maeda and coworkers in the 1980s, and has been clinically approved for liver cancer treatment.⁸⁵ The blood half-life of SMANCS is 10 times higher than that of NCS, that leads to enhanced tumor targeting via the EPR effect. Most importantly, the improved stability and tumor selectivity resulted in increased antitumor efficacy during hepatocellular carcinoma treatment.⁸⁶ In light of these promising findings, other types of polymer-drug conjugates are also gaining prominence, with dextran-doxorubicin, PEG-camptothecin, and polyglutamate–paclitaxel conjugates in phase I, II, and III clinical trials.⁸⁷ With regards to liposomal delivery systems, a doxorubicin-containing, PEGylated formulation, Doxil®, has been clinically approved to treat Kaposi’s sarcoma and several types of solid tumors.⁸⁸ While dendrimers have yet to find their way into clinical use, preliminary research with methotrexate-containing polyamidoamine dendrimers has shown growth reduction of subcutaneous tumors in mice.⁸⁹ Several micellar systems are currently in Phase I/II clinical trials for the delivery of doxorubicin (DOX) and paclitaxel. Among these, Kataoka and coworkers prepared DOX micelles from a poly(ethylene glycol)–poly(L-aspartic acid) block copolymer, resulting in significantly improved preclinical antitumor efficacy.⁷⁹ The micelle formulation, currently in clinical trials under the name NK911, nearly tripled the half-life of free drug (from 48 minutes to 2.3-2.8 hours) and reduced the clearance of the drug.⁸⁰

Table 1.1 shows the basic structures and properties of these nanoplateforms, serving to highlight differences that exist among them. Both polymer-drug conjugates

Table 1.1. Summary of different nanotherapeutic technologies proposed for cancer therapy

Nano Systems	Polymer-drug conjugates 	Dendrimers 	Polymer micelles 	Liposomes 
Size	< 10 nm	2-10 nm	10 - 100 nm	100 - 200 nm
Structural characteristics	Macromolecular structure	Macromolecular tree-like structure	Spherical, supramolecular core-shell structure	Spherical, bilayer vesicle structure
Carrier Composition	Water-soluble polymer	Hyperbranched polymer chains	Amphiphilic di- and tri-block copolymers	Phospholipid, cholesterol membrane lipids
Drug incorporation strategy	Covalent conjugation requiring functional groups on drug and polymer	Covalent conjugation requiring functional groups on drug and polymer	Non-covalent encapsulation/compatible with hydrophobic drugs	Non-covalent encapsulation/compatible with hydrophilic drugs
Clinical status	Clinical	Preclinical	Phase I/II clinical trials	Clinical

and dendrimer systems necessitate the covalent conjugation of drug molecules to the carriers.⁹⁰ This in turn would require the presence of functionalizable chemical groups on the drug molecules, limiting the generality of this approach. In light of the high chemical stability of covalent bonds, specific chemical strategies (e.g. enzymatic degradation, acid-catalyzed hydrolysis) is necessary to release the drug molecules at tumor sites.⁹¹ Moreover, due to the small size of these systems (typically <10 nm), they can easily cross basement membranes in the glomeruli of kidneys and be quickly cleared, leading to much shortened blood half-lives.^{92,93}

Liposomes are vesicular nanostructures self-assembled from the phospholipid and cholesterol molecules that typically form cell membranes.⁸⁴ As a result of their inner hydrophilic compartment, liposomes are more suitable for the delivery of water-soluble agents such as therapeutic proteins or DNAs. Poorly soluble drugs can be entrapped within the hydrophobic bilayer membrane, but the loading capacity is limited due to membrane destabilization effects.⁹⁴ Stealth liposomes, where hydrophilic polymers such as PEG have been conjugated on the liposomal surface, have considerably prolonged blood circulation times, and effective passive targeting to solid tumors through the EPR effect has been noted in numerous studies.^{95,96} However, due to intrinsic structural constraints, most liposomal particles are over 90 nm in diameter, which may considerably limit their transport in tumor tissues. For example, Yuan and coworkers have shown limited liposomal penetration to only 30 μm (a few cell layers) following particle extravasation.⁹⁷ Later studies have shown that fibril collagen is the main structural barrier for interstitial transport.⁹⁸ Moreover, drug release from conventional liposomal formulations is quite limited once these particles reach the tumor target. To overcome

this problem, thermo- and pH-sensitive liposomes have been explored to provide responsive release of drugs in hopes of improving bioavailability.^{99,100}

Polymeric micelles provide a unique and complementary nanoplatform to the above nanosystems for drug delivery applications. The hydrophobic cores of micelles provide a natural carrier environment that allows easy encapsulation of poorly soluble anticancer drugs. The non-covalent encapsulation strategy makes it feasible to entrap drugs without the requirement of reactive chemical groups. The size of polymeric micelles, 10-100 nm, can be easily controlled by varying the hydrophobic block of the amphiphilic copolymer.¹⁰¹ This size range allows for evasion of renal filtration while allowing for increased tumor penetration compared to liposomes¹⁰². In the sections below, we will discuss strategies employed to achieve micelle multifunctionalization, namely active targeting, stimulated drug release, and imaging sensitivity for cancer applications (Figure 1.7).

1.3.3 Targeted micellar systems

First generation polymer micelles preferentially accumulate at tumor sites via passive targeting, relying on extravasation to tumor sites through leaky vasculature to elicit a therapeutic effect via controlled release of the encapsulated drug. While mostly successful, as was noted in the cases of NK911 and Genexol-PM, more effective accumulation of micelles to specific tumor sites is warranted. Currently, active targeting strategies, involving the attachment of a moiety (e.g. ligand) to the micelle surface that allows for binding to a specific receptor on the tumor cells, are an intense area of recent study. While active targeting does not imply that the micelle will actually seek out the

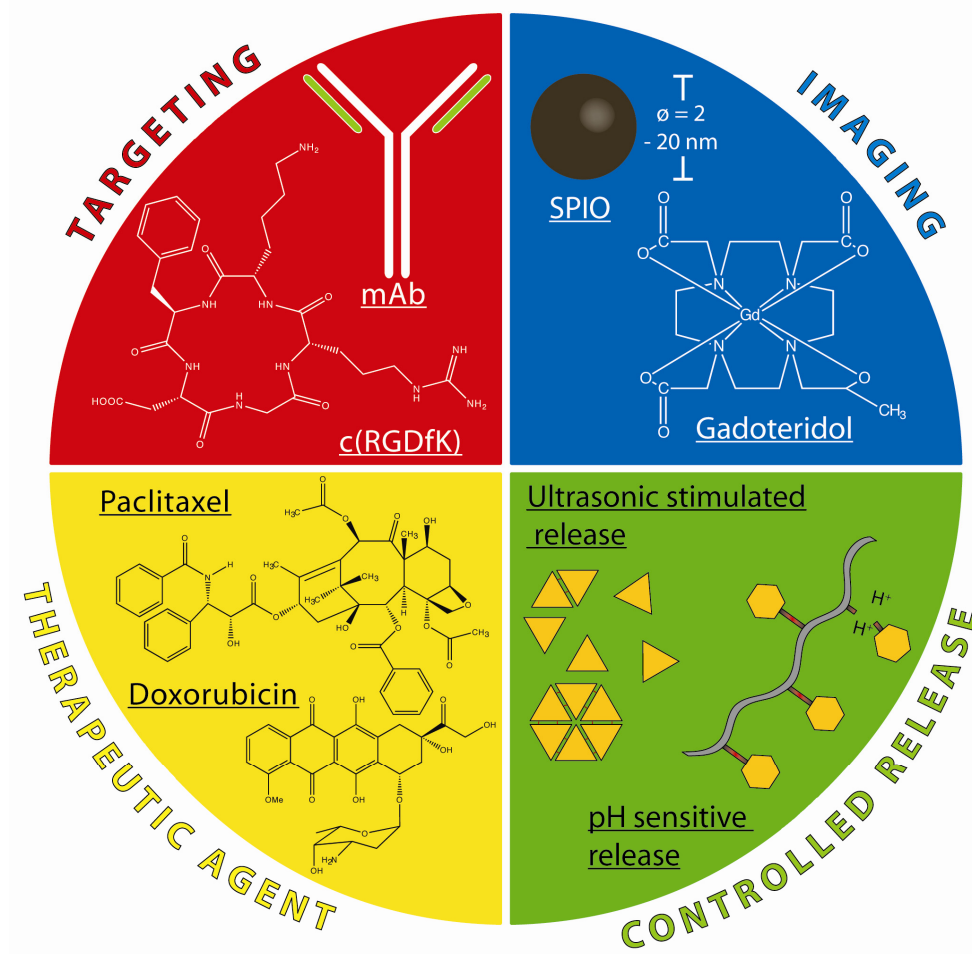


Figure 1.7. Multifunctional design of a micelle nanomedicine platform with cancer targeting, imaging, and controlled release properties.

tumor, the strategy has been shown to have several advantages, including increased accumulation at target sites as well as increased uptake into tumors via specific receptor-ligand interactions.¹⁰³ Typically, these ligands are grouped into the following classes: small organic molecules, peptides, carbohydrates, antibodies, and aptamers.

An example of a small organic molecule utilized with much success as a targeting ligand in micellar drug delivery is folic acid, whose receptor is overexpressed (100-300 times) on a variety of tumors and has a high binding affinity to its ligand.¹⁰⁴ Park and coworkers functionalized DOX-containing PEG-PLGA micelles with folic acid and were able to show increased uptake and cytotoxicity with these micelles in KB cells over nonfunctionalized micelles (IC₅₀ of 50 mM compared to 75 mM).¹⁰⁵ Work *in vivo* showed that folate-labeled micelles caused the tumor growth rates to decrease by a factor of two compared to non-targeted micelles. Further research by the same group into folate functionalization of micelles consisted of a folate-PEG-DOX system that self-assembled through hydrophobic doxorubicin association and functionalization of the hydrophobic portion of the PEG-PCL block with folate.^{106,107} The folate-PEG-DOX nanoaggregates showed a two-fold increase in cytotoxicity over non-targeted aggregates, as well as improved anti-tumor efficacy *in vivo* (40% decrease in tumor volume when compared to free drug administration), while the PEG-PCL micelles functionalized with folate on the hydrophobic portion also showed increased toxicity in MCF-7 and HeLa 229 cells.

Peptides, or short molecules composed of several α -amino acids linked together, are also being actively explored as ligand candidates for micellar active tumor targeting. Recently, Bae and coworkers were able to design a polymer micelle system containing

the cell penetrating peptide TAT conjugated to the PEG on the surface of PEG-PLLA micelles.¹⁰³ The overall system had an extra component that consisted of a pH-sensitive diblock copolymer of poly (methacryloyl sulfadimethoxine) (PSD) and PEG (PSD-b-PEG) that served to shield the micelles and expose TAT in low pH environments. This micelle system was able to internalize into cells upon exposure to low acidic environments, with the TAT peptide assisting in the translocation of the micelle into the cell and near the nucleus. Recent work by our own laboratory has involved the use of the cyclic(Arg-Gly-Asp-D-Phe-Lys) (cRGD) peptide, which targets the $\alpha_v\beta_3$ integrin, a cellular transmembrane protein shown to greatly affect tumor growth, local invasiveness, and metastatic potential, found overexpressed on the surface of angiogenic vessels and not readily detectable in quiescent vessels.¹⁰⁸

Recent research has also focused on the attachment of carbohydrate molecules such as galactose and lactose to micelles, with these ligands expressing high affinity to the asialoglycoprotein receptor (ASGPR) found overexpressed in hepatocellular carcinoma.¹⁰⁹ A galactose-labeled poly(ethylene glycol)-co-poly(γ -benzyl L-glutamate) block copolymer was used by Cho and coworkers to fabricate micelles encapsulating paclitaxel, with results showing a 30% increase in micellar uptake in an ASGPR cancer cell line *in vitro* compared to a non-ASGPR cancer cell line.¹¹⁰ Increased binding by carbohydrate-labeled micelles was demonstrated by Kataoka and coworkers, who developed lactose-encoded PEG-PLA micelles.¹¹¹ Lectin binding studies showed that 80% functionalized lactose-encoded micelles bound in a trivalent fashion with fast association kinetics ($k_a = 3.2 \times 10^4 \text{ M}^{-1}\text{s}^{-1}$) and slow dissociation constants ($k_d = 1.3 \times 10^{-4}$

s⁻¹), increasing the association constant by over two-fold, while decreasing the main dissociation constant by 145-fold compared to 20% functionalized micelles.

Tumor-specific monoclonal antibodies, which are large, customizable molecules with high binding affinities, represent another potential class of targeting ligands. Recently, Torchilin et al. developed diacyllipid-PEG (PE-PEG) micelles conjugated with either an anti-cancer monoclonal antibody (mAb 2C5) or an anti-myosin mAb 2G4 antibody to target lung cancer cells.²² mAb 2C5 micelles loaded with paclitaxel were able to increase drug accumulation within the tumor by four-fold after 2 h incubation time, an uptake that correlated directly with increased anti-tumor efficacy. Aptamers, or stable, tumor-specific DNA or RNA oligonucleotides identified from screening a random library to individual molecular targets, are also gaining potential as targeting ligands. PEG-PLA micelles were recently conjugated with an RNA aptamer specific for the prostate specific membrane antigen (PSMA) to treat prostate tumors.^{112,113} After showing a 77-fold increase in binding versus non-labeled micelles, docetaxel was loaded in the micelles and their antitumor activity in LNCaP prostate cancer cells examined. Aptamer-encoded micelles showed 50% greater lethality in LNCaP cells than non-targeted micelles. Studies *in vivo* consisting of intra-tumoral injections of targeted micelles into LNCaP xenografts in nude mice showed overall increased anti-tumor efficacy and lesser levels of systemic toxicity than non-targeted micelles, and more importantly, total tumor regression in five of the seven mice in the group.

1.3.4 *Stimulus-responsive micelle systems*

While active targeting can effectively lead to an increase in micelle accumulation in tumors, the issue of in what fashion the drug will be released once at the site represents another challenge in micellar drug delivery. In order to minimize systemic toxicity and improve patient morbidity, it is of paramount importance that the drug remain stably encapsulated and that only small amounts, if any, leach out of micelles during circulation and prior to uptake in tumors. Once at the intended site, it is desirable that the drug be released in a manner that guarantees a rapid exposure to toxic levels of the drug, followed by a sustained release at these levels, ensuring drug adequate bioavailability of the drug and subsequent therapeutic effect. Hence, several strategies aimed at achieving site-specific, stimulus responsive, delivery of drugs is being explored. These strategies, including pH, temperature, ultrasound and chemical sensitive release, are discussed below.

Cancer cells tend to have lower pH values (as low as 5.7) than normal tissue environments (pH: 7.4), due to their dependence on glycolysis for metabolism.¹¹⁴ Additionally, the process of endocytosis, or the sequestration of the nanocarriers into a vesicles (e.g. early endosome, late endosomes, and heavily degradative lysosomes) is one associated with low pH values of ~5.0-5.5. Hence, the changes in pH encountered by micelles upon intravenous injection provide a possible venue through which to achieve stimulus release of drug. Two commonly used strategies to induce pH sensitive release from micelles include the use of acid-labile bonds and non-covalent strategies involving selective protonation of pH-sensitive components inside the micelle.

In the first strategy, pH sensitivity arises from the formation of an acid labile linkage between the drug and the polymer forming the micelle, which leads to increased

loading but requires that the drug molecule possess functional groups that can be covalently modified. Park and coworkers were able to fabricate pH sensitive micelles by using either a hydrazone or cis-acotinyl bond to link doxorubicin to the PLA end of PEG-PLA micelles, with differences arising from the release of unmodified drug or modified drug from the hydrazone and cis-acotinyl linkages, respectively.¹¹⁵ Hydrazone linked micelles were then shown to have a five-fold greater cytotoxicity when compared with free drug. Kataoka and coworkers were able to formulate micelles in a similar manner, where doxorubicin was conjugated to polyethylene glycol-poly(aspartic acid) (PEG-pAsp) copolymer via a hydrazone linkage.¹¹⁶⁻¹¹⁸ The resulting micelles had high loadings of DOX (42.5%), and pH sensitive release, where only 3% of the drug was released after 48 h in pH 7.4 compared to 25% release of drug at the same time point in a pH environment of 5.5. Studies *in vivo* showed increased tumor accumulation, greater tolerance for drug, and tumor regression in 50% of the mice tested. Finally, Frechet and coworkers were able to design pH sensitive micelles in which the acid-labile bond was used as a structural component of the micelle polymer backbone, where drug release occurs as a result of acid catalyzed polymer degradation.¹¹⁹⁻¹²¹ Using hydrophobic groups attached to the hydrophobic dendrimer ends of a PEG-dendritic polylysine or PEG-dendritic polyester copolymer, these terminal hydrophobic trimethoxy benzyl groups were then linked to the dendrimer via acid-sensitive acetal linkages, yielding small micellar nanoparticles following self-assembly. The amount of degradation seen at pH 7.4 was negligible (less than 5%) after 24 h, but high levels of degradation (80-100%) were observed under pH 5.0 conditions for the same time period. DOX loaded micelles

showed favorable size and loading and excellent pH sensitivity in their release, with a ten-fold increase in release rate at pH 5.0 over pH 7.4.

pH sensitive release from polymer micelles can also be achieved via non-covalent strategies, whereupon an ionizable component within the micelle structure alters conformation upon protonation. Kataoka and coworkers were able to design a rather ingenious system that relies on charge-charge interactions to build a micelle core carrying a positively charged zinc porphyrin dendrimer that is neutralized by the negatively charged residues of a PEG-poly(L-aspartic acid) copolymer.^{122,123} Hence, the micelles are stable at neutral pH, but at pH below 6 or above 8, these micelles destabilize due to loss of charge balance in their core. Tang et al. devised a triblock polymer of PEG, poly(2-(dimethylamino) ethyl methacrylate) (DMA), and poly(2-diethylamino)ethyl acrylate (DEA) resulting in a system that dissolves completely in acidic solution but forms micelles at high pH (pH 8.0).¹²⁴ Acid sensitive release of dipyridamole was observed with a 50% increase of drug release at pH 3.0 over that at pH 7.4. Recently, poly(b-aminoester) polymer has been shown to be hydrophobic at neutral pH, but can become fully soluble at pH below 6.1.¹²⁵ Amiji and coworkers were thus able to fabricate paclitaxel-containing pH sensitive micelles by surrounding a hydrophobic poly(b-amino ester) core with a PEG corona from the pluronic copolymer F108, with *in vivo* results demonstrating improved drug deposition in the tumor over not only free drug (23-fold improvement) but also over non-pH sensitive pluronic PCL nanoparticles (threefold improvement).^{126,127}

With technological advances that permit for the local elevation of temperatures at localized sites in the body, temperature-sensitive drug release has gained much

momentum in micellar drug delivery, especially in cancer therapy, where recent findings suggest that tumors are susceptible to hyperthermia.¹²⁸ The polymer of choice for the formation of micelles with a temperature-sensitive corona is poly(N-isopropylacrylamide) or pNIPAM, that has a lower critical solution temperature (LCST) of 32°C.^{129,130} The principle rests on the fact that the micelles are stable below the LCST, but at higher temperatures than the LCST, the system becomes hydrophobic and precipitates out of solution. With this in mind, Okano and coworkers fabricated micelles in which poly(butyl methacrylate) (PBMA) was used to form the hydrophobic core while pNIPAM was used for the thermosensitive corona.¹³¹ The resulting pNIPAM-b-PBMA micelles were loaded with doxorubicin and showed significant temperature-sensitive based release, with only 15% of the drug released after 15 h at 30°C, compared to 90% drug release in the same time period at a temperature 37°C. Release of drug from these micelles could also be turned on and off by simply altering the temperature. More importantly, cytotoxicity experiments showed that almost no cell death occurred at 29°C (less than 5%) but greatly increased when the temperature was raised to 37°C (65% cell death). In a similar fashion, Yang et al. fabricated micelles consisting of pNIPAM copolymerized with dimethylacrylamide (DMMAAm) and consisting of a core of PLGA.^{132,133} Following paclitaxel loading, the micelle system showed temperature sensitivity over a very tight range, with a fourfold increase in paclitaxel release and eightfold increase in cytotoxicity at 39.5°C over those at 37°C.

While traditionally used for diagnostic purposes, ultrasound technology for therapeutic purposes in conditions involving strokes, osteoporosis, and cardiovascular disease is gaining popularity.¹³⁴ Therapeutically, it is also being used to trigger drug

release from drug delivery depots, due to such side effects as local temperature increases, cavitation which increases the permeability of cell membranes, and the production of highly reactive free radical species which can accelerate polymer degradation.^{134,135} For purposes of ultrasound-triggered nanoscale drug delivery, pluronic (triblock polymers of PEG-PPO-PEG) micelles are commonly used. As an example, Pitt and coworkers designed ultrasound-sensitive pluronic micelles containing the doxorubicin.¹³⁶⁻¹³⁸ Ultrasound treatment was shown to increase the toxicity of the DOX-containing micelles by six-fold over the free drug. It was proposed that micellar sequestration of the drug away from the cells assisted in toxicity, a sequestration that was impeded only by ultrasound,^{138,139} that was responsible for an increase in cell membrane permeability to DOX. Following stabilization of these pluronic micelles with PEG-phospholipid (PEG-DSPE), experiments *in vivo* showed that ultrasound was able to improve the antitumor efficacy of both free DOX and micelle incorporated DOX, with ultrasound delaying tumor growth an additional 2.6 days over micelles without ultrasound.

1.3.5 *Micelles for cancer imaging*

Currently, medical imaging modalities, such as magnetic resonance imaging (MRI), computed tomography (CT), single photon emission computed tomography (SPECT), positron emission tomography (PET), and ultrasonography, play vital roles in cancer diagnosis and therapy, ultimately resulting in significant improvements in cancer management. It is now well known that early and complete detection of the disease translates to successful patient treatment. As an example, recent research has shown that 5-year survival rates of up to 97% can be achieved in breast cancer patients if all tumors

are localized upon diagnosis.¹⁴⁰ With regards to therapy, image-guided procedures prove irreplaceable in gold-standard practices such as surgery, as well as novel strategies such as percutaneous ablation.^{141,142} And while device design optimization is a current constant in industry as well as in academia, nano-technological advances stand to make a significant impact in cancer diagnosis and therapy by enhancing the ability of the different modalities to differentiate cancerous tissue from normal tissue. With the emergence of novel contrast agents and imaging probes comes the ever-present challenge of having to effectively deliver these agents to the site of action. Polymer micelles prove excellent candidates for the delivery of imaging agents, given their ability to solubilize these water-insoluble, oftentimes non-biocompatible probes. Moreover, their ability to be functionalized with targeting ligands, in addition to their long blood-circulating times and preferential accumulation at tumor sites, can translate into accurate tumor localization, demarcation, as well as identification. While at a much less advanced clinical stage than therapeutic micelles, micelles for cancer imaging are a rising trend within the field of nanomedicine, with strategies proposed for a variety of modalities including MRI, CT, SPECT, and the growing field of fluorescent imaging.

Given its high spatial and temporal resolution, several micellar platforms have been established for use in MR imaging, and vary mainly with regards to whether a T1 or T2 contrast agent is used. Presently, the most commonly used contrast agent in MR imaging is gadolinium (Gd), an agent that increases image contrast by shortening the T1 relaxation time of water protons.¹⁴³ Noting its inability to target specific tumors, as well as its short half-life, several researchers have attempted to encapsulate Gd ions within polymer micelles so as to increase its bioavailability and accumulation in tumors.

Yokoyama and coworkers developed a responsive T1 contrast agent using a mixture of poly(ethylene glycol)-*b*-poly(aspartic acid) (PEG-P(Asp (DTPA-Gd))) and poly(allylamine) (PAA).¹⁴⁴ In micellar form, the macromolecular probe displayed low longitudinal relaxivity values (2.1 - 2.5 mmol⁻¹ s⁻¹) mainly because the Gd ions have limited accessibility to water protons for the relaxation process to take place. However, upon micellar dissociation, the relaxivity values increased to 10-11 mmol⁻¹ s⁻¹. This phenomenon is most likely due to the presence of the Gd chelates in the aqueous environment, resulting in more efficient relaxation of water protons. Recently, Li et al. established a Gd(III)-containing micellar system composed of a biodegradable poly(L-glutamic acid)-*b*-polylactide (PG-*b*-PLA) block copolymer.¹⁴⁵ In this approach, the Gd(III) ions were chelated to the outer surface of the shell of the micelle, via DTPA conjugation to the hydrophilic block. Micelles in the study measured 229.6 nm at physiological pH and did not exhibit cytotoxicity at concentrations up to 100 µg/mL. Relaxivity results indicate that the Gd-containing micelles led to an approximate two-times higher T1 relaxivity than the standard Gd-DTPA control utilized in the clinics. Last but not least, Torchilin and coworkers developed PEO-PE micelles containing Gd-DTPA-PE and ¹¹¹In-DTPA-PE for MR and scintigraphy imaging, respectively.¹⁴⁶ The resulting micelles were found to be highly stable and formed particles that ranged in size from 10-50 nm depending on molecular weight of the hydrophilic block. Once administered subcutaneously into rabbits, T1-weighted axial MR images showed that lymph vessels were visible as soon as 4 min after injection. Scintigraphy studies showed that the ¹¹¹In-labelled micelles accumulated at the popliteal lymph node and produced

high image contrast within seconds after injection. Gentle massaging of the injection site caused an increase in nodal accumulation and the thoracic duct became visible.

Another type of contrast agent actively being explored for use in T2-weighted MR imaging are the class of superparamagnetic iron oxide (SPIO) nanoparticles, proving to have better detection sensitivity and slower kidney clearance than Gd-based contrast agents.¹⁴⁷ Our laboratory recently developed a micellar formulation composed of poly(ethylene glycol)-poly(ϵ -caprolactone) (PEG-PCL) that contained a cluster of SPIO nanoparticles.¹⁴⁸ The resulting micelles consisted of a cluster of SPIO nanoparticles within the hydrophobic core, with the particles ranging in size from 4, 8 and 16 nm in size, which in turn yielded micelles ranging in size from 75 ± 4 , 97 ± 6 , and 110 ± 9 nm, respectively. While T1 relaxivities were found to be lower than typical hydrophilic SPIO formulations utilized in presently in the clinics, most likely due to the limited accessibility to water, T2 relaxivities were significantly larger. It was found that the clustering of hydrophobic SPIO nanoparticles inside the micelle core dramatically increased T2 relaxivity, proving to be a function of SPIO number and diameter within the core. Moreover, the micellar formulation showed detection sensitivity to nanomolar concentrations under MRI. Experiments *in vivo* are currently underway to examine the feasibility of this system in a clinical setting.

Polymer micelles for cancer imaging have also been developed for imaging modalities such as CT and SPECT. In the case of the former, Torchilin et al. developed iodine-containing PLL-PEG polymer micelles having an average diameter of 100 nm and iodine content of 45% (w/w).¹⁴⁹ Following subcutaneous injection of the formulation in the hind leg of rabbits, researchers were able to identify popliteal lymph nodes after 2 h.

Opacification of the liver and spleen were observed after IV injection of the micelles into rabbits, with vessels in the liver being demarcated within half an hour after injection. Our laboratory recently established 16% cRGD-labelled ^{111}In containing PEG-b-PCL polymeric micelles for SPECT imaging. Following *in vitro* calibration, the micelles formulation was injected into the tail vein of mice with breast tumors, SPECT-CT images were obtained after 24 h. Results demonstrate that a substantial amount of ^{111}In -containing micelles were found distributed throughout the body after 24 h, whereas only a limited amount of free ^{111}In was detected in the bladder and kidney, highlighting the ability of the micelles to avoid renal uptake and subsequent excretion.

Finally, it is worth mentioning the burgeoning area of quantum dots (QD) and the role that fluorescent imaging plays in cancer therapy. While lack of tissue penetration and possible toxicity may limit clinical translation of QDs, their *in vitro* and small-animal *in vivo* applications stand to make immense contributions to the field of molecular imaging by answering many fundamental questions regarding the underlying biology of tumors. As an example, QDs are presently an invaluable visualization resource in protein microarrays.¹⁵⁰ Micelles encapsulating quantum dots (CdSe, CdSe/ZnS, or CdSe/ZnSe/ZnS nanoparticles) have recently been developed for fluorescence imaging. Dubertret et al. reported quantum dot-encapsulated DSPE-PEG phospholipid micelles.¹⁵¹ The resulting micelles showed no acute toxicity *in vitro* and *in vivo*. The micelles were conjugated with DNA and showed efficient targeting to complementary sequences *in vitro*, and were also used to trace lineage in tadpole for studies in embryogenesis. Chen et al. prepared fluorescent micelles by encapsulating quantum dots inside siloxane surfactant $\text{C}_{16}\text{H}_{33}\text{-N}^+(\text{Me})_2\text{-CH}_2\text{CH}_2\text{CH}_2\text{-Si(OMe)}_3 \text{Cl}^-$.¹⁵² It was shown that each micelle

contained approximately 100 quantum dots producing an enhanced fluorescence that allowed for quantitative fluorescence measurements using a conventional fluorescence microscope. van Tilborg and coworkers produced a bimodal imaging probe for MRI and fluorescence imaging by encapsulating QDs inside paramagnetic lipid micelles.¹⁵³ The micelles were conjugated with annexin A5 for targeting of apoptotic cells, and the targeting efficiency was confirmed by MRI and fluorescence imaging.

1.3.6 *Multifunctional polymer micelles*

The unique chemistry of polymer micelles affords the possibility for customization of the basic platform, leading to the emergence of a new generation of multifunctional micelles. This trend seeks to capitalize on innate properties of tumors, such as the overexpression of specific cell surface receptors and low pH environments, so as to enhance uptake and release of therapeutics, as well as effective targeting of imaging agents. It is now believed that the most effective patient outcome can be achieved by merging several components all into one ‘theranostic’ entity, a highly integrated nanomedicine device that can diagnose, deliver targeted treatment in a controlled manner, and monitor response to cancer therapy.³⁰

Kataoka and coworkers explored the use of multifunctionality of polymer micelles by conjugating a targeting ligand, folate, to pH-sensitive doxorubicin-releasing polymer micelles composed of PEG-p(Asp-Hyd-ADR).¹¹⁷ In this case, the multifunctional platform consisting of the summation of the targeting and pH-stimulus parts proved more effective at treating KB cells (nearly 10-fold after a 24 h exposure) than the untargeted formulation. Similarly, when folate was introduced to their pH-

sensitive PEG-pHis DOX-containing micelles, Bae and coworkers observed three times more accumulation in MCF-7 tumors *in vivo* when compared to folate-free micelles, resulting in enhanced cytotoxicity.¹⁵⁴ Recently, Zhuo et al. formulated a thermoresponsive polymer micelle system composed of a P(NIPAAm-*co*-HMAAm) block for controlled release of methotrexate, as well as a targeting component consisting of biotin conjugated to PEG (biotin-PEG-*b*-P(NIPAAm-*co*-HMAAm)).¹⁵⁵ The authors of the study proposed to use a biotin-avidin system to target tumors by initially administering avidin-conjugated biotinylated monoclonal antibodies, and then having the biotinylated micelles “chase” the antibodies in a pretargeting approach. Results show that methotrexate release exhibited temperature-dependent behavior and that after preincubation of biotin-transferrin with HeLa cells, FITC-labeled biotinylated micelles showed an approximate two-fold increase in cellular uptake when compared to non-pretargeted HeLa cells. An alternate micellar platform developed by Kennedy and coworkers aimed to combine delivery of doxorubicin and imaging of tumors via ultrasound.¹⁵⁶ In this strategy, consisting of DOX-containing PEG-PLLA micelles and nanodroplets of perfluoropentane (PFP) stabilized by an outer layer of block copolymer, ultrasound would trigger drug release from micelles through a process called inertial cavitation and facilitate its entry into tumor cells by altering the cell membrane permeability. Moreover, during the process of bubble coalescence into micron-sized structures, the resulting particles would provide a strong ultrasound contrast for ultrasonography. Upon administration of the formulation (four IV injections of 3 mg/kg Dox encapsulated in 0.5% PEG-PLLA/2% PFP microbubbles, twice weekly), MDA-MB 231 tumors not treated with ultrasound showed a pattern of growth similar to control

tumors. On the contrary, tumors undergoing administration of the micelles and treated with ultrasound (30 second treatment at 3 MHz) showed significant regression. Additionally, within 4 hours after injection, ultrasonography revealed strong echoes within the center of the tumor, further demonstrating *in vivo* coalescing of nanobubbles.

In light of their many advantages, polymer micelles are rapidly emerging as potent nanotherapeutic constructs for cancer therapy. Representing only a small class of budding nanoscale devices aimed for biomedical use, polymer micelles nonetheless stand to make the greatest impact in cancer care given their increased drug and imaging agent solubilization, longer blood-circulation times, and heightened accumulation at tumor sites. While the recent translation of micellar technology to the clinics has yielded promising findings, improvements of the basic platform regarding enhanced site-specific and controlled release of drug are paramount in avoiding toxic side-effects. As a result, current research in the field of micellar therapeutics is directed towards exploring the versatility of polymer micelles. By having the micelle perform a myriad of tasks, synergizing for example its ability to deliver drugs in a targeted and controlled manner with tumor imaging, we have shown above that a maximal efficacy with regards to tumor management can be achieved (Figure 1.7). Hence, the present-day focus of multifunctional nanomedicine involves the attachment of ligands with high affinity for receptors that we now know are overexpressed on tumors (e.g. folic acid), and/or the exploration of ingenious ways to release drug using the tumors own microenvironment as a stimulus. However, the future of multifunctional nanomedicine depends highly on the evolution of the governing scientific disciplines that comprise cancer treatment. These include advances in the following: 1) the identification of novel target enzymes or

receptors within tumors that can be exploitable for therapy (cancer biology); 2) the development of novel compounds that can take advantage of these molecular targets, for therapeutic or imaging purposes (medicinal chemistry); 3) advances in imaging devices and software for accurate *in vivo* diagnostics; and 4) the synthesis of new, multifaceted materials that comprise the building blocks of polymer micelles (materials science). When innovations in these fields can converge, capitalize, and complement one another, we will be that much closer to Paul Ehrlich's vision of a "magic bullet" and one step closer to being able to offer personalized medicine for the treatment of cancer.

1.4 Overview and organization of the thesis

In an attempt to harness advancements in nanotechnology and give rise to a powerful nanomedicine platform for lung cancer therapy, this proposal aims at establishing β -lapachone-loaded polymeric micelles as a viable platform for the treatment of tumors. **Hence, the work presented herein aims to target lung tumors in two distinct ways: 1) pharmacokinetically through the use of polymer micelles as delivery vehicles that will ensure drug stability, bioavailability, and targeted localized delivery; and 2) pharmacodynamically through the use of an anticancer drug (β -lapachone) that is bioactivated by an enzyme overexpressed in NSCLC tumors (NQO1).** We hypothesize that achievement of the objectives outlined will result in the development of a nanotherapeutic system with high specificity, reduced toxicity, and efficacious antitumor responses.

To achieve this end goal, the research consisted of several stages, from device fabrication, to characterization *in vitro* and *in vivo*, that comprise the chapters of this

thesis work. Chapter 2 examines the pharmacodynamics of a currently used clinical formulation of β -lap (ARQ 501), and aims to establish a rationale for micellar encapsulation of the drug. Chapter 3 consists of the fabrication of β -lap polymer micelles and their *in vitro* characterization regarding size, morphology, and cell killing potential. Chapter 4 involves the translation of the micellar technology *in vivo*, and its antitumor effect in various animal models. Chapter 5 focuses on the development of quantum dot micelles for the purposes of tracking micelles *in vitro*, and to better understand particle transport and targeting of intracellular compartments.

The work encompassed within this thesis will contribute to the development of polymer nanotherapeutics for the targeted and localized treatment of lung cancer. Any results and knowledge obtained from this work should hopefully assist in propelling nanomedicine platforms towards the targeted and specific treatment of lung cancer, as well as other cancers with endogenous elevations of NQO1.

1.5 References

1. Jemal A, Siegel R, Ward E, Hao Y, Xu J, Murray T, Thun MJ. Cancer statistics, 2008. *CA Cancer J Clin* 2008;58(2):71-96.
2. Forgacs E, Zochbauer-Muller S, Olah E, Minna JD. Molecular genetic abnormalities in the pathogenesis of human lung cancer. *Pathol Oncol Res* 2001;7(1):6-13.
3. Collins LG, Haines C, Perkel R, Enck RE. Lung cancer: diagnosis and management. *Am Fam Physician* 2007;75(1):56-63.

4. Barbone F, Bovenzi M, Cavallieri F, Stanta G. Cigarette smoking and histologic type of lung cancer in men. *Chest* 1997;112(6):1474-9.
5. Travis WD, Travis LB, Devesa SS. Lung cancer. *Cancer* 1995;75(1 Suppl):191-202.
6. O'Mahony D, Kummar S, Gutierrez ME. Non-small-cell lung cancer vaccine therapy: a concise review. *J Clin Oncol* 2005;23(35):9022-8.
7. Elshaikh M, Ljungman M, Ten Haken R, Lichter AS. Advances in Radiation Oncology. *Annu Rev Med* 2005.
8. Gopal R. Pulmonary toxicity associated with the treatment of non-small cell lung cancer and the effects of cytoprotective strategies. *Semin Oncol* 2005;32(2 Suppl 3):S55-9.
9. Thanos L, Mylona S, Pomoni M, Kalioras V, Zoganas L, Batakis N. Primary lung cancer: treatment with radio-frequency thermal ablation. *Eur Radiol* 2004;14(5):897-901.
10. Suh R, Reckamp K, Zeidler M, Cameron R. Radiofrequency ablation in lung cancer: promising results in safety and efficacy. *Oncology (Williston Park)* 2005;19(11 Suppl 4):12-21.
11. Munro MH, Blunt JW, Dumdei EJ, Hickford SJ, Lill RE, Li S, Battershill CN, Duckworth AR. The discovery and development of marine compounds with pharmaceutical potential. *J Biotechnol* 1999;70(1-3):15-25.
12. Mukherjee AK, Basu S, Sarkar N, Ghosh AC. Advances in cancer therapy with plant based natural products. *Curr Med Chem* 2001;8(12):1467-86.

13. Chemotherapy in non-small cell lung cancer: a meta-analysis using updated data on individual patients from 52 randomised clinical trials. Non-small Cell Lung Cancer Collaborative Group. *Bmj* 1995;311(7010):899-909.
14. Pfister DG, Johnson DH, Azzoli CG, Sause W, Smith TJ, Baker S, Jr., Olak J, Stover D, Strawn JR, Turrisi AT and others. American Society of Clinical Oncology treatment of unresectable non-small-cell lung cancer guideline: update 2003. *J Clin Oncol* 2004;22(2):330-53.
15. Shepherd FA, Dancey J, Ramlau R, Mattson K, Gralla R, O'Rourke M, Levitan N, Gressot L, Vincent M, Burkes R and others. Prospective randomized trial of docetaxel versus best supportive care in patients with non-small-cell lung cancer previously treated with platinum-based chemotherapy. *J Clin Oncol* 2000;18(10):2095-103.
16. Nishimura N, Sugiura R, Ueda H, Ono H, Horinouchi H, Uchiyama N, Chohnabayashi N. Gemcitabine plus UFT combination chemotherapy as second- or third-line therapy in non-small cell lung cancer: a pilot study. *J Med Invest* 2008;55(3-4):260-6.
17. Salomon DS, Brandt R, Ciardiello F, Normanno N. Epidermal growth factor-related peptides and their receptors in human malignancies. *Crit Rev Oncol Hematol* 1995;19(3):183-232.
18. Silvestri GA, Rivera MP. Targeted therapy for the treatment of advanced non-small cell lung cancer: a review of the epidermal growth factor receptor antagonists. *Chest* 2005;128(6):3975-84.

19. Bonner JA, Harari PM, Giralt J, Azarnia N, Shin DM, Cohen RB, Jones CU, Sur R, Raben D, Jassem J and others. Radiotherapy plus cetuximab for squamous-cell carcinoma of the head and neck. *N Engl J Med* 2006;354(6):567-78.
20. Canal P, Gamelin E, Vassal G, Robert J. Benefits of pharmacological knowledge in the design and monitoring of cancer chemotherapy. *Pathol Oncol Res* 1998;4(3):171-8.
21. Ozben T. Mechanisms and strategies to overcome multiple drug resistance in cancer. *FEBS Lett* 2006.
22. Torchilin VP, Lukyanov AN, Gao Z, Papahadjopoulos-Sternberg B. Immunomicelles: targeted pharmaceutical carriers for poorly soluble drugs. *Proc Natl Acad Sci U S A* 2003;100(10):6039-44.
23. Langer R. Where a pill won't reach. *Sci Am* 2003;288(4):50-7.
24. Langer R. Drug delivery and targeting. *Nature* 1998;392(6679 Suppl):5-10.
25. Brem H, Lawson HC. The development of new brain tumor therapy utilizing the local and sustained delivery of chemotherapeutic agents from biodegradable polymers. *Cancer* 1999;86(2):197-9.
26. Langer R. Drug delivery. Drugs on target. *Science* 2001;293(5527):58-9.
27. Dupuy DE, DiPetrillo T, Gandhi S, Ready N, Ng T, Donat W, Mayo-Smith WW. Radiofrequency ablation followed by conventional radiotherapy for medically inoperable stage I non-small cell lung cancer. *Chest* 2006;129(3):738-45.
28. Gralla RJ, Edelman MJ, Detterbeck FC, Jahan TM, Loesch DM, Limentani SA, Govindan R, Peng G, Monberg MJ, Obasaju CK and others. Assessing quality of life following neoadjuvant therapy for early stage non-small cell lung cancer

- (NSCLC): results from a prospective analysis using the Lung Cancer Symptom Scale (LCSS). *Support Care Cancer* 2008.
29. Bernstein ED, Herbert SM, Hanna NH. Chemotherapy and radiotherapy in the treatment of resectable non-small-cell lung cancer. *Ann Surg Oncol* 2006;13(3):291-301.
 30. Sumer B, Gao J. Theranostic nanomedicine for cancer. *Nanomed* 2008;3(2):137-40.
 31. Winau F, Westphal O, Winau R. Paul Ehrlich--in search of the magic bullet. *Microbes Infect* 2004;6(8):786-9.
 32. Park HJ, Ahn KJ, Ahn SD, Choi E, Lee SW, Williams B, Kim EJ, Griffin R, Bey EA, Bornmann WG and others. Susceptibility of cancer cells to beta-lapachone is enhanced by ionizing radiation. *Int J Radiat Oncol Biol Phys* 2005;61(1):212-9.
 33. Pardee AB, Li YZ, Li CJ. Cancer therapy with beta-lapachone. *Curr Cancer Drug Targets* 2002;2(3):227-42.
 34. Tagliarino C, Pink JJ, Reinicke KE, Simmers SM, Wuerzberger-Davis SM, Boothman DA. Mu-calpain activation in beta-lapachone-mediated apoptosis. *Cancer Biol Ther* 2003;2(2):141-52.
 35. Bailly C. Topoisomerase I poisons and suppressors as anticancer drugs. *Curr Med Chem* 2000;7(1):39-58.
 36. Boothman DA, Trask DK, Pardee AB. Inhibition of potentially lethal DNA damage repair in human tumor cells by beta-lapachone, an activator of topoisomerase I. *Cancer Res* 1989;49(3):605-12.

37. Li CJ, Averboukh L, Pardee AB. beta-Lapachone, a novel DNA topoisomerase I inhibitor with a mode of action different from camptothecin. *J Biol Chem* 1993;268(30):22463-8.
38. Weller M, Winter S, Schmidt C, Esser P, Fontana A, Dichgans J, Groscurth P. Topoisomerase-I inhibitors for human malignant glioma: differential modulation of p53, p21, bax and bcl-2 expression and of CD95-mediated apoptosis by camptothecin and beta-lapachone. *Int J Cancer* 1997;73(5):707-14.
39. Li CJ, Li YZ, Pinto AV, Pardee AB. Potent inhibition of tumor survival *in vivo* by beta-lapachone plus taxol: combining drugs imposes different artificial checkpoints. *Proc Natl Acad Sci U S A* 1999;96(23):13369-74.
40. Reinicke KE, Bey EA, Bentle MS, Pink JJ, Ingalls ST, Hoppel CL, Misico RI, Arzac GM, Burton G, Bornmann WG and others. Development of beta-lapachone prodrugs for therapy against human cancer cells with elevated NAD(P)H:quinone oxidoreductase 1 levels. *Clin Cancer Res* 2005;11(8):3055-64.
41. Planchon SM, Pink JJ, Tagliarino C, Bornmann WG, Varnes ME, Boothman DA. beta-Lapachone-induced apoptosis in human prostate cancer cells: involvement of NQO1/xip3. *Exp Cell Res* 2001;267(1):95-106.
42. Tagliarino C, Pink JJ, Dubyak GR, Nieminen AL, Boothman DA. Calcium is a key signaling molecule in beta-lapachone-mediated cell death. *J Biol Chem* 2001;276(22):19150-9.
43. Pink JJ, Wuerzberger-Davis S, Tagliarino C, Planchon SM, Yang X, Froelich CJ, Boothman DA. Activation of a cysteine protease in MCF-7 and T47D breast

- cancer cells during beta-lapachone-mediated apoptosis. *Exp Cell Res* 2000;255(2):144-55.
44. Pink JJ, Planchon SM, Tagliarino C, Varnes ME, Siegel D, Boothman DA. NAD(P)H:Quinone oxidoreductase activity is the principal determinant of beta-lapachone cytotoxicity. *J Biol Chem* 2000;275(8):5416-24.
 45. Bey EA, Bentle MS, Reinicke KE, Dong Y, Yang CR, Girard L, Minna JD, Bornmann WG, Gao J, Boothman DA. An NQO1- and PARP-1-mediated cell death pathway induced in non-small-cell lung cancer cells by beta-lapachone. *Proc Natl Acad Sci U S A* 2007;104(28):11832-7.
 46. Bentle MS, Reinicke KE, Dong Y, Bey EA, Boothman DA. Nonhomologous end joining is essential for cellular resistance to the novel antitumor agent, beta-lapachone. *Cancer Res* 2007;67(14):6936-45.
 47. de Haan LH, Pot GK, Aarts JM, Rietjens IM, Alink GM. *In vivo* relevance of two critical levels for NAD(P)H:quinone oxidoreductase (NQO1)-mediated cellular protection against electrophile toxicity found *in vitro*. *Toxicol In vitro* 2005.
 48. Ough M, Lewis A, Bey EA, Gao J, Ritchie JM, Bornmann W, Boothman DA, Oberley LW, Cullen JJ. Efficacy of beta-lapachone in pancreatic cancer treatment: exploiting the novel, therapeutic target NQO1. *Cancer Biol Ther* 2005;4(1):95-102.
 49. Siegel D, Ross D. Immunodetection of NAD(P)H:quinone oxidoreductase 1 (NQO1) in human tissues. *Free Radic Biol Med* 2000;29(3-4):246-53.

50. Belinsky M, Jaiswal AK. NAD(P)H:quinone oxidoreductase1 (DT-diaphorase) expression in normal and tumor tissues. *Cancer Metastasis Rev* 1993;12(2):103-17.
51. Logsdon CD, Simeone DM, Binkley C, Arumugam T, Greenson JK, Giordano TJ, Misek DE, Kuick R, Hanash S. Molecular profiling of pancreatic adenocarcinoma and chronic pancreatitis identifies multiple genes differentially regulated in pancreatic cancer. *Cancer Res* 2003;63(10):2649-57.
52. Bentle MS, Reinicke KE, Bey EA, Spitz DR, Boothman DA. Calcium-dependent modulation of poly(ADP-ribose) polymerase-1 alters cellular metabolism and DNA repair. *J Biol Chem* 2006;281(44):33684-96.
53. Bentle MS, Bey EA, Dong Y, Reinicke KE, Boothman DA. New tricks for old drugs: the anticarcinogenic potential of DNA repair inhibitors. *J Mol Histol* 2006;37(5-7):203-18.
54. Planchon SM, Wuerzberger S, Frydman B, Witiak DT, Hutson P, Church DR, Wilding G, Boothman DA. Beta-lapachone-mediated apoptosis in human promyelocytic leukemia (HL-60) and human prostate cancer cells: a p53-independent response. *Cancer Res* 1995;55(17):3706-11.
55. Wuerzberger SM, Pink JJ, Planchon SM, Byers KL, Bornmann WG, Boothman DA. Induction of apoptosis in MCF-7:WS8 breast cancer cells by beta-lapachone. *Cancer Res* 1998;58(9):1876-85.
56. Park HJ, Choi EK, Choi J, Ahn KJ, Kim EJ, Ji IM, Kook YH, Ahn SD, Williams B, Griffin R and others. Heat-induced up-regulation of NAD(P)H:quinone

- oxidoreductase potentiates anticancer effects of beta-lapachone. *Clin Cancer Res* 2005;11(24 Pt 1):8866-71.
57. Boothman DA, Pardee AB. Inhibition of radiation-induced neoplastic transformation by beta-lapachone. *Proc Natl Acad Sci U S A* 1989;86(13):4963-7.
58. Nasongkla N, Wiedmann AF, Bruening A, Beman M, Ray D, Bornmann WG, Boothman DA, Gao J. Enhancement of solubility and bioavailability of beta-lapachone using cyclodextrin inclusion complexes. *Pharm Res* 2003;20(10):1626-33.
59. Li P, Zhao L, Yalkowsky SH. Combined effect of cosolvent and cyclodextrin on solubilization of nonpolar drugs. *J Pharm Sci* 1999;88(11):1107-11.
60. Rao VM, Stella VJ. When can cyclodextrins be considered for solubilization purposes? *J Pharm Sci* 2003;92(5):927-32.
61. Loftsson T. Cyclodextrins and the Biopharmaceutics Classification System of Drugs. *J Incl Phenom Macro* 2002;44(1-4):63-67.
62. Szejtli J. Introduction and General Overview of Cyclodextrin Chemistry. *Chem Rev* 1998;98(5):1743-1754.
63. Singh M, Sharma R, Banerjee UC. Biotechnological applications of cyclodextrins. *Biotechnol Adv* 2002;20(5-6):341-59.
64. LaVan DA, McGuire T, Langer R. Small-scale systems for *in vivo* drug delivery. *Nat Biotechnol* 2003;21(10):1184-91.

65. Gao J, Qian F, Szymanski-Exner A, Stowe N, Haaga J. *In vivo* drug distribution dynamics in thermoablated and normal rabbit livers from biodegradable polymers. *J Biomed Mater Res* 2002;62(2):308-14.
66. Qian F, Saidel GM, Sutton DM, Exner A, Gao J. Combined modeling and experimental approach for the development of dual-release polymer millirods. *J Control Release* 2002;83(3):427-35.
67. Qian F, Szymanski A, Gao J. Fabrication and characterization of controlled release poly(D,L-lactide-co-glycolide) millirods. *J Biomed Mater Res* 2001;55(4):512-22.
68. Weinberg BD, Ai H, Blanco E, Anderson JM, Gao J. Antitumor efficacy and local distribution of doxorubicin via intratumoral delivery from polymer millirods. *J Biomed Mater Res A* 2007;81(1):161-70.
69. Dong Y, Chin SF, Blanco E, Kabbani W, Bey EA, Boothman DA, Gao J. Efficacy of Intratumoral β -Lapachone Polymer Millirod Implant for Prostate Cancer Treatment. *Clin Cancer Res* 2008;In press.
70. Gros L, Ringsdorf H, Schupp H. Polymeric Anti-Tumor Agents on a Molecular and on a Cellular-Level. *Angewandte Chemie-International Edition in English* 1981;20(4):305-325.
71. Jones M, Leroux J. Polymeric micelles - a new generation of colloidal drug carriers. *Eur J Pharm Biopharm* 1999;48(2):101-11.
72. Torchilin VP. Structure and design of polymeric surfactant-based drug delivery systems. *J Control Release* 2001;73(2-3):137-72.

73. Sutton D, Nasongkla N, Blanco E, Gao J. Functionalized micellar systems for cancer targeted drug delivery. *Pharm Res* 2007;24(6):1029-46.
74. Soga O, van Nostrum CF, Fens M, Rijcken CJ, Schiffelers RM, Storm G, Hennink WE. Thermosensitive and biodegradable polymeric micelles for paclitaxel delivery. *J Control Release* 2005;103(2):341-53.
75. Torchilin VP. PEG-based micelles as carriers of contrast agents for different imaging modalities. *Adv Drug Deliv Rev* 2002;54(2):235-52.
76. Haag R. Supramolecular drug-delivery systems based on polymeric core-shell architectures. *Angewandte Chemie-International Edition* 2004;43(3):278-282.
77. Hashizume H, Baluk P, Morikawa S, McLean JW, Thurston G, Roberge S, Jain RK, McDonald DM. Openings between defective endothelial cells explain tumor vessel leakiness. *Am J Pathol* 2000;156(4):1363-80.
78. Maeda H. The enhanced permeability and retention (EPR) effect in tumor vasculature: the key role of tumor-selective macromolecular drug targeting. *Adv Enzyme Regul* 2001;41:189-207.
79. Nakanishi T, Fukushima S, Okamoto K, Suzuki M, Matsumura Y, Yokoyama M, Okano T, Sakurai Y, Kataoka K. Development of the polymer micelle carrier system for doxorubicin. *J Control Release* 2001;74(1-3):295-302.
80. Matsumura Y, Hamaguchi T, Ura T, Muro K, Yamada Y, Shimada Y, Shirao K, Okusaka T, Ueno H, Ikeda M and others. Phase I clinical trial and pharmacokinetic evaluation of NK911, a micelle-encapsulated doxorubicin. *Br J Cancer* 2004;91(10):1775-81.

81. Kim TY, Kim DW, Chung JY, Shin SG, Kim SC, Heo DS, Kim NK, Bang YJ. Phase I and pharmacokinetic study of Genexol-PM, a cremophor-free, polymeric micelle-formulated paclitaxel, in patients with advanced malignancies. *Clin Cancer Res* 2004;10(11):3708-16.
82. Li C, Wallace S. Polymer-drug conjugates: Recent development in clinical oncology. *Adv Drug Deliv Rev* 2008.
83. Lee CC, MacKay JA, Frechet JM, Szoka FC. Designing dendrimers for biological applications. *Nat Biotechnol* 2005;23(12):1517-26.
84. Torchilin VP. Recent advances with liposomes as pharmaceutical carriers. *Nat Rev Drug Discov* 2005;4(2):145-60.
85. Maeda H, Ueda M, Morinaga T, Matsumoto T. Conjugation of poly(styrene-co-maleic acid) derivatives to the antitumor protein neocarzinostatin: pronounced improvements in pharmacological properties. *J Med Chem* 1985;28(4):455-61.
86. Greish K, Fang J, Inutsuka T, Nagamitsu A, Maeda H. Macromolecular therapeutics: advantages and prospects with special emphasis on solid tumour targeting. *Clin Pharmacokinet* 2003;42(13):1089-105.
87. Duncan R. The dawning era of polymer therapeutics. *Nat Rev Drug Discov* 2003;2(5):347-60.
88. Gabizon AA. Pegylated liposomal doxorubicin: metamorphosis of an old drug into a new form of chemotherapy. *Cancer Invest* 2001;19(4):424-36.
89. Kukowska-Latallo JF, Candido KA, Cao Z, Nigavekar SS, Majoros IJ, Thomas TP, Balogh LP, Khan MK, Baker JR, Jr. Nanoparticle targeting of anticancer

- drug improves therapeutic response in animal model of human epithelial cancer. *Cancer Res* 2005;65(12):5317-24.
90. Gillies ER, Frechet JM. Dendrimers and dendritic polymers in drug delivery. *Drug Discov Today* 2005;10(1):35-43.
91. Gopin A, Ebner S, Attali B, Shabat D. Enzymatic activation of second-generation dendritic prodrugs: Conjugation of self-immolative dendrimers with poly(ethylene glycol) via click chemistry. *Bioconjug Chem* 2006;17(6):1432-40.
92. Greenwald RB, Choe YH, McGuire J, Conover CD. Effective drug delivery by PEGylated drug conjugates. *Adv Drug Deliv Rev* 2003;55(2):217-50.
93. Peer D, Karp JM, Hong S, Farokhzad OC, Margalit R, Langer R. Nanocarriers as an emerging platform for cancer therapy. *Nat Nanotechnol* 2007;2(12):751-60.
94. Liu J, Lee H, Huesca M, Young A, Allen C. Liposome formulation of a novel hydrophobic aryl-imidazole compound for anti-cancer therapy. *Cancer Chemother Pharmacol* 2006;58(3):306-18.
95. Kamaly N, Kalber T, Ahmad A, Oliver MH, So PW, Herlihy AH, Bell JD, Jorgensen MR, Miller AD. Bimodal paramagnetic and fluorescent liposomes for cellular and tumor magnetic resonance imaging. *Bioconjug Chem* 2008;19(1):118-29.
96. Zalipsky S, Saad M, Kiwan R, Ber E, Yu N, Minko T. Antitumor activity of new liposomal prodrug of mitomycin C in multidrug resistant solid tumor: insights of the mechanism of action. *J Drug Target* 2007;15(7-8):518-30.

97. Yuan F, Leunig M, Huang SK, Berk DA, Papahadjopoulos D, Jain RK. Microvascular permeability and interstitial penetration of sterically stabilized (stealth) liposomes in a human tumor xenograft. *Cancer Res* 1994;54(13):3352-6.
98. McKee TD, Grandi P, Mok W, Alexandrakis G, Insin N, Zimmer JP, Bawendi MG, Boucher Y, Breakefield XO, Jain RK. Degradation of fibrillar collagen in a human melanoma xenograft improves the efficacy of an oncolytic herpes simplex virus vector. *Cancer Res* 2006;66(5):2509-13.
99. Chen Q, Tong S, Dewhirst MW, Yuan F. Targeting tumor microvessels using doxorubicin encapsulated in a novel thermosensitive liposome. *Mol Cancer Ther* 2004;3(10):1311-7.
100. Li W, Huang Z, MacKay JA, Grube S, Szoka FC, Jr. Low-pH-sensitive poly(ethylene glycol) (PEG)-stabilized plasmid nanolipoparticles: effects of PEG chain length, lipid composition and assembly conditions on gene delivery. *J Gene Med* 2005;7(1):67-79.
101. Shuai X, Ai H, Nasongkla N, Kim S, Gao J. Micellar carriers based on block copolymers of poly(epsilon-caprolactone) and poly(ethylene glycol) for doxorubicin delivery. *J Control Release* 2004;98(3):415-26.
102. Torchilin VP. Micellar nanocarriers: pharmaceutical perspectives. *Pharm Res* 2007;24(1):1-16.
103. Sethuraman VA, Bae YH. TAT peptide-based micelle system for potential active targeting of anti-cancer agents to acidic solid tumors. *J Control Release* 2007;118(2):216-24.

104. Ross JF, Chaudhuri PK, Ratnam M. Differential regulation of folate receptor isoforms in normal and malignant tissues *in vivo* and in established cell lines. Physiologic and clinical implications. *Cancer* 1994;73(9):2432-43.
105. Yoo HS, Park TG. Folate receptor targeted biodegradable polymeric doxorubicin micelles. *J Control Release* 2004;96(2):273-83.
106. Park EK, Kim SY, Lee SB, Lee YM. Folate-conjugated methoxy poly(ethylene glycol)/poly(epsilon-caprolactone) amphiphilic block copolymeric micelles for tumor-targeted drug delivery. *J Control Release* 2005;109(1-3):158-68.
107. Park EK, Lee SB, Lee YM. Preparation and characterization of methoxy poly(ethylene glycol)/poly(epsilon-caprolactone) amphiphilic block copolymeric nanospheres for tumor-specific folate-mediated targeting of anticancer drugs. *Biomaterials* 2005;26(9):1053-61.
108. Eliceiri BP, Cheresch DA. The role of alphav integrins during angiogenesis: insights into potential mechanisms of action and clinical development. *J Clin Invest* 1999;103(9):1227-30.
109. Wands JR, Blum HE. Primary hepatocellular carcinoma. *N Engl J Med* 1991;325(10):729-31.
110. Jeong YI, Seo SJ, Park IK, Lee HC, Kang IC, Akaike T, Cho CS. Cellular recognition of paclitaxel-loaded polymeric nanoparticles composed of poly(gamma-benzyl L-glutamate) and poly(ethylene glycol) diblock copolymer endcapped with galactose moiety. *Int J Pharm* 2005;296(1-2):151-61.
111. Jule E, Nagasaki Y, Kataoka K. Lactose-installed poly(ethylene glycol)-poly(D,L-lactide) block copolymer micelles exhibit fast-rate binding and high affinity

- toward a protein bed simulating a cell surface. A surface plasmon resonance study. *Bioconjug Chem* 2003;14(1):177-86.
112. Farokhzad OC, Jon S, Khademhosseini A, Tran TN, Lavan DA, Langer R. Nanoparticle-aptamer bioconjugates: a new approach for targeting prostate cancer cells. *Cancer Res* 2004;64(21):7668-72.
113. Farokhzad OC, Cheng J, Teply BA, Sherifi I, Jon S, Kantoff PW, Richie JP, Langer R. Targeted nanoparticle-aptamer bioconjugates for cancer chemotherapy *in vivo*. *Proc Natl Acad Sci U S A* 2006;103(16):6315-20.
114. Engin K, Leeper DB, Cater JR, Thistlethwaite AJ, Tupchong L, Mcfarlane JD. Extracellular Ph Distribution in Human Tumors. *International Journal of Hyperthermia* 1995;11(2):211-216.
115. Yoo HS, Lee EA, Park TG. Doxorubicin-conjugated biodegradable polymeric micelles having acid-cleavable linkages. *J Control Release* 2002;82(1):17-27.
116. Bae Y, Fukushima S, Harada A, Kataoka K. Design of environment-sensitive supramolecular assemblies for intracellular drug delivery: polymeric micelles that are responsive to intracellular pH change. *Angew Chem Int Ed Engl* 2003;42(38):4640-3.
117. Bae Y, Jang WD, Nishiyama N, Fukushima S, Kataoka K. Multifunctional polymeric micelles with folate-mediated cancer cell targeting and pH-triggered drug releasing properties for active intracellular drug delivery. *Mol Biosyst* 2005;1(3):242-50.
118. Bae Y, Nishiyama N, Fukushima S, Koyama H, Yasuhiro M, Kataoka K. Preparation and biological characterization of polymeric micelle drug carriers

- with intracellular pH-triggered drug release property: tumor permeability, controlled subcellular drug distribution, and enhanced *in vivo* antitumor efficacy. *Bioconjug Chem* 2005;16(1):122-30.
119. Gillies ER, Frechet JMJ. A new approach towards acid sensitive copolymer micelles for drug delivery. *Chemical Communications* 2003(14):1640-1641.
120. Gillies ER, Frechet JMJ. pH-responsive copolymer assemblies for controlled release of doxorubicin. *Bioconjugate Chemistry* 2005;16(2):361-368.
121. Gillies ER, Goodwin AP, Frechet JMJ. Acetals as pH-sensitive linkages for drug delivery. *Bioconjugate Chemistry* 2004;15(6):1254-1263.
122. Stapert HR, Nishiyama N, Jiang DL, Aida T, Kataoka K. Poly-ion complex micelles encapsulating light-harvesting ionic Zn porphyrin dendrimers for PDT. *Abstracts of Papers of the American Chemical Society* 2000;219:U226-U226.
123. Stapert HR, Nishiyama N, Jiang DL, Aida T, Kataoka K. Polyion complex micelles encapsulating light-harvesting ionic dendrimer zinc porphyrins. *Langmuir* 2000;16(21):8182-8188.
124. Tang Y, Liu SY, Armes SP, Billingham NC. Solubilization and controlled release of a hydrophobic drug using novel micelle-forming ABC triblock copolymers. *Biomacromolecules* 2003;4(6):1636-45.
125. Lynn DM, Amiji MM, Langer R. pH-Responsive Polymer Microspheres: Rapid Release of Encapsulated Material within the Range of Intracellular pH *Angew Chem Int Ed Engl* 2001;40(9):1707-1710.

126. Potineni A, Lynn DM, Langer R, Amiji MM. Poly(ethylene oxide)-modified poly(beta-amino ester) nanoparticles as a pH-sensitive biodegradable system for paclitaxel delivery. *J Control Release* 2003;86(2-3):223-34.
127. Shenoy D, Little S, Langer R, Amiji M. Poly(ethylene oxide)-modified poly(beta-amino ester) nanoparticles as a pH-sensitive system for tumor-targeted delivery of hydrophobic drugs. 1. *In vitro* evaluations. *Mol Pharm* 2005;2(5):357-66.
128. van der Zee J. Heating the patient: a promising approach? *Ann Oncol* 2002;13(8):1173-84.
129. Chung JE, Yokoyama M, Okano T. Inner core segment design for drug delivery control of thermo-responsive polymeric micelles. *J Control Release* 2000;65(1-2):93-103.
130. Liu XM, Yang YY, Leong KW. Thermally responsive polymeric micellar nanoparticles self-assembled from cholesteryl end-capped random poly(N-isopropylacrylamide-co-N,N-dimethylacrylamide): synthesis, temperature-sensitivity, and morphologies. *Journal of Colloid and Interface Science* 2003;266(2):295-303.
131. Chung JE, Yokoyama M, Yamato M, Aoyagi T, Sakurai Y, Okano T. Thermo-responsive drug delivery from polymeric micelles constructed using block copolymers of poly(N-isopropylacrylamide) and poly(butylmethacrylate). *J Control Release* 1999;62(1-2):115-27.

132. Soppimath KS, Tan DCW, Yang YY. pH-triggered thermally responsive polymer core-shell nanoparticles for drug delivery. *Advanced Materials* 2005;17(3):318-+.
133. Liu SQ, Tong YW, Yang YY. Incorporation and *in vitro* release of doxorubicin in thermally sensitive micelles made from poly(N-isopropylacrylamide-co-N,N-dimethylacrylamide)-b-poly(D,L-lactide-co-glycolide) with varying compositions. *Biomaterials* 2005;26(24):5064-5074.
134. Mitragotri S. Healing sound: the use of ultrasound in drug delivery and other therapeutic applications. *Nat Rev Drug Discov* 2005;4(3):255-60.
135. Rapoport N, Smirnov AI, Timoshin A, Pratt AM, Pitt WG. Factors affecting the permeability of *Pseudomonas aeruginosa* cell walls toward lipophilic compounds: Effects of ultrasound and cell age. *Archives of Biochemistry and Biophysics* 1997;344(1):114-124.
136. Munshi N, Rapoport N, Pitt WG. Ultrasonic activated drug delivery from pluronic P-105 micelles. *Cancer Letters* 1997;118(1):13-19.
137. Rapoport NY, Herron JN, Pitt WG, Pitina L. Micellar delivery of doxorubicin and its paramagnetic analog, ruboxyl, to HL-60 cells: effect of micelle structure and ultrasound on the intracellular drug uptake. *J Control Release* 1999;58(2):153-62.
138. Marin A, Sun H, Hussein GA, Pitt WG, Christensen DA, Rapoport NY. Drug delivery in pluronic micelles: effect of high-frequency ultrasound on drug release from micelles and intracellular uptake. *Journal of Controlled Release* 2002;84(1-2):39-47.

139. Husseini GA, Runyan CM, Pitt WG. Investigating the mechanism of acoustically activated uptake of drugs from Pluronic micelles. *Bmc Cancer* 2002;2:-.
140. Etzioni R, Urban N, Ramsey S, McIntosh M, Schwartz S, Reid B, Radich J, Anderson G, Hartwell L. The case for early detection. *Nat Rev Cancer* 2003;3(4):243-52.
141. Clasen S, Pereira PL. Magnetic resonance guidance for radiofrequency ablation of liver tumors. *J Magn Reson Imaging* 2008;27(2):421-33.
142. Crocetti L, Lencioni R. Thermal ablation of hepatocellular carcinoma. *Cancer Imaging* 2008;8:19-26.
143. Sato H, Enmi J, Teramoto N, Hayashi T, Yamamoto A, Tsuji T, Naito H, Iida H. Comparison of Gd-DTPA-induced signal enhancements in rat brain C6 glioma among different pulse sequences in 3-Tesla magnetic resonance imaging. *Acta Radiol* 2008;49(2):172-9.
144. Nakamura E, Makino K, Okano T, Yamamoto T, Yokoyama M. A polymeric micelle MRI contrast agent with changeable relaxivity. *J Control Release* 2006;114(3):325-33.
145. Zhang G, Zhang R, Wen X, Li L, Li C. Micelles based on biodegradable poly(L-glutamic acid)-b-poly lactide with paramagnetic Gd ions chelated to the shell layer as a potential nanoscale MRI-visible delivery system. *Biomacromolecules* 2008;9(1):36-42.
146. Trubetskoy VS, Frank-Kamenetsky MD, Whiteman KR, Wolf GL, Torchilin VP. Stable polymeric micelles: lymphangiographic contrast media for gamma scintigraphy and magnetic resonance imaging. *Acad Radiol* 1996;3(3):232-8.

147. Wang YX, Hussain SM, Krestin GP. Superparamagnetic iron oxide contrast agents: physicochemical characteristics and applications in MR imaging. *Eur Radiol* 2001;11(11):2319-31.
148. Ai H, Flask C, Weinberg B, Shuai X, Pagel MD, Farrell D, Duerk J, Gao J. Magnetite-loaded polymeric micelles as ultrasensitive magnetic-resonance probes. *Advanced Materials* 2005;17(16):1949-1952.
149. Trubetskiy VS, Gazelle GS, Wolf GL, Torchilin VP. Block-copolymer of polyethylene glycol and polylysine as a carrier of organic iodine: design of long-circulating particulate contrast medium for X-ray computed tomography. *J Drug Target* 1997;4(6):381-8.
150. Shingyoji M, Gerion D, Pinkel D, Gray JW, Chen FQ. Quantum dots-based reverse phase protein microarray. *Talanta* 2005;67(3):472-478.
151. Dubertret B, Skourides P, Norris DJ, Noireaux V, Brivanlou AH, Libchaber A. *In vivo* imaging of quantum dots encapsulated in phospholipid micelles. *Science* 2002;298(5599):1759-62.
152. Chen YF, Rosenzweig Z. Luminescent CdSe quantum dot doped stabilized micelles. *Nano Letters* 2002;2(11):1299-1302.
153. van Tilborg GAF, Mulder WJM, Chin PTK, Storm G, Reutelingsperger CP, Nicolay K, Strijkers GJ. Annexin A5-conjugated quantum dots with a paramagnetic lipidic coating for the multimodal detection of apoptotic cells. *Bioconjugate Chemistry* 2006;17(4):865-868.

154. Lee ES, Na K, Bae YH. Doxorubicin loaded pH-sensitive polymeric micelles for reversal of resistant MCF-7 tumor. *Journal of Controlled Release* 2005;103(2):405-418.
155. Cheng C, Wei H, Shi BX, Cheng H, Li C, Gu ZW, Cheng SX, Zhang XZ, Zhuo RX. Biotinylated thermoresponsive micelle self-assembled from double-hydrophilic block copolymer for drug delivery and tumor target. *Biomaterials* 2008;29(4):497-505.
156. Rapoport N, Gao Z, Kennedy A. Multifunctional nanoparticles for combining ultrasonic tumor imaging and targeted chemotherapy. *J Natl Cancer Inst* 2007;99(14):1095-106.

CHAPTER TWO

Pharmacological Studies of β -lap•HP β -CD (ARQ 501): A Case for Micellar Encapsulation

2.1 Introduction

For most solid tumors, surgical resection remains the gold standard of therapy, yielding much improved patient outcomes. However, complete excision of the disease is not possible in the vast majority of cases, requiring the use of adjuvant therapies such as chemotherapy to combat recurrence.¹ Hence, in non-small cell lung cancer (NSCLC), the most prevalent type of lung cancer within the population, surgery is used to eliminate the majority of the tumor, followed by the administration of platinum-based therapeutics.² Most often, platinum-based drugs are coupled with third generation agents such as paclitaxel, gemcitabine, and docetaxel, especially in cases where platinum-based drugs have proved ineffective.³ The use of these chemotherapeutics has led to increases in 1-year survival rates, but have failed to make a significant impact on overall patient survival.⁴

Significant advances in the understanding of underlying molecular mechanisms of tumorigenesis has led to the design and discovery of several drugs capable of exerting effects on key molecular targets essential for tumor propagation. This should ideally allow for heightened antitumor specificity, and more importantly, decreased toxicity in healthy tissues and organs. As an example, β -lapachone (β -lap), is a naturally occurring antineoplastic agent that is bioactivated by the cytosolic enzyme NAD(P)H:quinone oxidoreductase-1 (NQO1), a flavoprotein found overexpressed in NSCLC. Preclinical in

vitro studies have shown that the drug effectively kills tumor cells in an NQO1-dependent fashion at μM doses, sparing those cells that do not express the enzyme.⁵⁻⁹ This fact, in combination with promising preclinical in vivo data,¹⁰ has warranted the translation of β -lap into the clinical arena.

In order to propel the drug into the clinics, a suitable delivery vehicle was required that would help overcome the low solubility of β -lap (0.04 mg/mL). Cyclodextrins (CDs) are cyclic oligosaccharides in the form of truncated cones, consisting of a hydrophobic core and a hydrophilic outer surface, which can effectively increase the solubility of otherwise water-insoluble drugs.¹¹⁻¹⁴ Following the exploration of several CDs with different numbers of glucopyranose units (e.g. α has 6, β has 7, and γ has 8), it was found that hydroxypropyl- β -cyclodextrin (HP β -CD) resulted in the greatest enhancement of solubility (400-fold increase).¹⁵ As a result, the efficacy of a complexed form of β -lap and HP β -CD (β -lap•HP β -CD) is currently being explored clinically in several different cancers, in combination with several different drugs, by Arqule, Inc. under the name of ARQ 501.¹⁶⁻¹⁹

A phase I trial of the drug involved a combination of ARQ 501 with docetaxel in patients with advanced solid tumors, where the dosing regimens consisted of administration of ARQ 501 for 5 consecutive days with one docetaxel infusion at day 3 at a dose of 50 to 100 mg/m², or a single dose of ARQ 501 and a single infusion of docetaxel on day 1.¹⁹ These regimens were deemed tolerable, and 12 of the 16 patients had stable disease. When used in combination with gemcitabine in a phase II clinical study, ARQ 501, showed modest antitumor activity against pancreatic cancer.¹⁸ In this study, 20 patients with unresectable tumors were evaluated 8 weeks after the start of a dosing

regimen that consisted of weekly infusions of ARQ 501 ($400\text{mg}/\text{m}^2$) and gemcitabine ($800\text{ mg}/\text{m}^2$). Of the 20 patients, 6 showed signs of tumor reduction, with 1 patient showing a significant regression of 29.6% of pancreatic lesions. However, an adverse side effect of ARQ 501 treatment was reported to be hemolysis, and has been found to be a severe limiting factor. For example, in a phase II multi-center study where 45 patients with leiomyosarcoma were being treated with ARQ 501, a single infusion at $450\text{ mg}/\text{m}^2$ led to extreme hemolysis, acute renal failure, and eventual treatment-related death.¹⁶ Antitumor efficacy from this study consisted of one partial remission and three patients with stable disease.

In light of findings suggesting that hemolysis is a considerable hurdle for the clinical progression of β -lap, our objective was to thoroughly examine the ARQ 501 formulation in hopes of uncovering the underlying cause of this toxicity. We also aimed to investigate the pharmacokinetics of β -lap•HP β -CD for purposes of better understanding the modest tumor regression patterns observed in clinical trials. Hemolysis assays were conducted by incubating RBCs with several different formulations of β -lap and HP β -CD. Blood and tissues of mice injected with β -lap•HP β -CD were analyzed for β -lap concentration over time. Results from this study suggest that the hemolysis observed clinically is likely the result of the cyclodextrin carrier used for β -lap solubilization purposes. It was found that β -lap did not cause any appreciable hemolysis, but did in fact convert hemoglobin to methemoglobin. Pharmacokinetic data point to a rapid clearance of the drug from the bloodstream, with the highest accumulation over time of β -lap seen in the liver and kidneys. Moreover, a micellar formulation of β -lap did not lead to any hemolysis, and significantly improved the blood

residence time and tumor accumulation of the drug. Findings from this study will prove beneficial in determining the utility of the current clinical formulation of β -lap, and the possibility of alternate delivery strategies such as polymer micelles.

2.2 Materials and methods

2.2.1 Materials

HP β -CD was obtained from Cyclodextrin Technologies Development, Inc. (CTD) (High Springs, FL) with >98% purity. β -Lap was synthesized following a previously reported procedure.²⁰ PEG5k-PLA5k block copolymer (Mn = 10,000 Da) was synthesized utilizing a ring-opening polymerization procedure published previously.²¹ Radiolabelled block copolymer (MeO-PEG-PLA-OCOC³H₃, 10kD) was synthesized by end capping of the terminus of the PLA block (5mCi of ³H). All organic solvents were of analytical grade. Phosphate buffered saline (PBS, pH 7.4) was purchased from Fisher Scientific (Pittsburgh, PA). Tritium labeled acetyl chloride (³H) was purchased from American Radiolabeled Chemicals Inc (St. Louis, USA). Tissue solubilizer (BTS-450) and scintillation cocktail (Ready Organic) were purchased from Beckman Coulter (Fullerton, CA). A549 lung tumors were grown in DMEM with 10% fetal bovine serum, 2 mM L-glutamine, 100 units/mL penicillin, and 100 mg/mL streptomycin at 37°C in a humidified incubator with a 5% CO₂-95% air atmosphere. Cells were routinely found free of mycoplasma infection.

2.2.2 Preparation of β -lap•HP β -CD complexes

β -Lap•HP β -CD complexes were produced by dissolving HP β -CD (25 g) in 50 mL of PBS. Once the HP β -CD was completely dissolved, a known amount of β -lap (1 g) was added to the HP β -CD solution and left stirring at room temperature for 48 h. After 48 h, the solution was filtered through 0.45 μ m nylon filters, after which the concentration of β -lap was determined using UV-Vis spectrophotometry ($\lambda_{\text{max}} = 257$ nm, $\epsilon = 105$ mL/(cm·mg β -lap) and a previously established calibration curve.

2.2.3 *β -lap micelle fabrication*

A film sonication procedure was utilized to fabricate β -lap micelles.²² Briefly, β -lap and PEG-PLA (5% w/w) were dissolved in acetone and the organic solvent was allowed to evaporate, yielding a solid film. Water was then added to the film and sonicated for 5 min. In each case, drug-loaded polymer micelles were filtered through 0.45 μ m nylon filters to remove non-encapsulated drug aggregates in solution, and the micelle solution was stored immediately at 4°C to prevent premature drug release. The solution of micelles was then concentrated by centrifugation at a rotational speed of 3,000 RPM at 4°C (Eppendorf Centrifuge 5804 R) using Amicon Ultra Centrifugal Filter Devices (MW cutoff = 100,000 Da). The concentration of β -lap was then determined by lyophilizing a known volume of solution, which was later dissolved in chloroform and analyzed via UV-Vis spectrophotometry with the aforementioned λ_{max} and calibration curve.

In the case where radiolabeled polymer was to be used for purposes of micelle distribution studies, a small amount of MeO-PEG-PLA-OCOC³H₃ (1% w/w) was

dissolved with PEG-PLA, and β -lap micelles were prepared in a similar method as described above.

2.2.4 Hemolysis assays

Blood was freshly obtained from athymic female nude mice. The blood was collected in a heparin-coated tube and centrifuged at 2800 RPM for 5 min, after which the red blood cells (RBCs) were isolated and washed three times (centrifugation at 2800 RPM for 5 min) with PBS buffer. After the three washings, the cells were resuspended in PBS and 100 μ L of the RBC suspension was incubated with 900 μ L of different concentrations of either HP β -CD alone, β -lap•HP β -CD, β -lap dissolved in DMSO, and β -lap polymer micelles. Complete hemolysis was obtained by incubating the same amount of erythrocytes with 0.2% Triton X-100. Additionally, a sample consisting of RBCs incubated with PBS was also included as a control. The samples were then placed in a New Brunswick Scientific C24 Incubator Shaker for 1 h at 37°C, after which the samples were centrifuged for 1 h at 10,000 RPM. The supernatant of all samples was then analyzed for hemoglobin (Hb) released via UV-Vis spectrophotometry at a wavelength of 576 nm, and % hemolysis was calculated based on Hb present in the 0.2% Triton X-100 (complete hemolysis) samples. All experiments were conducted in triplicate. The percentage (%) of hemolysis was then plotted as a function of concentrations of either HP β -CD or β -lap.

2.2.5 Pharmacokinetic analysis of β -lap•HP β -CD

Animal procedures adhered to the National Institutes of Health (NIH) guidelines and followed an approved protocol by the Institutional Animal Care and Use Committee (IACUC) at the University of Texas Southwestern Medical Center at Dallas. Pharmacokinetic studies involving blood concentration over time, as well as tissue of distribution of β -lap, were performed in tumor-bearing nude mice weighing 25 g. A549 lung cancer cells were grown to 80-90% confluence. The cells were then harvested, prepared at $5 \times 10^6 / 50 \mu\text{l}$ cell suspensions, and injected into the flanks of 6-8 week-old nude mice. Tumor size was measured regularly by means of a caliper and volume calculated using the formula: $\text{volume (mm}^3\text{)} = \text{length} \times \text{width} \times \text{width}/2$. Animals containing average tumor sizes of approximately 300 mm^3 were selected for pharmacokinetic studies. A solution of β -lap•HP β -CD (30 mg/Kg) was administered to the mice intravenously (IV). At predetermined times, the animals were sacrificed and blood was harvested via cardiac puncture and placed in heparin-coated tubes. The blood was then centrifuged at 2800 RPM for 5 min and the plasma collected. Tissues, including the lungs, brain, spleen, liver, kidney, and heart were removed, accurately weighed, and placed in liquid nitrogen.

Concentrations of β -lap in plasma and different tissues were determined using an LC/MS/MS method developed for the drug on an Applied Biosystems 3200 Q TRAP mass spectrometer coupled to a Shimadzu Prominence liquid chromatography instrument found in the Preclinical Pharmacology Core Laboratory at the University of Texas Southwestern Medical Center at Dallas. β -Lap was easily detected as a singly charged species with the two best daughter ions giving comparable results. The transitions monitored were 243.1 to 187.1 and 243.1 to 159.2. Chromatography was conducted

using a Synergi Fusion RP column (Phenomenex, 5 micron packing 4.6 X 150 mm). The following conditions were utilized: Buffer A: 0.1% formic acid in water; Buffer B: 25% isopropanol in methanol + 0.1% formic acid; flow rate 0.5 ml/min; 0-5 min 100% A, 5-9 min gradient to 100% B, 9-16 min 100% B, 16-17 min gradient to 0% B, 17-20 min 100% A. A Waters OASIS HLB solid phase extraction column was used to extract β -Lap from plasma and tissue. Briefly, tissue homogenates for both calibration curves and samples were prepared by adding a volume of PBS equal to 3X the weight of each tissue sample in grams. Total volume was calculated as 4x tissue weight in grams. Acetonitrile (200 μ L) was added to 100 μ L of either tissue homogenate or plasma in order to precipitate protein. The sample was then vigorously vortexed and allowed to incubate at RT for 10 min. PBS (700 μ L) was then added to the sample and spun for 5 min at 16,000 x g. The resulting supernatant was then mixed with 1 mL of dH₂O and passed over an OASIS HLB solid phase extraction column. Total drug was eluted with methanol after two 5% methanol in water washes, and the sample diluted to 50% methanol with water. Prior to running LC/MS/MS, 0.1% formic acid was added to each sample.

Calibration standards covering 10,000 to 5 ng/mL were prepared in blank plasma and tissue homogenate and a curve was fit to the data. Blank plasma or tissue was also included and established the limit of detection (LOD) as between 50-1600 (calculated mass area) for the 243.1 to 187.1 transition, which was used for all subsequent analysis. This represents a number 3-fold above that seen for blank plasma or tissue. The lower limit of quantitation (LLOQ) is 5 ng/ml for all tissues except brain, where it was found to be 10 ng/ml. Experiments were conducted in triplicate and data were analyzed assuming compartmental pharmacokinetics.

2.2.6 Pharmacokinetic analysis of β -lap micelles

Experiments involving radioactive materials were approved by the Radiation Safety Committee at UT Southwestern Medical Center. Pharmacokinetic studies regarding blood concentration over time, as well as tissue distribution of β -lap micelles, were performed in tumor-bearing nude mice weighing 25 g. A549 lung cancer cells were harvested, prepared, and injected as described in the previous section. β -Lap micelles containing 1% tritium (^3H)-labelled PEG-PLA were injected into the mice via the tail vein. Blood was collected from the ocular vein at 1 min, 30 min, 1 h, 2 h, 4 h, 6 h, 10 h, and 24 h after injection. Plasma was isolated from blood samples by centrifugation at 3000 RPM for 5 min. The plasma was then mixed with a tissue solubilizer (1 mL, BTS-450) at RT for 5 hrs followed by the addition of a liquid scintillation cocktail (10 mL, Ready Organic™) for 12 hrs. Radioactive isotope amounts in the samples were then measured by a Beckman LS 6000 IC liquid scintillation counter. Biodistribution studies of β -lap micelles in tissues and organs were conducted at 2 h and 24 h timepoints. At these timepoints, animals were sacrificed, organs were harvested, weighed, and suspended in dH_2O , and were subsequently homogenized. Tissue solubilizer (1 mL) was then added to an amount of tissue, followed by 30% hydrogen peroxide (100 μL), liquid scintillation cocktail (10 mL), and acetic acid (70 μL). Amounts of radioactive isotope in the tissues were then measured by a liquid scintillation counter. Radioactive isotope quantities were estimated using a predetermined calibration curve of the tritium-labeled β -lap micelle solution, and results were presented as percentage (%) of initial dose in

tissues. All experiments were conducted in triplicate and data were analyzed assuming compartmental pharmacokinetics.

2.3 Results

2.3.1 Hemolysis resulting from ARQ 501

Figure 2.1 depicts the percentage (%) of hemolysis as a result of different formulations of β -lap and HP β -CD. As can be observed from the figure, β -lap•HP β -CD (ARQ 501) indeed causes hemolysis. At a low β -lap concentration of 0.5 mg/mL, ARQ 501 resulted in a $38 \pm 2\%$ hemolysis. With increases in concentration, % hemolysis due to β -lap•HP β -CD increased only slightly, reaching levels of $47 \pm 1\%$ and $52 \pm 2\%$ at β -lap concentrations of 1.0 and 1.5 mg/mL, respectively. However, incubation of RBCs with β -lap dissolved in DMSO did not result in any perceivable hemolysis, reaching a maximum hemolysis at $7 \pm 2\%$ at a concentration of 0.5 mg/mL. When HP β -CD alone, at a low concentration of 5 mg/mL, was incubated with RBCs, a small % hemolysis was observed ($6 \pm 1\%$). However, at higher concentrations of HP β -CD, substantial hemolysis occurred. At a concentration of 10 mg/mL, HP β -CD led to $43 \pm 4\%$ hemolysis. At even higher concentrations of 17 and 50 mg/mL, the resulting hemolysis from HP β -CD was $92 \pm 4\%$ and $94 \pm 1\%$, respectively. By contrast, β -lap-containing PEG-PLA micelles were not shown to cause any noticeable hemolysis at comparable β -lap concentrations.

2.3.2 Interaction of β -lap with RBCs

The effect of β -lap on hemoglobin (Hb), the major component of RBCs, can be found in Figure 2.2. As can be observed from Figure 2.2A, the characteristic λ_{\max} of

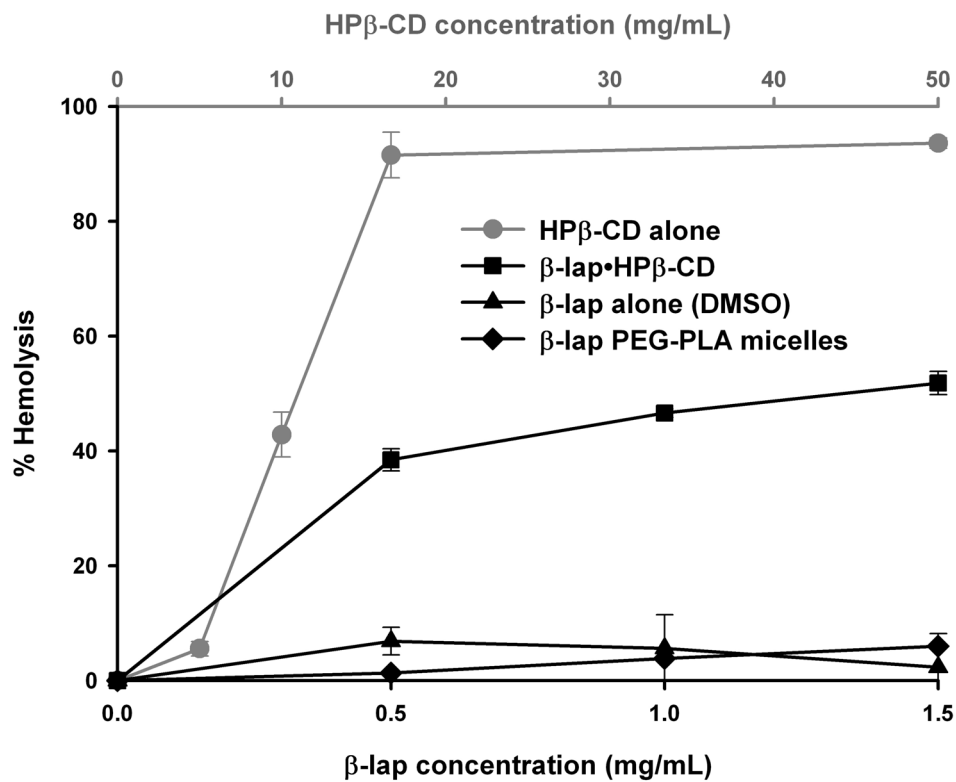


Figure 2.1. Percent (%) hemolysis as a result of β -lap in different formulations, including complexed with HP β -CD, dissolved in DMSO, and in micellar form. The top x-axis represents the concentration of HP β -CD with which RBCs were incubated and the bottom x-axis represents the corresponding β -lap concentration.

hemoglobin at 415 nm is visible in samples that were incubated with 0.2% Triton X-100. The Hb λ_{\max} can also be seen in samples treated with a high concentration (50 mg/mL) of HP β -CD. However, in samples where hemolysis occurred as a result of co-incubation of RBCs with β -lap•HP β -CD, the λ_{\max} of Hb at 415 nm has been blue-shifted to a lower wavelength of 408 nm. This change in λ_{\max} of hemoglobin was not apparent in β -lap micelle samples given their inability to cause lysis and release Hb.

Figure 2.2B depicts wavelength scans of hemoglobin at higher wavelength values. In samples where hemolysis has occurred as a result of 0.2% Triton X-100 treatment, two λ_{\max} of hemoglobin can be observed at 541 nm and 576 nm. These two characteristic peaks are also apparent in samples where hemolysis was induced by incubation with HP β -CD. In samples treated with β -lap•HP β -CD, the 576 nm peak is apparent, but not the peak at 541 nm, given the absorbance of β -lap at lower wavelengths. However, a new Hb prominent peak can be observed at a wavelength of 628 nm in β -lap•HP β -CD treated samples. This peak is absent in Triton and HP β -CD treated samples, as well as in β -lap-containing PEG-PLA micelles, indicating an interaction between the drug and hemoglobin.

2.3.3 Pharmacokinetic analysis of β -lap•HP β -CD

Figure 2.3A shows the blood concentration of β -lap over time. As can be seen from the figure, β -lap, when complexed with HP β -CD, is very short lived in the blood. The short phase half-life, $t_{1/2,\alpha}$, of ARQ 501 is approximately 3 min, while the elimination phase (long) half-life, $t_{1/2,\beta}$, is 24 min. The drug is almost completely cleared from the blood after 2 h, with the blood clearance found to be 13575 mL h⁻¹ Kg⁻¹. Taken together,

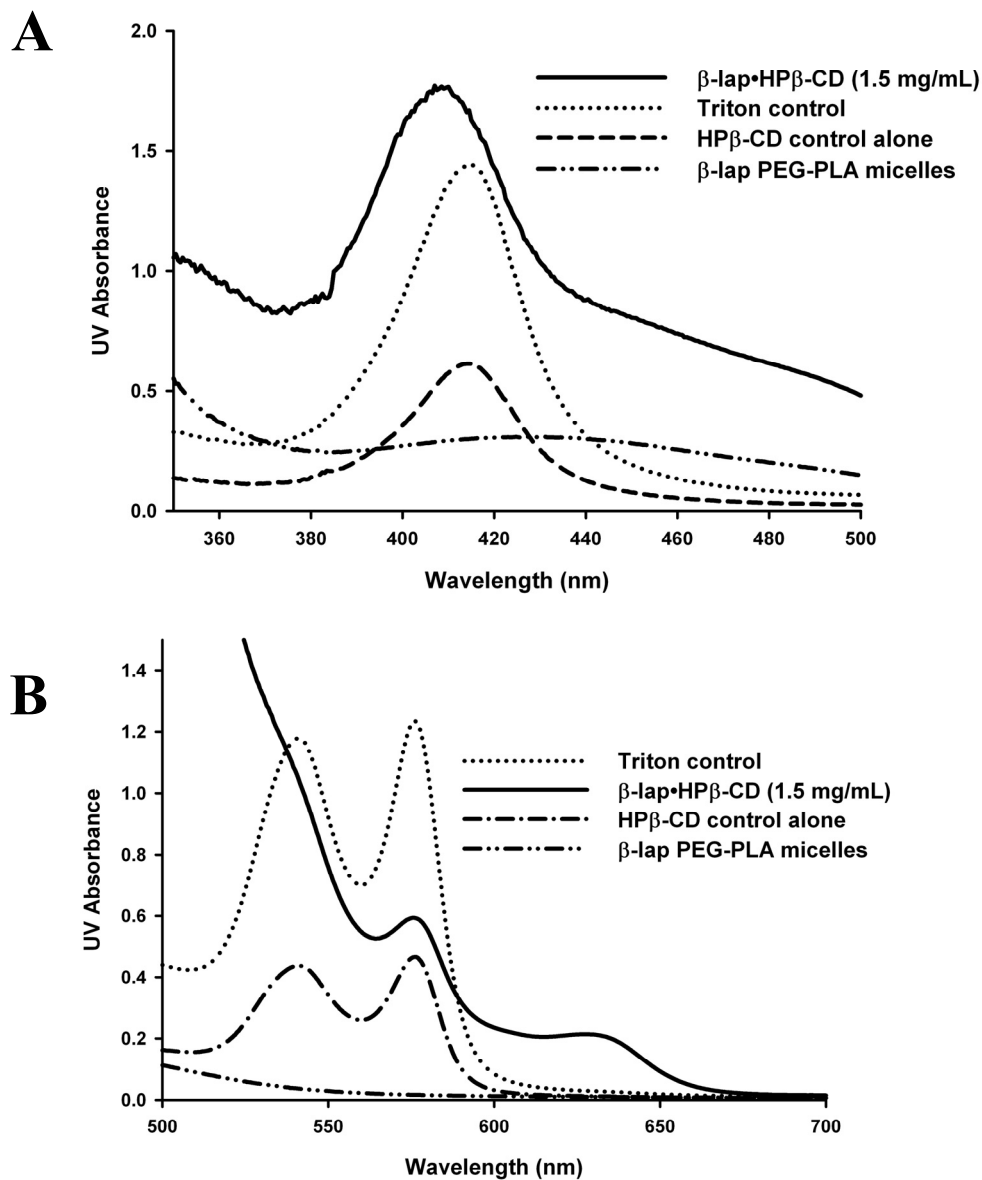


Figure 2.2. Examination of β -lap interaction with hemoglobin (Hb). (A) UV-Vis wavelength scans in the range of 350 nm to 500 nm showing the λ_{\max} of Hb at 415 nm. (B) UV-Vis wavelength scans in the range of 500 nm to 700 nm showing characteristic λ_{\max} of Hb at 541 nm and 576 nm.

the mean residence time (MRT), or the average time the drug remains in the blood, is very short, equating to 26 min.

Figure 2.3B shows the tissue distribution of β -lap in different tissues and organs of the mouse, including liver, kidney, spleen, lung, brain, heart, and tumor. At a time of 5 min after the injection, β -lap was found to distribute almost immediately and evenly among all of the major organs. Levels of β -lap were found to be at or above 10 $\mu\text{g/g}$ in all tissues within 5 min after injection, including the liver, kidney, spleen, and lungs. Surprisingly, there was a high accumulation of β -lap in the brain and heart early after drug administration. Levels of β -lap in the tumor, however, were found to be much lower than that compared to other organs, at a value of 1 $\mu\text{g/g}$. At a timepoint of 30 min after administration, the levels of β -lap in the liver remain high and above 10 $\mu\text{g/g}$, while the β -lap amount in all other tissues and organs has fallen to levels slightly above 1 $\mu\text{g/g}$. At this timepoint, there is still a particularly even distribution of the drug among the different organs, with levels still surprisingly high in organs such as the brain and heart. It is important to note that the levels of β -lap in the tumor have only decreased slightly relative to amounts in other organs. At a timepoint of 2 h postinjection, the amount of β -lap in the liver has remained relatively unchanged when compared to the early timepoints, representing the organ with most accumulation of β -lap over time. All the while, levels of β -lap have drastically fallen compared to early timepoints, with the concentrations hovering at a value of 0.1 $\mu\text{g/g}$, still significantly above the detection limit of 5 ng/g . Amounts of β -lap in the brain and heart are still heavily apparent at the 2 h timepoint despite the decreasing trend. It is important to note that the levels of β -lap in the tumor have fallen off drastically as well in the tumor.

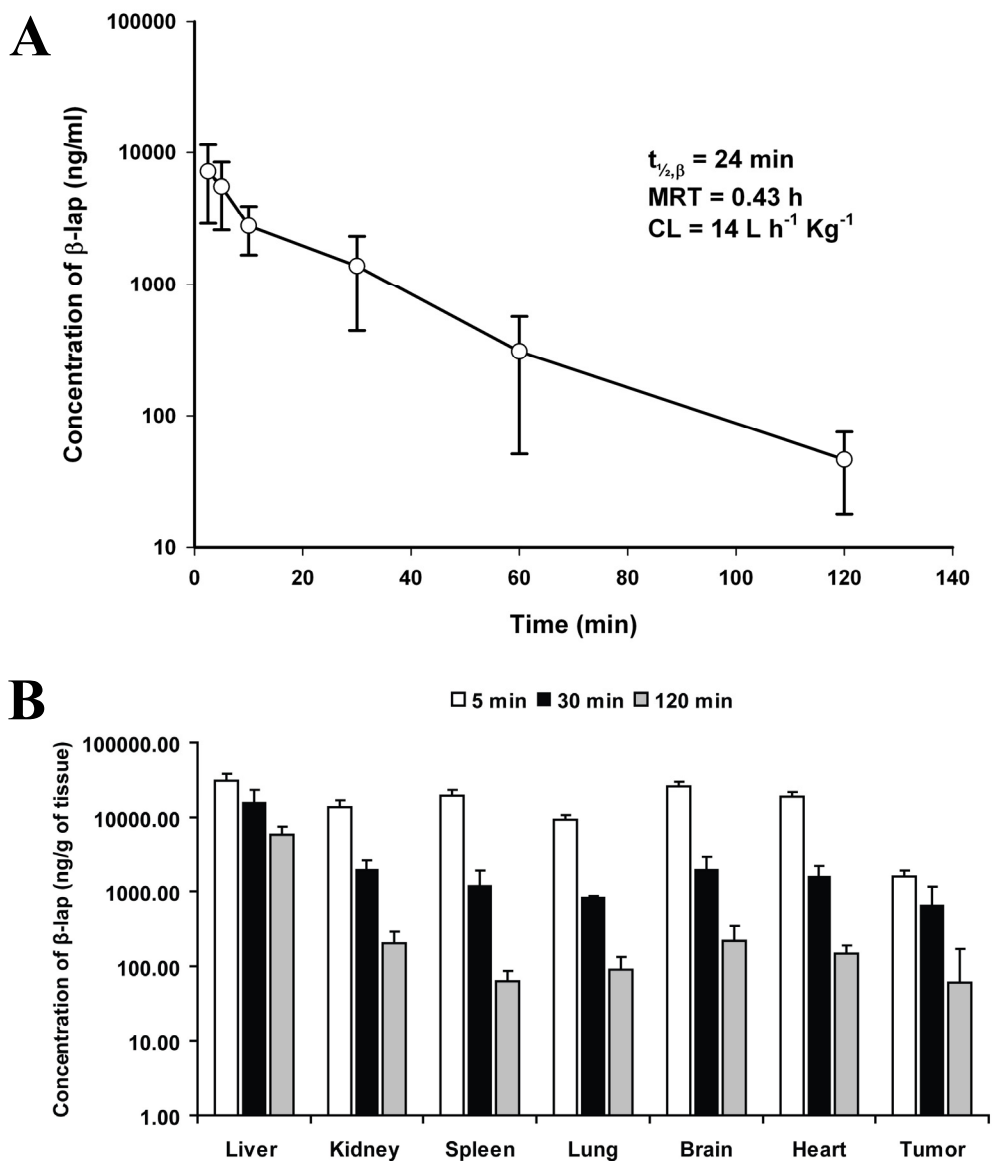


Figure 2.3. Pharmacokinetic analysis of β -lap•HP β -CD (single administration of 30 mg/Kg) in mice bearing A549 subcutaneous lung tumors. (A) Blood-concentration over time curve of β -lap. (B) Tissue distribution of β -lap among various organs of the body at specific timepoints after administration. All experiments were conducted in triplicate ($n = 3$). Error bars represent standard deviation.

2.3.4 Pharmacokinetic analysis of β -lap micelles

The pharmacokinetics of β -lap micelles were examined in tumor-bearing mice, the results of which comprise Figure 2.4A. As can be seen from Figure 2.4A, the blood concentration of β -lap micelles over time is rather prolonged over a 24 h time span, with a short phase half-life of 2 h, and an elimination half-life of 28 h. β -Lap micelles had a much slower clearance rate from the blood, approximately $2 \text{ mL h}^{-1} \text{ Kg}^{-1}$, and a long mean residence time (MRT) of 39 h. After 24 h, roughly 20% of the initial dose of β -lap micelles was still found in the blood stream (data not shown).

The tissue distribution of β -lap micelles at 2 and 24 h after administration is shown in Figure 2.4B, where micelle accumulation was examined in organs including the liver, spleen, lungs, heart, kidneys, muscle, brain, and tumor. Following injection, the largest accumulation of β -lap micelles after 2h can be seen in the spleen, with approximately 5.8% of the injected dose (ID) per gram of the organ (% ID/g), or approximately 1.6% of the injected dose. β -Lap micelles were also seen to accumulate in the liver and kidneys, but to a lesser extent as compared to the spleen, with 3.4% ID/g (7.7% ID) and 1.1% ID/g, respectively. In contrast, β -lap micelles were seen to accumulate in organs including the heart, lungs, and muscle in seemingly negligible amounts 2h after injection, with the brain showing almost no accumulation of micelles. Conversely, tumors were shown to amass a fair amount of β -lap micelles comparatively 2 h following injection, reaching levels of $\sim 1.5\%$ ID/g. This value of micellar uptake appears to remain constant for prolonged times, as 1.6% ID/g of β -lap micelles were observed in the tumor after 24 h. Micelle accumulation appears to decrease slightly over time in organs such as the lungs, heart, and kidney 24 h after injection. In contrast, β -lap

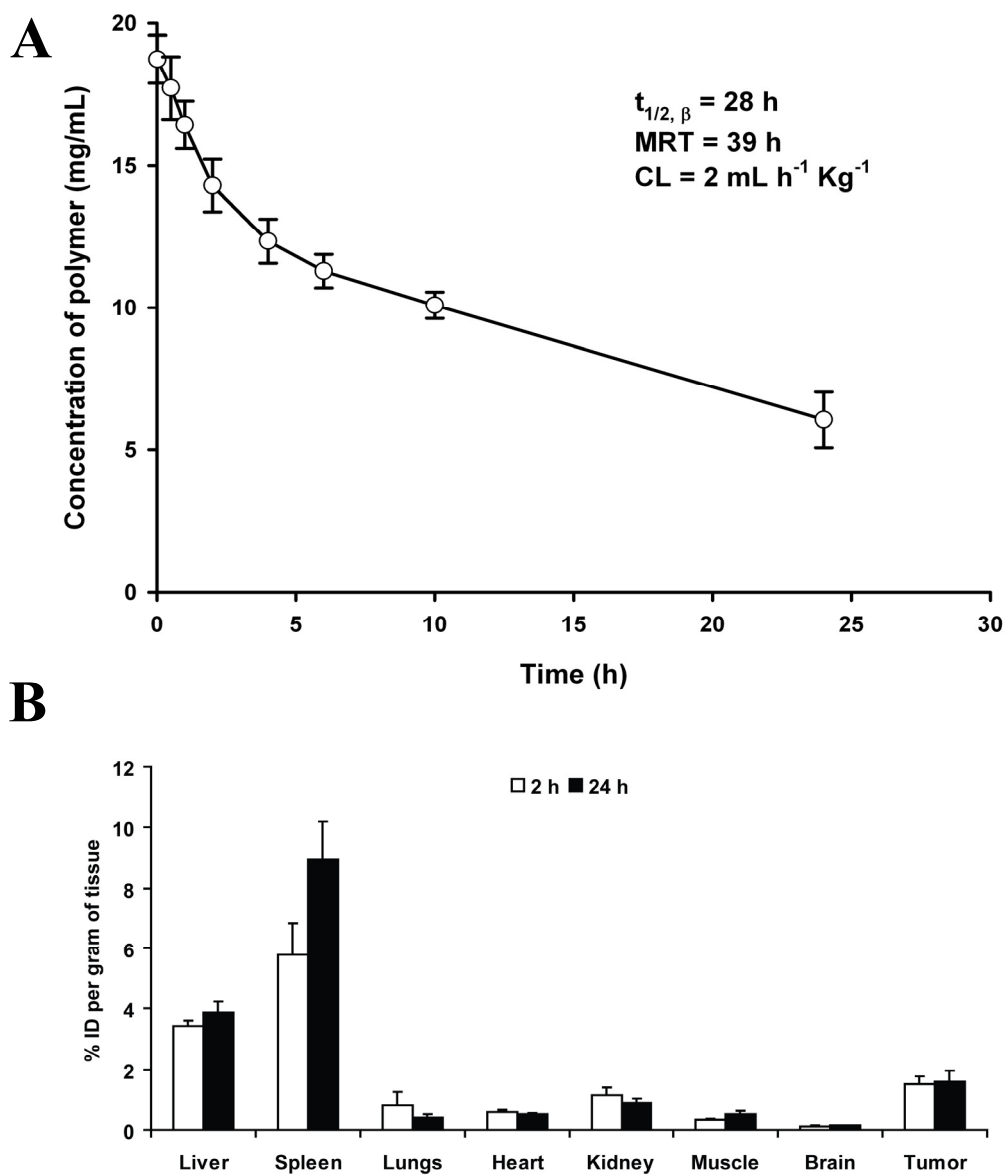


Figure 2.4. Pharmacokinetic analysis of β -lap PEG-PLA polymer micelles (single administration of 40 mg/Kg) in mice. (A) Concentration of polymer in blood over time curve of β -lap. (B) Tissue distribution of β -lap micelles among various organs of the body at specific timepoints after administration. All experiments were conducted in triplicate. Error bars represent standard error ($n = 3$ for all organs except tumors, where $n = 6$).

micelle amounts in liver were shown to be higher after 24 h when compared to the 2 h timepoint. Likewise, β -lap micelles were shown to collect to a greater degree in the spleen 24 h after injection (8.9% ID/g) when compared to the 2 h timepoint.

2.4 Discussion

2.4.1 *HP β -CD is a highly hemolytic solubilization vehicle*

Currently, cyclodextrins are extensively used as solubilizers for a variety of drugs for an equally broad range of conditions and diseases. As an example, Hohl and coworkers showed that complexation of camptothecin with several different CDs increased the solubility and stability of the drug.²³ Previously, we demonstrated a 400-fold increase in the aqueous solubility of β -lap through complexation of the drug with HP β -CD,¹⁵ which in turn increased the feasibility of using the drug in clinics. In various clinical trials, however, it was found that a formulation of β -lap•HP β -CD resulted in substantial patient hemolysis, proving a fatal factor in one trial.¹⁶ This toxic side effect of the drug formulation prevents dose-escalation, as well as increases in dosing frequency, and may well lead to discontinuation of the clinical translation of β -lap. In an attempt to uncover the cause for β -lap-induced hemolysis, it was found that β -lap•HP β -CD was approximately 50% hemolytic, but that this hemolysis resulted from the delivery vehicle HP β -CD and not the drug. When incubated alone with RBCs at concentrations necessary to solubilize β -lap, it was found that HP β -CD caused nearly complete hemolysis (Figure 2.1), similar to RBCs undergoing lysis with 0.2% Triton X-100. On the contrary, β -lap, when dissolved in DMSO, showed no appreciable signs of hemolysis.

It is now well known that the different cyclodextrins, including α , β , and γ , as well as modified forms of these, cause hemolysis.²⁴⁻²⁷ The order of hemolytic activity, as reported by Uekama et al., is γ -CD < α -CD < β -CD.²⁵ Stella and coworkers were able to show that a 30 min incubation of rabbit RBCs with HP β -CD at a concentration of 10 mM (equivalent to 14 mg/mL) yielded near complete hemolysis,²⁷ corroborating findings from this study. Results from several labs indicate that the mechanism by which CDs cause hemolysis involves interactions with membrane components, including cholesterol and phospholipid sequestration.²⁵ Briefly, CDs bring about shape changes in erythrocytes, progressing from biconcave discocytes to monoconcave stomatocytes to round spherocytes.²⁶ Hemolysis occurs following these transformations, with the exception being β -CD, which induces hemolysis prior to conversion to stomatocytes. In the process of these morphological changes, cyclodextrins remove phospholipids, cholesterol, and proteins from erythrocytes. The removal of cholesterol increases membrane fluidity, which in turn leads to membrane invagination and eventual cell lysis.²⁷ In light of the hemolytic effects of CDs, research in the field is focused on the modification of CDs to reduce their interactions with RBCs. For example, Uekama and coworkers were able to significantly hinder the hemolytic effects of heptakis(2,6-di-*O*-methyl)- β -cyclodextrin (DM- β -CyD) by introducing acetyl groups to the hydroxyl groups at the 3-position of the glucose units.²⁴ Hence, at 100 mM of CD concentration, a concentration where 100% hemolysis occurs for all CDs, the modified form of DM- β -CyD was shown to cause no perceivable hemolysis.

2.4.2 *β -lap oxidation of hemoglobin and potential anemia*

While the hemolysis observed as a result of incubation with β -lap•HP β -CD can be attributed to the solubilization vehicle used, β -lap was shown to interact with RBCs, specifically hemoglobin, through oxidation of the iron component of Hb (Fe^{2+} to Fe^{3+}). During UV-Vis scans of lysed cells treated with β -lap•HP β -CD, two separate phenomena become apparent. The first consisted of an Hb characteristic λ_{max} shift from 415 nm to 408 nm. The second consisted of the appearance of a new Hb peak at 628 nm in samples where hemolysis occurred as a result of incubation with β -lap•HP β -CD. Work by Matsuda and coworkers elucidated, through a series of studies involving slab optical waveguide (SOWG) spectroscopy, the adsorption and reduction processes of hemoglobin.²⁸ In this study, a peak shift to about 406 nm led the researchers to conclude that the adsorbed hemoglobin was actually an oxidized form of hemoglobin known as methemoglobin (metHb), a ferric (Fe^{3+}) form of the protein. The emergence of a new peak at 628 nm is also a telltale sign that is highly indicative of the presence of methemoglobin, as corroborated by Baseman and coworkers²⁹ as well as Tromberg et al.³⁰ The precise mechanism by which β -lap converts the ferrous form of hemoglobin to methemoglobin has not been thoroughly examined, but the belief involves metabolism of the drug by enzymes located in RBCs.³¹ It is now well known that β -lap is metabolized into at least 6 distinct metabolites upon incubation with RBCs.³² More importantly, the fact that RBCs contain cytochrome P450-like activity may hint at the fact that the drug is reduced in RBCs, whereby oxygen radicals are produced that can convert hemoglobin to methemoglobin.

Methemoglobinemia is a naturally occurring condition that results from the oxidation of the ferrous component of hemoglobin. The effects of methemoglobinemia

include abnormal oxygen affinity and a decreased ability to carry oxygen, with the end result being tissue hypoxia.³⁰ A number of different pathways exist to reduce methemoglobin back to hemoglobin enzymatically.²⁸ Methylene blue can be used to reduce methemoglobin back to its physiologically active state.³⁰ Nevertheless, methemoglobinemia is a serious condition that warrants attention, specifically when designing a drug delivery vehicle for an agent such as β -lap.

Clinically, methemoglobinemia manifests itself depending on the degree of severity. For mild methemoglobinemia, symptoms include skin discoloration, headaches, and dyspnea or difficulty breathing.³³ In the most severe cases, methemoglobinemia results in tachypnea, acidosis, seizures, and death.³⁴ Following injection of ARQ 501 into mice at doses close to and above the maximum tolerated dose (MTD), the mice react in a severe form to the drug, and we believe that this reaction may be brought about by methemoglobinemia. The reaction of the mice to ARQ 501 includes heavy and difficult breathing, fatigue, and eventual seizures. It is also believed that β -lap toxicity may stem from complications involving ischemia-reperfusion. β -Lap-induced cell death is very similar to cell death arising from ischemia-reperfusion, in that ROS cause DNA breaks that surpass a certain threshold, leading to PARP-1 hyperactivation, a known cellular response to ischemia-reperfusion.⁵ This condition may also explain the symptoms observed in mice following β -lap administration, although a more thorough investigation is warranted. It is important to note at this time that the polymer micelles involved in this study are designed to entrap β -lap within its hydrophobic core, thereby preventing its interaction with blood components, and should prevent methemoglobinemia and other side-effects brought about by the drug.

2.4.3 *β -lap•HP β -CD is rapidly cleared from blood and distributes evenly among organs*

Once injected intravenously, β -lap•HP β -CD was found to be very short-lived in the blood, with a long phase half-life of approximately 24 minutes and a clearance of roughly $14 \text{ L h}^{-1} \text{ Kg}^{-1}$, agreeing well with previously reported data concerning cyclodextrin pharmacokinetics.^{35,36} Lerk and coworkers studied the pharmacokinetics of β -CD and HP β -CD in the rat, and found that the half-life of HP β -CD was approximately 23 min.³⁵ Jin et al. found that baicalein complexed with HP β -CD was cleared extremely fast, with concentrations dropping to barely detectable levels 30 min after injection.³⁶ Previous work in our laboratory showed that the binding constant of β -lap with HP β -CD is $1.1 \times 10^{-3} \text{ M}^{-1}$.¹⁵ The relatively weak binding affinity may result in fast β -lap dissociation from HP β -CD upon IV injection. Taken together, the very short blood half-lives indicate a very fast distribution of the drug into the different organs of the mouse, which was shown in the present study with β -lap, where the drug evenly distributed in the organs in a matter of minutes following injection. Meijer and coworkers were able to show that two model drugs, naproxen and flurbiprofen, distributed relatively evenly among the liver, kidney, and spleen 10 min after injection.³⁷ The implications for very rapid elimination of the drug from the blood and equally rapid distribution into the organs are detrimental to therapy for two reasons. Firstly, the drug does not have enough time to accumulate at the tumor site and exert its effects. This was shown herein, where tumor concentrations of β -lap were much lower than those of other organs. Secondly, the rapid distribution of drug into organs has the potential to lead to substantial toxicity in healthy

tissues and organs. Results from this study show that β -lap accumulated in all organs, including the brain and heart, within minutes after administration.

Research by Meijer and coworkers,³⁷ as well as Gibaud et al.,³⁸ have attempted to shed light on the in vivo disposition of cyclodextrin-complexed drugs. Both groups were able to show that cyclodextrin complexation indeed changed the pharmacokinetics of the drug, with concentrations proving higher in all organs as compared to free drug alone. However, the difference is not immensely significant, leading to the conclusion that upon IV administration, only a small amount of drug remains in the complexed form. Upon injection, HP β -CD and plasma proteins compete for drug binding, as does cholesterol and drug for HP β -CD. Therefore, in vivo fate of complexed drugs depends more on complexation efficiency and the affinity of the drug for plasma proteins. Increases in organ concentrations may be due to the ability of CDs to shuttle drugs to biological membranes more efficiently than plasma proteins.³⁷

2.4.4 β -lap micelles display prolonged blood residence and distribute to specific organs

Currently, nanocomposite materials such as polymer-drug conjugates,³⁹ liposomes,⁴⁰ and polymer micelles,⁴¹ are emerging as powerful nanomedicine platforms. Polymer micelles are supramolecular core-shell structures that prove highly advantageous for drug delivery purposes given their ability to encapsulate hydrophobic anticancer agents within a small-sized (10-100 nm) and stable structure. Moreover, the presence of polyethylene glycol (PEG) on their exterior corona, as well as their small size, proves beneficial with regards to enhancing the carrier's pharmacokinetics. PEG on the surface

of micelles hinders recognition and subsequent uptake by macrophages of the reticuloendothelial system (RES) and prevents micellar aggregation.⁴² Additionally, their small size range allows them to evade filtration by the kidneys, all the while avoiding uptake by macrophages that attempt to engulf larger, foreign particles in the bloodstream.⁴³ Last but not least, the small size of polymer micelles should contribute to their preferential accumulation in tumors through the enhanced permeability and retention (EPR) effect.⁴⁴

In this study, β -lap polymer micelles were shown to be long-lived in the bloodstream, with an elimination phase half-life of 28 h. Moreover, 20% of the injected dose was still present in blood stream 24 h after injection. This agrees fairly well with similar studies concerning micelle pharmacokinetics. Kataoka and coworkers, while examining the pharmacokinetics of poly(ethylene glycol)–poly(D,L-lactide) PEG-PDLLA, were able to show that 25% of the injected micelles were found in blood 24 h after injection. The authors also reported a long half-life, $t_{1/2,\beta}$, of approximately 19 h. The long mean residence times of micelles in the blood is very beneficial for therapeutic purposes, given that micelles will be able to circulate for longer periods of time, all the while increasing the possibility of extravasating to tumor sites in multiple passes.

It is well known that the reticuloendothelial system is part of the immune system and consists of monocytes and macrophages in the spleen, and Kupffer cells of the liver. In this study, β -lap polymer micelles were shown to accumulate mostly in the aforementioned organs, with data agreeing well with previous findings concerning micellar distribution following IV injection. Kataoka and coworkers have thoroughly investigated the pharmacokinetics of micelles in several studies, examining a wide array

of drugs and block copolymers.⁴⁵⁻⁴⁷ In the aforementioned system consisting of PEG-PDLLA block copolymer, Kataoka et al. showed accumulation of the micelles in the liver and spleen at low %ID values of 6-8% and 0.8-1%, respectively.⁴⁷ These values are very close to the %ID observed in this study, which were 7-8% and 1-2% for liver and spleen, respectively. The reason for the low percentage of initial dose in these organs is most likely due to the small size of β -lap micelles, which were shown to be approximately 30 nm in diameter (Chapter 3), akin to the size of those used in Kataoka's PEG-PDLLA study. It has been shown that micelles with diameters larger than 100 nm result in an increase in liver and spleen accumulation, reaching values of 20-40%.⁴⁷ Moreover, the reduced uptake of micelles in these organs also serves to corroborate the core-shell morphology of the β -lap polymer micelles, where the hydrophobic PLA core is shielded by an outer corona of PEG, effectively minimizing opsonization by the complement system of the RES. It is important to note at this time that in another study, where cisplatin was incorporated into poly-(ethylene glycol)-poly(glutamic acid) block copolymers, Kataoka and coworkers showed that the accumulation of micelles in these two organs gradually increased from 3 min to 24 h, mirroring our own findings.⁴⁶ This is most likely due to the prolonged blood residence time of the resulting β -lap polymer micelles.

Of immense importance to the field of micellar drug delivery is the potential for accumulation of micelles in organs where toxicity may arise. In this study, it was shown that micelles did not accumulate to a large degree in the heart, lungs, or muscle, and was negligible in the brain. The minimal uptake of micelles in the brain is expected however, given that the size of the micelles is too large to pass through the blood brain barrier.

The extent at which β -lap micelles accumulate in tumors is of immense importance to the eventual clinical translation of β -lap therapeutics. In this study, we showed a comparatively higher accumulation of β -lap micelles in tumors. This high collection of micelles within the tumor is most likely due to the enhanced permeability and retention (EPR) effect observed in tumors. It is now well known that the EPR effect, also known as passive targeting, arises from the fact that tumor blood vessels are unusually 'leaky' when compared to normal blood vessels because of their ongoing angiogenic state.^{48,49} It has been shown that fenestrations in tumor vasculature can be as big as 550 nm,⁵⁰ which should allow for extravasation and accumulation of the 30 nm-sized β -lap micelles. Moreover, this amassing of micelles within the tumor seemed constant over a 24 h time course, increasing only slightly. The slight increase in micelle collection in the tumor at the 24 h timepoint may be a result of the increased blood residence time of the micelles. The constant values of the micelles within the tumor agree well with findings suggesting that the lymphatic drainage of tumor tissue is impaired.⁵¹ Hence, β -lap micelles can reside in the tumor tissue for longer times, undergoing a slower elimination rate than would normally occur in organs such as the lungs and kidney. Taken together, these data suggest that β -lap micelles would effectively extravasate to tumors, accumulate to a greater extent over time, and remain within the tumor for prolonged times, all the while exerting antitumor effects through drug release.

2.5 Conclusions

Results from this study serve to shed light on the potentially fatal toxic side effects from a clinical formulation of β -lap, ARQ 501. We have shown that the delivery vehicle, and not the drug, is the major cause of hemolysis. However, it was shown that β -lap oxidizes the ferrous form of hemoglobin, bringing about a conversion to methemoglobin. Pharmacokinetically, complexation of the drug led to a rapid blood clearance of the drug, as well as a high and equal distribution of the drug to the different organs of the body. Conversely, incorporation of β -lap within polymer micelles increased the blood residence time of the drug and led to heightened accumulation within the tumor, all the while avoiding uptake in vital organs.

2.6 Acknowledgements

We wish to thank Dr. Noelle Williams and the Preclinical Pharmacology Core Laboratory at the University of Texas Southwestern Medical Center at Dallas for analysis of β -lap•HP β -CD pharmacokinetics. We also wish to thank Dr. Erik A. Bey for assistance with animal experiments, as well as Dr. Su-Guen Yang and Dr. Jagadeesh Setti Guthi for assistance with β -lap micelle pharmacokinetic experiments. This work was supported by NIH grants CA122994 and CA102792, as well as DOD grant W81XWH-04-1-0164. Elvin Blanco is grateful for the support of a minority supplement grant from the NIH, as well as predoctoral DOD grant BC043453.

2.7 References

1. O'Mahony D, Kummar S, Gutierrez ME. Non-small-cell lung cancer vaccine therapy: a concise review. *J Clin Oncol* 2005;23(35):9022-8.

2. Bouchard N, Laberge F, Raby B, Martin S, Lacasse Y. Adjuvant chemotherapy in resected lung cancer: two-year experience in a university hospital. *Can Respir J* 2008;15(5):270-4.
3. Pfister DG, Johnson DH, Azzoli CG, Sause W, Smith TJ, Baker S, Jr., Olak J, Stover D, Strawn JR, Turrisi AT and others. American Society of Clinical Oncology treatment of unresectable non-small-cell lung cancer guideline: update 2003. *J Clin Oncol* 2004;22(2):330-53.
4. Silvestri GA, Rivera MP. Targeted therapy for the treatment of advanced non-small cell lung cancer: a review of the epidermal growth factor receptor antagonists. *Chest* 2005;128(6):3975-84.
5. Bentle MS, Reinicke KE, Bey EA, Spitz DR, Boothman DA. Calcium-dependent modulation of poly(ADP-ribose) polymerase-1 alters cellular metabolism and DNA repair. *J Biol Chem* 2006;281(44):33684-96.
6. Bey EA, Bentle MS, Reinicke KE, Dong Y, Yang CR, Girard L, Minna JD, Bornmann WG, Gao J, Boothman DA. An NQO1- and PARP-1-mediated cell death pathway induced in non-small-cell lung cancer cells by beta-lapachone. *Proc Natl Acad Sci U S A* 2007;104(28):11832-7.
7. Pink JJ, Planchon SM, Tagliarino C, Varnes ME, Siegel D, Boothman DA. NAD(P)H:Quinone oxidoreductase activity is the principal determinant of beta-lapachone cytotoxicity. *J Biol Chem* 2000;275(8):5416-24.
8. Planchon SM, Pink JJ, Tagliarino C, Bornmann WG, Varnes ME, Boothman DA. beta-Lapachone-induced apoptosis in human prostate cancer cells: involvement of NQO1/xip3. *Exp Cell Res* 2001;267(1):95-106.

9. Reinicke KE, Bey EA, Bentle MS, Pink JJ, Ingalls ST, Hoppel CL, Misico RI, Arzac GM, Burton G, Bornmann WG and others. Development of beta-lapachone prodrugs for therapy against human cancer cells with elevated NAD(P)H:quinone oxidoreductase 1 levels. *Clin Cancer Res* 2005;11(8):3055-64.
10. Ough M, Lewis A, Bey EA, Gao J, Ritchie JM, Bornmann W, Boothman DA, Oberley LW, Cullen JJ. Efficacy of beta-lapachone in pancreatic cancer treatment: exploiting the novel, therapeutic target NQO1. *Cancer Biol Ther* 2005;4(1):95-102.
11. Li P, Zhao L, Yalkowsky SH. Combined effect of cosolvent and cyclodextrin on solubilization of nonpolar drugs. *J Pharm Sci* 1999;88(11):1107-11.
12. Loftsson T. Cyclodextrins and the Biopharmaceutics Classification System of Drugs. *J Incl Phenom Macro* 2002;44(1-4):63-67.
13. Rao VM, Stella VJ. When can cyclodextrins be considered for solubilization purposes? *J Pharm Sci* 2003;92(5):927-32.
14. Szejtli J. Introduction and General Overview of Cyclodextrin Chemistry. *Chem Rev* 1998;98(5):1743-1754.
15. Nasongkla N, Wiedmann AF, Bruening A, Beman M, Ray D, Bornmann WG, Boothman DA, Gao J. Enhancement of solubility and bioavailability of beta-lapachone using cyclodextrin inclusion complexes. *Pharm Res* 2003;20(10):1626-33.
16. Hartner L, Rosen L, Hensley M, Mendelson D, Staddon A, Chow W, Kovalyov O, Ruka W, Skladowski K, Jagiello-Grusfeld A and others. Phase 2 dose multi-

- center, open-label study of ARQ 501, a checkpoint activator, in adult patients with persistent, recurrent or metastatic leiomyosarcoma (LMS). *Journal of Clinical Oncology*, 2007 ASCO Annual Meeting Proceedings Part I. 2007;25(18S):20521.
17. Kawecki A, Adkins DR, Cunningham CC, Vokes E, Yagovane DM, Dombal G, Koralewski P, Hotko Y, Vladimirov V. A phase II study of ARQ 501 in patients with advanced squamous cell carcinoma of the head and neck. *J Clin Oncol (Meeting Abstracts)* 2007;25(18_suppl):16509-.
 18. Khong HT, Dreisbach L, Kindler HL, Trent DF, Jeziorski KG, Bonderenko I, Popiela T, Yagovane DM, Dombal G. A phase 2 study of ARQ 501 in combination with gemcitabine in adult patients with treatment naive, unresectable pancreatic adenocarcinoma. *J Clin Oncol (Meeting Abstracts)* 2007;25(18_suppl):15017-.
 19. Li C, Nemunaitis J, Senzer N, Edelman G, Glasner S, Dombal G, Dovholuk A, Cunningham C. A phase Ib trial of ARQ 501, a selective checkpoint activator, in combination with docetaxel in patients with advanced solid tumors. *J Clin Oncol (Meeting Abstracts)* 2006;24(18_suppl):13053-.
 20. Planchon SM, Wuerzberger S, Frydman B, Witiak DT, Hutson P, Church DR, Wilding G, Boothman DA. Beta-lapachone-mediated apoptosis in human promyelocytic leukemia (HL-60) and human prostate cancer cells: a p53-independent response. *Cancer Res* 1995;55(17):3706-11.

21. Shuai X, Ai H, Nasongkla N, Kim S, Gao J. Micellar carriers based on block copolymers of poly(epsilon-caprolactone) and poly(ethylene glycol) for doxorubicin delivery. *J Control Release* 2004;98(3):415-26.
22. Blanco E, Bey EA, Dong Y, Weinberg BD, Sutton DM, Boothman DA, Gao J. Beta-lapachone-containing PEG-PLA polymer micelles as novel nanotherapeutics against NQO1-overexpressing tumor cells. *J Control Release* 2007;122(3):365-74.
23. Kang J, Kumar V, Yang D, Chowdhury PR, Hohl RJ. Cyclodextrin complexation: influence on the solubility, stability, and cytotoxicity of camptothecin, an antineoplastic agent. *Eur J Pharm Sci* 2002;15(2):163-70.
24. Hirayama F, Mieda S, Miyamoto Y, Arima H, Uekama K. Heptakis(2,6-di-O-methyl-3-O-acetyl)-beta-cyclodextrin: A water-soluble cyclodextrin derivative with low hemolytic activity. *J Pharm Sci* 1999;88(10):970-5.
25. Motoyama K, Arima H, Toyodome H, Irie T, Hirayama F, Uekama K. Effect of 2,6-di-O-methyl-alpha-cyclodextrin on hemolysis and morphological change in rabbit's red blood cells. *Eur J Pharm Sci* 2006;29(2):111-9.
26. Ohtani Y, Irie T, Uekama K, Fukunaga K, Pitha J. Differential effects of alpha-, beta- and gamma-cyclodextrins on human erythrocytes. *Eur J Biochem* 1989;186(1-2):17-22.
27. Shiotani K, Uehata K, Irie T, Uekama K, Thompson DO, Stella VJ. Differential effects of sulfate and sulfobutyl ether of beta-cyclodextrin on erythrocyte membranes in vitro. *Pharm Res* 1995;12(1):78-84.

28. Matsui M, Nakahara A, Takatsu A, Kato K, Matsuda N. In Situ Observation of Reduction Behavior of Hemoglobin Molecules Adsorbed on Glass Surface. *IEICE Trans Electron* 2006;E89-C(12):1741-1745.
29. Kannan TR, Baseman JB. Hemolytic and Hemoxidative Activities in *Mycoplasma penetrans*. *Infect. Immun.* 2000;68(11):6419-6422.
30. Lee J, El-Abaddi N, Duke A, Cerussi AE, Brenner M, Tromberg BJ. Noninvasive in vivo monitoring of methemoglobin formation and reduction with broadband diffuse optical spectroscopy. *J Appl Physiol* 2006;100(2):615-22.
31. Miao XS, Song P, Savage RE, Zhong C, Yang RY, Kizer D, Wu H, Volckova E, Ashwell MA, Supko JG and others. Identification of the in vitro metabolites of 3,4-dihydro-2,2-dimethyl-2H-naphthol[1,2-b]pyran-5,6-dione (ARQ 501; beta-lapachone) in whole blood. *Drug Metab Dispos* 2008;36(4):641-8.
32. Yang RY, Kizer D, Wu H, Volckova E, Miao XS, Ali SM, Tandon M, Savage RE, Chan TC, Ashwell MA. Synthetic methods for the preparation of ARQ 501 (beta-Lapachone) human blood metabolites. *Bioorg Med Chem* 2008;16(10):5635-43.
33. Wurdeman RL, Mohiuddin SM, Holmberg MJ, Shalaby A. Benzocaine-induced methemoglobinemia during an outpatient procedure. *Pharmacotherapy* 2000;20(6):735-8.
34. Hahn IH, Hoffman RS, Nelson LS. EMLA-induced methemoglobinemia and systemic topical anesthetic toxicity. *J Emerg Med* 2004;26(1):85-8.

35. Frijlink HW, Visser J, Hefting NR, Oosting R, Meijer DK, Lerk CF. The pharmacokinetics of beta-cyclodextrin and hydroxypropyl-beta-cyclodextrin in the rat. *Pharm Res* 1990;7(12):1248-52.
36. Liu J, Qiu L, Gao J, Jin Y. Preparation, characterization and in vivo evaluation of formulation of baicalein with hydroxypropyl-beta-cyclodextrin. *Int J Pharm* 2006;312(1-2):137-43.
37. Frijlink HW, Franssen EJ, Eissens AC, Oosting R, Lerk CF, Meijer DK. The effects of cyclodextrins on the disposition of intravenously injected drugs in the rat. *Pharm Res* 1991;8(3):380-4.
38. Ben Zirar S, Astier A, Muchow M, Gibaud S. Comparison of nanosuspensions and hydroxypropyl-beta-cyclodextrin complex of melarsoprol: Pharmacokinetics and tissue distribution in mice. *Eur J Pharm Biopharm* 2008.
39. Duncan R. Polymer conjugates as anticancer nanomedicines. *Nat Rev Cancer* 2006;6(9):688-701.
40. Torchilin VP. Recent advances with liposomes as pharmaceutical carriers. *Nat Rev Drug Discov* 2005;4(2):145-60.
41. Sutton D, Nasongkla N, Blanco E, Gao J. Functionalized micellar systems for cancer targeted drug delivery. *Pharm Res* 2007;24(6):1029-46.
42. Torchilin VP. PEG-based micelles as carriers of contrast agents for different imaging modalities. *Adv Drug Deliv Rev* 2002;54(2):235-52.
43. Nishiyama N, Kataoka K. Current state, achievements, and future prospects of polymeric micelles as nanocarriers for drug and gene delivery. *Pharmacol Ther* 2006;112(3):630-48.

44. Torchilin VP. Micellar nanocarriers: pharmaceutical perspectives. *Pharm Res* 2007;24(1):1-16.
45. Nishiyama N, Kato Y, Sugiyama Y, Kataoka K. Cisplatin-loaded polymer-metal complex micelle with time-modulated decaying property as a novel drug delivery system. *Pharm Res* 2001;18(7):1035-41.
46. Nishiyama N, Okazaki S, Cabral H, Miyamoto M, Kato Y, Sugiyama Y, Nishio K, Matsumura Y, Kataoka K. Novel cisplatin-incorporated polymeric micelles can eradicate solid tumors in mice. *Cancer Res* 2003;63(24):8977-83.
47. Yamamoto Y, Nagasaki Y, Kato Y, Sugiyama Y, Kataoka K. Long-circulating poly(ethylene glycol)-poly(D,L-lactide) block copolymer micelles with modulated surface charge. *J Control Release* 2001;77(1-2):27-38.
48. Hashizume H, Baluk P, Morikawa S, McLean JW, Thurston G, Roberge S, Jain RK, McDonald DM. Openings between defective endothelial cells explain tumor vessel leakiness. *Am J Pathol* 2000;156(4):1363-80.
49. Maeda H. The enhanced permeability and retention (EPR) effect in tumor vasculature: the key role of tumor-selective macromolecular drug targeting. *Adv Enzyme Regul* 2001;41:189-207.
50. Jain RK, di Tomaso E, Duda DG, Loeffler JS, Sorensen AG, Batchelor TT. Angiogenesis in brain tumours. *Nat Rev Neurosci* 2007;8(8):610-22.
51. Maeda H, Wu J, Sawa T, Matsumura Y, Hori K. Tumor vascular permeability and the EPR effect in macromolecular therapeutics: a review. *J Control Release* 2000;65(1-2):271-84.

CHAPTER THREE

Development and Characterization of β -Lapachone Micelle Nanotherapeutics**3.1 Introduction**

Presently, the development of integrated cancer nanomedicine, which consists of drugs that exploit cancer-specific molecular targets combined with effective carriers for tumor-targeted drug delivery, has shown significant promise in expanding therapeutic indices for chemotherapy. β -Lapachone (β -lap) (Figure 3.1A) is a novel, plant-derived anticancer drug whose cytotoxic effect is significantly enhanced by NAD(P)H:quinone oxidoreductase 1 (NQO1), a flavoprotein found overexpressed (up to 20-fold) in a variety of human cancers, including those of the lung,¹ prostate,² pancreas,³ and breast.⁴ Upon administration of β -lap, NQO1 induces a futile cycling of β -lap that depletes the cell of NAD(P)H and leads to the generation of DNA damaging hydroxyl radicals.⁵ Additionally, β -lap treatment leads to an NQO1-dependent rise in cytosolic Ca^{2+} that results in the loss of mitochondrial membrane potential, ATP depletion, unique substrate proteolysis, DNA fragmentation, and cell apoptosis.⁶ The mechanism of action is independent of caspases, p53 status, and cell cycle stage.⁷ Given its central role in β -lap-mediated lethality, NQO1 is a vital, exploitable target for the treatment of cancer cells that overexpress this enzyme.

While β -lap proves to be a very promising agent from a pharmacodynamic standpoint, several factors hinder conventional intravenous administration for preclinical evaluation and clinical translation. Firstly, its non-specific distribution can lead to low tumor concentrations and systemic toxicity.⁸ Moreover, its polycyclic nature makes it

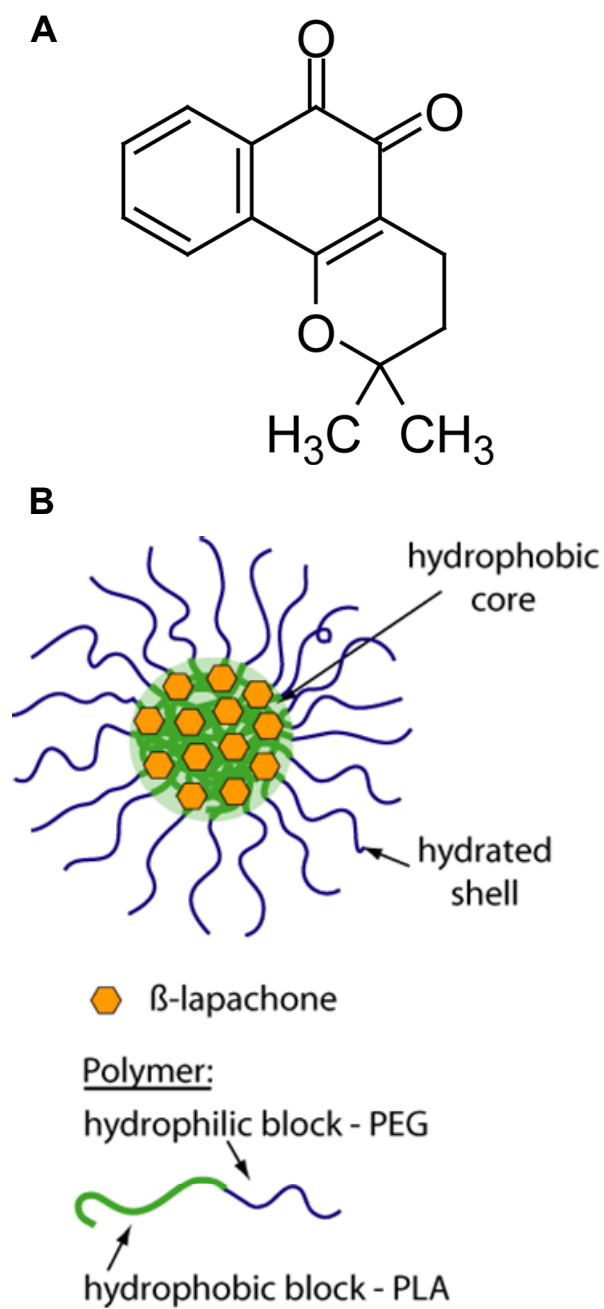


Figure 3.1. (A) Chemical structure of β -lap (MW = 242 Da). (B) Schematic of a β -lap-containing polymer micelle and constituent components.

highly hydrophobic, with an aqueous solubility of 0.04 mg/mL.⁹ Prior work by our laboratory focused on attempts to increase the aqueous solubility of β -lap through its complexation with hydroxypropyl- β -cyclodextrin (HP β -CD). However, the fast dissociation of β -lap and cyclodextrin makes the drug susceptible to aggregation and rapid clearance, suggesting for the use of an effective nanotherapeutic delivery vehicle that can efficiently solubilize the drug and deliver it to solid tumors.

Polymer micelles are spherical, nanosized (10-100 nm) supramolecular constructs that are garnering significant attention as a versatile drug delivery platform for cancer therapy.¹⁰⁻¹² Polymer micelles have a unique core-shell structure as a result of the self-assembly of amphiphilic block copolymers in aqueous environments (Figure 3.1B). The hydrophobic core acts as a solubilizing reservoir for water insoluble drugs, such as β -lap, providing protection from enzymatic degradation and inactivation.¹³ The hydrophilic micellar corona, in turn, forms a hydrating layer on the surface of the micelle that hinders plasma protein adsorption and subsequent rapid phagocytic clearance by the reticuloendothelial system (RES).¹⁴ Additionally, small micellar size, along with low critical micelle concentrations (CMCs), result in long-circulating, stable constructs that do not easily dissociate *in vivo*,¹⁵ and contribute to the preferential accumulation of micelles in tumor tissue through the enhanced permeability and retention (EPR) effect.^{16,17}

To exploit these numerous advantages of polymer micelles, our objective was to develop β -lap-containing micelles for an NQO1-specific therapy. In this study, we report the development of a film sonication method to fabricate β -lap micelles with relatively high loading of the drug, adequate micelle size, core-shell formation, and favorable

release characteristics. Using three different cancer cell lines, β -lap micelle treatment showed a substantial increase in cytotoxicity in NQO1+ cells over NQO1- cells, highlighting the system as a potential treatment strategy against NQO1-overexpressing tumors.

3.2 Materials and Methods

3.2.1 Materials

β -Lap was synthesized following a previously reported procedure.¹⁸ PEG5k-PLA5k block copolymer (Mn = 10,000 Da) was synthesized utilizing a ring-opening polymerization procedure published previously.¹⁹ Poly(D,L-lactide) (PLA) (Mn = 27,344 Da) was purchased from Birmingham Polymers (Pelham, AL). All organic solvents were of analytical grade. H596 non-small cell lung carcinoma (NSCLC) cells, DU-145 prostate, and MDA-MB-231 breast cancer cells, were grown in DMEM with 10% fetal bovine serum, 2 mM L-glutamine, 100 units/mL penicillin, and 100 mg/mL streptomycin at 37°C in a humidified incubator with a 5% CO₂-95% air atmosphere. All cells were routinely found free of mycoplasma infection.

3.2.2 Differential scanning calorimetry (DSC) analysis

DSC measurements of the solid-state solubility of β -lap in PLA were performed using a Shimadzu Differential Scanning Calorimeter (DSC-60, Columbia, USA) with samples under a nitrogen atmosphere. The procedure was adapted from a method published by Panyam et al.²⁰ and previously utilized by our laboratory to determine the solid-state solubility of β -lap in poly(D,L-lactide-*co*-glycolide) (PLGA).²¹ Briefly,

known quantities of β -lap (13 mg) and PLA (27.8 mg) were separately dissolved in acetone. Different amounts of drug were mixed with polymer, and transferred to aluminum pans. The solvent was then evaporated, and pans were crimped and weighed. Samples were heated to 180°C at a rate of 10°C/min. The heats of melting of β -lap were obtained using the peak integration calculation method provided by the DSC software. The solid-state solubility value of β -lap was determined by plotting enthalpy values as a function of the percentage of β -lap loading. The X-intercept resulting from a linear regression of the data represents the solid state solubility value of β -lap in PLA.

3.2.3 *β -Lap micelle fabrication*

Three distinct micelle preparation methods (dialysis, solvent evaporation, film sonication) were used to encapsulate β -lap within PEG-PLA micelles. In the dialysis method, the drug and polymer were dissolved in acetone, placed within a dialysis bag (MW cutoff = 2,000 Da), and dialyzed against water overnight at 4°C. The solvent evaporation method consisted of dissolving β -lap and PEG-PLA in acetone and adding the mixture dropwise to water under sonication by a Fisher Scientific Sonic Dismembrator 60 (Hampton, NH) with an output power of 0.010 W, after which the solvent was allowed to evaporate overnight. Finally, the film sonication procedure involved the dissolution of β -lap and PEG-PLA in acetone and evaporation of the solvent, yielding a solid film. Water was then added to the film and sonicated for 5 min. In each case, drug-loaded polymer micelles were filtered through 0.45 μ m nylon filters to

remove non-encapsulated drug aggregates in solution, and all micelle preparations above were stored immediately at 4°C to hinder premature drug release.

Drug loading was determined by centrifuging 0.5 mL of micelle solution at a rotational speed of 2,000 RPM for 30 minutes at 4°C (Eppendorf Centrifuge 5804 R) using Amicon Ultra Centrifugal Filter Devices (MW cutoff = 100,000 Da). Absorbance of β -lap in the resulting supernatant was measured ($\lambda_{\text{max}} = 257.2$ nm, $\epsilon = 105$ mL/(cm·mg β -lap)) using a Perkin Elmer Lambda 20 UV-Vis Spectrophotometer (Fremont, CA). Micelle solutions were then lyophilized overnight and the resulting freeze-dried powder was accurately weighed, dissolved in chloroform, and analyzed via UV-Vis spectrophotometry to provide the total amount of β -lap (free and micelle encapsulated). Loading efficiency and density of β -lap were then determined utilizing the following set of equations:

$$\% \text{ drug loading efficiency} = \frac{\text{amount } \beta\text{-lap in micelles}}{\text{initial amount of } \beta\text{-lap in system}} \times 100 \quad (1)$$

$$\% \text{ drug loading density} = \frac{\text{amount } \beta\text{-lap in micelles}}{\text{amount of micelles - free } \beta\text{-lap}} \times 100 \quad (2)$$

Micelle fabrication experiments were conducted in triplicate and following data tabulation, statistical analyses between different groups were performed using a Student's two-tailed t-test ($P < 0.05$).

3.2.4 β -Lap micelle characterization

3.2.4.1 Size characterization

Following fabrication, micelle size was determined using a Viscotek Dynamic Light Scattering (DLS) instrument (Houston, TX). Scattered light was detected at a 90° angle. Data was obtained from 10 measurements of 5 s duration and averaged utilizing the instrumental software to determine micelle size and size distribution.

β -Lap micelle size was corroborated via transmission electron microscopy (TEM) with images obtained using a JEOL 1200 EX. Formvar coated-copper grids were glow discharged using a Vacuum Coating Unit. A glow discharged grid was allowed to float on a small drop of the micelle solution for 2 min, after which the excess liquid was removed by blotting the grid against a filter paper. The grid was then treated with 2% PTA solution for 30 s after being treated with the micelle solution. All TEM images of β -lap micelles were obtained at an accelerating voltage of 80 kV.

3.2.4.2 Core-shell morphology and drug encapsulation

Micelles were analyzed by $^1\text{H-NMR}$ to verify core-shell architecture. β -Lap-loaded PEG-PLA micelles were prepared using the film sonication technique at 10% w/w theoretical drug loading. Following micelle fabrication and filtration, the micelle solution was split among two Amicon Ultra Centrifugal Filter Devices (MW cutoff = 100,000 Da) and concentrated by centrifugation at a speed of 2,000 RPM at 4°C to minimize premature drug loss. Micelles were then washed with water to remove free drug. Once the absorbance of both supernatants was well below a value of 0.1, micelles were freeze-dried. One batch of micelles was resuspended in D_2O , while another batch was dissolved in deuterated chloroform. The two samples were then analyzed utilizing a 400-MHz Varian NMR spectrometer (Palo Alto, CA) and the resulting spectra were

compared to spectra obtained from β -lap dissolved in D₂O and PEG-PLA dissolved in chloroform.

3.2.4.3 Examination of β -lap release from micelles

Release studies of β -lap-containing PEG-PLA micelles were performed to examine β -lap release kinetics. Approximately 100 mg of β -lap-loaded polymer micelles were prepared utilizing the film sonication technique at a theoretical loading of 10% w/w. After micelle fabrication, the amount of loaded drug and micelles was determined, and equal amounts of micelles were aliquoted among Spectrum Float-A-Lyzer dialysis devices with a molecular weight cutoff of 100,000 Da. Release studies were conducted in triplicate in PBS at a pH of 7.4. At predetermined times, the buffer solution (12 mL) was removed and replaced with an equal amount of fresh buffer solution. The amount of β -lap released from micelles was determined by measuring the absorbance of the supernatant at 257.2 nm via UV-Vis spectrophotometry.

3.2.4.4 Modeling of β -lap release kinetics from micelles

Theoretical models were developed to simulate the drug release profiles from polymer micelles. Previous work has shown that drug release from a micelle core occurs in two successive stages: early release that can be well described by a Higuchi dissolution model (Equations 3 and 4) and late release that is well approximated by Fickian diffusion (Equation 5):²²

$$\frac{M(t)}{M(\infty)} = 1 - \left[\left(\frac{a'}{a_0} \right)^3 + \frac{1}{2} \frac{c_s}{c_0} \left(\left(\frac{a'}{a_0} \right) + \left(\frac{a'}{a_0} \right)^2 - 2 \left(\frac{a'}{a_0} \right)^3 \right) \right] \quad (3)$$

$$c_0 (a_0^3 + 2a'^3 - 3a_0 a'^2) + c_s \left(4a'^2 a_0 + a_0^3 \ln \frac{a_0}{a'} - a_0^3 - a_0^2 a' - 2a'^3 \right) = 6Dc_s a_0 t \quad (4)$$

$$\frac{M(t)}{M(\infty)} = p \left(1 - \frac{6}{\pi^2} \exp \left(\frac{-\pi^2 D t}{a_0^2} \right) \right) \quad (5)$$

where $M(t)$ is the mass of drug released at time t and $M(\infty)$ is the amount of drug released as time approaches infinity. The Higuchi model approximates drug release as a steadily moving front of dissolving drug moving inward from the periphery of the micelle core, where the drug is contained.²³ This model has five parameters: the radius of the micelle core, a_0 ; the distance of the moving front from the center of the core at time t , a' ; the initial micelle drug loading, c_0 ; the solubility of drug in solution, c_s ; and the diffusivity of the drug in the micelle core, D_h . Later drug release was shown to be correctly approximated by Fickian diffusion out of a sphere, which has three parameters: the fraction of the drug released at infinite time, p_0 ; the radius of the micelle core, a_0 ; and the diffusivity of drug in the micelle core, D_f .^{24,25} β -Lap solubility and micelle loading were known: $c_s = 0.04$ mg/mL and $c_0 = 8.68$ mg/mL. The radius of gyration of the 5 kD PEG corona (6.16 nm) was subtracted from the hydrodynamic micelle radius (14.6 nm) to determine the size of the micelle core, $a_0 = 8.44$ nm, as reported previously.²² The drug released by 360 hours was used as the drug released at infinite time, p_0 . Estimates of the two remaining unknowns, the rates of β -lap diffusion, D_h and D_f , were then calculated

using non-linear least squares parameter estimation (Matlab 7.1). D_h and D_f were estimated using release data from 0-18 and 18-360 hours, respectively.

3.2.5 Cytotoxicity of β -lap micelles in vitro

Relative survival assays based on DNA content were performed in three different cancer cell lines with isogenic expression (or inhibition of enzyme activities with dicoumarol) of NQO1 as previously described.⁵ H596 non-small cell lung cancer and MDA-MB-231 breast cancer cells contain homozygous *2 NQO1 polymorphisms and thereby lack NQO1 expression. Isogenic NQO1+ counterparts were generated and characterized for β -lap free drug responses as described.^{5,26} In contrast, DU-145 human prostate cancer cells endogenously over-express NQO1, and its enzyme activity can be blocked by coadministration of dicoumarol, mimicking an NQO1-deficient cell. Briefly, NQO1+ or NQO1- H596 and MDA-MB-231 cells were seeded (10,000 cells/well) into each well of 48-well plates. DU-145 cells were seeded similarly. On the following day, media were removed, and media containing predetermined doses of free β -lap drug or β -lap micelles (prepared via the film sonication method) were added for 2 h. For DU-145 cells, dicoumarol at a concentration of 40 μ M was coadministered to cells to inhibit NQO1. After 2 h exposures, media were then removed, control growth media added, and cells were allowed to grow for an additional 7 days. DNA content was determined by DNA fluorescence Hoescht dye 33258, using an adaptation of the method of Labarca and Paigen.²⁷ Samples were read in a Perkin Elmer HTS 7000 Bio Assay Reader (Waltham, MA) and data were expressed as means \pm SE relative growth and graphed as treated/control (T/C) values from six wells per treatment.

3.2.6 DNA damage and cell death assays

Distinct biological assays were conducted in NQO1+ and NQO1- H596 cells to corroborate the mechanism of action of β -lap-mediated cell death via micellar drug delivery versus responses known for free drug.^{7,26,28,29} The first consisted of reactive oxygen species (ROS) analyses. Following β -lap micelle exposure to cells, ROS formation was ascertained using the conversion of non-fluorescent 5, 6-Chloromethyl-2V, 7V-dichlorodihydrofluorescein diacetate (CM-H₂DCFDA) to its fluorescent derivative (DCF) by flow cytometry (FC-500 flow cytometer, Beckman Coulter Electronics, Miami, FL) as described.³⁰

DNA damage analyses, or alkaline comet assays, were also performed. DNA lesions, including DNA single and double strand breaks (SSBs, DSBs, respectively), as well as DNA base damage, were assessed in single cells treated with β -lap micelles using alkaline comet assays as previously described.^{28,31} Slides were stained with SYBR-green and visualized using a Nikon Eclipse TE2000-E fluorescence microscope (Melville, NY), after which digital photomicrographs were taken.

Lastly, nucleotide analyses were conducted, where changes in intracellular nicotinamide adenine dinucleotide (NAD⁺) levels were measured in cells after β -lap micelle exposure as described.²⁸ Intracellular NAD⁺ levels were expressed as percentage of treated divided by control (%T/C).

3.3 Results

3.3.1 Solubility of β -lap in PLA polymer

In order to gain insight into interactions between β -lap and the core-forming material (i.e. PLA), solid-state solubility studies were performed using DSC. Values of ΔH_m (J/g) were plotted as a function of β -lap loading percentage (Figure 3.2A). The X-intercept, provided by linear regression of the data, yields the solid-state solubility of β -lap in PLA at 31%. The dissolution behavior of β -lap within PLA helps to explain discrepancies in drug loading among the different micelle fabrication procedures. Close inspection of images of β -lap/PEG5k-PLA5k films at different loading percentages illustrate the dissolution of drug within the polymer (Fig. 3.2B). At levels below the solid-state solubility value, the drug and polymer appear as a continuous film. However, at higher loading percentages (20%), where relative β -lap to PLA density is 40%, β -lap crystals appeared in the film, indicative of drug loading above the solubility threshold of β -lap in PLA core.

3.3.2 *Effect of different micelle fabrication methods on drug loading*

Several different micelle fabrication techniques were examined with the purpose of generating β -lap micelles with an adequate size, yield, and drug loading density and efficiency. Table 1 depicts the size, yield, and loading values obtained from the three different fabrication methods. As shown in the table, from an initial 10% theoretical loading, the dialysis method produced micelles with an extremely low drug loading at $0.02 \pm 0.01\%$, as well as a poor loading efficiency ($0.08 \pm 0.04\%$) and micelle yield ($36.3 \pm 3.40\%$). The solvent evaporation procedure provided a marked improvement in β -lap loading over the dialysis method, with a loading percentage of $0.39 \pm 0.05\%$, but with a low loading efficiency of $4.12 \pm 0.64\%$. Conversely, the film sonication method

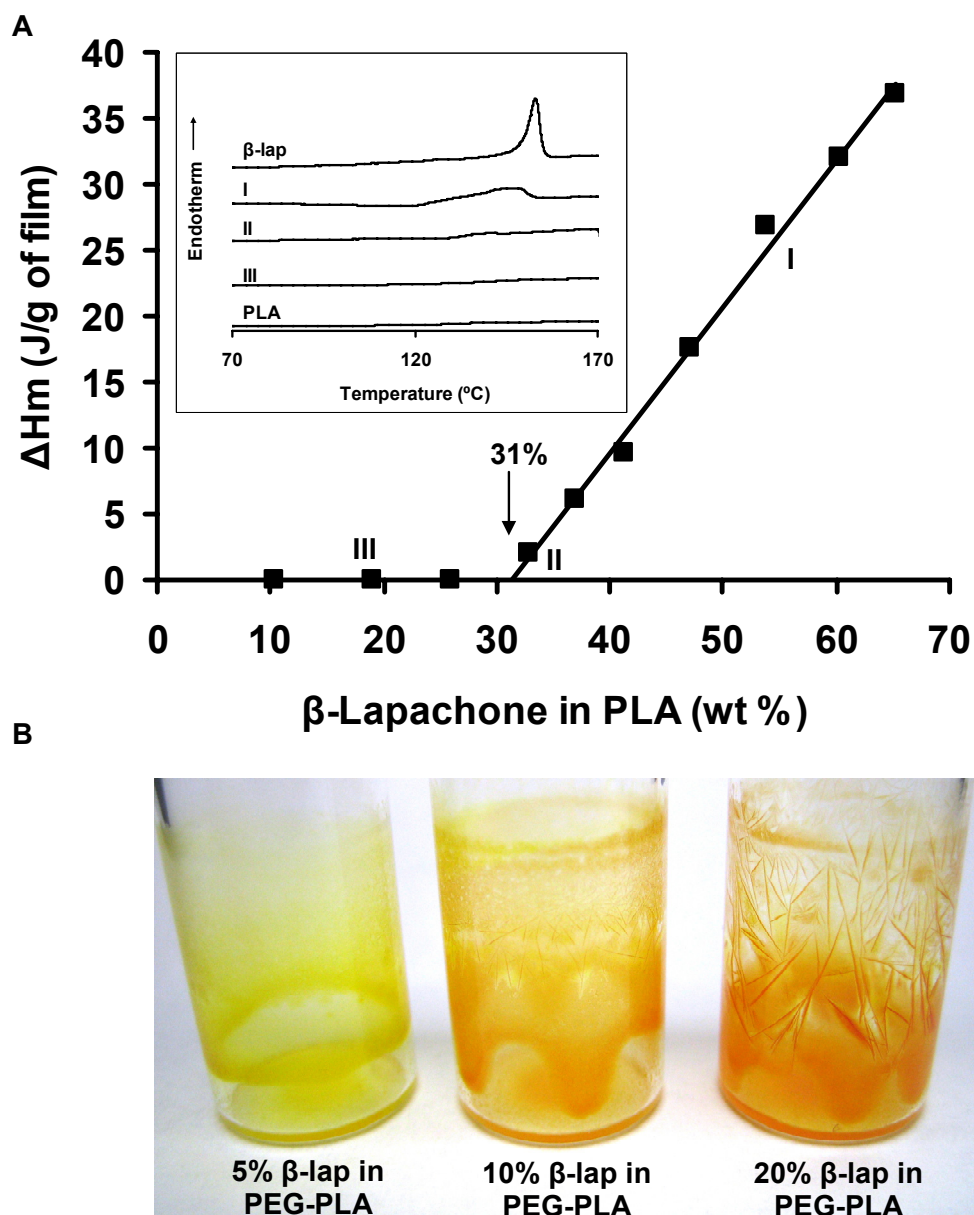


Figure 3.2. Solid state solubility studies of β -lap in PLA polymer. Figure 2A depicts β -lap melting enthalpy (ΔH_m) as a function of β -lap loading percentage. The X-intercept indicates the solubility limit of β -lap in PLA. Figure 2B represents images of β -lap and PLA films at different loading percentages for qualitative comparison.

Table 3.1 β -Lapchone micelle size, yield, and drug loading parameters from different fabrication procedures

Micelle fabrication method	Theoretical loading (%)	Micelle size (nm)	Yield (%)	efficiency (%)	Loading density (%)
Dialysis	10	23.3 \pm 1.2	36.3 \pm 3.4	0.08 \pm 0.04	0.02 \pm 0.01
Solvent evaporation	10	17.3 \pm 0.2	95.0 \pm 1.8	4.1 \pm 0.6	0.4 \pm 0.1
Film sonication	5	28.4 \pm 2.7	88.6 \pm 3.7	39.8 \pm 1.0	2.2 \pm 0.1
	10	29.6 \pm 1.5	85.3 \pm 6.7	41.9 \pm 5.6	4.7 \pm 1.0
	20	26.8 \pm 3.2	85.2 \pm 3.0	32.9 \pm 5.9	6.5 \pm 1.0

produced the highest β -lap loading of micelles among all three fabrication methods, with a $4.7 \pm 1.0\%$ drug loading at a theoretical loading of 10%, a loading efficiency of $41.9 \pm 5.6\%$, and a high micelle yield of $85.3 \pm 6.7\%$. With a subsequent increase in theoretical drug loading to 20%, β -lap loading in micelles increased to $6.5 \pm 1.0\%$. Meanwhile, a lowered loading efficiency to $32.9 \pm 5.9\%$ was observed at this composition. Taken together, these data highlight the effectiveness of the film sonication method at producing higher loaded β -lap micelles over other micelle fabrication methods, with differences in loading percentage values being statistically significant ($P < 0.05$).

3.3.3 Examination of β -lap crystal formation

During the course of experimentation, a phenomenon associated with crystallization of β -lap was observed (Figure 3.3) and is worth mentioning. As can be seen from Figure 3.3A, upon heating of the drug to temperatures equivalent to 68°C , the aqueous solubility of β -lap was increased. Therefore, initially the drug existed in a solubilized state, and DLS recordings of the sample registered only micelle within solution. However, upon cooling of the sample to RT, crystals with approximate dimensions of $250 \mu\text{m}$ in length and $3 \mu\text{m}$ (Figure 3.3B) in diameter began to appear in solution and precipitated to the bottom of the DLS cuvette following sample cooling. Work is currently underway to examine the tolerability of these crystals in vivo, and their therapeutic potential remains to be determined, but certainly opens an alternate avenue of therapy. For the subsequent characterization and animal studies, these crystals were removed as part of the filtering process and only β -lap micelles were used for therapeutic

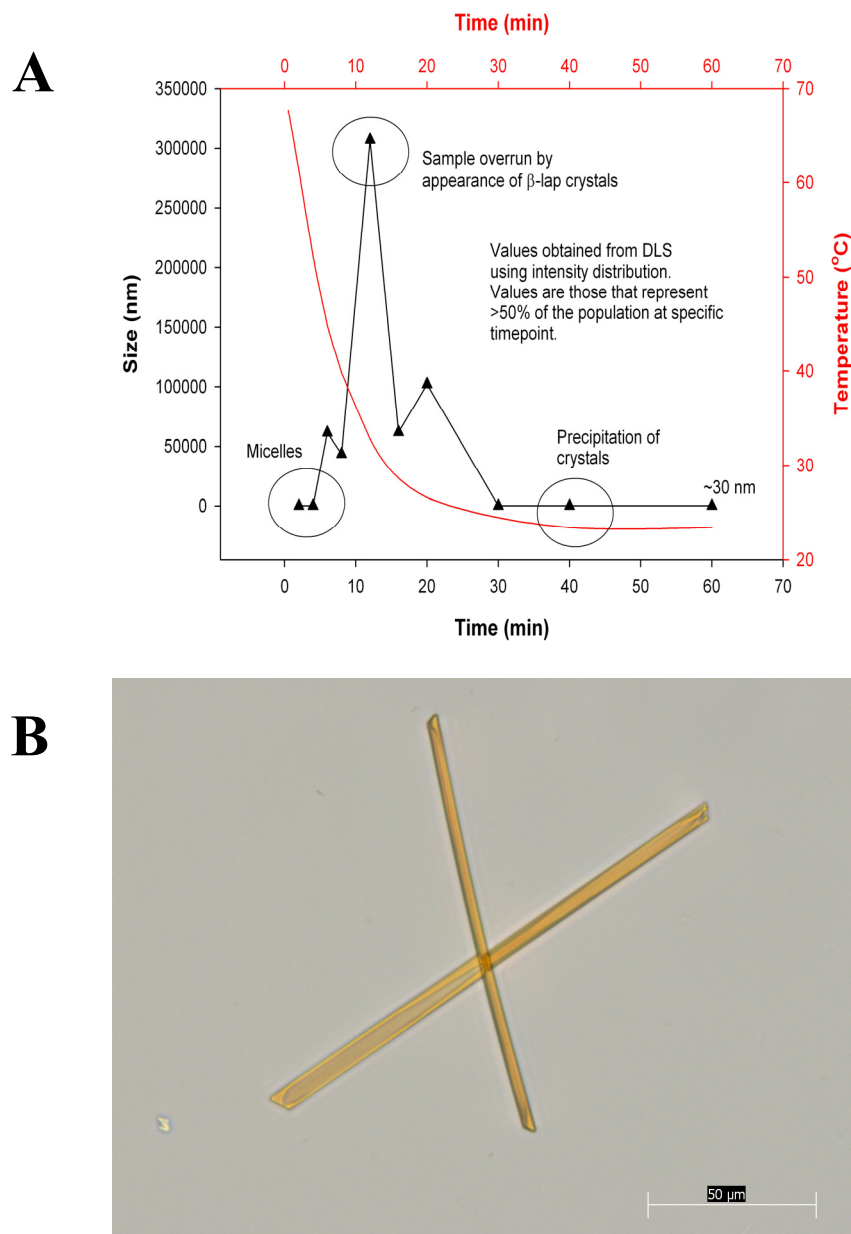


Figure 3.3. (A) DLS size measurements of a sample of micelles in which crystallization of β -lap can be observed to occur over time as a function of temperature. (B) A representative micrograph of β -lap crystals in solution. The scale bar represents 50 μ m.

evaluations.

3.3.4 *β -Lap micelle characterization*

Drug-loaded micelle size was determined utilizing dynamic light scattering (DLS) for each of the fabrication methods examined (Table 1). The three different methods all produced micelles of an adequate size (e.g. 10-100 nm), with the dialysis and solvent evaporation procedures yielding micelle sizes of 23.3 ± 1.2 nm and 17.3 ± 0.2 nm, respectively. The film sonication procedure produced micelles with a slightly greater average diameter (29.6 ± 1.5 nm), possibly due to the increased loading of the drug within the micelle core.³² Transmission electron microscopy examination of the β -lap micelles corroborates the size findings, showing micelles that measure ~ 30 nm in diameter and which are highly monodisperse (Figure 3.4). The TEM findings also serve to highlight the spherical nature of the micelles.

Encapsulation of β -lap inside micelle cores was demonstrated by comparing ^1H -NMR spectra of micelle samples in deuterated chloroform (CDCl_3) and deuterated water (D_2O) (Figure 3.5). In CDCl_3 , prominent resonance peaks of β -lap were observed in addition to those of PLA and PEG blocks, indicating that the micelle contains both copolymer and β -lap. In contrast, only the PEG resonance peaks were detected in D_2O , while both the PLA and β -lap resonance peaks were absent. The micelle shells consisting of PEG blocks were well solvated in D_2O and therefore showed clear ^1H -NMR signal. In contrast, when β -lap was encapsulated inside micelle cores, resonance peaks of PLA blocks and β -lap were not observed due to their insufficient chain motion in D_2O , demonstrating the core-shell structure of β -lap-loaded micelles.

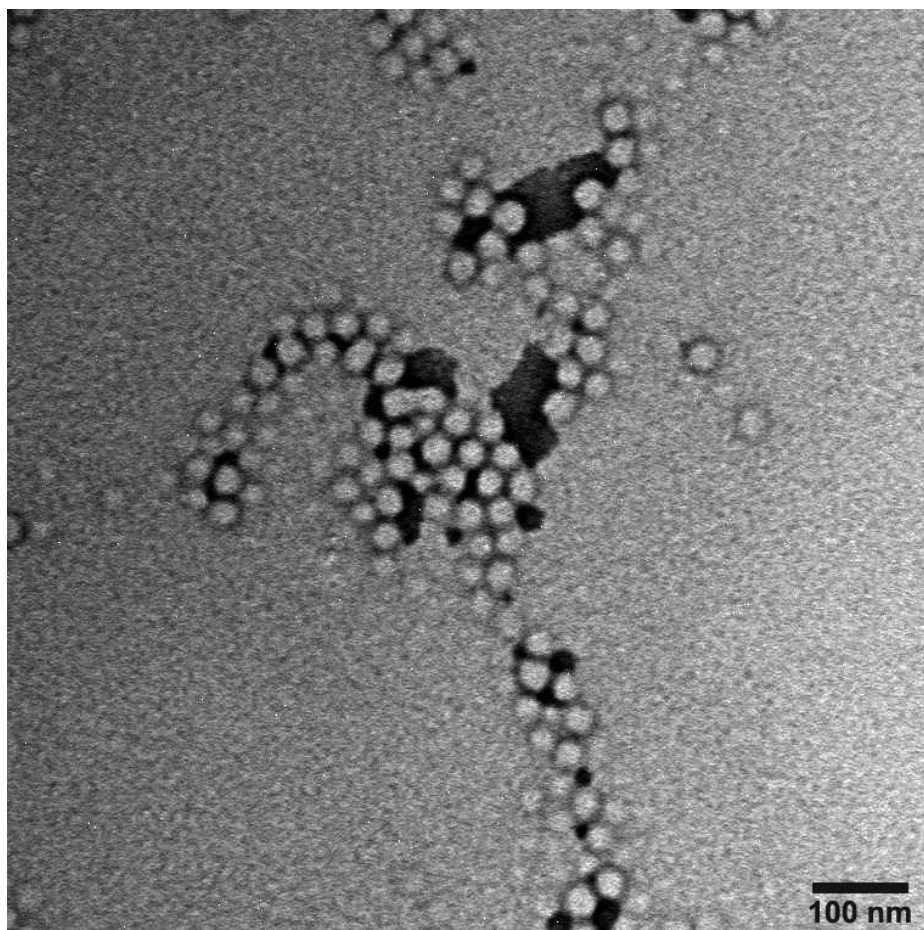


Figure 3.4. TEM image of β -lap micelles.

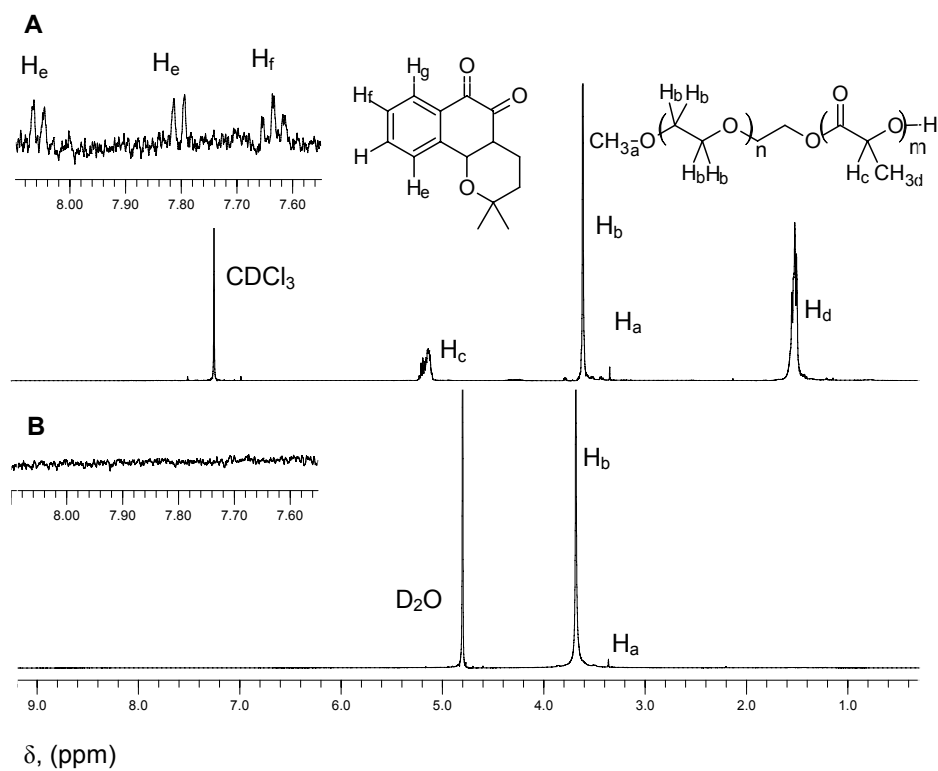


Figure 3.5. ^1H NMR spectra of β -lap-loaded PEG-PLA micelles in (A) deuterated chloroform (CDCl_3) and (B) deuterated water (D_2O). Figure insets represent magnifications of the aromatic protons from β -lap.

The release kinetics of β -lap from PEG-PLA polymer micelles were examined *in vitro* (Figure 3.6). As can be seen from the figure, the time for 50% of drug release ($t_{1/2}$) is 18 h, with the majority of the drug (~75%) being released over the course of 4 days. Simulated model drug release is shown along with experimentally measured cumulative release data. The Higuchi based model²³ output was successfully fit to the experimental measurements from 0-18 hours. D_h had an estimated value of $4.2 \times 10^{-17} \text{ cm}^2/\text{s}$ (95% confidence interval: $4.0\text{-}4.4 \times 10^{-17} \text{ cm}^2/\text{s}$). After 18 hours, the Fickian^{24,25} diffusion approximation begins to fit the data and continues to fit the data until the end of the study. For the Fick approximation, the value of diffusion, D_f , is $2.3 \times 10^{-19} \text{ cm}^2/\text{s}$ (95% confidence interval: $2.0\text{-}2.5 \times 10^{-19} \text{ cm}^2/\text{s}$), almost 200 times slower than drug transport for the first 18 hours. The quality of the model fits and low error of the parameter estimates indicate that both models well approximate the drug release data at different times of drug release. However, the diffusion rates at each stage of drug release differed considerably, suggesting that two different processes may be taking place. In the first 18 hours, drug release occurs relatively quickly through a Higuchi-like mechanism. Drug released in this period of time could be precipitated in and around the micelle core but may have good access to the surrounding aqueous environment through micelle surface. However, diffusion after 18 hours is dramatically slower, which may reflect drug that has less access to the surrounding hydrophilic corona. This fraction of the drug loading could be entrapped in or even dissolved in dense solid regions of the hydrophobic core, where polymer entanglement serves as a much greater impediment to drug transport.

3.3.5 Mechanism of action of cell death induced by β -lap micelles

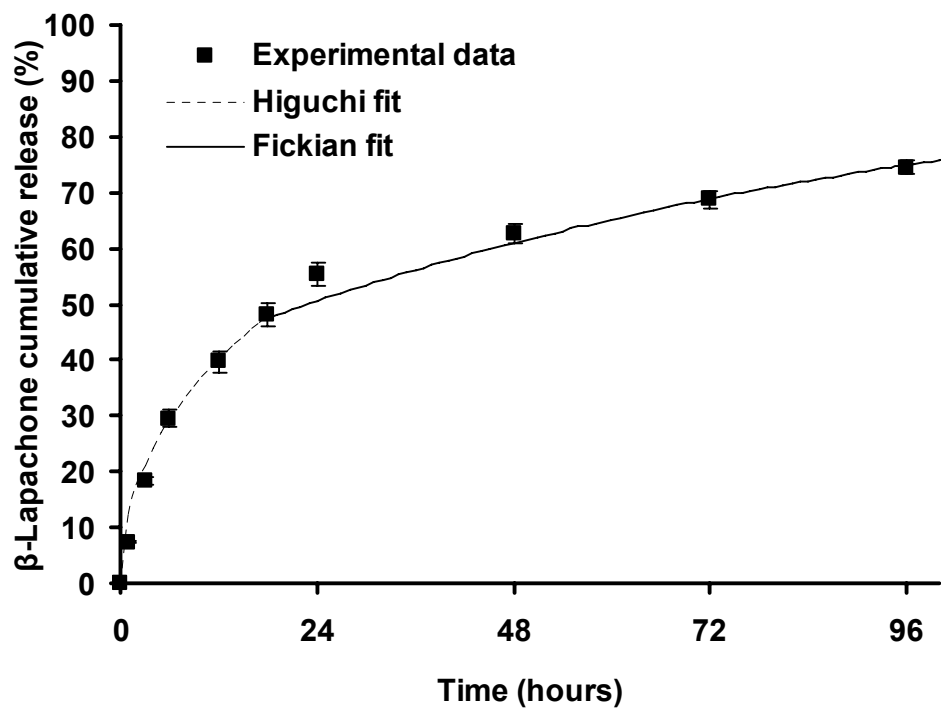


Figure 3.6. β -Lap release profiles *in vitro* from PEG-PLA polymer micelles in PBS at pH 7.4 and 37°C. The error bars were calculated as standard deviation from triplicate samples.

Growth assays were performed to examine the mechanism of action of β -lap micelles on NQO1-overexpressing tumor cells compared to NQO1-null tumor cells. NQO1- cells also serve to mimic normal tissues that are NQO1 deficient. Figure 3.7 depicts relative survival curves (%T/C) *in vitro* of three different tumor cell lines (lung, prostate, and breast) treated with free β -lap and β -lap micelles at different drug doses. Results show that after a 2 h incubation with β -lap micelles, a significant increase in cytotoxicity can be observed in NQO1+ over NQO1- cells in all three cell lines. In H596 cells, a 26% loss in survival in NQO1+ cells following 5 μ M β -lap micelle administration was noted, and at 10 μ M an approximate 85% loss in survival was observed. Values for β -lap micelles were consistently less cytotoxic than for free drug exposures. β -Lap micelle cytotoxicity was equal to that of free β -lap drug administration at 10 μ M, with the difference in cytotoxicities at smaller doses attributed to a delay in drug release from the micelles. Finally, while free β -lap leads to an approximate 25% loss in survival in NQO1- cells at a 15 μ M dose, β -lap micelles have minimal toxicity in NQO1- cells (~7% loss in survival at 20 μ M dose).

The same pattern of cell cytotoxicity for the NQO1+ cells and survival in the NQO1- cells was evident in human prostate and breast cancer cells. In DU-145 and MDA-MB-231 cells, β -lap micelles kill more than 50% of NQO1+ cells at a dose of 6 μ M. At further dose increases, β -lap micelle cytotoxicity approached that of free β -lap. NQO1- cells were resistant to β -lap micelles. In DU-145 cells, there was less than a 10% loss in cell survival after coadministration of dicoumarol (NQO1 inhibitor) with β -lap micelles. Similarly, NQO1- MDA-MB-231 cells were resistant to β -lap micelles. Importantly drug-free micelles were shown to have no cytotoxic effect on tumor cells

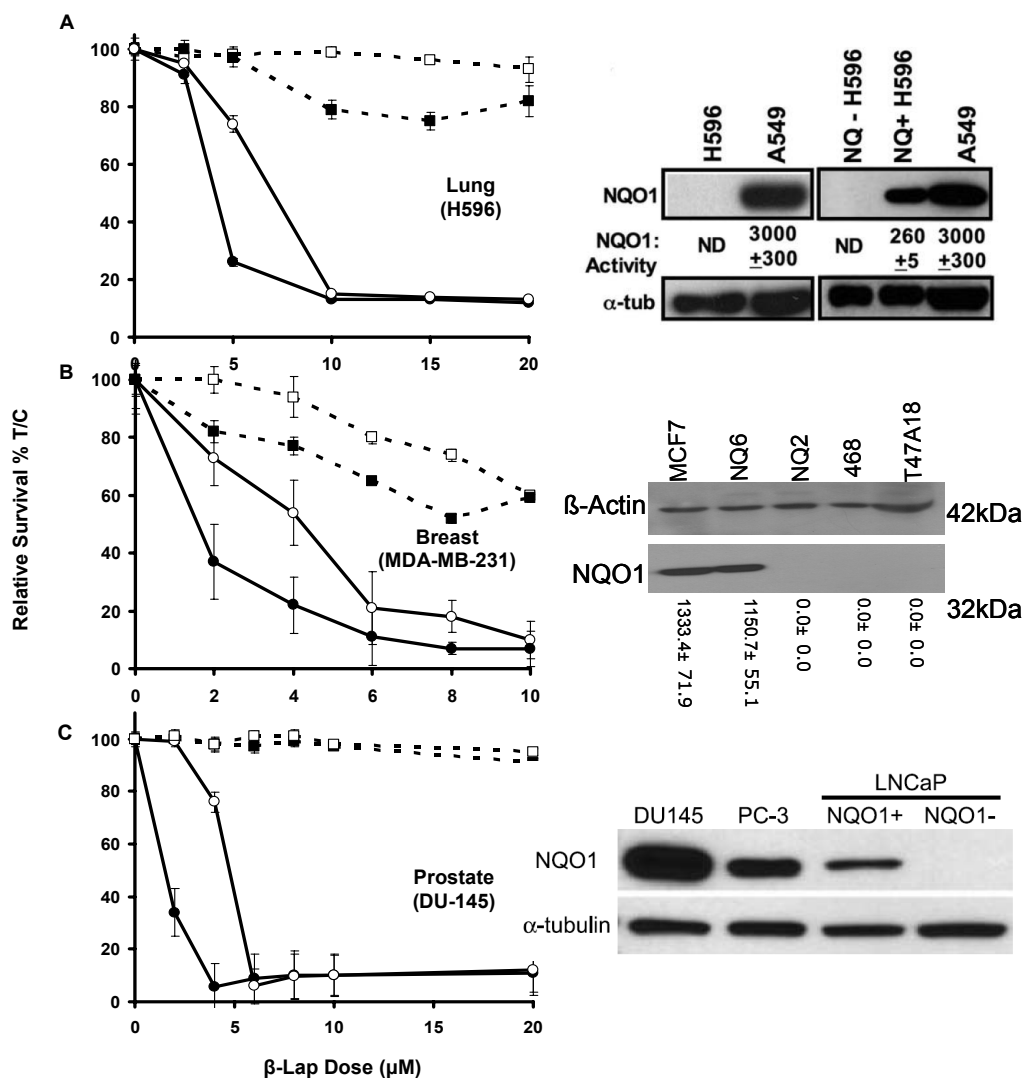


Figure 3.7. Long-term, relative survival assays of (A) H596 lung, (B) DU-145 prostate, and (C) MDA-MB-231 breast cancer cells treated with β -lap at indicated doses for 2 h. To the right of the figure are corresponding NQO1 enzyme expression assays extracted from Refs. 34 (lung), 35 (prostate), and unpublished data pertaining to Patra, B et al. (breast). In the figures, the following symbols pertain to the corresponding treatment groups:

- β -lap micelles NQO1(-)
- Free β -lap NQO1(-)
- β -lap micelles NQO1(+)
- Free β -lap NQO1(+)

(data not shown). To the right of each of the relative survival assays are NQO1 enzyme assays³³⁻³⁵ that correspond to the specific tumor line examined, serving to highlight the presence of NQO1 in the cells and the dependence of cell death on its expression.

In attempts to elucidate whether the unique mechanism of action of β -lap was preserved through micellar delivery of the drug, several key biological assays were performed in H596 cells to identify vital components of β -lap-mediated cell death in NSCLC, as reported by Bey et al.²⁶ Figure 3.8 shows the results of the three biological assays (ROS analysis, comet assays, and NAD loss) conducted to examine vital characteristics of β -lap-induced cell death. Administration of β -lap micelles at a dose of 10 μ M leads to oxidative stress in NQO1+ cells in a manner identical to that of free β -lap drug administration. In contrast, β -lap-induced oxidative stress was absent in NQO1- cells. In the NQO1- cells, no DNA damage was evident after exposure with free β -lap drug or β -lap micelles. However, in the NQO1+ cells, extensive comet tail formation can be observed, indicating DNA damage. Lastly, Figure 3.8C shows NAD loss associated with β -lap micelle administration to H596 cells at the 10 μ M dose. As can be observed from the figure, no NAD loss occurs in the NQO1- cells, while an exponential decrease in NAD is observed with increasing dose in micelle delivered β -lap. Taken together, these results serve to show that the unique mechanism of action of β -lap is preserved through micellar delivery.

3.4 Discussion

The objective of the present study was to develop polymer micelles that can effectively encapsulate β -lap with adequate loading density and minimal loss of drug and

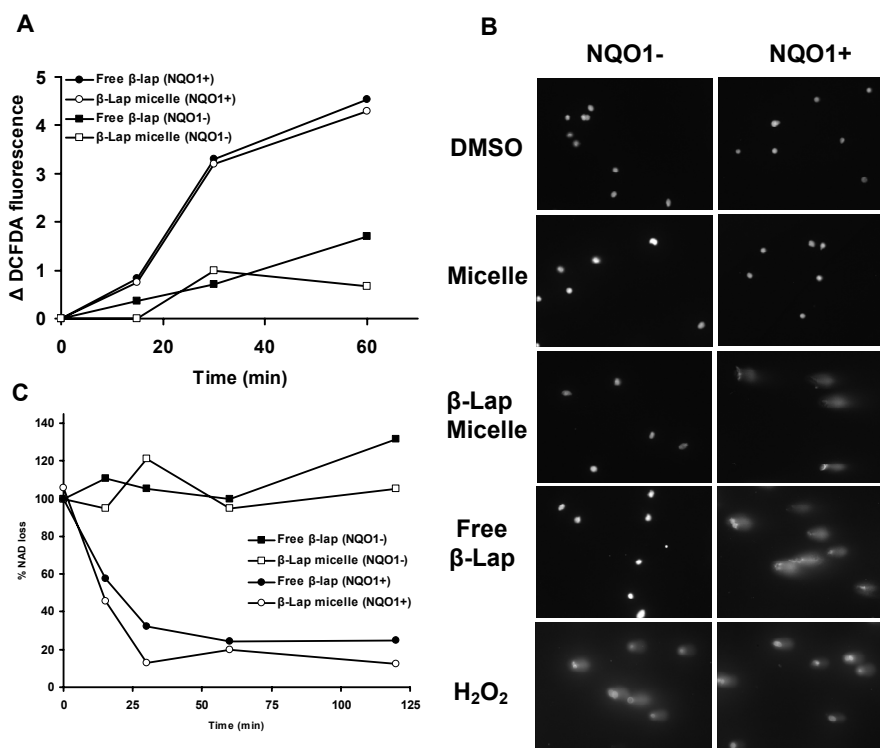


Figure 3.8. Cell death and DNA damage assays conducted in NQO1+ and NQO1- H596 NSCLC cells at a dose of 10 μ M of free β -lap or β -lap containing micelles. (A) Induction of ROS in H596 cells incubated for 20 minutes with CM-H₂DCFDA and then treated with the dose and assessed at the times indicated. (B) Alkaline comet assays of H596 following a 2 h exposure. Vehicle alone (DMSO), micelles alone, and H₂O₂ (for NQO1 independent DNA damage) served as controls. (C) Nucleotide loss following exposure and assessed at the times indicated.

polymer. Of the three methods examined in this study, film sonication yielded micelles with the highest loading density and loading efficiency. The dialysis method has been shown to be effective in cases where the encapsulated agent is very water insoluble. Despite the low water solubility (0.04 mg/mL) of β -lap, this value is still much higher compared to agents such as paclitaxel (0.34 μ g/mL).³⁶ Hence, the majority of β -lap can still be lost to the surrounding aqueous medium during dialysis, leaving only a very minimal amount ($0.02 \pm 0.01\%$) within the micelles. The solvent evaporation technique is another widely used method for micelle formation, and we have successfully formed PEG-PLA polymer micelles with high doxorubicin loading.³⁷ However, this method also proved inefficient at loading β -lap within micelles (loading density = $0.39 \pm 0.05\%$), mainly because of the crystallization behavior of β -lap. Both the dialysis and solvent evaporation methods have slow processes of micellar formation, requiring time for organic solvent to exchange with an aqueous environment or evaporate organic solvent, respectively. In contrast, β -lap crystallization is a faster kinetic process, which can result in the loss of the majority of drug to crystal formation.

The film sonication method proved effective at achieving higher drug loading density within micelles. This increased loading can be best explained by the formation of a molecular level mixture between β -lap and PLA. During the film formation process, β -lap dissolves within the PLA core at a solid-state solubility of 31% (Figure 3.2A). At values below this limit, β -lap forms a homogeneous molecular-level mixture with the PLA matrix. The dissolution of drug within the polymer matrix prevents β -lap from crystallizing during micelle formation, leading to higher drug loading density within the micelles. Similar phenomenon was observed previously by Panyam et al. where an

increase in drug loading correlated with increases in solid-state solubility.²⁰ While the film sonication method led to a significant increase in drug loading density, the loading efficiency was only approximately 40%. We hypothesize that β -lap mixed with PEG chains in the film may not be efficiently loaded inside the micelle core upon sonication. One possible strategy to overcome this limitation is to use longer core forming blocks as demonstrated by Allen *et al.*,³⁸ or the addition of PLA within the film.

The film sonication method leads to micelles with an increased amount of β -lap encapsulated within the core ($4.7 \pm 1.0\%$ to $6.5 \pm 1.0\%$). Additionally, the hydrodynamic diameter of the micelles (29.6 ± 1.5 nm) as measured by DLS and TEM also proves adequate for future *in vivo* delivery applications. Micelles of similar diameters (e.g. SP1049C and Genexol) have shown prolonged blood circulation times and increased maximum tolerated toxicity during clinical trials.³⁹ ¹H NMR studies clearly demonstrated the core-shell structure of the polymer micelles produced by the film sonication procedure. The results indicate that the drug is encapsulated within the PLA micelle core and the micelle surface is stabilized with a mobile PEG corona. Such a core-shell structure has the potential advantage in the protection of the drug from enzymatic degradation while the PEG layer hinders plasma protein adsorptions and particle aggregation. Structural characterization from ¹H NMR serves to confirm the formation of a highly effective drug carrier that ensures drug stability and long circulation times.

In vitro growth inhibition assays demonstrate that β -lap micelles effectively kill a variety of tumor cells overexpressing NQO1 while sparing NQO1- cells. Close examination shows that micelle-delivered β -lap is less toxic to both NQO1+ and NQO1-

cells compared to the free drug (Figure 3.5). Several reasons may explain this discrepancy. Firstly, the actual intracellular concentration of β -lap may be smaller in cells incubated with β -lap micelles than those with free drug. This is possible since most anticancer agents are lipophilic (as well as hydrophobic) and can easily cross cell membranes. PEG-stabilized nanoparticles are typically internalized through fluidic phase endocytosis,¹⁴ and PEG shielding can effectively reduce cell uptake, leading to a smaller drug concentration inside the cells. Secondly, after cell internalization, micelle-delivered β -lap may not be immediately available due to micelle encapsulation. *In vitro* drug release studies showed the value of $t_{1/2}$ is 18 hrs (Figure 3.4). This delayed drug availability may also contribute to a lesser cytotoxicity as shown in both NQO1+ and NQO1- cells. Despite reduced *in vitro* toxicity, the value of β -lap micelles will likely reside in the increased drug solubility and improved pharmacokinetics over free drug during *in vivo* applications. In polymer-drug conjugate systems developed by Li et al.⁴⁰ and Ulbrich et al.⁴¹ for the delivery of paclitaxel and doxorubicin respectively, the conjugated drugs showed less *in vitro* cytotoxicity compared to the free drugs, however, their antitumor efficacy responses were considerably higher due to increased accumulation in tumors.

Comprehensive biological studies show that the unique mechanism of action of β -lap, as shown previously by Bey et al.²⁶ is preserved through micellar drug delivery. In NQO1-overexpressing tumor cells incubated with β -lap micelles, reactive oxygen species (ROS) was generated (Figure 3.6A) as a result of NQO1-dependent futile cycling of the β -lap and subsequent depletion of NAD(P)H from the cell (Figure 3.6C). Accumulation of ROS such as hydroxyl radicals causes massive DNA damages as shown

in comet assay for β -lap micelles as well as the free drug (Figure 3.6B). This NQO1-specific cytotoxicity combined with micellar drug delivery bodes well for *in vivo* translation of the platform, where upon administration, β -lap micelles will accumulate in tumor tissue through passive targeting and release β -lap, which will only be bioactivated in the presence of high levels of NQO1. Concurrently, normal healthy tissues will be spared from the cytotoxic effect of β -lap due to lack of NQO1 expression and reduced micelle uptake.

3.5 Conclusions

In summary, we have successfully developed β -lap-PEG-PLA polymer micelles with adequate loading density, optimal size, core-shell structure, and diffusion-based release kinetics. Upon administration to NQO1+ and NQO1- cells, we were able to show an NQO1-dependent cytotoxicity that resembles that of free drug administration, where NQO1+ cells are effectively killed and NQO1- cells are spared. Future studies will focus on the preclinical evaluation of these micelles in NQO1-overexpressing animal tumor models.

3.6 Acknowledgements

This work was supported by an NIH grant CA90696 to JG, NIH grant CA102792 to DAB, and DOD grant W81XWH-04-1-0164 to DAB. EB is grateful for the support of a National Institutes of Health minority supplement grant. This is report CSCNP10 from the Program in Cell Stress and Cancer Nanomedicine at UT Southwestern Medical Center at Dallas.

3.7 References

1. Belinsky M, Jaiswal AK. NAD(P)H:quinone oxidoreductase1 (DT-diaphorase) expression in normal and tumor tissues. *Cancer Metastasis Rev* 1993;12(2):103-17.
2. Logsdon CD, Simeone DM, Binkley C, Arumugam T, Greenson JK, Giordano TJ, Misek DE, Kuick R, Hanash S. Molecular profiling of pancreatic adenocarcinoma and chronic pancreatitis identifies multiple genes differentially regulated in pancreatic cancer. *Cancer Res* 2003;63(10):2649-57.
3. Lewis AM, Ough M, Du J, Tsao MS, Oberley LW, Cullen JJ. Targeting NAD(P)H:Quinone oxidoreductase (NQO1) in pancreatic cancer. *Mol Carcinog* 2006.
4. Siegel D, Ross D. Immunodetection of NAD(P)H:quinone oxidoreductase 1 (NQO1) in human tissues. *Free Radic Biol Med* 2000;29(3-4):246-53.
5. Pink JJ, Planchon SM, Tagliarino C, Varnes ME, Siegel D, Boothman DA. NAD(P)H:Quinone oxidoreductase activity is the principal determinant of beta-lapachone cytotoxicity. *J Biol Chem* 2000;275(8):5416-24.
6. Tagliarino C, Pink JJ, Dubyak GR, Nieminen AL, Boothman DA. Calcium is a key signaling molecule in beta-lapachone-mediated cell death. *J Biol Chem* 2001;276(22):19150-9.
7. Reinicke KE, Bey EA, Bentle MS, Pink JJ, Ingalls ST, Hoppel CL, Misico RI, Arzac GM, Burton G, Bornmann WG and others. Development of beta-lapachone prodrugs for therapy against human cancer cells with elevated

- NAD(P)H:quinone oxidoreductase 1 levels. *Clin Cancer Res* 2005;11(8):3055-64.
8. Ough M, Lewis A, Bey EA, Gao J, Ritchie JM, Bornmann W, Boothman DA, Oberley LW, Cullen JJ. Efficacy of beta-lapachone in pancreatic cancer treatment: exploiting the novel, therapeutic target NQO1. *Cancer Biol Ther* 2005;4(1):95-102.
 9. Nasongkla N, Wiedmann AF, Bruening A, Beman M, Ray D, Bornmann WG, Boothman DA, Gao J. Enhancement of solubility and bioavailability of beta-lapachone using cyclodextrin inclusion complexes. *Pharm Res* 2003;20(10):1626-33.
 10. Kwon GS, Forrest ML. Amphiphilic block copolymer micelles for nanoscale drug delivery. *Drug Development Research* 2006;67(1):15-22.
 11. Otsuka H, Nagasaki Y, Kataoka K. PEGylated nanoparticles for biological and pharmaceutical applications. *Adv Drug Deliv Rev* 2003;55(3):403-19.
 12. Torchilin VP. Micellar nanocarriers: pharmaceutical perspectives. *Pharm Res* 2007;24(1):1-16.
 13. Jones M, Leroux J. Polymeric micelles - a new generation of colloidal drug carriers. *Eur J Pharm Biopharm* 1999;48(2):101-11.
 14. Savic R, Luo L, Eisenberg A, Maysinger D. Micellar nanocontainers distribute to defined cytoplasmic organelles. *Science* 2003;300(5619):615-8.
 15. Torchilin VP, Lukyanov AN, Gao Z, Papahadjopoulos-Sternberg B. Immunomicelles: targeted pharmaceutical carriers for poorly soluble drugs. *Proc Natl Acad Sci U S A* 2003;100(10):6039-44.

16. Hashizume H, Baluk P, Morikawa S, McLean JW, Thurston G, Roberge S, Jain RK, McDonald DM. Openings between defective endothelial cells explain tumor vessel leakiness. *Am J Pathol* 2000;156(4):1363-80.
17. Maeda H. The enhanced permeability and retention (EPR) effect in tumor vasculature: the key role of tumor-selective macromolecular drug targeting. *Adv Enzyme Regul* 2001;41:189-207.
18. Planchon SM, Wuerzberger S, Frydman B, Witiak DT, Hutson P, Church DR, Wilding G, Boothman DA. Beta-lapachone-mediated apoptosis in human promyelocytic leukemia (HL-60) and human prostate cancer cells: a p53-independent response. *Cancer Res* 1995;55(17):3706-11.
19. Shuai X, Ai H, Nasongkla N, Kim S, Gao J. Micellar carriers based on block copolymers of poly(epsilon-caprolactone) and poly(ethylene glycol) for doxorubicin delivery. *J Control Release* 2004;98(3):415-26.
20. Panyam J, Williams, D, Dash, A, Leslie-Pelecky, D, Labhasetwar, V. Solid-state solubility influences encapsulation and release of hydrophobic drugs from PLGA/PLA nanoparticles. *J Pharm Sci* 2004;93(7):1804 - 1814.
21. Wang F, Blanco E, Ai H, Boothman DA, Gao J. Modulating beta-lapachone release from polymer millirods through cyclodextrin complexation. *J Pharm Sci* 2006;95(10):2309-19.
22. Sutton D, Wang S, Nasongkla N, Dormidontova E, Gao J. Doxorubicin and beta-lapachone release and interaction with micellar core materials. *Experimental Biology and Medicine* 2007;Submitted.

23. Higuchi T. Mechanism of Sustained-Action Medication. Theoretical Analysis of Rate of Release of Solid Drugs Dispersed in Solid Matrices. *J Pharm Sci* 1963;52:1145-9.
24. Crank J. *The Mathematics of Diffusion*. New York, NY: Oxford University Press; 1975. 89-103 p.
25. Ritger PL, Peppas NA. A simple equation for description of solute release I. Fickian and non-fickian release from non-swellable devices in the form of slabs, spheres, cylinders or discs. *Journal of Controlled Release* 1987;5(1):23-36.
26. Bey EA, Bentle MS, Reinicke KE, Dong Y, Yang CR, Girard L, Minna JD, Bornmann WG, Gao J, Boothman DA. An NQO1- and PARP-1-mediated cell death pathway induced in non-small-cell lung cancer cells by beta-lapachone. *Proc Natl Acad Sci U S A* 2007;104(28):11832-7.
27. Labarca C, Paigen K. A simple, rapid, and sensitive DNA assay procedure. *Anal Biochem* 1980;102(2):344-52.
28. Bentle MS, Reinicke KE, Bey EA, Spitz DR, Boothman DA. Calcium-dependent modulation of poly(ADP-ribose) polymerase-1 alters cellular metabolism and DNA repair. *J Biol Chem* 2006;281(44):33684-96.
29. Tagliarino C, Pink JJ, Reinicke KE, Simmers SM, Wuerzberger-Davis SM, Boothman DA. Mu-calpain activation in beta-lapachone-mediated apoptosis. *Cancer Biol Ther* 2003;2(2):141-52.
30. Panduri V, Weitzman SA, Chandel NS, Kamp DW. Mitochondrial-derived free radicals mediate asbestos-induced alveolar epithelial cell apoptosis. *Am J Physiol Lung Cell Mol Physiol* 2004;286(6):L1220-7.

31. Olive PL, Banath JP, Durand RE. Heterogeneity in radiation-induced DNA damage and repair in tumor and normal cells measured using the "comet" assay. *Radiat Res* 1990;122(1):86-94.
32. Torchilin VP. Targeted polymeric micelles for delivery of poorly soluble drugs. *Cell Mol Life Sci* 2004;61(19-20):2549-59.
33. Bae Y, Fukushima S, Harada A, Kataoka K. Design of environment-sensitive supramolecular assemblies for intracellular drug delivery: polymeric micelles that are responsive to intracellular pH change. *Angew Chem Int Ed Engl* 2003;42(38):4640-3.
34. Bey EA, Bentle MS, Reinicke KE, Dong Y, Yang CR, Girard L, Minna JD, Bornmann WG, Gao J, Boothman DA. An NQO1- and PARP-1-mediated cell death pathway induced in non-small-cell lung cancer cells by beta-lapachone. *Proc Natl Acad Sci U S A* 2007;104(28):11832-11837.
35. Dong Y, Chin SF, Blanco E, Kabbani W, Bey EA, Boothman DA, Gao J. Efficacy of Intratumoral β -Lapachone Polymer Millirod Implant for Prostate Cancer Treatment. *Clin Cancer Res* 2008;In press.
36. Bouquet W, Ceelen W, Fritzinger B, Pattyn P, Peeters M, Remon JP, Vervaet C. Paclitaxel/beta-cyclodextrin complexes for hyperthermic peritoneal perfusion - Formulation and stability. *Eur J Pharm Biopharm* 2006.
37. Nasongkla N, Bey E, Ren J, Ai H, Khemtong C, Guthi JS, Chin SF, Sherry AD, Boothman DA, Gao J. Multifunctional polymeric micelles as cancer-targeted, MRI-ultrasensitive drug delivery systems. *Nano Lett* 2006;6(11):2427-30.

38. Allen C, Maysinger D, Eisenberg A. Nano-engineering block copolymer aggregates for drug delivery. *Colloids and Surfaces B-Biointerfaces* 1999;16(1-4):3-27.
39. Sutton D, Nasongkla N, Blanco E, Gao J. Functionalized micellar systems for cancer targeted drug delivery. *Pharm Res* 2007;24(6):1029-46.
40. Canal P, Gamelin E, Vassal G, Robert J. Benefits of pharmacological knowledge in the design and monitoring of cancer chemotherapy. *Pathol Oncol Res* 1998;4(3):171-8.
41. Ulbrich K, Etrych T, Chytil P, Jelinkova M, Rihova B. HPMA copolymers with pH-controlled release of doxorubicin - In vitro cytotoxicity and in vivo antitumor activity. *Journal of Controlled Release* 2003;87(1-3):33-47.

CHAPTER FOUR

In vivo examination of β -lap micelle efficacy in lung tumor models

4.1 Introduction

With adequate treatment regimens to combat lung cancer still lacking, a new trend in chemotherapeutics aims at identifying exploitable molecular targets unique to lung cancer cells so as to design tumor-specific drugs. These agents would be able to therapeutically target only cancer cells, all the while sparing normal, healthy tissues and organs. This principle has guided the development of drugs such as gefitinib and erlotinib, two tyrosine kinase (TK) inhibitors,¹ as well as cetuximab, a monoclonal antibody that prevents ligand binding to the extracellular domain of epidermal growth factor receptor.²

β -Lapachone (β -lap) is a novel, naturally existing anticancer agent whose mechanism of action is highly dependent on the enzyme NAD(P)H:quinone oxidoreductase-1 (NQO1), a flavoprotein found overexpressed in NSCLC.³ In the presence of the enzyme, β -lap undergoes a futile cycling, which leads to depletion of NADH and NADPH from the cell, resulting in the generation of reactive oxygen species (ROS).⁴ The ROS then produces single-stranded breaks (SSBs) in the DNA, and Ca^{2+} release from the endoplasmic reticulum (ER). DNA lesions, in combination with Ca^{2+} , causes the repair enzyme poly(ADP-ribose)polymerase-1 (PARP-1) to become hyperactivated.⁵ It is this hyperactivation that exhausts the NAD^+ and ATP supplies of the cell, resulting in a pattern of cell death called “programmed necrosis” or “necroptosis.”⁶ In light of its unique mechanism of action, it is expected that β -lap would only lead to cell death in tumor tissues overexpressing NQO1, sparing tissues and organs

with endogenous or low levels of the enzyme. This principle has been shown *in vitro*, where NQO1-overexpressing breast,⁷ prostate,⁸ and lung cancer⁵ cells were killed at low μM doses (2-5 μM) of the drug, while NQO1 non-expressing cells were unaffected at these doses.

In an attempt to translate β -lap to the clinic, Arqule Inc. examined a formulation of β -lap complexed with hydroxypropyl- β -cyclodextrin (HP β -CD) (β -lap•HP β -CD, ARQ 501) in a variety of cancers, ranging from pancreatic⁹ to leiomyosarcoma.¹⁰ In all the trials, patient morbidity due to ARQ 501 presented itself in the form of hemolysis, proving fatal in one patient in the latter trial. After examining β -lap-induced hemolysis, our laboratory was able to show that the vehicle, HP β -CD, was responsible for the condition, with the drug itself causing no perceivable hemolysis (Chapter 2). The blood half-life of the formulation was also found to be 24 min, with the drug shown to distribute evenly among all organs, including the brain and heart. The short half-life, as well as the rapid and uniform distribution of the drug, appear to explain the limited efficacy of the formulation, necessitating the use of an alternate carrier for a more targeted and efficacious antitumor response.

Polymer micelles are emerging as powerful drug delivery vehicles with immense potential for cancer therapeutics. These spherical, nanosized (~10-100 nm) supramolecular constructs are formed from the self-assembly of biocompatible amphiphilic block copolymers in aqueous environments.¹¹ The core-shell architecture of polymer micelles is beneficial for drug delivery, because the hydrophobic core can act as a reservoir or cargo space that shields away lipophilic drugs, while the outer shell provides a hydrating layer that hinders plasma protein interactions that would otherwise

lead to rapid particle clearance.¹² Additionally, the small size of micelles hinders RES uptake and subsequent accumulation in the liver and spleen.¹³ Moreover, the critical micelle concentration (CMC), or the concentration at which monomeric amphiphiles form micelles, is very low for amphiphilic polymers, typically on the order of 10^{-6} - 10^{-7} M, resulting in very stable constructs that do not easily dissociate *in vivo*.¹⁴ Taken together, polymer micelles have longer circulation times, which in turn aids in the preferential accumulation of micelles in tumor tissue, a result of the enhanced permeability and retention (EPR) effect.^{15,16}

Previously, we developed β -lap PEG-PLA polymer micelles for lung cancer therapy (Chapter 3).¹⁷ We were able to fabricate β -lap micelles with small size (30 nm), core-shell morphology, and favorable release kinetics. In addition, β -lap micelles demonstrated an NQO1-dependent mechanism of action against a wide array of tumors upon a 2 h exposure *in vitro*. Last but not least, findings indicate that β -lap micelles were long-circulating in the bloodstream ($t_{1/2} = 28 \pm 3$ h) and preferentially accumulated in tumors for prolonged periods of time.

Given their potential to provide for a safe and efficacious vehicle for the delivery of β -lap, our objective was to examine the *in vivo* antitumor efficacy of the β -lap micelle platform. We hypothesize that β -lap micelles will provide for an efficacious nanotherapeutic platform for the treatment of lung tumors, given their ability to pharmacokinetically and pharmacodynamically target tumors overexpressing NQO1. To examine this, two different lung tumor xenografts were used, which included a subcutaneous A549 lung tumor and a tail vein orthotopic Lewis lung carcinoma (LLC) model. Micelles were administered either intratumorally (IT) or intravenously (IV) in the

case of subcutaneous models, and intravenously in the case of orthotopic models. Results from this study show that β -lap micelles were effective at suppressing tumor growth over time in subcutaneous models, and were able to prolong animal survival in an aggressive orthotopic model. Minimal weight loss as a result of the formulation also proves the tolerability of the formulation. These preclinical findings are essential for the eventual development and clinical translation of β -lap micelles for use as a nanotherapeutic treatment option for lung cancer.

4.2 Materials and methods

4.2.1 *Materials*

β -Lap was synthesized following a previously reported procedure.¹⁸ PEG5k-PLA5k block copolymer (Mn = 10,000 Da) was synthesized utilizing a ring-opening polymerization procedure published previously.¹⁹ All organic solvents were of analytical grade. Isoflurane was obtained from Webster Veterinary (Sterling, MA). D-Luciferin was obtained from Gold Bio Technology Inc. (St. Louis, MO). A549 lung tumors and Lewis lung carcinoma (LLC) cells were grown in DMEM with 10% fetal bovine serum, 2 mM L-glutamine, 100 units/mL penicillin, and 100 mg/mL streptomycin at 37°C in a humidified incubator with a 5% CO₂-95% air atmosphere. Cells were routinely found free of mycoplasma infection.

4.2.2 *Preparation β -lap•HP β -CD complexes*

β -Lap•HP β -CD complexes were produced by dissolving HP β -CD (25 g) in 50 mL of PBS. Once the HP β -CD was completely dissolved, a known amount of β -lap (1 g)

was added to the HP β -CD solution and left stirring at room temperature for 48 h. After 48 h, the solution was filtered through 0.45 μ m nylon filters, after which the concentration of β -lap was determined using UV-Vis spectrophotometry ($\lambda_{\text{max}} = 257$ nm, $\epsilon = 105$ mL/(cm \cdot mg β -lap) and a previously established calibration curve.

4.2.3 *β -Lap micelle fabrication*

β -Lap micelles were produced using a film sonication procedure.¹⁷ Briefly, β -lap and PEG-PLA (5% w/w) were dissolved in acetone and the organic solvent was allowed to evaporate, yielding a solid film. Water was then added to the film and sonicated for 5 min. In each case, drug-loaded polymer micelles were filtered through 0.45 μ m nylon filters to remove non-encapsulated drug aggregates in solution, and the micelle solution was stored immediately at 4°C to hinder premature drug release. The solution of micelles was then concentrated by centrifugation at a rotational speed of 3,000 RPM at 4°C (Eppendorf Centrifuge 5804 R) using Amicon Ultra Centrifugal Filter Devices (MW cutoff = 100,000 Da). The concentration of β -lap was then determined by lyophilizing a known volume of solution, which was later dissolved in chloroform and analyzed via UV-Vis spectrophotometry with a previously established calibration curve.

4.2.4 *Establishment and treatment of subcutaneous A549 lung tumors in mice*

Animal procedures adhered to the National Institutes of Health (NIH) guidelines and followed an approved protocol by the Institutional Animal Care and Use Committee (IACUC) at the University of Texas Southwestern Medical Center at Dallas. Efficacy studies were performed in tumor-bearing nude (Nu/Nu) female mice weighing

approximately 25 g. A549 lung cancer cells were grown to 80-90% confluence. The cells were then harvested, prepared at $5 \times 10^6 / 50 \mu\text{l}$ cell suspensions, and injected into the flanks of 6-8 week-old nude mice. Tumor size was measured regularly by means of a caliper and volume calculated using the formula: $\text{volume (mm}^3\text{)} = \text{length} \times \text{width} \times \text{width}/2$. Animals were monitored over time and those containing adequate tumor size range were used in a study to examine the efficacy of β -lap•HP β -CD against A549 subcutaneous lung tumors, the results of which were compared to control micelles in tumors with a starting range of 100-200 mm³. Intratumoral (IT) efficacy studies of β -lap micelles were conducted in tumors with slightly larger tumors (ranging from 400-500 mm³) given the fact that solution had to be injected directly into the tumor. Tumors for intravenous (IV) studies examining the efficacy of β -lap micelles compared to control (blank) micelle treatment groups ranged from 200-400 mm³.

For intravenous studies conducted with β -lap•HP β -CD, a 30 mg/Kg or a 60 mg/Kg solution were injected into the tail vein of the mice (n = 10) every other day (e.o.d.) over the course of 9 days. The size of tumors was monitored over the course of treatment by means of a caliper, and tumor volume was calculated as described previously. For intratumoral treatment of subcutaneous tumors, mice were anesthetized via isoflurane inhalation, and a β -lap micelle solution or control micelle solution (20 μL , 2 mg/Kg) was injected directly into the tumor every other day over the course of 13 days. The size of tumors (n = 6) was monitored over the course of treatment as described previously. Intravenous treatment of subcutaneous A549 tumors (n = 4) consisted of injecting a 40 mg/Kg solution of β -lap micelles into the tail vein of mice every other day over the course of 13 days. The size of tumors was monitored as described previously.

Animal weight loss experiments were conducted in mice, where β -lap micelles (40 mg/Kg) were injected intravenously in a regimen consisting of every other day treatments over the course of 13 days. The weights of mice ($n = 3$) were recorded and compared to mice receiving control (blank) micelles in a similar fashion and regimen.

4.2.5 *Establishment and treatment of orthotopic lung tumors in mice*

A lung orthotopic tumor model was used to examine the efficacy of β -lap micelles. Briefly, 16 female Nu/Nu mice (25 g) were injected IV with a suspension containing 5×10^5 Lewis lung carcinoma cells. Mice were randomly assigned into either one of two groups ($n = 8$ in each group) consisting of a β -lap micelle or control (blank) micelle treatment group. Animals were monitored every other day using bioluminescence imaging (BLI) for signs of tumor growth. The animals were placed under anesthesia via isoflurane inhalation, and were administered 2.5 mg of D-luciferin subcutaneously. After 5 min, bioluminescent images of animals were obtained by placing the mice within a Xenogen Vivovision IVIS Lumina, and imaged for 1 min. Relative light intensity units (RLU) ranging from 75,000 to 3.0×10^5 was used as a marker for tumor presence in the lungs (Figure 4.1). Day 0 was designated as the day of initial detection of the disease, and the day prior to the start of treatment. On the following day, a 40 mg/Kg solution of β -lap micelles was administered via the tail vein, and this regimen was repeated five times over the course of 9 days. Animals were monitored every day for survival. While BLI can be used as a method to monitor the presence of disease, it cannot reliably be used as an indicator of tumor efficacy in the case of LLC tumors as shown in Figure 4.1B. As can be seen in the figure, an animal undergoing

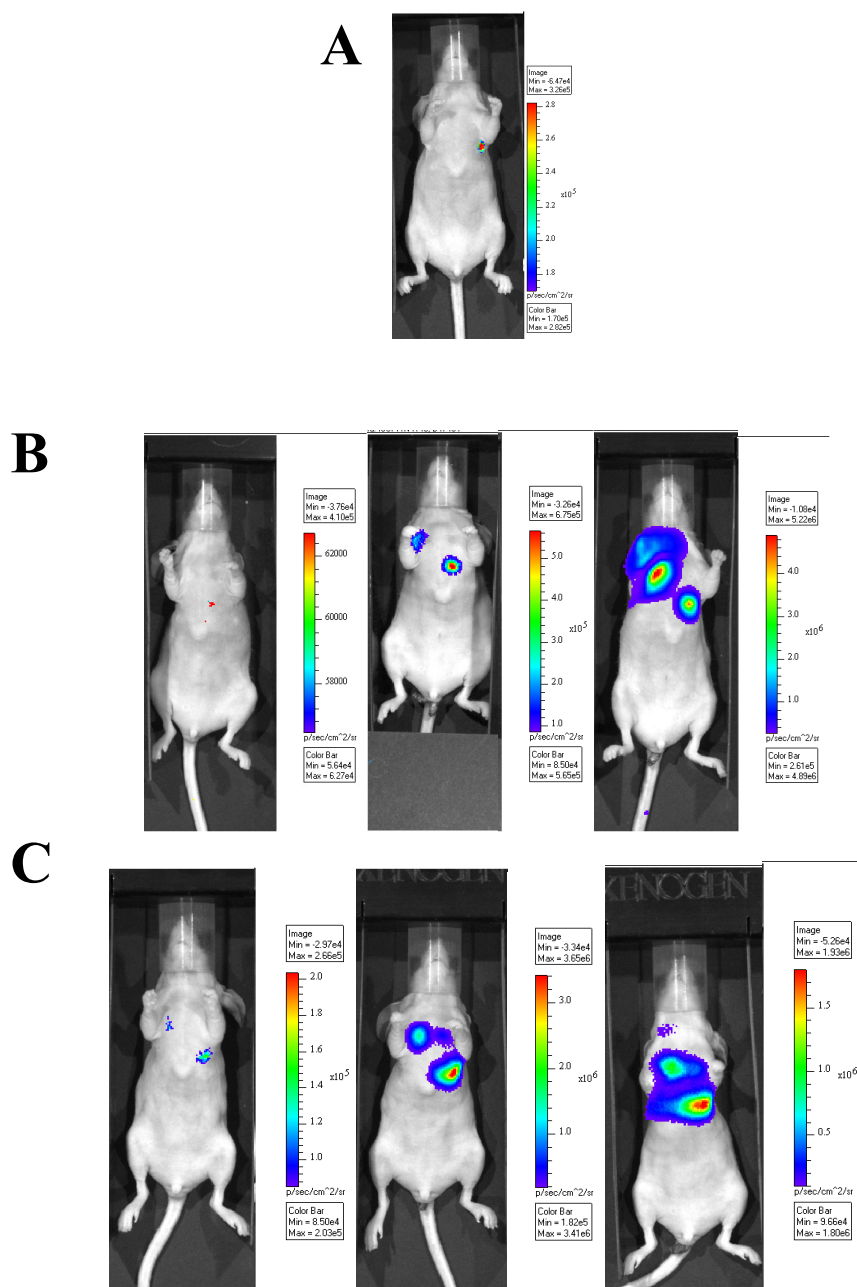


Figure 4.1. (A) Representative image of Lewis lung carcinoma orthotopic model in a nude mouse at stage of initial treatment (Day 0). (B) Time progression (5 d) of mice undergoing treatment (40 mg/Kg β -lap micelles). (C) Time progression (5 d) of control mice (blank micelles).

β -lap micelle treatment that is responding favorably to the treatment in terms of animal survival (survived 13 d prior to initial detection of disease), has failed to show a decrease or disappearance in BLI intensity. By comparison, a control mouse showing similar intensity of BLI, has only survived 6 d prior to initial detection of disease.

4.3 Results

4.3.1 *β -Lap•HP β -CD treatment of subcutaneous lung tumors*

Figure 4.2 constitutes the antitumor response of A549 subcutaneous lung tumors treated with β -lap•HP β -CD. As can be seen from the figure, tumors in all groups began at roughly the same size (100 mm³) and remained at this same size for the entire duration of treatment (day 9). It is important to note at this time that only 1 mouse out of the initial 5 in the 60 mg/Kg group survived past the 4th day of treatment, with all animals in this group dying as a result of the formulation. Moreover, the sizes of both tumors were comparable in size, with the 30 mg/Kg treatment group measuring 115 ± 13 mm³ and the control groups measuring 124 ± 12 mm³. After day 9, tumors in all groups began to grow at the same rate and remained relatively at equal sizes. As an example, 26 days after the start of the initial treatment, the average size of tumors in the control and 30 mg/Kg group were equal, measuring 314 ± 53 mm³ and 314 ± 45 mm³ in treatment and control groups, respectively. It was not until after day 35, where tumors in the control and 30 mg/Kg treated group were approximately 486 mm³ in size that a separation between the two groups occurred. After day 35, β -lap•HP β -CD treated tumors (30 mg/Kg) grew to sizes greater than those in the control group, and this trend remained until completion of

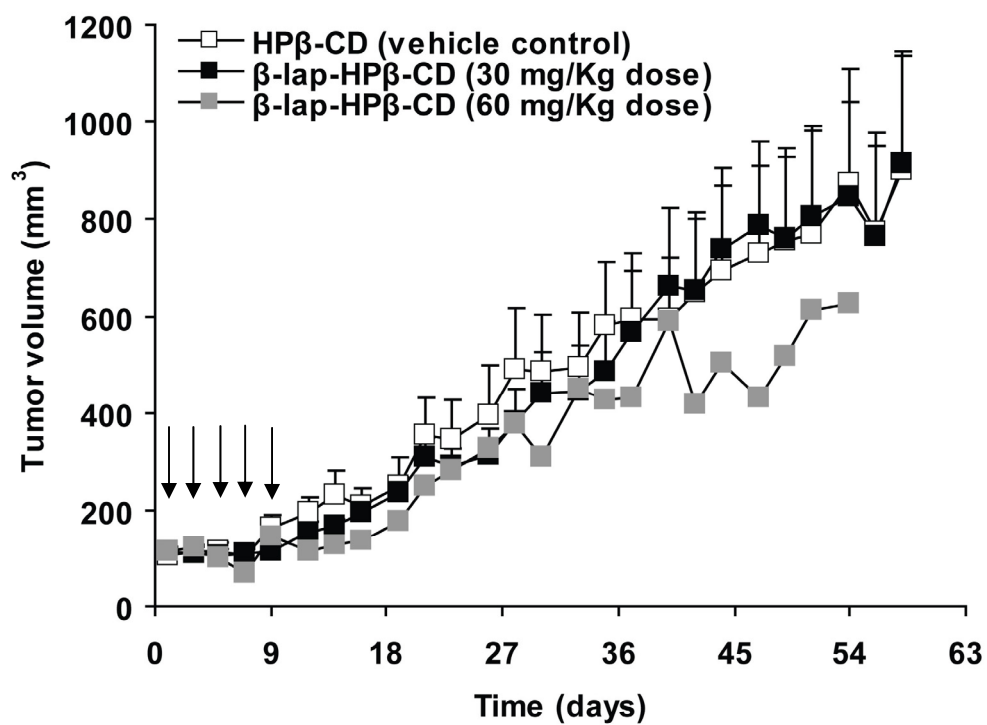


Figure 4.2. Efficacy of intravenous injection of β -lap•HP β -CD in subcutaneous A549 lung tumors. β -Lap•HP β -CD solution (30 mg/Kg) were administered via the tail vein e.o.d. for the duration of 9 days, as indicated by the arrows. Error bars indicate standard error (n = 10).

animal monitoring. At day 58, β -lap treated tumors (30 mg/Kg) measured 916 ± 222 mm³, while control tumors measured 651 ± 113 mm³ in size. It is important to note at this time that no statistical difference between the two groups was found throughout the duration of the study. While the tumor size of the lone survivor in the 60 mg/Kg β -lap•HP β -CD group grew at the same rate as control and 30 mg/Kg treated tumors, this finding fails to shed light on the efficacy of β -lap•HP β -CD at higher doses, due to the reduced number of animals. It does, however, prove that higher doses of β -lap•HP β -CD (ARQ 501) result in substantial toxicity and death, with 60 mg/Kg proving to be very close to the maximum tolerated dose of the drug.

4.3.2 *β -Lap micelle efficacy in subcutaneous A549 lung tumors*

The efficacy of β -lap micelles was examined in subcutaneous A549 lung tumors via two routes of administration, which included intratumoral and intravenous injection. The results of injections of β -lap micelles directly into the tumor can be found in Figure 4.3. As can be observed from the figure, β -lap micelle administration directly into the tumor resulted in initial decrease in tumor volume over the first few days of treatment. The starting size of the tumors in the treatment group was approximately 485 mm³. At day 7, the average size of tumors had decreased to 433 ± 77 mm³. The size of treated tumors did not grow to the initial average until 13 days after the start of treatment, when the average size was found to be 442 ± 58 mm³. After this last treatment day, the tumor began to grow once more, reaching a size of 574 ± 97 mm³ on day 36. It is important to note at this time that tumors were not affected by administration of control micelles. The tumors grew from a starting volume of 452 ± 106 mm³ to 629 ± 138 mm³ over the first 13

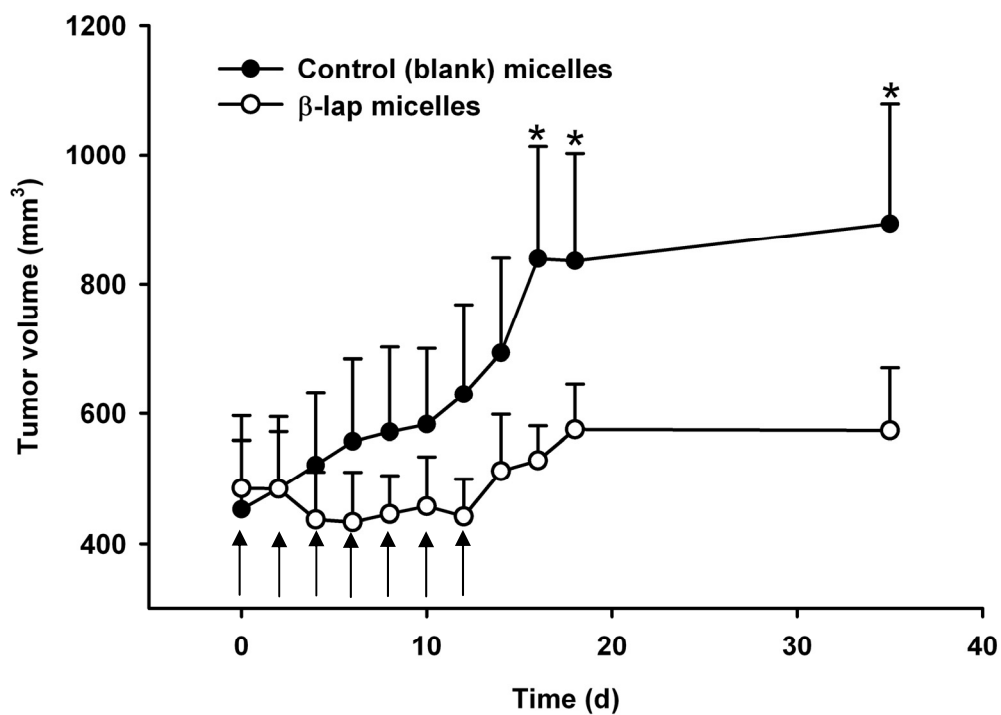


Figure 4.3. Intratumoral (IT) efficacy of β -lap micelles in subcutaneous A549 lung tumors. β -Lap micelles were injected intratumorally e.o.d. for the duration of 13 days, as indicated by the arrows. Error bars indicate standard error ($n = 6$). Asterisk marks over error bars indicate differences in tumor volume averages that were significant ($p = 0.05$).

days of treatment, reaching a size of $894 \pm 185 \text{ mm}^3$ by day 36. Tumors volumes in both groups appear to plateau at later timepoints, likely the result of necrosis stemming from repeated perforation of the tumor and subsequent injection of solution.

The efficacy of β -lap micelles was also examined following intravenous administration (Figure 4.4A). The average starting size of tumors in the treatment group was found to be $297 \pm 55 \text{ mm}^3$. For the first 9 days of treatment, growth of the tumors seemed subdued, reaching an average size of $361 \pm 85 \text{ mm}^3$ at this timepoint. By comparison, control tumors grew from a starting size of $385 \pm 62 \text{ mm}^3$ to an average size of $550 \pm 76 \text{ mm}^3$ at day 9. At day 18, tumors in the control group have continued to grow and have reached an average size of $744 \pm 63 \text{ mm}^3$ while β -lap micelle treated tumor sizes averaged $405 \pm 75 \text{ mm}^3$ at this time. It is important to note that from this point forward, difference in tumor sizes between the treatment and control groups were found to be statistically significant ($p \leq 0.05$) throughout the course of the study. This is due to the fact that the growth of treated tumors has been significantly hampered, with the average size hovering around the 400 mm^3 mark. As an example, at day 50, treated tumors measured an average of $368 \pm 90 \text{ mm}^3$. This is in stark contrast to control tumors, which have reached average values of $880 \pm 95 \text{ mm}^3$. By day 77, treated tumors have regressed to an average size of $255 \pm 25 \text{ mm}^3$, while control tumors reached $1349 \pm 301 \text{ mm}^3$.

In a separate experiment, animal weight of mice was monitored in mice receiving 40 mg/Kg of β -lap micelles and compared to those receiving control (blank) micelles (Figure 4.4B). As is evident from the figure, animal weight between the treated and control groups did not vary significantly from one another, with minimal weight loss

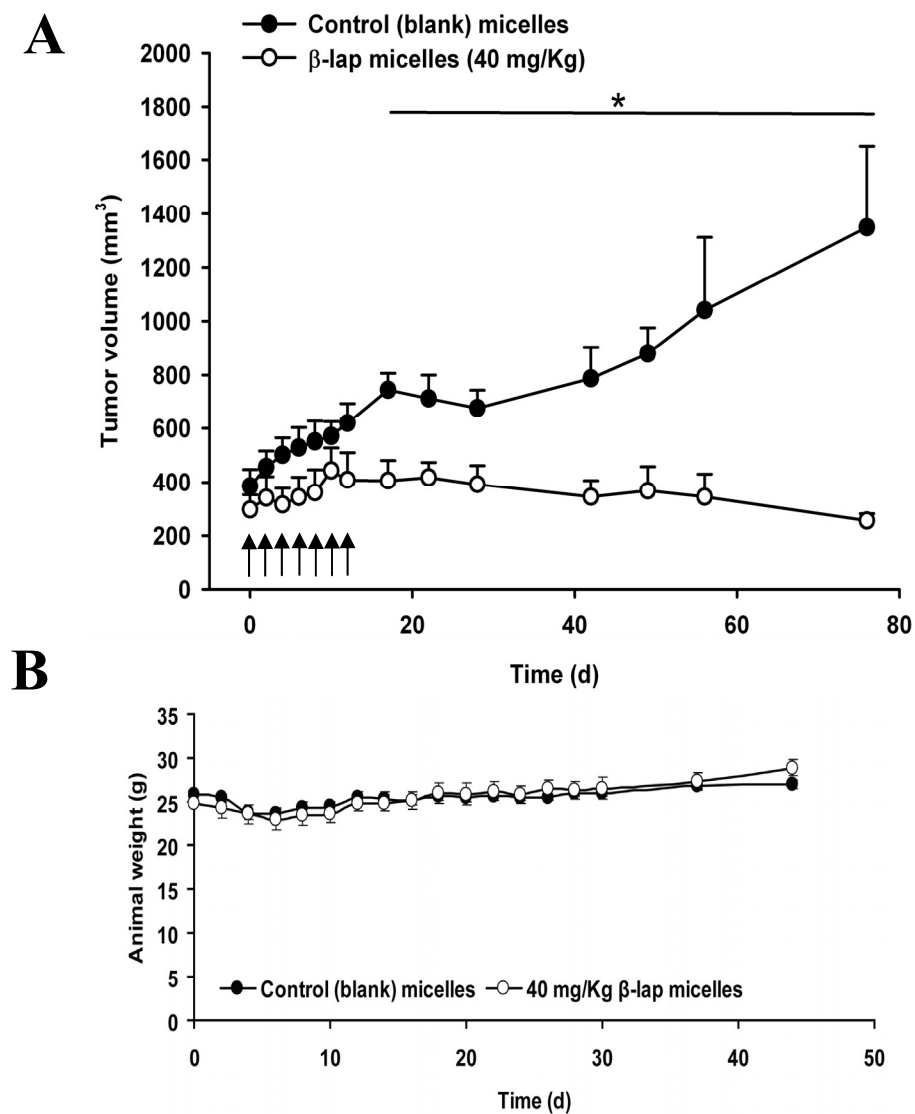


Figure 4.4. (A) Efficacy of β -lap micelles in subcutaneous A549 lung tumors. β -Lap micelles (40 mg/Kg) were injected intravenously e.o.d. for the duration of 13 days, as indicated by the arrows in the figure. Error bars represent standard error ($n = 4$), and the asterisk indicates data points in which statistical significance ($p = 0.05$) is achieved. (B) Weight change over time of mice treated with 40 mg/Kg of β -lap micelles and control micelles. Error bars represent stand error ($n = 3$)

occurring in any of the two groups.

4.3.3 *β -lap micelle treatment of orthotopic lung tumors*

The efficacy of β -lap micelles was examined in a pulmonary model using Lewis lung carcinoma cells, with results shown in the form of an animal Kaplan-Meier survival curve in Figure 4.5. In the figure, Day 0 represents the day that tumor was found at detectable levels in mice through the use of bioluminescence imaging (Figure 4.1). As can be seen from the data, 50% of control animals died from the disease at day 6. At this same timepoint in the treated animals, 75% of the animals were still surviving. Moreover, 50% of the deaths in the treated group were not found to occur until day 9. All of the animals in the control group expired on day 7, one week after initial detection of the disease. While animal survival in the treated group appeared to steadily decline past the 7 day timepoint, 100% of animal deaths did not occur until day 17. This represents a 10 day prolongation of survival when compared to control animals.

4.4 Discussion

4.4.1 *β -lap•HP β -CD proved ineffective at inhibiting tumor growth*

β -Lapachone is a novel anticancer agent whose mechanism of action relies on the presence of a particular enzyme, NQO1, found overexpressed in several cancers, specifically lung cancer. This unique cell killing effect has been well-documented *in vitro*, where NQO1-overexpressing cells were effectively killed at μ M doses of the drug, while NQO1-nonexpressing cells were spared.^{5,7} Despite this specific tumor targeting, delivery strategies are required to not only solubilize the drug, but protect it from

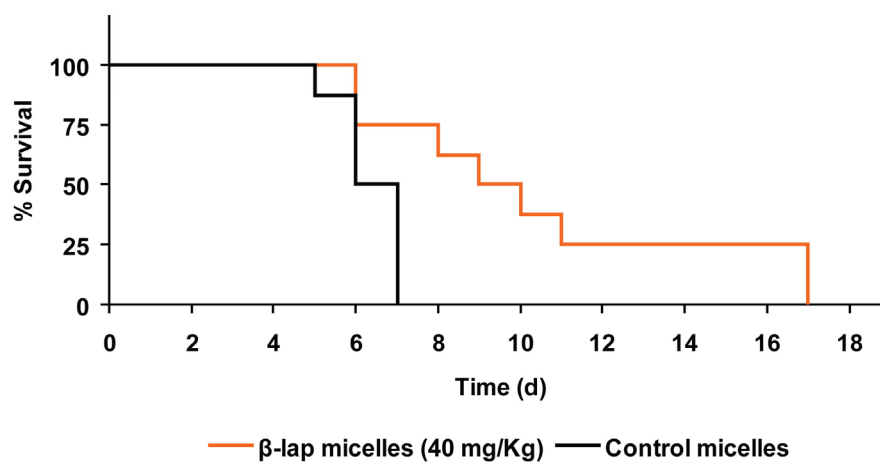


Figure 4.5. Kaplan-Meier curve displaying % of animal survival over time for nude mice with lung orthotopic Lewis lung carcinoma treated with β -lap micelles. Micelle solutions were administered e.o.d. for the duration of 9 days, if permitting. Experiments were conducted with $n = 8$ in each group.

enzymatic degradation and rapid clearance from the blood. A formulation of β -lap, β -lap•HP β -CD (ARQ 501), is currently undergoing various phases of clinical trials, but toxicity in the form of hemolysis and modest antitumor results have hindered its widespread use. Previously, we demonstrated that the delivery vehicle, HP β -CD, was the causal factor for hemolysis, and that complexation with cyclodextrins led to non-specific and rapid distribution of the drug to all organs. We also demonstrated that β -lap was rapidly cleared from the bloodstream, and that tumor levels of the drug were low when compared to other organs (Chapter 2). Taken together, these findings suggested a low antitumor efficacy of the formulation, which was demonstrated herein. As shown, tumors treated with an IV injection of β -lap•HP β -CD failed to induce growth inhibition, with tumors exhibiting the same growth kinetics as controls (Figure 4.2). These findings are highly analogous to other *in vivo* results regarding drug complexation with HP β -CD. Cullen and coworkers demonstrated that a systemic administration of β -lap•HP β -CD did not have a significant antitumor effect when compared to vehicle alone controls.²⁰ Cinatl et al. showed that a higher dose of a cyclodextrin formulation of the anticancer drug aphidicolin was necessitated to bring about the same effect as a low dose of a nanoparticle (liposomal) formulation of the drug.²¹ Last but not least, Aggarwal and colleagues highlighted the disadvantages associated with paclitaxel cyclodextrin formulations *in vivo*, stating that precipitation of the drug out of the complex upon blood dilution was a major deterrent to the clinical use of the formulation.²²

4.4.2 *β -Lap micelles prove effective at hindering tumor growth and prolonging survival*

In view of the shortcomings associated with cyclodextrins, an alternate drug delivery platform was required to fully harness the antitumor effects of β -lap. We previously showed the effective encapsulation of β -lap within PEG-PLA polymer micelles.¹⁷ These micelles exhibited small size (~ 30 nm), core-shell morphology, and favorable release kinetics. Moreover, *in vitro* experiments showed the preservation of NQO1-dependent cell toxicity. When examined *in vivo*, pharmacokinetic findings foreshadowed favorable antitumor activity, with long blood circulation times ($t_{1/2} = 28$ h) and adequate micelle accumulation and residence in tumors (Chapter 2). As hypothesized, β -lap micelles proved effective at inhibiting tumor growth *in vivo*. An intratumoral injection of β -lap micelles was found to suppress tumor growth when compared to control tumors, and these findings agree well with similar published studies. Lavasanifar and coworkers were able to show that an intratumoral injection of cucurbitacin I-containing poly(ethylene oxide)-block-poly(alpha-benzyl carboxylate epsilon-caprolactone) (PEO-b-PBCL) micelles resulted in regression of B16.F10 mouse melanoma tumors.²³ And while the chemistry and design of polymer micelles favors its use as a systemic platform for drug delivery, especially in the case of lung tumors, it is important to note the work by Goldberg and coworkers concerning intratumoral injection of chemotherapeutics in lung cancer.²⁴⁻²⁶ Termed “endobronchial intratumoral chemotherapy,” their approach involves the use of a flexible bronchoscope to deliver anticancer drugs directly into tumor tissue by means of a needle-catheter.²⁴ The advantages include site-specific delivery, high intratumoral drug concentrations, and reduced toxic side effects. Through the use of this technique, the authors found an initial shrinkage of tumors after the injection of cisplatin, which paved the way for resection and

resulted in 3-year survival rates of 65%.²⁴ In light of these findings, it is possible to consider the intratumoral injection of β -lap micelles as a viable option for lung cancer therapy.

As shown in this study, β -lap micelles are highly effective as a systemic chemotherapeutic platform for the treatment of lung cancer. When administered IV, β -lap micelles were able to inhibit tumor growth over a prolonged period of time when compared to control tumors (Figure 4.4A). When an orthotopic model was examined, β -lap micelles were shown to prolong animal survival in an otherwise very aggressive tumor model. These results are akin to those found by Kataoka and coworkers, where a micellar formulation of cisplatin-containing poly-(ethylene glycol)-poly(glutamic acid) block copolymers was shown to lead to tumor regression against Lewis lung carcinoma in mice.²⁷ In contrast, no effect on tumor growth was observed with free cisplatin administration, which mirrors our own findings from this study. Cho and coworkers were able to show that adriamycin-containing poly(γ -benzyl L-glutamate)/poly(ethylene oxide) polymer micelles, administered 4 times for 6 days, showed significant tumor growth suppression to control tumors.²⁸ Last but not least, Matsumura et al. developed poly(ethylene glycol)-poly(glutamic acid) block copolymer micelles that encapsulate 7-Ethyl-10-hydroxy-camptothecin (SN-38), an active metabolite of irinotecan hydrochloride (CPT-11).²⁹ *In vivo* antitumor studies showed that a micellar formulation of the drug was significantly more effective at suppressing subcutaneous tumor growth than free drug controls.

The heightened antitumor efficacy of β -lap micelles is most likely the result of the improved pharmacokinetics of the drug. Where β -lap•HP β -CD is very short-lived in the

blood ($t_{1/2} = 24$ min), β -lap micelles have a much higher mean residence time and half-life ($t_{1/2} = 28$ h). The increased circulation time of the micelles increases the chances of the micelles extravasating into the tumor through the enhanced permeability and retention (EPR) effect. Indeed, previous findings showed that micelles accumulated in A549 subcutaneous lung tumors to a relatively large degree (Chapter 2). In a study by Bey et al., it was shown *in vitro* that the A549 lung tumors that were implanted subcutaneously into the flanks of mice in the studies carried out herein expressed endogenous levels of NQO1 activity of $3 \pm 0.03 \mu\text{mol}\cdot\text{min}^{-1}\cdot\mu\text{g}^{-1}$.⁵ These high levels of NQO1 will have contributed to the efficacy observed *in vivo*, as the micelles localized and remained within the tumor, releasing drug that could be bioactivated by NQO1. In the case of orthotopic lung tumors, this effect of micelle accumulation may be further enhanced given the high vascularity of the lungs. In addition, the impaired lymphatic drainage of tumors means that micelles will remain within tumors for longer times without being eliminated, hence increasing exposure of the tumors to high levels of the drug. It is also important to note that Kataoka and coworkers also observed minimal weight loss with cisplatin micelles,²⁷ which also agrees with our own findings in this study. Previously, it was found that β -lap micelles accumulated most in organs such as the liver, spleen, and kidneys (Chapter 2), and hence, toxicity to these organs is expected, especially in light of their increasing accumulation over time. However, Alink and coworkers showed that in mice, the endogenous levels of NQO1 in organs of nude mice, including the liver, kidney, and lungs, were low, and agreed fairly well with findings by other researchers.³⁰ While we have yet to examine NQO1 levels in the organs of the mice, these findings may shed light on the minimal toxicity observed in mice throughout the study. Regardless of

NQO1 levels in mice, it is now well known that the levels of NQO1 in organs of humans is very low,³ which in turn should result in low levels of toxicity from the drug. Taken together, the findings of this study highlight the importance of a drug delivery vehicle capable of enhancing the pharmacokinetics of the encapsulated drug.

4.5 Conclusion

Efficacy *in vivo* findings from this study show that β -lap micelles are effective against different animal models of lung cancer. In contrast to a cyclodextrin formulation of β -lap, which was not effective at all against a subcutaneous model of A549 lung cancer, β -lap micelles were able to significantly hinder tumor growth over a prolonged period of time. Moreover, β -lap micelles at a 40 mg/Kg dose were found to be tolerable, and resulted in minimal and insignificant animal weight loss. When examined in orthotopic tumors, β -lap micelles were shown to prolong survival in an otherwise aggressive animal tumor model. Results from this study highlight the *in vivo* therapeutic potential of β -lap micelles and comprise promising preclinical data for the eventual translation of β -lapachone for lung cancer treatment.

4.6 Acknowledgements

We wish to thank Dr. Erik A. Bey for assistance with animal experiments. This work was supported by NIH grants CA122994 and CA102792 to Jinming Gao, as well as DOD grant W81XWH-04-1-0164 David A. Boothman. Elvin Blanco is grateful for the support of a minority supplement grant from the NIH, as well as predoctoral DOD grant BC043453.

4.7 References

1. Silvestri GA, Rivera MP. Targeted therapy for the treatment of advanced non-small cell lung cancer: a review of the epidermal growth factor receptor antagonists. *Chest* 2005;128(6):3975-84.
2. Bonner JA, Harari PM, Giralt J, Azarnia N, Shin DM, Cohen RB, Jones CU, Sur R, Raben D, Jassem J and others. Radiotherapy plus cetuximab for squamous-cell carcinoma of the head and neck. *N Engl J Med* 2006;354(6):567-78.
3. Belinsky M, Jaiswal AK. NAD(P)H:quinone oxidoreductase1 (DT-diaphorase) expression in normal and tumor tissues. *Cancer Metastasis Rev* 1993;12(2):103-17.
4. Pink JJ, Planchon SM, Tagliarino C, Varnes ME, Siegel D, Boothman DA. NAD(P)H:Quinone oxidoreductase activity is the principal determinant of beta-lapachone cytotoxicity. *J Biol Chem* 2000;275(8):5416-24.
5. Bey EA, Bentle MS, Reinicke KE, Dong Y, Yang CR, Girard L, Minna JD, Bornmann WG, Gao J, Boothman DA. An NQO1- and PARP-1-mediated cell death pathway induced in non-small-cell lung cancer cells by beta-lapachone. *Proc Natl Acad Sci U S A* 2007;104(28):11832-7.
6. Bentle MS, Bey EA, Dong Y, Reinicke KE, Boothman DA. New tricks for old drugs: the anticarcinogenic potential of DNA repair inhibitors. *J Mol Histol* 2006;37(5-7):203-18.

7. Bentle MS, Reinicke KE, Dong Y, Bey EA, Boothman DA. Nonhomologous end joining is essential for cellular resistance to the novel antitumor agent, beta-lapachone. *Cancer Res* 2007;67(14):6936-45.
8. Dong Y, Chin SF, Blanco E, Kabbani W, Bey EA, Boothman DA, Gao J. Efficacy of Intratumoral β -Lapachone Polymer Millirod Implant for Prostate Cancer Treatment. *Clin Cancer Res* 2008;In press.
9. Khong HT, Dreisbach L, Kindler HL, Trent DF, Jeziorski KG, Bonderenko I, Popiela T, Yagovane DM, Dombal G. A phase 2 study of ARQ 501 in combination with gemcitabine in adult patients with treatment naive, unresectable pancreatic adenocarcinoma. *J Clin Oncol (Meeting Abstracts)* 2007;25(18_suppl):15017-.
10. Hartner L, Rosen L, Hensley M, Mendelson D, Staddon A, Chow W, Kovalyov O, Ruka W, Skladowski K, Jagiello-Grusfeld A and others. Phase 2 dose multi-center, open-label study of ARQ 501, a checkpoint activator, in adult patients with persistent, recurrent or metastatic leiomyosarcoma (LMS). *Journal of Clinical Oncology*, 2007 ASCO Annual Meeting Proceedings Part I. 2007;25(18S):20521.
11. Jones M, Leroux J. Polymeric micelles - a new generation of colloidal drug carriers. *Eur J Pharm Biopharm* 1999;48(2):101-11.
12. Torchilin VP. Structure and design of polymeric surfactant-based drug delivery systems. *J Control Release* 2001;73(2-3):137-72.
13. Haag R. Supramolecular drug-delivery systems based on polymeric core-shell architectures. *Angewandte Chemie-International Edition* 2004;43(3):278-282.

14. Torchilin VP, Lukyanov AN, Gao Z, Papahadjopoulos-Sternberg B. Immunomicelles: targeted pharmaceutical carriers for poorly soluble drugs. *Proc Natl Acad Sci U S A* 2003;100(10):6039-44.
15. Hashizume H, Baluk P, Morikawa S, McLean JW, Thurston G, Roberge S, Jain RK, McDonald DM. Openings between defective endothelial cells explain tumor vessel leakiness. *Am J Pathol* 2000;156(4):1363-80.
16. Maeda H. The enhanced permeability and retention (EPR) effect in tumor vasculature: the key role of tumor-selective macromolecular drug targeting. *Adv Enzyme Regul* 2001;41:189-207.
17. Blanco E, Bey EA, Dong Y, Weinberg BD, Sutton DM, Boothman DA, Gao J. Beta-lapachone-containing PEG-PLA polymer micelles as novel nanotherapeutics against NQO1-overexpressing tumor cells. *J Control Release* 2007;122(3):365-74.
18. Planchon SM, Wuerzberger S, Frydman B, Witiak DT, Hutson P, Church DR, Wilding G, Boothman DA. Beta-lapachone-mediated apoptosis in human promyelocytic leukemia (HL-60) and human prostate cancer cells: a p53-independent response. *Cancer Res* 1995;55(17):3706-11.
19. Shuai X, Ai H, Nasongkla N, Kim S, Gao J. Micellar carriers based on block copolymers of poly(epsilon-caprolactone) and poly(ethylene glycol) for doxorubicin delivery. *J Control Release* 2004;98(3):415-26.
20. Ough M, Lewis A, Bey EA, Gao J, Ritchie JM, Bornmann W, Boothman DA, Oberley LW, Cullen JJ. Efficacy of beta-lapachone in pancreatic cancer

- treatment: exploiting the novel, therapeutic target NQO1. *Cancer Biol Ther* 2005;4(1):95-102.
21. Michaelis M, Zimmer A, Handjou N, Cinatl J, Cinatl J, Jr. Increased systemic efficacy of aphidicolin encapsulated in liposomes. *Oncol Rep* 2005;13(1):157-60.
 22. Singla AK, Garg A, Aggarwal D. Paclitaxel and its formulations. *Int J Pharm* 2002;235(1-2):179-92.
 23. Molavi O, Ma Z, Mahmud A, Alshamsan A, Samuel J, Lai R, Kwon GS, Lavasanifar A. Polymeric micelles for the solubilization and delivery of STAT3 inhibitor cucurbitacins in solid tumors. *Int J Pharm* 2008;347(1-2):118-27.
 24. Celikoglu F, Celikoglu SI, Goldberg EP. Bronchoscopic intratumoral chemotherapy of lung cancer. *Lung Cancer* 2008;61(1):1-12.
 25. Celikoglu SI, Celikoglu F, Goldberg EP. Endobronchial intratumoral chemotherapy (EITC) followed by surgery in early non-small cell lung cancer with polypoid growth causing erroneous impression of advanced disease. *Lung Cancer* 2006;54(3):339-46.
 26. Celikoglu F, Celikoglu SI, York AM, Goldberg EP. Intratumoral administration of cisplatin through a bronchoscope followed by irradiation for treatment of inoperable non-small cell obstructive lung cancer. *Lung Cancer* 2006;51(2):225-36.
 27. Nishiyama N, Okazaki S, Cabral H, Miyamoto M, Kato Y, Sugiyama Y, Nishio K, Matsumura Y, Kataoka K. Novel cisplatin-incorporated polymeric micelles can eradicate solid tumors in mice. *Cancer Res* 2003;63(24):8977-83.

28. Jeong YI, Na HS, Cho KO, Lee HC, Nah JW, Cho CS. Antitumor activity of adriamycin-incorporated polymeric micelles of poly(γ -benzyl L-glutamate)/poly(ethylene oxide). *Int J Pharm* 2008.
29. Koizumi F, Kitagawa M, Negishi T, Onda T, Matsumoto S, Hamaguchi T, Matsumura Y. Novel SN-38-incorporating polymeric micelles, NK012, eradicate vascular endothelial growth factor-secreting bulky tumors. *Cancer Res* 2006;66(20):10048-56.
30. de Haan LH, Pot GK, Aarts JM, Rietjens IM, Alink GM. *In vivo* relevance of two critical levels for NAD(P)H:quinone oxidoreductase (NQO1)-mediated cellular protection against electrophile toxicity found *in vitro*. *Toxicol In vitro* 2006;20(5):594-600.

CHAPTER FIVE

Summary and Future Work

5.1 Summary of the project

Currently, lung cancer accounts for 15% of estimated new cancer cases in 2008 and is expected to result in 30% of cancer mortalities.¹ With five-year relative survival rates as low as 3% for distant disease, the prognosis for the disease remains extremely bleak, with patients warranting more effective treatment strategies to combat the disease. The gold standard for lung cancer therapy involves surgical excision, followed by the adjuvant use of platinum-based therapeutics.² However, many patients prove unresponsive to this therapy, and/or suffer from adverse effects to the treatment.³ Hence, a recent trend in cancer chemotherapy involves the development of anticancer agents whose mechanism of action is dependent on unique molecular targets found overexpressed in tumors.

β -Lapachone is a novel anticancer drug whose mechanism of action is bioactivated by the enzyme NQO1, found overexpressed in lung tumors. Our objective was to develop polymer micelles that could effectively encapsulate β -lap in order to target lung tumors in two distinct ways: 1) pharmacokinetically by using a delivery vehicle that ensures tumor accumulation and drug stability; and 2) pharmacodynamically through the use of a drug whose mechanism of action relies on its interaction with an overexpressed enzyme in tumors. Hence, in Chapter 2 of the present work, we made a case for micellar encapsulation of β -lap, showing that an existing clinical formulation of the drug, β -lap•HP β -CD, proved too toxic for administration. β -Lap•HP β -CD, or ARQ

501, was shown to cause patient hemolysis due to the delivery vehicle, HP β -CD, used for solubilization. Moreover, β -lap was shown to be very short lived in the blood, and was shown to distribute uniformly to all organs, with low uptake in tumors. In contrast, a micellar formulation of β -lap resulted in increased blood residence times, and showed heightened and sustained accumulation in the tumor, with minimal uptake in organs such as the brain and heart.

In Chapter 3 of this thesis, we thoroughly characterized the β -lap micelle platform, showing that micelles were indeed small in size (30 nm), possessed core-shell morphology, and displayed favorable release kinetics. Moreover, β -lap micelles killed NQO1-overexpressing tumors in an NQO1-dependent fashion, all the while sparing cells with no NQO1-expression, or whose expression had been knocked down. In chapter 4 of this work, we demonstrated the *in vivo* efficacy of β -lap micelles in different models of lung cancer, including subcutaneous and orthotopic models. In subcutaneous A549 tumors, β -lap micelles were shown to hinder tumor growth compared to controls, both in intratumoral and intravenous administration regimens. It is important to note that β -lap•HP β -CD failed to result in tumor treatment in A549 subcutaneous lung tumors. In orthotopic models, β -lap micelles were shown to prolong animal survival in an otherwise aggressive cell line. Last but not least, minimal weight loss in the β -lap micelle treated mice served to highlight the tolerability of the formulation and its reduced toxicity.

Taken together, results from this study demonstrate the potential of β -lap micelle nanotherapeutics for lung cancer treatment.

5.2 Future directions

A comprehensive and in-depth validation of the β -lap micelle nanotherapeutic platform remains the immediate future direction of the current project. Further examination of the strategy in alternate preclinical models, including higher order species, is required prior to the eventual clinical translation of the technology. However, several improvements can be incorporated into the basic platform so as to enhance the antitumor efficacy of β -lap micelle nanotherapeutics. These include, among others, micellar functionalization with targeting ligands and the combination of synergistic and adjuvant therapies, and are discussed below.

5.2.1 Synergy of β -lap micelles with ionizing radiation (IR) and DNA repair inhibitors

Currently, radiation therapy is a powerful therapeutic option for the treatment of several cancers, including lung cancer, where advancements have been aimed at compensating for motion artifacts and accurate localization of all tumor nodules.⁴ However, the ever-present dilemma in radiation therapy involves the administration of a sufficient dose to kill tumors, all the while sparing healthy tissue. An active area of research involves the synergy of IR with several chemotherapeutics, with the ultimate goal consisting of the minimization of the required dose of radiation therapy needed to bring about therapeutic benefit.

It has been shown previously that IR synergizes with β -lapachone.⁵⁻⁷ Park and coworkers showed that exposure of FSall tumors to 2.5 Gy prior to treatment with β -lap led to a synergistic pattern of cell killing,⁶ mirroring results from studies conducted by Boothman and coworkers.⁵ Park et al. concluded that IR led to an increase in NQO1 within the cells, which in turn resulted in synergy. However, recently it has been

postulated by Boothman and coworkers that the synergy observed by β -lap treatment and IR is the result of the inhibition of DNA repair brought about by β -lap-mediated hyperactivation of PARP-1. This has also been supported by Song et al. who states that synergy is the result of upregulation of NQO1, in addition to reduced ability to repair DNA.⁷ In light of this overwhelming evidence for synergy, β -lap micelles could be used in a combinatorial fashion with IR. In this strategy, the synergy between the two modalities would mean that sublethal or subtoxic doses would be administered to the patients, significantly reducing morbidity and side effects.

As mentioned previously, the inability of the cell to repair the extensive DNA damage brought about by β -lap leads to the eventual demise of the cell. Hence, it is expected that any agents that could assist in DNA damage overwhelming DNA repair would greatly enhance the therapeutic efficacy of β -lap. In this strategy, β -lap micelles could be administered to the patient concomitantly with DNA repair inhibitors to potentiate the cytotoxic effect of β -lap-induced reactive oxygen species generation. Co-encapsulation within the micelle of β -lap and DNA repair inhibitors, such as Nu7026, is a viable possibility.⁸

5.2.2 *Exploration of micelles containing prodrugs of β -lap*

Recently, prodrug formulations of β -lap (mono(arylimino) derivatives) were developed, which were shown to convert to β -lap through spontaneous hydrolytic reaction.⁹ The rates of hydrolysis were shown to be highly dependent on the strength of the electron-withdrawing substituent groups on the molecule, as well as the pH of the solution. Therefore, micelles containing prodrugs of β -lap would release their contents

preferentially in tumor tissue, where the pH has been shown to be as low as 6.¹⁰ In contrast, little release would occur in environments such as the blood, where the pH has been found to be 7.4. This pH-sensitive release would in turn reduce the possible toxic side effects that can arise from β -lap, by having the micelle only release its contents at the intended site of action. These prodrugs were also shown to be less water soluble than the parent drug, which has been shown to enhance their loading within micelles. Taken together the incorporation of these prodrugs within micelles stand to have a significant impact in β -lapachone therapeutics by increasing even more the specificity of therapy.

5.2.3 *Functionalization of β -lap micelles*

A recent trend in polymer micelle therapeutics involves the functionalization of micelles with targeting ligands for enhanced tumor specificity and imaging moieties for tracking purposes.¹¹

Currently, active targeting strategies, where a targeting moiety is attached to the micelle surface that allows for binding to a specific receptor on the tumor cells are an active area of research. Advantages to this strategy include the increased accumulation at target sites as well as increased uptake into tumors via specific receptor-ligand interactions.¹² Hence, β -lap micelles could be fashioned with folic acid in order to target a receptor which has been shown to be expressed on the surface of tumors up to 100-300 times over normal tissue.¹³ Our laboratory has also recently established polymer micelles functionalized with the cyclic(Arg-Gly-Asp-D-Phe-Lys) (cRGD) peptide, which targets the $\alpha_v\beta_3$ integrin, a cellular transmembrane protein found overexpressed on the surface of angiogenic vessels and not readily detectable in quiescent vessels.¹⁴ Results from in vitro

micellar studies show enhanced cellular uptake, and subsequently, increased cell-killing potential.^{15,16}

In addition to targeting ligands, imaging agents may be incorporated within the platform in order to track micelles and image treatment progression. Our laboratory has also recently established polymer micelles encapsulating superparamagnetic iron oxide (SPIO) nanoparticles for T2-weighted MR imaging.¹⁵ Incorporation of this imaging agent would not only enable clinicians to localize tumors for combinatorial therapy (i.e. ionizing radiation, surgery), but would allow them to visualize β -lap micelle therapy and extent of treatment.

In light of these strategies for β -lap micelles, there remains great excitement over the future of this potential therapy for lung cancer, with special focus on possible improvements in patient outcomes.

5.3 References

1. Jemal A, Siegel R, Ward E, Hao Y, Xu J, Murray T, Thun MJ. Cancer statistics, 2008. *CA Cancer J Clin* 2008;58(2):71-96.
2. Bouchard N, Laberge F, Raby B, Martin S, Lacasse Y. Adjuvant chemotherapy in resected lung cancer: two-year experience in a university hospital. *Can Respir J* 2008;15(5):270-4.
3. Pfister DG, Johnson DH, Azzoli CG, Sause W, Smith TJ, Baker S, Jr., Olak J, Stover D, Strawn JR, Turrisi AT and others. American Society of Clinical Oncology treatment of unresectable non-small-cell lung cancer guideline: update 2003. *J Clin Oncol* 2004;22(2):330-53.

4. Bucci MK, Bevan A, Roach M, 3rd. Advances in radiation therapy: conventional to 3D, to IMRT, to 4D, and beyond. *CA Cancer J Clin* 2005;55(2):117-34.
5. Boothman DA, Pardee AB. Inhibition of radiation-induced neoplastic transformation by beta-lapachone. *Proc Natl Acad Sci U S A* 1989;86(13):4963-7.
6. Park HJ, Ahn KJ, Ahn SD, Choi E, Lee SW, Williams B, Kim EJ, Griffin R, Bey EA, Bornmann WG and others. Susceptibility of cancer cells to beta-lapachone is enhanced by ionizing radiation. *Int J Radiat Oncol Biol Phys* 2005;61(1):212-9.
7. Suzuki M, Amano M, Choi J, Park HJ, Williams BW, Ono K, Song CW. Synergistic effects of radiation and beta-lapachone in DU-145 human prostate cancer cells in vitro. *Radiat Res* 2006;165(5):525-31.
8. Bentle MS, Reinicke KE, Dong Y, Bey EA, Boothman DA. Nonhomologous end joining is essential for cellular resistance to the novel antitumor agent, beta-lapachone. *Cancer Res* 2007;67(14):6936-45.
9. Reinicke KE, Bey EA, Bentle MS, Pink JJ, Ingalls ST, Hoppel CL, Misico RI, Arzac GM, Burton G, Bornmann WG and others. Development of beta-lapachone prodrugs for therapy against human cancer cells with elevated NAD(P)H:quinone oxidoreductase 1 levels. *Clin Cancer Res* 2005;11(8):3055-64.
10. Vaupel P, Kallinowski F, Okunieff P. Blood flow, oxygen and nutrient supply, and metabolic microenvironment of human tumors: a review. *Cancer Res* 1989;49(23):6449-65.

11. Sutton D, Nasongkla N, Blanco E, Gao J. Functionalized micellar systems for cancer targeted drug delivery. *Pharm Res* 2007;In Press.
12. Sethuraman VA, Bae YH. TAT peptide-based micelle system for potential active targeting of anti-cancer agents to acidic solid tumors. *J Control Release* 2007;118(2):216-24.
13. Ross JF, Chaudhuri PK, Ratnam M. Differential regulation of folate receptor isoforms in normal and malignant tissues in vivo and in established cell lines. Physiologic and clinical implications. *Cancer* 1994;73(9):2432-43.
14. Eliceiri BP, Cheresh DA. The role of alphav integrins during angiogenesis: insights into potential mechanisms of action and clinical development. *J Clin Invest* 1999;103(9):1227-30.
15. Nasongkla N, Bey E, Ren J, Ai H, Khemtong C, Guthi JS, Chin SF, Sherry AD, Boothman DA, Gao J. Multifunctional polymeric micelles as cancer-targeted, MRI-ultrasensitive drug delivery systems. *Nano Lett* 2006;6(11):2427-30.
16. Nasongkla N, Shuai X, Ai H, Weinberg BD, Pink J, Boothman DA, Gao J. cRGD-functionalized polymer micelles for targeted doxorubicin delivery. *Angew Chem Int Ed Engl* 2004;43(46):6323-7.

APPENDIX A

Quantum Dot (QD) Polymer Micelles for *In vitro* Tracking

A.1 Introduction

Recently, optical imaging modalities such as fluorescent imaging represent a rising trend, given their cost-effectiveness, rapidity, and ease of use, with present-day advances proving promising in significantly broadening our understanding of tumor biology. Fluorescent imaging relies on the excitation of markers such as fluorescent proteins and dyes for light emission from labeled cells. Quantum dots (QDs) have garnered much attention as emerging fluorescent markers with the potential to image tumor processes *in vivo*. Quantum dots (QDs) are nanosized (~2-10 nm in diameter) semiconductor crystals, composed of a CdSe or CdTe core encased by an inert protective shell, that fluoresce brightly when excited.¹ QDs are fluorescently activated by absorbing a photon of light, which creates an electron-hole pair, or exciton. The exciton recombines, and a lower-energy photon is emitted, the energy of which is determined by the size of the quantum dot.

Current fluorophores have numerous disadvantages, chief among them photobleaching and narrow excitation. Conversely, QDs are brighter and more resistant to photobleaching. Whereas organic fluorophores lose >90% of their fluorescence signal within one minute, QDs are fluorescently very stable for more than 30 minutes under the same experimental conditions, allowing for crisp images.² Waggoner *et al.* were able to show that QDs coated with an amphiphilic poly(acrylic acid) polymer were fluorescent *in vivo* for at least 4 months.³ QDs also have quantum yields of up to 80%, a value which is

unaffected through biomolecule conjugation.⁴ Quantum dots are also fluorescently tunable to a desired narrow emission spectrum because the emission wavelength is dependent on quantum dot size, with smaller quantum dots emitting blue and larger QDs emitting red.

The fact that they are customizable, along with their long-term stability and brightness, make QDs ideal for small-animal biomedical imaging, with immunofluorescence studies showing that it is possible to detect single QDs over long periods of time. For biological applications, quantum dots are often coated with a polymer shell such as *n*-poly(ethylene glycol) phosphatidylethanolamine (PEG-PE)⁵ so as to avoid adsorption and aggregation, and are functionalized with a ligand such as EGF.⁶ Bruchez and coworkers were able to show that QDs conjugated to immunoglobulin G (IgG) and streptavidin were able to target the breast cancer cell surface receptor Her2, cytoskeleton components, and nuclear antigens.⁷ Jain *et al.* was able to use multiphoton microscopy techniques to track quantum dots in mice *in vivo*, and was able to differentiate between tumor vasculature, perivascular cells, and cell matrix.⁸ Finally, Nie and coworkers developed bioconjugated QD probes for *in vivo* mouse imaging.⁹ Quantum dots were encapsulated within a polymer coating consisting of tri-*n*-octylphosphine (TOPO) and an amphiphilic block copolymer, with subsequent linking to PEG, and the researchers noticed that the optical properties of the construct did not change. They then conjugated a prostate-specific membrane antigen (PSMA) monoclonal antibody to the modified QD and demonstrated active targeting to prostate cancer cell lines in mice *in vivo*.

Given their superior optical properties such as increased brightness, tunable wavelength emission, and resistance to photobleaching, as well as their functionalization capabilities, QDs are an exciting platform for *in vitro* and cancer imaging in small animals. Therefore, our objective was to develop quantum dot-containing polymer micelles for purposes of micellar tracking (Figure A.1). The longterm goal involves utilizing QD micelles to provide for accurate localization of target tissues *in vivo*, which in turn should also lead to an effective evaluation of proposed therapy. To achieve this, QDs were incorporated into PEG-PLA using a solvent evaporation procedure for micellization. The QD micelles were then characterized for size via dynamic light scattering (DLS) and transmission electron microscopy (TEM), morphology by TEM, and fluorescence intensity. Their uptake in SLK tumor cells were also evaluated using confocal laser scanning microscopy. Results show that QDs were successfully incorporated into PEG-PLA micelles, encapsulated into micelles in a clustered form and were small in size. QD micelles were also shown to retain their high fluorescence intensity. Last but not least, QD micelles were shown to incorporate into SLK cells after cellular incubation. Findings from this study represent a major step toward the development of QD micellar technology for *in vitro* and small animal imaging of cancer.

A.2 Materials and Methods

A.2.1 Materials

PEG5k-PLA5k block copolymer ($M_n = 10,000$ Da) was synthesized utilizing a ring-opening polymerization procedure published previously.¹⁰ Quantum dots emitting at 576 nm, named YCS, were generously provided by Dr. Fanqing “Frank” Chen at the

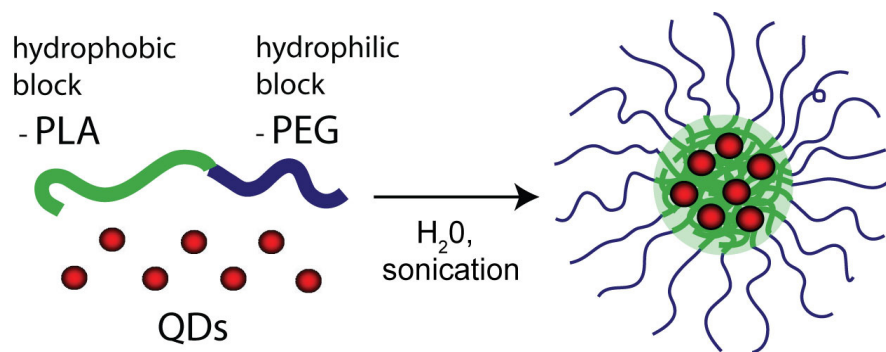


Figure A.1. Schematic of a QD micelle, including constituent components.

Lawrence Berkeley National Laboratory. All organic solvents were of analytical grade and were purchased from Sigma-Aldrich Chemical Co. (St. Louis, MO). SLK cells were cultured in DMEM medium with 10% fetal bovine serum (FBS) at 37°C in 5% CO₂ atmosphere.

A.2.2 QD encapsulation within micelles

The QDs obtained, coated with tri-octylphosphine oxide (TOPO) and in a solution of 1-butanol, were first precipitated. Briefly, a small volume of QDs (100 µL) were added to 1 mL of hexane, after which, 3 mL of ethanol were added under vortex. Following centrifugation at 4350 RPM for 10 minutes at room temperature, the supernatant was removed and the QDs dried under vacuum for 1 h. The QDs were then resuspended in THF.

QD micelles were prepared using a previously established solvent evaporation procedure.¹¹ A small volume of QDs (100 µL) was added to a solution of PEG-PLA dissolved in THF (8 mg/mL). The solution of polymer and QDs was then added dropwise to 5 mL of water under sonication (60 Sonic Dismembrator, Fisher Scientific), after which, the THF was allowed to evaporate overnight. Following evaporation, the micelle solution was filtered using a 0.45 µm nylon filter and stored under 4°C conditions.

A.2.3 Transmission electron microscopy and size analysis with DLS

QD encapsulation and size was determined via transmission electron microscopy (TEM) with images obtained using a JEOL 1200 EX. Formvar coated-copper grids were

glow discharged using a Vacuum Coating Unit. For each micelle sample, a glow discharged grid was allowed to float on a small drop of the micelle solution for 2 min, after which the excess liquid was removed by blotting the grid against a filter paper. For negative stained images, the grid was treated with 2% PTA solution for 30 s after being treated with the micelle solution. All TEM images of QD-micelles were obtained at an accelerating voltage of 80 kV.

Dynamic light scattering (DLS) was used to determine the size of quantum dot encapsulated micelles. Briefly, 0.5 mL of sample was placed within a Viscotek Dynamic Light Scattering instrument so as to determine micelle size, with scattered light detected at a 90° angle and collected on an autocorrelator. Data was obtained from 10 measurements of 5 s duration and averaged utilizing the instrumental software to determine particle size and size distribution.

A.2.4 Fluorescence characterization of QD micelles

Fluorescence analysis of QD micelles was conducted using a Perkin Elmer LS 45 Luminescence Spectrometer. Approximately 2 mL of the sample was placed in a cuvette and analyzed at an excitation wavelength of 350 nm from 300 to 700 nm. Peak information such as λ_{max} was obtained using instrumental software.

A.2.5 In vitro tumor cell uptake of QD micelles

Uptake of QD micelles was examined in SLK cells, an endothelial tumor cell line derived from human Kaposi's sarcoma. Cells were seeded onto 35 mm MatTek glass bottom microwell dishes at a seeding density of 125,000 cells/well (Ashland, MA). After

24 h, the cells were incubated with various concentrations of QD-containing micelles (100 $\mu\text{g/g}$ of media) for a duration of 72 h. Following incubation, the media was removed, and the cells were washed 3X with PBS. Cells were then imaged for QD micelle uptake using a Nikon Eclipse TE-2000 Confocal Laser Scanning Microscope (CLSM) (Melville, NY). The excitation wavelength chosen was 404 nm and the emission wavelength was 595 nm. The experiment was also conducted in control cells that were not incubated with QD micelles in attempts to negate autofluorescence effects.

A.3 Results

A.3.1 Morphology and size analysis of QD micelles

Bright-field transmission electron microscopy (TEM) highlights the morphology of QD micelles (Figure A.2). As can be seen from the figure, QDs were successfully incorporated within PEG-PLA micelles. Given that the polymer does not significantly attenuate electron beams, QD micelles are shown as clusters of QD particles. Indeed in the figure, the QDs, which measure approximately 5 nm, are shown to be closely packed in large numbers within the hydrophobic compartment of polymer micelles. The size of QD micelles, as ascertained from TEM microscopy, is approximately 40 nm, which agrees fairly well with dynamic light scattering results, demonstrating that QD micelles were 38 ± 6 nm in diameter.

A.3.2 Fluorescence analysis of QD micelles

The fluorescence intensity of QDs within micelles was examined and is demonstrated in Figure A.3. As can be observed from the figure, the YCS QDs emit at a

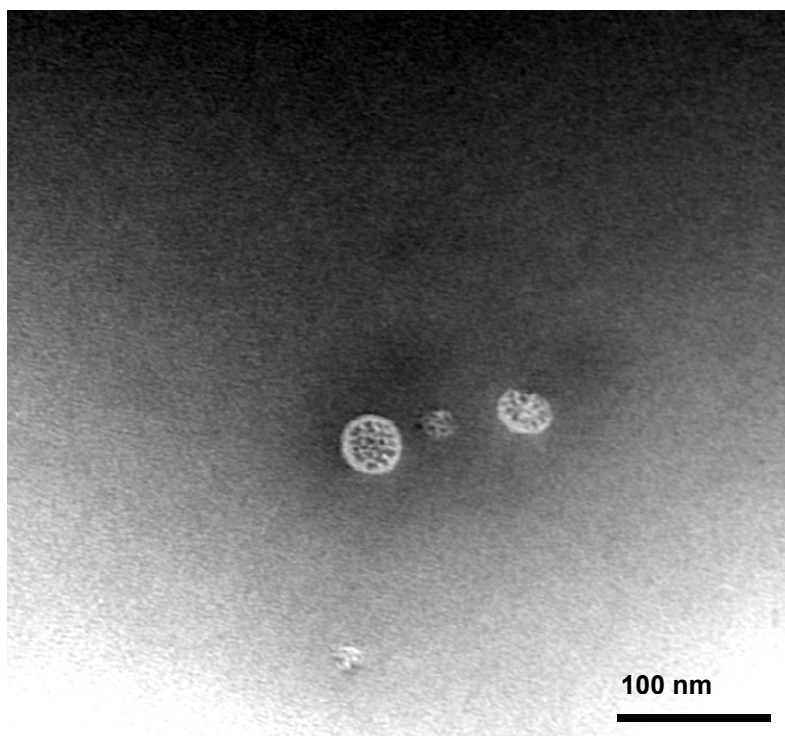


Figure A.2. Transmission electron microscopy image of QD polymer micelles. A 2% PTA counterstain was used for contrast enhancement.

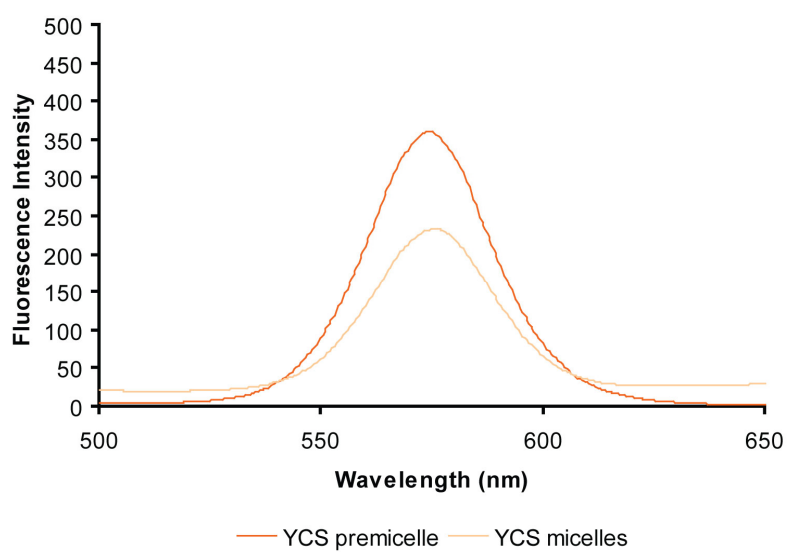


Figure A.3. Fluorescence spectra of QD micelles prior to and following micellization.

wavelength of 576 nm when excited in hexane at a wavelength of 350 nm. Upon encapsulation within polymer micelles, QDs retain their fluorescence, albeit, with a slight decrease in intensity as compared to an equivalent concentration of QDs in hexane. This decrease corresponds to an approximate 1.5-fold decrease in fluorescence, and no significant quenching following micellization appears to be taking place.

A.3.3. Confocal microscopy examination of QD micelles in vitro

Figure A.4 depicts confocal laser scanning microscopy images of SLK cells incubated with QD micelles and compared to control micelles. As can be seen from the image, QD micelles were shown to accumulate within SLK cells 72 h after initial incubation. While minimal information can be ascertained regarding intracellular localization of the QD micelles, it is known that the micelles distribute to the cytoplasm and are not found within the nucleus of the cell, as seen in Figure A.4F. In contrast, no fluorescence was detected in control cells, demonstrating that the fluorescence detected in the QD-incubated cells is not due to cellular autofluorescence.

A.4 Discussion

Currently, quantum dots represent a powerful tool within the realm of molecular imaging given their tunable emission wavelengths, resistance to bleaching, and immense brightness.¹² While the clinical use of QDs is not presently feasible, given the limited tissue penetration of external light sources, their utility in *in vitro* assays, *ex vivo* tissue analysis, and small animal imaging is of great biological significance. Technological advancements have made it possible for the functionalization of QDs with ligands with

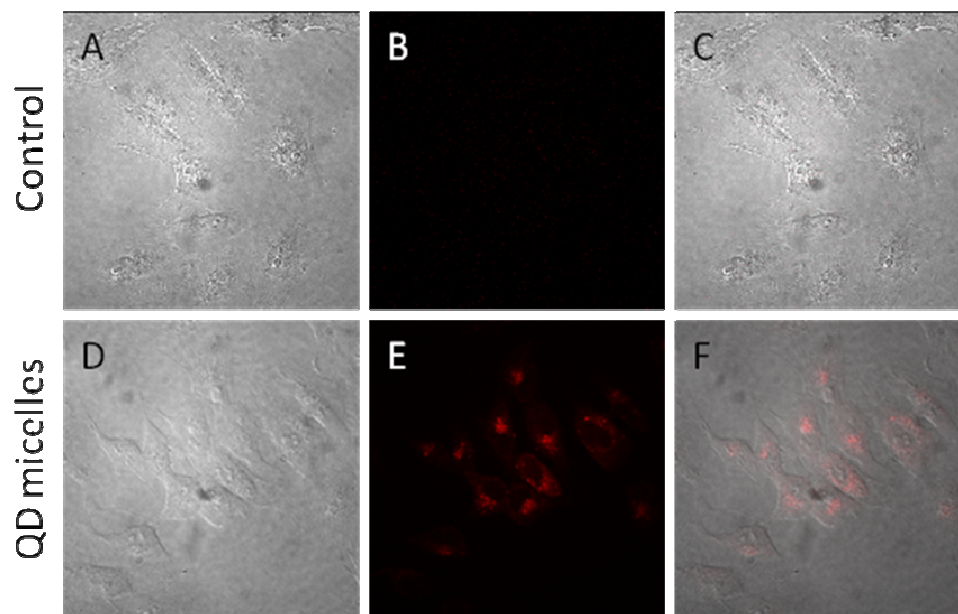


Figure A.4. Confocal laser scanning microscopy of control SLK cells (A-C) and SLK cells incubated with QD micelles (D-F). (A) and (D) represent differential interference contrast (DIC) images, while (B) and (E) represent fluorescence micrographs. (C) and (F) are merged images of DIC and fluorescence for the respective cells. The magnification is 60X and the λ_{ex} and λ_{em} are 404 nm and 595 nm, respectively.

high affinity for receptors on cells,¹³ as well as for their use in proteomics and genomics,¹⁴ allowing for a greater insight and understanding of novel molecular targets in tumors and underlying processes of tumorigenesis. Our objective in this study was to encapsulate quantum dots within micelles for purposes of *in vitro* tracking of therapeutic micelles. The ultimate end goal is the use of QD micelle technology to gain a better understanding of processes including: 1) uptake pathways regarding micelles following exposure to cells; 2) intracellular distribution of micelles following internalization; and 3) fate of micelles over time. Moreover, QD micelles may be used in subcutaneous models in small animals to gain a better understanding of *in vivo* micellar tumor targeting specificity and efficiency. Therefore, work outlined previously proves an important step in the eventual achievement of these goals.

Herein, we demonstrated that quantum dots are effectively incorporated within the hydrophobic core of PEG-PLA polymer micelles. Similar to previous findings by our laboratory concerning super paramagnetic iron oxide (SPIO) nanoparticles,^{15,16} quantum dots were shown to form a cluster within the micelle core (Figure A.2). This result is expected if we take into account the hydrophobic nature of the QDs, as well as their similar sizes to SPIOs (~4 nm). As in the case of SPIOs, the original properties of the QD nanoparticles are also retained upon micellization, resulting in micelles with fluorescence. However, there appears to be a slight decrease in fluorescence intensity upon micellization. This result is in contrast to our findings regarding SPIO micellar encapsulation, wherein an increased MRI relaxivity (i.e. enhanced contrast) was observed.¹⁵ Conversely, this data agrees extremely well with a previous publication by Chen and coworkers, who were able to show that upon clustering of QDs within C₁₆H₃₃-

$N^+(Me)_2-CH_2CH_2CH_2-Si(OMe)_3 Cl^-$ micelles, an approximate 2-fold decrease in signal intensity was observed. The reason for this phenomenon appears to be caused by potential Förster resonance energy transfer (FRET) effects that occur between the QDs within the micelles. This is substantiated by the fact that FRET is found to occur when the Förster radius (i.e. the radius at which energy transfer is 50% efficient) is 8 nm.¹⁷ In other words, if two quantum dots are within a close enough proximity to each other within the core of the micelle, FRET is seen to occur and the intensity of fluorescence is quenched. In spite of this finding, QD micelles retained a considerable fluorescence signal for imaging purposes.

In this study, cells were incubated with quantum dot micelles for purposes of micellar tracking. As observed in Figure A.4, QD micelles were internalized by SLK tumors and were found to distribute in the cytoplasm, with no intensity observed in the nucleus. While preliminary with regards to the end goal of the project, these findings open several avenues of future research. As an example, QD micelles could be fashioned with targeting ligands to examine intricacies in different internalization pathways. It is also possible to combine QD micelles with the use of dyes for specific cytoplasmic organelles to examine the cellular localization of micelles after internalization. Last but not least, different colored quantum dots can be equipped with and without targeting ligands to examine differences in *in vivo* tumor targeting in subcutaneous mouse models using intravital microscopy. Results from these future studies should shed significant light on micellar therapeutics and provide necessary information for micellar optimization.

A.5 Conclusion

Findings from this study serve to highlight the feasibility and potential of QD micelle platforms for use in cancer imaging. We have shown that the encapsulation of quantum dots within polymer micelles occurs in a clustered form and that fluorescence intensity is preserved. Moreover, incubation of tumors with QD micelles showed cytoplasmic accumulation of the micelles. Results from this study can be potentially used towards the development of QD micelles for *in vitro* micellar tracking purposes following the addition of targeting ligands, as well as for small animal imaging studies.

A.6 Acknowledgements

We wish to thank Dr. Fanqing “Frank” Chen for the generous gift of quantum dots. We also wish to thank Chalermchai Khemtong and Chase W. Kessinger for experimental help. This work was supported by NIH grants CA122994 and CA102792, as well as DOD grant W81XWH-04-1-0164. Elvin Blanco is grateful for the support of a minority supplement grant from the NIH, as well as predoctoral DOD grant BC043453.

A.7 References

1. Michalet X, Pinaud FF, Bentolila LA, Tsay JM, Doose S, Li JJ, Sundaresan G, Wu AM, Gambhir SS, Weiss S. Quantum dots for live cells, *in vivo* imaging, and diagnostics. *Science* 2005;307(5709):538-44.
2. Gao X, Nie S. Molecular profiling of single cells and tissue specimens with quantum dots. *Trends Biotechnol* 2003;21(9):371-3.

3. Ballou B, Lagerholm BC, Ernst LA, Bruchez MP, Waggoner AS. Noninvasive imaging of quantum dots in mice. *Bioconjug Chem* 2004;15(1):79-86.
4. Watson A, Wu X, Bruchez M. Lighting up cells with quantum dots. *Biotechniques* 2003;34(2):296-300, 302-3.
5. Dubertret B, Skourides P, Norris DJ, Noireaux V, Brivanlou AH, Libchaber A. *In vivo* imaging of quantum dots encapsulated in phospholipid micelles. *Science* 2002;298(5599):1759-62.
6. Lidke DS, Nagy P, Heintzmann R, Arndt-Jovin DJ, Post JN, Grecco HE, Jares-Erijman EA, Jovin TM. Quantum dot ligands provide new insights into erbB/HER receptor-mediated signal transduction. *Nat Biotechnol* 2004;22(2):198-203.
7. Wu X, Liu H, Liu J, Haley KN, Treadway JA, Larson JP, Ge N, Peale F, Bruchez MP. Immunofluorescent labeling of cancer marker Her2 and other cellular targets with semiconductor quantum dots. *Nat Biotechnol* 2003;21(1):41-6.
8. Stroh M, Zimmer JP, Duda DG, Levchenko TS, Cohen KS, Brown EB, Scadden DT, Torchilin VP, Bawendi MG, Fukumura D and others. Quantum dots spectrally distinguish multiple species within the tumor milieu *in vivo*. *Nat Med* 2005;11(6):678-82.
9. Gao X, Cui Y, Levenson RM, Chung LW, Nie S. *In vivo* cancer targeting and imaging with semiconductor quantum dots. *Nat Biotechnol* 2004;22(8):969-76.
10. Shuai X, Ai H, Nasongkla N, Kim S, Gao J. Micellar carriers based on block copolymers of poly(epsilon-caprolactone) and poly(ethylene glycol) for doxorubicin delivery. *J Control Release* 2004;98(3):415-26.

11. Nasongkla N, Shuai X, Ai H, Weinberg BD, Pink J, Boothman DA, Gao J. cRGD-functionalized polymer micelles for targeted doxorubicin delivery. *Angew Chem Int Ed Engl* 2004;43(46):6323-7.
12. Gao X, Yang L, Petros JA, Marshall FF, Simons JW, Nie S. *In vivo* molecular and cellular imaging with quantum dots. *Curr Opin Biotechnol* 2005;16(1):63-72.
13. Yang D, Chen Q, Wang W, Xu S. Direct and indirect immunolabelling of HeLa cells with quantum dots. *Luminescence* 2008;23(3):169-74.
14. Waggoner A. Fluorescent labels for proteomics and genomics. *Curr Opin Chem Biol* 2006;10(1):62-6.
15. Ai H, Flask C, Weinberg B, Shuai X, Pagel MD, Farrell D, Duerk J, Gao J. Magnetite-loaded polymeric micelles as ultrasensitive magnetic-resonance probes. *Advanced Materials* 2005;17(16):1949-1952.
16. Nasongkla N, Bey E, Ren J, Ai H, Khemtong C, Guthi JS, Chin SF, Sherry AD, Boothman DA, Gao J. Multifunctional polymeric micelles as cancer-targeted, MRI-ultrasensitive drug delivery systems. *Nano Lett* 2006;6(11):2427-30.
17. Anni M, Manna L, Cingolani R, Valerini D, Creti A, Lomascolo M. Förster energy transfer from blue-emitting polymers to colloidal CdSe/ZnS core shell quantum dots. *Applied Physics Letters* 2004;85(18):4169-4171.

APPENDIX B

**Intratumoral Delivery of β -Lapachone via Polymer Implants for Prostate Cancer
Therapy**

Ying Dong,¹ Shook-Fong Chin,¹ Elvin Blanco,¹ Erik A. Bey,¹ Wareef Kabbani,²
Xian-Jin Xie,^{1,3} William G. Bornmann,⁴ David A. Boothman,¹ Jinming Gao^{1,*}

¹Simmons Comprehensive Cancer Center,

²Department of Pathology,

³Department of Clinical Sciences,

University of Texas Southwestern Medical Center,

Dallas, Texas 75390

⁴Department of Experimental Diagnostic Imaging,
University of Texas M. D. Anderson Cancer Center,

Houston, TX 77030

Running Title: β -Lap Polymer Implant Therapy for Prostate Tumors

Key Words:

β -Lapachone, controlled release drug delivery, poly(D,L-lactide-co-glycolide)
(PLGA), prostate cancer, intratumoral chemotherapy

* To whom correspondence should be addressed

Email: jinming.gao@utsouthwestern.edu

Telephone: 1-214-645-6370

Fax: 1-214-645-6347

Abstract

β -Lapachone (β -lap) is a novel anticancer agent with selectivity against prostate cancer cells over-expressing the NAD(P)H:quinone oxidoreductase-1 (NQO1) enzyme. Lack of solubility and an efficient drug delivery strategy limits this compound in clinical applications. In this study, we report the development of β -lap-containing polymer implants (millirods) for direct implantation into prostate tumors, with the hypothesis that the combination of a tumor-specific anticancer agent, β -lap, with localized and site-specific release of the agent will enhance antitumor efficacy. Survival assays show that β -lap kills three different prostate cancer cell lines in an NQO1-dependent fashion, highlighting the unique mechanism of action of the drug and its potential use in targeted therapy. Results demonstrate that upon incorporation of solid-state inclusion complexes of β -lap with hydroxypropyl- β -cyclodextrin (HP β -CD) into poly(D,L-lactide-co-glycolide) (PLGA) millirods, an initial burst of β -lap followed by a sustained release of the drug was observed in phosphate buffered saline (PBS, pH 7.4) at 37°C up to 30 days. β -Lap release kinetics *in vivo* showed sustained release of β -lap (~0.4 mg/kg/day) comparable to that observed *in vitro*. Antitumor efficacy studies in PC-3 prostate tumor xenografts in athymic nude mice demonstrated significant inhibition of tumor growth by β -lap millirods compared to controls ($p < 0.0001$, $n=10$ /group). Kaplan-Meier survival curves showed that mice treated with β -lap millirods survived nearly two-fold longer than controls, without observable systemic toxicity, as indicated by negligible weight loss and normal histology of liver and kidney tissues. These results demonstrate the outstanding potential and therapeutic value of β -lap for the treatment of prostate tumors.

Introduction

The incidence of prostate cancer in the US is the highest of all estimated new cancer cases in males, nearly doubling that of lung cancer, and is the second leading cause of cancer-related deaths in men in 2007 (1). Novel strategies in the diagnosis and therapy of prostate cancer have resulted in increased survival, but have failed to significantly impact mortality rates, particularly in advanced stage tumors. Currently, the gold standard for prostate cancer therapy is radical prostatectomy, which depending on Gleason score, can result in increases in mortality of 7% (Gleason score 2-4) or 60% (Gleason score 8-10) (2). While prostate surgery is efficacious in low-stage tumors, the procedure has notable side-effects, including high rates of incontinence and impotence. In light of the invasiveness of the procedure, alternate strategies have been explored to treat the disease, while aiming to preserve quality of life. Radiofrequency ablation, cryoablation, and brachytherapy have shown promise in treating prostate cancer, but local recurrence of tumor remains a significant problem (3). Several chemotherapeutic agents, such as docetaxel, are viable treatment options for prostate cancer, but suffer from drug resistance and poor delivery to the tumor site, with high levels of systemic toxicity frequently observed (4). Hence, the development of targeted strategies that can exclusively kill prostate cancer cells in a tumor- and site-specific manner should yield increased efficacy, reducing normal tissue toxicity and improving quality of life.

β -Lapachone (β -lap) is a novel, 1,2-orthonaphthoquinone originally derived from the bark of the lapacho tree in South America. It possess a wide range of activities including antifungal, antiviral, antitrypanosomal, and antitumor properties (5). Recent studies have shown that the mechanism of action of β -lap is highly specific and depends on expression of NAD(P)H:quinone oxidoreductase-1 (NQO1). NQO1 is a flavoprotein found overexpressed up to 20-fold compared to normal adjacent tissue in a variety of tumors, including those of

the pancreas (6), lung (7), breast (8) and prostate (9). NQO1 induces a futile cycling of drug that exhausts NAD(P)H from the cell, leading to a substantial amount of reactive oxygen species (ROS) that causes DNA damage (7). A concomitant rise in endoplasmic reticulum-derived cytosolic Ca^{2+} results in PARP1 hyperactivation, NAD^+ /ATP depletion, followed by unique apoptotic substrate proteolysis, DNA fragmentation, and cell death (10). This unique mechanism of action of β -lap sets it apart from traditional chemotherapeutic agents, in that it kills cells independent of caspases, p53 status, and cell cycle stage (11). In light of its heightened antitumor activity in cells overexpressing NQO1, β -lap is a powerful agent capable of offering tumor-selective cell killing.

Despite the unique mechanism of action of β -lap, its low solubility in water (0.038 mg/ml or 0.16 mM) (12) hinders its clinical translation through traditional routes such as intravenous administration (13). Moreover, the lack of site-specificity following IV injection may result not only in low tumor concentrations, but possible toxicity as well. Recently, several biodegradable polymer depot devices have been developed with the hope of achieving intratumoral, controlled release of anticancer drugs. This strategy proves advantageous, since therapeutic levels of a desired anticancer agent are maintained for prolonged periods of time (14). In this way, an 'inside-out' approach to tumor treatment is achieved while reducing systemic side effects. Given these potential advantages, several implantable polymer-drug depot devices have been developed for use in a wide variety of cancers. Gliadel®, a carmustine (BCNU)-containing polymer implant, was approved by the FDA in 1996 for the treatment of glioblastoma multiforme (15-18). Recent research by Qiao and coworkers has led to the development of 5-fluorouracil (5-FU)-releasing silicone implants, capable of zero-order drug release for 24 weeks *in vitro* (19). Work by our own laboratory has resulted in the fabrication of cylindrical, poly(D,L-lactide-

co-glycolide) (PLGA) polymer implants (millirods) for the intratumoral treatment of liver cancers, releasing such drugs as carboplatin and doxorubicin (20-22). Upon incorporation of the latter drug within millirods, the antitumor efficacy *in vivo* was evidenced by decreased tumor sizes 4 and 8 days after millirod implantation in VX2 liver tumors in rabbits (23). In the same study, intratumoral doxorubicin distribution was shown to be high within the tumor core, with penetration distances of 2.8 ± 0.5 and 1.3 ± 0.4 mm at days 4 and 8, respectively.

Based on this concept, we produced several polymer millirod formulations containing β -lap complexed with different cyclodextrins (CDs) to achieve variable release kinetics (24). Depending on the cyclodextrin utilized, as well as the presence or lack of excipient molecules in the millirod, release of drug could be modulated between fast and sustained release kinetics. For example, when complexed with hydroxypropyl- β -cyclodextrin (HP β -CD), release of β -lap showed burst release kinetics (~80% release after 2 days), while the drug alone released in a more sustained manner (~9% after 22 days). The goal of our current study was to examine the *in vivo* antitumor efficacy of a β -lap millirod formulation possessing optimal release profiles, with the hypothesis that β -lap-containing polymer millirods will provide an efficacious response in prostate tumor-bearing mice. HP β -CD was used to form an inclusion complex with β -lap to achieve an initial burst release of drug from PLGA millirods, while free, non-complexed drug was incorporated to provide a prolonged release. PLGA millirods were directly implanted inside PC-3 tumor xenografts and *in vivo* drug release, antitumor efficacy, and systemic toxicity were examined over time. The significantly improved antitumor response highlights the unique advantage of integrating a novel therapeutic agent (β -lap) with enabling drug delivery technology (polymer millirods) to achieve tumor- and site-specific treatment of human prostate cancers.

Materials and methods

Materials. Poly(D,L-lactide-co-glycolide) (lactide:glycolide=50/50, MW 50,000 Da, inherent viscosity 0.65 dl/g) was purchased from Birmingham Polymers, Inc. (Birmingham, AL). β -Lap was synthesized following a previously published procedure (25). HP β -CD was obtained from Cyclodextrin Technologies Development, Inc. (High Springs, FL) with >98% purity. Glucose anhydrous was obtained from Fisher Scientific (Pittsburgh, PA). Dicoumarol (Dic), an NQO1 inhibitor, was purchased from Sigma (Dallas, TX).

Cell culture. DU-145, PC-3, and LNCaP human prostate cancer cells were originally obtained from Dr. George Wilding (University of Wisconsin-Madison). DU-145 and PC-3 cells were grown in GIBCO™ RPMI Medium 1640 (1X) (Invitrogen) with 5% fetal bovine serum (FBS) and LNCaP cells were grown in Dulbecco's minimal essential medium (DMEM) with 10% FBS. All media contained 2 mM/L L-glutamine, penicillin (100 units/ml) and streptomycin (100 mg/mL). Cells were cultured at 37 °C in a 5% CO₂, 95% air humidified atmosphere and were free of mycoplasma contamination.

Immunoblotting of NQO1 expression. Western blots were prepared using standard methods. Briefly, cultured cells or xenograft tissues were harvested for detection of NQO1 expression levels. Cells were washed in ice-cold PBS buffer and lysed in loading buffer (62.5 mM Tris, pH 6.8, 6 M urea, 10% glycerol, 2% SDS, 0.003% bromophenol blue, 5% 2-mercaptoethanol). Samples were then sonicated with a Fisher Scientific Sonic Dismembrator (model 550), fit with a microtip probe, and boiled for 5 min before being stored at -20°C for future analyses. Western blots were first incubated with PBS containing 0.2% Tween 20 and 5% milk for 1 h to prevent nonspecific binding. An anti-human NQO1 antibody was kindly provided by Dr. David Ross (University of Colorado Health

Science Center, Denver, CO) and used at a 1:5,000 dilution at 4 °C overnight. α -Tubulin or GAPDH was used as a loading control. The blots were developed with enhanced chemiluminescence (ECL) substrate (Amesham, Arlington Heights, IL), and exposed using Fuji X-ray film.

NQO1 enzyme assays. Cells were harvested by trypsinization (0.25% trypsin and 1mM EDTA), washed twice in ice-cold PBS, and resuspended in PBS containing 10 mg/ml aprotinin. Cell suspensions were sonicated four times on ice using a 10 s pulse followed by centrifugation at 14,000g for 20 min to get S9 supernatants. Enzymatic reactions contained 77 μ M cytochrome *c* (Sigma) and 0.14% bovine serum albumin in Tris-HCl buffer (50 mM, pH 7.5). NQO1 activity was measured using NADH (200 μ M) as an immediate electron donor and menadione (10 μ M) as an intermediate electron acceptor. A 40 μ M dicoumarol dose was used to block NQO1 activity, and each experiment was conducted in triplicate. Enzymatic activities were calculated as nmol cytochrome *c* reduced/min/mg protein, based on the initial rate of change in OD (absorbance) at 550 nm.

Relative survival assays. Cell survival was examined using a DNA assay as described (9). Briefly, cells were seeded at 5×10^3 per well in a 48-well plate and allowed to attach overnight. Cells were then treated for 2 h with various β -lap concentrations, alone or in conjunction with 40 μ M dicoumarol, followed by replenishment with drug-free medium and were allowed to grow for 5-7 days until control cells grew to 100% confluence. DNA content was then determined by Hoescht dye staining and fluorescence detection using a Perkin-Elmer plate reader (Boston, MA). Reported results are means \pm standard error (SE) from at least three experiments performed in triplicate.

Preparation of β -lap-HP β -CD inclusion complexes. Following a previously published procedure (12), 25 g of HP β -CD were weighed and

dissolved in 50 mL of PBS (pH 7.4). After complete dissolution, approximately 1 g of β -lap was added to the HP β -CD solution. The solution was covered and allowed to stir at room temperature for 3 days, after which the contents were filtered using a 0.45 μ m nylon filter, yielding a solution of β -lap-HP β -CD complex. The solution was then lyophilized and the resulting solid powder ground using a mortar and pestle.

Fabrication of polymer millirods. Polymer millirods were produced using a previously established compression-heat molding procedure (21). The composition of the millirods was modified to achieve the desired drug release profile. Briefly, millirod components (31% β -lap-HP β -CD complex, 19% free β -lap, and 50% PLGA) were weighed separately, placed in a mortar, and well mixed utilizing a pestle. Control millirods were composed of 26% HP β -CD and 74% PLGA. The contents were then placed into a Teflon tube (1.6 mm I.D.) within a stainless steel mold. The mold was then placed in an oven (Fisher Model 282A) at 90°C for 2 h with a compression pressure of 4.6 MPa. The resulting cylindrical millirods, with a diameter of 1.6 mm, were cut to a length of 4 mm for subsequent studies (Figure 1).

***In vitro* drug release studies.** β -Lap-loaded PLGA millirods ($n = 3$) were placed in a glass scintillation vial that contained 5 mL of PBS (pH 7.4) at 37°C. Sample vials were placed in an orbital shaker (C24 model, New Brunswick Scientific) with a rotating speed of 150 rpm. At various time points, the millirods were removed from the solution and placed into a new scintillation vial containing 5 mL of fresh buffer at 37 °C. The concentration of released β -lap was measured using a UV-Vis spectrophotometer (Perkin-Elmer Lambda 20 model) at the maximum absorption wavelength of the drug ($\lambda_{\text{max}} = 257.2$ nm).

Characterization of *in vivo* release of β -lap from polymer millirods. Drug release studies *in vivo* were conducted by intratumorally implanting β -lap

millirods into PC-3 xenograft-bearing athymic nude mice. At different time points, mice were sacrificed and millirods retrieved. Millirods were dissolved in acetonitrile to recover the remaining drug. Drug solutions were then passed through 100 μm filters and analyzed by HPLC using a ZORBAX C-18 column (150 x 4.6 mm, 5.0 mm) with a mobile phase consisting of 70% acetonitrile and 30% 25 mM ammonium formate buffer at pH 7.0.

Subcutaneous xenograft animal models and anti-tumor efficacy study.

All animal procedures were approved by the UT Southwestern IACUC committee. PC-3 cells were grown to 80-90% confluence. Cells were then harvested, prepared at $5 \times 10^6 / 50 \mu\text{l}$ cell suspensions, and injected into the flanks of 6-8 week-old athymic mice (Charles River Labs). Tumor size was measured regularly with a caliper and volume calculated using the formula: volume (mm^3) = length X width X width/2. When tumor sizes reached about 300 mm^3 , β -lap loaded (2.6mg) or control millirods measuring 4 mm in length were implanted intratumorally using a 13-gauge trochar. Tumor sizes were measured every other day after millirod implantation. Mice were sacrificed when tumors reached 2 cm^3 or 10% of body weight. After sacrifice, tumor, liver, and kidney tissues were removed and sent for histological examination. Portions of tumor tissues were also frozen in liquid nitrogen for immunoblotting.

Histological staining. Tumor, liver, and kidney tissues were harvested at desired time points and fixed in a 10% formalin solution overnight. Standard paraffin embedding and processing was performed by the Department of Pathology, UT Southwestern Medical Center. Briefly, paraffin-embedded tissues were sectioned 5 μm in thickness and baked overnight at 37°C. Hematoxylin and eosin (H&E) staining was conducted and histology images were taken using a Nikon E400 microscope and Nikon coolpix 4500 camera.

Statistical analysis. Tumor growth profiles in two tested groups were analyzed using a mixed model approach. Log-rank tests were applied to survival analysis (Kaplan-Meier curve). *P* values <0.05 were considered significant. All statistical analyses were performed using SAS 9.1.3 Service Pack 3.

Results

β -Lap killed prostate cancer cells in an NQO1-dependent manner. As mentioned previously, NQO1 has been found to be highly elevated in multiple types of tumors, including prostate cancers (5). Immunoblotting and enzymatic methods were used to confirm and quantify NQO1 expression levels in three different prostate cancer cell lines including DU145, PC-3 and LNCaP (Figure 2A; Table 1). The data demonstrate that DU145 cells naturally have a higher NQO1 expression level and activity (556 ± 18 nmol cytochrome *c* reduced/min/mg protein) when compared to PC-3 cells (108 ± 17 nmol cytochrome *c* reduced/min/mg protein). LNCaP cells do not express NQO1, even though they have a wild-type NQO1 gene (26). In a previous study, we established an isogenic LNCaP system in which cells expressed or lacked NQO1 expression by an NQO1-bearing retrovirus or vector only, respectively (5). LNCaP NQO1+ cells showed similar NQO1 activity (108 ± 21 nmol cytochrome *c* reduced/min/mg protein) as PC-3 cells after selection.

Following examination of NQO1 levels in human prostate tumors, relative survival assays of the three cell lines after exposure to β -lap were conducted to determine cytotoxicity (Figure 2B). After a 2 h exposure of β -lap at a dose of 2 μ M, the relative survival of DU145 and LNCaP NQO1+ cells remained essentially unaffected (<10% lethality). However, the same exposure time and dose in PC-3 cells led to a >50% decrease in survival. An increase in dose to 4 μ M of β -lap led to a >95% lethality of both DU145 and PC-3 cells. By

comparison, only a 30% lethality of LNCaP NQO1+ cells was achieved at this same dose, and it was not until a dose of 6 μM of β -lap that a >80% lethality of LNCaP cells was achieved. It is important to note at this time that dicoumarol, an NQO1 inhibitor administered at a dose of 40 μM , effectively rescued DU145 and PC-3 cells from β -lap-induced cell death, confirming the NQO1-dependent cell killing mechanism of β -lap. Examination of dicoumarol administered to DU145 and PC-3 cells, as well as NQO1- LNCaP cells, showed that >95% of cells in all three cell lines were able to survive a 6 μM dose, with increasing doses (e.g. 8 μM and 10 μM) resulting in greater lethality for the 2 h exposure time. However, at 20 μM , there was no distinction with regard to lethality between NQO1-expressing and NQO1-null cells for LNCaP, as well as the failure of dicoumarol to rescue DU145 and PC-3 cells, suggesting that other NQO1-independent mechanisms might be involved in β -lap cytotoxicity at supralethal doses. The LD₅₀ values of the three cell lines following a 2 h exposure of β -lap can be found in Table 1.

Incorporation of free β -lap together with β -lap.HP β -CD complex into millirods led to an initial burst followed by sustained release of β -lap. Polymer millirods for the purposes of intratumoral delivery of β -lap to prostate tumors were produced and the release kinetics of the drug *in vitro* examined. Given the fact that a 2 h exposure of the drug results in irreversible cell death, an initial burst of the drug was desired to rapidly achieve therapeutic levels, followed by a sustained release over a prolonged period of time. As shown in Figure 3, a burst release of ~0.4 mg occurs within the first 12 h, due predominantly to the presence of β -lap complexed with HP β -CD, which has been shown previously to enhance drug release (24). After this time, release of drug decreased over time, with an approximate release rate of 0.05 mg of drug/day for the next 3 days. By the sixth day, 0.6 mg of drug was released from the millirod, and the release rate

for the subsequent 4 days was 0.01 mg of drug/day. By day 23, the release of the drug from the millirod is 0.7 mg, highlighting the sustained release of drug due most likely to the fraction of free drug remaining as a molecular dissolution in the PLGA polymer (24).

The inset in Figure 3 serves to demonstrate similarities of β -lap release kinetics in an *in vitro* setting compared to *in vivo* release in PC-3 tumor xenografts within 48 h after millirod implantation. After 6 h *in vivo*, a burst dose of 0.3 mg of the drug has been released from the millirod, compared to an approximate 0.2 mg released in the *in vitro* experiment. At the transition point between burst and sustained release (12 h), 0.47 mg of drug has been released from implanted millirods compared to 0.39 mg for *in vitro* millirods. After 1 day, the drug amount released *in vitro* is 0.44 mg, compared to 0.58 mg *in vivo*, eventually rising to 0.5 mg and 0.72 mg, respectively, after 2 days. Although release of drug *in vivo* is slightly greater than release *in vitro*, this difference is not statistically significant at all timepoints.

Intratumoral delivery of β -lap-loaded millirods led to significant antitumor efficacy. In order to examine antitumor effects, β -lap-containing millirods were implanted into subcutaneous PC-3 xenografts located on the flanks of athymic nude mice. Tumor sizes were measured every other day and compared with tumors containing control (blank) millirods. The average tumor size at the beginning of the study was approximately 300 mm³ (Figure 4A). Within 3 days following implantation, the control tumors nearly doubled in size to an average volume of 551 \pm 39 mm³, while treated tumors regressed to a size of 204 \pm 12 mm³. This pattern of tumor regression quickly becomes one of tumor size maintenance and delayed growth, a pattern that contrasts considerably with the continued and uninhibited growth in control tumors. At day 11, the average size of the control tumors surpassed 1000 mm³ (1039 \pm 92 mm³), while β -lap-treated

tumors have yet to grow back to their original size of 300 mm³ (282 ± 31 mm³). It is important to note that it took 25 days for tumors in the treatment group to surpass the 1000 mm³ mark. This highlights the delayed tumor growth achieved with implantation of β-lap-loaded millirods. After 13 days, the treated tumors have surpassed their initial size and measured an average of 371 ± 54 mm³, while control tumors measured 1130 ± 98 mm³. After day 17, the tumors treated with β-lap millirods began to grow at a similar rate as control tumors, as evidenced by comparable growth rates (51.1 mm³/day for control tumors and 55.6 mm³/day for treatment tumors). In spite of tumor regrowth, statistical analyses at each time point demonstrated significant tumor volume differences (P-value < 0.01) between treated and control groups. Mixed model statistical analyses showed a more pronounced difference (p-value < 0.0001) in total tumor growth behavior between these two groups.

In an attempt to establish possible toxicity resulting from the proposed strategy, animal weights were recorded over the duration of the study (Figure 4B). As can be seen from the figure, the weights in both control and treated groups remain highly similar throughout the course of the experiment, with the average weight being 25 g. No statistical difference was found between the average weights of the two groups, indicating no difference in toxicity between mice treated with β-lap millirods and mice with control millirods. While there appears to be no difference in systemic toxic side effects, the two groups possess differences in animal survival, as evidenced by the Kaplan-Meier survival curve in Figure 4C. The rapid growth of subcutaneous tumors in mice with control millirods led to animal loss at earlier timepoints compared to mice in the treated group. An approximate 50% loss in animals was observed after 25 days in the control group. By comparison, all the animals in the β-lap millirod treatment group survived at this timepoint, and a 50% loss in survival did not occur until

after 35 days. At 35 days, all animals in the control group were lost, while a small fraction of mice in the treatment group survived past 40 days. A Log-rank test of the Kaplan-Meier survival curve indicates that there is a significant delay for the tumor in the treatment group to reach the size for sacrifice when compared to control tumors (P-value = 0.0024).

Histological examination of tumor tissues following treatment with β -lap millirods confirmed significant antitumor response. To determine whether or not PC-3 tumor xenografts maintained NQO1 expression, a key target for achieving cancer specificity by β -lap-loaded PLGA millirods *in vivo*, xenograft tissues were harvested and immunoblotting was conducted to measure NQO1 levels (Figure 5A). The results indicate that high NQO1 expression levels were preserved following subcutaneous implantation and growth in the flanks of mice, and that these levels were comparable to PC-3 cells harvested *in vitro*.

Histological examination of tumor tissues explanted from mice 6 days after millirod implantation shed insight into the mechanism of treatment afforded by β -lap-loaded millirods. As shown in Figure 5B, the area immediately adjacent to control millirods contained numerous viable tumor cells in H&E stained sections, easily identifiable by clusters of dark staining nuclei. Magnification of this implant boundary (Figure 5D) showed tumor cells that have large nuclei, irregular in shape and size, and undergoing mitosis. These observations served to corroborate the presence of viable tumor cells in this area. At regions farther away from the implant, a typical patchy necrotic area (region labeled *), due to fast proliferation rates in high-grade tumors, can also be observed. In contrast, β -lap-treated tumors (Figure 5C) showed a pronounced area of coagulative necrosis in the region surrounding the β -lap millirod implant. Easily discernible from the image is a sharp demarcation line between necrosis and dark staining cells at distances away from the implant. A higher magnification image of this zone

(Figure 5E) shows the presence of a large number of inflammatory cells, mostly neutrophils and lymphocytes, whose incidence is caused mainly by tumor treatment. Immediately adjacent to the inflammatory cells are viable tumor cells (again evidenced by large nuclei, irregular shape, and mitotic state), that become more and more pronounced at distances farther away from the treatment radius. As in control tumors, an area of patchy necrosis at distances farther away from the implant can also be observed, interspersed with viable cells, necrotic cells, apoptotic cells, and inflammatory cells.

In order to further evaluate possible systemic side-effects of β -lap-loaded millirods, we performed histological examination of liver and kidney tissues 1 month after millirod implantation (Figure 6). H&E staining of the tissues did not show any pathological changes in either tissue after β -lap treatment compared to those with control millirods. The absence of tissue damage or cell abnormalities in the liver and kidney strongly suggest that there were no noticeable signs of systemic toxicity brought about by millirod-delivered β -lap.

Discussion

The objective of the present study was to evaluate the *in vivo* antitumor efficacy of β -lap, a novel and unique anticancer drug, delivered intratumorally via a polymer depot. Currently, 10-15 year survival rates for patients with primary prostate cancer are 65% after surgery (27), and 67-87% after brachytherapy (28). Invasiveness of the surgical procedure and high local recurrence rates provide the motivation for the search for efficacious alternative and supplemental therapies. Docetaxel is a frequently used drug for chemotherapy of prostate cancer that offers moderate success, but results in high systemic toxicity (4, 29). Moreover, human prostate tumors are inherently resistant to many other clinically used drugs, given the fact that loss of androgen dependence and tumor suppressor

genes (e.g. p53) are important factors in prostate cancer progression (30-32). Additionally, these tumors are commonly dysregulated with regard to calcium homeostasis (33), and lack caspases that mediate apoptosis (34). To overcome the shortcomings of current treatments, a novel agent is required that can offer an effective prostate tumor-specific treatment while sparing normal cells. The unique mechanism of action of β -lap, involving its bioactivation through the NQO1 enzyme, makes it an ideal agent for the treatment of tumors that overexpress this enzyme, such as prostate cancer. Results from cell culture studies demonstrate that a short exposure of β -lap for 2 h causes irreversible cell death, contrasting tremendously with other known anticancer drugs, where a prolonged drug exposure time may be required to elicit cytotoxicity.

In light of the aforementioned data, it would be expected that an intravenous administration of β -lap would prove a highly effective treatment modality for prostate cancer. However, results from this study also show that high-dose administration of the drug led to significant toxicity of NQO1-nonexpressing prostate cancer cells. Indeed, prior research showed significant antitumor response in pancreatic cancer xenografts after systemic administration of β -lap, but caused mortality at high therapeutic doses (6). Additionally, β -lap administration at different time points was only able to bring about a minor delay in tumor growth, and was unable to produce long-term tumor regression. Thus, treatment with β -lap warrants an effective delivery vehicle that can offer site-specific and sustained administration of the drug.

Matrix-based drug delivery devices represent a rising trend in cancer chemotherapy yielding advantages such as: 1) exposure of tumors to therapeutic levels of the drug for a prolonged time; 2) reduction of toxicity to healthy cells; and 3) potential tailoring of release kinetics for design of the most efficacious delivery regimen. Several implant strategies have been explored for intratumoral

treatment of cancers. For example, Gliadel® wafers, consisting of BCNU incorporated into a 1,3-bis-(*p*-carboxyphenoxy)propane and sebacic acid polymer matrix, have been shown to result in a 27% reduction in risk of mortality from malignant glioma (35). Moreover, Wientjes et al. developed a doxorubicin-releasing poly(lactide-co-glycolide) (PLG) implant for the treatment of prostate tumors, demonstrating feasibility for *in vivo* use as well as low systemic concentrations of the drug after implantation into the prostate of beagle dogs (36). Recently, we reported β -lap-loaded millirods with tailorable release kinetics depending on inclusion of excipient molecules (e.g. glucose) or complexation with different cyclodextrin complexes (e.g. α -CD, β -CD, and γ -CD) (24). We were able to demonstrate that β -lap complexation with HP β -CD allowed for faster release of β -lap from the millirods, in part due to the increase in drug solubility from 0.038 mg/mL to 16 mg/mL. On the other hand, free drug showed the slowest release due to the formation of a molecular-level mixture with the PLGA polymer and the lack of excipient molecules in the polymer matrix.

Based on the fact that a 2 h exposure of β -lap leads to irreversible cell death, we designed a polymer millirod that featured a burst release of the drug within a short time period so as to achieve an elevated, therapeutic dose of the drug, followed by a sustained release of the drug over a prolonged period of time. This was achieved by incorporating both complexed and free drug within the millirod, with the complexed form of the drug providing a burst release of the drug (~0.4 mg released within the first 12 h) and the free form providing a sustained release of the drug (release rate of 0.01 mg of drug/day). The burst release would lead to an elevation of the drug concentration within tumors and quickly exert tumor cell killing effects, while the sustained release would maintain the drug concentration inside the tumor. Data show that *in vivo* burst

release kinetics of β -lap correlated very closely with release *in vitro*, with no statistical difference between the two conditions.

To evaluate antitumor efficacy and systemic toxicity, β -lap-loaded polymer millirods were implanted into PC-3 prostate tumor xenografts ($\sim 300 \text{ mm}^3$). Results from this study showed significant tumor regression and delayed growth after intratumoral implantation of the β -lap millirods. Moreover, survival of animals treated with β -lap millirods was significantly increased compared with untreated mice. Minimal, if any, systemic toxicity was observed, as evidenced by the lack of weight loss and normal appearing histology of major organs (e.g. liver, kidney). Taken together, this data serves to highlight the potential of utilizing intratumoral delivery of β -lap via polymer millirods as a viable treatment option for prostate cancer.

Results from this study showed tumor recurrence as a potential limitation of the current treatment. Tumor regrowth was found 2 weeks after millirod implantation (Figure 4A), which is likely due to viable cancer cells in the region adjacent to the treatment area (Figure 5B-E). To overcome this limitation, it may be necessary to combine the current treatment with another therapeutic modality, in an adjuvant or neoadjuvant fashion. For example, patients may undergo radiation therapy or a minimally invasive ablative technique (cryotherapy or radiofrequency ablation), followed by the implantation of a β -lap-containing polymer millirod in order to maximize therapeutic potential. Previously, our laboratory demonstrated that the combination of radiofrequency ablation of VX2 liver tumors followed by the intratumoral implantation of a doxorubicin-containing millirod resulted in increased efficacy as compared to millirod implants alone (37). The selective killing feature of β -lap makes it more appealing than other drugs due to its tumor selectivity and reduced toxicity in tissues that do not express NQO1. Furthermore, previous studies have shown that

β -lap functions as a radiosensitizer, with *in vitro* studies demonstrating that a low dose of β -lap together with a low dose of IR leads to synergistic cell death (38). Therefore, β -lap millirods may be implanted initially, followed by low-dose ionizing radiation (IR) in order to provide synergy between the two treatment modalities and enhance antitumor efficacy. The combination can be achieved by applying either external beam or co-implantation of low dose irradiation materials such as brachyseeds together with β -lap millirods. All in all, several viable combination strategies exist that can potentially maximize the therapeutic outcome of intratumoral β -lap implants.

Conclusion

β -Lap-containing polymer millirods represent an exciting therapeutic option for the targeted treatment of prostate tumors that overexpress the enzyme NQO1. By combining a novel drug, β -lap, whose mechanism of action is enhanced by an enzyme overexpressed in prostate tumors, with a local polymer delivery device capable of controlled-release, we were able to demonstrate significantly improved antitumor efficacy. Moreover, results from this study demonstrate minimal systemic toxicity and prolonged animal survival. Work is currently in progress to further maximize treatment efficacy by combining the therapy with existing radiotherapy strategies.

Acknowledgements

This work was supported by NIH grant CA90696 to JG and DOD grant W81XWH-04-1-0164 to DAB. EB is grateful for the support of an NIH minority supplement grant and DOD predoctoral grant W81XWH-05-1-0258. This is report CSCN016 from the Cell Stress and Cancer Nanomedicine program in the

Simmons Comprehensive Cancer Center at the University of Texas Southwestern Medical Center at Dallas.

References

1. Jemal A, Siegel R, Ward E, Murray T, Xu J, Thun MJ. Cancer statistics, 2007. *CA Cancer J Clin* 2007;57: 43-66.
2. Malaeb BS, Rashid HH, Lotan Y, *et al.* Prostate cancer disease-free survival after radical retropubic prostatectomy in patients older than 70 years compared to younger cohorts. *Urol Oncol* 2007;25: 291-7.
3. Bracarda S, de Cobelli O, Greco C, *et al.* Cancer of the prostate. *Crit Rev Oncol Hematol* 2005;56: 379-96.
4. Small EJ. Docetaxel in prostate cancer. *Anticancer Drugs* 2001;12 Suppl 1: S17-20.
5. Planchon SM, Pink JJ, Tagliarino C, Bornmann WG, Varnes ME, Boothman DA. beta-Lapachone-induced apoptosis in human prostate cancer cells: involvement of NQO1/xip3. *Exp Cell Res* 2001;267: 95-106.
6. Ough M, Lewis A, Bey EA, *et al.* Efficacy of beta-lapachone in pancreatic cancer treatment: exploiting the novel, therapeutic target NQO1. *Cancer Biol Ther* 2005;4: 95-102.
7. Bey EA, Bentle MS, Reinicke KE, *et al.* An NQO1- and PARP-1-mediated cell death pathway induced in non-small-cell lung cancer cells by beta-lapachone. *Proc Natl Acad Sci U S A* 2007;104: 11832-7.
8. Bentle MS, Reinicke KE, Bey EA, Spitz DR, Boothman DA. Calcium-dependent modulation of poly(ADP-ribose) polymerase-1 alters cellular metabolism and DNA repair. *J Biol Chem* 2006;281: 33684-96.
9. Pink JJ PS, Tagliarino C, Varnes ME, Siegel D, Boothman D. A. NAD(P)H:Quinone oxidoreductase activity is the principal determinant of beta-lapachone cytotoxicity. *J Biol Chem* 2000;275: 5416-24.
10. Tagliarino C, Pink JJ, Dubyak GR, Nieminen AL, Boothman DA. Calcium is a key signaling molecule in beta-lapachone-mediated cell death. *J Biol Chem* 2001;276: 19150-9.
11. Reinicke KE BE, Bentle MS, Pink JJ, Ingalls ST, Hoppel CL, Misico RI, Arzac GM, Burton G, Bornmann WG, Sutton D, Gao J, Boothman DA. Development of beta-lapachone prodrugs for therapy against human cancer cells with elevated NAD(P)H:quinone oxidoreductase 1 levels. *Clin Cancer Res* 2005;11: 3055-64.
12. Nasongkla N, Wiedmann AF, Bruening A, *et al.* Enhancement of solubility and bioavailability of beta-lapachone using cyclodextrin inclusion complexes. *Pharm Res* 2003;20: 1626-33.

13. Tewari A, Raman JD, Chang P, Rao S, Divine G, Menon M. Long-term survival probability in men with clinically localized prostate cancer treated either conservatively or with definitive treatment (radiotherapy or radical prostatectomy). *Urology* 2006;68: 1268-74.
14. LaVan DA, McGuire T, Langer R. Small-scale systems for *in vivo* drug delivery. *Nat Biotechnol* 2003;21: 1184-91.
15. Fleming AB, Saltzman WM. Pharmacokinetics of the carmustine implant. *Clin Pharmacokinet* 2002;41: 403-19.
16. Ewend MG, Elbabaa S, Carey LA. Current treatment paradigms for the management of patients with brain metastases. *Neurosurgery* 2005;57: S66-77; discussion S1-4.
17. Limentani SA, Asher A, Heafner M, Kim JW, Fraser R. A phase I trial of surgery, Gliadel wafer implantation, and immediate postoperative carboplatin in combination with radiation therapy for primary anaplastic astrocytoma or glioblastoma multiforme. *J Neurooncol* 2005;72: 241-4.
18. Westphal M, Ram Z, Riddle V, Hilt D, Bortey E. Gliadel wafer in initial surgery for malignant glioma: long-term follow-up of a multicenter controlled trial. *Acta Neurochir (Wien)* 2006;148: 269-75; discussion 75.
19. He YC, Chen JW, Cao J, Pan DY, Qiao JG. Toxicities and therapeutic effect of 5-fluorouracil controlled release implant on tumor-bearing rats. *World J Gastroenterol* 2003;9: 1795-8.
20. Qian F, Stowe N, Liu EH, Saidel GM, Gao J. Quantification of *in vivo* doxorubicin transport from PLGA millirods in thermoablated rat livers. *J Control Release* 2003;91: 157-66.
21. Qian F, Szymanski A, Gao J. Fabrication and characterization of controlled release poly(D,L-lactide-co-glycolide) millirods. *J Biomed Mater Res* 2001;55: 512-22.
22. Szymanski-Exner A, Gallacher A, Stowe NT, Weinberg B, Haaga JR, Gao J. Local carboplatin delivery and tissue distribution in livers after radiofrequency ablation. *J Biomed Mater Res A* 2003;67: 510-6.
23. Weinberg BD, Ai H, Blanco E, Anderson JM, Gao J. Antitumor efficacy and local distribution of doxorubicin via intratumoral delivery from polymer millirods. *J Biomed Mater Res A* 2007;81: 161-70.
24. Wang F, Blanco E, Ai H, Boothman DA, Gao J. Modulating beta-lapachone release from polymer millirods through cyclodextrin complexation. *J Pharm Sci* 2006;95: 2309-19.
25. Planchon SM, Wuerzberger S, Frydman B, *et al.* Beta-lapachone-mediated apoptosis in human promyelocytic leukemia (HL-60) and human prostate cancer cells: a p53-independent response. *Cancer Res* 1995;55: 3706-11.
26. Steiner M, Hillenbrand M, Borkowski M, Seiter H, Schuff-Werner P. 609 C --> T polymorphism in NAD(P)H:quinone oxidoreductase gene in patients with

prostatic adenocarcinoma or benign prostatic hyperplasia. *Cancer Lett* 1999;135: 67-71.

27. Huang WC, Lee CL, Eastham JA. Locally ablative therapies for primary radiation failures: a review and critical assessment of the efficacy. *Curr Urol Rep* 2007;8: 217-23.

28. Heysek RV. Modern brachytherapy for treatment of prostate cancer. *Cancer Control* 2007;14: 238-43.

29. Beer TM, El-Geneidi M, Eilers KM. Docetaxel (taxotere) in the treatment of prostate cancer. *Expert Rev Anticancer Ther* 2003;3: 261-8.

30. Martel CL, Gumerlock PH, Meyers FJ, Lara PN. Current strategies in the management of hormone refractory prostate cancer. *Cancer Treat Rev* 2003;29: 171-87.

31. Downing SR, Jackson P, Russell PJ. Mutations within the tumour suppressor gene p53 are not confined to a late event in prostate cancer progression. a review of the evidence. *Urol Oncol* 2001;6: 103-10.

32. Downing SR, Russell PJ, Jackson P. Alterations of p53 are common in early stage prostate cancer. *Can J Urol* 2003;10: 1924-33.

33. Prevarskaya N, Skryma R, Shuba Y. Ca²⁺ homeostasis in apoptotic resistance of prostate cancer cells. *Biochem Biophys Res Commun* 2004;322: 1326-35.

34. Coffey RN, Watson RW, Fitzpatrick JM. Signaling for the caspases: their role in prostate cell apoptosis. *J Urol* 2001;165: 5-14.

35. Perry J, Chambers A, Spithoff K, Laperriere N. Gliadel wafers in the treatment of malignant glioma: a systematic review. *Curr Oncol* 2007;14: 189-94.

36. Ortiz R, Au JL, Lu Z, Gan Y, Wientjes MG. Biodegradable intraprostatic doxorubicin implants. *Aaps J* 2007;9: E241-50.

37. Weinberg BD, Blanco E, Lempka SF, Anderson JM, Exner AA, Gao J. Combined radiofrequency ablation and doxorubicin-eluting polymer implants for liver cancer treatment. *J Biomed Mater Res A* 2007;81: 205-13.

38. Miyamoto S, Huang TT, Wuerzberger-Davis S, *et al.* Cellular and molecular responses to topoisomerase I poisons. Exploiting synergy for improved radiotherapy. *Ann N Y Acad Sci* 2000;922: 274-92.

Figure 1. Schematic of complexation and incorporation of β -lap and β -lap•HP β -CD complex into PLGA millirods.

Figure 2. β -Lap killed human prostate cancer cells in an NQO1-dependent mechanism. (A) NQO1 protein expression levels in various human prostate cancer cell lines. LNCaP cells have an NQO1 polymorphism and are NQO1-deficient. Cells were transfected with NQO1 creating an isogenic NQO1 \pm -system. (B) Relative survival assays of three different cell lines exposed to either β -lap alone or β -lap and a 40 μ M dose of dicoumarol (Dic) for 2h at indicated doses. Error bars represent standard error mean (SEM) from six replicates.

Figure 3. Cumulative amount of β -lap released from PLGA millirods was plotted as a function of time. The figure inset depicts the cumulative β -lap released *in vitro* as compared to *in vivo* following millirod implantation into PC-3 tumor xenografts within 48 h. Values are mean \pm SEM (n=3).

Figure 4. Intratumoral delivery of β -lap using polymer millirods as a vehicle significantly enhanced antitumor efficacy in PC-3 tumor xenograft models. (A) Comparison of tumor volume after intratumoral implantation of either β -lap-loaded millirods or control millirods containing HP β -CD alone. Values are means \pm SEM (n=10). (B) Animal weight data over time in both control and treatment groups. Values are means \pm SEM (n=10). (C) Kaplan-Meier curves comparing the antitumor efficacy of two different types of millirods as shown in (A). Open circle represents either accidentally animal loss at day 27 or animal survival at the end of the experiment.

Figure 5. Histological examination (H&E) of PC-3 tumor xenograft sections after millirod implantation confirmed significant anti-tumor effects of β -lap *in vivo*. (A) Western blot demonstrating NQO1 expression in explanted PC-3 xenografts. Cell lysate of parental LNCaP cells (NQO1-) was used as negative control. (B) A cross section of tumor treated with HP β -CD-loaded millirod (4x magnification).

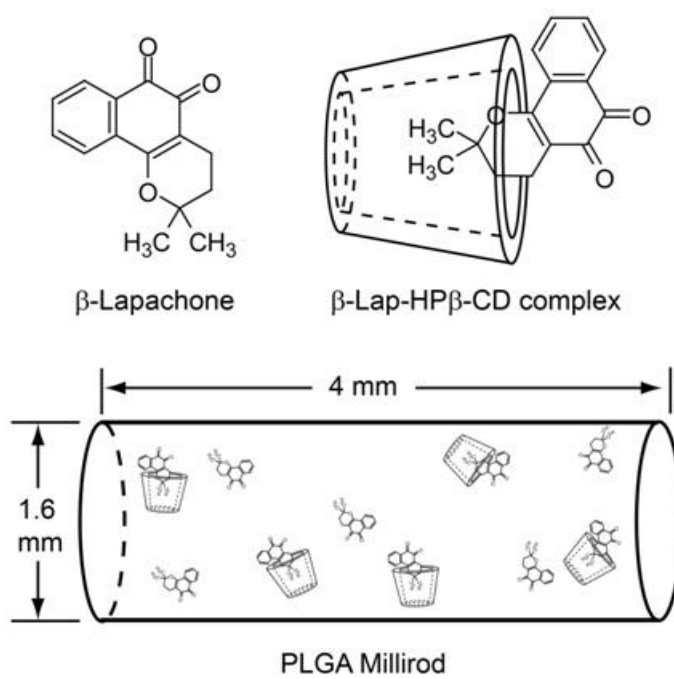
Circled 'R' represents the millirod implantation site, while * serves to show areas of patchy necrosis. (C) A cross section (4x magnification) of a tumor xenograft 6 days after implantation of β -lap-loaded millirod. (D) and (E) represent increased magnifications (40x) of (B) and (C) respectively.

Figure 6. Histological examination (H&E, 40X magnification) of liver and kidney tissues further corroborated negligible systemic toxicity observed with implant-delivered β -lap. (A) and (B) represent liver tissues while (C) and (D) represent kidney tissue. (A) and (C) are labeled as blank and refer to samples from control groups, while (B) and (D) represent tissues from experiments involving β -lap-loaded millirods.

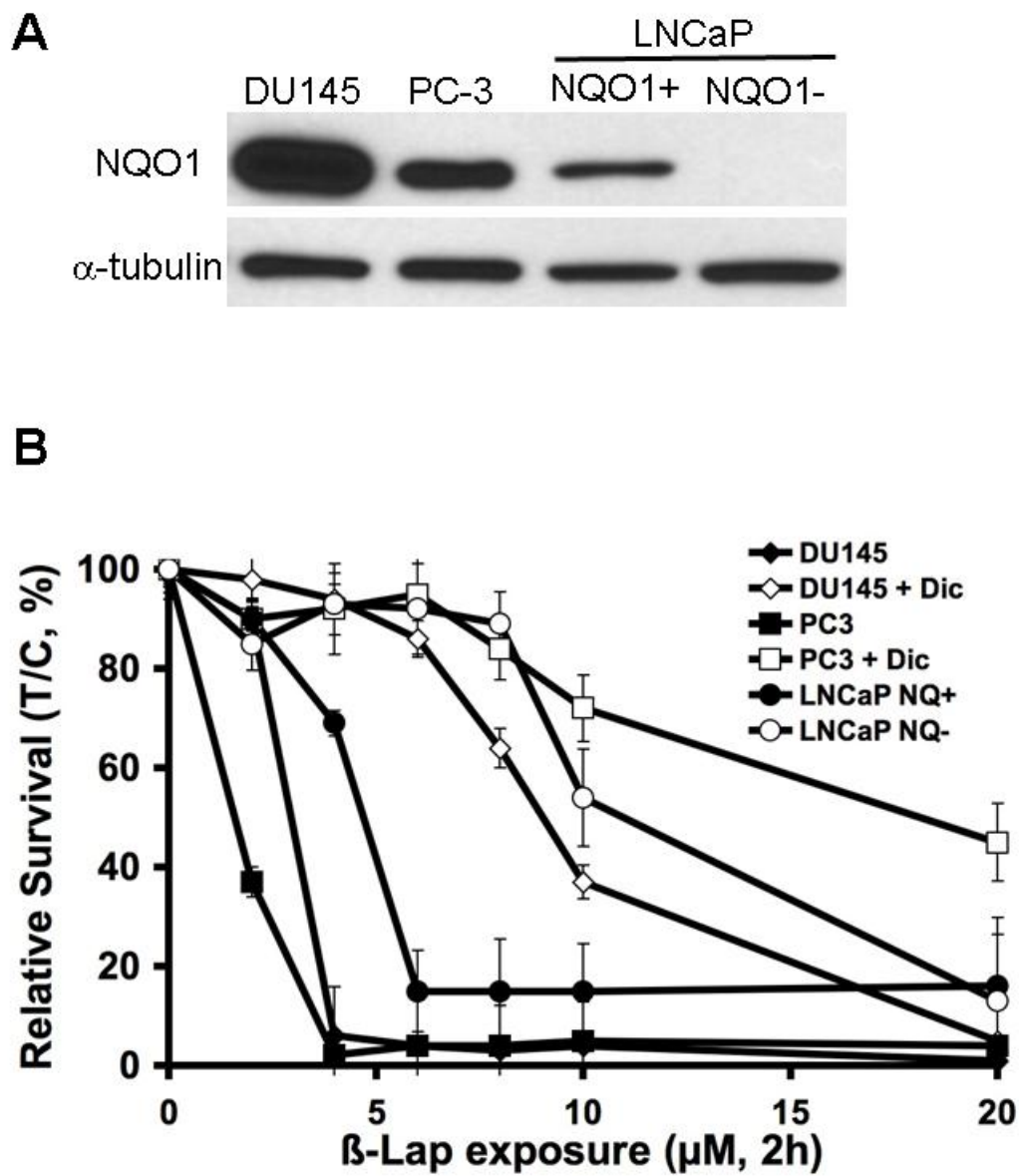
Table 1. NQO1 enzymatic activity and LD₅₀ of β -lap \pm Dic in three different prostate cancer cell lines

Cell Lines	NQO1 level (nmol cytochrome <i>c</i> reduced/min/mg protein)	β -Lap exposure LD ₅₀ (μ M, 2 h)	
		Dicoumarol (-)	Dicoumarol (+)
DU145	556 \pm 18	3.0 \pm 0.1	9.1 \pm 0.6
LNCaP NQO1+	108 \pm 21	2.7 \pm 0.9	> 20
LNCaP NQO1-	2.4 \pm 0.1	11.8 \pm 1.7	ND
PC-3	107 \pm 17	1.5 \pm 0.1	20.0 \pm 4.4

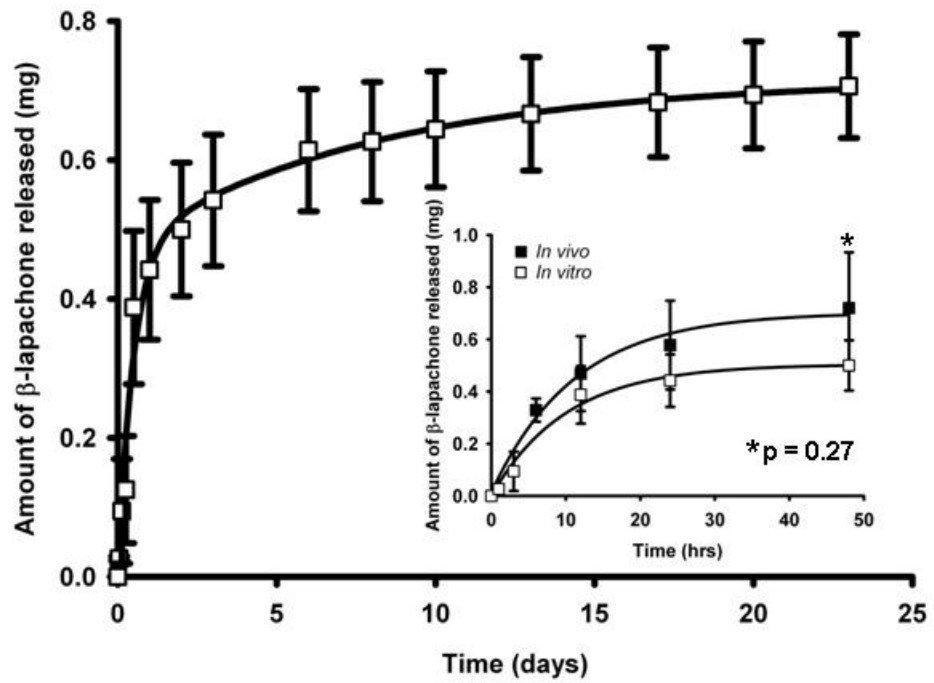
* Values are mean \pm SEM; n = 6 per group.



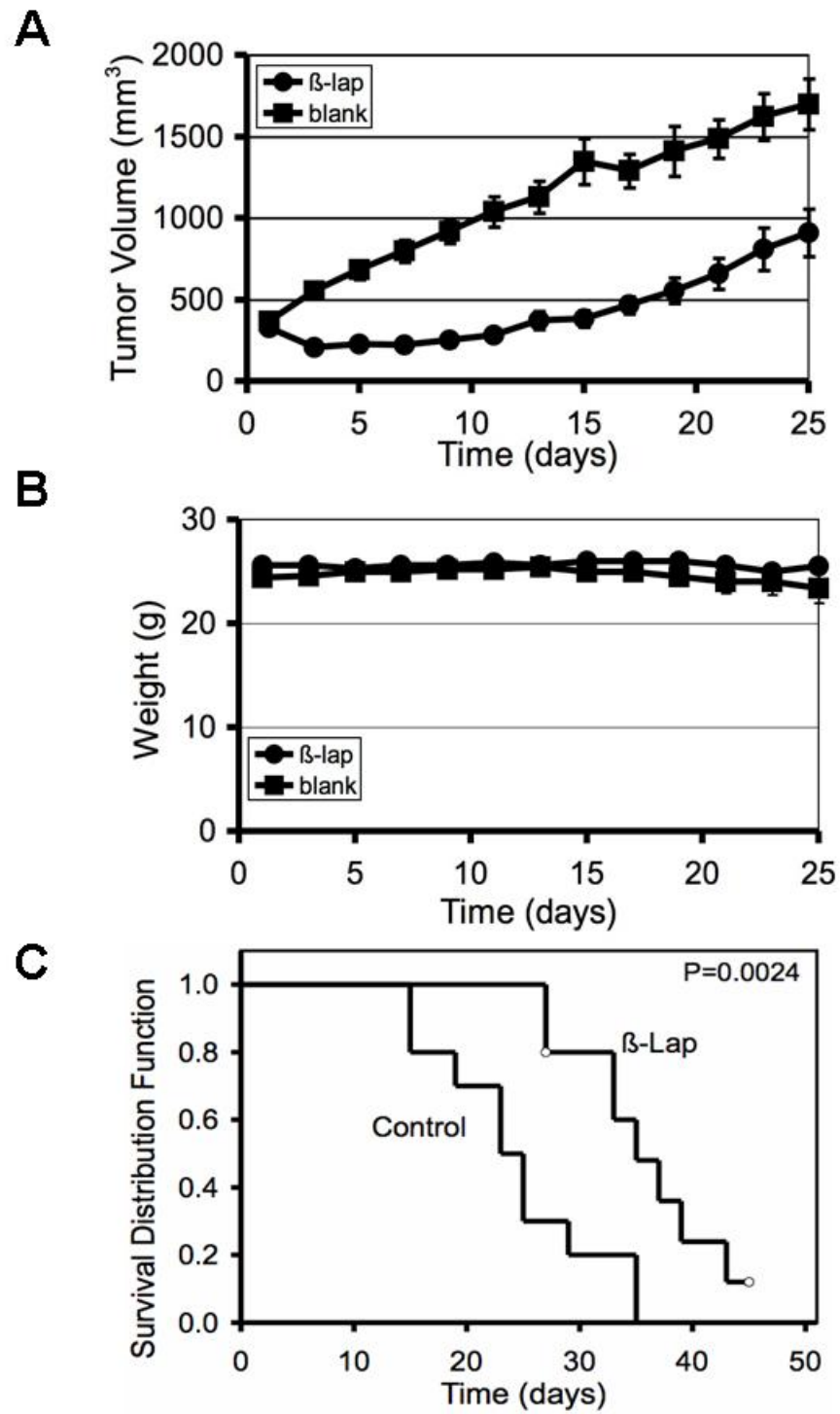
Dong et al. Fig. 1



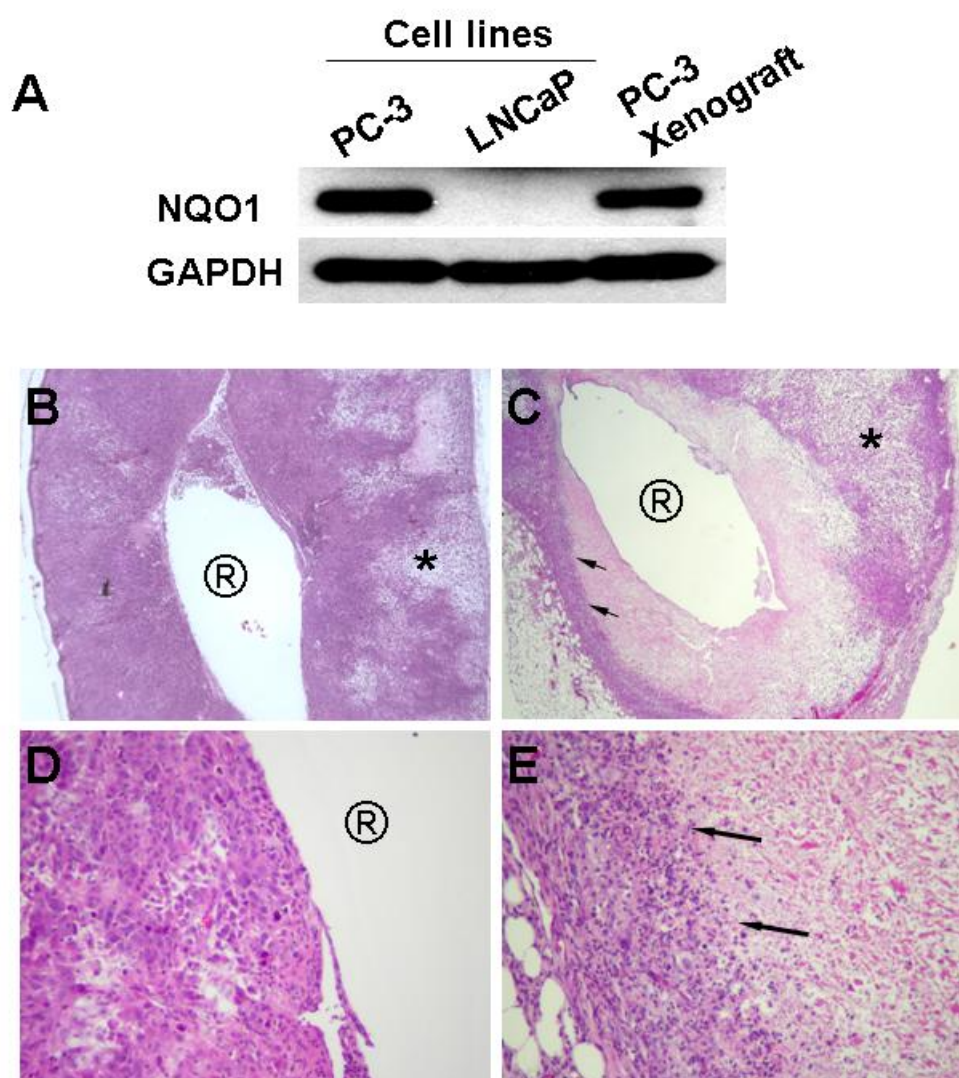
Dong et al. Fig. 2



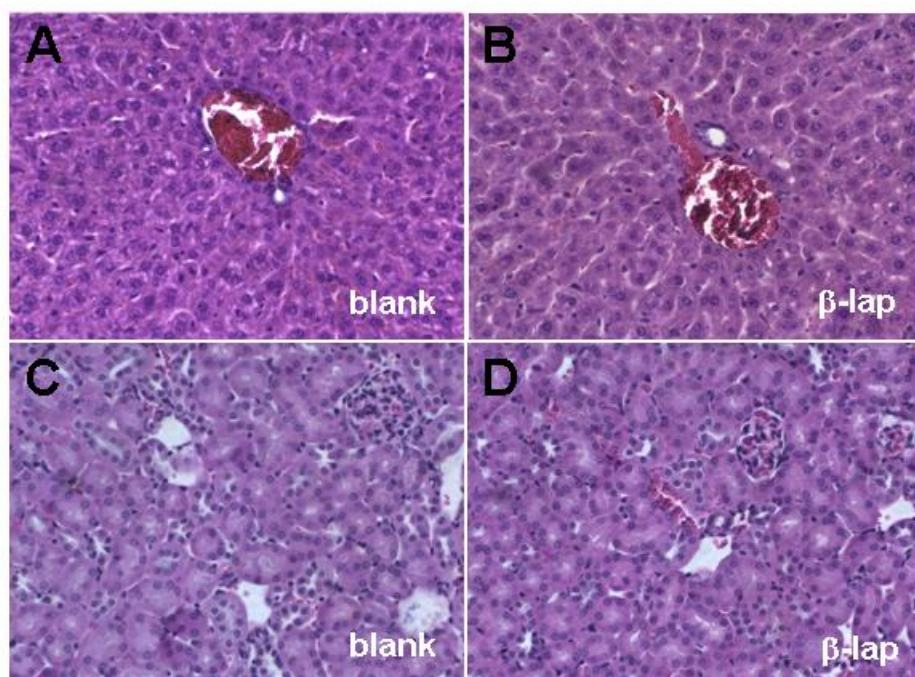
Dong et al. Fig. 3



Dong et al. Fig. 4



Dong et al. Fig. 5



Dong et al. Fig. 6

APPENDIX C
Published Manuscripts

Model simulation and experimental validation of intratumoral chemotherapy using multiple polymer implants

Brent D. Weinberg · Ravi B. Patel · Hanping Wu ·
Elvin Blanco · Carlton C. Barnett · Agata A. Exner ·
Gerald M. Saidel · Jinming Gao

Received: 12 December 2007 / Accepted: 8 May 2008 / Published online: 4 June 2008
© International Federation for Medical and Biological Engineering 2008

Abstract Radiofrequency ablation has emerged as a minimally invasive option for liver cancer treatment, but local tumor recurrence is common. To eliminate residual tumor cells in the ablated tumor, biodegradable polymer millirods have been designed for local drug (e.g., doxorubicin) delivery. A limitation of this method has been the extent of drug penetration into the tumor (<5 mm), especially in the peripheral tumor rim where thermal ablation is less effective. To provide drug concentration above the therapeutic level as needed throughout a large tumor, implant strategies with multiple millirods were devised using a computational model. This dynamic, 3-D mass balance model of drug distribution in tissue was used to simulate the consequences of various numbers of implants in different locations. Experimental testing of model predictions was performed in a rabbit VX2 carcinoma model. This study demonstrates the value of multiple implants to provide therapeutic drug levels in large ablated tumors.

Keywords Biodegradable implant · Liver cancer · Radiofrequency (RF) ablation · Mathematical model · Drug transport simulation

1 Introduction

Radiofrequency (RF) ablation has emerged as a viable alternative to surgery for the treatment of hepatocellular carcinoma (HCC) and colorectal metastases to the liver (CRM) [1, 25]. While its ease of use and minimally invasive nature have allowed this treatment modality to reach the forefront of ablative cancer treatments, tumor recurrence has been significant, particularly when RF ablation is applied percutaneously [2, 4, 10]. To address this limitation, biodegradable polymer implants were designed to release chemotherapeutic drugs into tumors after RF ablation. These polymer implants in the form of millirods have been tested in normal liver tissue [20, 23] as well as in experimental liver tumors in rabbits [28, 29]. Despite promising *in vivo* results, the clinical use of millirods may be limited by the inability to deliver a drug to distal regions of the remnant tumor. While ablation increases the extent of drug penetration into the tumor, therapeutic concentrations of drug are only found within 5 mm of the implant surface [29]. Unfortunately, this distance may be inadequate to treat HCC or CRM, which are often greater than 2 cm in diameter [6, 26]. Therefore, a polymer millirod treatment strategy should be developed that can deliver drugs to targeted regions and thus be applicable to clinically encountered tumors.

Multiple polymer millirods can be implanted within a tumor to increase the volume in which the drug concentration is above the therapeutic level. This approach has a number of potential advantages. First, multiple implants can increase the total amount of drug delivered to the tumor without a large increase in systemic drug exposure. Second, multiple implants in a single tumor can decrease the average distance between implants and the target tissue at the ablated periphery, where the risk for recurrence is highest.

B. D. Weinberg · R. B. Patel · G. M. Saidel · J. Gao
Department of Biomedical Engineering,
Case Western Reserve University, Cleveland, OH 44106, USA

H. Wu · A. A. Exner
Department of Radiology, Case Western Reserve University,
Cleveland, OH 44106, USA

B. D. Weinberg · E. Blanco · C. C. Barnett · J. Gao (✉)
Simmons Comprehensive Cancer Center, University of Texas
Southwestern Medical Center, 6001 Forest Park,
Rm ND2.210, Dallas, TX 75390, USA
e-mail: jinming.gao@utsouthwestern.edu

Previous work suggests that using multiple polymer millirods in a single tumor is a feasible treatment strategy. In an attempt to more thoroughly eradicate the tumor, most hepatic lesions are treated by “overlapping” zones of ablation applied via minimally invasive, laparoscopic or open procedures [1, 24]. In each of these cases, an implant could be inserted after each RF application to achieve a favorable geometric distribution of implants. Other cancer treatments have also adopted the multiple implant approach. For example, prostate cancer treatment with brachytherapy has embraced geometric distribution of implants, using the placement of multiple radioactive seeds to deliver ionizing radiation to tumors [8]. In this treatment, seed placement is planned by an experienced medical physicist, but considerable effort has been directed towards designing software to predict radiation coverage and speed treatment design [14]. Intratumoral treatment designs have also used multiple drug containing implants to optimize the spread of drug within the treated region. For treating gliomas, up to 8 BCNU-impregnated polyanhydride implants (Gliadel[®] wafers) are placed into the resection cavity after surgery [9]. Clinical trials have used up to 5 stereotactic injections per patient of 5-fluorouracil (5-FU)-containing microspheres into brain tumors [15, 16]. One recent report on the placement of multiple doxorubicin implants into dog prostates indicated that multiple implants could be highly effective in locally delivering chemotherapy to potential tumors [17]. These precedents suggest that placing multiple polymer millirods in a single tumor is a feasible and potentially effective strategy.

Although a multiple implant scheme is likely to improve drug distribution throughout a tumor, the ideal treatment approach and degree of benefit provided are not known. Simulation of drug distribution in tumors using a mathematical model of drug transport can be effective in the assessment of multiple implants. Results from model simulations can be used to predict drug exposure throughout the tumor, analogous to using computational tools to plan tumor radiation doses during prostate brachytherapy [12, 31]. A major advantage of using model simulation is that drug exposures can be rapidly evaluated and can minimize costly animal experiments. Based on predicted drug concentrations, simulated implant configurations can be compared based on predicted treatment efficacy. Additionally, model simulations can be used to evaluate drug exposures in different regions of the ablated tumor, especially near the tumor periphery where the thermal dose may not be sufficient to cause cell death [7].

In this study, we report the development of a multiple implant strategy for treating RF ablated tumors. A three-dimensional (3-D) model of drug transport in tissue was developed to simulate local drug concentrations in ablated

liver tissue and liver tumors. Comparisons were made between millirod treatments using center, peripheral, and combined arrangements of 1–6 doxorubicin containing polymer implants. Experiments with a liver tumor model in rabbits were used to determine the extent to which simulation results were valid. To our knowledge, this paper describes the first use of RF ablation combined with multiple chemotherapy implants to treat experimental tumors. Additionally, the use of the drug transport model provides new insight into predicting drug distribution after a multimodal treatment that can be used to design future treatments.

2 Methods

2.1 Drug transport model

The dynamic distribution of drug concentrations was simulated for two tissue conditions: (1) normal liver tissue with an ablated central core (Fig. 1a) and (2) normal tissue surrounding a tumor with an ablated central core (Fig. 1b). For these tissue conditions, one or more polymer millirods were placed in various arrangements. From each polymer millirod, doxorubicin (DOX) diffused into tissue according to a dynamic, 3-D transport model. In tumor tissue, DOX can be bound, i.e., coupled to molecules in the cell which prevent its diffusion, and unbound, i.e., free to move by convection or diffusion. Measurement of DOX concentrations in murine tumors has demonstrated DOX bound to intracellular molecules such as DNA can account for as much as 95% of total DOX [13]. Modeling free and bound DOX transport requires two transport equations. However, when the binding rate is rapid, the local free and bound DOX are nearly in equilibrium so that only one equation of total DOX concentration is sufficient to describe the drug distribution dynamics in tissue [5]. Furthermore, DOX transport in ablated livers can be adequately modeled without including a convection term [19]. Under these conditions, the governing equation for total DOX concentration C is:

$$\frac{\partial C}{\partial t} = D\nabla^2 C - \gamma C \quad (1)$$

where D is the apparent diffusion rate coefficient ($\text{m}^2 \text{s}^{-1}$) and γ is the apparent rate coefficient of elimination (s^{-1}) by perfusion and metabolism. Initially, no drug is in the tissue:

$$t = 0 : C = 0 \quad (2)$$

At the implant (im) surface, the drug concentration was assumed to vary with time and was linearly interpolated from experimental measurements from single implants placed in tumors and ablated tumors [29]:

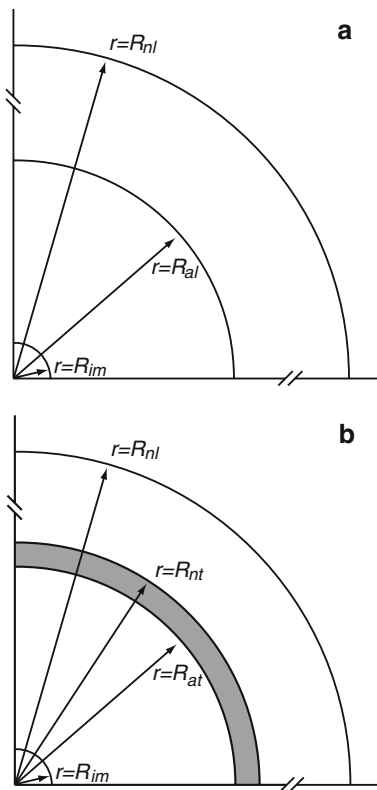


Fig. 1 Schematic representation of regions around the polymer implant assumed in simulating drug distribution in tissue: (a) normal liver with an ablated core; and (b) liver with a partially ablated tumor. The radii of the implant (im), ablated liver tissue (al), non-ablated liver (nl), ablated tumor (at), and non-ablated tumor (nt) are indicated by the arrows. The dark region at the periphery of ablated tumor is considered to have greater risk of tumor recurrence because of lower heat exposure. Distances not to scale

$$r = R_{im} : C_{im} = f(t) \tag{3}$$

This boundary condition, $f(t)$, is a constant plateau for the first 4 days, after which the concentration slowly decreases between days 4 and 8. This boundary condition is similar to previously published experimental measurements from rat livers [19]. Far enough into the non-ablated normal liver (nl), the drug concentration was assumed negligible because of the elimination process:

$$r = R_{nl} : C_{nl} = 0 \tag{4}$$

For condition (A) with normal tissue, the drug concentration and flux were assumed continuous at the boundary between the ablated normal liver (al) and non-ablated liver (nl):

$$r = R_{al} : C_{al} = C_{nl}, \quad D\nabla C_{al} = D\nabla C_{nl} \tag{5}$$

For condition (B) with a tumor surrounded by normal tissue, the drug concentration and flux were assumed continuous at the boundary between the ablated tumor core (at) and non-ablated tumor (nt):

$$r = R_{at} : C_{at} = C_{nt}, \quad D\nabla C_{at} = D\nabla C_{nt} \tag{6}$$

and at the boundary between the non-ablated tumor (nt) and surrounding normal liver (nl):

$$r = R_{nt} : C_{nt} = C_{nl}, \quad D\nabla C_{nt} = D\nabla C_{nl} \tag{7}$$

2.2 Simulation strategy

This model was used to simulate the dynamics of doxorubicin concentration distributions in tissue from implanted polymer millirods over 8 days based on finite-element code COMSOL 3.3 (Burlington, MA) with Cartesian coordinates. All geometries were meshed using the fine adaptive mesh setting within COMSOL, which provided a spatial resolution of <0.1 cm within regions of geometric complexity. Further decreases in mesh size had a negligible effect on the simulation outcomes.

For tissue condition (A) without a tumor, we assumed a spherical ablated region, $R_{im} \leq r \leq R_{al} = 0.9$ cm, surrounded by normal liver tissue, $R_{al} < r \leq R_{nl} = 4$ cm. Under this condition, simulations were performed to emulate placement of implants in an ablated rabbit liver for model validation. For condition (B), we assumed a spherical tumor with an ablated tumor core, $R_{im} \leq r \leq R_{at} = 0.9$ cm; a non-ablated tumor rim, $R_{at} \leq r \leq R_{nt} = 1.0$ cm, and surrounding region of normal liver tissue, $R_{nt} < r \leq R_{nl} = 4$ cm. This condition, which corresponded to an incompletely ablated tumor with a peripheral rim of viable tumor, was used to predict drug concentration distributions in scenarios with various, multiple implant tumor placements (Fig. 2). Two scenarios used either a short (8 mm) or long (16 mm) millirod implanted centrally; four scenarios used only short millirods peripherally implanted; four scenarios used short millirods peripherally implanted and a long millirod centrally implanted. All peripheral implants were placed 7 mm from the center of the ablated region. Short and long implants contained 3.4 and 6.8 mg of doxorubicin, respectively, which resulted in total doxorubicin doses in these scenarios ranging from 3.4 to 23.6 mg. This compared well to the recommended intravenously administered therapeutic dose of doxorubicin, which was 7.9–14.8 mg for rabbits [27]. All simulated doses were well below the estimated lethal dose (LD50) of 63.3 mg [3].

2.3 Diffusion and elimination parameter values

Model parameters were chosen based on previous estimates made from experimental doxorubicin distributions in ablated rat liver and ablated rabbit tumors [19, 30]. Parameter values are listed in Table 1. The doxorubicin diffusion and elimination rate coefficients could be considered constant under certain conditions and as functions of position and time under other conditions. In non-ablated

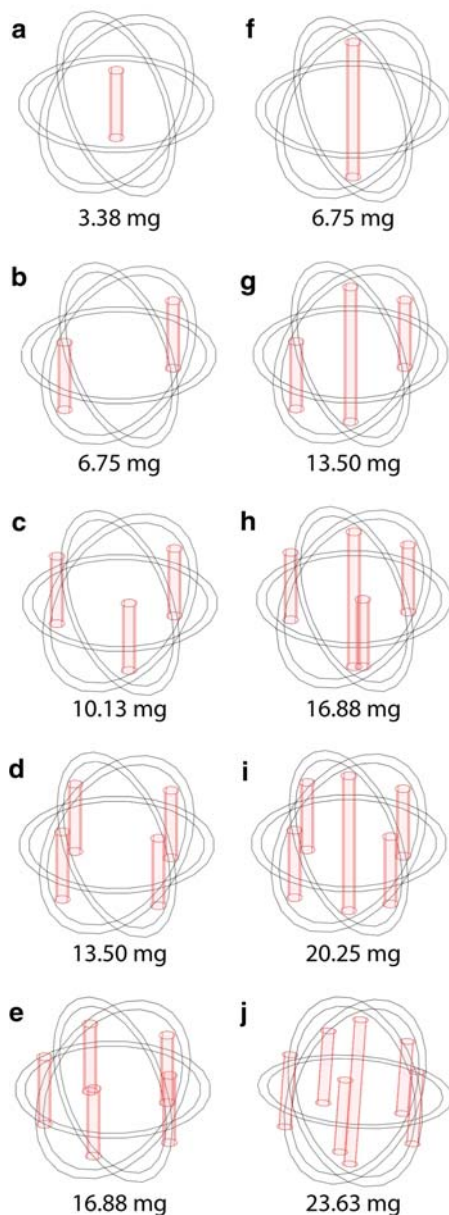


Fig. 2 Multiple implant configurations for simulating drug distribution in tissue with a 2.0 cm diameter tumor (denoted by the *outer sphere*) with a 1.8 cm diameter ablated tumor core (denoted by the *inner sphere*). Single central implant with different lengths: (a) 8 mm; (f) 16 mm. Two to five peripheral 8-mm long implants (b–e). Peripheral 8-mm long implants and a central 16-mm long implant (g–j). Total doxorubicin doses are shown below each design

and ablated normal liver tissue as well as non-ablated tumor, these coefficients have constant values. In ablated tumor regions, diffusion and elimination rate coefficients had to be considered as functions of position or time in order to simulate available data. Previous studies suggested that the DOX diffusion rate coefficient D in ablated tumors depends on position: higher in the central ablation region and lower in the outer region as indicated by histology [30]. For this study, the diffusion rate coefficient in ablated

Table 1 Simulation parameter values

Parameter	Abbreviation	Value
Diffusion, non-ablated liver ^a	D_{nl}	$6.7 \times 10^{-11} \text{ m}^2 \text{ s}^{-1}$
Diffusion, ablated liver ^a	D_{al}	$1.1 \times 10^{-11} \text{ m}^2 \text{ s}^{-1}$
Diffusion, non-ablated tumor ^b	D_{nt}	$5.0 \times 10^{-11} \text{ m}^2 \text{ s}^{-1}$
Diffusion, ablated tumor center ^b	D_{at}	$8.8 \times 10^{-11} \text{ m}^2 \text{ s}^{-1}$
Elimination, non-ablated liver ^a	γ_{nl}	$9.6 \times 10^{-4} \text{ s}^{-1}$
Elimination, non-ablated tumor ^a	γ_{nt}	$0.6 \times 10^{-4} \text{ s}^{-1}$
Elimination, ablated tumor (day 0) ^b	$\gamma_{at}(\text{day } 0)$	0 s^{-1}
Elimination, ablated tumor (day 8) ^b	$\gamma_{at}(\text{day } 8)$	$0.6 \times 10^{-4} \text{ s}^{-1}$

^a Qian et al. [19]

^b Weinberg et al. [30]

tumor ($R_{im} \leq r \leq R_{at}$) was expressed as a function of position (r):

$$R_{im} \leq r \leq \alpha R_{at} : D = D_{at};$$

$$\alpha R_{at} < r \leq R_{at} : D = D_{at} - \left[\frac{r - \alpha R_{at}}{R_{at} - \alpha R_{at}} \right] [D_{at} - D_{nt}] \quad (8)$$

where $\alpha = 0.47$ was chosen so that the diffusion rate coefficient was constant within a central region of the ablated tumor (D_{at}) and decreased linearly to the value in non-ablated tumor (D_{nt}). Previous estimates of doxorubicin diffusion in ablated tumors required coefficients that varied as a function of position and were greater near the centrally placed ablation probe, where temperature distributions are likely higher. This theory has been substantiated by histological findings in the ablated tissues [30]. In the ablated tumor, the elimination rate coefficient was expressed as a function of time $\gamma = \gamma_{at}(t)$:

$$0 \leq t \leq t_1 : \gamma_{at}(t) = 0; \quad t_1 \leq t \leq t_2 : \gamma_{at}(t) = \left[\frac{t - t_1}{t_2 - t_1} \right] \gamma_{at}(t_2) \quad (9)$$

For comparison to experimental results, $t_1 = 4$ days and $t_2 = 8$ days. The elimination rate coefficient is expected to be negligible for the first 4 days after an ablation that destroys tumor and vascular cells, abolishing both metabolism and perfusion. Between days 4 and 8, tissue and vascular cells develop as inflammation is resolved in the ablated region [30].

2.4 Evaluation of simulated drug treatments

The presumed efficacy of treatments was related to drug (doxorubicin) concentration [DOX] distribution. Several measures were computed for comparison. For these calculations, the tumor was divided into two regions: an inner core (75% of tumor volume) and an outer risk volume (25% of tumor volume). Average drug concentrations were

calculated for the whole tumor volume or risk volume over time ($t_2 = 8$ days). Treatments were further compared by calculating the fractions of whole tumor and risk volume for which drug concentrations were greater than a therapeutic target concentration, $[DOX^*] = 12.8 \mu\text{g/g}$, or two times the therapeutic value of doxorubicin in VX2 tumor [21, 22]. Two times the therapeutic concentration was chosen to provide a safety margin above which most cells could be assumed to be killed by the drug.

2.5 Manufacture of polymer implants

Doxorubicin-containing millirods were fabricated by combining 65% poly(D,L-lactide-co-glycolide) (PLGA) microspheres, 13.5% doxorubicin, and 21.5% NaCl (w/w) using a previously published compression-heat molding procedure [18]. The mixture was blended with a mortar and pestle, packed into a Teflon tube (1.6 mm inside diameter), and compressed with steel plungers (1.6 mm outside diameter) at 90°C for 2 h. Final implants were cylindrical with an approximate diameter of 1.6 mm and length of 8.0 mm.

2.6 Animal model and treatment

All animal experiments were approved by the Institutional Animal Care and Use Committee at Case Western Reserve University and followed all applicable guidelines. One multiple implant scenario selected from the simulated scenarios was tested both in ablated liver tissue and ablated liver tumors. To test in ablated liver, the abdomens of New Zealand White rabbits ($n = 2$) were opened just below the sternum. The liver was gently exposed and lifted, and a 17-G, 1 cm exposed tip ablation probe (Radionics, Burlington, MA) was inserted into the middle lobe of the liver. Tissue in contact with the tip was heated to a temperature of 90°C, as measured by a thermocouple sensor in the ablation probe, for 9 min. After ablation, polymer millirods were inserted into the ablated region in the pattern selected. If necessary, implants were secured in place by covering the puncture with resorbable gelatin foam and suturing it in place with a 6-0 monocril suture. The abdomen was then closed.

A combined treatment of rabbit liver tumors with RF ablation and doxorubicin millirods was performed based on a modification of a previous technique [29]. VX2 carcinomas ($n = 2$) were implanted in the liver and were allowed to grow for 28 days until they reached an approximate diameter of 2.0 cm. After 28 days, the abdomen was reopened, and a 17-G ablation probe with a 2-cm exposed tip (Radionics) was placed into the center of the tumor. The tissue was heated and maintained at a temperature of 90°C for 9 min to ablate a sphere with a

diameter of approximately 1.8 cm in the center of the tumor. After ablation, DOX-containing millirods were placed into the ablated tumor. In each of the groups, one of the rabbits was euthanized at each time point, 4 and 8 days after ablation.

2.7 Tumor evaluation

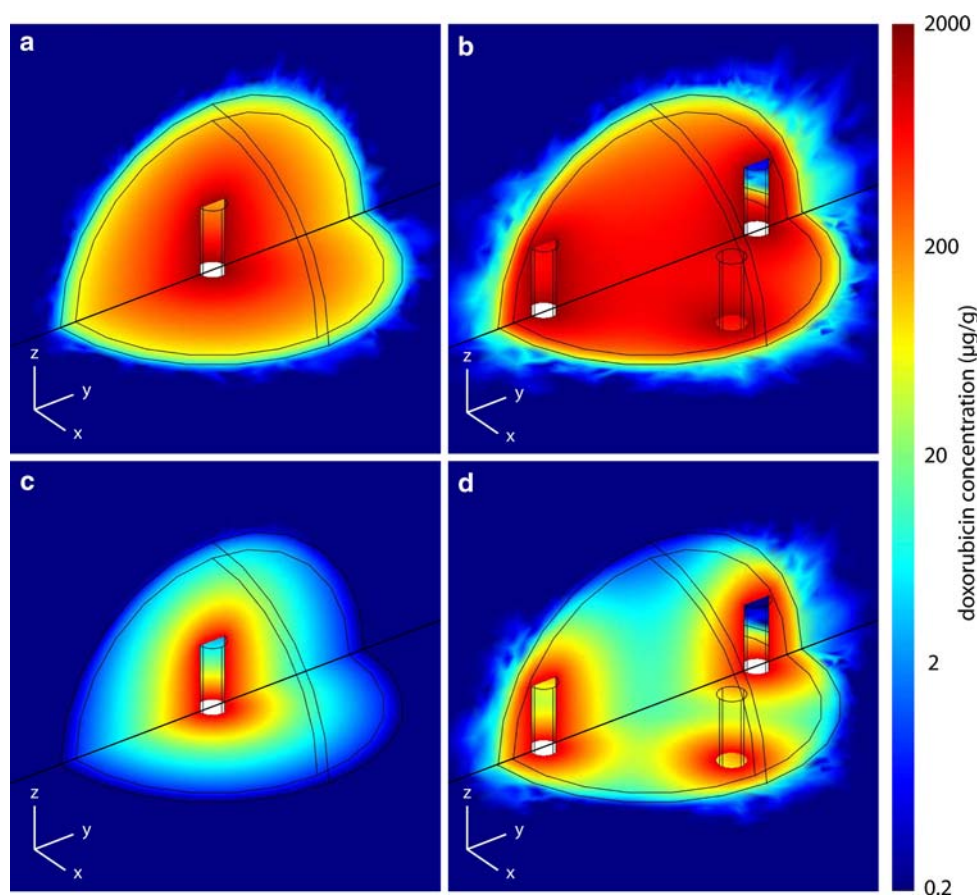
Tumors were removed from the surrounding liver tissue and sliced in half parallel to the front surface of the liver. One half of the tumor was fixed in formalin solution and the other half of the tumor was frozen at -20°C . Frozen liver sections 100 μm thick were sliced from each section using a cryostat microtome (Leica CM3050S) and then scanned with a fluorescent imager (Molecular Dynamics Fluorimager SI). The fluorescence value of ablated tissue background was subtracted using a background subtraction algorithm. The net fluorescence intensity (NFI) was empirically related to $[DOX]$ ($\mu\text{g/g}$), $\text{NFI} = 194 \cdot [DOX]^{0.67}$ [28]. The fixed tissue was embedded in paraffin, sliced, and stained with hematoxylin and eosin (H&E) or Masson's trichrome (MTC). Histology slides were subsequently used to identify the location of each tissue region in the DOX concentration maps.

3 Results

3.1 Simulated drug distributions using multiple implants

To quantify the advantage of multiple implants over a single implant in treating incompletely ablated tumors, a comparison was made between using one central implant and four peripheral implants. These scenarios correspond to the configurations shown in Fig. 2a and d, respectively. Doxorubicin (DOX) concentration distributions determined from model simulations for the two scenarios at 4 and 8 days after implantation are shown in Fig. 3. On day 4, DOX concentrations in the ablated tissue were high in both scenarios (Fig. 3a, b). However, the doxorubicin concentration $[DOX]$ of the non-ablated tumor rim, or risk volume, was higher in the multiple implant case. This pattern continued to day 8, when it was more evident because of decreasing $[DOX]$ in the single implant case (Fig. 3c, d). Over the 8 day period, the average $[DOX]$ in the whole tumor was 119 $\mu\text{g/g}$ using 1 implant and 290 $\mu\text{g/g}$ using 4 peripheral implants. In the risk volume, average $[DOX]$ over 8 days was 16.9 and 99.3 $\mu\text{g/g}$, respectively, for the two scenarios. Much of this advantage was expected, as the total DOX dose had been increased by a multiple of 4. However, the risk volume exposure increased roughly sixfold, indicating that repositioning the implants offered

Fig. 3 Simulated drug concentration distributions in tissue with 2.0 cm diameter tumor and 1.8 cm ablated tumor core on day 4 (**a, b**) and day 8 (**c, d**). Single implant in the center (**a, c**). Four implants spaced around the periphery (**b, d**)



more than a dose dependent increase in drug delivery to the periphery. On day 4, the [DOX] was above the therapeutic threshold concentration ($[\text{DOX}^*]$) in 100% of the risk volume with 4 implants, but only in 78% of the risk volume with a single implant.

3.2 Comparison of multiple implant configurations

Multiple implant strategies were quantitatively compared using measures of average [DOX] in the whole tumor and the risk volume (Figs. 4a, b). The average [DOX] increased almost linearly with total DOX dose, which depended primarily on the number of implants rather than implant configuration. In the risk volume, however, average [DOX] depended on the implant distribution in the tumor. For the same DOX dose, the average [DOX] in the risk volume from peripheral configurations was approximately $20 \mu\text{g/g}$ above the average [DOX] from peripheral + center configurations with equivalent dosage.

Implant configurations were also compared based on the duration for which 100% of the risk volume had [DOX] above $[\text{DOX}^*]$ (Fig. 4c, d). Center only configurations never reached the $[\text{DOX}^*]$ for 100% of the risk

volume, nor did the peripheral configuration with only 2 millirods. All other configurations with total DOX dose $\geq 10 \text{ mg}$ achieved $[\text{DOX}^*]$ for 100% of the risk volume and the duration of $[\text{DOX}] \geq [\text{DOX}^*]$ in 100% of the risk volume increased with DOX dose. No significant difference was seen between peripheral and peripheral + center treatment strategies. Configurations were also compared based on the time required for [DOX] to reach $[\text{DOX}^*]$ in 100% of the risk volume. Shorter times are more desirable because the cells around the periphery have had less time to recover from the heat exposure and may have a decreased tolerance to DOX. More implants decreased the time required for $[\text{DOX}] \geq [\text{DOX}^*]$ in 100% of the risk volume. At high doses of DOX, the peripheral + center strategy offered an advantage, primarily because it decreased the elapsed time until drug was delivered to the poles of the tumor. Otherwise, all treatments for which $[\text{DOX}] \geq [\text{DOX}^*]$ in 100% of the risk volume did so in 11–68 h. Configurations with equivalent total DOX doses did have some qualitative treatment differences. As expected, the peripheral implants provided $[\text{DOX}] \geq [\text{DOX}^*]$ over much of the tumor equator, but relatively less at the poles of the tumor. The advantage of the peripheral + center strategy was $[\text{DOX}] \geq [\text{DOX}^*]$

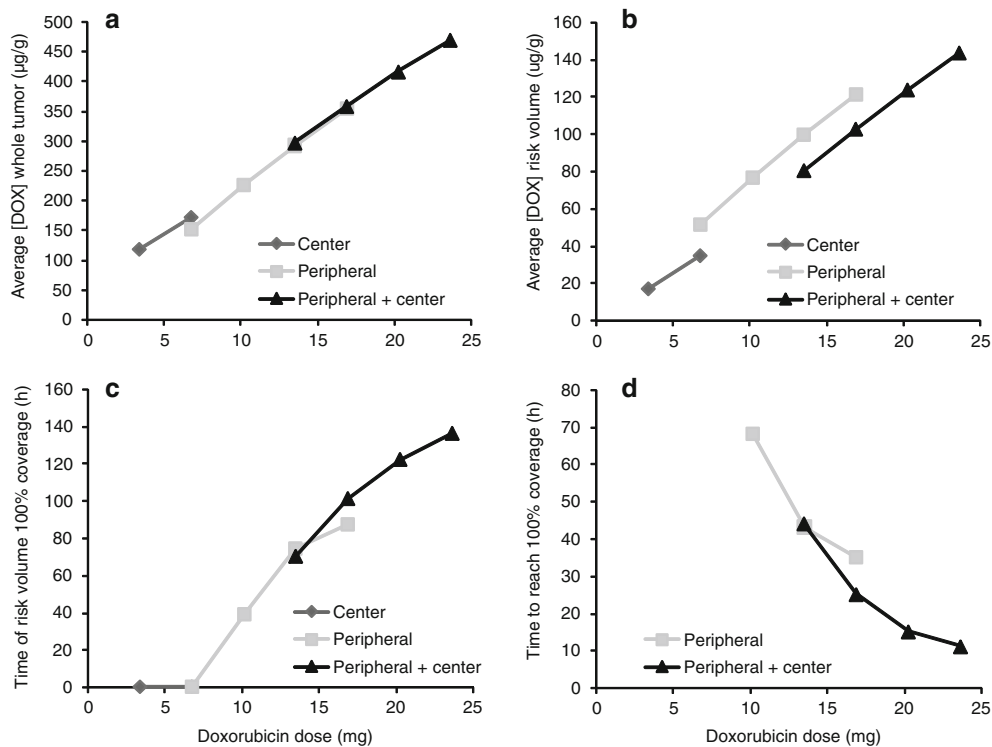


Fig. 4 Characteristics of simulated drug distribution with central implant, peripheral implants, or peripheral + central implants as a function of total DOX dose. Average doxorubicin concentration [DOX] over 8 days in (a) the entire tumor or (b) outer tumor rim (risk

volume). (c) Simulated duration for which [DOX] $\geq 12.8 \mu\text{g/g}$ in entire risk volume. (d) Time after implantation at which [DOX] $\geq 12.8 \mu\text{g/g}$ in entire risk volume

around much of the poles of the tumor rather than at lateral regions of the tumor surface.

3.3 Multiple implant treatment of ablated liver

In an *in vivo* experiment, normal rabbit livers were implanted after thermal ablation with 4 peripheral polymer millirods with DOX (Fig. 2d). A comparison of [DOX] predicted from the model simulation and measured from experimental data is shown in Fig. 5. From model simulation, [DOX] was high in the tissue surrounding the implants on day 4. The distribution of DOX continued throughout the ablated region, particularly toward the center of the ablated region by day 8. A similar trend was observed in the experimental data, but the observed [DOX] was markedly higher than predicted. Median [DOX] in the ablated region was almost three times higher from experimental data as compared to simulated data. However, the model accurately predicted that [DOX] $\geq [\text{DOX}^*]$ in more than 98% of the ablated tissue at days 4 and 8. From experimental data, the drug penetration distance, i.e. the distance from the ablation center at which [DOX] $< [\text{DOX}^*]$, was 8.5 mm on day 4 and 9.5 mm on day 8. A summary of [DOX] information is compiled in Table 2.

3.4 Multiple implant treatment of liver with ablated tumor

In an *in vivo* experiment, VX2 liver tumors in rabbits were thermally ablated and implanted with 4 peripheral polymer millirods with DOX (Fig. 2d). Although the model simulation tumor size was 2 cm in diameter, tumors were approximately 2.5 cm and had a cystic core when treated. Distribution of [DOX] from model simulations and experimental slices are shown in Fig. 6. Measured [DOX] distributions (Fig. 6b, d) were more irregular in experimental tumors than in the simulated spheres, reflecting the underlying asymmetry and inhomogeneity of the liver tumors. [DOX] could not be measured in the center of the tumor because of the cystic core of the tumor, but at the periphery of the ablated tumor [DOX] distributions appeared similar in simulation and experimental data. A quantitative summary of [DOX] in the tumors is given in Table 2. With respect to [DOX] $\geq [\text{DOX}^*]$ in the non-ablated tumor rim, the experimental data were similar to model predictions. On day 4, however, [DOX*] was attained in 87% of this region instead of the predicted 100%. Median [DOX] was also similar between model predictions and experimental measurements. For the non-ablated tumor rim on day 4, the

Fig. 5 Simulated drug distribution in ablated normal tissue compared to DOX distribution in images of ablated normal liver from in vivo rabbit experiments with four peripheral implants (located at *white asterisks*). Ablated regions are within *white dashed lines*. Thermal ablation source located at *white dots*. Model simulated DOX distributions on day 4 (**a**) and day 8 (**c**). DOX distributions from experimental images on day 4 (**b**) and day 8 (**d**). Fixation or preservation artifact in experimental images arose from fracture of brittle ablated tissue during slicing. Scale bars are 5 mm

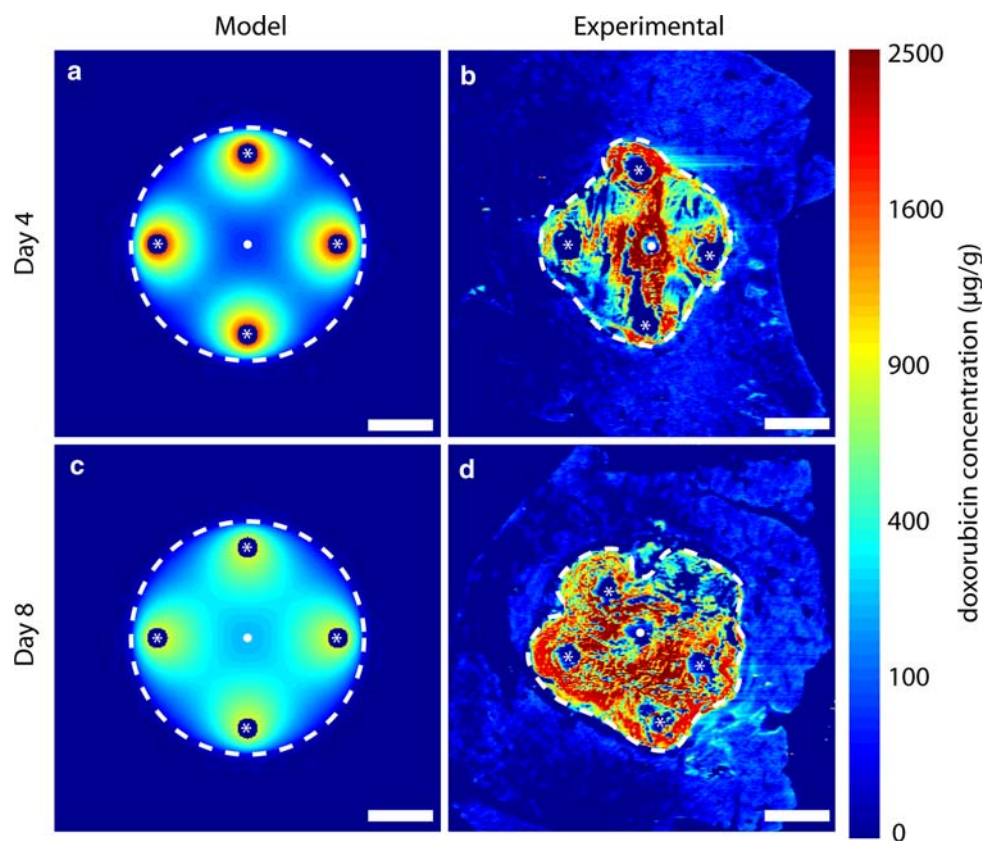


Table 2 Doxorubicin coverage of simulated and experimental tissues

	Model		Experimental	
	Day 4	Day 8	Day 4	Day 8
Ablated liver model (Condition A)				
Area of ablated liver (mm ³)	254	254	155	186
Ablated liver over [DOX*] (%)	98.3%	98.8%	98.0%	98.3%
[DOX] in ablated liver (µg/g) ^a	205 (117–430)	295 (192–398)	590 (166–1311)	1008 (361–1796)
Ablated tumor model (Condition B)				
Area of ablated tumor (mm ³)	254	254	343	418
Area of non-ablated tumor (mm ³)	60	60	195	90
Non-ablated tumor over [DOX*] (%)	100%	61%	87%	65%
[DOX] in non-ablated tumor (µg/g) ^a	140 (78–232)	20 (8–56)	79 (30–173)	26 (7–87)

^a Values shown are the median concentration. Brackets contain the 25th and 75th percentiles

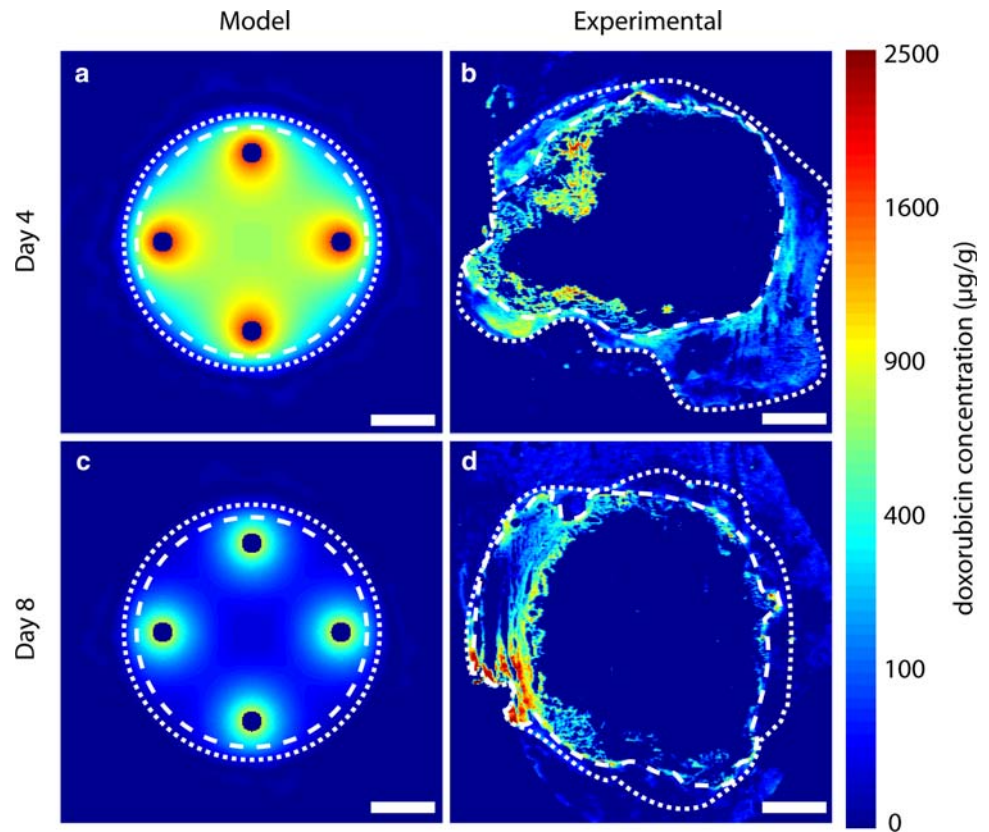
median model predicted [DOX] = 140 µg/g was higher than the experimentally measured median [DOX] = 79 µg/g. However, there was considerable overlap between the middle 50% of the points. On day 8, the model predicted median concentration [DOX] = 20 µg/g, which corresponded to the experimentally measured median [DOX] = 26 µg/g. Overall, the experimental values for [DOX] in the non-ablated tumor rim were close to the model-predicted values. Both experimental and model simulated regions in which [DOX] ≥ [DOX*] exhibited the same trend: peaking on day 4 and decreasing slightly by day 8.

4 Discussion

4.1 Computational model

From drug-containing polymer millirods implanted in tissue after thermal ablation, drug enters surrounding tissue and produces concentration distribution patterns that depend on the location of the implants. Especially with several implanted millirods, prediction of spatial distribution dynamics of the drug concentration requires a mathematical model and computer simulation. Simulations

Fig. 6 Simulated drug distribution in ablated tumor tissue compared to DOX distribution in images of ablated tumor liver from in vivo rabbit experiments with four peripheral implants. The outer extent of the ablated regions is within *white dashed lines* and the outer extent of the non-ablated tumor is within *white dotted lines*. Model simulated DOX distributions on day 4 (**a**) and day 8 (**c**). DOX distributions from experimental images on day 4 (**b**) and day 8 (**d**). Central portion of ablated tumor is not visible in experimental images because of extensive necrosis. *Scale bars* are 5 mm



were obtained using a commercial code (COMSOL 3.3) that implements a finite-element method (FEM). This code was used to deal with the complexity of asymmetric placements of multiple implants and a wide range of inputs, boundary conditions, and tissue properties. Furthermore, this code was able to deal with diffusion and elimination rate coefficients that vary with time and location in tissue. This computational model could be used in the future to simulate complex treatment scenarios based on imaging data.

The boundary conditions in this study are based on the assumptions that the rate of drug release measured experimentally from a single implant would be uniform on all surfaces of the implant and that they would be the same for each of the multiple implants placed asymmetrically within a tumor. As a practical matter, the variation of these boundary conditions from implant to implant is probably of second-order importance relative to the spatial variability of tissue properties.

4.2 Simulation of drug distributions in ablated tissue

Model simulation of drug distributions using multiple implants provided a basis for quantifying the expected effects on tumor recurrence. In the peripheral rim of the ablated tumor (i.e., risk volume), the risk of tumor recurrence is higher because it may be exposed to

sublethal heating during ablation [11]. As shown in Fig. 3, peripheral implants can significantly increase the drug concentration in the risk volume. However, different central and peripheral implant configurations can result in different levels of therapeutic drug levels in the entire tumor and in the risk volume and the time at which these levels are reached (Fig. 4). In general, the therapeutic level was reached more quickly and over a greater tumor volume with more implants that have a greater total dose. Within the ablated tumor, where the rate of drug diffusion is relatively quick and the rate of elimination is relatively low, different configurations are less important than the total drug dose in determining drug levels over the entire tumor volume. Peripheral implants, however, can lead to higher drug concentration in the risk volume, but this requires multiple implants in appropriate locations.

4.3 Central and peripheral implant configurations

Using peripheral implants either with or without a central implant allowed the drug concentration to reach therapeutic levels throughout the entire tumor, a finding which was not seen with a single central implant (Fig. 4). With a central implant, much of the drug dose was delivered to the core of the ablated region tumor instead of the risk volume. Increasing the total drug dose to achieve therapeutic drug

levels can potentially have systemic side effects. Appropriate placement of peripheral implants can reach therapeutic levels more quickly and in more of the risk volume without a central implant even with the same total drug dose (Fig. 4b, d). The accuracy of model simulations must be tested by comparison to data from in vivo experiments.

4.4 Comparison of simulated and in vivo drug distributions

Of the simulated configuration of multiple implants, four peripheral implants produced therapeutic drug levels in the entire tumor over a relatively short time period. Comparable in vivo experimental studies were performed with four implants in ablated rabbit livers, either normal or with tumors. In normal ablated liver, [DOX] from experimental images was much higher than simulated drug concentrations in the central ablated region (Fig. 5). One reason for the lower simulated drug concentration is that model parameter values were taken from studies with ablated rat liver [19], which may differ from ablated rabbit liver because different tissue types have different vascularity and density. Additionally, the assumed drug concentration at the implant boundary was taken from a single implant placed in a small ablated tumor [29], which may inadequately represent boundary drug concentrations with multiple implants in close proximity. Nevertheless, model simulation of the overall trend in average drug concentration corresponds to that observed experimentally. Moreover, the model predicted that 98% of the ablated region would reach therapeutic target concentrations in accord with estimates from experimental [DOX] images.

Model predictions of [DOX] distribution in ablated liver tumors were compared to experimental [DOX] measurements from ablated VX2 liver tumors in rabbits (Fig. 6). Experimental tumors were larger than anticipated and had a necrotic center from which no [DOX] data was available (Fig. 6b, d). Furthermore, since the location of the thermal ablation source could not be located from the experimental images, the relative locations of the experimental implant could only be estimated. However, at the periphery of the ablated tumors, particularly in the non-ablated rim, [DOX] was well above the therapeutic [DOX*]. Average [DOX] and the fraction of the area where [DOX] was above the therapeutic [DOX*] from model predictions were in agreement with corresponding measures from experimental images. Whereas simulated [DOX] values exceeded [DOX*] over the entire tumor on day 4, experimental [DOX] measurements exceeded [DOX*] in 87% of the tumor rim. Factors that could explain this disparity include the heterogeneity of the experimental tumor tissue or variability in the size and shape of the tumor and the ablated

regions. Despite the difference, the average drug concentration values in the non-ablated tumor overlapped considerably between simulated and experimental data (Table 2). On day 8, coverage of the non-ablated tumor correlated much more closely between the model and experimental data, which have values of 61 and 65%, respectively. Overall, for tumor areas $>5 \text{ cm}^2$ in the central cross section, [DOX] surpassed [DOX*] in a large fraction of the tumor rim on both days. The success of achieving this therapeutic drug level with polymer millirods in such a large tumor is a major step toward the use of these implants in practical clinical situations.

5 Conclusion

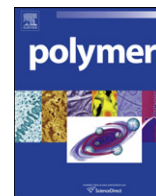
Simulation of drug concentration distribution in ablated tissue from multiple implants can be successful in predicting optimal implant strategies that can be tested experimentally. The combination of model simulations with a small set of animal experiments is much more efficient in determining an optimal implant strategy for treating large tumors than a much larger set of animal experiments alone.

Acknowledgments This work was supported by NIH grant R01 CA90696 to JG. BW and RP are supported in part by the NIH grant T32 GM07250 to the Case Western Reserve University Medical Scientist Training Program. BW is also supported by DOD predoctoral fellowship BC043453. This is manuscript CSCN P012 from the ‘Cell Stress and Cancer Nanomedicine’ program in the Simmons Comprehensive Cancer Center at the University of Texas Southwestern Medical Center at Dallas.

References

1. Barnett CC Jr, Curley SA (2001) Ablative techniques for hepatocellular carcinoma. *Semin Oncol* 28:487–496
2. Berber E, Siperstein AE (2007) Perioperative outcome after laparoscopic radiofrequency ablation of liver tumors: an analysis of 521 cases. *Surg Endosc* 21:613–618
3. Bertazzoli C, Chieli T, Grandi M et al (1970) Adriamycin: toxicity data. *Experientia* 26:389–390
4. Curley SA, Marra P, Beaty K et al (2004) Early and late complications after radiofrequency ablation of malignant liver tumors in 608 patients. *Ann Surg* 239:450–458
5. Fung LK, Shin M, Tyler B et al (1996) Chemotherapeutic drugs released from polymers: distribution of 1, 3-bis(2-chloroethyl)-1-nitrosourea in the rat brain. *Pharm Res* 13:671–682
6. Gannon CJ, Curley SA (2005) The role of focal liver ablation in the treatment of unresectable primary and secondary malignant liver tumors. *Semin Radiat Oncol* 15:265–272
7. Goldberg SN (2001) Radiofrequency tumor ablation: principles and techniques. *Eur J Ultrasound* 13:129–147
8. Grimm P, Sylvester J (2004) Advances in brachytherapy. *Rev Urol* 6:S37–S48
9. Guerin C, Olivi A, Weingart JD et al (2004) Recent advances in brain tumor therapy: local intracerebral drug delivery by polymers. *Invest New Drugs* 22:27–37

10. Harrison LE, Koneru B, Baramipour P et al (2003) Locoregional recurrences are frequent after radiofrequency ablation for hepatocellular carcinoma. *J Am Coll Surg* 197:759–764
11. Johnson PC, Saidel GM (2002) Thermal model for fast simulation during magnetic resonance imaging guidance of radio frequency tumor ablation. *Ann Biomed Eng* 30:1152–1161
12. Kaplan ID, Meskell P, Oldenburg NE et al (2006) Real-time computed tomography dosimetry during ultrasound-guided brachytherapy for prostate cancer. *Brachytherapy* 5:147–151
13. Laginha KM, Verwoert S, Charrois GJ et al (2005) Determination of doxorubicin levels in whole tumor and tumor nuclei in murine breast cancer tumors. *Clin Cancer Res* 11:6944–6949
14. Lessard E, Kwa SL, Pickett B et al (2006) Class solution for inversely planned permanent prostate implants to mimic an experienced dosimetrist. *Med Phys* 33:2773–2782
15. Menei P, Jadaud E, Faisant N et al (2004) Stereotaxic implantation of 5-fluorouracil-releasing microspheres in malignant glioma. *Cancer* 100:405–410
16. Menei P, Capelle L, Guyotat J et al (2005) Local and sustained delivery of 5-fluorouracil from biodegradable microspheres for the radiosensitization of malignant glioma: a randomized phase II trial. *Neurosurgery* 56:242–248 discussion 242–248
17. Ortiz R, Au JL, Lu Z et al (2007) Biodegradable intraprostatic doxorubicin implants. *AAPS J* 9:E241–E250
18. Qian F, Szymanski A, Gao J (2001) Fabrication and characterization of controlled release poly(D,L-lactide-co-glycolide) millirods. *J Biomed Mater Res* 55:512–522
19. Qian F, Stowe N, Liu EH et al (2003) Quantification of in vivo doxorubicin transport from PLGA millirods in thermoablated rat livers. *J Control Release* 91:157–166
20. Qian F, Stowe N, Saidel GM et al (2004) Comparison of doxorubicin concentration profiles in radiofrequency-ablated rat livers from sustained- and dual-release PLGA millirods. *Pharm Res* 21:394–399
21. Ridge JA, Collin C, Bading JR et al (1988) Increased adriamycin levels in hepatic implants of rabbit Vx-2 carcinoma from regional infusion. *Cancer Res* 48:4584–4587
22. Swistel AJ, Bading JR, Raaf JH (1984) Intraarterial versus intravenous adriamycin in the rabbit Vx-2 tumor system. *Cancer* 53:1397–1404
23. Szymanski-Exner A, Gallacher A, Stowe NT et al (2003) Local carboplatin delivery and tissue distribution in livers after radiofrequency ablation. *J Biomed Mater Res* 67A:510–516
24. Tanabe KK, Curley SA, Dodd GD et al (2004) Radiofrequency ablation: the experts weigh in. *Cancer* 100:641–650
25. Tateishi R, Shiina S, Teratani T et al (2005) Percutaneous radiofrequency ablation for hepatocellular carcinoma. An analysis of 1000 cases. *Cancer* 103:1201–1209
26. Ueno S, Tanabe G, Sako K et al (2001) Discrimination value of the new western prognostic system (CLIP score) for hepatocellular carcinoma in 662 Japanese patients. *Cancer of the Liver Italian Program. Hepatology* 34:529–534
27. Wallace KB (2003) Doxorubicin-induced cardiac mitochondriopathy. *Pharmacol Toxicol* 93:105–115
28. Weinberg BD, Ai H, Blanco E et al (2007) Antitumor efficacy and local distribution of doxorubicin via intratumoral delivery from polymer millirods. *J Biomed Mater Res A* 81:161–170
29. Weinberg BD, Blanco E, Lempka SF et al (2007) Combined radiofrequency ablation and doxorubicin-eluting polymer implants for liver cancer treatment. *J Biomed Mater Res A* 81:205–213
30. Weinberg BD, Patel RB, Exner AA et al (2007) Modeling doxorubicin transport to improve intratumoral drug delivery to RF ablated tumors. *J Control Release* 124:11–19
31. Yamada Y, Bhatia S, Zaider M et al (2006) Favorable clinical outcomes of three-dimensional computer-optimized high-dose-rate prostate brachytherapy in the management of localized prostate cancer. *Brachytherapy* 5:157–164



Folate-encoded and Fe₃O₄-loaded polymeric micelles for dual targeting of cancer cells

Xiaoqiang Yang^{a,1}, Yinghua Chen^{b,1}, Renxu Yuan^a, Guihua Chen^b, Elvin Blanco^c, Jinming Gao^c, Xintao Shuai^{a,*}

^aBME Center, State Key Laboratory of Optoelectronic Materials and Technologies, School of Chemistry and Chemical Engineering, Sun Yat-Sen University, Guangzhou 510275, PR China

^bThe Third Affiliated Hospital, Sun Yat-Sen University, Guangzhou 510630, PR China

^cSimmons Comprehensive Cancer Center, University of Texas Southwestern Medical Center at Dallas, Dallas, TX 75390, USA

ARTICLE INFO

Article history:

Received 11 March 2008
Received in revised form 4 June 2008
Accepted 5 June 2008
Available online 11 June 2008

Keywords:

Micelles
Block copolymers
Drug delivery

ABSTRACT

Diblock copolymers of poly(ethylene glycol) (PEG) and poly(ϵ -caprolactone) (PCL) bearing a tumor-targeting ligand, folate, were self-assembled into micelles. Superparamagnetic iron oxide (SPIO) nanoparticles and an anticancer drug doxorubicin (DOX) were coencapsulated within the micelles less than 100 nm in diameters. These SPIO–DOX-loaded micelles were superparamagnetic at room temperature, but turned ferrimagnetic at 10 K, consistent with magnetic properties of primary SPIO nanoparticles. Cell culture experiments demonstrated the potential of these polymeric micelles as an effective dual targeting nanopatform for the delivery of anticancer drugs. Folate attachment to micelles resulted in the recognition of the micelles by tumor cells over-expressing folate receptors, leading to facilitation in cellular uptake of micelles, and the transport efficiency of the SPIO-loaded and folate-functionalized micelles into the tumor cells can be further enhanced by applying an external magnetic field to the cells.

© 2008 Elsevier Ltd. All rights reserved.

1. Introduction

Over the past decades, polymeric micelles have drawn considerable interests because of their great potential in anticancer drug delivery and diagnostic imaging applications [1–4]. These nano-sized particles, formed from the self-assembly of amphiphilic block copolymers, provide a unique core–shell architecture wherein the hydrophobic core serves as a natural carrier environment for hydrophobic drugs or imaging agents while the hydrophilic shell enables particle stabilization in aqueous solutions [5–7]. Despite of their numerous advantages such as drug solubilization and prolonged blood circulation, micelles lack the ability to achieve high targeting efficiency at tumor sites. Moreover, insufficient cell uptake further decreases the therapeutic efficacy of the administered drug, and nonspecific accumulation in healthy tissues leads to serious side effects and limits the dosage that can be administered. Hence, studies involving means to further improve the tumor specificity of micelles in therapeutic and diagnostic applications are a growing trend in micellar research. A well-known strategy to

achieve active tumor targeting is to encode the micellar outer layer with specific ligands that can recognize molecular signatures on the cancer cell surface. Targeting ligands that can serve such a purpose include folic acid, peptides such as cyclic (Arg–Gly–Asp–D–Phe–Lys) (cRGD), transferrin and monoclonal antibodies [8–11]. However, in order for the nanoparticles to be able to recognize cell surface receptors, they need to be directed to tumor sites in the first place. Therefore, an external targeting strategy, such as a guided magnetic field, which can hold the micelles in and/or effectively drive the micelles into tumor tissues is expected to improve drug delivery efficiency. Pioneering work in the area of external magnetic field-aided drug delivery dates back to the late 1970s, when Widder et al. developed the first magnetic microsphere as a drug carrier and used an external magnetic field to guide the drug/carrier to the targeted site [12,13]. Following this groundbreaking work, research on tumor targeted chemotherapy with magnetic nanoparticles has increased considerably over the past two decades [14–17]. Despite various advances, major success in drug targeting has been limited when compared to the application of magnetic particles as diagnostic contrast agents in magnetic resonance imaging (MRI) [18–20]. Further development and testing of novel magnetic carriers are necessary to achieve the therapeutic potential of magnetic targeting. Although regarded as a promising class of drug delivery vehicles, polymeric micelles combining dual magnetic and

* Corresponding author. Tel.: +86 20 84110365; fax: +86 20 84112245.

E-mail address: shuaixt@mail.sysu.edu.cn (X. Shuai).

¹ These authors contributed equally to this work.

molecular targeting functions to tumor tissues and associated cells have rarely been exploited.

In this article, we describe dual targeting micelles that contain a molecular targeting ligand on the micelle surface as well as a cluster of superparamagnetic iron oxide (SPIO) nanoparticles in the cores for magnetic targeting. Micelles based on copolymers of poly(ϵ -caprolactone) (PCL) and poly(ethylene glycol) (PEG) bearing folate on the PEG distal ends, denoted as folate-PEG-PCL, were used to encapsulate the anticancer drug doxorubicin (DOX) and SPIO, after which cell culture experiments were conducted as a proof of concept to demonstrate their potential as a dual targeting system that can transport anticancer drugs to tumor cells effectively.

2. Experimental section

2.1. Materials

Phenyl ether (99%), benzyl ether (99%), 1,2-hexadecanediol (97%), oleic acid (99%), oleylamine (>70%) and iron(III) acetylacetonate were purchased from Sigma-Aldrich and used without further purification. Doxorubicin hydrochloride (DOX) was supplied by Shenzhen Main Luck Pharmaceutical Inc., Shenzhen, China, and was used as-received. MTT (3-(4,5-dimethylthiazol-2-yl)-2,5-diphenyltetrazolium bromide) was purchased from Sigma-Aldrich. RPMI-1640 medium, Dulbecco's phosphate-buffered saline (PBS), and 0.25% trypsin were purchased from Gibco BRL. All other chemicals used in experiments were of analytical grade, and used without further purification. A KB cell line derived from human oral cavity squamous carcinoma was obtained from the center of experimental animal, Sun Yat-sen University.

2.2. Synthesis of copolymers and Fe₃O₄ nanoparticles

The targeting and non-targeting copolymers, folate-PEG-PCL and allyl-PEG-PCL, were synthesized via multistep synthesis as described in our recent publication [21]. Fe₃O₄ nanoparticles (SPIO) were synthesized according to a reported method [22]. Briefly, iron(III) acetylacetonate (2 mmol), 1,2-hexadecanediol (10 mmol), oleic acid (6 mmol), oleylamine (6 mmol), and benzyl ether (20 mL) were mixed and magnetically stirred under a flow of nitrogen. The mixture was heated to 200 °C for 2 h and then, under a blanket of nitrogen, heated to reflux (300 °C) for 1 h. The black-colored mixture was cooled to room temperature by removing the heat source. The product, 6 nm Fe₃O₄ nanoparticles, was then precipitated with ethanol, centrifuged (6000 rpm, 10 min) to remove the solvent, and re-dispersed into hexane. A black-brown hexane dispersion of 6 nm Fe₃O₄ nanoparticles was then produced.

2.3. Preparation of SPIO-DOX-loaded micelles

SPIO and DOX-encapsulated micelles were prepared via the dialysis method. Briefly, 10 mg of folate-PEG-PCL, 2 mg of doxorubicin hydrochloride, triethylamine (1.3 mL), and SPIO (1.5 mg) were dissolved in a mixed solvent consisting of THF (1 mL) and DMSO (1 mL). The above solution was slowly added into 5 mL of deionized water under sonication using an UP 50H Dismembrator (Hielscher, Germany) and then dialyzed against deionized water for 2 days to allow the formation of SPIO-DOX-loaded micelles and to remove organic solvents and unencapsulated DOX dissolved in aqueous solution (M_w cut-off: 14,000 Da). Afterwards, the micelle solution was removed from the dialysis bag and filtered through a 0.22 μ m membrane to remove large aggregates.

2.4. Micelle size and morphology

Micelles obtained were characterized with photon correlation spectroscopy, performed at 25 °C on a BI-200 SM dynamic laser scattering system from Brookhaven Instruments. Scattered light was detected at a 90° angle and collected on an autocorrelator. Sizes given are the means of five runs \pm standard deviation. Samples for transmission electron microscopy (TEM, JEM-2010HR, Japan) analysis were prepared by drying a dispersion of the particles on a copper grid coated with amorphous carbon. Subsequently, a small drop of phosphotungstic acid (PTA) solution (2 wt.% in water) was added to the copper grid, and after 30 s the grid was blotted with filter paper for TEM observation.

2.5. Determination of DOX and SPIO-loading contents

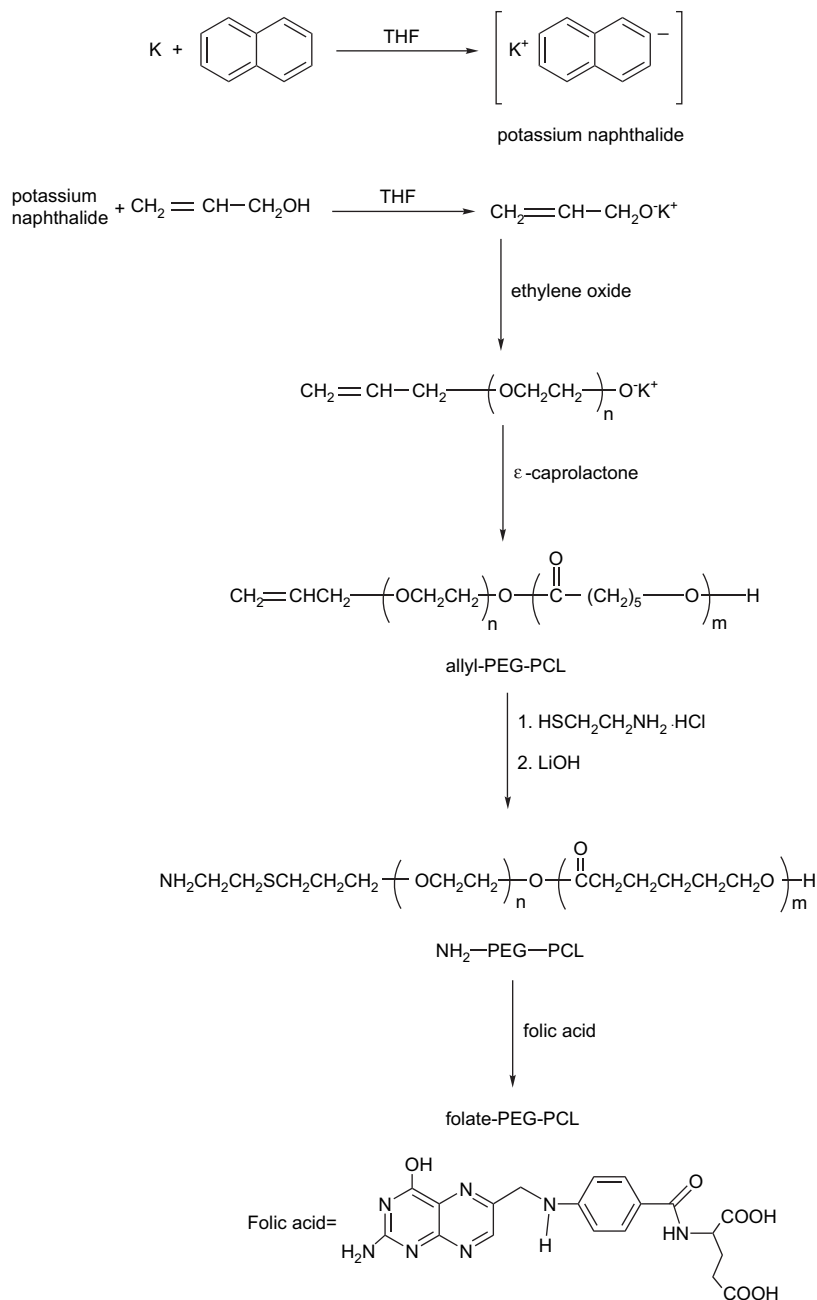
The DOX-loading content (DLC), defined as the weight percentage of DOX in micelles, was quantified by UV-vis analysis using a Unico UV-2000 UV-vis spectrophotometer. First, DOX-SPIO-loaded micelle solutions were lyophilized to yield the solid micelle samples. Then the dried micelle samples were weighed and re-dissolved in a mixture of chloroform and DMSO (1:1, v/v). After the insoluble SPIO particles were removed from the solution by magnetic field-guided accumulation, the absorbance of DOX at 480 nm was measured to determine drug content in the solution using a previously established calibration curve. The loading density of SPIO inside polymeric micelles was determined using a polarized Zeeman Atomic Absorption Spectrophotometer (Model: Z-2000 series). Briefly, the freeze-dried micelles were weighed and then added into 1 M HCl solution to allow the disaggregation of micelles and complete dissolution of SPIO crystals. Iron concentration was determined at the specific Fe absorption wavelength (248.3 nm) based on a previously established calibration curve. SPIO loading density was calculated as the ratio of iron oxide over the total weight of micelles.

2.6. Release of DOX from micelles

Freeze-dried micelle samples were resuspended in PBS (pH 7.4) or sodium acetate buffered solution (pH 5.0) and then transferred into a dialysis bag (M_w cut-off: 14,000 Da). The bag was placed into the same buffered solution (25 mL). The release study was performed at 37 °C in a Shanghai Yiheng Scientific DKZ incubator shaker. At selected time intervals, solution outside of the dialysis bag was removed for UV-vis analysis and replaced with fresh buffer solution. DOX concentration was calculated based on the absorbance intensity of DOX at 480 nm. In the assessment of drug release behavior, the cumulative amount of released drug was calculated, and the percentages of drug released from micelles were plotted against time. Release of free DOX (initial DOX concentration in dialysis bag: 40 μ g/mL) from the dialysis bag at different pHs was performed as controls following the same procedure as described above.

2.7. Magnetic properties of SPIO-DOX-micelles

The magnetization data of SPIO and SPIO-DOX-loaded micelles were determined using a MPMS XL-7 Quantum Design SQUID magnetometer at 10 K and 300 K. Temperature control is achieved by the components within the Temperature Control Module (TCM) under the active control of the Model 1822 Controller and the control system software. The applied magnetic field was varied from 2×10^4 Oe to -2×10^4 Oe in order to generate hysteresis loops. The magnetic responsiveness of SPIO nanoparticles and SPIO-DOX-micelles in solution was tested by simply placing a magnet near the glass vial. A cylindrical sintered N-35 Nd-Fe-B



Scheme 1. Synthetic approach of folate-PEG-PCL.

magnet purchased from Ningbo permanent magnetics Co., Ltd (China) (Dimension: $d = 18$ mm, $h = 15$ mm; field strength: ≈ 0.42 T) was used.

2.8. Dual targeting study

KB cells were seeded at 5×10^5 cells/well in 60 mm petri dish and maintained in 4 mL of RPMI-1640 medium supplemented with 10% heat-inactivated fetal bovine serum (FBS). After incubation for 24 h in a humidified incubator (37°C , 5% CO_2) at 37°C , a pre-determined amount of micelles in PBS was added into each dish to adjust for a DOX concentration of $5 \mu\text{g}/\text{mL}$. To evaluate the influence of magnetic field on cell uptake of micelles, a cylindrical sintered N-35 Nd-Fe-B magnet (Dimension: $d = 18$ mm, $h = 15$ mm; field strength: ≈ 0.42 T) was placed against the outer

bottom wall of the petri dish at different distances (i.e. 0 cm, 1 cm and 2 cm, respectively) to vary the magnetic field strength applied to the cells. For the Prussian blue staining experiment, cells were incubated and then washed twice with PBS, fixed by adding 2 mL of 4% paraformaldehyde-containing PBS fixative solution for 30 min. Media in the dish were replaced with the same but fresh paraformaldehyde-containing PBS. Each dish received a 2.5 mL of a 2:1 (v/v) mixture of 2% potassium ferrocyanide(II) trihydrate and 2% HCl solutions, after which cells were incubated for 20 min at 37°C . Cells were then washed three times with PBS, and the Prussian blue staining result and DOX fluorescence were assessed on a Nikon TE2000-U inverted fluorescence microscope. For the flow cytometry analysis, cells were incubated with 2 mL of RPMI-1640 medium (DOX concentration: $5 \mu\text{g}/\text{mL}$). Afterwards, cells were washed with PBS, trypsinized, centrifuged, resuspended in 1 mL of PBS, and

analyzed via flow cytometry. For the control experiment in which free folate was added to compete with the folate-functionalized micelles, KB cells were first incubated with free folate (10 mM) for 1 h, and then co-incubated with folate-functionalized micelles for 0.5 h.

2.9. *In vitro* cytotoxicity against KB cells

KB cells were seeded onto 24-well plates with a seeding density of 10,000 cells per well, maintained in 1 mL RPMI-1640 medium supplemented with 10% inactivated FBS, and incubated for 1 day at 37 °C in a humidified atmosphere with 5% CO₂. Cells were then incubated in 1 mL RPMI-1640 medium containing DOX-loaded micelles (DOX concentration: 2.5 µg/mL) for 3 days. A 0.415 T magnetic field was applied to cells throughout the course of cell incubation. In control experiments, micelles loaded with SPIO alone were added to the culture media, and the cells were then incubated for 4 days. Afterwards, cells were washed twice with PBS, and incubated for 4 h in 1 mL RPMI-1640 medium containing 100 µL MTT (5 mg/mL in PBS). The precipitate was dissolved in 750 µL DMSO and analyzed on a BIO-RAD microplate reader.

2.10. Statistical analysis

All data were repeated three times in experiments and are reported as mean values with standard deviations. Statistical analysis was carried out using Student's *t*-test. Differences were considered statistically significant when $p < 0.05$.

3. Results and discussion

Amphiphilic block copolymers, folate-PEG-PCL ($M_n = 5.1$ kDa, $M_n(\text{PEG}) = 2.9$ kDa, $M_n(\text{PCL}) = 0.87$ kDa) and allyl-PEG-PCL ($M_n = 3.8$ kDa, $M_n(\text{PEG}) = 2.9$ kDa, $M_n(\text{PCL}) = 0.87$ kDa), were used for micelle fabrication. They were synthesized by multi-step chemical reactions as shown in Scheme 1. The polymer structure has been characterized and the molecular weight was determined by Gel permeation chromatography (GPC) in our recent publication [21]. GPC measurement indicated that the M_n of folate-PEG-PCL is 5.1 kDa. Hydrophobic SPIO nanoparticles, measuring ~6 nm in diameter, were synthesized with precise control of particle diameter (Fig. 1A). The selected area electron diffraction (SAED) pattern (inset in Fig. 1A) indicates that the particle composition is

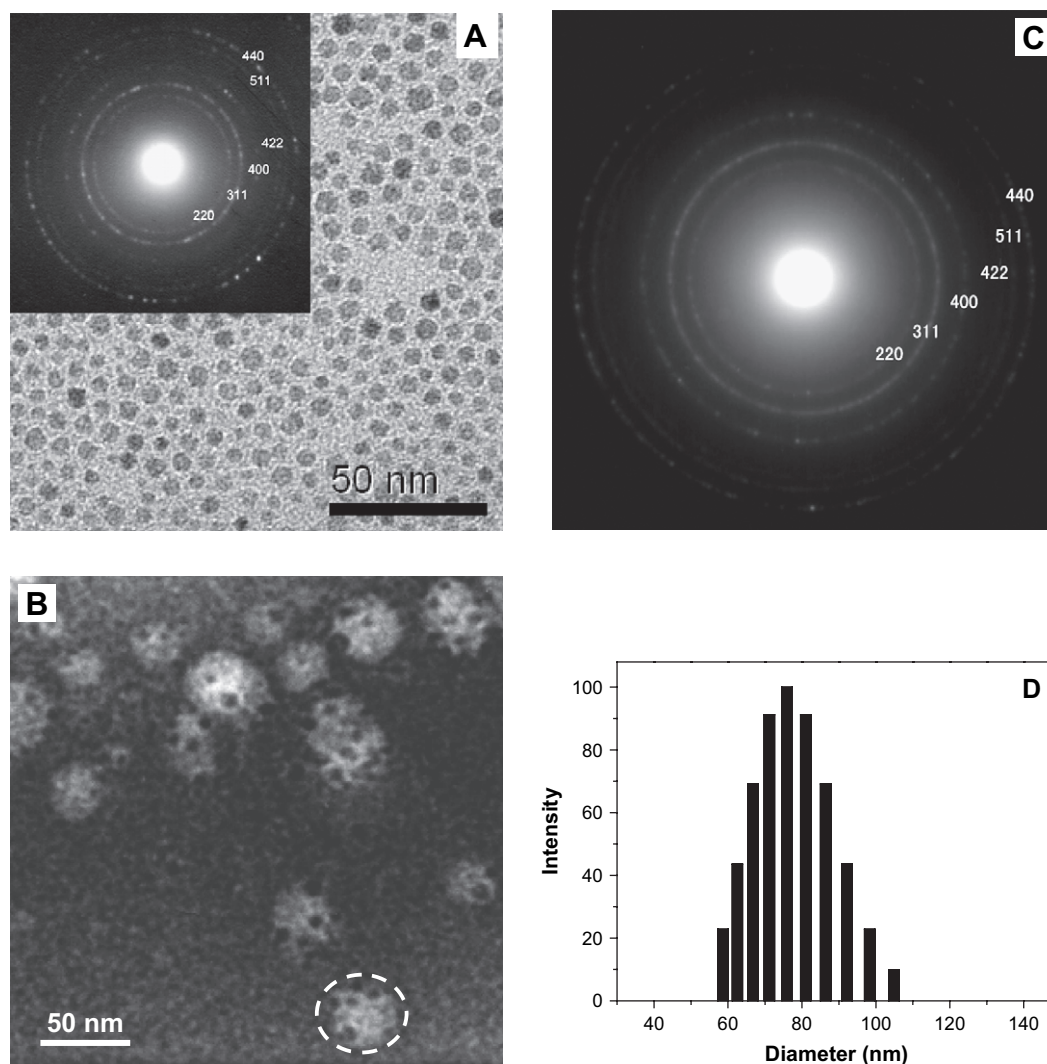
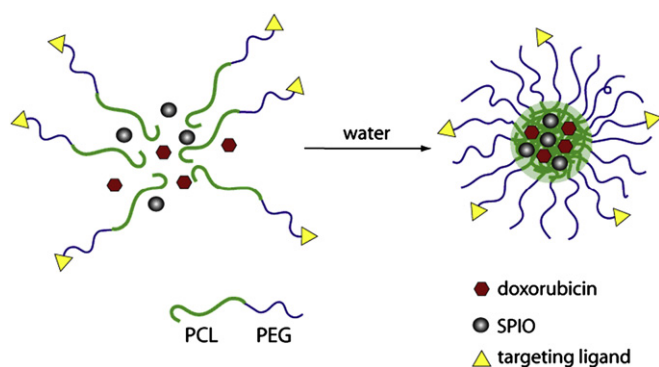


Fig. 1. Transmission electron microscopy (TEM) image of (A) 6 nm Fe₃O₄ nanoparticles; selected area electron diffraction (SAED) pattern (B); TEM image (C) and dynamic light scattering (DLS) histogram (D) of SPIO-DOX-loaded magnetic micelle based on folate-PEG-PCL copolymer. Sample for TEM measurement was negatively stained by 2% PTA. Inset in (A) shows the SAED pattern acquired from 6 nm Fe₃O₄ nanoparticles. As an example, one micelle particle was marked with a dashed white circle.

magnetite (Fe_3O_4) [4]. SPIO and anticancer drug DOX were jointly loaded into the targeting micelles, as shown in Scheme 2. The loading contents of SPIO and DOX in the micelles are summarized in Table 1. TEM image (Fig. 1C) of DOX and SPIO-loaded micelles shows that they are uniform in shape and size distribution, and SPIO particles were successfully encapsulated into micelles. Dynamic light scattering (DLS) measurements showed that the mean diameters were 29 ± 2 nm and 30 ± 2 nm for blank micelles (i.e. SPIO and DOX-free micelles), and 71 ± 1 nm and 75 ± 3 nm for SPIO and DOX-loaded micelles. The SPIO and DOX-loaded micelles showed a significant increase in size, mainly due to SPIO loading [23]. The SAED pattern of these magnetic micelles shows no difference from that of the 6 nm SPIO nanoparticles (Fig. 1B), indicating that SPIO nanoparticle has not changed its crystalline structure during the encapsulation process. Magnetization measurements also provided evidence that the SPIO nanoparticle encapsulated in micelles maintained its crystalline structure (Fig. 2). Both SPIO and micelles are superparamagnetic at room temperature, and the saturation magnetization (83.5Fe emu/g) of the magnetic micelles is slightly higher than that of SPIO (78.1Fe emu/g). At 10 K, both SPIO and SPIO-loaded micelles displayed ferromagnetic properties with a coercivity of 244 Oe for SPIO and 120 Oe for SPIO–DOX–micelles.

Release of DOX from SPIO–DOX-loaded micelles was pH-dependent, and loading of the SPIO nanoparticles within micelle core did not lead to an obvious change in the DOX-release profile. In control experiments, free DOX quickly diffused out of the dialysis bag at both pHs 7.4 and 5.0. The release of free DOX was completed in 3 h. As shown in Fig. 3, DOX release in the two media revealed a biphasic release pattern consisting of an initial burst release followed by a sustained and slow release over a prolonged time of up to several weeks. Within 2 weeks, SPIO loading did not obviously affect the release profile of DOX at pH 5. However, for time points after 15 days, faster DOX release occurs from SPIO–DOX–micelles compared to DOX–micelles. At pH 7.4, DOX release was relatively slow for both formulations, with less than 10 wt.% of DOX released



Scheme 2. Formation of SPIO–DOX-encapsulated micelles.

Table 1

Micelle size, SPIO and DOX loading densities

Micelle formulation	Micelle diameter (nm)	SPIO loading (wt.%)	DOX loading (wt.%)
Allyl-PEG–PCL	SPIO–DOX-free micelle	30 ± 2.0	–
	SPIO-free micelle	33 ± 1.0	2.5 ± 0.1
	SPIO–DOX-micelle	71 ± 1.0	12.2 ± 2.4
Folate-PEG–PCL	SPIO–DOX-free micelle	29 ± 2.0	–
	SPIO-free micelle	30 ± 1.0	3.0 ± 0.1
	SPIO–DOX-micelle	75 ± 3.0	10.2 ± 2.1

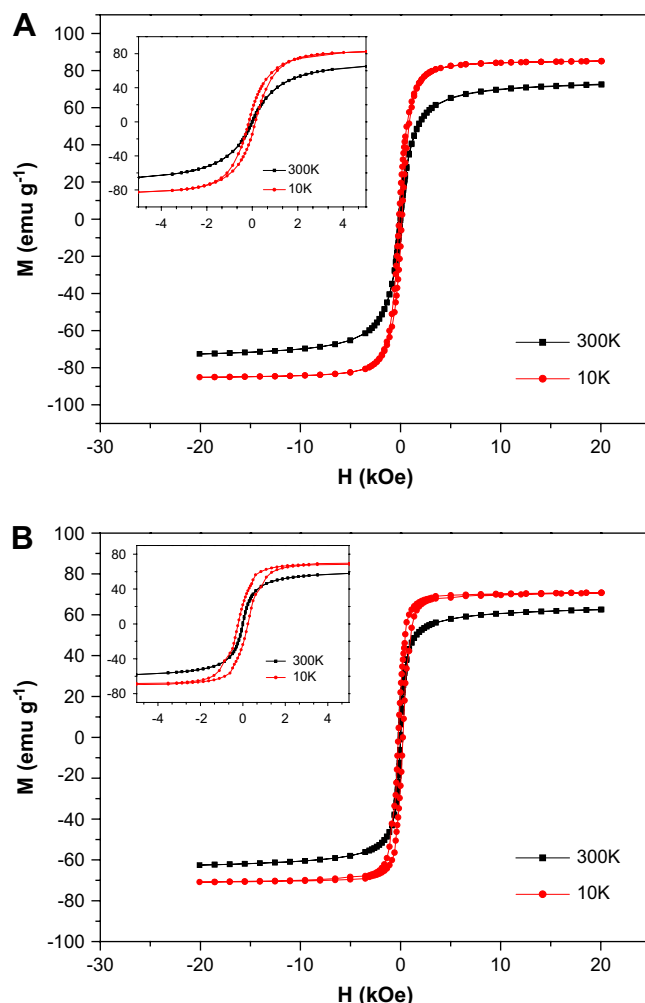


Fig. 2. Hysteresis loops of SPIO–DOX-micelle based on allyl-PEG–PCL (A) and 6 nm Fe_3O_4 nanoparticles (B) measured at 300 K and 10 K. The two insets in the figure show the local magnification.

in 5 days, and only 18 wt.% of DOX released after 35 days for both micellar formulations. DOX release at pH 5.0 was much faster than that at pH 7.4 from both formulations, with the difference in release being statistically significant. More than 30 wt.% and 70 wt.% of DOX was released in 5 and 35 days, respectively. It is likely due to the re-protonation of the amino group of DOX and faster degradation of micelle core at lower pH, and this type of faster release of DOX in acidic conditions was also observed by Kataoka and coworkers with the DOX-loaded polymeric micelles [2b]. This observed pH-dependent DOX release behavior is hypothesized to potentiate drug release from micelles once the micelles enter the tumor cells via endocytosis and are trapped within acidic endosomal compartments.

The magnetic responsiveness of SPIO nanoparticles and SPIO–DOX–micelles in solution was visualized by a simple experiment in which a 0.42 T magnet was placed near the glass vials (Fig. 4). Both SPIO nanoparticles in hexane and SPIO–DOX–micelles in water deposited notably on the wall adjacent to the magnet within 30 s. These observations provide direct evidence that SPIO–DOX–micelles, like SPIO nanoparticles, possess prompt responsiveness to an external magnetic field. In addition, we can easily deduce that DOX and SPIO were coencapsulated successfully into the micelle core based on the fact that the SPIO–DOX–micelle solution became transparent and colorless due to the magnetically induced separation of micelles from solution. Magnetic micro-devices such as

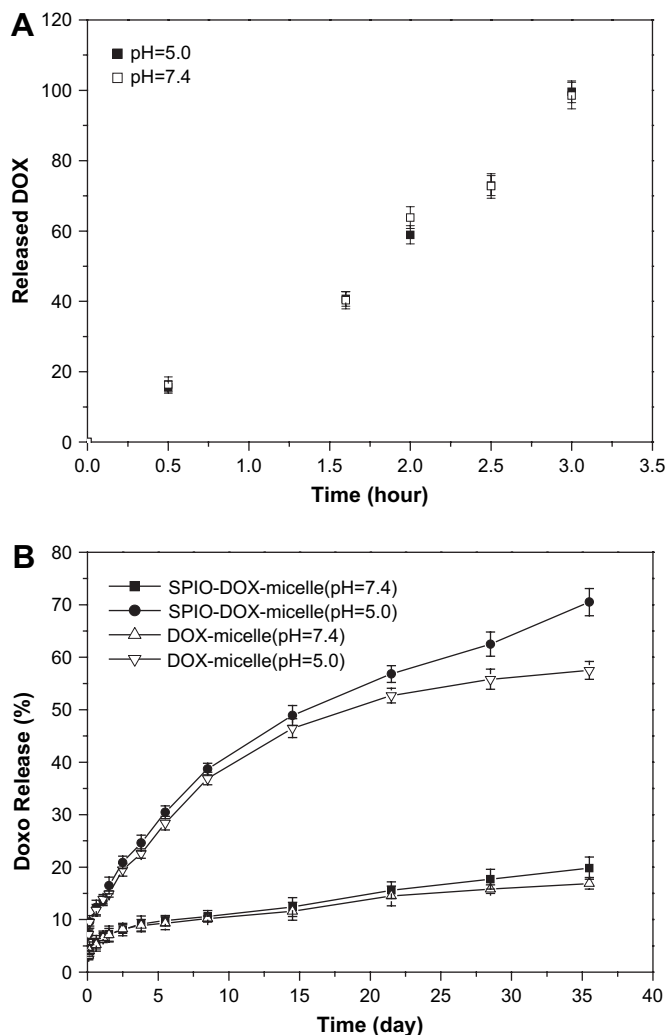


Fig. 3. (A) Release profiles of free DOX from solutions at pH 5.0 and pH 7.4. (B) In vitro DOX-release profiles from micelles based on folate-PEG-PCL at neutral (pH 7.4) and acidic conditions (pH 5.0) at 37 °C. Data are presented as mean \pm SD ($n = 3$).

magnetic nanotubes and silica coated nanoparticles have demonstrated potential in magnetic-field assisted bio-separation and cell sorting in addition to specific targeting applications [24,25]. Our experiments served to highlight the potential of using an easy and effective way to direct drug-loaded nanoparticles from a solution to the targeted locations under an external magnetic field. In particular, the magnetic micelles developed herein are highly sensitive to external magnetic field and thus have potential as a magnetically guided nanopatform for drug delivery.

As a proof of concept, we designed simple in vitro cell culture experiments to test the dual magnetic and folate targeting effects of SPIO-DOX-loaded micelles. The experimental design is shown in Fig. 5. A commercially available 0.42 T Nd-Fe-B magnet was placed against the outer bottom surface of the petri dish, and the large black circle shows the position of the magnet. Cells in two locations within the petri dish, referred to as circle 1 and 2 areas, were investigated regarding DOX fluorescent intensity and Prussian blue staining. Circle 1 is within the black circle showing the magnet position and thus is in the strongest magnetic field, while the magnetic field applied to circle 2 is much weaker. As visualized under microscopy, both Prussian blue and DOX fluorescence intensities indicate that cells located inside circle 1 have taken up considerably more folate-functionalized and SPIO-DOX-loaded micelles than cells located inside circle 2 after 3 h incubation (see Fig. 5A vs B for Prussian blue, and C vs D for fluorescence images). To evaluate the effect of magnetic field strength on cell uptake, we vertically positioned the magnet at different distances from the dish bottom at 0 cm, 1 cm, and 2 cm. The magnetic field strengths applied to the cells in circle 1 in three magnet positions are 4150 G, 1280 G and 450 G, respectively, as measured with a LakeShore 421 gaussmeter. We incubated the cells with folate-encoded and folate-free SPIO-DOX-loaded micelles in the presence of the external magnetic field to further compare the magnetic and molecular targeting effects. After 0.5 h cell incubation time with micelle-containing media in varied magnetic field strengths, DOX fluorescence of cells was analyzed with inverted fluorescence microscopy and flow cytometry to investigate the cell uptake level of micelles. Fig. 6A and B shows the DOX fluorescence images and quantitative fluorescence intensity of cells from circle 1. Two major findings were observed: first, a strong magnetic field has a considerable

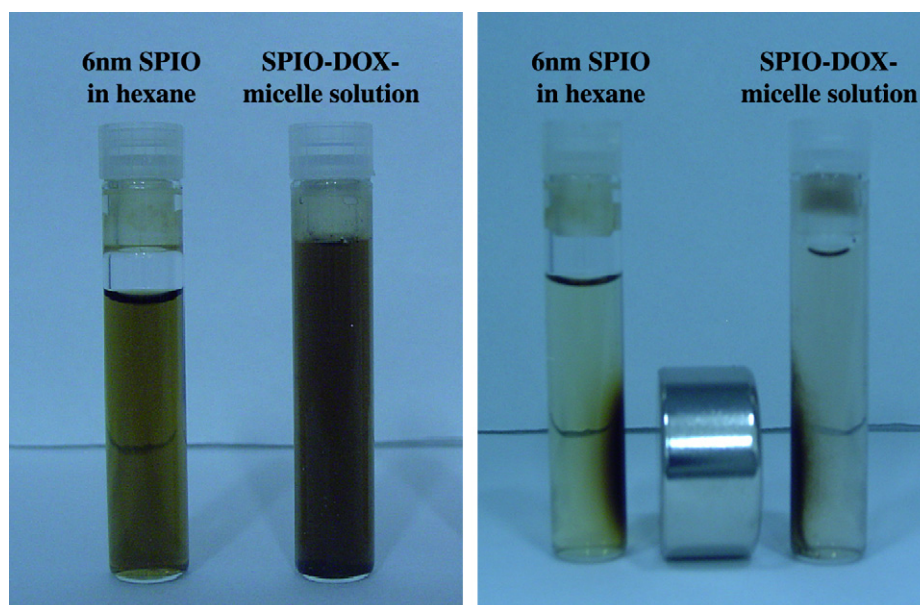


Fig. 4. Samples before and after imposing an external magnetic field. Micelles based on folate-PEG-PCL.

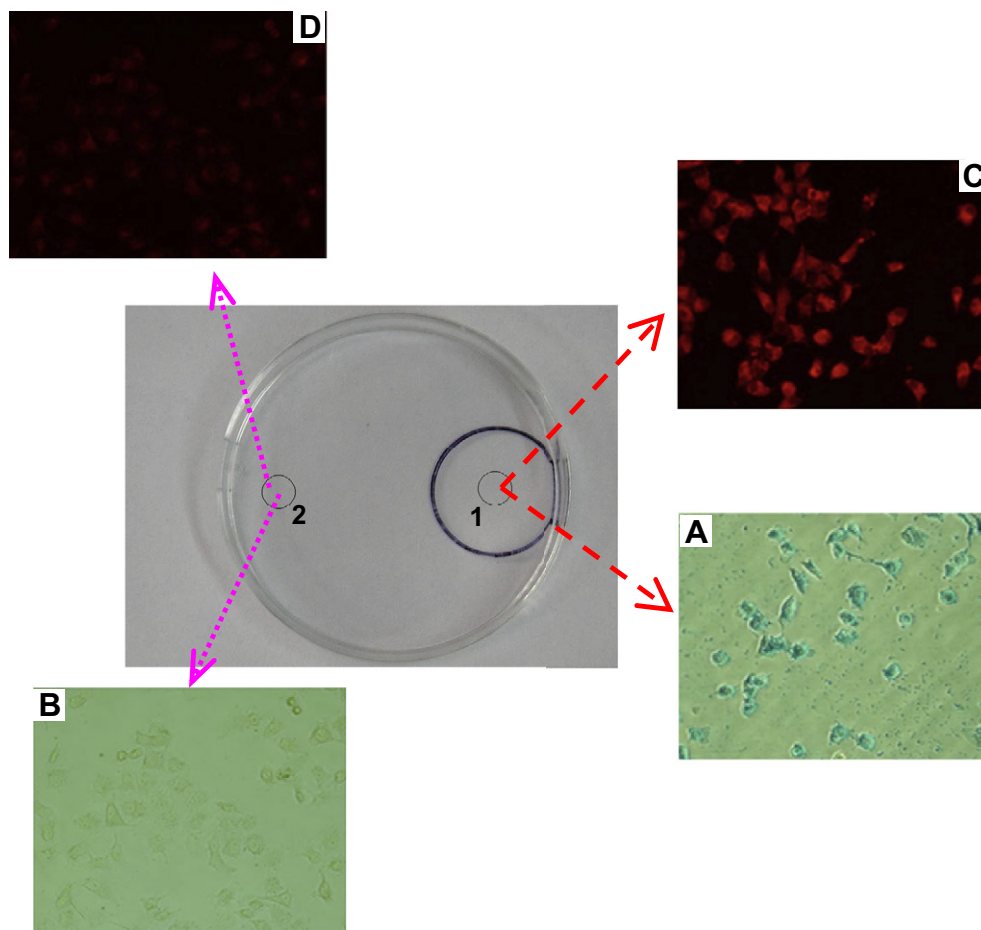


Fig. 5. Micrographs of SPIO–DOX-loaded micelles based on folate–PEG–PCL after 3 h incubation in an external magnetic field. (A) and (B) refer to the Prussian blue staining of cells located in circle 1 and circle 2; (C) and (D) refer to the DOX fluorescent intensity of cells located in circle 1 and circle 2, respectively. Circle 1 and circle 2 indicate the different positions of magnet, respectively. Determined magnetic field strength: 4150 G for cycle 1; 150 G for cycle 2.

influence on the cell uptake of the magnetic micelles. The relative fluorescence intensity of cells as determined by flow cytometry decreased 84% and 92%, respectively, for folate-encoded and folate-free micelles when the magnetic field strength was decreased to 0 G from 4150 G. At high magnetic field strength (i.e. 4150 G), the magnetic targeting effect is more apparent than that from folate targeting. In comparison, at the weaker magnetic field strength (450 G), data show no obvious magnetic-induced targeting effect on the cell uptake of micelles. Hence, we conclude from this experiment that the strong external magnetic field can effectively increase the local concentration of micelles in media near the investigated cells. Additionally, folate-mediated cell targeting became much more evident when the external magnetic field was weakened. As shown in Fig. 6B, folate targeting in a 4150 G magnetic field led to a 1.2-fold increase in DOX fluorescence in cells, while the same targeting resulted in an increase by a factor of 2.3 and 2.4 in 450 G and 0 G magnetic fields, respectively. Similar results can be observed via fluorescence microscopy analysis as well (Fig. 6A). The fluorescence disparity between the samples demonstrated the dynamic interplay of magnetic targeting vs biological targeting via folate under different experimental conditions. In the ligand competing assay at 0 G magnetic field, cell uptake of targeting micelle dropped back to almost the same level of folate-free micelle when large amount of free folate (10 mM) was present in the cell culture medium.

The potential of these Fe₃O₄-loaded and folate-encoded micelles as a novel drug delivery platform was further demonstrated by the MTT cytotoxicity assay. Two groups of experimental controls,

micelles without DOX and SPIO loaded inside as well as micelles loaded with SPIO alone, did not show significant cell growth inhibition, indicating minimal cell cytotoxicity of DOX-free micelles. The cytotoxicity of four DOX-loaded micelles with or without magnetic responsiveness was compared in order to further verify the dual targeting effect. The external magnetic field strength applied to cells during the course of cell incubation was set to 4150 G. As shown in Fig. 7, after 3 days cell incubation in the given magnetic field, four micelles exhibited significantly different cytotoxicities in KB cells. Although magnetic targeting resulted in an ideal cell growth inhibition even for the non-folate magnetic micelle, the best outcome (i.e. $9 \pm 3\%$ cell viability) was achieved with folate-encoded and Fe₃O₄-loaded micelles. Furthermore, in the two micelles without Fe₃O₄ loading, folate targeting showed increased cytotoxic effects, with cell viabilities consisting of $77 \pm 2\%$ and $57 \pm 3\%$ for the folate-free and the folate-encoded micelles, respectively ($p < 0.05$). It is noteworthy that as a whole, these two DOX-encapsulated micelle formulations without magnetic responsiveness were much less effective in cell growth inhibition. These MTT cytotoxicity data are in agreement with results obtained in the cell uptake study, and revealed once more the dual targeting effect of Fe₃O₄-loaded and folate-encoded micelles to target cells in the presence of a strong external magnetic field. In the dual targeting strategy, the external magnetic field will first guide the accumulation of micelles to tumor tissues after which a targeting ligand would allow for binding to the cell membrane receptors to facilitate micelle uptake inside tumor cells. Animal experiments are currently in progress to evaluate the efficacy of this dual targeting micelle *in vivo*.

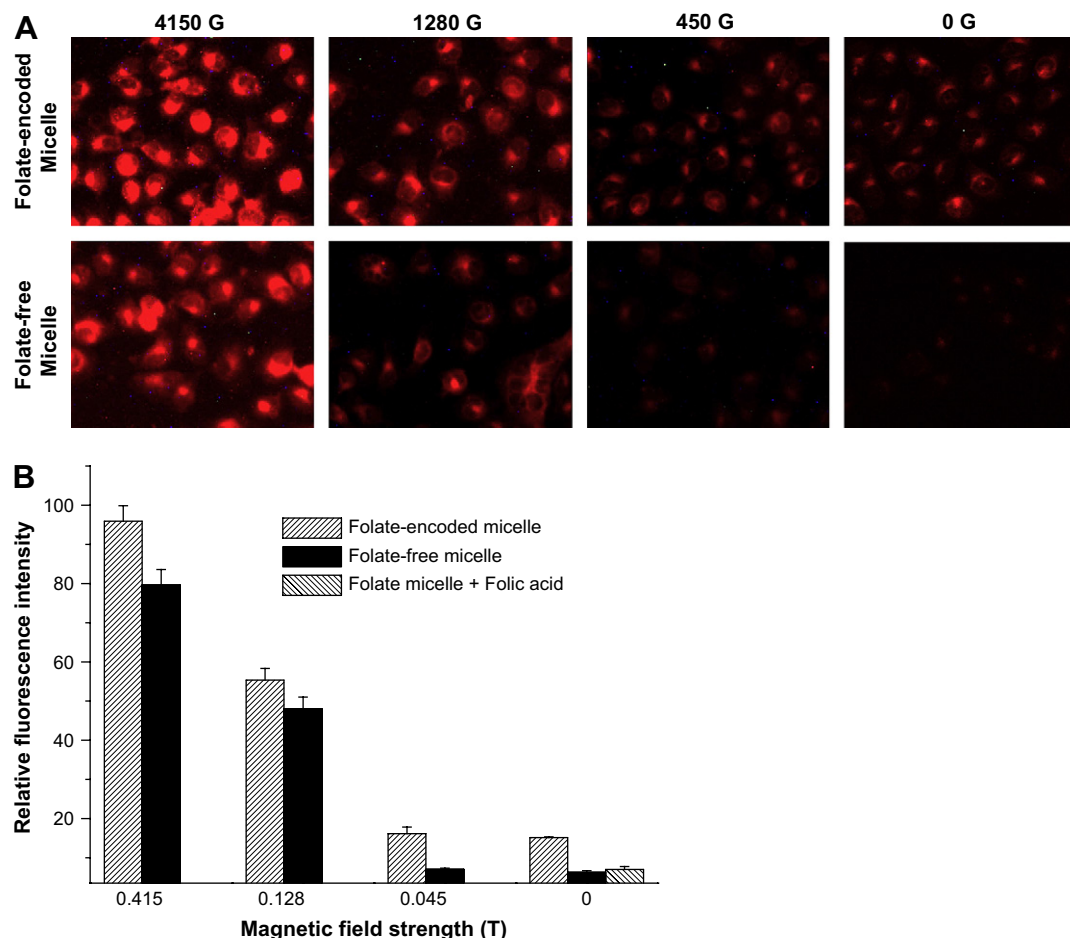


Fig. 6. Fluorescence microscopy images (A) and flow cytometry data (B) for KB cells upon treatment with the SPIO–DOX-loaded micelles in different magnetic field strengths. Relative fluorescence intensities obtained in flow cytometry are presented as mean \pm SD ($n = 3$). Cell incubation time: 0.5 h. Folate competing assay was performed in the presence of large amount of free folate (10 mM) in solution. $p < 0.05$ for all data points when comparing between folate-encoded and folate-free micelles.

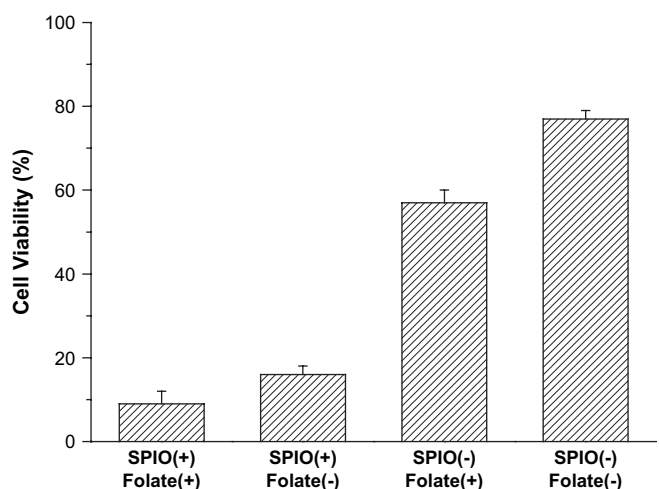


Fig. 7. (A) Cytotoxicity of four DOX-encapsulated micelle formulations with or without magnetic responsiveness. Cells were incubated for 3 days in micelle-containing media (DOX concentration: 2.5 $\mu\text{g}/\mu\text{L}$), and an external magnetic field (0.415 T) was applied to cells during the whole course of cell incubation. Micelle characteristics are shown below the X-axis as follows: SPIO (+) and SPIO (-) for micelles with and without SPIO loading, while folate (+) and folate (-) for micelles with and without folate functionalization. For example, under such denotation, SPIO (+) and folate (+) together indicate SPIO-loaded and folate-encoded micelles. Data are presented as mean \pm SD ($n = 3$).

4. Conclusions

In summary, we report a novel dual targeting strategy to maximize drug delivery efficacy to tumor cells. A nanoscale, micellar carrier from a block copolymer, folate-PEG-PCL, has been developed to encapsulate superparamagnetic Fe_3O_4 and to deliver an anticancer drug, doxorubicin. These micelles demonstrate the potential to achieve dual tumor targeting (i.e. magnetic field-guided and ligand-directed targeting) of micelles to tumor cells. The dual targeting strategy opens up several opportunities for enhancing drug delivery efficiency and cancer specificity during chemotherapy.

Acknowledgement

This work was supported by the National Natural Science Foundation of China (Grant Nos. 20474076, 20728403 and 50673103).

References

- [1] (a) Xiong DA, He ZP, An YL, Zhe Li, Wang H, Chen X, et al. *Polymer* 2008;49: 2548–52; (b) Kim SY, Shin G, Lee YM. *Biomaterials* 1999;20:1033–42.
- [2] (a) Li JB, Shi LQ, An YL, Li Y, Chen X, Dong HJ. *Polymer* 2006;47:8480–7; (b) Kataoka K, Matsumoto T, Yokoyama M, Okano T, Sakurai Y, Fukushima S, et al. *J Controlled Release* 2000;64:143–53; (c) Liu DH, Zhong CL. *Polymer* 2008;49:1407–13.

- [3] (a) Chen C, Yu CH, Cheng YC, Yu PHF, Cheung MK. *Biomaterials* 2006;27:4804–14;
(b) Huynh DP, Shim WS, Kim JH, Lee DS. *Polymer* 2006;47:7918–26.
- [4] Ai H, Flask C, Weinberg B, Shuai X, Pagel MD, Farrell D, et al. *Adv Mater* 2005;17:1949–52.
- [5] Savic R, Luo L, Eisenberg A, Maysinger D. *Science* 2003;300:615–8.
- [6] (a) Hu YQ, Kim MS, Kim BS, Lee DS. *Polymer* 2007;48:3437–43;
(b) Kataoka K, Harada A, Nagasaki Y. *Adv Drug Delivery Rev* 2001;47:113–31.
- [7] Sutton D, Nasongkla N, Blanco E, Gao J. *Pharm Res* 2007;24:1029–46.
- [8] Licciardi M, Giammona G, Du JZ, Armes SP, Tang YQ, Lewis AL. *Polymer* 2006;47:2946–55.
- [9] Nasongkla N, Shuai X, Ai H, Weinberg BD, Pink J, Boothman DA, et al. *Angew Chem* 2004;116:6483–7.
- [10] Daniels TR, Delgado T, Helguera G, Penichet ML. *Clin Immunol* 2006;121:159–76.
- [11] Dinauer N, Balthasar S, Weber C, Kreuter J, Langer K, Briesen HV. *Biomaterials* 2005;26:5898–906.
- [12] Widder KJ, Senyei AE, Scarpelli DG. *Proc Soc Exp Biol Med* 1978;58:141–6.
- [13] Widder KJ. *Proc Natl Acad Sci USA Biol Sci* 1981;78:579–81.
- [14] Alexiou C, Arnold W, Klein RJ, Parak FG, Hulin P, Bergemann C, et al. *Cancer Res* 2000;60:6641–8.
- [15] Häfeli UO. *Int J Pharm* 2004;277:19–24.
- [16] Alexiou C, Jurgons R, Schmid R, Hilpert A, Bergemann C, Parak F, et al. *J Magn Magn Mater* 2005;293:389–93.
- [17] Lübke AS, Bergemann C, Riess H, Schriever F, Reichardt P, Possinger K, et al. *Cancer Res* 1996;56:4686–93.
- [18] Schillinger U, Brill T, Rudolph C, Huth S, Gersting S, Krötz F, et al. *J Magn Magn Mater* 2005;293:501–8.
- [19] Rudge SR, Kurtz TL, Vessely CR, Catterall LG, Williamson DL. *Biomaterials* 2000;21:1411–20.
- [20] Nasongkla N, Bey E, Ren J, Ai H, Khemtong C, Guthi JS, et al. *Nano Lett* 2006;6:2427–30.
- [21] Yang X, Deng W, Fu L, Gao J, Quan D, Shuai X. *J Biomed Mater Res A* 2008;86A:48–60.
- [22] Sun S, Zeng H, Robinson DB, Raoux S, Rice PM, Wang SX, et al. *J Am Chem Soc* 2004;126:273–9.
- [23] Shuai X, Ai H, Nasongkla N, Kim S, Gao J. *J Controlled Release* 2004;98:415–26.
- [24] Yoon TJ, Yu KN, Kim E, Kim JS, Kim BG, Yun SH, et al. *Small* 2006;2:209–15.
- [25] Son SJ, Reichel J, He B, Schuchman M, Lee SB. *J Am Chem Soc* 2005;127:7316–7.

Folate-functionalized polymeric micelles for tumor targeted delivery of a potent multidrug-resistance modulator FG020326

Xiaoqiang Yang,^{1*} Wenjing Deng,^{2*} Liwu Fu,² Elvin Blanco,³ Jinming Gao,³ Daping Quan,¹ Xintao Shuai¹

¹BME Center, State Key Laboratory of Optoelectronic Materials and Technologies, School of Chemistry and Chemical Engineering, Sun Yat-Sen University, Guangzhou 510275, China

²Cancer Center, Sun Yat-Sen University, Guangzhou 510060, China

³Simmons Comprehensive Cancer Center, University of Texas Southwestern Medical Center at Dallas, Dallas, Texas

Received 25 November 2006; revised 16 April 2007; accepted 18 May 2007

Published online 16 October 2007 in Wiley InterScience (www.interscience.wiley.com). DOI: 10.1002/jbm.a.31537

Abstract: To overcome multidrug resistance (MDR) existing in tumor chemotherapy, polymeric micelles encoded with folic acid on the micelle surface were prepared with the encapsulation of a potent MDR modulator, FG020326. The micelles were fabricated from diblock copolymers of poly(ethylene glycol) (PEG) and biodegradable poly(ϵ -caprolactone) (PCL) with folate attached to the distal ends of PEG chains. The folate-conjugated copolymers, folate-PEG-PCL, were synthesized by multistep chemical reactions. First, allyl-terminated copolymer (allyl-PEG-PCL) was synthesized through a ring-opening polymerization of ϵ -caprolactone in bulk employing monoallyl-PEG as a macroinitiator. Second, the allyl terminal groups of copolymers were converted into primary amino groups by a radical addition reaction, followed by conjugation of the carboxylic group of folic acid. *In vitro* studies at 37°C demonstrated that

FG020326 release from micelles at pH 5.0 was faster than that at pH 7.4. Cytotoxicity studies with MTT assays indicated that folate-functionalized and FG020326-loaded micelles resensitized the cells approximately five times more than their folate-free counterparts ($p < 0.01$) in human KB_{v200} cells treated with vincristine (VCR). The *in vitro* Rhodamine 123 efflux experiment using MDR KB_{v200} cells revealed that when cells were pretreated with folate-attached and FG020326-loaded micelles, the P-glycoprotein (P-gp) drug efflux function was significantly inhibited. © 2007 Wiley Periodicals, Inc. *J Biomed Mater Res* 86A: 48–60, 2008

Key words: multidrug resistance; polymeric micelles; poly(ethylene glycol)-poly(ϵ -caprolactone); folate functionalization; tumor targeting

INTRODUCTION

The resistance of cancer cells to multiple structurally unrelated chemotherapeutic drugs termed “multidrug resistance (MDR)” has been recognized as a major cause of failure in human cancer chemotherapy. It is well known that various mechanisms are involved in drug resistance in cancer, chief among them the classical efflux mechanism associated with the function of P-glycoprotein (P-gp). P-gp is an ABC transporter and a plasma membrane glycoprotein encoded by the human *MDR1* gene, which acts as a drug efflux pump that extrudes a wide range of

structurally and mechanistically different chemotherapeutic drugs out of cancer cells.^{1–3} The mechanism of action of various drugs, including vinca alkaloids, anthracyclines, epipodophyllotoxins, taxanes and other natural products, have been reported to be affected by classical MDR.¹ Hence, a common way to circumvent P-gp-based MDR is to use MDR modulators that inhibit P-gp-mediated drug efflux, resulting in resensitization of MDR cancer cells to treatment with chemotherapeutic agents when coadministered with MDR modulators.⁴ Recently, several effective MDR modulators have been reported including verapamil, quinidine, PSC833, etc.⁵ One of the authors (LF) of the present work and coworkers have demonstrated that the small molecular FG-020326, an imidazole derivative (E)-methyl 3-(4-(4,5-bis(4-(isopropyl(methyl)amino)phenyl)-1H-imidazol-2-yl)phenyl)acrylate as shown in Figure 1, can significantly inhibit the function of P-gp, and consequently increase the intracellular accumulation and

*These authors contributed equally to this work.

Correspondence to: X. Shuai; e-mail: shuaixt@mail.sysu.edu.cn

Contract grant sponsor: National Natural Science Foundation of China; contract grant numbers: 20474076, 50673103, 30371659

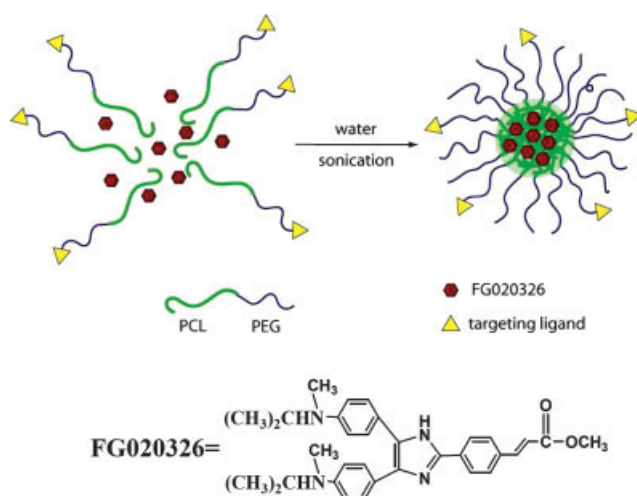


Figure 1. Schematic formation of FG020326-encapsulated micelle by adding THF solution containing FG020326 and copolymer to water under sonication, followed by evaporation of THF. [Color figure can be viewed in the online issue, which is available at www.interscience.wiley.com.]

efficacy of vincristine (VCR), a commonly used anticancer agent. Notably, FG020326 increased the sensitivity of KB_{v200} cells to VCR by ~52-fold.^{6,7}

Despite remarkable promise for concomitant delivery of FG020326 and anticancer drugs, the low water solubility of the unprotonated FG020326 remains a problem for traditional *in vivo* administration. Moreover, the implementation of P-gp inhibition in cancer treatment with MDR modulators has faced two major obstacles. Firstly, it is often associated with exacerbated toxicity of anticancer drugs because this approach may also block the excretory functions of P-gp expressed in healthy tissues, and thus markedly reduces clearance of anticancer agents from these sites.⁸ Secondly, MDR modulators, even if soluble in physiological aqueous media, undergo quick renal clearance following *in vivo* administration, resulting in short blood retention that prevents tumors from receiving therapeutic concentrations.

Several studies over the past decade have extensively documented the advantages of polymeric micelles as anticancer drug carriers, specifically their ability to overcome limitations stemming from toxicity, and agent solubilization and long circulation time.^{9,10} Polymer micelles consist of a hydrophobic core that acts as a carrier compartment that accommodates hydrophobic agents, and the soluble shell consists of a brush-like protective corona that stabilizes the nanoparticles in aqueous solution. Upon encapsulation within the micelles, solubility limits for hydrophobic drugs can be exceeded.¹¹ Until now, most reported micelle systems have focused on the delivery of hydrophobic anticancer drugs, with examples including micelles based on PEGylated polyesters such as poly(ethylene glycol)-*b*-poly(D,L-

lactide) (PEG-PLA) and poly(ethylene glycol)-*b*-poly(ϵ -caprolactone) (PEG-PCL), which have been reported for the delivery of doxorubicin and paclitaxel.^{12,13} Owing to their nanoscaled dimension, these micellar particles are also expected to escape the quick kidney excretion. Despite several advantages, a significant challenge for micelle delivery systems is how to achieve high targeting efficiency at the tumor sites and associated cells. One strategy, adopted by many researchers is the functionalization of the micelles with a ligand that can selectively bind to a specific receptor over-expressed on the cell surface (i.e. active targeting). However, only a handful of reports have dealt with the modification of micelles with an active targeting ligand, specifically PEG-PCL micelles, in this fashion. Among them, a cyclic pentapeptide, cRGDFK, which is specific to the $\alpha v \beta 3$ receptor, was demonstrated to significantly enhance the uptake of micelles by SLK tumor endothelial cells.¹⁴ Furthermore, Lee and coworkers showed that PEG-PCL micelles, with folate acid conjugated to the PCL block, demonstrated a folate-directed targeting of micelles to MCF-7 cells and HeLa 229 cells for the delivery of doxorubicin.¹⁵

The purpose of the present work is to propose a novel, tumor-targeted polymeric micelle platform for the delivery of FG020326. Until now, only passive targeting of P-gp inhibitor Cyclosporin A (CsA) by PEO-*b*-PCL micelles has been reported by Lavasani et al.^{16,17} We propose micelle particles fabricated from the biodegradable copolymer poly(ethylene glycol)-*b*-poly(ϵ -caprolactone) (PEG-PCL) containing FG020326 and functionalized with folate on their surface layer to target tumor cells possessing an over-expression of folate receptors on the cellular membrane. In contrast to the strategy by Lee and coworkers in which folate was conjugated to the PCL block, we attached folate to the PEG distal ends in the present work in hopes that the targeting ligand would have a better chance of being presented out of the surface layer of micelles for a further enhancement of targeting effect of the folate-bearing PEG-PCL micelles. In the present work, copolymers for fabrication of targeting micelles were synthesized via multistep, sequential syntheses of allyl-PEG-PCL by anionic reaction, NH₂-PEG-PCL by radical addition reaction in water with potassium persulfate (K₂S₂O₈) as a catalyst, and folate-PEG-PCL by conjugation of folic acid. FG020326 loading and its *in vitro* release were investigated. Efficient cell internalization of FG020326-loaded targeting micelles was demonstrated using a Rhodamine 123 efflux assay. As hypothesized, FG020326 transported with folate-bearing micelles rather than folate-free micelles remarkably resensitized MDR KB_{v200} cells to VCR as demonstrated by cell culture experiments. Taking into consideration the fact that folate recep-

tors are known to over-express in various types of tumors, including ovarian, lung, colorectal, renal, breast cancers, and non-Hodgkin's lymphomas,¹⁸ we expect that this novel platform of folate-directed delivery of MDR modulators is of great potential for cancer treatment purposes.

MATERIALS AND METHODS

Materials

ϵ -Caprolactone (ϵ -CL, from Sigma-Aldrich) and allyl alcohol (from Guangzhou Chemical Reagent Factory, China) were both purified by vacuum distillation over calcium hydride (CaH_2). Tetrahydrofuran (THF, from Sigma-Aldrich) was dried by refluxing over a sodium-potassium alloy and distilled under dry argon. 18-Crown-6 (from Sigma-Aldrich) was vacuum-dried overnight at 46°C. 2-Aminoethanethiol hydrochloride, folic acid, *N*-hydroxysuccinimide (NHS), naphthalene, potassium persulfate ($\text{K}_2\text{S}_2\text{O}_8$), dicyclohexylcarbodiimide (DCC), azobisisobutyronitrile (AIBN) were purchased from Sigma-Aldrich and used as received. Ethylene oxide (EO, purity 99%) stored inside a gas tank were obtained from Foshan Kedi Gas Chemical Industry (China) and used as received. All organic solvents are of analytic grade. Phosphate-buffered solutions (PBS, pH 7.4 and 5) were prepared in our laboratory. Potassium naphthalide solution was prepared by adding potassium into an anhydrous THF solution of naphthalene and then stirring the mixture at room temperature for 1 h under dry argon, just prior to use. FG020326 was synthesized according to a previously published procedure in the literature.^{19,20} VCR was purchased from ShenZhen Main Luck Pharmaceuticals, China. MTT (3-(4,5-dimethylthiazol-2-yl)-2,5-diphenyltetrazolium bromide) was purchased from Sigma-Aldrich. Dulbecco's modified Eagle's medium (DMEM) and RPMI-1640 were purchased from Gibco BRL (USA). KB_{v200} is a human epidermoid carcinoma MDR cell line with high expression of P-gp as well as folate receptors on the cell membrane. KB_{v200} cells were cultured with RPMI-1640 culture medium containing 10% FBS at 37°C in a humidified atmosphere of 95% air plus 5% CO_2 .

Synthesis of allyl-terminated diblock copolymer of PCL and PEG (allyl-PEG-PCL)

The copolymer was synthesized by sequential anionic ring-opening polymerization of EO and ϵ -CL in one pot using potassium alkoxide as an initiator. THF solution (4 mL) of potassium naphthalide was allowed to mix with 0.5-mL allyl alcohol, and then the mixture was stirred for 15 min into a flame-dried reaction flask equipped with a magnetic stirring bar and two capillary gas inlets for EO and argon, respectively. Subsequently, 20 mL anhydrous THF and 1.5 g 18-crown-6 predissolved in 5-mL anhydrous THF in another flamed flask were then transferred into the first reaction flask under argon. After stirring for another 15 min, the mixture was cooled with a salted ice-water bath

of -5°C . A precalculated amount of dry EO was slowly blown and condensed into the reaction mixture. Afterwards, the EO polymerization was conducted at 0°C for 24 h and then at room temperature for 3 days to ensure a thorough conversion of EO. In the second step, a predesigned amount of ϵ -CL was injected into the reaction flask under argon protection and then polymerized at room temperature for 48 h. The polymerization was finally quenched by adding a small amount of acetic acid. The crude copolymer collected by precipitation in hexane was redissolved in dichloromethane and added to ten-fold diethyl ether under vigorous stirring. A white powder was sequentially isolated by filtration and washed with hexane and diethyl ether.

Conversion of allyl-PEG-PCL into NH_2 -PEG-PCL

This procedure was carried out by a radical addition reaction of 2-aminoethanethiol hydrochloride, which was modified based on a previously reported method by Kataoka and coworkers for converting allyl-PEG into NH_2 -PEG.²¹ The reaction was conducted in an aqueous micelle solution, which was prepared by slowly adding a THF solution (2 mL) of allyl-PEG-PCL (0.5 g) into distilled water (20 mL) under stirring, and then allowing evaporation of THF and formation of micelles as previously reported.²² The micelle solution was first bubbled with nitrogen for 1 h to remove oxygen, and then $\text{K}_2\text{S}_2\text{O}_8$ (0.8 molar equivalent of allyl-PEG-PCL) and 2-aminoethanethiol hydrochloride (10-fold molar equivalent of allyl-PEG-PCL) were added into the above solution. Subsequently, the micelle solution was sealed in a nitrogen atmosphere and stirred for 5 h at 52°C . Unreacted 2-aminoethanethiol hydrochloride and $\text{K}_2\text{S}_2\text{O}_8$ were removed by dialysis against water for 24 h at room temperature (MW cut-off: 8000 Da). Lithium hydroxide solution (1M) was then added in a dropwise fashion into the micelle solution to adjust the pH from 7.4 to 9.4, which converts the terminal amine salt into primary amino groups. The obtained micelle solution was immediately freeze-dried. After lyophilization, the micelle powder was redissolved in THF, filtered across a 220-nm pore-size membrane to remove lithium chloride and unreacted lithium hydroxide, and finally precipitated into hexane to recover pure copolymer (yield > 78%). Conversion rate of allyl- to NH_2 - was calculated based on the analysis of NMR spectra of allyl-PEG-PCL and NH_2 -PEG-PCL, as shown in Figure 2. Integral values of absorption peaks "a" and "h" in Figure 2(a), "d" and "h" in Figure 2(b) (denoted as I_{a-2a} , I_{h-2a} , I_{d-2b} , and I_{h-2b} , respectively) were used for the calculation. The conversion rate of allyl-PEG-PCL into NH_2 -PEG-PCL was calculated as $(I_{d-2b}/I_{h-2b})/(I_{a-2a}/I_{h-2a})$.

Preparation of folate-conjugated copolymer (folate-PEG-PCL)

Folate was first activated with NHS according to a previously published procedure.²³ Briefly, folic acid (1 g) dissolved in anhydrous DMSO (30 mL) was reacted overnight with NHS (0.9 g) in the presence of DCC (0.5 g) under argon at room temperature, and the major byproduct, 1,3-dicyclohexylurea (DCU), was removed by filtration. Subse-

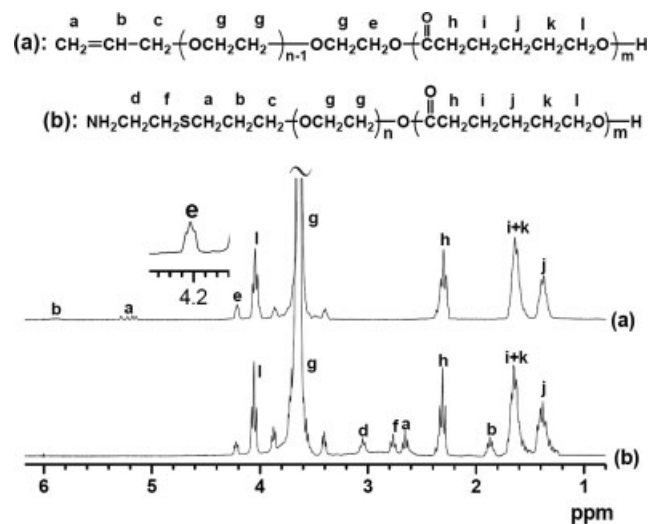


Figure 2. ^1H NMR spectra of allyl-PEG3k-PCL1k (a) and NH_2 -PEG3k-PCL1k (b) in CDCl_3 . The expanded peak “e” at ~ 4.2 ppm indicates the successful synthesis of block copolymer.

quently, the above activated folate solution (3 mL) was added to a DMSO solution (5 mL) containing NH_2 -PEG-PCL (0.4 g) and triethylamine (0.05 mL). The reaction was performed at room temperature for 10 h under argon. The resulting solution was centrifuged and filtered. The filtrate thus obtained was dialyzed against water for 24 h (MW cut-off: 1000 Da). The aqueous solution inside the dialysis bag was then freeze-dried. The powdery sample was redissolved in THF (3 mL), and the filtrate was added dropwise to distilled water under stirring. After overnight evaporation of THF, the resultant micelle solution was dialyzed against water for 5 days to completely remove unreacted folic acid and any residual THF. The micelle solution was finally freeze-dried to yield a solid powder (yield > 82%). To evaluate the conversion rate of NH_2 -PEG-PCL into folate-PEG-PCL, copolymer was dissolved in DMSO and folate absorbance at 363 nm was measured by a Unico UV-2000 UV-Vis spectrophotometer to quantify the folate mass content in the sample. Absorbance of folate at 363 nm in DMSO with various concentrations was measured to generate a calibration curve.

Characterization of copolymers

Nuclear magnetic resonance (NMR) spectra were recorded on a Varian 300-MHz NMR spectrometer in deuterated water (D_2O), chloroform (CDCl_3), or DMSO depending on sample solubility at room temperature. Gel permeation chromatography (GPC) was employed to determine molecular weight and molecular weight distribution. GPC analysis was carried out using a SHODEX[®] 7.8 mm \times 300 mm column with chloroform as an eluent (1 mL/min) and polystyrene standards for column calibration. Twenty microliter samples were injected with a microsyringe, and the eluent was analyzed with a differential refractive index (RI) detector Waters 2414 from Waters (USA). High performance liquid chromatograph (HPLC)

was performed in pH 7.4 PBS using an Agilent(HP)1100 chromatographic instrument to analyze the content of free folate in the folate-conjugated copolymer samples. Folate solutions with various concentrations were first analyzed with HPLC to generate a calibration curve. The total folate amount in each sample was determined by measuring the absorbance of folate at 363 nm in DMSO with a Unico UV-2000 UV-Vis spectrophotometer.

Determination of critical micellization concentration

The critical micellization concentration (CMC) of folate-targeted copolymers was determined by fluorescence measurements using pyrene as an extrinsic probe, as previously reported.²⁴ The fluorescence spectra of pyrene were measured at varying polymer concentrations using a Shimadzu RF-5301PC fluorescence spectrometer (Japan) at 25°C. The excitation wavelength was adjusted to 339 nm, and the detection of fluorescence was performed at 375 and 385 nm, which correspond to the wavelength of the (0,0) band and the (0,2) band of pyrene fluorescence, respectively. CMC was measured from the onset of a rise in the intensity ratio of peaks at 385 nm to peaks at 375 nm in the fluorescence spectra of pyrene plotted *versus* the logarithm of polymer concentration.

Preparation of FG020326-loaded micelles

Polymeric micelles containing FG020326 were prepared as follows: 10 mg of copolymer (allyl-PEG-PCL or folate-PEG-PCL) and 2 mg of FG020326 were codissolved in 2-mL THF in a glass vial. The solution was then added to pure water (20 mL) under sonication using a UP 50H Dismembrator (Hielscher, Germany). THF was allowed to slowly evaporate overnight, leading to the formation of micelles (Fig. 1). Residual THF was completely removed by vacuum evaporation at room temperature with a rotary evaporator. The micelle solution, concentrated to 5 mL, was filtered with a syringe filter (pore size: 0.22 μm) to eliminate polymer and FG020326 aggregates, and then dialyzed against pure water for 24 h to remove unencapsulated FG020326 (MW cut-off: 8000 Da). The micelles thus obtained were characterized with photon correlation spectroscopy, which was performed at 25°C on a BI-200 SM dynamic laser scattering system from Brookhaven Instruments. Scattered light was detected at 90° and collected on an autocorrelator. For each sample, data obtained from five measurements were averaged to yield the size and size distribution. The polymer concentration in size measurement studies was $\sim 10^{-3}$ mg/mL. Solid micelle samples for NMR, GPC and UV-Vis experiments were obtained by lyophilization of micelle solutions.

Determination of drug-loading content

The drug-loading content (DLC) was defined as the weight percentage of FG020326 in the micelle. DLC was quantified by determining the absorbance at 411.5 nm

using a Unico UV-2000 UV-Vis spectrophotometer. The freeze-dried micelle samples were redissolved in THF for the UV-Vis measurement. FG020326 solutions of various concentrations in THF were prepared, and the absorbance at 411.5 nm was measured to generate a calibration curve for the DLC calculations for various micelles. The extinction coefficient of FG020326 at THF is $\epsilon_{411.5} = 1.67 \times 10^4 \text{ M}^{-1} \text{ cm}^{-1}$. The drug-loading content was calculated using the following equation:

$$\text{DLC} = \frac{\text{Amount of FG020326 in micelle (mg)}}{\text{Amount of FG020326 - loaded micelle (mg)}} \times 100$$

***In vitro* release of FG020326 from micelles**

Freeze-dried micelle samples (10 mg each) were resuspended in PBS (pH 7.4 or 5) and transferred into a dialysis bag (MW cut-off: 8000 Da). The bag was placed into 25 mL PBS (pH 7.4 or 5). The release study was performed at 37°C in a Shanghai Yiheng Scientific DKZ incubator shaker. At selected time intervals, solution outside the dialysis bag was removed for UV-Vis analysis and replaced with fresh buffer solution. FG020326 concentration was calculated based on the absorbance intensity of FG020326 at 411.5 nm. In the assessment of drug release behavior, the cumulative amount of the released drug was calculated, and the percentages of drug released from each micelle were plotted against time. Release of free drug from the dialysis bag at both pHs were performed as control following the same procedure as described above.

MTT cytotoxicity assay

The inhibition of cell growth was evaluated by the MTT method using triplicate assays. Human epidermoid carcinoma cell lines KB_{v200} cells were harvested during logarithmic growth phase, seeded in 96-well plates at 0.3×10^4 cells/well, and then adjusted to a final volume of 170 μL with RPMI-1640 culture medium containing 10% FBS. After 24 h incubation, the cells were incubated with culture media containing VCR and FG020326-free or FG020326-loaded micelles at predesigned concentrations in each well. FG020326 concentration in FG020326-containing media, i.e. media containing either free FG020326 or FG020326-loaded micelle, was set to 2 $\mu\text{mol/L}$. Cell incubation with VCR and copolymers below the CMC was also performed as control. VCR and micelle at various gradient concentrations in the culture media were obtained by media dilution. After 72 h, 10 μL of MTT solution (5 mg/mL in 0.9% NaCl saline) was added to each well and the incubation was continued for an additional 4 h in a 37°C incubator containing 5% CO₂, allowing the viable cells to reduce the yellow MTT into dark-blue formazan crystals, which were then dissolved in 100 μL of DMSO. The absorbance in individual wells was determined at 540 and 655 nm by a microplate reader (BIO-RAD). The VCR concentration required to inhibit cell growth by 50% (IC₅₀) was calculated from the cytotoxicity curves (Bliss's software). Free FG020326 in its protonated form was also

tested as a control. The MDR reversal effect was assessed by quantifying the VCR IC₅₀ values with or without the presence of FG020326 in the culture media.

Rhodamine 123 efflux studies

KB_{v200} cells were exposed for 2 h to media containing one of the following: blank micelles, copolymers below the CMC, FG020326-loaded micelles, and free FG020326. In a control experiment, KB_{v200} cells were first incubated with free folate (10 mM) for 1 h, and then cocultured with folate-functionalized and FG020326-loaded micelles for 2 h. FG020326 concentration in media containing FG020326-loaded micelles or free FG020326 was 2 $\mu\text{mol/L}$. The cells were collected and washed once and then resuspended in 1 mL RPMI-1640 at the concentration of 1×10^5 cells/mL. The cells were then loaded with 5 $\mu\text{g/mL}$ of Rhodamine 123 for 30 min at 37°C. After one wash with dye-free RPMI-1640, cells were allowed to efflux the dye for 10 min in dye-free RPMI 1640 at 37°C. The cells were then washed out and suspended in 1 mL RPMI 1640, after which flow cytometric analysis was carried out using a FACScan flow cytometer to evaluate the MDR strength of KB_{v200} cells.

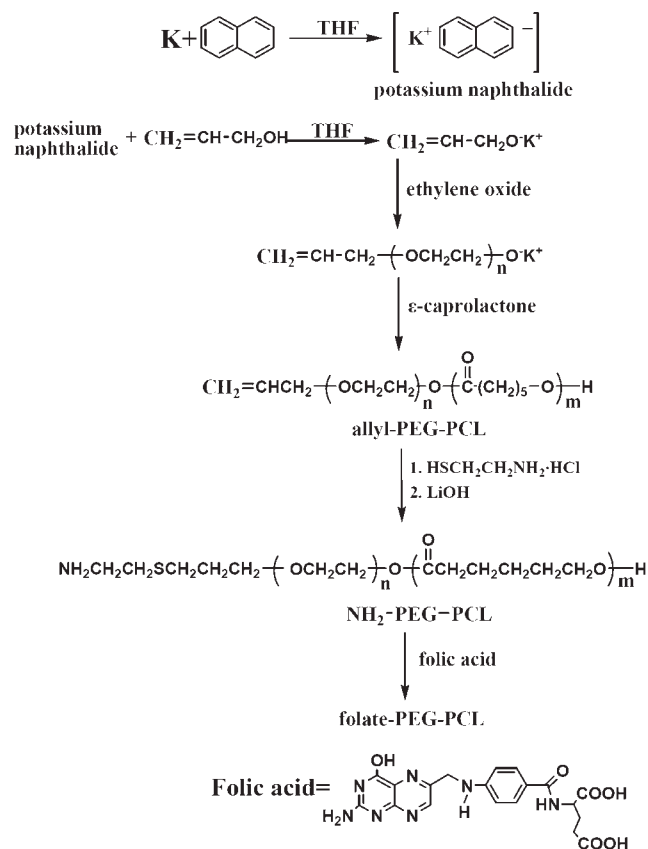
Statistical analysis

The experimental data were measured as mean values with standard deviations. Statistical analysis was carried out using the Student's *t*-test. Differences were considered statistically significant with $p < 0.05$.

RESULTS AND DISCUSSION

Syntheses of block copolymers

Synthesis of allyl-terminated PEG using allyl alkoxide as an initiator during anionic polymerization of EO, and subsequent conversion of allyl groups to primary amino groups by radical addition reaction of 2-aminoethanethiol hydrochloride, has been reported earlier by Kataoka and coworkers.²¹ Using a similar approach, we synthesized primary amino group-capped PEG-PCL for folate conjugation. The synthetic route for the targeting copolymer, folate-PEG-PCL, as shown in Scheme 1, outlines three major reaction steps involved in the synthesis. The synthesis of allyl-terminated diblock copolymer (allyl-PEG-PCL) by stepwise anionic ring-opening polymerization of EO and ϵ -CL was performed in a well controlled manner regarding the copolymer molecular weight as well as the length of individual blocks. To carry out the conversion of allyl groups of copolymers into primary amino groups, we first attempted the radical addition reaction of 2-aminoethanethiol hydrochloride with copolymer in DMF at 70°C using AIBN as an initiator, according to the



Scheme 1. Synthetic approach to folate-PEG-PCL.

method reported by Kataka et al. for the conversion of allyl-ended PEG into PEG mono-amine. However, the loss of PCL blocks of copolymers was noted under such reaction conditions for neat PEG, which is likely due to the susceptibility of the PCL carbonyl group to a nucleophilic attack of 2-aminoethanethiol hydrochloride at the elevated temperature 70°C. Indeed, the primary amino groups, even if protonated, have been reported to show some nucleophilic activity.²⁵ Therefore, we modified the reaction conditions of the above radical addition reaction, which allowed us to achieve complete allyl conversion while avoiding loss of integrity of PCL blocks. The major difference between our procedure and Kataka's is that, in the present work, the radical addition of thiol groups to the allyl double bonds was performed at a lower temperature (50°C) in an aqueous micelle solution, in which the PCL blocks are insoluble and thus well protected, rather than in an organic phase that may dissolve both PEG and PCL, and as a result, water-soluble K₂S₂O₈ rather than AIBN was used as an initiator. After the radical addition reaction, 1M lithium hydroxide solution was added dropwise to deprotonate the terminal amine chloride salt into the primary amino group. After freeze-drying of the micelle solution, micelle powder was dissolved in THF and filtered to remove

lithium chloride and unreacted lithium hydroxide. About 100% conversion of allyl to amino group has been obtained for both allyl-PEG3k-PCL1k and allyl-PEG3k-PCL2k. There is no evidence in the GPC and NMR measurements that the above process caused PCL cleavage (Table I). Finally, folic acid was activated and then conjugated to the PEG distal ends of copolymers. Although folic acid possesses α- and γ-carboxylic acid groups, which could both be activated by NHS, the γ-carboxylic acid group has much higher reactivity.^{26,27} Therefore, copolymers conjugating folate through the γ-carboxylic acid reaction should be produced predominantly. We obtained a conversion rate of 82.2% for folate-PEG3k-PCL1k, and 81.5% for folate-PEG3k-PCL2k respectively from their NH₂-PEG-PCL intermediates.

Spectroscopic methods were employed to characterize diblock intermediates (i.e., allyl- and NH₂-terminated copolymers) and folate-PEG-PCLs. As shown in Figures 2 and 3, the copolymer structures were confirmed by ¹H NMR measurements in which the characteristic resonances of both PCL and allyl-ended PEG were observed, indicating the coexistence of both blocks in the purified samples. Notably, the ¹H NMR absorption around 4.2 ppm in Figure 2, i.e., the triplet peak "e," strongly demonstrated the linkage structure between PCL and PEG blocks, complying with the expected copolymer structure in Scheme 1. By comparing the integrals of characteristic peaks of PEG blocks (e.g., the singlet of -OCH₂- at 3.65 ppm) and PCL blocks (e.g., the triplet of -C(=O)-CH₂- at 2.25 ppm) with that of characteristic peaks of the terminal allyl groups (e.g., the multiplet of CH₂=CH- at 4.90 ppm) in the ¹H NMR spectrum, the length of PEG and PCL blocks was calculated and reported as molecular weights in Table I.

GPC measurements also demonstrated the successful synthesis of the diblock copolymer by revealing a unimodal molecular weight distribution in the GPC chromatograms (data not shown). Only a negli-

TABLE I
Characteristics of the Prepared Block Copolymers

Code	Polymer	M _n ^a	M _n ^b	M _w /M _n ^a
1	Allyl-PEG3k-OH	2943	NA	1.106
2	Allyl-PEG3k-PCL1k	3808	3724	1.097
	NH ₂ -PEG3k-PCL1k	4018	3870	1.215
	Folate-PEG3k-PCL1k	5090	NA	1.261
3	Allyl-PEG3k-PCL2k	5125	5047	1.092
	NH ₂ -PEG3k-PCL2k	5224	5026	1.132
	Folate-PEG3k-PCL2k	6079	NA	1.271

NA: data not available.

^aDetermined by GPC with RI detector.

^bCalculated based on ¹H NMR spectra. The GPC-determined molecular weight of PEG block, 2943, was used for calculation.

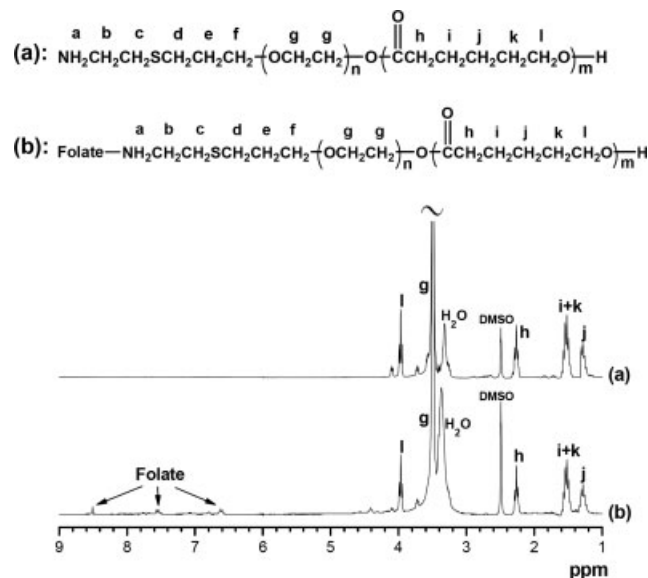


Figure 3. ¹H NMR spectra of NH₂-PEG3k-PCL1k (a) and folate-PEG3k-PCL1k (b) in DMSO-*d*₆.

gible increase in molecular weight of copolymer upon radical addition process was detected (Table I). By comparison, folate conjugation induced an increase in the copolymer molecular weight in GPC measurements (about 800–1000), due to the molecular weight addition effect of folate molecules (M_n of folic acid: 441). This molecular weight increase in GPC measurements is acceptable considering the detection variation of GPC analysis. GPC measurements with the UV detector did not detect a secondary peak in the chromatogram of the folate-conjugated copolymers (data not shown). Furthermore, the amount of unattached folate molecules determined by HPLC measurement in these copolymers is negligible (i.e. less than 0.9 wt % of the total amount of folate in each sample). This small residual amount of free folic acid should have little effect on micelle targeting to KB_{v200} cells. On the whole, both NMR and GPC measurements suggested that the radical addition reaction of aminoethanethiol hydrochloride with the allyl-bearing copolymer did not lead to a significant increase in copolymer molecular weight, implying that radical polymerization of allyl groups was suppressed to a great extent under our modified reaction conditions.

The critical micellization concentration determined by fluorescence measurements using pyrene as a probe was 9.6×10^{-6} g/mL for folate-PEG3k-PCL1k, and 3.8×10^{-6} g/mL for folate-PEG3k-PCL2k.

Micelle properties

Similar to the earlier observations for the doxorubicin or paclitaxel-loaded PEG-PCL micelles,^{22,28} Figure 4

demonstrates that FG023026 was encapsulated inside the PCL core of the core-shell-structural micelles. In CDCl₃, prominent resonance peaks (about 1.2, 2.08 ppm) of FG020326 were clearly observed in the ¹H NMR spectrum, in addition to those of PCL and allyl-PEG blocks, indicating that the micelle contains both copolymer and FG020326. However, in D₂O, only the PEG resonance peaks were detected while both the PCL and FG020326 resonance peaks were hardly observed. Based on these phenomena, we reasoned that the micelle shells consisting of PEG blocks were solvated in D₂O and therefore showed clear ¹H NMR signals. In contrast, resonance peaks of PCL blocks and FG020326 confined inside the solid micelle core were hardly observed due to their insufficient chain mobility in D₂O.

As shown in Table II, micelles predominantly less than 100 nm in diameter were successfully prepared, and the micelle size appears to be dependent on both copolymer composition and drug-loading. In general, similar to the doxorubicin or paclitaxel-loaded PEG-PCL micelles reported earlier,^{22,28} copolymers with longer PCL blocks formed larger micelle particles. Folate functionalization of copolymers does not lead to an obvious change in micelle size. However, unlike the previously reported data for the doxorubicin or paclitaxel-loaded PEG-PCL micelles, where micelle size is mostly independent

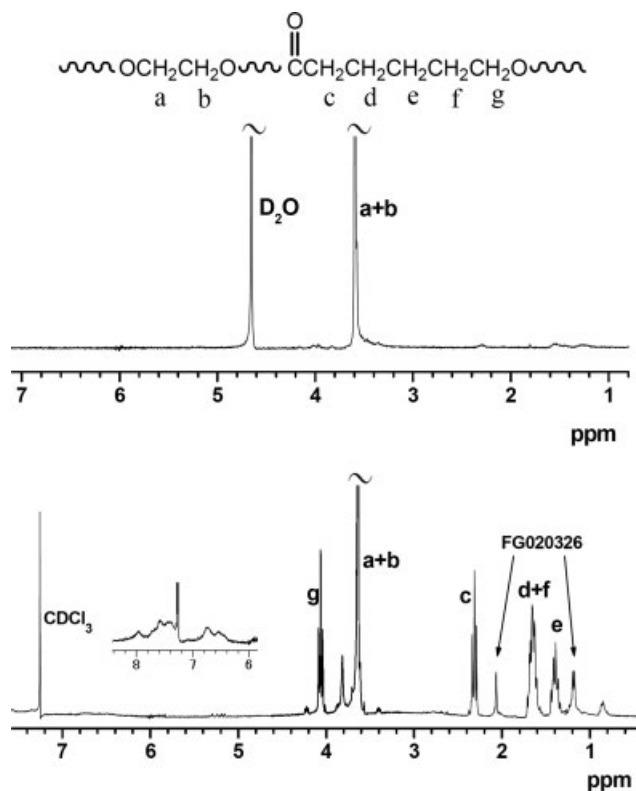


Figure 4. ¹H NMR spectra of FG020326-loaded allyl-PEG3k-PCL2k micelles in D₂O (a) and CDCl₃ (b).

TABLE II
Influence of Copolymer Composition on Micellar Properties

Copolymers	Micelle Size (nm)		Drug Loading Content (%)
	FG020326 Unencapsulated	FG020326-Loaded	
Allyl-PEG3k-PCL1k	51.4 ± 2	76.7 ± 3	5.3 ± 0.2
Allyl-PEG3k-PCL2k	82.4 ± 2	98.8 ± 3	6.1 ± 0.3
Folate-PEG3k-PCL1k	54.1 ± 2	73.6 ± 2	5.6 ± 0.2
Folate-PEG3k-PCL2k	81.8 ± 3	117.8 ± 4	6.4 ± 0.4

of drug-loading, FG020326-loading apparently led to the increase in particle size for both folate-free and folate-bearing micelles. FG020326-loading for the most part did not change the narrow size distributions of micelles. In addition, the loading content of FG020326 (DLC) in folate-PEG-PCL micelles increased from 5.6% to 6.4% with an increase of PCL molecular weight from 1 to 2 kDa, likely due to the fact that longer PCL brings about more micellar hydrophobic space for the drug to embed in, as well as stronger hydrophobic interaction between copolymer and FG020326.

In vitro FG020326 release properties

In the control experiments, free FG020326 quickly diffused out of the dialysis bag at both pH values [Fig. 5(a)]. The release of free FG020326 reached 100% in 3.5 h. The *in vitro* release profiles of FG020326-loaded micelles in two different buffered solutions (PBS at pH 7.4 and 5.0) were shown in Figure 5(b). The considerably slower release rate of micelle encapsulated drug than that of the free drug indicates the negligible effect of the dialysis bag on the detected rate of drug release from the micelles. The release behavior of FG020326 from the PEG-PCL micelles is similar to that of doxorubicin from the same type of micelles.²² Briefly, a relatively rapid release in the first phase, followed by a sustained and slower release over a prolonged time up to several weeks, was observed in both solutions. Furthermore, in comparison with the release at pH 5.0, FG020326 release from micelles at pH 7.4 was obviously slower ($p < 0.05$ for both formulations). It is important to note that FG020326, like doxorubicin, can be protonated at low pH resulting in an increase of drug solubility in aqueous solutions. Indeed, we determined the solubility values of FG020326 at pH5 and at pH7.4 to be 9.2×10^{-5} g/mL and 2.4×10^{-5} g/mL, respectively. Therefore, it is expected that FG020326 can be released faster when the micelle solution becomes acidic, e.g. at pH 5. Another reason causing the faster release of FG020326 at pH 5 might be that the micelle core hydrolyzed faster at

lower pH. For our FG020326-loaded micelles, the amount of released FG020326 for 24 h was about 15 wt % at pH 7.4, while it reached about 30 wt % at pH 5.0. This type of pH-dependent releasing behavior of drugs is of particular interest for tumor-targeted drug delivery using polymeric micelles. In the present case, a fast FG020326 release can be anticipated to occur once the micelle particles are internalized inside the tumor cells via folate-mediated endocytosis and trapped inside the lysosomal compartments where the pH value is known to drop to around 5.0.²⁹ Consequently, much enhanced bioavailability of the micelle-transported FG020326 is likely to occur, which is essential for achieving the desirable MDR reversal effect. FG020326 release rates

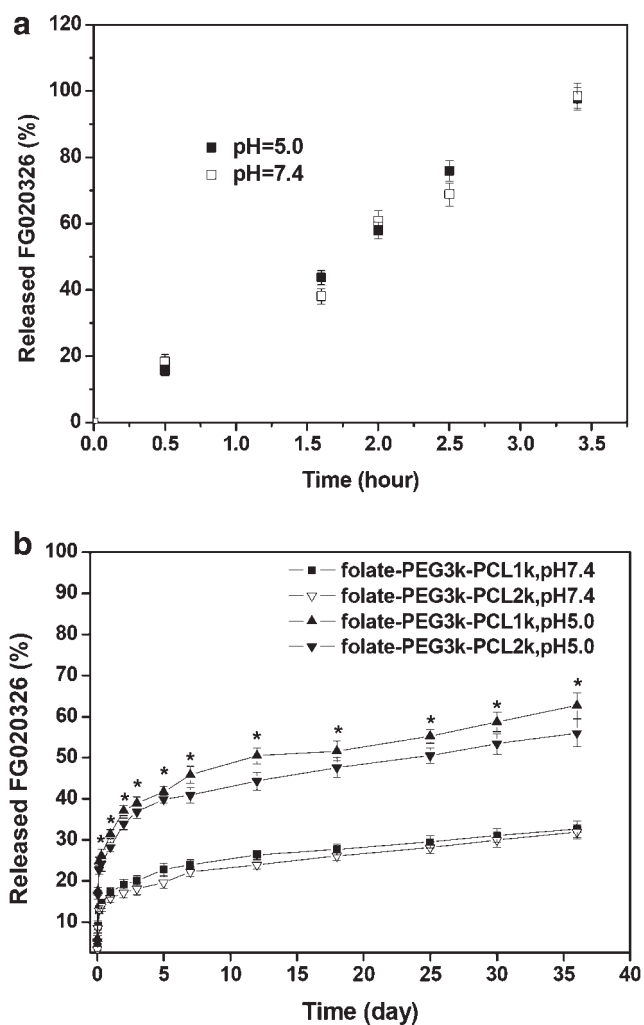


Figure 5. (a) Release profiles of free FG020326 from saturated solutions at pH 5.0 and pH 7.4. Data are presented as mean \pm SD ($n = 3$). (b) *In vitro* FG020326-release profiles for two micelle formations, folate-PEG3k-PCL1k and folate-PEG3k-PCL2k, at neutral (pH 7.4) and acidic (pH 5.0) conditions at 37°C. Data are presented as mean \pm SD ($n = 3$). *Denotes a significant difference between FG020326 release at that time point ($p < 0.05$, same formulation at different pH).

from the two micelles at pH 7.4 are similar within 35 h, which is to some extent consistent with the observation that CsA release from PEO-b-PCL micelles was almost not affected by the PCL length.¹⁶ At pH 5, FG020326 release from the PEG3k-PCL2k micelle appears to be slower than that from the PEG3k-PCL1k micelle ($p < 0.05$ for most time points starting from 24 h). At this condition, it is likely that FG020326 traversing the larger micelle particle may be retarded because of the longer diffusion path.³⁰

Although polymeric micelles provide an effective solution for the delivery of poorly soluble drugs, drug leaking out from micelles at the initial hours after injection is a commonly existing problem. Our research indicates that, at pH 7.4, which is close to the pH of normal biological fluids, the percentage of FG020326 released in 24 h for both formulations is about 15%, i.e. 85% of the encapsulated FG020326 is still trapped in micelles after 24 h. Note that micelle in solution can be freeze-dried to keep its intactness before use and 24 h is considerably long compared to the circulation time of small molecular drugs in blood. Although not perfect, these micelle systems still provided a biologically meaningful platform for FG020326 delivery. Further research in our labs is underway to get more desirable FG020326 release profile, i.e. reducing release at first hours and enhancing the release rate in the following sustained release stage, by varying the carrier polymer structure.

MDR reversal

A number of experimental and clinical approaches have been studied to overcome MDR effects in cancer cells.³¹ For instance, either conjugating drug to a soluble polymer carrier like *N*-(2-hydroxypropyl) methacrylamide (pHPMA) or transporting drug with a polymeric micelle was demonstrated as an effective

approach to overcome MDR. Unlike free drugs which cross the membrane by diffusion, a pathway that is affected by P-gp in MDR cells, polymer-drug conjugates or drug-encapsulated polymeric micelles are most likely transported into the cells via endocytosis, which is not affected by P-gp.^{8,32,33} In addition, the use of MDR modulators, e.g. cyclosporine A and some surfactants such as Pluronic[®] block copolymer below the CMC, were demonstrated to be a common and effective approach to inhibit P-gp-mediated drug efflux.^{31,34} Passive targeting of P-gp inhibitor Cyclosporin A by PEO-b-PCL micelles has been reported recently by Lavasanifar and coworkers. Their study focused on the pharmacokinetics and biodistribution of micelle-transported drug, and no information is available on the MDR reversal effect of this system.^{16,17}

In the present work, the MDR reversal potency was evaluated by MTT assays that revealed the cytotoxicity of anticancer VCR with and without the presence of FG020326 in the culture media. Previous studies have demonstrated that Pluronic[®] block copolymers below the CMC, i.e. block unimers of poly(polyethylene oxide) and poly(propylene oxide), are very effective P-gp function inhibitors, and Pluronic micelles do not possess such function of P-gp inhibition.³¹ To clarify whether PEG-PCL itself may inhibit the P-gp function like Pluronic unimers do, we tested the MDR reversal effect of these copolymers without the presence of FG020326. Cells were treated with copolymer solutions either above or below the polymer CMC. Our results indicate that in either case, above or below CMC, neither folate-PEG3k-PCL1k nor folate-PEG3k-PCL2k obviously improved the cytotoxicity of VCR to KB_{v200} cells [Table III and Fig. 6(a,b)]. This implies that folate-PEG-PCL alone cannot suppress the P-gp drug efflux function of KB_{v200} cells regardless of whether it is in unimer or micellar form. By contrast, FG020326 and

TABLE III
IC₅₀ of VCR in KB_{v200} Cells Determined by MTT Assay

Modulator Used in VCR Toxicity Test		IC ₅₀ ± SD	
FG020326-loaded allyl-PEG3k-PCL1k micelle ^a		0.0202 ± 0.0051	
FG020326-loaded allyl-PEG3k-PCL2k micelle ^a		0.0207 ± 0.0042	
FG020326-loaded folate-PEG3k-PCL1k micelle ^a		0.0046 ± 0.0031 ^b	
FG020326-loaded folate-PEG3k-PCL2k micelle ^a		0.0089 ± 0.0022	
Free FG020326 ^a		0.0059 ± 0.0013	
None		0.3157 ± 0.1102	
FG020326-free unimers or micelles	Folate-PEG3k-PCL1k	9.6 × 10 ⁻⁵ (>CMC)	0.3523 ± 0.0923
		1.0 × 10 ⁻⁶ (<CMC)	0.3489 ± 0.1045
	Folate-PEG3k-PCL2k	3.8 × 10 ⁻⁵ (>CMC)	0.3681 ± 0.0758
		1.0 × 10 ⁻⁷ (<CMC)	0.3315 ± 0.0824

Various experiments were conducted to clarify the performance of the FG020326-loaded micelles in terms of the MDR reversal.

^aKB_{v200} cells were incubated at the same FG020326 concentration of 2 μmol L⁻¹.

^b $p < 0.01$ (folate-PEG3k-PCL1k vs. allyl-PEG3k-PCL1k).

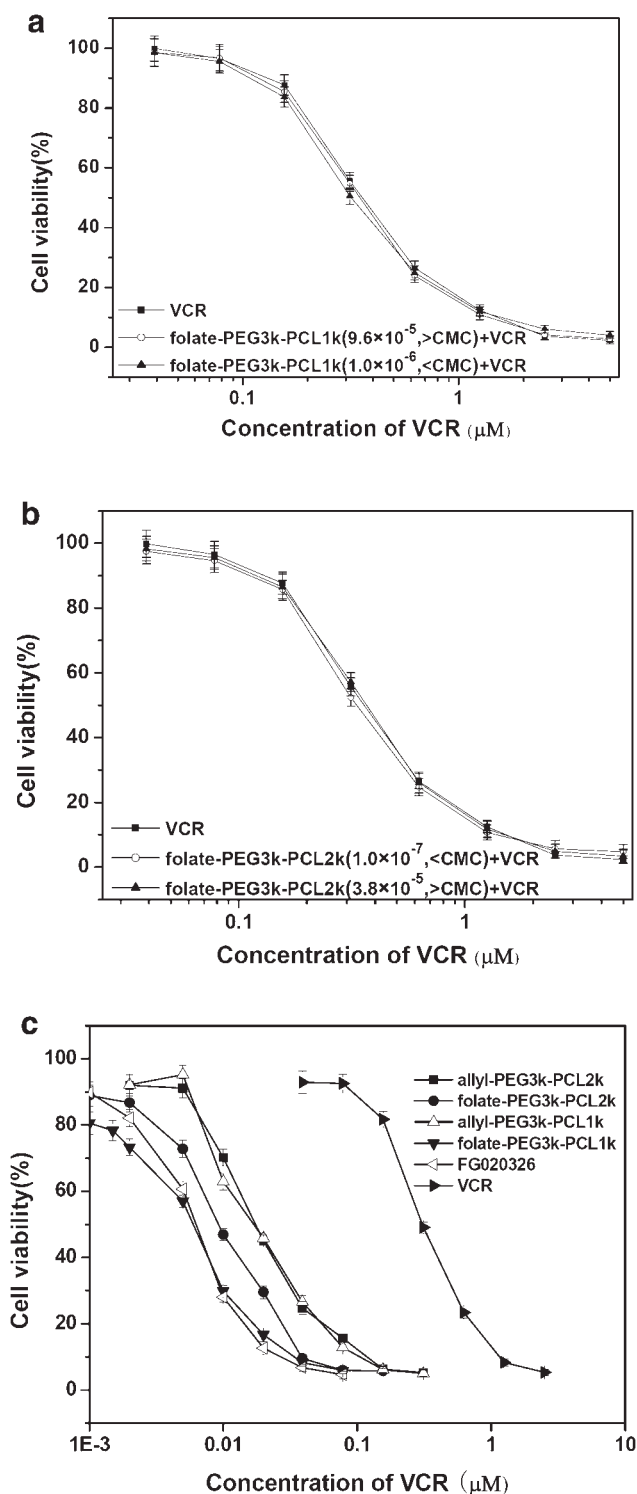


Figure 6. (a, b) Effect of FG020326-free unimers (below CMC) and micelles (above CMC) on the cytotoxicity of VCR in KB_{v200} cells. Data are presented as mean \pm SD ($n = 3$). (c) Effect of FG020326 or FG020326-loaded polymeric micelles on the cytotoxicity of VCR in KB_{v200} cells. Cells were incubated at the same FG020326 concentration $2 \mu\text{mol L}^{-1}$. Data is presented as mean \pm SD ($n = 3$).

FG020326-loaded micelles showed significant MDR reversal effect on KB_{v200} cells. It is known that FG020326 re-sensitizes KB_{v200} cells by inhibiting the function of P-gp associated with the resistance of cancerous cells to anticancer drugs.⁶ As can be seen, FG020326 transported by micelles functioned the MDR reversal of KB_{v200} cells.

In the VCR concentration-effect curves shown in Figure 6(c), the concentration yielding half-maximal inhibition to cell growth (IC_{50}) was detected at $0.316 \mu\text{M}$ for KB_{v200} cells not treated with FG020326 or FG020326-containing micelles (i.e. the negative control group). In comparison, IC_{50} values lower than $0.021 \mu\text{M}$ were detected for cells treated with FG020326 or FG020326-containing micelles, which is at least one order of magnitude lower than that for the negative control. Moreover, in comparison with the cells exposed to the folate-free and FG020326-loaded micelles, cells exposed to the folate-bearing and FG020326-loaded micelles are apparently even more sensitive to VCR treatment. For example, MTT assays with the PEG3k-PCL1k micelles revealed a significant IC_{50} decrease from 0.02 to $0.0046 \mu\text{M}$ upon folate functionalization of micelles. A major cause for this significant IC_{50} decrease of VCR in MTT assay upon folate-functionalization of micelles may be the augmented internalization of FG020326-loaded micelles into KB_{v200} cells, which overexpress the folate receptors on the cell membrane, i.e. more FG020326 transported into the cells by targeting micelles resulted in better suppression of the P-gp-mediated drug efflux. This hypothesis was supported by the Rhodamine 123 efflux study as will be discussed in the next section. In addition, cellular attachment of drug-loaded micelles was enhanced when the micelles were functionalized with folate. Even if the micelles attached to KB_{v200} cells did not undergo further endocytosis, enhanced cellular attachment of micelles will still increase FG020326 amounts in the replaced culture media, which will likely lead to better MDR reversal as well.

Although the strong MDR reversal activity of FG020326 was demonstrated previously,^{6,7} the mechanism of this MDR modulator was not completely understood. P-gp is a plasma membrane protein that mediates the ATP-dependent efflux of cancer therapeutics. On the basis of its amino acid sequence, P-gp is predicted to consist of two similar halves, each containing six putative transmembrane segments and a nucleotide-binding domain.³⁴ In a previously published report, an MDR modulator OC144-093, which is a substituted diarylimidazole ($M = 495$) and structurally very similar to FG020326, was found to inhibit the P-gp ATPase activity and block the binding of [^3H]azidopine to P-gp.³⁵ Moreover, [^3H]azidopine was known to block the binding of VCR to P-gp,³⁶ and inhibition of the ATPase activity

means that higher concentrations of intracellular ATP would be required for functioning of P-gp.³¹ Based on these literature reports, we assume that there might exist two pathways that the internalized FG020326 led to the MDR reversal of KB_{v200} cells. First, FG020326, like [³H]azidopine, may share a common P-gp binding site for VCR as well. Consequently, FG020326 transported into the cells may interact with this P-gp binding site and block the P-gp binding of VCR from the cytoplasm. Second, like OC144-093, FG020326 may inhibit the intracellular ATPase activity resulting in the suppression of P-gp functioning. FG020326 transported by micelles via endocytosis are believed to release in the lysosome and afterwards may act in the same way as free FG020326 taken up by the cells. If this be the case, it is not difficult to understand why the enhanced endocytosis of micelles by attachment of a targeting ligand would lead to better MDR reversal effects of micelle-transported FG020326. However, future studies are needed to confirm these hypotheses, and it must be noted that in our study, free FG020326 still showed the best MDR reversal than any micellar formulation in the present study.

It is noteworthy that, in the MTT assays, only the folate-PEG3k-PCL1k micelle-delivered FG020326 resulted in a VCR cytotoxicity comparable to that induced by free FG020326, and FG020326 transported by other micelles appeared to be less effective [Fig. 6(c)]. One underlying reason for the lower reversal potency of FG020326-loaded micelles compared to that of free FG020326 is likely the sustained release of FG020326 from micelles. Although FG020326 loaded inside the PEG-PCL micelles is believed to release quickly in acidic lysosomal compartments based on the *in vitro* FG020326 release data, it still may not be utilized as quickly as free FG020326 inside the cells. Furthermore, we assume that the considerably high VCR cytotoxicity induced by the folate-PEG3k-PCL1k micelle-delivered FG020326 is that, in this particular formulation, the cellular uptake of micelles have been significantly enhanced due to the folate-functionalization and relative small micelle size, resulting in a strong compensation to the above mentioned drawback in the bioavailability of the micelle encapsulated drug.

Rhodamine 123 efflux studies

Rhodamine 123 has been known to be the P-gp substrate, and MDR modulators could affect intracellular Rhodamine 123 levels by inhibiting the function of P-gp in human MDR cancer cells.³⁷ Pretreatment of cells with blank copolymer in either concentrations (above or below CMC) did not increase the amount of Rhodamine 123 remaining in

KB_{v200} cells, which is in good agreement with the cytotoxicity data that blank copolymer did not improve VCR cytotoxicity. The results shown in Figure 7(a) demonstrate that the amount of Rhodamine 123 remaining in KB_{v200} cells was obviously increased upon pretreatment of the cells with either FG020326 or FG020326-loaded micelles. Moreover, the accumulation of Rhodamine 123 inside KB_{v200} cells was significantly enhanced by attaching a tumor-targeting ligand, folate, to the micellar delivery vehicles and then using these FG020326-loaded targeting micelles to pretreat the cells. Rhodamine 123 efflux appeared unhindered when a large amount of free folate was introduced to compete with the targeting micelles containing FG020326, as evidenced in Figure 7(b). Apparently, targeting micelles transport FG020326 more efficiently than their nontargeting counterparts. Finally, the Rhodamine 123 fluorescence intensity detected by flow cytometry when using FG020326-loaded folate-PEG3k-PCL1k micelles rather than any other micelle formula, including the FG020326-

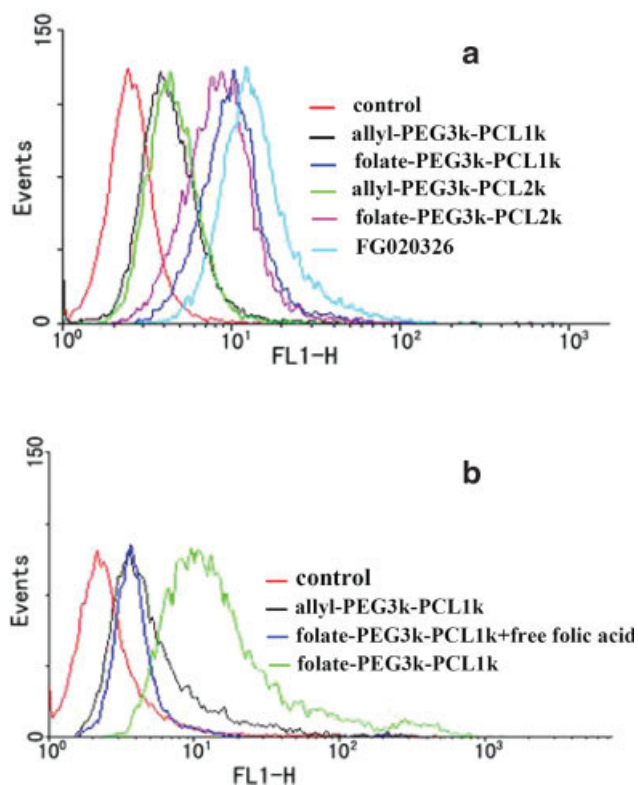


Figure 7. (a) Effect of FG020326 and FG020326-loaded polymeric micelles on Rhodamine 123 efflux in KB_{v200} cells, incubated at the same FG020326 concentration 2 $\mu\text{mol L}^{-1}$. (b) Flow cytometry histogram of micelle uptake in KB_{v200} cells implies that cell uptake of targeting micelle is inhibited by the presence of free folate ligands (10 mM) in solution. Fluorescence height represents the Rhodamine 123 amounts remained in KB_{v200} cells. [Color figure can be viewed in the online issue, which is available at www.interscience.wiley.com.]

loaded folate-PEG3k-PCL2k micelles, approached the fluorescence intensity detected when using free FG020326 [Fig. 7(a)]. These results, which are in agreement with the cytotoxicity data discussed in the previous section, indicate once again that, in addition to the folate-induced targeting effect, micelle composition is also decisive and thus must be properly adjusted to achieve the highest FG020326 delivery efficiency.

CONCLUSION

Biodegradable diblock copolymers, folate-PEG-PCL, of different molecular weights and compositions were successfully synthesized by multistep reactions. These copolymers self-assembled into tumor-targeted core-shell micelle structures smaller than 100 nm in diameter with a hydrophobic PCL core capable of encapsulating FG020326, a potent MDR modulator, at a DLC of up to 6.4 wt %. The targeting micelles can deliver FG020326 into the human MDR KB_{v200} cells more efficiently than their nontargeting counterparts. FG020326 delivered by the folate-encoded micelles demonstrates strong MDR reversal activity, comparable to that of free FG020326 in the KB_{v200} cells. Although preliminary, our studies provide the first evidence of effectively delivering a cancer MDR modulator using biodegradable and targeted polymeric micelles that can recognize molecular signatures on cancer cells surface. Because of their enormous therapeutic potential in drug delivery, such as prolonged blood circulation, EPR effect, and active targeting to tumor cells, these MDR modulator-loaded and folate-encoded micelles may find application in cancer chemotherapy to overcome drug resistance. We are currently conducting animal tests with these folate-functionalized and FG020326-loaded micelles to investigate their *in vivo* antitumor efficacy.

References

- Gottesman MM, Fojo T, Bates SE. Multidrug resistance in cancer: Role of ATP-dependent transporters. *Nat Rev Cancer* 2002;2:48–58.
- Ambudkar S, Kimchi-Sarfaty C, Sauna ZE, Gottesman MM. P-glycoprotein: From genomics to mechanism. *Oncogene* 2003;22:7468–7485.
- Gottesman MM, Pastan I, Ambudkar SV. P-glycoprotein and multi drug resistance. *Curr Opin Genet Dev* 1996;6:610–617.
- Fojo T, Bates S. Strategies for reversing drug resistance. *Oncogene* 2003;22:7512–7523.
- Tan BJM, Piwnica-Worms D, Ratner L. Multidrug resistance transporters and modulation. *Curr Opin Oncol* 2000;12:450–458.
- Chen LM, Wu XP, Ruan JW, Liang YJ, Ding Y, Shi Z, Wang XW, Gu LQ, Fu LW. Screening novel, potent multi-drug resistant modulators from imidazole derivatives. *Oncol Res* 2004;14:355–362.
- Chen LM, Liang YJ, Ruan JW, Ding Y, Wang XW, Shi Z, Gu LQ, Yang XP, Fu LW. Reversal of P-gp mediated multidrug resistance in vitro and in vivo by FG020318. *J Pharm Pharmacol* 2004;56:1061–1066.
- Lee ES, Na K, Bae YH. Doxorubicin loaded pH-sensitive polymeric micelles for reversal of resistant MCF-7 tumor. *J Control Release* 2005;103:405–418.
- Kataoka K, Harada A, Nagasaki Y. Block copolymer micelles for drug delivery: Design, characterization and biological significance. *Adv Drug Deliv Rev* 2001;47:113–131.
- Ai H, Flask C, Weinberg B, Shuai X, Pagel MD, Farrell D, Duerk J, Gao J. Magnetite-loaded polymeric micelles as ultrasensitive magnetic-resonance probe. *Adv Mater* 2005;17:1949–1952.
- Savic R, Luo L, Eisenburg A, Maysinger D. Micellar nanocontainers distributed to defined cytoplasmic organelles. *Science* 2003;300:615–618.
- Kim SY, Lee YM. Taxol-loaded block copolymer nanospheres composed of methoxy poly(ethylene glycol) and poly(ϵ -caprolactone) as novel anticancer drug carriers. *Biomaterials* 2001;22:1697–1704.
- Zhang X, Jackson JK, Burt HM. Development of amphiphilic diblock copolymers as micellar carriers of taxol. *Int J Pharm* 1996;132:195–206.
- Nasongkla N, Shuai X, Ai H, Weinberg BD, Pink J, Boothman DA, Gao J. cRGD-functionalized polymer micelles for targeted doxorubicin delivery. *Angew Chem Int Ed* 2004;43: 6323–6327.
- Park EK, Kim SY, Lee SB, Lee YM. Folate-conjugated methoxy poly(ethylene glycol)/poly(ϵ -caprolactone) amphiphilic block copolymeric micelles for tumor-targeted drug delivery. *J Control Release* 2005;109:158–168.
- Aliabadi HM, Mahmud A, Sharifabadi AD, Lavasanifar A. Micelles of methoxy poly(ethylene oxide)-*b*-poly(*q*-caprolactone) as vehicles for the solubilization and controlled delivery of cyclosporine A. *J Control Release* 2005;104:301–311.
- Aliabadi HM, Brocks DR, Lavasanifar A. Polymeric micelles for the solubilization and delivery of cyclosporine A: Pharmacokinetics and biodistribution. *Biomaterials* 2005;26:7251–7259.
- Sudimach BAJ, Lee RJ. Targeted drug delivery via the folate receptor. *Adv Drug Deliv Rev* 2000;41:147–162.
- Ruan JW, Fu LW, Huang ZS, Chen LM, Ma L, Gu LQ. Studies on synthesis of multiaryl-substituted imidazoles and reversal activity on the multidrug resistance. *Chem J Chin Univ* 2004;25:870–873.
- Sarshar S, Zhang CZ, Moran EJ, Krane S, Rodarte JC, Benbatoul KD, Dixon R, Mjallik AMM. 2,4,5-Trisubstituted imidazoles novel nontoxic modulators of P-glycoprotein mediated multidrug resistance, Part 1. *Bioorg Med Chem Lett* 2000;10: 2599–2601.
- Cammas S, Nagasaki Y, Kataoka K. Heterobifunctional poly(ethylene oxide): Synthesis of α -methoxy- ω -amino and α -hydroxy- ω -amino PEOs with the same molecular weights. *Bioconjug Chem* 1995;6:226–230.
- Shuai X, Ai H, Nasongkla N, Kim S, Gao J. Micellar carriers based on block copolymers of poly(ϵ -caprolactone) and poly(ethylene glycol) for doxorubicin delivery. *J Control Release* 2004;98:415–426.
- Yoo HS, Park TG. Folate-receptor-targeted delivery of doxorubicin nano-aggregates stabilized by doxorubicin-PEG-folate conjugate. *J Control Release* 2004;100:247–256.
- Yasugi K, Nagasaki Y, Kato M, Kataoka K. Preparation and characterization of polymer micelles from poly(ethylene glycol)-poly(D,L-lactide) block copolymers as potential drug carrier. *J Control Release* 1999;62:89–100.
- Dimitrov IV, Berlinova IV, Vladimirov NG. Synthesis of Poly(oxyethylene)-poly(Z-L-lysine) hybrid graft copolymers. *Macromolecules* 2006;39:2423–2426.

26. Wang S, Lee RJ, Mathias CJ, Green MA, Low PS. Synthesis, purification, and tumor cell uptake of ^{67}Ga -Deferoxamine-folate, a potential radiopharmaceutical for tumor imaging. *Bioconjug Chem* 1996;7:56–62.
27. Mathias CJ, Wang S, Low PS, Waters DJ, Green MA. Receptor-mediated targeting of ^{67}Ga -deferoxamine-folate to folate-receptor-positive human KB tumor xenografts. *Nucl Med Biol* 1999;26:23–25.
28. Shuai X, Merdan T, Schaper AK, Xi F, Kissel T. Core cross-linked polymeric micelles as paclitaxel carriers. *Bioconjug Chem* 2004;15:441–448.
29. Bae Y, Fukushima S, Harada A, Kataoka K. Design of environment-sensitive supramolecular assemblies for intracellular drug delivery: Polymeric micelles that are responsive to intracellular pH change. *Angew Chem Int Ed* 2003;42:4640–4643.
30. Liu J, Zeng F, Allen C. Influence of serum protein on polycarbonate-based copolymer micelles as a delivery system for a hydrophobic anti-cancer agent. *J Control Release* 2005;103:481–497.
31. Kabanov AV, Batrakova EV, Alakhov VY. Pluronic block copolymers for overcoming drug resistance in cancer. *Adv Drug Deliv Rev* 2002;54:759–779.
32. Minko T, Kopeckova P, Pozharov V, Kopecek J. HPMA copolymer bound adriamycin overcomes *MDR1* gene encoded resistance in a human ovarian carcinoma cell line. *J Control Release* 1998;54:223–233.
33. Omelyanenko V, Kopeckova P, Gentry C, Kopecek J. Targetable HPMA copolymer–adriamycin conjugates. Recognition, internalization, and subcellular fate. *J Control Release* 1998;53:25–37.
34. List AF, Kopecky KJ, Willman CL, Head DR, Persons DL, Slovak ML, Dorr R, Karanes C, Hynes HE, Doroshow JH, Shurafa M, Appelbaum FR. Benefit of cyclosporine modulation of drug resistance in patients with poor-risk acute myeloid leukemia: A southwest oncology group study. *Blood* 2001;98:3212–3220.
35. Newman MJ, Rodarte JC, Benbatoul KD, Romano SJ, Zhang CZ, Krane S, Moran EJ, Uyeda RT, Dixon R, Guns ES, Mayer LD. Discovery and characterization of OC144-093, a novel inhibitor of P-glycoprotein-mediated multidrug resistance. *Cancer Res* 2000;60:2964–2972.
36. Safa AR, Glover CJ, Meyers MB, Biedler JL, Felsted RL. Vinblastine photo affinity labeling of a high molecular weight surface membrane glycoprotein specific for multidrug-resistant cells. *J Biol Chem* 1986;261:6137–6140.
37. Shi Z, Liang YJ, Chen ZS, Wang XW, Wang XH, Ding Y, Chen LM, Yang XP, Fu LW. Reversal of MDR1/P-glycoprotein-mediated multidrug resistance by vector-based RNA interference in vitro and in vivo. *Cancer Biol Ther* 2006;5:39–47.

Polymer Implants for Intratumoral Drug Delivery and Cancer Therapy

BRENT D. WEINBERG,¹ ELVIN BLANCO,² JINMING GAO²

¹Department of Biomedical Engineering, Case Western Reserve University, 10900 Euclid Ave, Cleveland, Ohio 44106

²Simmons Comprehensive Cancer Center, University of Texas Southwestern Medical Center at Dallas, 5323 Harry Hines Blvd., Dallas, Texas 75390

Received 26 January 2007; accepted 17 April 2007

Published online in Wiley InterScience (www.interscience.wiley.com). DOI 10.1002/jps.21038

ABSTRACT: To address the need for minimally invasive treatment of unresectable tumors, intratumoral polymer implants have been developed to release a variety of chemotherapeutic agents for the locoregional therapy of cancer. These implants, also termed “polymer millirods,” were designed to provide optimal drug release kinetics to improve drug delivery efficiency and antitumor efficacy when treating unresectable tumors. Modeling of drug transport properties in different tissue environments has provided theoretical insights on rational implant design, and several imaging techniques have been established to monitor the local drug concentrations surrounding these implants both *ex vivo* and *in vivo*. Preliminary antitumor efficacy and drug distribution studies in a rabbit liver tumor model have shown that these implants can restrict tumor growth in small animal tumors (diameter <1 cm). In the future, new approaches, such as three-dimensional (3-D) drug distribution modeling and the use of multiple drug-releasing implants, will be used to extend the efficacy of these implants in treating larger tumors more similar to intractable human tumors. © 2007 Wiley-Liss, Inc. and the American Pharmacists Association *J Pharm Sci* 97:1681–1702, 2008

Keywords: biodegradable polymers; imaging methods; cancer chemotherapy; drug transport; controlled release; mathematical model; drug targeting

INTRODUCTION

Cancer is an enormous health concern in the United States and in recent years has surpassed heart disease as the predominant cause of death for all but the most elderly Americans.¹ Currently, the most curative treatment option for solid tumors is surgical resection followed by adjuvant

chemotherapy or radiation therapy to minimize the risk of recurrence. Many cancers respond well to this treatment strategy, but many patients are not eligible for surgical resection. For example, out of 70000 newly diagnosed colon cancer metastases to the liver in the US per year, the number of patients who are actually candidates for surgery is disappointingly low at 2500–4500.² Reasons limiting resection include tumor size, involvement of more than one liver lobe, or a co-existing liver condition (e.g., cirrhosis).^{2,3} In addition, the overall survival rates for these patients even after surgery are often low.⁴ Other

Correspondence to: Jinming Gao (Telephone: 214-648-9278; Fax: 214-648-0264; E-mail: jinming.gao@utsouthwestern.edu)

Journal of Pharmaceutical Sciences, Vol. 97, 1681–1702 (2008)

© 2007 Wiley-Liss, Inc. and the American Pharmacists Association

abdominal cancers, such as those of the pancreas and stomach, also have low resection rates and poor overall patient survival.¹ Intravenously administered chemotherapy for these tumors also has limited effectiveness. Since only a small amount of the systemic blood flow is directed to the tumor, only a fraction of the total dose reaches the tumor site.⁵ The remainder of the dose is distributed throughout healthy organs and tissues, leading to a variety of undesirable side effects ranging from neutropenia to cardiomyopathy.^{6,7} Many chemotherapeutic drugs also have very rapid plasma clearance, leading to short tumor exposure times.⁸ To improve the outcome of these cancer patients, a new paradigm of minimally invasive and locoregional cancer therapies has rapidly evolved and received considerable attention in the recent years.⁹

Image-guided, minimally invasive techniques for therapeutic interventions use regional tumor destruction as an alternative to surgical resection.¹⁰ Strategies for tumor ablation include thermal heating,^{11,12} cryosurgery,^{13,14} or chemical ablation.^{15,16} In each of these techniques, an interventional needle or electrode is inserted into the tumor with image guidance.^{17,18} Then, the ablation is applied to destroy the tumor and a surrounding margin of normal tissue. Since they can be applied percutaneously, these minimally invasive treatments typically are viable alternatives to surgery that can be used in patients with poor overall health as an outpatient procedure. Additionally, local administration of the treatment maximizes destruction to the tumor target while limiting damage to the surrounding normal tissue. Ablation has been used for the treatment of several unresectable cancers, including those in the liver,¹⁹ prostate,²⁰ and lung.²¹

Other attempts to improve treatment of unresectable tumors have focused on means to increase the tumor specificity of chemotherapeutic drugs through locoregional delivery.²² Administering an anticancer drug either to the region that contains a tumor or directly within the tumor has the advantage of increasing tumor exposure to a drug while limiting systemic toxicity. One strategy for locoregional chemotherapy is to infuse a solution of a chemotherapeutic agent into the region of the malignancy. Intravesicular chemotherapy has become a common treatment for bladder tumors, and has been shown to be associated with a reduced tumor recurrence rate after surgery.²³ Local chemotherapy infusion has also been used with some success in the case of

advanced nonsmall cell lung cancer when patients have a malignant pleural effusion.²⁴ Additionally, several studies have shown significant benefits in treating ovarian cancers with intraperitoneal (IP) infusions.²⁵ All of these treatments require that malignant cells be in close contact with the surrounding space to which the chemotherapy is administered.

For tumors that are not externally accessible, local perfusion, or the administration of a chemotherapeutic agent to a segment of the circulation that preferentially perfuses the tumor, is an alternative. Intra-arterial administration of drugs can maximize drug delivery to blood vessels supplying tumors. For example, transarterial chemoembolization (TACE) benefits from the fact that most hepatocellular carcinomas (HCCs) receive the vast majority of their blood supply from their hepatic artery while normal liver receives its blood supply largely from the portal vein.²⁶ In this treatment, a catheter is selectively placed in the branches of the hepatic artery which feed the tumor. Once arterial selection has been achieved, a solution of chemotherapeutic agents dissolved in an oily solvents followed by embolic agents is infused into the artery.²⁶ This approach has been shown to increase concentrations of chemotherapy in the tumor by 10- to 100-fold²⁶ and to improve 1-year survival of patients with unresectable HCC by as much as 20%.²⁷ As a result, TACE has become a commonly administered therapy for unresectable HCC.²⁸ Another strategy to improve delivery is through regional perfusion, in which the portion of the systemic circulation containing a tumor is isolated from the rest of the circulation.²⁹ Isolated thoracic perfusion (ITP) is achievable by closing off the descending aorta and vena cava with balloon catheters, blocking blood flow to the arms with inflated cuffs, and introducing chemotherapy into the right atrium. This approach has been used to increase the concentration of chemotherapy delivered to lung cancers by 6- to 10-fold,³⁰ and an analogous approach exists for isolated abdominal perfusion. Each of these locoregional chemotherapy methods had been shown to increase tumor exposure to drug while reducing systemic toxicity.

Intratumoral cancer treatments extend the locoregional treatment concept by attempting to further limit the scope of chemotherapy exposure. Treatments that have been studied extensively include intratumoral infusions, injections, and implantable devices that deliver either

chemotherapeutic drugs or other therapeutic agents.²² Infusion of chemotherapeutic agents has been heavily studied in the area of brain tumors, where it has spawned a field known as convection-enhanced delivery (CED).³¹ In CED, a microcatheter is inserted into a tumor and the therapeutic agent is slowly administered to the surrounding tissue using positive pressure infusion. Major advantages of CED to brain tumors include bypassing the blood–brain barrier and delivering drugs further from the infusion site due to convection.³² CED has been used to deliver conventional chemotherapeutic drugs³³ but has shown considerable promise for the delivery of targeted bacterial toxins³¹ and therapeutic antibodies.³⁴ Intratumoral injections of therapeutic solutions have also shown success in treating tumors in locations other than the brain, such as the lung,³⁵ pancreas,³⁶ and liver.³⁷ Several studies have been performed in an attempt to determine optimal parameters for injection and to determine which tumor features, such as collagen content, contribute to the extent of drug delivery.^{38,39} Furthermore, recent studies have shown that using intratumoral injection to deliver viral gene therapy vectors minimizes nonspecific expression of gene products.^{40,41} Since intratumorally injected liquids may distribute irregularly and be cleared quickly, several investigators have introduced injectable drug depots to prolong the extent of drug release. Examples of intratumoral depots include PLGA,^{42–44} alginate,⁴⁵ and albumin⁴⁶ microspheres as well as injectable gels which solidify upon intratumoral injection.^{47–49} Injectable depots have the advantage of easy administration and prolonged tumor drug exposure.

Intratumoral, drug-releasing implants are a subset of the intratumoral drug delivery paradigm and have shown increasing promise in recent years. Driven by developments for the treatment of prostate^{50,51} and brain cancers,^{52,53} implantable devices containing either radioactive elements or chemotherapeutic drugs have become viable treatment options. The only clinically approved chemotherapeutic implant for cancer treatment is the Gliadel wafer, a carmustine(BCNU)-eluting implant fabricated from a polyanhydride copolymer, 1,3-bis-(p-carboxyphenoxy) propane/poly(sebacic acid) (pCPP:SA).⁵⁴ These implants were designed to treat glioblastoma multiforme, an aggressive brain cancer with extremely limited patient survival, through placement in the surgical cavity after primary surgical resection.

After placement, the implants release their drug load over a period of approximately 5 days,⁵⁵ and drug has been shown to penetrate several millimeters into the brain parenchyma.⁵⁶ A recent long-term study showed that the Gliadel implant placement after surgery increased patient survival to 13.8 months versus 11.6 months for control and maintained this survival advantage for at least 3 years after initial treatment.⁵⁷ Despite the clinical success of the Gliadel implant, the use of chemotherapeutic implants has yet to become widespread in the treatment of other cancers, such as those of the pancreas, liver, or lungs. However, it is likely that future chemotherapeutic implants can be optimized for use in a variety of different tumors to maximize patient comfort and survival.

This review article describes work in extending the use of intratumoral implants to treat unresectable liver tumors. The proposed treatment strategy is primary treatment of the tumor bulk with radiofrequency (RF) ablation followed by the placement of drug-eluting polymer implants in the ablated tumor region. These biodegradable polymer millirods have been fabricated from poly(D,L-lactide-co-glycolide) (PLGA) to deliver chemotherapeutic agents through and beyond the RF ablated tumor, thus maximizing tumor destruction and reducing the risk of tumor recurrence. The first section describes the overall goals that must be considered when developing any local delivery device, including the use of models to predict local drug transport. The second section describes techniques for measuring local drug concentrations and the use of these measurements to customize drug release. In the third section, this review describes the preliminary results from using these implants to treat a rabbit liver cancer model. Finally, the last section presents some conclusions drawn from the early use of these implants and some future goals to facilitate using these implants to treat larger tumors similar to unresectable human cancers.

OVERVIEW OF DRUG DELIVERY GOALS

Definition of Pharmacokinetic Goals for Local Drug Delivery to Unresectable Tumors

In considering the use of an intratumoral implant for tumor treatment, it is necessary to consider the generic characteristics that would benefit the device. First, the implant should be able to

minimize shortcomings associated with systemically administered chemotherapy. Second, it should provide an optimal drug delivery profile to the tumor, which is to say that it should be able to provide effective drug concentrations to the desired region over a prolonged period of time. Third, the device should be part of a comprehensive and complete treatment strategy that is versatile and applicable in a wide range of realistic situations. Achieving these goals should maximize the treatment success of these intratumoral implants.

When delivering their drug cargo to tumors, intratumoral implants must provide an optimal drug release profile that is characterized by the ability to deliver drug to a large volume, to rapidly reach the therapeutic concentration, and to maintain the therapeutic concentration for an extended time. Previous studies have shown that limited penetration distance is one of the major restrictions on the efficacy of intratumoral treatments.^{55,56} Any successful implant must be designed in such a way that takes into consideration ways to maximize the drug delivery distance. Additionally, the implant must provide drug to the surrounding tissue at an appropriate rate.⁵⁸

A schematic of ideal drug release rates is shown in Figure 1. Consider implant A, an implant which releases drug at a constant rate somewhere above the elimination rate. While local drug concentration will slowly rise, it may take too long to reach tissue concentrations that are toxic to the surrounding cancer cells. Alternatively, implant B provides a rapid dose of chemotherapy that will quickly surpass the effective concentration. However, the release rate after the initial burst is insufficient to maintain this concentration for any extended length of time. Such a release rate is undesirable, as it could allow cancer cells to recover, perhaps even with newly acquired drug resistance.⁵⁹ The ideal implant, implant C, combines the best characteristics of both implants: rapid ascent to the effective concentration followed by a maintenance dose to remain at a useful drug level. While this explanation is a simplification (e.g., elimination is almost certainly not constant, etc.), it serves as an example of how different drug release rates might affect local drug concentrations. Additionally, it offers some insight on how the situation can be changed by modifying the elimination rate or therapeutic concentration. For the most part, however, local drug concentrations surrounding implants must be determined experimentally.

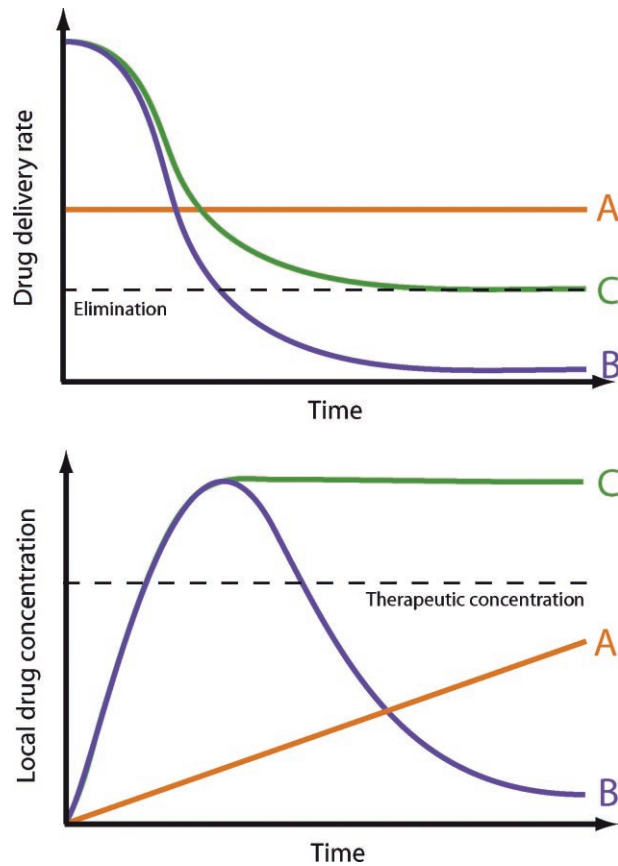


Figure 1. Scheme illustrating drug release and local drug concentration from three theoretical implant types. A zero-order release implant (A) releases drug at a constant rate, but it may take a long period of time to reach the therapeutic concentration. A burst-release implant (B) releases large amounts of drug early, but may not extended release to maintain a therapeutic concentration. A dual-release implant (C) combines an early burst of drug to accelerate the rise to therapeutic concentrations with sustained release to maintain therapeutic concentrations.

The success of chemotherapeutic implants for cancer treatment also depends on their inclusion in a comprehensive tumor treatment strategy. As an example, with the previously mentioned Gliadel treatment, the tumor is first surgically resected (“debulked”) followed by the placement of multiple BCNU-impregnated implants in the surgical cavity.⁵² The design of a liver cancer treatment using polymer millirods proposes a similar strategy to Gliadel treatment: using RF ablation to destroy the majority of the tumor mass followed by placement of polymer implants in the tumor to kill any residual cancer cells and limit tumor recurrence. RF ablation is already used clinically to treat liver tumors, but tumor

recurrence, particularly around the ablation boundary, has greatly limited the clinical success of tumor ablation.^{60,61} Using chemotherapeutic implants with ablation may maximize the benefit compared to using the implants alone. The ablation destroys the majority of the tumor cells, leaving the implants to kill only the remaining cells, thereby reducing the risk of recurrence. Furthermore, tumor ablation may facilitate drug delivery from the implants by changing the fundamental rates governing drug transport in the tumors.⁵⁸ To develop this strategy, drug-impregnated, PLGA polymer millirods with different release rates were developed and tested in animal models, first in nonablated and ablated liver tissue^{62–65} and then in nonablated and ablated liver tumors.^{66,67} Results from these studies are described in “Measuring and Modulating Local Drug Pharmacokinetics” and “Treatment of Animal Tumor Models Sections.”

Interstitial Drug Transport Models in Tumor and Surrounding Tissues

In addition to generic considerations on drug release from implants, the mechanisms of drug transport and elimination in the surrounding tumor tissue have a major effect on how an implant delivers drug to the tumor.⁶⁸ Drug released locally into the tumor has several possible fates that will ultimately affect the outcome of the treatment. Primarily, drug molecules can either move to another location through a transport process or be eliminated such that they no longer exert their desired effect.

Drug can typically be transported by two mechanisms: diffusion and convection.^{55,69,70} In diffusion, free drug moves from a region of higher drug concentration to an adjacent region of lower drug concentration at a rate proportional to the concentration gradient. Diffusion is a primary mode of transport, particularly when drug is being released from a local implant. Convection, on the other hand, is the transport of drug along with the bulk flow of a fluid. In organs that have a high rate of interstitial fluid flow, convection is especially important. Convection also has a significant role in the flow of systemically administered chemotherapeutic agents from the vascular space to the tumor, where it travels along the same flow that delivers nutrients to the tumor.⁶⁸ The relative importance of diffusion or convection in drug transport depends on the delivery system

and tissue type. For instance, in the brain, where interstitial fluid constantly flows from the ventricles to the surrounding parenchyma, convection has a significant effect on the extent of drug penetration.⁷¹ In situations with small molecular drugs where flow is more limited, diffusion is the predominant mode of drug transport.

Drug elimination can occur through several different mechanisms. One route of drug elimination is through metabolism. Once in a cell, drug can be altered or bound in a variety of ways. Some drug molecules, such as 5-fluorouracil, bind irreversibly to their therapeutic target, after which they are no longer in the population of available drug.⁷² More generally, cells have a variety of nonspecific methods for detoxification, such as organelles for breaking down foreign molecules through enzymatic or pH-mediated degradation. Alternatively, cells contain protective molecules, such as glutathione, which are designed specifically to bind foreign molecules and render them more hydrophilic and less potent.⁷³ Either of these metabolic pathways essentially inactivates the drug. When considering implantable drug delivery systems, another mechanism of drug loss is perfusion away from the target region.⁵⁸ In this situation, drug is transported by either diffusion or convection into one of two systemic circulations, the blood or the lymph. The vasculature is a fast-moving circulation which rapidly moves drugs away from the target region and into other parts of the body. Since most chemotherapeutic agents have short plasma half-lives, once the drug reaches the plasma it is unlikely to return to the target tumor, and for practical purposes can be considered eliminated. While the lymph is a slower-moving body of fluid that can contribute to drug convection, its effects are probably less influential than those of blood because tumors are known to have limited and poorly organized lymphatic drainage.⁷⁰ Any drug contained in lymphatic fluid eventually moves into the venous circulation, where it undergoes the same fate as drug that directly diffuses into blood vessels.

Consider the example of drug transport shown in Figure 2, in which drug is being delivered to a liver tumor from a cylindrical implant in the center of the tumor. Previous work has shown that transport in liver can be reasonably approximated without including convection.⁵⁸ Drug leaving the implant is transported away from the implant into the tumor tissue based on a tumor diffusion rate, D_{tumor} . Once in the tumor, drug can be eliminated

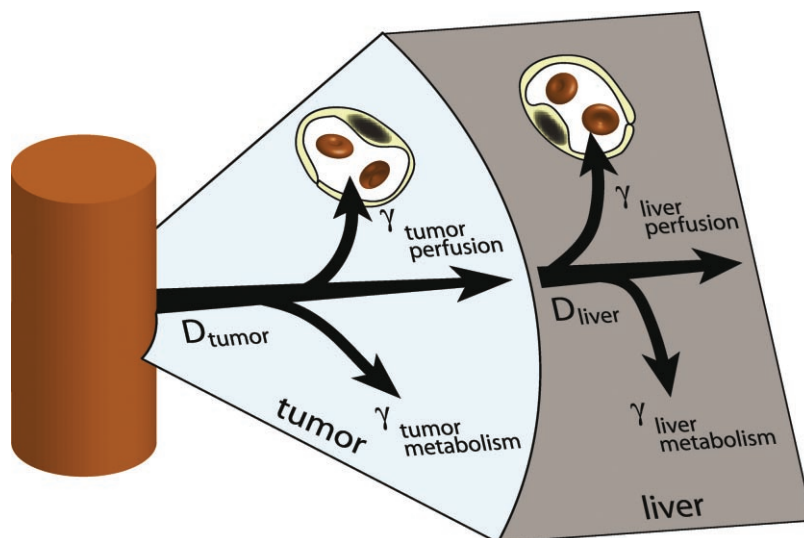


Figure 2. Simplified scheme of drug transport from an implant centrally placed in a liver tumor. Transport of the drug into the tumor tissue is governed by the diffusion constant of drug in tumor (D_{tumor}), and two simultaneous modes of elimination: metabolism to inactive forms in tumor cells ($\gamma_{\text{tumor metabolism}}$) or transport into nearby blood vessels which wash drug out of the region ($\gamma_{\text{tumor perfusion}}$). Once drug reaches the surrounding normal tissue, it continues to diffuse outward into liver tissue (D_{liver}), where it has different rates of elimination by metabolism ($\gamma_{\text{liver metabolism}}$) or perfusion ($\gamma_{\text{liver perfusion}}$).

in one of two ways, through blood flow and metabolism, proportional to two different constants which sum to contribute to a total elimination, γ_{tumor} . Once drug reaches the outer boundary of the tumor, it can diffuse into the surrounding normal liver tissue, where its fate is again governed by new diffusion and elimination rates. If elimination can be considered approximately first order, the drug transport in each tissue is governed by the following equation:

$$\frac{\partial C}{\partial t} = D\nabla^2 C - \gamma C \quad (1)$$

where C is the drug concentration, t the time, ∇ the gradient operator, and D and γ are the tissue-specific rates of diffusion and elimination, respectively. Drug transport properties in each tissue can be estimated by solving this equation computationally and minimizing the error between model output and experimentally collected data.

The use of such a model provides insight into factors that can facilitate or impede drug transport from a local implant. First, any factor that increases the rate of drug transport or lowers the rate of drug elimination will increase the permeation of drug within the tissue. For instance, some work in ex vivo tumors has shown that prolonged

drug exposure raises drug diffusion coefficients, presumably by killing cells and destroying overall structure.⁷⁴ Other work by Saltzman and coworkers⁵⁶ has shown that including high molecular weight molecules, such as dextrans, can increase transport away from implants by increasing the convective fluid flow contribution while decreasing blood perfusion. Similarly, it can be expected that any factor that reduces elimination will also have a beneficial effect, facilitating deeper drug penetration into the tumor. On the other hand, any action that decreases transport or increases elimination will act as a barrier to drug delivery that will effectively reduce the distance over which an implant can be effective. Inflammation, such as that occurring after RF ablation, may raise blood flow and decrease drug diffusion rates as a result of collagen deposition around the wound.⁷⁵ These side effects could certainly impede successful drug transport from a local tumor treatment. The distance at which an implant can have an effect on a tumor depends on the drug release rate from the implant as well as the balance between local transport and elimination. Unfortunately, several studies have indicated that antitumor implants are likely only effective for a few millimeters away from the implant surface.⁷⁶ Studies into local drug concentration

and local transport mechanisms, however, have provided useful information on ways to overcome these limitations.

MEASURING AND MODULATING LOCAL DRUG PHARMACOKINETICS

Overview of Methods to Investigate Local Drug Release and Tissue Distribution

In developing an intratumoral chemotherapy device, techniques for monitoring local drug concentrations are necessary to optimize implant design. Measuring drug concentration as a function of time provides a quantitative method to compare multiple treatments. Many different techniques can be used to monitor drug release from intratumoral implants. While certain techniques require extraction of tissue and measurement of drug concentration *ex vivo*, alternate, noninvasive imaging based-techniques can be used to measure concentrations *in vivo*. New implant designs or treatment conditions can be tested by creating an implant that has the ideal characteristics described in the Introduction Section; a rapid ascent to and prolonged stay above the therapeutic concentration. Additionally, drug concentration information can then be used as input to estimate tissue transport properties. Then, ideal implants can be created through a combination of empirical testing and engineering design.

Considerable information has been obtained by monitoring local drug concentrations using *ex vivo* analysis of extracted tissues. Two main categories of *ex vivo* analysis exist: bulk tissue analysis by conventional spectroscopic methods or tissue section analysis by imaging-based methods. The key principle of bulk tissue measurements is the removal of a sizeable piece of tissue followed by the use of a spectroscopic method to determine the average drug concentration in that tissue.⁷⁷ For targeted drug delivery to tumors, drug concentrations in different tumor regions are the most important, so these tissues are often removed in different sections. To determine tissue drug concentrations, tissues are weighed and either mechanically or chemically homogenized according to the desired detection mechanism. Examples of techniques to measure drug concentration in the extracted tissues include fluorescence detection, high performance liquid chromatography (HPLC),^{77,78} mass spectrometry, and atomic

absorption spectroscopy (AAS).⁶² If the drug target is radiolabeled, drug concentrations can also be measured using liquid scintigraphy. Key advantages of measuring drug concentrations in removed tissues include definitive drug detection, high sensitivity, and the ability to detect low drug concentrations. However, these techniques are restricted by low spatial resolution and accuracy, as measurements are an average over an entire piece of tissue. Achieving spatial measurements depends on the size of pieces cut from the tissue, which usually limits spatial resolution from these techniques to the millimeter range.

Imaging of *ex vivo* tissues can help overcome the spatial resolution limitations of bulk tissue analysis methods. For imaging-based methods, the tissue is removed and sliced into a thin piece followed by drug detection through imaging the slice. At least two techniques have been used for imaging drug detection: autoradiography and fluorescence.⁷⁴ For autoradiography, the drug target is radiolabeled and then detected by exposing the tissue section to a flat panel detector or X-ray film.^{56,74} Advantages of this technique include high sensitivity, very low detection limits, and high resolution, while the major limitation is working with a radiolabeled drug. Fluorescent detection of drug concentration in tissues is an alternate strategy. In this method, tissue slices are analyzed using a fluorescence scanner or fluorescent microscope to detect drug.⁷⁸ To use this technique, the drug must either be intrinsically fluorescent or labeled with a fluorescent tag, such as fluorescein isothiocyanate (FITC).⁷⁹ While also offering low detection limits, reasonable sensitivity, and good resolution, only a few small molecule drugs are fluorescent, and labeling of drugs inevitably modifies their transport and efficacy, unlike radiolabeling methods. For large molecules, such as protein drugs or antibodies, fluorescent labeling may have only a minimal effect on the overall drug properties and may not adversely affect the delivery system, making the approach more tenable. *Ex vivo* drug detection is a major tool in developing local drug delivery methods, but temporal information is limited because every time point requires animal euthanasia and removal of tissue.

Noninvasive imaging methods for measuring local drug concentrations represent a growing trend in attempts to address the temporal limitations of *ex vivo* approaches. Driven by advances in imaging technology as well as proliferation of scanner availability, noninvasive

imaging methods likely hold the future for monitoring drug concentrations from local delivery strategies. With noninvasive imaging, a single subject can be imaged several times throughout the study period, greatly increasing the data available from a smaller number of animal subjects. The most straightforward extension of previous detection technologies is use of radiolabeled drugs coupled with positron emission tomography (PET)⁸⁰ or single photon emission tomography (SPECT) for drug detection.⁵ These detection methods have existed clinically for several years, but recent development of specialized small animal scanners, often coupled with CT for anatomical information, has improved resolution and usability, making nuclear medicine techniques key for development of targeted therapies. Additionally, these techniques can be easily translated to clinical use for monitoring of clinical trials of newly developed devices or treatment strategies. Other imaging techniques, such as *in vivo* fluorescence imaging, have been specifically developed for use in small animals and can contribute primarily to small animal studies. With *in vivo* fluorescence imaging, fluorescently labeled molecules are imaged directly in the animal.⁸¹ Most fluorescent imaging suffers from greater background noise than radiographic imaging and limitation to two dimensions, but developments in tomographic fluorescence offer the potential to reduce noise and provide three-dimensional (3-D) localization of drug.⁸² Beyond radiolabeling and fluorescence, magnetic resonance imaging (MRI) detection of drugs or drug carriers labeled with an MRI contrast agent, such as gadolinium or superparamagnetic iron oxide (SPIO), also offers the potential to noninvasively image anatomical detail and drug concentrations simultaneously.^{83–85} Recent advances and the benefits afforded by noninvasive imaging make it likely that these techniques will dominate the future landscape of monitoring local drug delivery strategies.

A novel noninvasive method used in the development of polymer millirods for liver cancer treatment is drug detection using X-ray computed tomography (CT).^{86–88} Polymer implants were loaded with the anticancer drug carboplatin and tested in both normal and ablated rat liver tissue. Carboplatin has a unique property among cancer drugs in that it contains the heavy metal platinum ($Z = 78$), which has high X-ray attenuation and provides inherent CT contrast. Polymer millirods containing carboplatin were implanted in non-

ablated or RF ablated rat livers, and carboplatin was detected by performing CT scans at multiple time points after implantation.⁸⁸ A representative CT scan of one of these rats is shown in Figure 3. Slices perpendicular to the long axis of the implant clearly show the higher absorption of the implant compared to the surrounding tissue. By comparing the intensity of the implant to premeasured implants with known concentrations, the remaining carboplatin in the implant was determined. The drug concentrations in the implants and surrounding tissue were determined by subtracting the background signal and converting to drug concentrations based on scans of

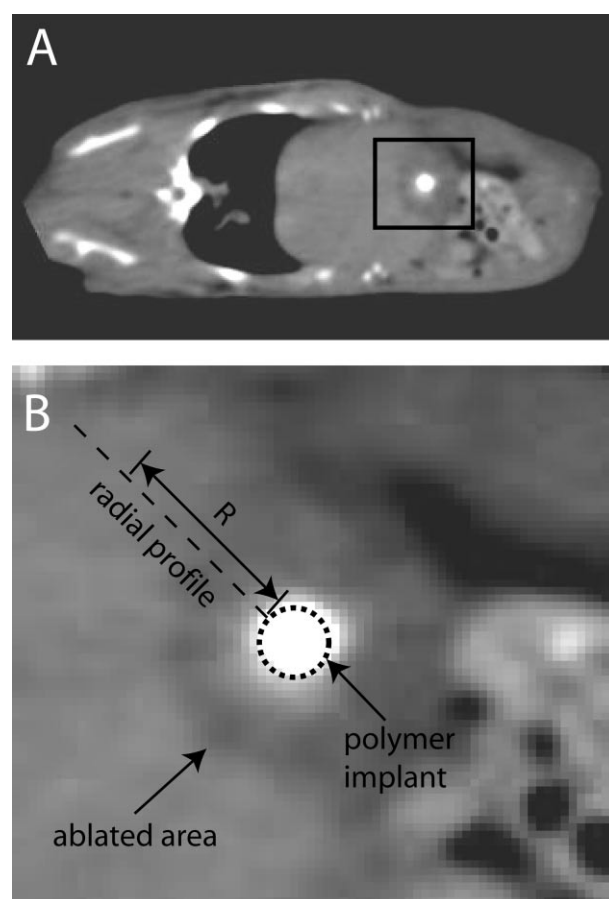


Figure 3. Computed tomography (CT) scan of rat with a polymer millirod containing the anticancer agent carboplatin placed in a region of liver treated by radio-frequency ablation. A: Oblique slice through the rat showing the general location of the polymer implant in the liver (black square). B: Enlargement of the implant region showing the ablated region and implant. Drug concentrations can be approximated by measuring the image intensity arising from carboplatin as a function of distance, R , from the implant surface. Adapted from Reference⁸⁸ with permission.

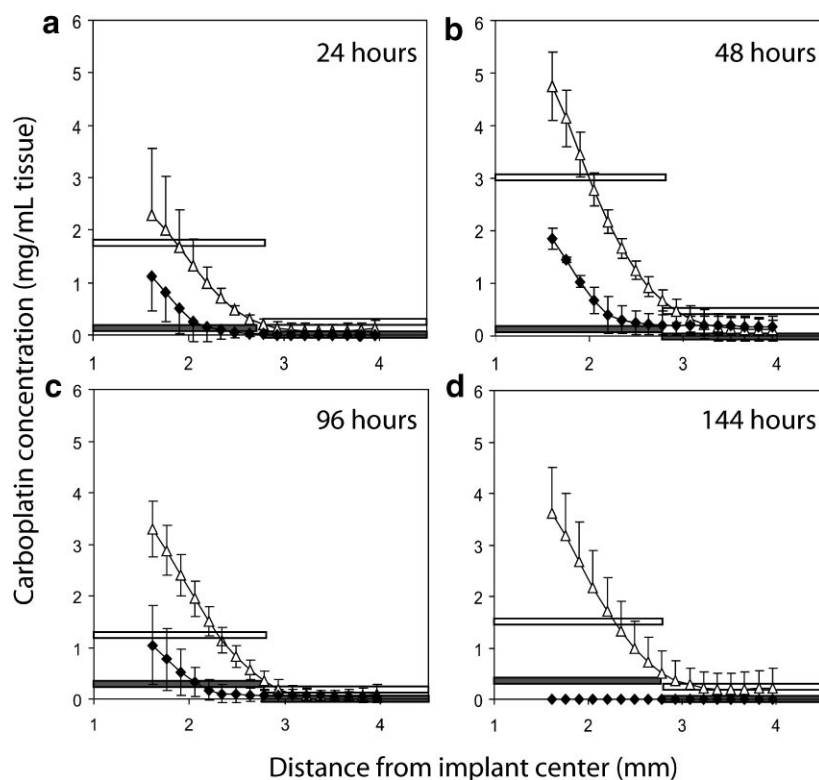


Figure 4. Carboplatin distribution in normal (\blacklozenge) and ablated (\triangle) liver tissue measured by CT. Values reflect mean \pm SD between animals. Atomic absorption spectroscopy (AAS) measurements confirm drug concentrations in tissue sections 2 mm wide from both ablated (white rectangle) and normal (gray rectangle) liver tissue. AAS data represent the average drug concentration determined over a tissue sample the width of the rectangle. Adapted from Reference⁸⁸ with permission.

premeasured standards. Tissue concentrations of carboplatin determined from CT images are shown in Figure 4 along with validation measurements determined using AAS of platinum concentration in extracted tissues. CT provided higher spatial resolution than AAS and revealed differences in drug distribution in nonablated and ablated tissues not appreciated by AAS. Ablated tissue retained carboplatin for longer times and at greater distances from the implant than nonablated tissue, illustrating a fundamental difference between drug transport in these tissue environments. Additionally, these results validated the use of a noninvasive imaging strategy to monitor local drug release from implants.

Further studies of local drug concentration around implants using fluorescent imaging allowed for greater quantification of the differences between ablated and normal tissue.⁸⁹ Doxorubicin, a topoisomerase II inhibitor commonly used in liver cancer treatment,³ also has the fortuitous property of natural fluorescence. Polymer millirods containing doxorubicin were

implanted in nonablated and RF ablated rat livers.⁹⁰ Liver tissues were removed at various times after implantation, and local doxorubicin concentrations were determined by measuring the fluorescence of the extracted slices. Average doxorubicin concentrations at time points ranging from 1 h to 4 days after implant placement were used to estimate the transport properties of liver tissues within the framework of a theoretical model of drug distribution as described in the Overview of Drug Delivery Goals Section.⁵⁸ The resulting estimates are shown in Table 1. These studies established the baseline transport properties of doxorubicin in normal rat liver as well as

Table 1. Doxorubicin Transport Properties in Rat Liver

	Normal Liver	Ablated Liver
Apparent diffusion, D^* , ($\text{cm}^2 \cdot \text{s}^{-1}$)	6.7×10^{-7}	1.1×10^{-7}
Apparent elimination, γ^* , ($\text{cm}^2 \cdot \text{s}^{-1}$)	9.6×10^{-4}	n/a

how ablation modifies them. Ablation reduced the diffusion coefficient, perhaps by destroying cell structure and making more sites available for drug binding. Even more notably, ablation virtually abolished elimination, which is sensible since RF ablation might be expected to reduce elimination both due to metabolism in cells (by killing them) and perfusion related losses (by coagulating and destroying blood vessels). This reduction in drug elimination can largely explain why drug penetration distances and retention were higher in ablated liver tissue.

In summary, techniques for measuring local drug concentrations surrounding implants are fundamentally important for the development of a local drug delivery system for tumors. Many methods exist for measuring drug concentrations, each with advantages and disadvantages, and it is likely that a combination of methods provide the best overall information about drug delivery. After obtaining local drug concentrations, they can be compared empirically to determine qualitative differences in delivery or interpreted through the use of a model to obtain quantitative transport information. Both sets of data can then be used to modify implant properties to provide the best drug coverage to the tumor.

Controlling Drug Release and Local Pharmacokinetics from Polymer Implants

Development of techniques to monitor local drug pharmacokinetics allows for the design and assessment of different implant types. As described in the Overview of Drug Delivery Goals Section, an ideal implant should provide a rapid ascent to the therapeutic concentration and maintenance of this dose for as long as possible. The first generation polymer millirod provided rapid release of a drug mimic, largely within the first few days.⁶⁵ However, through modification of the implant design it is possible to customize the delivery profile of the implants. Consequently, local drug concentrations arising around the implants can be compared and evaluated based on overall tissue drug exposure.

Several modifications to the initial compression-heat molded millirods can either prolong drug release or change the timing of the released dose. One modification is the addition of a semi-permeable membrane around the outside of the implant, which can be made either by wrapping the cylindrical device with a membrane⁶³ or by dip

coating the implant.⁶⁴ Using these methods, polymer membranes containing NaCl (10–50% w/w) or poly(ethylene oxide) (PEO) (5–20% w/w) were placed around monolithic millirods. When placed in an aqueous environment, the water-soluble component of the outer membrane rapidly dissolved, leaving a semi-permeable membrane with porosity that could be modulated by controlling the water-soluble fraction. These membrane-encased millirods substantially prolonged the drug release from the resulting implants over a period as long as 5 weeks.^{63,64}

By further modifying the polymer millirods, it is possible to create an implant that adds an additional burst dose to the millirods with sustained drug release. As discussed in the Overview of Drug Delivery Goals Section, the tissue surrounding a sustained release implant may not reach the therapeutic concentration for some time, delaying the onset of action of the drug. To accelerate the rise to the therapeutic concentration, a burst dose can be added to the implant to act as a loading dose. Dual-release implants combining the benefits of a drug burst followed by sustained release were then created by supplementing the implant with two drug coatings.⁵⁸ Monolithic millirod implants were first created by compression molding followed by the addition of two subsequent coatings. To sustain the release of drug from this implant, it was dip coated with a layer of PLA/PEG as described above. Then, a second coating consisting of doxorubicin and PEO was added to provide an additional burst dose. The total burst dose of drug could be controlled by applying multiple coatings to increase the thickness of the burst layer. The resulting implants, termed dual-release millirods, released a burst dose of doxorubicin followed by a sustained dose of doxorubicin for as long as 10 days.⁵⁸ In this manner, polymer millirods that could release doxorubicin into tumors with different dose timings were created.

To evaluate the differences in local drug distribution generated by different implant types, these burst, sustained, and dual-release millirod formulations were tested *in vivo*.⁶⁴ In the rat model, liver tissue was ablated for 2 min at 90°C to create an ablation region 8–10 mm in diameter. Subsequently, polymer millirods of each type were placed in the ablation needle tract and sutured into place. At specified time points, the rats were euthanized, and the polymer implants and surrounding liver tissue were extracted. Doxorubicin remaining in the implant was quantified by an

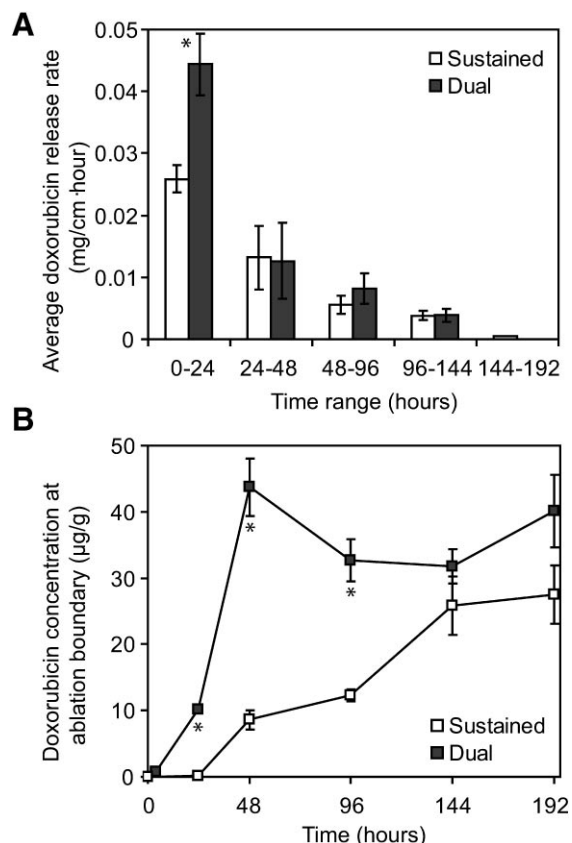


Figure 5. In vivo relationship between drug release rate and local tissue concentrations. A: Average rate of drug release from two implant formulations in vivo in ablated rat livers. B: Doxorubicin concentration at the outer edge of the ablated region for the same two implant formulations. Adapted from Reference⁶⁴ with permission.

extraction procedure and used to calculate average release rates, which are shown in Figure 5A. As expected, the dual-release implants released a higher amount of drug in the first 24 h,

but after this time the drug release rates were not statistically different. Tissue doxorubicin concentrations were determined using fluorescence scanning of sliced tissues, and the doxorubicin concentration at the outer ablation boundary is shown in Figure 5B. The dual-release implants provided a more rapid ascent to therapeutically relevant concentrations that was statistically different from the sustained-release implants. The similarity between the experimental results and the desired theoretical profiles shown in Figure 1 (panel 2, curves A and C) is notable. More detailed fluorescent images of tissues that confirm this finding are shown in Figure 6. Dual-release implants led to local doxorubicin concentrations as high as 1000 $\mu\text{g/g}$ within 1 day, while it took nearly 4 days for the drug distributions around the sustained implant to reach this extent. This study established that differences in implant formulation could have a substantial impact on local drug concentrations.

Controlling Host Tissue Response in Local Drug Therapy

Histology studies of treated tissue from ablated livers were performed to provide a more detailed understanding of the effect of changing tissue properties on drug transport.⁷⁵ Ablated rat livers were treated with doxorubicin-containing polymer implants, and tissues were subsequently removed at time points ranging from 1 h to 8 days after ablation. Throughout the first 4 days after ablation, an area of coagulation necrosis surrounding the implant was gradually infiltrated by inflammatory cells, particularly neutrophils and

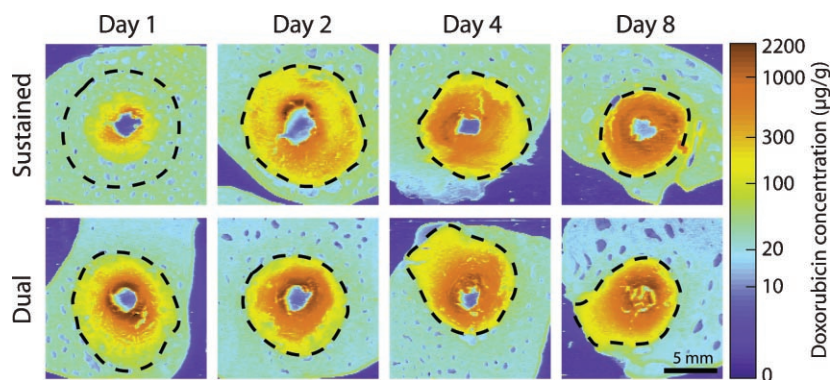


Figure 6. Fluorescence imaging comparing the rate of local doxorubicin accumulation due to two implant formulations (sustained-release and dual-release millirod) in ablated liver over 8 days. The dotted line is the ablation boundary, and the scale bar is 5 mm. Adapted from Reference⁶⁴ with permission.

monocytes. By 8 days after ablation, fibroblasts and the formation of a dense, collagenous fibrous capsule were evident at the ablation boundary. Furthermore, it was found that doxorubicin concentrations leading up to the fibrous capsule were high but dropped precipitously in the nascent fibrous capsule. From these results, it appeared that the wound healing response after ablation could have a major role in drug diffusion, acting as a barrier to transport outside the ablation region.⁷⁵ This finding reiterates the importance of considering the tissue surrounding the implant not as a static environment, but instead as a dynamic milieu that can ultimately affect the success of the treatment itself.

Since the tissue surrounding the implant has a large impact on the efficacy of drug therapy, one strategy to overcome this is to modify the response of the surrounding tissue in a way that favors effective drug dispersion. One way to modify the properties of ablated tissue is to moderate the ensuing inflammatory response with an anti-inflammatory agent. To test this hypothesis, the potent corticosteroid dexamethasone (DEX) was loaded into PLGA millirod implants.⁹¹ To facilitate the subsequent release of DEX, a highly hydrophobic drug, a more water soluble DEX formulation complexed with hydroxypropyl β -cyclodextrin (HP β -CD) was incorporated in the implants. These implants were tested for their ability to reduce fibrous capsule formation following liver ablation in rats. Histology with Masson's trichrome stain showed that the DEX-impregnated implants drastically suppressed the thickness of the collagen fibrous boundary compared to a control ablation treatment (Fig. 7). The average thickness of the fibrous capsule was 0.04 ± 0.01 mm in subjects receiving a DEX implant, reduced both compared to a control ablation (0.29 ± 0.08 mm) or ablation followed by an IP DEX injection (0.26 ± 0.07 mm).⁹¹

In addition to enhancing drug delivery by reducing fibrous capsule formation, DEX administration after ablation may have other beneficial effects as well as some disadvantages. DEX is expected to reduce chemokine and growth factor production and angiogenic processes that have been implicated in tumor growth and recurrence after ablation.⁹²⁻⁹⁴ At least one report has suggested that liver tumor recurrence after ablation is potentiated by inflammation,⁶⁰ which may allow DEX to improve the primary outcome of ablation. On the other hand, the inflammatory state of the tissue following ablation may con-

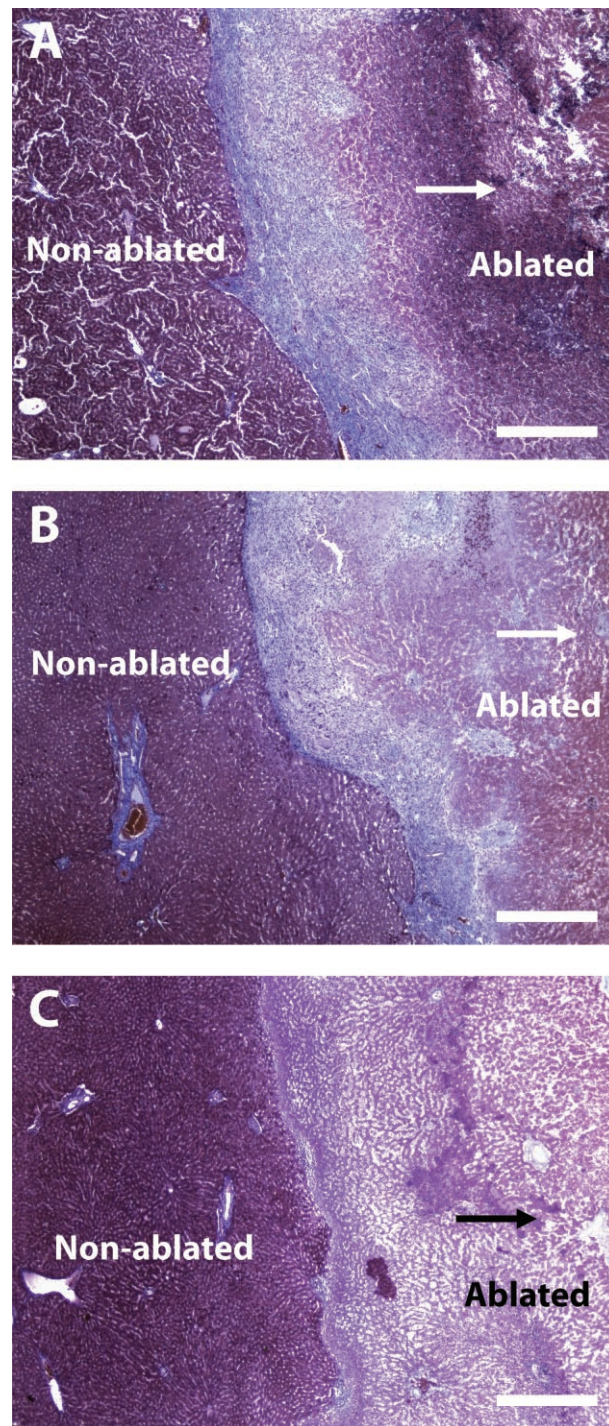


Figure 7. Masson's trichrome stained histology images of ablated liver samples 8 days after RF ablation and millirod implantation. A: Ablated liver receiving control PLGA millirod. B: Sample that received a control PLGA millirod and intraperitoneal (IP) injection of DEX. C: Ablated liver receiving DEX-loaded millirod. The arrows point to the center of the liver ablation/millirod implantation site. All scale bars are 0.5 mm. Adapted from Reference⁹¹ with permission.

tribute to tumor destruction. In several reported studies, considerable damage has been found to occur following the initial thermal damage.^{95,96} The authors have speculated that this progressive ablation damage could be a result of inflammatory activation or altered cytokine expression after ablation. If this process is interrupted, DEX could adversely affect the therapeutic outcome of ablation. This complication might be avoided by stopping revascularization using more specific drugs, such as a new class of drugs known as vascular disrupting agents.⁹⁷ Future study of implants containing multiple agents should allow for specific modification of tissue properties after ablation to achieve the most favorable tumor destruction with the combined treatment.

Summary

Several different implant types were developed and evaluated in thermal ablation models of rat and rabbit livers. Two factors appeared to have a role in the extent of drug delivery: the rate of drug release and the properties of the surrounding tissue. Dual-release implants, consisting of two dip-coated layers, provided the fastest ascent to therapeutic concentrations and maintained local concentrations for at least 8 days. RF ablation, by destroying the surrounding vasculature, potentiated drug release into the surrounding tissue but may have ultimately restricted it by instigating the encapsulation of the ablated region within a thick fibrous shell. One approach, including DEX complexed with β -cyclodextrin in the implants, showed the potential to overcome this limitation. Overall, studies of drug release from implants demonstrated that PLGA implants are a versatile platform for drug delivery that is capable of different release kinetics and local pharmacokinetics following RF ablation.

TREATMENT OF ANIMAL TUMOR MODELS

Drug Distribution and Antitumor Efficacy from Liver Tumor Treatment with Polymer Implants

After extensive pharmacokinetic study of polymer millirods in normal livers, preliminary studies of drug distribution and treatment efficacy in tumor tissue were performed. One study assessed the use of implants alone for treatment and local control of small liver tumors;⁶⁶ the second study explored drug distribution and therapeutic effects

of an approach combining RF ablation followed by implant placement.⁶⁷ Both of these studies were performed using the rabbit VX2 model of liver carcinoma, which has been widely used in the assessment of new interventional therapies and is considered a realistic model of human HCC.⁹⁸⁻¹⁰⁰ Together, these studies provide insight on the efficacy of liver tumor treatment with implantable polymer devices.

The first study established the use of polymer millirods as a standalone strategy for the treatment of small, unresectable liver cancers.⁶⁶ The primary goal of this work was to determine the drug distribution and the resulting treatment efficacy from using polymer implants to treat tumors smaller than 1 cm in diameter. Such a scenario might be encountered in humans in advanced HCC, when multiple small tumors might be found throughout the liver. In this case, surgery is often excluded because of insufficient liver function or the involvement of both liver lobes.¹⁰¹ Small VX2 liver tumors (diameter = 8 mm) in New Zealand White rabbits were treated with the implantation of a burst-release doxorubicin millirod into the center of the tumor.⁶⁶ On a gross level, the implants demonstrated considerable tumor control at both time points, as tumors were 50% and 90% smaller than their respective controls. The treated tumors had a substantially different morphology than controls, showing considerable necrosis and cell damage. Drug penetration was seen at distances of 2.8 mm (day 4) and 1.3 mm (day 8) away from the implant. A plot of day 4 drug concentrations within the tumor as a function of distance from the implant is shown in Figure 8. Outside the tumor, drug concentrations dropped sharply and were below the detectable levels of drug. Furthermore, untreated tumor cells, which are likely to grow into recurrent tumors over time, were found outside the main tumor boundary. This study established that the polymer implants could be used to treat small tumors in a palliative or neoadjuvant role. Future studies with larger numbers of animal subjects will be further pursued to establish treatment success rates.

Drug Distribution and Antitumor Efficacy from Combined Liver Tumor Treatment with Radiofrequency (RF) Ablation and Polymer Implants

After demonstrating the drug coverage and treatment effects provided by the implants alone,

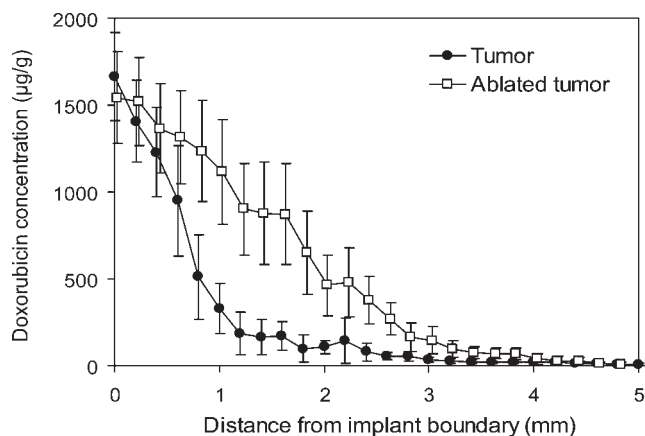


Figure 8. Average doxorubicin concentration in nonablated (●) or ablated (□) rabbit liver tumors as a function of distance from the implant 4 days after tumor treatment. Error bars show 95% confidence interval of the mean.

polymer millirods containing doxorubicin were tested as part of a combined liver cancer treatment.⁶⁷ The combined treatment consisted of RF ablation of the center of the tumor followed by the placement of a doxorubicin-containing implant. For liver tumor treatment, this approach has two distinct advantages. First, the RF treatment destroys the majority of the tumor mass, leading to a considerable reduction of viable tumor. Remnant tumor cells may also have increased susceptibility to drug because of their sublethal hyperthermia exposure. Second, RF ablation of the tumor mass facilitates drug distribution to greater distances from the implant, an effect established in earlier studies in normal liver.^{62,90} This property should provide greater drug exposure to the tumor, and hence, a greater degree of success, than either treatment alone. Additionally, the combined treatment may be more clinically relevant, as combined treatments for human tumors are often regarded as more effective than single treatments.¹⁰²

RF ablation followed by polymer implant placement was also tested in the VX2 liver carcinoma model in rabbits.⁶⁷ VX2 tumors of 1.1 cm in diameter were treated with RF ablation insufficient to destroy the entire tumor to mimic the human scenario in which a tumor is not completely treated. Following ablation, doxorubicin-containing polymer millirods were implanted into the ablation tract in the center of the tumors. Results from the combined treatment allowed for comparison of drug distribution properties between nonablated and ablated tumors. Radially averaged drug concentrations from the ablated tumors on day 4 are shown compared to those in

nonablated tumors in Figure 8. In both cases, drug concentrations in the center of the tumor are over 1000 µg/g at the implant tissue interface. However, the drug penetrates more deeply into ablated tumor tissues, providing greater drug coverage to the tumor 4 mm away from the implant boundary. Doxorubicin penetration distances in the ablated tumor tissue were found to be 3.7 mm on day 4 and 2.1 mm on day 8 (compared to 2.8 and 1.3 mm on day 4 and day 8 in nonablated tumors, respectively). Ablation almost tripled the total mass drug estimated to be in the tumor on day 4, increasing the value from 210 ± 120 µg without ablation to 590 ± 300 µg with ablation. The overall half-life of drug removal from the tumor volume was found to be 2.0 ± 0.1 days, slower than the 1.6 ± 0.2 days seen in nonablated tumor. These results support the conclusion that tumor ablation provides a reduction in drug elimination similar to that found in ablated normal liver, leading to greater penetration into the tumor tissue, and ultimately, greater coverage of the tumor with therapeutic drug values. Such data were qualitatively confirmed in images of drug distribution, which showed greater amounts of drug further from the tumor.

Gross pathological and histological observations after the combined treatment also allowed for preliminary assessment of the success of the combined treatment. The total area of coagulation necrosis and inflammatory tissue surrounding the ablated area was similar regardless of which type of implant was used. Totalling both time points, two out of seven animals treated with ablation and a control implant were found to have significant regions of residual tumor; similarly, two out of

seven animals treated with ablation and a doxorubicin implant had residual tumor. None of the animals (0/3) in the 8 day ablation plus implant group had areas of residual tumor, indicating a possible, although not statistically significant improvement in this group. Considerable knowledge on why the residual tumors remain untreated was determined from histological assessment. In the two residual tumors in the treatment group, areas of residual tumor began on average 4.1 mm away from the implant location, with 50% of the viable tumor found within 7.9 mm. Some residual tumor cells were found as far as 12.0 mm away from the implant. Comparison of tumor histology with fluorescence microscopy images provided further insight into why the treatment did not reach the entire tumor. Starting at day 4 and more considerable by day 8, fibrous capsule formation around the coagulated zone was evident. Fluorescence attributed to doxorubicin was seen up to the fibrous boundary on day 8, but little fluorescence was seen beyond this barrier, suggesting that collagen deposition in the boundary may have inhibited drug transport to untreated regions outside the ablated region (Fig. 9). The two main barriers to treatment success revealed by this study were drug penetration distance from the millirod implant and the formation of a fibrous barrier to drug transport.⁶⁷

Together, the two studies of liver tumor treatment with polymer millirods provide several interesting findings about the probability of success for tumor treatment with implantable polymer devices. With doxorubicin containing millirods alone, relatively small lesions (<1.0 cm diameter) were controlled in terms of tumor size but may not have been ultimately cured because of the presence of residual cells around the periphery.⁶⁶ However, these results suggest that these implants may be successful in reducing tumor load and could serve as a palliative and life-prolonging strategy in patients who are not good candidates for surgical resection. For instance, patients with multiple small metastatic lesions to the liver could be treated with percutaneous, image-guided placement of an implant in each lesion. The study of the combined treatment was unable to elicit statistically significant values in likelihood of remnant viable tumor, but did reveal that fibrous capsule formation and therapeutic distance from the implant limit treatment of residual tumor.⁶⁷ Future studies can now address these issues, perhaps by including DEX in the implants to reduce fibrous capsule formation⁹¹

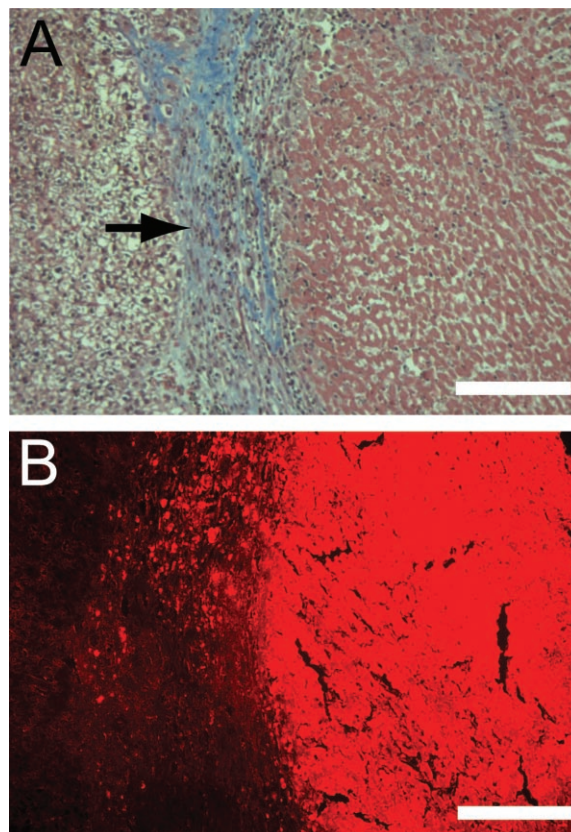


Figure 9. A: Masson's trichrome stained images of the ablation boundary 8 days after treatment. Ablated tissue is on the right and normal tissue on the left, with the boundary marked by the black arrow. A thick fibrous capsule was found at the ablation boundary. B: Fluorescent microscopy image of the matching regions showing doxorubicin accumulation just inside the ablation boundary. Scale bars are 200 μm . Adapted from Reference⁶⁷ with permission.

and using multiple polymer millirods placed peripherally around the tumor to minimize the distance between the implants and risk areas for tumor recurrence.

Three-Dimensional Modeling of Intratumoral Drug Delivery

Current research is focusing on the development of a 3-D finite element model to evaluate the effects of different implant designs and treatment strategies, such as the incorporation of an anti-inflammatory agent and the use of multiple millirods, on local cancer therapy. This approach limits the number of animal experiments and allows for rapid prototyping of different treatment

strategies. To model drug distribution into ablated tissues, transport properties of nonablated and ablated tumor were estimated. The resulting properties were then used to simulate drug distribution to ablated tumors with different types or arrangement of implants.

Tumor drug transport parameters were estimated by minimizing the error between a finite element solution to the transport mass balance equation and experimental data previously determined.^{66,67} Nonablated tumor was found to have drug diffusion slightly less than normal liver tissue and elimination considerably less than normal liver tissue. Ablated tumor, on the other hand, had a doxorubicin diffusion rate higher than either normal liver or nonablated tumor. As was found in normal liver, ablation completely stopped drug elimination for 4 days, but due to reperfusion of the ablated tumor areas elimination returned to values similar to that in normal tumor between day 4 and day 8. This finding

indicates that much as in normal liver tissue, ablation provides a clear window for improved drug delivery that lasts 4–8 days.

The estimated tissue parameters were then used to simulate 3-D drug distribution profiles using multiple, peripherally placed implants to treat larger tumors. Exemplary scenarios using RF ablation followed by placement of 1 or 4 burst-release doxorubicin polymer millirods to treat a single tumor are shown in Figure 10. In this instance, a tumor measuring 2 cm in diameter has been treated with RF ablation insufficient to treat the entire tumor (1.8 cm ablation diameter). Drug transport was then simulated using a finite element solution to determine the drug concentrations throughout the tumor over an 8-day period. The resulting model predicted drug concentrations on day 8 are shown in Figure 10C,D. The drug distributions from four peripheral distributions show considerably higher drug concentrations, particularly in the nonablated tumor

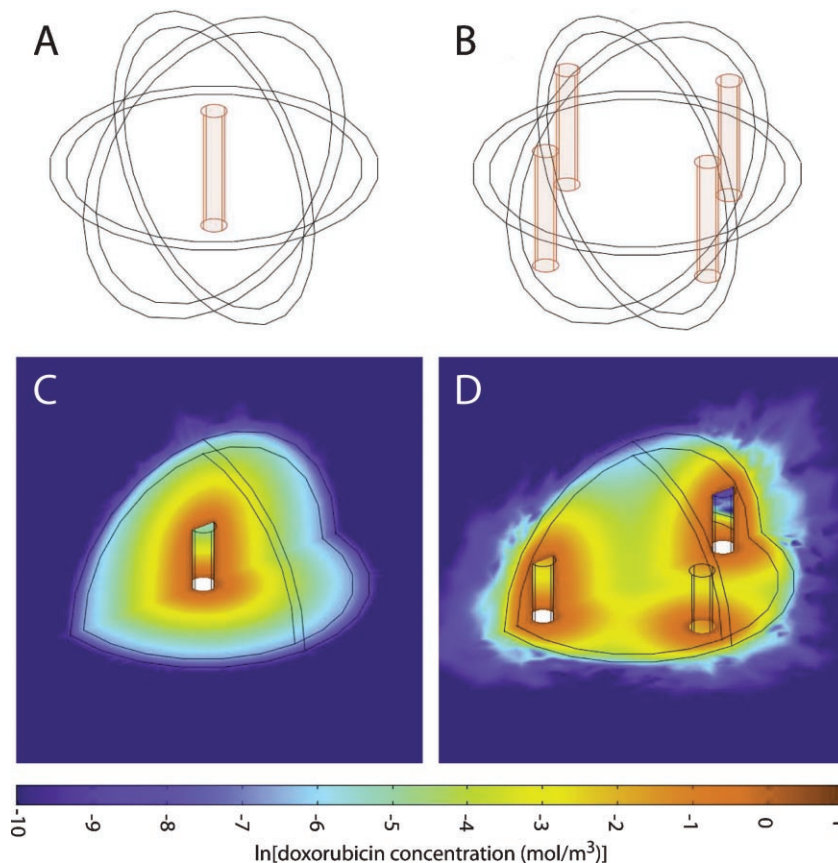


Figure 10. Simulated three-dimensional (3-D) geometry of a 2 cm diameter tumor containing a central RF ablated region of diameter 1.8 cm and treated with either one central implant (A) or four peripheral implants at a radius of 0.7 cm from the tumor center (B). Model predicted doxorubicin concentrations on day 8 for the single implant (C) and four implant (D) scenarios.

around the periphery of the lesion, where the tumor is most likely to recur. The four peripherally placed implants maintained the entire tumor volume at greater than two times the therapeutic concentration ($>12.8 \mu\text{g/g}$) for 74 h, while the single implant never reached 100% tumor coverage during the simulated 8 days. These findings indicate that a multiple implant strategy may be advantageous over a single, centrally placed implant. However, this strategy could be limited by the ability of a physician to easily place multiple solid implants into a tumor. An alternative method is to use an injectable polymer gel that forms a solid depot in situ. The advantage of this strategy is that these depots can be injected as a liquid through a smaller needle, allowing for easier administration of drug in multiple positions. Several types of in situ forming implants are available, with their precipitation triggered by pH,¹⁰³ temperature,¹⁰⁴ or solvent exchange.⁴⁷ Future studies could be used to establish the benefits of using one of these delivery systems along with RF ablation.

Using drug distribution simulations, many different treatments can be rapidly compared to determine which has the maximum likelihood of success. Future extensions to this model can be used to predict how implants with different release profiles, such as dual-release doxorubicin implants, could improve tumor coverage. Additionally, the model will be able to evaluate how other changes to implant design that modify tissue properties, such as including DEX within the implants, can affect drug distribution in the tumors. Ultimately, a drug transport model may be used as part of a comprehensive treatment planning tool. Image-based data obtained from CT or MRI could be used to determine tumor geometry. Subsequently, ablation treatment could be planned using a thermal damage model,¹⁰⁵ after which drug coverage in the ablated tumor could be predicted using this 3-D finite element model. Using a computational tool to plan combined treatment would allow assessment of the best ways to treat complex lesions and extension of the findings from smaller tumors already reported into larger, more clinically relevant tumor models.

CONCLUSIONS AND FUTURE OUTLOOK

Conventional systemic chemotherapy for tumors is restricted by lack of tumor specificity and severe

side effects associated with intrinsic drug toxicity.⁵⁻⁷ With the emergence of minimally invasive, image-guided interventional technology, tumor chemotherapy is at the threshold of a major breakthrough because of such technological advances in targeting strategies that overcome the previous limitations. Tumor-directed therapies, such as focal ablation and locoregional chemotherapy, are being developed to increase the specificity of tumor destruction and reduce undesired side effects. Intratumoral implants reduce systemic drug exposure by using image-guided placement directly into the target region, thus delivering the entire drug dose with reduced systemic exposure. The key consideration with intratumoral chemotherapy is to design an implant system that provides optimal drug distribution and therefore maximal tumor destruction.

Polymer millirod implants were specifically designed to treat unresectable liver tumors in conjunction with RF ablation. Implants with different drug release rates have been developed and extensively studied in both nonablated and ablated liver tissues, where they effectively delivered drugs into the surrounding tissue. Particularly, dual-release implants combining a burst of drug release with sustained drug release maximized drug coverage in the ablated region.⁶⁴ Modeling of tissue properties using a pharmacokinetic transport model emphasized the importance of tumor pretreatment with RF ablation, which facilitated drug delivery to tissues further away from the implant by preventing drug elimination. Polymer millirods were further tested in a rabbit model of HCC. Tumor control was achieved within a limited distance from the implant, but several of the treated animals had regions of viable tumor just beyond the boundary of the ablation. The success of the tumor treatment appeared to be limited by two factors: drug transport distance from the implant and the formation of a fibrous capsule that restricted drug transport.

The future of polymer millirods for tumor treatment depends on optimizing drug delivery efficiency to the tumor periphery. One way of achieving this goal is to include an anti-inflammatory agent and doxorubicin in a single implant. DEX-containing polymer millirods have already been shown to prevent fibrous capsule formation and decrease new blood vessel formation after ablation.⁹¹ These effects should promote drug delivery by increasing doxorubicin diffusion

and reducing elimination. Another anticipated improvement is placing multiple implants around the periphery of a larger tumor to improve the probability of treatment success. Placing implants closer to the boundary increases the likelihood of drug exposure at and beyond the ablation periphery, where recurrence is most likely to occur. The focus of a multiple implant strategy will be maximizing drug coverage of the tumor periphery while maintaining a reasonable and safe number of implants and total drug dose. 3-D modeling will be an essential tool for rapidly evaluating different treatment protocols as well as gaining mechanistic insights to optimize dosage regimen design. The integrated modeling and experimental approach should greatly assist the clinical translation of polymer implants as a viable option for locoregional chemotherapy of unresectable tumors.

ACKNOWLEDGMENTS

This work was supported by the NIH grant R01 CA090696 to JG. BW is supported by a DOD predoctoral fellowship BC043453 and the NIH grant T32 GM07250 to the Case Western Reserve University Medical Scientist Training Program. EB is supported by a NIH minority supplement. This is manuscript CSCNP009 from the "Cell Stress and Cancer Nanomedicine" program in the Simmons Comprehensive Cancer Center at UT Southwestern Medical Center at Dallas.

REFERENCES

1. Jemal A, Siegel R, Ward E, Murray T, Xu J, Smigal C, Thun MJ. 2006. Cancer statistics, 2006. *CA Cancer J Clin* 56:106–130.
2. Bentrem DJ, Dematteo RP, Blumgart LH. 2005. Surgical therapy for metastatic disease to the liver. *Annu Rev Med* 56:139–156.
3. Leung TW, Johnson PJ. 2001. Systemic therapy for hepatocellular carcinoma. *Semin Oncol* 28:514–520.
4. Geller DA, Tsung A, Marsh JW, Dvorchik I, Gambin TC, Carr BI. 2006. Outcome of 1000 liver cancer patients evaluated at the UPMC Liver Cancer Center. *J Gastrointest Surg* 10:63–68.
5. Dowell JA, Sancho AR, Anand D, Wolf W. 2000. Noninvasive measurements for studying the tumoral pharmacokinetics of platinum anticancer drugs in solid tumors. *Adv Drug Deliv Rev* 41:111–126.
6. Crawford J, Dale DC, Lyman GH. 2004. Chemotherapy-induced neutropenia: Risks, consequences, and new directions for its management. *Cancer* 100:228–237.
7. Wallace KB. 2003. Doxorubicin-induced cardiac mitochondrionopathy. *Pharmacol Toxicol* 93:105–115.
8. El-Kareh AW, Secomb TW. 2000. A mathematical model for comparison of bolus injection, continuous infusion, and liposomal delivery of doxorubicin to tumor cells. *Neoplasia* 2:325–338.
9. Gillams AR. 2005. Image guided tumour ablation. *Cancer Imaging* 5:103–109.
10. Barnett CC, Jr., Curley SA. 2001. Ablative techniques for hepatocellular carcinoma. *Semin Oncol* 28:487–496.
11. Goldberg SN. 2001. Radiofrequency tumor ablation: Principles and techniques. *Eur J Ultrasound* 13:129–147.
12. Vogl TJ, Mack MG, Muller PK, Straub R, Engelmann K, Eichler K. 1999. Interventional MR: Interstitial therapy. *Eur Radiol* 9:1479–1487.
13. Han KR, Beldegrun AS. 2004. Third-generation cryosurgery for primary and recurrent prostate cancer. *BJU Int* 93:14–18.
14. Dale PS, Souza JW, Brewer DA. 1998. Cryosurgical ablation of unresectable hepatic metastases. *J Surg Oncol* 68:242–245.
15. Livraghi T, Benedini V, Lazzaroni S, Meloni F, Torzilli G, Vettori C. 1998. Long term results of single session percutaneous ethanol injection in patients with large hepatocellular carcinoma. *Cancer* 83:48–57.
16. Shah SS, Jacobs DL, Krasinkas AM, Furth EE, Itkin M, Clark TW. 2004. Percutaneous ablation of VX2 carcinoma-induced liver tumors with use of ethanol versus acetic acid: Pilot study in a rabbit model. *J Vasc Interv Radiol* 15:63–67.
17. Francica G, Marone G. 1999. Ultrasound-guided percutaneous treatment of hepatocellular carcinoma by radiofrequency hyperthermia with a 'cooled-tip needle'. A preliminary clinical experience. *Eur J Ultrasound* 9:145–153.
18. Merkle EM, Boll DT, Boaz T, Duerk JL, Chung YC, Jacobs GH, Varnes ME, Lewin JS. 1999. MRI-guided radiofrequency thermal ablation of implanted VX2 liver tumors in a rabbit model: Demonstration of feasibility at 0.2 T. *Magn Reson Med* 42:141–149.
19. Curley SA, Izzo F, Delrio P, Ellis LM, Granchi J, Vallone P, Fiore F, Pignata S, Daniele B, Cremona F. 1999. Radiofrequency ablation of unresectable primary and metastatic hepatic malignancies: Results in 123 patients. *Ann Surg* 230:1–8.
20. Varshney S, Sewkani A, Sharma S, Kapoor S, Naik S, Sharma A, Patel K. 2006. Radiofrequency ablation of unresectable pancreatic carcinoma: Feasibility, efficacy and safety. *JOP* 7:74–78.

21. Nguyen CL, Scott WJ, Goldberg M. 2006. Radio-frequency ablation of lung malignancies. *Ann Thorac Surg* 82:365–371.
22. Goldberg EP, Hadba AR, Almond BA, Marotta JS. 2002. Intratumoral cancer chemotherapy and immunotherapy: Opportunities for nonsystemic preoperative drug delivery. *J Pharm Pharmacol* 54:159–180.
23. Wientjes MG, Badalament RA, Au JL. 1996. Penetration of intravesical doxorubicin in human bladders. *Cancer Chemother Pharmacol* 37:539–546.
24. Seto T, Ushijima S, Yamamoto H, Ito K, Araki J, Inoue Y, Semba H, Ichinose Y. 2006. Intrapleural hypotonic cisplatin treatment for malignant pleural effusion in 80 patients with non-small-cell lung cancer: A multi-institutional phase II trial. *Br J Cancer* 95:717–721.
25. Alberts DS, Delforge A. 2006. Maximizing the delivery of intraperitoneal therapy while minimizing drug toxicity and maintaining quality of life. *Semin Oncol* 33:8–17.
26. Ramsey DE, Kernagis LY, Soulen MC, Geschwind JF. 2002. Chemoembolization of hepatocellular carcinoma. *J Vasc Interv Radiol* 13:S211–S221.
27. Kokudo N, Makuuchi M. 2004. Current role of portal vein embolization/hepatic artery chemoembolization. *Surg Clin North Am* 84:643–657.
28. Ramsey DE, Geschwind JF. 2002. Chemoembolization of hepatocellular carcinoma—what to tell the skeptics: Review and meta-analysis. *Tech Vasc Interv Radiol* 5:122–126.
29. Muller H, Hilger R. 2003. Curative and palliative aspects of regional chemotherapy in combination with surgery. *Support Care Cancer* 11:1–10.
30. Muller H. 2002. Combined regional and systemic chemotherapy for advanced and inoperable non-small cell lung cancer. *Eur J Surg Oncol* 28:165–171.
31. Hall WA, Sherr GT. 2006. Convection-enhanced delivery: Targeted toxin treatment of malignant glioma. *Neurosurg Focus* 20:E10.
32. Raghavan R, Brady ML, Rodriguez-Ponce MI, Hartlep A, Pedain C, Sampson JH. 2006. Convection-enhanced delivery of therapeutics for brain disease, and its optimization. *Neurosurg Focus* 20:E12.
33. Mardor Y, Roth Y, Lidar Z, Jonas T, Pfeffer R, Maier SE, Faibel M, Nass D, Hadani M, Orenstein A, Cohen JS, Ram Z. 2001. Monitoring response to convection-enhanced taxol delivery in brain tumor patients using diffusion-weighted magnetic resonance imaging. *Cancer Res* 61:4971–4973.
34. Sampson JH, Akabani G, Friedman AH, Bigner D, Kunwar S, Berger MS, Bankiewicz KS. 2006. Comparison of intratumoral bolus injection and convection-enhanced delivery of radiolabeled anti-tenascin monoclonal antibodies. *Neurosurg Focus* 20:E14.
35. Celikoglu SI, Celikoglu F, Goldberg EP. 2006. Endobronchial intratumoral chemotherapy (EITC) followed by surgery in early non-small cell lung cancer with polypoid growth causing erroneous impression of advanced disease. *Lung Cancer* 54:339–346.
36. Order SE, Siegel JA, Principato R, Zeiger LE, Johnson E, Lang P, Lustig R, Wallner PE. 1996. Selective tumor irradiation by infusional brachytherapy in nonresectable pancreatic cancer: A phase I study. *Int J Radiat Oncol Biol Phys* 36:1117–1126.
37. Mok TS, Kanekal S, Lin XR, Leung TW, Chan AT, Yeo W, Yu S, Chak K, Leavitt R, Johnson P. 2001. Pharmacokinetic study of intralesional cisplatin for the treatment of hepatocellular carcinoma. *Cancer* 91:2369–2377.
38. McGuire S, Yuan F. 2001. Quantitative analysis of intratumoral infusion of color molecules. *Am J Physiol Heart Circ Physiol* 281:H715–721.
39. McGuire S, Zaharoff D, Yuan F. 2006. Nonlinear dependence of hydraulic conductivity on tissue deformation during intratumoral infusion. *Ann Biomed Eng* 34:1173–1181.
40. Wang Y, Liu S, Li CY, Yuan F. 2005. A novel method for viral gene delivery in solid tumors. *Cancer Res* 65:7541–7545.
41. Wang Y, Yuan F. 2006. Delivery of viral vectors to tumor cells: Extracellular transport, systemic distribution, and strategies for improvement. *Ann Biomed Eng* 34:114–127.
42. Emerich DF, Snodgrass P, Lafreniere D, Dean RL, Salzberg H, Marsh J, Perdomo B, Arastu M, Winn SR, Bartus RT. 2002. Sustained release chemotherapeutic microspheres provide superior efficacy over systemic therapy and local bolus infusions. *Pharm Res* 19:1052–1060.
43. Menei P, Capelle L, Guyotat J, Fuentes S, Assaker R, Bataille B, Francois P, Dorwling-Carter D, Paquis P, Bauchet L, Parker F, Sabatier J, Faisant N, Benoit JP. 2005. Local and sustained delivery of 5-fluorouracil from biodegradable microspheres for the radiosensitization of malignant glioma: A randomized phase II trial. *Neurosurgery* 56:242–248; discussion 242–248.
44. Menei P, Jadaud E, Faisant N, Boisdron-Celle M, Michalak S, Fournier D, Delhaye M, Benoit JP. 2004. Stereotaxic implantation of 5-fluorouracil-releasing microspheres in malignant glioma. *Cancer* 100:405–410.
45. Arica B, Calis S, Kas H, Sargon M, Hincal A. 2002. 5-Fluorouracil encapsulated alginate beads for the treatment of breast cancer. *Int J Pharm* 242:267–269.
46. Almond BA, Hadba AR, Freeman ST, Cuevas BJ, York AM, Detrisac CJ, Goldberg EP. 2003. Efficacy

- of mitoxantrone-loaded albumin microspheres for intratumoral chemotherapy of breast cancer. *J Control Release* 91:147–155.
47. Krupka TM, Weinberg BD, Ziats NP, Haaga JR, Exner AA. 2006. Injectable polymer depot combined with radiofrequency ablation for treatment of experimental carcinoma in rat. *Invest Radiol* 41: 890–897.
 48. Jackson JK, Gleave ME, Yago V, Beraldi E, Hunter WL, Burt HM. 2000. The suppression of human prostate tumor growth in mice by the intratumoral injection of a slow-release polymeric paste formulation of paclitaxel. *Cancer Res* 60:4146–4151.
 49. Vogl TJ, Engelmann K, Mack MG, Straub R, Zangos S, Eichler K, Hochmuth K, Orenberg E. 2002. CT-guided intratumoural administration of cisplatin/epinephrine gel for treatment of malignant liver tumours. *Br J Cancer* 86:524–529.
 50. Merrick GS, Wallner KE, Butler WM. 2003. Permanent interstitial brachytherapy for the management of carcinoma of the prostate gland. *J Urol* 169:1643–1652.
 51. Grimm P, Sylvester J. 2004. Advances in Brachytherapy. *Rev Urol* 6:S37–S48.
 52. Guerin C, Olivi A, Weingart JD, Lawson HC, Brem H. 2004. Recent advances in brain tumor therapy: Local intracerebral drug delivery by polymers. *Invest New Drugs* 22:27–37.
 53. Wang PP, Frazier J, Brem H. 2002. Local drug delivery to the brain. *Adv Drug Deliv Rev* 54:987–1013.
 54. Brem H, Gabikian P. 2001. Biodegradable polymer implants to treat brain tumors. *J Control Release* 74:63–67.
 55. Fleming AB, Saltzman WM. 2002. Pharmacokinetics of the carmustine implant. *Clin Pharmacokinetics* 41:403–419.
 56. Strasser JF, Fung LK, Eller S, Grossman SA, Saltzman WM. 1995. Distribution of 1,3-bis(2-chloroethyl)-1-nitrosourea and tracers in the rabbit brain after interstitial delivery by biodegradable polymer implants. *J Pharmacol Exp Ther* 275:1647–1655.
 57. Westphal M, Ram Z, Riddle V, Hilt D, Bortey E. 2006. Gliadel wafer in initial surgery for malignant glioma: Long-term follow-up of a multicenter controlled trial. *Acta Neurochir (Wien)* 148:269–275; discussion 275.
 58. Qian F, Saidel GM, Sutton DM, Exner A, Gao J. 2002. Combined modeling and experimental approach for the development of dual-release polymer millirods. *J Control Release* 83:427–435.
 59. Chu G. 1994. Cellular responses to cisplatin. The roles of DNA-binding proteins and DNA repair. *J Biol Chem* 269:787–790.
 60. Harrison LE, Koneru B, Baramipour P, Fisher A, Barone A, Wilson D, Dela Torre A, Cho KC, Contractor D, Korogodsky M. 2003. Locoregional recurrences are frequent after radiofrequency ablation for hepatocellular carcinoma. *J Am Coll Surg* 197:759–764.
 61. Yu HC, Cheng JS, Lai KH, Lin CP, Lo GH, Lin CK, Hsu PI, Chan HH, Lo CC, Tsai WL, Chen WC. 2005. Factors for early tumor recurrence of single small hepatocellular carcinoma after percutaneous radiofrequency ablation therapy. *World J Gastroenterol* 11:1439–1444.
 62. Szymanski-Exner A, Gallacher A, Stowe NT, Weinberg B, Haaga JR, Gao J. 2003. Local carboplatin delivery and tissue distribution in livers after radiofrequency ablation. *J Biomed Mater Res* 67A:510–516.
 63. Qian F, Nasongkla N, Gao J. 2002. Membrane-encased polymer millirods for sustained release of 5-fluorouracil. *J Biomed Mater Res* 61:203–211.
 64. Qian F, Stowe N, Saidel GM, Gao J. 2004. Comparison of doxorubicin concentration profiles in radiofrequency-ablated rat livers from sustained- and dual-release PLGA millirods. *Pharm Res* 21: 394–399.
 65. Qian F, Szymanski A, Gao J. 2001. Fabrication and characterization of controlled release poly(D, L-lactide-co-glycolide) millirods. *J Biomed Mater Res* 55:512–522.
 66. Weinberg BD, Ai H, Blanco E, Anderson JM, Gao J. 2006. Antitumor efficacy and local distribution of doxorubicin via intratumoral delivery from polymer millirods. *J Biomed Mater Res A* 81:161–170.
 67. Weinberg BD, Blanco E, Lempka SF, Anderson JM, Exner AA, Gao J. 2006. Combined radiofrequency ablation and doxorubicin-eluting polymer implants for liver cancer treatment. *J Biomed Mater Res A* 81:205–213.
 68. Jain RK. 1999. Transport of molecules, particles, and cells in solid tumors. *Annu Rev Biomed Eng* 1:241–263.
 69. Sinek J, Frieboes H, Zheng X, Cristini V. 2004. Two-dimensional chemotherapy simulations demonstrate fundamental transport and tumor response limitations involving nanoparticles. *Biomed Microdevices* 6:297–309.
 70. Jain RK. 2001. Delivery of molecular and cellular medicine to solid tumors. *Adv Drug Deliv Rev* 46:149–168.
 71. Kalyanasundaram S, Calhoun VD, Leong KW. 1997. A finite element model for predicting the distribution of drugs delivered intracranially to the brain. *Am J Physiol* 273:R1810–R1821.
 72. Longley DB, Harkin DP, Johnston PG. 2003. 5-fluorouracil: Mechanisms of action and clinical strategies. *Nat Rev Cancer* 3:330–338.
 73. Tanner B, Hengstler JG, Dietrich B, Henrich M, Steinberg P, Weikel W, Meinert R, Kaina B, Oesch F, Knapstein PG. 1997. Glutathione, glutathione

- S-transferase alpha and pi, and aldehyde dehydrogenase content in relationship to drug resistance in ovarian cancer. *Gynecol Oncol* 65: 54–62.
74. Au JL, Jang SH, Wientjes MG. 2002. Clinical aspects of drug delivery to tumors. *J Control Release* 78:81–95.
 75. Blanco E, Qian F, Weinberg B, Stowe N, Anderson JM, Gao J. 2004. Effect of fibrous capsule formation on doxorubicin distribution in radiofrequency ablated rat livers. *J Biomed Mater Res A* 69:398–406.
 76. Wang CC, Li J, Teo CS, Lee T. 1999. The delivery of BCNU to brain tumors. *J Control Release* 61:21–41.
 77. Haaga JR, Exner AA, Wang Y, Stowe NT, Tarcha PJ. 2005. Combined tumor therapy by using radiofrequency ablation and 5-FU-laden polymer implants: Evaluation in rats and rabbits. *Radiology* 237:911–918.
 78. Zheng JH, Chen CT, Au JL, Wientjes MG. 2001. Time- and concentration-dependent penetration of doxorubicin in prostate tumors. *AAPS PharmSci* 3:E15.
 79. Lu Y, Segal E, Leamon CP, Low PS. 2004. Folate receptor-targeted immunotherapy of cancer: Mechanism and therapeutic potential. *Adv Drug Deliv Rev* 56:1161–1176.
 80. Roselt P, Meikle S, Kassiou M. 2004. The role of positron emission tomography in the discovery and development of new drugs; as studied in laboratory animals. *Eur J Drug Metab Pharmacokinet* 29:1–6.
 81. Moon WK, Lin Y, O'Loughlin T, Tang Y, Kim DE, Weissleder R, Tung CH. 2003. Enhanced tumor detection using a folate receptor-targeted near-infrared fluorochrome conjugate. *Bioconjug Chem* 14:539–545.
 82. Ntziachristos V. 2006. Fluorescence molecular imaging. *Annu Rev Biomed Eng* 8:1–33.
 83. Weinmann HJ, Ebert W, Misselwitz B, Schmitt-Willich H. 2003. Tissue-specific MR contrast agents. *Eur J Radiol* 46:33–44.
 84. Ye F, Ke T, Jeong EK, Wang X, Sun Y, Johnson M, Lu ZR. 2006. Noninvasive visualization of in vivo drug delivery of poly(L-glutamic acid) using contrast-enhanced MRI. *Mol Pharm* 3: 507–515.
 85. Nasongkla N, Bey E, Ren J, Ai H, Khemtong C, Guthi JS, Chin SF, Sherry AD, Boothman DA, Gao J. 2006. Multifunctional polymeric micelles as cancer-targeted, MRI-ultrasensitive drug delivery systems. *Nano Lett* 6:2427–2430.
 86. Szymanski-Exner A, Stowe NT, Lazebnik RS, Salem K, Wilson DL, Haaga JR, Gao J. 2002. Noninvasive monitoring of local drug release in a rabbit radiofrequency (RF) ablation model using X-ray computed tomography. *J Control Release* 83:415–425.
 87. Szymanski-Exner A, Stowe NT, Salem K, Lazebnik R, Haaga JR, Wilson DL, Gao J. 2003. Non-invasive monitoring of local drug release using X-ray computed tomography: Optimization and in vitro/in vivo validation. *J Pharm Sci* 92:289–296.
 88. Exner AA, Weinberg BD, Stowe NT, Gallacher A, Wilson DL, Haaga JR, Gao J. 2004. Quantitative computed tomography analysis of local chemotherapy in liver tissue after radiofrequency ablation. *Acad Radiol* 11:1326–1336.
 89. Gao J, Qian F, Szymanski-Exner A, Stowe N, Haaga J. 2002. In vivo drug distribution dynamics in thermoablated and normal rabbit livers from biodegradable polymers. *J Biomed Mater Res* 62:308–314.
 90. Qian F, Stowe N, Liu EH, Saidel GM, Gao J. 2003. Quantification of in vivo doxorubicin transport from PLGA millirods in thermoablated rat livers. *J Control Release* 91:157–166.
 91. Blanco E, Weinberg BD, Stowe NT, Anderson JM, Gao J. 2006. Local release of dexamethasone from polymer millirods effectively prevents fibrosis after radiofrequency ablation. *J Biomed Mater Res A* 76:174–182.
 92. Coussens LM, Werb Z. 2002. Inflammation and cancer. *Nature* 420:860–867.
 93. Raz A, Levine G, Khomiak Y. 2000. Acute local inflammation potentiates tumor growth in mice. *Cancer Lett* 148:115–120.
 94. Wang JM, Deng X, Gong W, Su S. 1998. Chemokines and their role in tumor growth and metastasis. *J Immunol Methods* 220:1–17.
 95. Nikfarjam M, Malcontenti-Wilson C, Christophi C. 2005. Focal hyperthermia produces progressive tumor necrosis independent of the initial thermal effects. *J Gastrointest Surg* 9:410–417.
 96. Nikfarjam M, Muralidharan V, Christophi C. 2005. Mechanisms of focal heat destruction of liver tumors. *J Surg Res* 127:208–223.
 97. Tozer GM, Kanthou C, Baguley BC. 2005. Disrupting tumour blood vessels. *Nat Rev Cancer* 5:423–435.
 98. Ramirez LH, Zhao Z, Rougier P, Bognel C, Dzodic R, Vassal G, Ardouin P, Gouyette A, Munck JN. 1996. Pharmacokinetics and antitumor effects of mitoxantrone after intratumoral or intraarterial hepatic administration in rabbits. *Cancer Chemother Pharmacol* 37:371–376.
 99. Yoon CJ, Chung JW, Park JH, Yoon YH, Lee JW, Jeong SY, Chung H. 2003. Transcatheter arterial chemoembolization with paclitaxel-lipiodol solution in rabbit VX2 liver tumor. *Radiology* 229: 126–131.
 100. Boehm T, Malich A, Goldberg SN, Hauff P, Reinhardt M, Reichenbach JR, Muller W, Fleck M, Seifert B, Kaiser WA. 2002. Radio-frequency ablation of VX2 rabbit tumors: Assessment of

- completeness of treatment by using contrast-enhanced harmonic power Doppler US. *Radiology* 225:815–821.
101. Kashef E, Roberts JP. 2001. Transplantation for hepatocellular carcinoma. *Semin Oncol* 28:497–502.
 102. Ashby LS, Ryken TC. 2006. Management of malignant glioma: Steady progress with multimodal approaches. *Neurosurg Focus* 20:E3.
 103. Shim WS, Kim JH, Kim K, Kim YS, Park RW, Kim IS, Kwon IC, Lee DS. 2007. pH- and temperature-sensitive, injectable, biodegradable block copolymer hydrogels as carriers for paclitaxel. *Int J Pharm* 331:11–18.
 104. Jeong B, Bae YH, Lee DS, Kim SW. 1997. Biodegradable block copolymers as injectable drug-delivery systems. *Nature* 388:860–862.
 105. Johnson PC, Saidel GM. 2002. Thermal model for fast simulation during magnetic resonance imaging guidance of radio frequency tumor ablation. *Ann Biomed Eng* 30:1152–1161.

Functionalized Micellar Systems for Cancer Targeted Drug Delivery

Damon Sutton,¹ Norased Nasongkla,^{1,2} Elvin Blanco,¹ and Jinming Gao^{1,3}

Received November 6, 2006; accepted December 21, 2006; published online March 24, 2007

Abstract. Polymer micelles are rapidly becoming a powerful nanomedicine platform for cancer therapeutic applications due to their small size (10–100 nm), *in vivo* stability, ability to solubilize water insoluble anticancer drugs, and prolonged blood circulation times. Recent data from clinical trials with three micelle formulations have highlighted these and other pharmacokinetic advantages with reduced systemic toxicity and patient morbidity compared to conventional drug formulation. While the initial anti-tumor efficacy of these systems seems promising, a strong research impetus has been placed on micelle functionalization in order to achieve tumor targeting and site-specific drug release, with the hope of reaching a more pronounced tumor response. Hence, the purpose of this review is to draw attention to the new developments of multi-functional polymer micelles for cancer therapy with special focus on tumor targeting and controlled drug release strategies.

KEY WORDS: active targeting; cancer nanomedicine; micelle pharmacokinetics; polymer micelles; responsive drug release.

INTRODUCTION

Recently, polymer micelles have gained considerable attention as a versatile nanomedicine platform with greatly improved drug pharmacokinetics and efficacious response in cancer treatment. Typical chemotherapeutic agents have low water solubility, short blood half-lives, narrow therapeutic indices, and high systemic toxicity, which lead to patient morbidity and mortality while compromising the desirable therapeutic outcome of the drugs. Polymer micelles have been shown to increase the aqueous solubility of chemotherapeutic agents and prolong their *in vivo* half-lives with lessened systemic toxicity. This is demonstrated in early phases of clinical trials in Japan, Korea, and the United States (1–3).

Several excellent reviews are currently available in the literature on micellization behavior, drug encapsulation, and general use of micelles as drug delivery systems (4–13). The purpose of this review is to provide an updated, comprehensive review on recent breakthroughs and applications of polymer micelles for tumor-specific therapy. First, a brief overview on micelle structure and composition will be presented, followed by a summary on the clinical pharmacokinetics of “stealth” micelles. This will be followed by a comprehensive review of micelle systems consisting of

additional functionality. Special emphasis will be placed on micellar systems that exploit unique molecular signatures on cancer cells for active targeting applications or responsive mechanisms (e.g. pH, temperature) for site-specific drug release.

MICELLE STRUCTURE AND COMPOSITION

Polymer micelles are composed of amphiphilic macromolecules that have distinct hydrophobic and hydrophilic block domains, with the structure of the copolymers usually being a di-block, tri-block, or graft copolymer. Within each copolymer system, aqueous exposure induces the hydrophobic and hydrophilic segments to phase separate and form nanoscopic supramolecular core/shell structures (Fig. 1). Depending on the relative size of the hydrophobic and hydrophilic segments and solvent conditions, Eisenberg *et al.* have demonstrated the formation of structures of many morphologies, including spheres, rods, vesicles, tubules, and lamellae (14–17). Although aggregates of different morphology may provide drastically different pharmacokinetic properties, as in the case of filamentous nanocarriers which can provide different flow behavior over spherical particles due to anisotropic alignment (18–20), most current applications have focused on spherical micelles and thus will be the subject of this review.

Many types of copolymers have been used for micelle formation, but the requirements of biocompatibility and oftentimes biodegradability have limited the choice of copolymers in clinical applications. Table I provides the names and structures of common copolymers for drug delivery applications. For the hydrophilic segment, the most commonly used polymer is polyethylene glycol (PEG) with a molecular weight of 2–15 kD. PEG is completely water

¹ Simmons Comprehensive Cancer Center, University of Texas Southwestern Medical Center at Dallas, 5323 Harry Hines Blvd., Dallas, Texas 75390, USA.

² Present address: Department of Biopharmaceutical Sciences and Pharmaceutical Chemistry, School of Pharmacy, University of California, San Francisco, 513 Parnassus Avenue, Health Science East 1145 B, San Francisco, California 94143, USA.

³ To whom correspondence should be addressed. (e-mail: jinming.gao@utsouthwestern.edu)

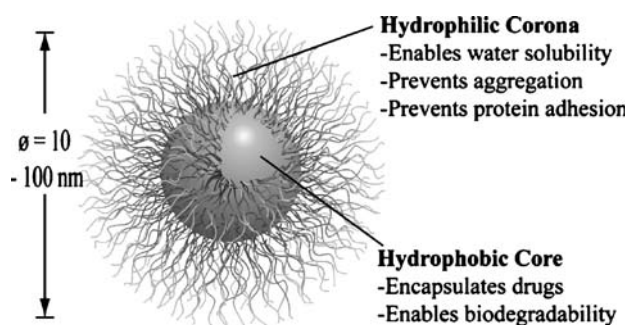


Fig. 1. Schematic illustration of the core-shell structure of a polymer micelle with intended functions of each component.

soluble, non-toxic, and uncharged, the latter property serving to lessen the possibility of undesired electrostatic interactions with plasma proteins. Other hydrophilic polymers such as poly(*N*-vinyl pyrrolidone) (PVP) (21) or poly(*N*-isopropyl acrylamide) (pNIPAM) (22–24) have also been used to form the micelle corona layer. For the hydrophobic segments, the most common materials are hydrophobic polyesters, but other materials, such as polyethers, polypeptides, or poly(β -amino ester) have also been used. Polyesters and polyamides can undergo hydrolytic and enzyme-catalyzed degradations, respectively, and are considered biodegradable. As an example of a micelle forming copolymer, Pluronic is a ternary copolymer of PEG and poly(propylene oxide) (PPO) oriented in a PEG-PPO-PEG configuration. Upon micellization, the hydrophobic PPO segments form the core while the PEG segments form the corona.

The core-shell structure of polymer micelles affords several advantages for drug delivery applications. Firstly, drug encapsulation within the micelle core allows for solubilization of water insoluble drugs. For example, the water solubility of paclitaxel can be increased by several orders of magnitude from 0.0015 to 2 mg/ml through micelle incorporation (25). Secondly, micelles have prolonged blood half-lives because PEG prevents opsonization, effectively reducing micelle uptake by the reticuloendothelial system (RES) (26,27). Thirdly, their small size (10–100 nm) makes them suitable for injection and enhanced tumor deposition due to the enhanced permeability and retention (EPR) effect stemming from the leakiness of tumor vasculature (28). Finally, their chemistry allows for the development of multifunctional modalities that can enhance micelle accumulation in cancerous tissues and facilitate drug internalization inside cancer cells.

CLINICAL PHARMACOKINETICS OF STEALTH MICELLES

Currently, clinical data on three polymer micelle systems, SP1049C, NK911, and Genexol-PM have been reported (1–3). All three are ‘stealth’ micelle formulations, i.e. they all have stabilizing PEG coronas to minimize opsonization of the micelles and maximize blood circulation times. SP1049C is formulated as doxorubicin (DOX)-encapsulated Pluronic micelles, NK911 is DOX-encapsulated micelles from a copolymer of PEG and DOX-conjugated poly(aspartic acid),

and Genexol-PM is a paclitaxel-encapsulated PEG-PLA micelle formulation. The pharmacokinetic results of the three formulations are summarized in Table II. These data were compared to free DOX (doxorubicin hydrochloride) (29) as well as liposome-delivered DOX (Doxil[®]) (30) and Cremophor[®] EL-delivered paclitaxel (31).

Comparison among the various formulations of doxorubicin reveals several distinguishing characteristics. Free DOX has an elimination phase half-life ($t_{1/2,\beta}$), or physiological excretion half-life, of 48 min. Both polymer micelle formulations roughly triple the half-life, bringing it to a range of 2.3–2.8 h whereas the liposomal form greatly increases the half-life to 45.9 h. Since different formulations are evaluated using differing compartmental models, quantitative comparison of half-lives between formulations can be difficult. However, comparison of the common parameters, such as clearance rates, is more illustrative. The drug clearance rates (C_L) from different formulations serve to highlight further differences. The C_L of the free DOX is 14.4 ± 5.6 ml/(min kg), while pluronic micelles did not significantly improve the C_L value (12.6 ml/(min kg)), presumably due to the low stability of Pluronic micelles which may rapidly dissociate upon dilution. In contrast, DOX encapsulation within the more stable NK911 micelles reduced the clearance rate by almost half (6.7 ± 1.1 ml/(min kg)). Liposomal DOX has a remarkably decreased clearance rate (0.02 ml/(min kg)), which is two orders of magnitude smaller than either micellar formulation. This very slow clearance rate may at first appear ideal, however several factors indicate otherwise. Firstly, the extremely low volume of distribution ($V_{ss} = 0.08$ l/kg) suggests that liposomal DOX may remain in the bloodstream and not extravasate into tumor tissue as widely as comparable micelles. Micelles, on the other hand, have been shown to accumulate more readily inside tumors compared to liposomes, primarily due to the smaller micellar size (32). Interestingly, another study found that the high blood residence times of liposomally formulated DOX may cause increased levels of stomatitis (33).

The other major chemotherapeutic drug which has been clinically used in micelles is paclitaxel (Taxol[®]), a potent anticancer drug with very low water solubility (1.5 μ g/cc). As a result, this agent already requires administration with a surfactant carrier. Currently, the clinically approved carrier to solubilize the drug is Cremophor[®] EL, a polyethylene glycol modified castor oil. Though useful in drug administration, the delivery agent itself has negative side effects such as hypersensitivity reactions (HSR) and neuropathy. To overcome this limitation, an alternate delivery system using PEG-PLA micelles, Genexol-PM, has been developed.

Cremophor[®] EL and Genexol-PM formulations have similar drug pharmacokinetics at 230 mg/m² dose (Table II). Both have similar half-lives (8.9 ± 1.8 and 11.0 ± 1.9 h from Cremophor[®] EL and Genexol-PM, respectively), and clearance rates (3.9 ± 1.1 and 4.8 ± 1.0 ml/(min kg), respectively). However, the Genexol-PM formulation shows marked improvement in patient morbidity. None of the patients observed in the Genexol-PM trial showed HSRs. Moreover, a lower degree of myelosuppression was observed in the Genexol-PM formulation than in the conventional one. Consequently, the PEG-PLA micelles allow for a consider-

Table I. Commonly Used Block Segments of Copolymers used in Micellar Drug Delivery

Copolymers	Abbreviations	Repeating Unit Structure
Corona segment		
Poly(ethylene glycol)	PEG, PEO	
Poly(N-vinyl pyrrolidone)	PVP	
Poly(N-isopropyl acrylamide)	pNIPAM, NIPAM	
Core segment		
<i>Polyethers</i>		
Poly(propylene oxide)	PPO	
<i>Polyesters</i>		
Poly(L-lactide), Poly(D, L-lactide)	PLA, PDLLA*	
Poly(lactide-co-glycolide)	PLGA	
Poly(ε-caprolactone)	PCL	
Poly(β-amino ester)		
<i>Polyamides</i>		
Poly(L-histidine)	pHis	
Poly(L-aspartic acid) derivatives	pAsp	
Poly(L-glutamic acid) derivatives	pGlu	
* Depending on stereochemistry		

able increase in maximum tolerated dose (MTD) with an MTD of 390 mg/m² compared to 230 mg/m² for Cremophor[®] EL. A final interesting note is that in the Genexol-PM trial, two patients showed tumor response despite previous paclitaxel failure in their treatments (3).

Clinical data demonstrates the distinct pharmacokinetic advantages of micelle-delivered drugs over free drugs. All of the doxorubicin micelle formulations show improved half-lives, slower clearance rates and increased area under plasma concentration (AUC) values over unencapsulated doxorubicin. Polymer micelles have also shown advantages in paclitaxel delivery in that they minimize toxicity associated with more traditional delivery systems. These data underscore the therapeutic potential of polymer micelles to improve cancer therapy.

FUNCTIONALIZED POLYMER MICELLES

Although stealth micelles allow for passive accumulation inside tumors with leaky vasculature, the majority of these nanoparticles are still cleared by the RES system, resulting in short half lives and unwanted micelle deposition in the liver and spleen. Development of multifunctional micelles, either through conjugation of targeting ligands on the micelle surface or a triggered release mechanism, can lessen these problems by increasing particle/drug exposure to the tumor. Fig. 2 illustrates the different types of functionality that have been introduced to micelle structures.

LIGAND-TARGETED POLYMER MICELLES

Targeting ligands are conjugated to the corona of the micelle in order to induce specific targeting and uptake of the micelle by tumor cells. These ligands tend to fall into the categories of small organic molecules, carbohydrates, antibodies, and aptamers. Table III provides an overview of reported ligand-targeted micelle formulations.

Micelles with small organic molecules as targeting ligands. The receptor for folic acid is a cell-proliferation protein that is over-expressed in many types of cancer cells including ovarian, breast, brain, and lung (34–36). The expression levels in tumors have been reported to be 100–300 times higher than those observed in normal tissue (37). It is a glycosyl-phosphatidylinositol-anchored glycoprotein that has high binding affinity to folic acid (K_d 10⁻¹⁰ M). Yoo and Park exploited the folate receptor by functionalizing folic acid onto DOX-loaded PEG-PLGA micelles by covalently conjugating the ligand via its γ -carboxyl group (38). *In vitro* cytotoxicity studies of the folate-micelles against KB cells (human nasopharyngeal epidermal carcinoma cell line) showed enhancement in cell uptake and cytotoxicity over non-targeted micelles, with the IC₅₀ of DOX/FOL micelles, DOX micelles and free DOX being 50, 70 and 75 μ M, respectively. Despite this small increase in *in vitro* cytotoxicity, the targeted micelles showed marked improvement in *in vivo* antitumor efficacy with two times decrease in the growth rate compared to non-targeted micelle control. Folate targeting was also used by these researchers to produce a DOX-based micellar system that did not contain polymer in the core (39). These targeted micellar nanoaggregates are based on a folate-PEG-DOX system which is self-assembled through hydrophobic doxorubicin association. This strategy leads to larger particles of approximately 200 nm in diameter with drug loading content as high as 57% since the majority of the nanoparticle is constructed from drug. Similar to the PLGA system, the folate-PEG-DOX nanoaggregate system showed twofold increased cytotoxicity over non-targeted aggregates, and an improved anti-tumor efficacy by a 40% decrease in tumor volume over free drug administration.

Park *et al.* also used folic acid as a targeting ligand but with a different folate conjugation strategy. In this case, folic acid was attached to the hydrophobic end of PEG-PCL block copolymer. Paclitaxel was then encapsulated (40,41). While it is unusual to couple a targeting ligand to the hydrophobic portion of the micelle, the authors reported folate to be

Table II. Comparison of Clinical Pharmacokinetics for Different Micellar Nanocarriers and Corresponding Commonly Used Formulations

Formulation	Free DOX ^a	SP1049C ^a	NK911 ^a	Doxil ^{®b}	Taxol ^{®c}	Genexol ^c
Drug Carrier	DOX DOX-HCl in 0.9% NaCl	DOX Pluronic micelles, mixture of L61 and F127	DOX PEG5k-pAsp ₃₀ - (DOX) _{45micelles}	DOX PEG-stabilized liposome	Paclitaxel Cremophor [®] EL	Paclitaxel PEG-PLA
Diameter (nm)	–	22–27	40	80–90	–	20–50
No. Patients	8	26	23	14	34	21
$t_{1/2,\alpha}$ (min)	2.4 ± 0.9	6.0 ± 2.7	7.5 ± 0.7	84	21.8 ± 13.9	–
$t_{1/2,\beta}$ (h)	0.8 ± 1.1	2.4 ± 2.1	2.8 ± 0.3	45.9	8.9 ± 1.8	11.0 ± 1.9
$t_{1/2,\gamma}$ (h)	25.8 ± 11.4	50.2 ± 29.2	64.2 ± 8.9	–	–	–
V _{ss} (L/kg)	24 ± 12	–	14.9 ± 3.6	0.08	–	–
C _L (ml/(min kg))	14.4 ± 5.6	12.6 ± 0.6	6.7 ± 1.1	0.02	3.9 ± 1.1	4.8 ± 1.0
MTD (mg/m ²)	50	70	67	50	230	390
AUC μ g h/ml	1.6 ± 1.1	1.8 ± 0.3	3.3 ± 0.4	902	25 ± 6.5	27.5 ± 8.2
Reference	(29)	(1)	(2)	(30)	(31)	(3)

^a Reported pharmacokinetic data at dose of 50 mg/m².

^b Only two doses were tested in this trial, 25 and 50 mg/m², the reported values are at 50 mg/m².

^c Reported pharmacokinetic data at 230 mg/m².

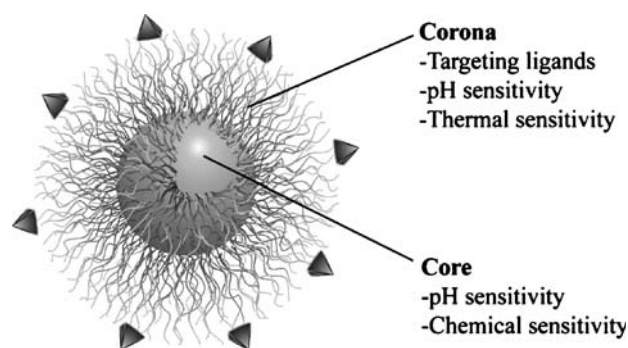


Fig. 2. Schematic diagram of functionalized polymer micelles with active targeting to tumors and responsive drug release properties.

present at the surface of the micelles via X-ray photoelectron spectroscopy (XPS) studies. These folate-encoded micelles were tested against non-malignant human fibroblasts and two cancer cell lines (MCF-7 and HeLa 229 cells). While non-targeted PEG-PCL micelles did not show significant toxicities in all three cell lines (15–22% cell death), the folate-encoded micelles increased toxicity in the two cancer cell lines (44–45% cell death) with folate receptor expression, but not in the normal fibroblasts (20%). Side-by-side comparisons of folate conjugation through hydrophilic PEG vs. hydrophobic PCL terminal ends should provide useful insight on the ligand functionalization strategy.

Micelles functionalized with peptide ligands. Small, tightly binding peptides have also been utilized for cancer-targeted drug delivery. The polypeptide nature of these ligands allows for optimization of ligand behavior via adjustment of the peptide sequence or conformation. One example of this is the cRGD peptide which targets the $\alpha_v\beta_3$ integrin. This integrin is a cellular transmembrane protein that has not only been shown to greatly affect tumor growth, local invasiveness, and

metastatic potential, but is also not readily detectable in quiescent vessels (42–44). Moreover, this membrane receptor is highly expressed in angiogenic vessels, making it a target for treating tumors, which are in a constant state of new vasculature growth. Cyclic(Arg-Gly-Asp-D-Phe-Lys) (cRGD) peptides have been developed by Kessler *et al.* to provide specific binding to $\alpha_v\beta_3$ integrins, proving to be 170 times more active than the linear form with an IC_{50} of 8 nM (45–49). Cheresch *et al.* have used ligands targeting the $\alpha_v\beta_3$ integrin to induce complete tumor regression via targeted gene delivery (50). Previous work in our lab has established the formation of cRGD-labeled polymer micelles and micelle targeting to $\alpha_v\beta_3$ -overexpressing tumor endothelial cells (SLK cells) (51). Maleimide-terminated poly(ethylene glycol)-poly(ϵ -caprolactone) (MAL-PEG-PCL) copolymer was synthesized and conjugated to cRGD ligand after micelle formation. Doxorubicin was encapsulated inside the micelle core and its intrinsic fluorescent properties ($\lambda_{ex}=485$ nm, $\lambda_{em}=595$ nm) permit for the study of cell uptake by flow cytometry and confocal laser scanning microscopy. Flow cytometry studies show that the percentage of cell uptake increased with increasing cRGD density on the micelle surface. With 5% cRGD surface density, a modest threefold increase of cell uptake was observed, while a more pronounced 30-fold increase was observed by flow cytometry with 76% cRGD attachment. In the presence of excess free RGD ligands, the $\alpha_v\beta_3$ -mediated cell uptake can be completely inhibited (51).

Micelles functionalized with carbohydrate ligands. Asialoglycoprotein receptor (ASGPR) is a membrane lectin receptor that is commonly found in liver cells (52). Carbohydrate molecules such as galactose and mannose are found as specific ligands to this receptor (53,54). As it is relatively particular to the liver, ASGPR-based strategies have been used to target drugs for treatment of liver diseases (55). In addition to being present in normal liver cells, ASGPR is also

Table III. Ligand-targeted Micelle Formulations

Ligand Type	Ligand	Polymer Composition	Micelle Size (nm)	Drug	<i>In Vitro</i> Model	Animal Model	Ref	
Small Organic Molecule	Folic Acid	PEG-PLGA	105	DOX	KB cell	KB in nu/nu mouse	(38)	
	Folic Acid	PEG-Dox	200	DOX	KB cell, A549	KB in nu/nu mouse	(39)	
Peptide	Folic Acid	PEG-PCL	50-130	Paclitaxel	MCF-7, HeLa		(40,41)	
	cRGD peptide	PEG-PCL	20-40	DOX	SLK		(51)	
	Carbohydrate	Galactose	poly(L-benzyl l-glutamate)-PEG	104	Paclitaxel	P388, SK-Hep 01, HepG2		(57)
		Lactose, Galactose, Mannose, Glucose	PEG-PLA	38–42				(58)
Antibody	Galactose	PEG-PLA	32				(59)	
	Lactose	PEG-PLA	20–40				(60,61)	
	Anti-GFA Ab mAb 2C5 mAb 2G4	Pluronic PEG-PE	Not reported 20	Haloperidol Paclitaxel	LLC, EL4 T, BT20	Mouse LLC in C57BL/6J mice	(62) (63)	
RNA Aptamer	Anti-PSMA aptamer	PEG-PLA	168	Docetaxel	LNCaP	LNCaP in BALB/c mouse	(66,67)	

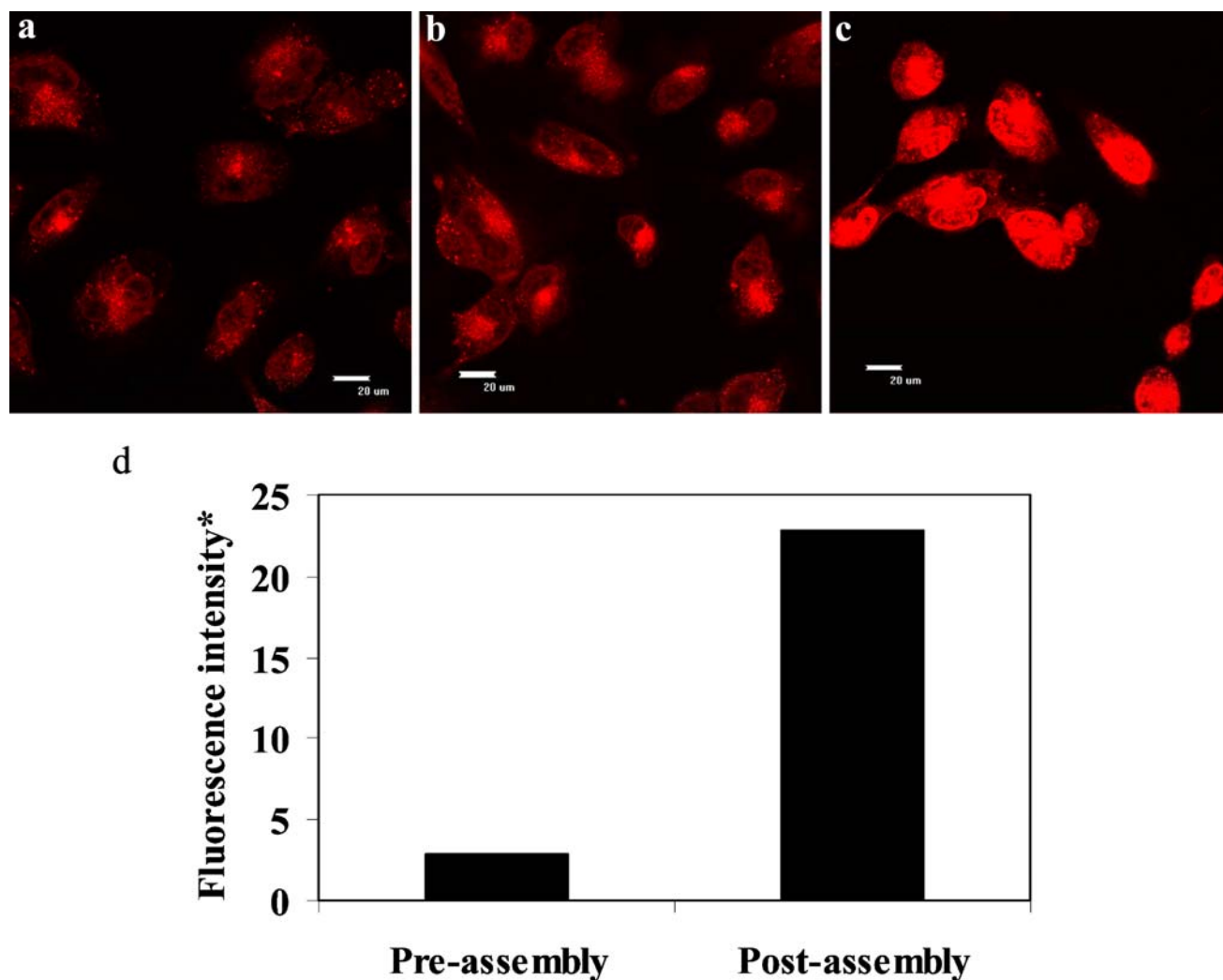


Fig. 3. Confocal laser scanning microscopy of DOX fluorescence of SLK cells after incubation for 1 h with **a** 0%, **b** 50% pre-, and **c** 50% post-micelle ligand attachment, respectively. DOX fluorescent images were obtained with $\lambda_{\text{ex}} = 485$ nm, $\lambda_{\text{em}} = 595$ nm. The scale bars are 20 μm in all three images. **d** Relative mean fluorescence intensity of 50% cRGD-DOX micelle with pre- and post-micelle ligand attachment in SLK tumor endothelial cells as measured by flow cytometry. *Fluorescence intensity corrected for non-targeted DOX-containing micelles.

overexpressed in hepatocellular carcinoma (56), which makes it a useful target for liver-specific chemotherapy. Cho *et al.* synthesized galactose-conjugated poly(ethylene glycol)-copoly(γ -benzyl L-glutamate) block copolymer (gal-PEG-b-PBLG), and loaded paclitaxel inside the micelles (57). *In vitro* cytotoxicity studies showed that an ASGPR-expressing cancer cell line had greater uptake of these micelles with a 30% increase in cytotoxicity compared to an analogous non-ASGPR expressing cell line SK-Hep01.

Kataoka *et al.* developed carbohydrate-conjugated PEG(4.9 kD)-b-PLA(4.5 kD) micelles and evaluated their binding affinity to a representative cell surface receptor, *ricinus communis* lectin *in vitro* (58–61). First, galactose and glucose were attached to a PEG-PLA copolymer (58). The chemistry is of note since the ligand was used as the initiator from which the PEG-PLA was synthesized through ring-opening polymerization. The high reaction efficiency and low polydispersity of the resulting copolymer allowed for the formation of micelles with up to 90% of the PEG chains functionalized with ligands.

The carbohydrate lactose was also used to produce targeted PEG-PLA micelles (60,61). In this case, a different but equally noteworthy chemistry was used to make the micelles, 3, 3' diethoxypropanol (DEP) was used to initiate the ring opening polymerizations and the resulting acetal-PEG-PLA was then self-assembled into micelles and incubated at pH 2 whereupon the acetal converts to an aldehyde. The aldehyde end groups on the micelle were then reacted with an amine-containing lactose via Schiff base formation, which was then reduced using NaH_3BCN . This chemistry has the advantage of creating low polydispersity block copolymers while keeping the versatility of allowing any amine-containing ligand to be attached to the micelles. Lectin binding studies of the resulting micelles demonstrated multivalent advantage of micelles over ligand-conjugated small molecules (60,61). As an example, 80% functionalized lactose-encoded micelles were found to bind in a trivalent manner with fast association kinetics ($k_a = 3.2 \times 10^4 \text{ M}^{-1}\text{s}^{-1}$) but very slow dissociation constants ($k_d = 1.3 \times 10^{-4} \text{ s}^{-1}$). This multivalent effect increased the association constant by over

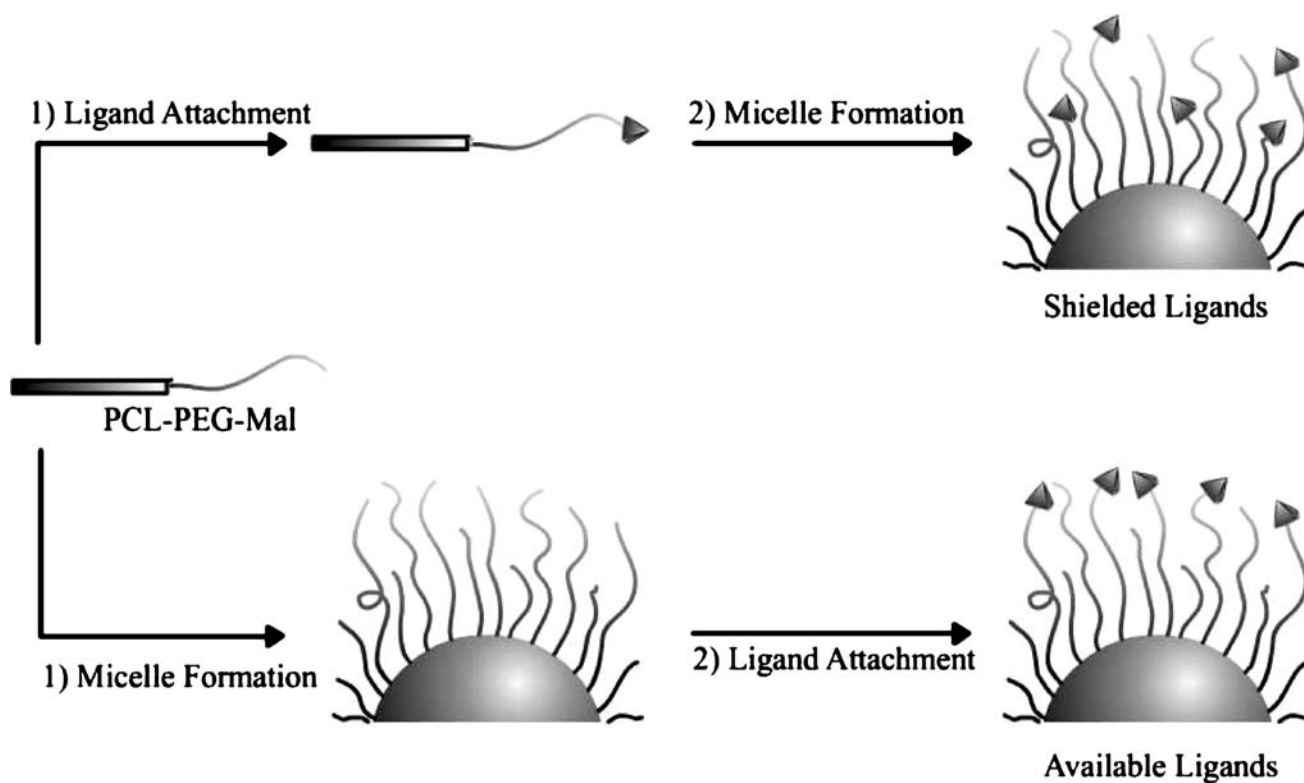


Fig. 4. Scheme showing hypothesized ligand availability through ligand attachment before (*top path*) or after micelle formation (*bottom path*).

twofold while decreasing the main dissociation constant by 145-fold compared to the 20% functionalized micelles, which behaved like monovalent systems. This was attributed to the additional ligands being able to bind to additional surface receptors after initial binding. This additional binding helps micelles to remain attached to receptor covered surfaces and prevents detachment.

Micelles with monoclonal antibodies as targeting ligands.

Another promising class of tumor targeting ligand is cancer-specific monoclonal antibodies. These large (~150 kD) and high affinity ($K_d \sim 0.1$ nM) ligands have the advantage of being able to be customized to bind specifically to a large variety of targets such as cancer cell specific antigens. These were among the first ligands used for micelle targeting, with Kabanov *et al.* using them to target haloperidol loaded pluronic micelles (the major application proposed was for psychiatric treatment). Brain specific antibody conjugation increased the neuroleptic action of the loaded micelles by fivefold over non-targeted micelles and 20-fold over free drug (62).

Torchilin *et al.* developed these ligands to target micelles to lung cancer cells. Diacyllipid-PEG-conjugated polymer (PEG-PE) micelles were functionalized with one of two antibodies, either an anti-cancer monoclonal antibody (mAb 2C5), or an anti-myosin mAb 2G4 (63). Both antibodies retained their ability to bind to their substrates after conjugation to micelles. Moreover, the 2C5 antibody targeted micelle was loaded with paclitaxel and induced a fourfold increase in drug accumulation at the tumor after 2 h, with a corresponding increase in anti-tumor efficacy. Another advantage of the use of antibodies is their high binding affinity that can result in improved behavior with as few as ten antibody ligands per micelle. As high levels of surface

modification can lead to unintended non-specific uptake of micelles, it is a great advantage to be able to target micelles with small levels of surface modification. These immunomicelles illustrate this, showing increased tumor accumulation and anti-tumor efficacy but no significant change in blood clearance rate from the non-targeted control samples (63).

Micelles functionalized with aptamers. Aptamers are DNA or RNA oligonucleotides that can be identified from screening a random library to specific molecular targets (64,65). These agents are stable *in vitro*, tumor specific, generally considered non-immunogenic and provide a new targeting platform for micellar drug delivery applications. Farokhzad *et al.* used an RNA aptamer for the prostate-specific membrane antigen (PSMA) to target PEG-PLA micelles to prostate tumors (66,67). These nanoparticles showed specific binding to PSA-expressing cancer cells, with the aptamer inducing a 77-fold increase in binding versus the control group (66), and were subsequently loaded with docetaxel and examined in prostate cancer treatment (67). *In vitro* assays using LNCaP prostate cancer cells demonstrated that aptamer-encoded micelles had a significantly increased cytotoxicity over non-targeted counterparts (the targeted particles showing roughly 50% greater lethality). *In vivo* studies were carried out via intra-tumoral injection of the micelle nanoparticles into LNCaP xenografts in a nude mouse model. The targeted nanoparticles were able to not only show significant increase in anti-tumor efficacy over their non-targeted control, but they were also able to induce total tumor regression in five of the seven mice in the group (in comparison, the non-targeted nanoparticles resulted in only two of the seven mice). In addition, the surviving mice also showed lesser levels of systemic toxicity as determined

by weight loss, than the mice treated with non-targeted counterparts. The presence of DNA or RNA degrading enzymes in the blood may prevent the use of these ligands during intravenous administration, however their initial promise warrants exploration of methodologies (such as development of aptamer analogues) that can increase the *in vivo* stability.

Strategies to optimize ligand presentation. Ligand targeting strategies have had mixed results, with some instances of striking success (38,39,68,69) as well as some with less than successful outcome (70,71). In the latter cases, lack of ligand binding had been attributed to the dynamic nature of the PEG corona which can take on conformations that buries the ligand within the hydrophilic chains (70). Moreover, the polydisperse nature of the PEG chains contributes to this problem as ligands can attach to shorter PEG chains and end up shielded by longer chains. These factors indicate that components within the micelle design can have a negative impact on the binding of attached targeting ligands to cell surfaces. These considerations have led to a series of studies and micelle designs aimed at optimizing the binding efficiency of the targeted micelles, focusing on methods that minimize the shielding effects of the PEG corona and maximize the chemical availability of the targeting ligand.

Ligand optimization strategies have been explored experimentally by our laboratory. In this case, a single ligand/micelle system was used, but two different strategies were applied for ligand attachment to the micelle. In one case, the cRGD ligand was attached to the PEG-PLA copolymer before micelle self assembly. In the second case, the micelles were assembled first, and the ligand attached afterwards, a method that would ensure that the ligand was attached to chemically available sites on the micelle surface. In both cases, doxorubicin was loaded into the micelles and uptake measured by doxorubicin fluorescence. As shown in Fig. 3, ligand attachment before micelle assembly (Fig. 3b) led to only a modest increase in cellular uptake when compared to a non-targeted micelle control (Fig. 3a). However, cRGD attachment to already formed micelles resulted in a marked increase in uptake (Fig. 3c), suggesting that the alternate ligand attachment route aided ligand availability. Confocal microscopy demonstrated this as well as flow cytometric studies (Fig. 3d). Although the two methods would appear to be similar, they are different upon consideration of the polydisperse nature of the PEG corona. As Fig. 4 illustrates, when the ligands are attached to the copolymer before micelle formation, they are likely conjugated to the shorter PEG chains within the population and suffer from shielding effects (Fig. 4, top path). This may be worsened by higher chemical reactivity of shorter polymer chains, which induces an additional selection pressure for ligands to be tethered to the short chains. There is also the possibility that some hydrophobic ligands may have aggregated inside the micelle core rather than being presented at the surface. In contrast, the post-micelle ligand addition strategy would select for ligands attaching to longer PEG chains which aids in ligand presentation for subsequent binding to cell surfaces (Fig. 4, bottom path).

Computer modeling has also been used to investigate ways to optimize ligand presentation to improve targeting. Chen and Dormidontova explored ligand valency and

bidisperse PEG layers as methods to increase ligand presentation (72) (Fig. 5). As cells are very large ($\sim 10 \mu\text{m}$ in diameter) in comparison to micelles (10–100 nm), the cell surface was modeled as a flat plane and the micelle corona modeled as a polymer brush with surface binding ligands on the chain ends. In this case, it was found that multivalency did aid in binding ability, but only when the receptors were closely packed on the cell surface. This can also be used to aid in ligand choice, as some ligand receptors, such as the $\alpha_v\beta_3$ integrin, are known to cluster together upon binding (73), bringing the receptors closer together and aiding in the efficacy of multivalent ligands. Moreover, use of a bidisperse corona design where the ligand is conjugated on the terminal end of longer PEG chains but the corona is composed of shorter PEG chains, also leads to a theoretically increased

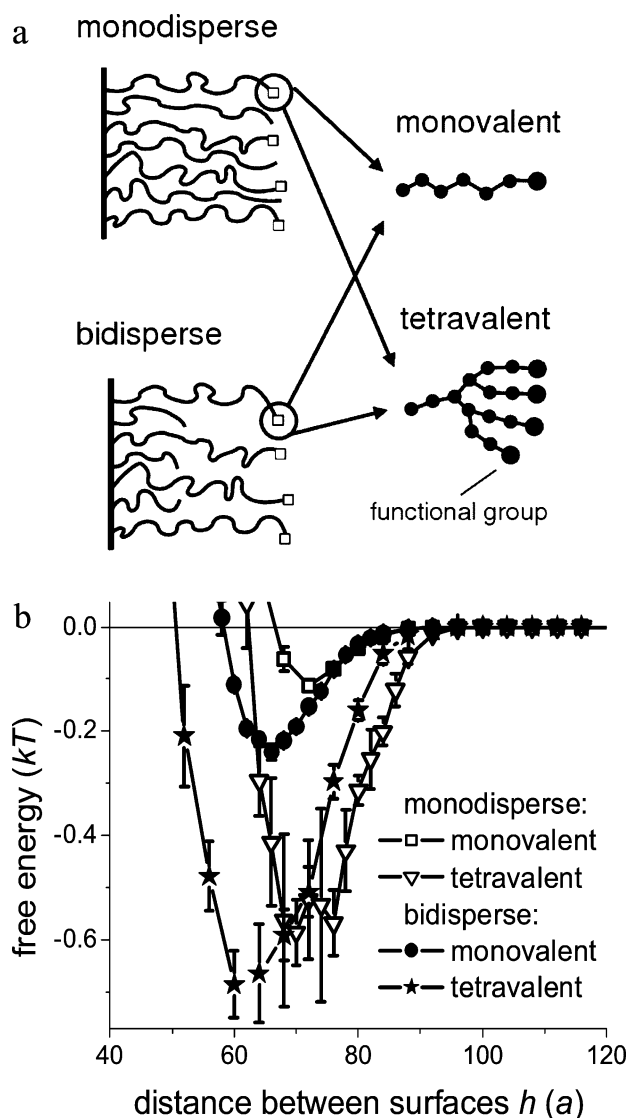


Fig. 5. **a** Schematic describing the tetravalent/monovalent ligand design and bidisperse PEG corona layers to enhance ligand presentation. See reference (72) for more details. **b** Free energy diagram describing the binding energy profile for the ligand/corona types (72).

Table IV. Micelle Formulations that Allow for Site-specific Drug Release

Polymer Composition	Release Mechanism	Size (nm)	Drug	Cancer Cell Line	Animal Model	Ref
<u>pH Sensitivity</u>						
<u>Acid Labile Bonds</u>						
(Covalent)						
PEG-PLA-DOX	Acid Labile Bond	89	DOX	HSB-2		(75)
PEG-p(Asp-Hyd-DOX)	Acid Labile Bond	65	DOX	SBC-3, KB cells, C26	Mouse	(76–78)
PEG-Acetal Linked Dendritic Polyester/ Polylysine	Acid Labile Bond	35	Nile red, DOX	MDA-MB-231		(79–81)
<u>Non-covalent pH Sensitivity</u>						
<u>Hydrophobic Core</u>						
Cationic Porphyrin Dendrimer, PEG-pAsp	Charge Neutralization	55	Porphyrin dendrimer	LLC		(82–83)
PEG-DMA-DEA	Amine protonation	30–50	Dipyridamloe			(84)
PLA-PEG PHis-PEG	Histidine protonation	50–114	DOX	MCF-7	BALB Mice	(85,87,88)
Pluronic+ β -amino ester	Beta amino ester protonation	130	Paclitaxel	BT-20, MDA-MB-231	Nu/Nu Mice	(90–92)
pNIPAM Copolymer	Protonation of Undecanoate	160–200	DOX			(93)
pNIPAM copolymer	Protonation of Undecanoate	35	AlCIPc	EMT-6		(94–96,129)
<u>Hydrophillic Core</u>						
PEG-EAMA	Nanogel Swelling	49–681				(97)
PEG-PMA	Nanogel Swelling	130	Cisplatin			(98)
<u>Temperature Sensitivity</u>						
PNIPAM-	LCST Transition	12–31	DOX	Bovine Aorta Endothelial		(23)
PNIPAM-PLA	LCST transition	40–65	DOX	Bovine Aorta Endothelial		(105)
PNIPAM-PBMA	LCST Transition	338	DOX	Bovine Aorta Endothelial		(24)
PNIPAM-copol-PLGA	LCST Transition	85–120	Paclitaxel	MDA-MB-435S		(103,105,107)
Cholesterol Endcapped Acrylamides	LCST Transition	100–200	Pyrene			(103)
<u>Ultrasound Activation</u>						
Pluronic, PEG-lipid	Ultrasound	12.9	DOX, Ruboxyl	HL-60, A2780, A2780/ADR, MCF-7	Nu/Nu mice	(115–120)
NNDEA Pluronic	Ultrasound	50–100	DOX	HL-60, DHD/ K12/TRb	BDIX Rat	(121–124)
<u>Enzyme Response</u>						
PEG-Peptide pNIPAM	Phosphorylation	50–100				(125)
<u>Oxidation</u>						
PEG-Polysulphide	Sulphide Oxidation	75				(126)

binding affinity (as calculated via free energy minimum in Fig. 5b). In this case, the shorter PEG chains provide a steric barrier preventing the ligand from curling back into the micelle corona layer.

The use of ligand targeting strategies in micelles has enabled the development of site-specific nanodevices with improved uptake and efficacy. Advances in the understanding of tumorigenesis have led to the discovery of a growing number of unique surface markers whose expression differentiates tumor from normal tissue and provides a means of achieving active targeting to tumors. This variety of ligands allows for the customization of micelles to a diverse number of cancer types.

SITE-SPECIFIC DRUG RELEASE

Drug encapsulation inside polymer micelles will considerably alter drug pharmacokinetics leading to an increase in drug targeting to tumor tissues. After reaching the targeted site, efficient drug release from micelle carriers becomes critically important to ensure drug bioavailability, and hence achieve the desired cytotoxic effect. In the section below, we review the various engineering strategies concerning the tailoring of micelle structures to trigger drug release at the tumor site. Table IV provides an overview of micelles designed for site-specific drug release.

pH sensitive drug release. Despite the general impression that the body has a uniform pH of 7.4, intravenously

administered nanodevices can encounter several instances of pH change that can facilitate drug delivery. Firstly, tumors tend to have lower pH values (as low as 5.7) than normal tissue environment (pH 7.4) (74). This acidification is due to the general characteristic of cancer cells to rely on glycolysis for metabolism. Changes in pH are also encountered once nanodevices enter cells via endocytosis. Endocytosis is the sequestration of the nanocarriers into an early endosome, which is accompanied by an increase of acidity inside the vesicle as it matures into late endosomes and heavily degradative lysosomes (pH 5.0–5.5). Both the acidic nature of tumor tissue and endocytosis provide ample applications for pH responsive micelles which release their contents upon exposure to acidic environments. Two strategies are generally used to induce pH sensitivity into a micellar system. The first is a covalent strategy involving the use of acid-labile bonds, while the second is a non-covalent strategy involving the selective protonation of pH-sensitive components inside the micelle.

Acid-labile bonds. pH sensitivity can arise from the creation of an acid labile linkage between the drug and the polymer forming the micelle (75–78). Covalent modification of the polymer with the drug allows for extremely high loading since the drug is itself an integral part of the micelle rather than merely an encapsulated agent during micelle formation. However, the main disadvantage of this method is the requirement of functional groups on the drug molecule that can be covalently modified, and since not all drugs are capable of being conjugated to a polymer in such a way, the scope of this method is limited. The most effective uses of acid labile bonds have been the direct conjugation of doxorubicin to the hydrophobic portion of a micelle forming block copolymer. Initially this was demonstrated by Park *et al.*, who used either a hydrazone or *cis*-acotinyl bond to link doxorubicin to the PLA end of PEG-PLA micelles (75). Although the *cis*-acotinyl linkage has a greater level of pH sensitivity in drug release with a roughly tenfold increase in release rate at pH 5.0 over 7.4, the *cis*-acotinyl linkage results in the release of a chemically modified drug whereas the hydrazone linkage, with a roughly fourfold increase in release rate, degrades cleanly and releases unmodified drug. The hydrazone linked micelles also have a fivefold greater cytotoxicity than free drug, given that endocytosis leads to greater uptake in the micellar DOX than passive diffusion does of the free drug. Though the PEG-PLA end modification in this case leads to favorable results, drug conjugation solely on the end group leads to a functional micelle with a relatively low loading (3.7%).

Kataoka *et al.* took a different approach and conjugated the drug to the aspartic acid residues of a polyethylene glycol poly (aspartic acid) (PEG-pAsp) copolymer via a hydrazone linkage (76–78). Though the precursor block copolymer is fully hydrophilic, the bonding of doxorubicin to the aspartic acid residues induces hydrophobicity in the pAsp segments. The resulting micelles achieved a DOX loading content as high as 42.5%; to date the highest drug loading content reported in a micelle of this size (less than 100 nm). These micelles had almost no release of drug at pH 7.4 (less than 3% after 48 h) but released drug in solutions of pH 5.5 with 25% of the drug released after 48 h. Near complete release of drug was observed at pH 3.0, with HPLC

analysis demonstrating release of functional drug. Though these micelles have less *in vitro* cytotoxicity than unconjugated drug (the IC_{50} of micelles being tenfold that of DOX), it was demonstrated via fluorescence microscopy that the micelles were indeed taken up by the cells after 3 h of exposure and drug released to the nucleus. *In vivo* studies demonstrated the utility of this micellar system. Biodistribution studies showed that while only 2% of free drug deposits in the tumor, micellar encapsulated drug improves this value to 10%. This additional tumor deposition was accompanied by a great increase in the tolerance for drug (15 mg/kg for free drug, compared to 40 mg/kg for micelle encapsulated drug). The micelles were then able to not only demonstrate greater tumor growth inhibition in mice, as well as induce complete tumor regression in 50% of the mice tested, outperforming the highest tolerated doxorubicin dose which only resulted in a complete cure in 17% of the mice (78).

Acid-labile bonds have also been used as a structural component of the micelle polymer backbone (79–81). In this way, the micelle itself can degrade as a function of pH resulting in a micelle that should be pH sensitive regardless of the drug used. These micelles are designed to release drugs as a result of acid catalyzed polymer degradation. Frechet and co-workers achieved this in a micellar system using hydrophobic groups attached to the hydrophobic dendrimer ends of a PEG-dendritic polylysine or PEG-dendritic polyester copolymer. These terminal hydrophobic trimethoxy benzyl groups were linked to the dendrimer via acid-sensitive acetal linkages. These unusual copolymers self-assembled into small micellar nanoparticles of between 20 and 50 nm with cores designed to degrade via acid catalyzed hydrolysis. Hydrolysis of the structures could be directly followed by UV/Vis spectrometry due to trimethoxybenzaldehyde residues that are released from the micelles upon degradation. The acetal group is easily hydrolyzed under acidic conditions and the resulting micelles show pH dependent degradation that is alterable via the change of the characteristics of the non-acetal portion of the hydrophobic dendrimer, with more hydrophilic cores degrading more quickly than more hydrophobic ones. In most cases, the amount of degradation seen at pH 7.4 was negligible (less than 5%) after 24 h, but high levels of degradation (80–100%) could be observed under pH 5.0 conditions for the same time period (79,81). In order to explore the use of this system for drug delivery, doxorubicin was loaded into these micelles. The DOX loaded micelles showed favorable size and loading (35 nm, 12% loading) and excellent pH sensitivity in their release, with a tenfold increase in release rate at pH 5.0 over pH 7.4. In order to account for innate DOX pH sensitivity, controls were performed by releasing DOX from a comparable non-pH responsive micellar assembly which showed only a twofold increase in release at acidic pH.

Non-covalent strategies. The other commonly used method to achieve pH sensitivity is a non-covalent strategy whereupon an ionizable component within the micelle structure alters conformation upon protonation. As an example, Kataoka *et al.* used charge–charge interactions to build a micelle core carrying a positively charged zinc porphyrin dendrimer. The core of the micelle in this case is composed of a positively charged porphyrin dendrimer which

has been neutralized by the negatively charged residues of a PEG-poly(L-aspartic acid) copolymer. This micelle is stable at neutral pH, but at pH above 8 or below 6, these micelles destabilize due to loss of charge balance in their core. This pH dependent stability results in a system which will remain stable until it is taken up by cells, whereupon the micelle will degrade after cellular uptake. These spherical 55 nm particles demonstrated roughly one third the uptake of non-encapsulated photosensitizer due to charge neutralization of the porphyrin preventing charge-charge interactions of the positively charged porphyrin with negatively charged cell membranes. While the uptake of the porphyrin was impeded by micelle encapsulation, the photodynamic efficiency of the micelles was 40 times higher than that of free porphyrin, a result of the micelle preventing porphyrin aggregation (82,83).

Whereas the above system uses a polyanion in the micelle, it is more common to build pH responsive micelles based on hydrophobic polycationic systems. Tang *et al.* designed a triblock polymer of PEG, poly(2-(dimethylamino)ethyl methacrylate) (DMA), and poly(2-diethylamino)ethyl acrylate (DEA) resulting in a system that dissolves completely in acidic solution but forms micelles at high pH (pH 8.0). Pyrene exclusion studies demonstrated that these micelles reversibly form at pH 7.0 and above, and break apart when the pH is less than 6.0. This group used the acid sensitivity of this copolymer alongside an acid sensitive model drug (dipyridamole) to make a high loading micelle (19%) without a requirement for organic solvent. Acid sensitive release of the agent was observed with a 50% increase of drug release at pH 3.0 over that at pH 7.4 (84).

Bae *et al.* used a block copolymer of polyethylene glycol and poly(L-histidine) (PEG-pHis) to fabricate pH sensitive micelles (85–88), where the histidine residues are hydrophobic at neutral pH (histidine has a pKa of 6.1) but protonate at the endosomal pH (5.5), resulting in a buffering effect that can induce micelle destabilization (85,87,88). Titration studies confirmed that the polyhistidine residues retained their buffering capacity within the physiologically relevant range between pH 8.0 and 6.0. Variable protonation of the histidine residues resulted in a copolymer whose CMC was tenfold greater at pH 5.0 than 7.4. Pyrene exclusion assays and light transmittance studies both confirmed that the micelles underwent dissociation when suspended in buffers with pH below 7.4. PEG-pHis micelles are unstable at pH 7.4 (85), but inclusion of a more stable PEG-PLA component to the micelle formulation resulted in micelles stable enough for clinical use (88). The inclusion of the second component also brings the activation pH to between 6.6 and 7.2, making these micelles viable for tumor targeting via pH changes. These micelles were further functionalized with folate targeting ligands and are more comprehensively discussed in the section on 'multifunctional micelles.'

Recently, the pH dependent solubility of poly(β -amino ester) (89) has been established for the creation of pH-sensitive micelles (90–92). These biodegradable polymers are hydrophobic at neutral pH but can become fully soluble at pH below 6.1. This pH dependent solubility can lead to almost instantaneous release of their contents from microparticles upon acidification (89). Amiji *et al.* used a strategy of surrounding a hydrophobic poly(β -amino ester) core with a PEG corona from the pluronic copolymer F108 (90–92) in

order to fabricate nanoparticles. These resulting micellar nanoparticles were loaded with paclitaxel (90) and found to form particles between 100 and 150 nm in diameter with loading content of 1% but a remarkable loading efficiency of 97%. *In vitro* microscopy studies using FITC encapsulated particles were used to demonstrate intracellular release. The pH sensitive particles showed release of FITC into the cytoplasm of the cells while a non-pH sensitive FITC nanoparticles control showed punctate fluorescence indicative of no release (91). *In vivo* studies demonstrated that the pluronic modified β -amino ester nanoparticles shared the long residence times and improved half-life that is seen in similar nanoparticles, but shows improved drug deposition in the tumor over not only free drug (23-fold improvement) but also over non-pH sensitive pluronic PCL nanoparticles (threefold improvement) (92).

To a lesser extent, poly(N-isopropylacrylamide) (pNIPAM) has been used in the design of pH sensitive micellar systems. Although pNIPAM is most known for its lower critical solution temperature (LCST) behavior in water, the temperature of the LCST can be adjusted by the incorporation of hydrophobic groups and titratable moieties such as undecanoic acid (93) or methacrylic acid (94–96) to the backbone. In the undecanoic acid case, copolymerization into a poly(N-isopropylacrylamide) backbone in order to act as a titratable group results in a temperature sensitive polymer becoming pH sensitive one. At physiological pH (7.4), the acid is deprotonated and the resulting polymer has a higher than body temperature LCST (38°C), however at lower pH (4.5), the acid becomes neutral and lowers the LCST (29°C). The resulting polymer can have an LCST above 37°C which will shift below this point in response to pH. As a result, it is believed that these polymers will become hydrophobic inside the endosome and disrupt the endosomal vesicle in the cell. Polymer micelles containing DOX were fabricated and a threefold increase of DOX release was observed upon a very sharp pH change of 6.6 over 7.4.

More extensive exploration has been done using pNIPAM with methacrylic acid and octadecylacrylate as the titratable moieties (94–96). This strategy allowed for the customization of the polymer solubility to be water insoluble above pH 6.0, but to solubilize completely at pH below 5.5. Despite the random copolymer structure, these polymers were able to form small nanoparticles of 35 nm. The small size, lack of surfactant required in creation, and critical aggregation concentration suggest micellar characteristics, such as a hydrophilic corona preventing aggregation, leading to the conclusion that these nanoparticles are indeed micelles. The photosensitizer aluminum chloride phthalocyanine (AlClPc) was incorporated into these micelles for applications involving photodynamic therapy against tumors. *In vitro* studies demonstrated the efficacy of this encapsulated photosensitizer against EMT-6 mouse mammary cells with the micelles showing no toxicity unless exposed to light, after which the LD₉₀ was found to be 6 μ m after 24 h of light exposure (94). Subsequent studies demonstrated these molecules were effective *in vivo* in EMT-6 flank tumors, with the micellar formulation providing complete tumor regression observed at a dose of 0.25 μ mol/kg (95).

Hydrophilic core micellar systems have also been developed for the purpose of pH sensitive drug release.

These systems function by creating a cross-linked hydrophilic core which swells and contracts in response to pH much like a hydrogel. Hayashi *et al.* used emulsion polymerization of a PEG-vinyl benzene with 2-(diethylamino)ethyl methacrylate using a diacrylate as a crosslinker to design such a system (97). These nanogels could be as small as 49.5 nm but swelled to over double their previous size within a very small and biologically relevant pH range (7.4–6.0). Kabanov's group used a similar strategy in his crosslinked PEG-poly(methacrylic acid) micelles (98). First calcium was used to induce micellization followed by crosslinking with a diamine. These micelles swelled under basic conditions as the acidic residues would deprotonate and a negative charge would build up within the micelle core, almost doubling the micellar size from 170 to 290 nm. Cisplatin could also be loaded into these cross-linked micelles with a 55% loading efficiency. And while the nanogel strategy for cancer targeted micelles is currently in its infancy, the large pH induced size variations suggest this strategy has a bright future.

Temperature sensitive drug release. The ability to raise local temperatures inside the body makes temperature triggered drug release a viable strategy in site-specific drug release (99). Additionally, tumors have been shown to be more vulnerable to hyperthermia than normal tissue as a result of their chaotic vasculature (99). These two factors give temperature sensitive nanosystems the capability of providing a synergistic therapy, whereupon the elevated temperature not only causes local drug release but also serves to inflict additional damage to tumor cells. Elevated temperatures have also been proposed as a way to induce micellar aggregation at the tumor site, improving biodistribution of the administered agent. In the case of the creation of temperature sensitive micelles, the most common technique is the use of an LCST behavior polymer as the corona of the micelle (23,24,100–104). The most extensively used polymer for this purpose is Poly(N-isopropylacrylamide), or pNIPAM. Pure pNIPAM homopolymer has an LCST of 32°C which can be adjusted by random copolymerization with monomers such as dimethylacrylamide in order to obtain LCST values within a desired range. The resulting micelles are stable below the LCST, but temperature increase above the LCST induces the entire system to be hydrophobic and precipitate out of solution.

Okano *et al.* initially used polystyrene (PS) to form the hydrophobic core while pNIPAM was used for the thermo-sensitive corona (23). The resulting micelles had a transition temperature of 32°C and did indeed show reversible aggregation behavior as shown by optical transmittance. Unfortunately, they did not show temperature-triggered drug release. An alternative was later found by this group in a hydrophobic core of poly(D,L-Lactide) (105). The pNIPAM/PLA micelles also showed reversible aggregation behavior, but again had a transition temperature that was too low for immediate *in vivo* use (32°C). This group developed a temperature responsive release system by using a low Tg hydrophobic polymer such as poly(butyl methacrylate) (PBMA) (24) as the core-forming segment. pNIPAM-bPBMA micelles showed reversible aggregation at a transition temperature of 34°C, and could be loaded with doxorubicin with a pronounced temperature release sensitivity, only 15% of the drug was released after 15 h at 30°C, as compared to a temperature to 37°C, where 90% drug release in the same time period. The

release could also be conditionally switched on and off using temperature cycling. Additionally, these micelles demonstrated temperature sensitive cytotoxicity, since the loaded micelles showed almost no toxicity at a 0.1 µg/ml dose at 29°C (less than 5% cell death) but greatly increased toxicity when the temperature was increased to 37°C (65% cell death). In order to determine the mechanism for release, fluorescent probes were incorporated into these micelles, revealing alterations in the core micropolarity upon heating despite the fact that the core itself is not thermoresponsive. It was proposed that a low Tg polymer core (PBMA has a Tg of 20°C) is more subject to core deformation than a high Tg core upon temperature transition of the corona forming polymer. Side-by-side comparisons with an analogous system using a high Tg core (polystyrene core, Tg=105°C) confirmed this hypothesis, as the higher Tg core micelles were designed to have the same LCST corona behavior as the lower Tg system, but showed little or no temperature dependent cytotoxicity or drug release (106). This group refined the design further by incorporating hydrophobic dimethylacrylamide (DMA) into the pNIPAM segment in order to raise the LCST temperature (105,107). These resulting systems were able to show biologically relevant transition temperatures as high as 42.5°C. The core polymer used, in this case, was PDLA, chosen for its low Tg (35°C). The DOX loaded pNIPAM-coDMA-bPDLA micelles was sufficiently mobile for temperature sensitive doxorubicin release (4–5-fold faster release at 42.5°C over 37°C), and temperature sensitive cytotoxicity was retained despite the higher Tg core.

pNIPAM/PLGA micelles have also been reported (93,108) by Yang *et al.* In this case, pNIPAM copolymerization with dimethylacrylamide (DMMAAm) resulted in materials with a desirable LCST of 39°C. The low Tg core of these micelles was also able to be sufficiently deform for temperature sensitive drug release, in particular when the PLGA segment length was short when compared to the hydrophilic region. This demonstrates a balance that must be considered when designing these systems, for longer hydrophobic segments appear to result in larger drug loading contents but a lesser intensity of temperature sensitivity to the release kinetics. In this case, paclitaxel was loaded in the micelles, rather than DOX. The more hydrophobic nature of paclitaxel allowed for very high loading (20%) and functional loading efficiency (50%). Fine tuning of the temperature sensitive and hydrophobic segment lengths allowed for the creation of a system which showed temperature sensitivity over a very tight range, with a fourfold increase in paclitaxel release and eightfold increase in cytotoxicity at 39.5°C over those at 37°C.

Other methods have been used to adjust the LCST behavior of pNIPAM. Hydrophobic grafting and end capping also results in polymers capable of temperature sensitive micellar systems (103). These systems tend to produce larger micellar particles than block copolymer strategies, but manipulation of the LCST behavior of the materials simply consists of adjusting graft density or copolymer content. Liu *et al.* attached cholesterol onto a pNIPAM copolymer in this fashion, resulting in an amphiphilic polymer capable for forming micellar constructs and encapsulating drug (103). Cholesterol end-capping resulted in a polymer with an LCST too low for use *in vivo* (33°C), but the grafting strategy

resulted in a material with LCST in the desirable range of slightly above body temperature (38°C). In spite of this, temperature increase only induced a roughly 50% increase in drug release, possibly due to the inability of the pNIPAM transition to sufficiently deform the micelle core.

Ultrasound-triggered drug release. Ultrasound is used in medicine for diagnostic and therapeutic applications and has proven to be a non-invasive method to access and treat many problems including strokes, osteoporosis, and cardiovascular disease (109). This method is also currently being explored as a trigger for drug release for either implanted drug depots (110) or injected nanodevices such as liposomes (111). The complexity of interactions of tissue with ultrasound gives insight as to the utility of this method for drug delivery. The most immediate effect is the local increase in temperature of the exposed tissue as a result of ultrasound waves which was shown to be sufficient to induce drug release in appropriately designed micelles. Cavitation also occurs, where small oscillating bubbles are rapidly produced and collapsed. This exposure has been shown to induce shear forces on tissue and has many effects including increasing the permeability of the cell membrane (112) and increasing the uptake of gene delivery vectors (109). Finally, ultrasound treatment produces small amounts of highly reactive free radical species which could possibly serve as a chemical trigger to an ably designed system.

To date, the most extensive exploration of ultrasound triggered drug release in polymer micelles has been done with pluronic micelles. As mentioned previously, pluronic is a ternary copolymer of PEG and PPO that has been shown to have little cytotoxicity and has been used for many biological applications including as a bioadhesive, hydrogel matrix (113), and in gene delivery (7). The polymer also appears to have a synergistic effect with some chemotherapeutic agents and has been proposed to inhibit the p-glycoprotein that causes multi-drug resistance in many cancer cells (114). Pitt *et al.* explored ultrasound as a means to induce drug release of doxorubicin from pluronic micelles (115,119). Even without ultrasound, pluronic has a synergistic effect with the doxorubicin, increasing the toxicity of the chemotherapeutic agent twofold in spite of decreased uptake of the doxorubicin into the cells. Ultrasound treatment further increased the toxicity of the drug containing micelles another sixfold (118). In order to explain this, it was proposed that the presence of pluronic unimers aided the toxicity of the drug (119) but the micelles actually sequestered drug away from the cells until ultrasound induced drug release (115,119). The presence of sequestered drug inside the hydrophobic core was determined fluorescently using a doxorubicin analogue, ruboxyl, and it was found that up to 70% of the ruboxyl was sequestered inside of the micelles (118). This hypothesis was further confirmed upon exploration of DNA damage to the treated cells, where micelle encapsulated doxorubicin did not show detectable DNA damage (via Comet assay) unless ultrasound was applied. Flow cytometric exploration suggested that ultrasound also increased the permeability of the cell membrane as well as induced DOX release from the micelles (119). The frequency of ultrasound was also found to affect drug release from pluronic micelles, with an increase of the ultrasound frequency from 67 kHz to 1 MHz lessening the degree of drug release from the micelles by threefold. Despite the decrease in

drug release, the increased frequency did increase cell uptake, suggesting that the ultrasound increased cell permeability.

Pluronic micelles have the disadvantage of being less stable upon dilution than most other polymer micelle systems, with micelle degradation being reported upon injection (120). As a result, this group incorporated a PEG-phospholipid (PEG-DSPE) making a mixed, stabilized micelle for use in animal studies (120). This system was used in extensive *in vivo* tests exploring anti-tumor efficacy and flow-cytometric biodistribution studies. In these studies, micelles were administered to mice followed by removal of the organs and flow cytometric characterization of the DOX uptake within the tissues. Ultrasound was found to improve the anti-tumor efficacy of both free DOX and micelle incorporated DOX. In the latter case, the ultrasound was able to delay tumor growth an additional 2.6 days over micelles without ultrasound. The biodistribution studies also demonstrated advantages to ultrasound mediated release, with application of ultrasound not only increasing the level of drug accumulation in the tumor (as measured by flow cytometry of recovered tissue), but also lowering the level of drug accumulation in the kidneys. This lower level of kidney exposure, as compared to tumor exposure, was attributed to released drug being eliminated by the kidney rather than micelles, which could be retained. Heart exposure was also lessened, an important result as cardiotoxicity is a major side-effect of traditional doxorubicin administration. In this study, DOX loaded PEG-pAsp(Z) micelles were also studied, and found to convey the same levels of biodistribution improvement as the stabilized pluronics.

Another way to stabilize pluronic micelles is to use an interpenetrating poly(diethylacrylamide) (NNDEA) network inside the micelle core (121–124). These plurogel micelles are equally able to encapsulate doxorubicin, release it upon ultrasonic stimulation, and show the same synergistic effects with drug toxicity as unstabilized pluronics. The plurogels are, however, much more stable upon dilution, with a half-life of roughly 17 h whereas unstabilized micelles rupture almost immediately upon dilution (122). The ability to remain stable upon dissolution allowed these micelles to be used *in vivo* with success. A mouse animal model was implanted with two tumors and given these core-stabilized pluronic micelles loaded with doxorubicin. One of the tumors was sonicated while the other was not and it was demonstrated that the sonicated tumors showed greater response to the chemotherapeutic treatment (124). It is difficult to determine the exact mechanism by which the ultrasound aided the pluronic micelles *in vivo*. The improvement can be due to increased release of the drug at the site, improved extravasation of the micelles as a result of ultrasound exposure to the angiogenic vessels, or a complex interplay of the two effects.

Drug release due to chemical sensitivity. Attempts have been made in micellar systems that respond to more specialized chemical stimulus than pH, temperature, or ultrasound. Although these are in the minority of the functionalized micelle research, they are worth noting.

An enzyme responsive system was designed based on a polypeptide that is a substrate of protein kinase A (125). This polypeptide was linked to pNIPAM and PEG moieties resulting in a micelle-forming polymer at 36°C. These micelles

had a core of pNIPAM and peptide with a PEG corona. Upon exposure to the protein kinase, the peptide portion of the micelle became phosphorylated and hydrophilic, driving the LCST to 40°C, and disintegrating from 200 nm particles to 100 nm, with a corresponding change of the aggregate mass of the nanoparticles from 10 to 2 million Daltons. This is the first report of an attempt at a protein kinase responsive micelle system.

Hydrogen peroxide (H₂O₂) and superoxide radicals are reactive oxygen species that are present in many cancer cells. One system sought to use these as a trigger for a responsive system by creating large polymer vesicles that collapse into smaller micelles upon H₂O₂ exposure (126). These vesicles were based on polymers with a poly(propylene sulphide) hydrophobic segment and a PEG hydrophilic segment. Presence of H₂O₂ oxidizes the sulphide residues into more hydrophilic sulphoxide residues disrupting the vesicles (200–500 nm) that result in formation of much smaller wormlike micelles (~20 nm), the structures and sizes of which were observed via TEM. These nanosystems required an unusually high H₂O₂ concentration (3%) for this conversion to happen, but this method of micelle stimulus shows promise and may yet prove to be more applicable once it has become more finely tuned.

Multi-functional micellar systems. The newest generation of cancer-targeted polymer micelles is based on systems with multiple functionalities. The architecture of a micelle with distinguishable surface, corona, and core allows for the customization of each region to provide functionality. These novel systems use the synergy of receptor mediated endocytosis and pH sensitivity to result in systems that both show enhanced tumor targeting as well as enhanced intracellular drug bioavailability.

Kataoka's group used folic acid to enhance their previous PEG-p(Asp-Hyd-Dox) micelles. As mentioned earlier, the untargeted formulation does show anti-tumor efficacy, but the micelle formulation appears to lessen the cytotoxicity of the encapsulated DOX. The folic acid ligand was linked to the micelle surface in order to selectively increase the uptake of the micelles, increasing their cytotoxicity while retaining low toxicity to non-folate receptor expressing tissues. Ligand targeting improved the cytotoxicity of the micelles, roughly doubling the toxicity of the micelles to KB cells after a 3 h exposure. Given a 24 h exposure, the targeted micelles showed to be equally as cytotoxic as free DOX and tenfold more cytotoxic than the untargeted formulation. Flow cytometry confirmed that the enhanced toxicity is a result of increased uptake of the ligand targeted micelles (77).

Bae *et al.* expanded on their PEG-pHis pH sensitive system (85,87,88) by adding ligand targeting function. Folic acid was conjugated to the pH sensitive micelles resulting in a multi-functional system which incorporated both ligand targeting for enhanced cell uptake and pH sensitivity for enhanced intracellular release. This system performed well *in vitro*, showing equal cytotoxicity as free DOX against MCF-7 cells (88). Further studies on multi-drug resistant MCF-7 cells showed this system to be more than 90% cytotoxic at a concentration of 10 µg/ml while free DOX shows only 10% cytotoxicity (87). This overcoming of the MDR phenotype may have resulted from the alteration of the mechanism of DOX uptake, with the folate targeted micelles being taken up via receptor mediated endocytosis, as

opposed to free drug passively diffusing across the membrane. The authors hypothesized that folate mediated receptor endocytosis may overcome the multi-drug efflux pumps. The *in vivo* efficacy was evaluated in mice bearing normal MCF-7 and drug resistant MCF-7 xenografts, with the pH sensitive folate-DOX-micelles showing a 3.6–4.5-fold and a 2.7-fold lesser tumor growth than free drug administration, respectively. Biodistribution studies also showed a much longer circulation time of DOX in blood for both folate and folate-free micelles compared to free DOX. Tumor distribution studies showed that folate-micelles allowed for 20 times more accumulation of DOX in solid tumors than free DOX and three times more than folate-free micelles, which correlates with the improved tumor efficacy with folate-micelles.

Bae *et al.* have also added a previously unsuggested aspect of pH sensitive ligand presentation to the above system. In this case, the targeting ligand was linked to a short block of histidine residues. At neutral pH, the hydrophobic histidine chain draws the ligand near the core of the micelle. Upon acidification, the protonated histidine chain brings the ligand out to the corona where it can be presented to receptor sites (86). These micelles showed pH sensitive cell uptake over a narrow pH change from 7.2 to 7.0, with a tenfold increase in cell uptake at pH 7.0 over that at 7.2. This functionality results in a micellar system that could travel through the bloodstream, specifically present its binding ligands to cells in acidic tumor environments, undergo receptor mediated endocytosis, selectively release drug inside the cell, while preventing non-specific uptake.

Torchilin *et al.* also designed a pH-controlled targeted micelle system via a multidisperse pH sensitive corona design (127). In this system, two targeting ligands are employed on PEG-phospholipid micelles. The first is an antibody attached to the end of a long PEG chain (Mw 3400). The second is a secondary targeting ligand, such as TAT peptide, which is attached to the micelle core via short PEG chains (Mw 2000). The majority of the corona, in this case, is composed of intermediate length PEG chains tethered to the micelle core via pH sensitive hydrazone linkages. Under neutral pH, these 7–15 nm micelles can bind tightly to cell surfaces via the antibody targeting, aiding in micelle accumulation at tumor sites. At low pH environments, shedding of many of the PEG chains led to 'de-shielding' the secondary ligand, which induces delivery of the payload to desired sites within the cell, such as the nucleus. Chemical availability of the antibody was preserved at both pH 8.0 and 5.0 as determined by ELISA assay. Biotin was used as a model 'hidden function,' and micelle retention in an avidin column showed the shielding effects. These dual-targeted micelles showed small amounts of retention in avidin columns (15%), however, when incubated at pH 5.0 for 15 min before column exposure, micelle retention increased to 75%, demonstrating deshielding of the biotin allowing for binding. Similar experiments using the TATp moiety as a hidden ligand demonstrated this effect in cancer cell lines. In both the cases of micelles and liposomes, little or no cell uptake was observed with the shielded systems, but short incubations (30 min) at pH 5.0 resulted in de-shielding and visible increase in uptake as detected by fluorescence microscopy.

A tri-functional micelle design has also been recently published (128). This design carries ligand targeting, pH

sensitivity, and image contrast. Gao *et al.* incorporated superparamagnetic iron oxide (SPIO) nanoparticles into a doxorubicin loaded, cRGD targeted, PEG-PLA micelle. The resulting 46 nm micelles enhanced cell specificity and uptake due to the cRGD ligand, demonstrated pH-triggered release of doxorubicin, and achieved MRI ultrasensitivity. In this case, increased cell uptake could be measured via flow cytometry, a method that can only be used *in vitro*, as well as via magnetic resonance imaging in tumor-bearing animals *in vivo*. This micelle design has the capability of not only treating tumors, but also being imaged non-invasively *in vivo*, so that micelle deposition can be correlated to tumor regression.

CONCLUSION AND FUTURE DIRECTIONS

Polymer micelles are becoming a powerful nanotherapeutic platform that affords several advantages for cancer-targeted drug delivery, including increased drug solubilization, prolonged blood half-lives, preferential accumulation in tumor sites, and a decrease in toxic side effects. Even in their simplest form, when a chemotherapeutic agent is solubilized in the micelle core, micelles have shown marked benefits to cancer therapy. However, the technology is still lacking in tumor specificity and controlled release of the entrapped agents. Hence, the focus has gradually shifted from passive targeting micelles to active targeting and responsive systems that carry additional mechanisms to aid in micelle accumulation at the site of action as well as site-specific release. The picture of the ideal micelle delivery system harkens back to the original vision of Paul Ehrlich's 'magic bullet' more than 100 years ago, where an agent introduced into the bloodstream is able to selectively target diseased tissue while leaving healthy tissue untouched. Great strides in cancer biology have yielded numerous new cancer-specific molecular targets that distinguish tumors from normal tissue. Despite these advances, cancer is an extremely heterogeneous disease and its treatment will likely involve a multifaceted approach rather than a single functionality. The previously discussed ligand targeted, pH sensitive formulations are promising examples of how micelle multifunctionality can lead to a fusion of chemical customization with biological insight so as to exploit multiple routes for tumor treatment. In the years to come, it is expected that knowledge gained in cancer biology and polymer chemistry will catalyze the further development of novel multifunctional micellar systems with greater customization to achieve more efficacious anti-tumor response.

ACKNOWLEDGEMENT

We thank the National Institutes of Health (R01-CA-90696 and R21-EB-005394) for their financial support. NN acknowledges the Royal Thai Government for a predoctoral fellowship support. EB acknowledges the predoctoral support from the NCI Minority Supplement Program. This is manuscript CSCNP008 from the "Cell Stress and Cancer Nanomedicine" program in the Simmons Comprehensive Cancer Center at the University of Texas Southwestern Medical Center at Dallas.

REFERENCES

1. S. Danson, D. Ferry, V. Alakhov, J. Margison, D. Kerr, D. Jowle, M. Brampton, G. Halbert, and M. Ranson. Phase I dose escalation and pharmacokinetic study of pluronic polymer-bound doxorubicin (SP1049C) in patients with advanced cancer. *Br. J. Cancer* **90**:2085–2091 (2004).
2. Y. Matsumura, T. Hamaguchi, T. Ura, K. Muro, Y. Yamada, Y. Shimada, K. Shirao, T. Okusaka, H. Ueno, M. Ikeda, and N. Watanabe. Phase I clinical trial and pharmacokinetic evaluation of NK911, a micelle-encapsulated doxorubicin. *Br. J. Cancer* **91**:1775–1781 (2004).
3. T. Y. Kim, D. W. Kim, J. Y. Chung, S. G. Shin, S. C. Kim, D. S. Heo, N. K. Kim, and Y. J. Bang. Phase I and pharmacokinetic study of Genexol-PM, a cremophor-free, polymeric micelle-formulated paclitaxel, in patients with advanced malignancies. *Clin. Cancer Res.* **10**:3708–3716 (2004).
4. Y. Kakizawa and K. Kataoka. Block copolymer micelles for delivery of gene and related compounds. *Adv. Drug Deliv. Rev.* **54**:203–222 (2002).
5. V. P. Torchilin. Structure and design of polymeric surfactant-based drug delivery systems. *J. Control. Release* **73**:137–172 (2001).
6. M. Jones and J. Leroux. Polymeric micelles—a new generation of colloidal drug carriers. *Eur. J. Pharm. Biopharm.* **48**:101–111 (1999).
7. A. V. Kabanov, P. Lemieux, S. Vinogradov, and V. Alakhov. Pluronic((R)) block copolymers: novel functional molecules for gene therapy. *Adv. Drug Deliv. Rev.* **54**:223–233 (2002).
8. G. S. Kwon and K. Kataoka. Block-Copolymer Micelles as Long-Circulating Drug Vehicles. *Adv. Drug Deliv. Rev.* **16**:295–309 (1995).
9. G. S. Kwon. Polymeric micelles for delivery of poorly water-soluble compounds. *Crit. Rev. Ther. Drug Carr. Syst.* **20**:357–403 (2003).
10. V. P. Torchilin. Block copolymer micelles as a solution for drug delivery problems. *Expert Opin. Ther. Pat.* **15**:63–75 (2005).
11. V. P. Torchilin. Targeted polymeric micelles for delivery of poorly soluble drugs. *Cell Mol. Life Sci.* **61**:2549–2559 (2004).
12. G. Gaucher, M. H. Dufresne, V. P. Sant, N. Kang, D. Maysinger, and J. C. Leroux. Block copolymer micelles: preparation, characterization and application in drug delivery. *J. Control. Release* **109**:169–188 (2005).
13. V. P. Torchilin. Micellar nanocarriers: pharmaceutical perspectives. *Pharm. Res.* **24**:1–16 (2007).
14. A. Choucair and A. Eisenberg. Control of amphiphilic block copolymer morphologies using solution conditions. *Eur. Phys. J., E* **10**:37–44 (2003).
15. A. Choucair and A. Eisenberg. Interfacial solubilization of model amphiphilic molecules in block copolymer micelles. *J. Am. Chem. Soc.* **125**:11993–12000 (2003).
16. Y. S. Yu, L. F. Zhang, and A. Eisenberg. Morphogenic effect of solvent on crew-cut aggregates of amphiphilic diblock copolymers. *Macromolecules* **31**:1144–1154 (1998).
17. H. W. Shen, L. F. Zhang, and A. Eisenberg. Multiple pH-induced morphological changes in aggregates of polystyrene-block-poly(4-vinylpyridine) in DMF/H₂O mixtures. *J. Am. Chem. Soc.* **121**:2728–2740 (1999).
18. P. Dalhaimer, F. S. Bates, H. Aranda-Espinoza, and D. Discher. Synthetic cell elements from block copolymers—hydrodynamic aspects. *Comptes Rendus. Physique* **4**:251–258 (2003).
19. P. Dalhaimer, A. J. Engler, R. Parthasarathy, and D. E. Discher. Targeted worm micelles. *Biomacromolecules* **5**:1714–1719 (2004).
20. P. Dalhaimer, F. S. Bates, and D. E. Discher. Single molecule visualization of stable, stiffness-tunable, flow-conforming worm micelles. *Macromolecules* **36**:6873–6877 (2003).
21. A. Benahmed, M. Ranger, and J. C. Leroux. Novel polymeric micelles based on the amphiphilic diblock copolymer poly(N-vinyl-2-pyrrolidone)-block-poly(D,L-lactide). *Pharm. Res.* **18**:323–328 (2001).
22. J. E. Chung, M. Yokoyama, T. Aoyagi, Y. Sakurai, and T. Okano. Effect of molecular architecture of hydrophobically modified poly(N-isopropylacrylamide) on the formation of

- thermosensitive core-shell micellar drug carriers. *J. Control. Release* **53**:119–130 (1998).
23. J. E. Chung, M. Yokoyama, and T. Okano. Inner core segment design for drug delivery control of thermo-responsive polymeric micelles. *J. Control. Release* **65**:93–103 (2000).
 24. J. E. Chung, M. Yokoyama, M. Yamato, T. Aoyagi, Y. Sakurai, and T. Okano. Thermo-responsive drug delivery from polymeric micelles constructed using block copolymers of poly(N-isopropylacrylamide) and poly(butylmethacrylate). *J. Control. Release* **62**:115–127 (1999).
 25. O. Soga, C. F. van Nostrum, M. Fens, C. J. Rijcken, R. M. Schiffelers, G. Storm, and W. E. Hennink. Thermosensitive and biodegradable polymeric micelles for paclitaxel delivery. *J. Control. Release* **103**:341–353 (2005).
 26. K. Kataoka, G. S. Kwon, M. Yokoyama, T. Okano, and Y. Sakurai. Block copolymer micelles as vehicles for drug delivery. *J. Control. Release* **24**:119–132 (1993).
 27. G. S. Kwon, M. Yokoyama, T. Okano, Y. Sakurai, and K. Kataoka. Enhanced tumor accumulation and prolonged circulation times of micelle-forming poly(ethylene oxide-aspartate) block copolymer-Adriamycin conjugates. *J. Control. Release* **28**:334–335 (1994).
 28. H. Maeda, K. Greish, and J. Fang. The EPR effect and polymeric drugs: a paradigm shift for cancer chemotherapy in the 21st century. *Polymer Therapeutics II: Polymers as Drugs, Conjugates and Gene Delivery Systems* **193**:103–121 (2006).
 29. K. Mross, P. Maessen, W. J. van der Vijgh, H. Gall, E. Boven, and H. M. Pinedo. Pharmacokinetics and metabolism of epidoxorubicin and doxorubicin in humans. *J. Clin. Oncol.* **6**:517–526 (1988).
 30. A. Gabizon, R. Catane, B. Uziely, B. Kaufman, T. Safra, R. Cohen, F. Martin, A. Huang, and Y. Barenholz. Prolonged circulation time and enhanced accumulation in malignant exudates of doxorubicin encapsulated in polyethylene-glycol coated liposomes. *Cancer Res.* **54**:987–992 (1994).
 31. P. H. Wiernik, E. L. Schwartz, J. J. Strauman, J. P. Dutcher, R. B. Lipton, and E. Paietta. Phase I clinical and pharmacokinetic study of taxol. *Cancer Res.* **47**:2486–2493 (1987).
 32. V. Weissig, K. R. Whiteman, and V. P. Torchilin. Accumulation of protein-loaded long-circulating micelles and liposomes in subcutaneous Lewis lung carcinoma in mice. *Pharm. Res.* **15**:1552–1556 (1998).
 33. R. L. Hong and Y. L. Tseng. Phase I and pharmacokinetic study of a stable, polyethylene-glycolated liposomal doxorubicin in patients with solid tumors: the relation between pharmacokinetic property and toxicity. *Cancer* **91**:1826–1833 (2001).
 34. J. Cummings and C. S. McArdle. Studies on the *in vivo* disposition of adriamycin in human tumours which exhibit different responses to the drug. *Br. J. Cancer* **53**:835–838 (1986).
 35. D. Goren, A. T. Horowitz, D. Tzemach, M. Tarshish, S. Zalipsky, and A. Gabizon. Nuclear delivery of doxorubicin via folate-targeted liposomes with bypass of multidrug-resistance efflux pump. *Clin. Cancer Res.* **6**:1949–1957 (2000).
 36. S. D. Weitman, A. G. Weinberg, L. R. Coney, V. R. Zurawski, D. S. Jennings, and B. A. Kamen. Cellular-localization of the folate receptor—potential role in drug toxicity and folate homeostasis. *Cancer Res.* **52**:6708–6711 (1992).
 37. J. F. Ross, P. K. Chaudhuri, and M. Ratnam. Differential regulation of folate receptor isoforms in normal and malignant-tissues *in-vivo* and in established cell-lines—physiological and clinical implications. *Cancer* **73**:2432–2443 (1994).
 38. H. S. Yoo and T. G. Park. Folate receptor targeted biodegradable polymeric doxorubicin micelles. *J. Control. Release* **96**:273–283 (2004).
 39. H. S. Yoo and T. G. Park. Folate-receptor-targeted delivery of doxorubicin nano-aggregates stabilized by doxorubicin-PEG-folate conjugate. *J. Control. Release* **100**:247–256 (2004).
 40. E. K. Park, S. Y. Kim, S. B. Lee, and Y. M. Lee. Folate-conjugated methoxy poly(ethylene glycol)/poly(epsilon-caprolactone) amphiphilic block copolymeric micelles for tumor-targeted drug delivery. *J. Control. Release* **109**:158–168 (2005).
 41. E. K. Park, S. B. Lee, and Y. M. Lee. Preparation and characterization of methoxy poly(ethylene glycol)/poly(epsilon-caprolactone) amphiphilic block copolymeric nanospheres for tumor-specific folate-mediated targeting of anticancer drugs. *Biomaterials* **26**:1053–1061 (2005).
 42. J. A. Varner and D. A. Cheresh. Tumor angiogenesis and the role of vascular cell integrin alphavbeta3. *Important Adv. Oncol.* **69**–87 (1996).
 43. A. Teti, S. Migliaccio, and R. Baron. The role of the alphaVbeta3 integrin in the development of osteolytic bone metastases: a pharmacological target for alternative therapy? *Calcif. Tissue Int.* **71**:293–299 (2002).
 44. C. Ruegg, O. Dormond, and A. Foletti. Suppression of tumor angiogenesis through the inhibition of integrin function and signaling in endothelial cells: which side to target? *Endothelium* **9**:151–160 (2002).
 45. J. Wermuth, S. L. Goodman, A. Jonczyk, and H. Kessler. Stereoisomerism and biological activity of the selective and superactive alpha(v)beta(3) integrin inhibitor cyclo(-RGDfV-) and its retro-inverso peptide. *J. Am. Chem. Soc.* **119**:1328–1335 (1997).
 46. H. Kessler, B. Diefenbach, D. Finsinger, A. Geyer, M. Gurrath, S. L. Goodman, G. Holzemann, R. Haubner, A. Jonczyk, G. Muller, E. G. von Roedern, and J. Wermuth. Design of superactive and selective integrin receptor antagonists containing the RGD sequence. *Lett. Pept. Sci.* **2**:155–160 (1995).
 47. R. Haubner, W. Schmitt, G. Holzemann, S. L. Goodman, A. Jonczyk, and H. Kessler. Cyclic RGD peptides containing beta-tartronic mimetics. *J. Am. Chem. Soc.* **118**:7881–7891 (1996).
 48. R. Haubner, R. Gratiats, B. Diefenbach, S. L. Goodman, A. Jonczyk, and H. Kessler. Structural and functional aspects of RGD-containing cyclic pentapeptides as highly potent and selective integrin alpha(v)beta(3) antagonists. *J. Am. Chem. Soc.* **118**:7461–7472 (1996).
 49. S. L. Goodman, G. Holzemann, G. A. G. Sulyok, and H. Kessler. Nanomolar small molecule inhibitors for alpha v beta 6, alpha v beta 5, and alpha v beta 3 integrins. *J. Med. Chem.* **45**:1045–1051 (2002).
 50. P. C. Brooks, R. A. Clark, and D. A. Cheresh. Requirement of vascular integrin alpha v beta 3 for angiogenesis. *Science* **264**:569–571 (1994).
 51. N. Nasongkla, X. Shuai, H. Ai, B. D. Weinberg, J. Pink, D. A. Boothman, and J. M. Gao. cRGD-functionalized polymer micelles for targeted doxorubicin delivery. *Angewandte Chemie-International Edition* **43**:6323–6327 (2004).
 52. G. Ashwelland and J. Harford. Carbohydrate-specific receptors of the liver. *Ann. Rev. Biochem.* **51**:531–554 (1982).
 53. M. Goto, H. Yura, C. W. Chang, A. Kobayashi, T. Shinoda, A. Maeda, S. Kojima, K. Kobayashi, and T. Akaike. Lactose-carrying polystyrene as a drug carrier—investigation of body distributions to parenchymal liver-cells using I-125 labeled lactose-carrying polystyrene. *J. Control. Release* **28**:223–233 (1994).
 54. R. W. Jansen, G. Molema, T. L. Ching, R. Oosting, G. Harms, F. Moolenaar, M. J. Hardonk, and D. K. Meijer. Hepatic endocytosis of various types of mannose-terminated albumins. What is important, sugar recognition, net charge, or the combination of these features. *J. Biol. Chem.* **266**:3343–3348 (1991).
 55. J. Kopacek and R. Duncan. Targetable polymeric prodrugs. *J. Control. Release* **6**:315–327 (1987).
 56. J. R. Wands and H. E. Blum. Primary hepatocellular carcinoma. *N. Engl. J. Med.* **325**:729–731 (1991).
 57. Y. I. Jeong, S. J. Seo, I. K. Park, H. C. Lee, I. C. Kang, T. Akaike, and C. S. Cho. Cellular recognition of paclitaxel-loaded polymeric nanoparticles composed of poly(gamma-benzyl L-glutamate) and poly(ethylene glycol) diblock copolymer endcapped with galactose moiety. *Int. J. Pharm.* **296**:151–161 (2005).
 58. K. Yasugi, T. Nakamura, Y. Nagasaki, M. Kato, and K. Kataoka. Sugar-installed polymer micelles: Synthesis and micellization of poly(ethylene glycol)-poly(D,L-lactide) block copolymers having sugar groups at the PEG chain end. *Macromolecules* **32**:8024–8032 (1999).

59. Y. Nagasaki, K. Yasugi, Y. Yamamoto, A. Harada, and K. Kataoka. Sugar-installed block copolymer micelles: their preparation and specific interaction with lectin molecules. *Biomacromolecules* **2**:1067–1070 (2001).
60. E. Jule, Y. Nagasaki, and K. Kataoka. Surface plasmon resonance study on the interaction between lactose-installed poly(ethylene glycol)-poly(D,L-lactide) block copolymer micelles and lectins immobilized on a gold surface. *Langmuir* **18**:10334–10339 (2002).
61. E. Jule, Y. Nagasaki, and K. Kataoka. Lactose-installed poly(ethylene glycol)-poly(D,L-lactide) block copolymer micelles exhibit fast-rate binding and high affinity toward a protein bed simulating a cell surface. A surface plasmon resonance study. *Bioconjug. Chem.* **14**:177–186 (2003).
62. A. V. Kabanov, V. P. Chekhonin, V. Y. Alakhov, E. V. Batrakova, A. S. Lebedev, N. S. Meliknubarov, S. A. Arzhakov, A. V. Levashov, G. V. Morozov, E. S. Severin, and V. A. Kabanov. The neuroleptic activity of haloperidol increases after its solubilization in surfactant micelles—micelles as microcontainers for drug targeting. *FEBS Lett.* **258**:343–345 (1989).
63. V. P. Torchilin, A. N. Lukyanov, Z. Gao, and B. Papahadjopoulos-Sternberg. Immunomicelles: targeted pharmaceutical carriers for poorly soluble drugs. *Proc. Natl. Acad. Sci. USA.* **100**:6039–6044 (2003).
64. C. Tuerkand and L. Gold. Systematic evolution of ligands by exponential enrichment—Rna Ligands to Bacteriophage-T4 DNA-Polymerase. *Science* **249**:505–510 (1990).
65. A. D. Ellington and J. W. Szostak. *In vitro* selection of Rna molecules that bind specific ligands. *Nature* **346**:818–822 (1990).
66. O. C. Farokhzad, S. Y. Jon, A. Khadelmhosseini, T. N. T. Tran, D. A. LaVan, and R. Langer. Nanoparticle-aptamer bioconjugates: A new approach for targeting prostate cancer cells. *Cancer Res.* **64**:7668–7672 (2004).
67. O. C. Farokhzad, J. J. Cheng, B. A. Teply, I. Sherifi, S. Jon, P. W. Kantoff, J. P. Richie, and R. Langer. Targeted nanoparticle-aptamer bioconjugates for cancer chemotherapy *in vivo*. *Proc. Natl. Acad. Sci. USA.* **103**:6315–6320 (2006).
68. J. D. Hood, M. Bednarski, R. Frausto, S. Guccione, R. A. Reisfeld, R. Xiang, and D. A. Cheresh. Tumor regression by targeted gene delivery to the neovasculature. *Science* **296**:2404–2407 (2002).
69. T. J. Wickham. Ligand-directed targeting of genes to the site of disease. *Nat. Med.* **9**:135–139 (2003).
70. K. Kunath, T. Merdan, O. Hegener, H. Haberlein, and T. Kissel. Integrin targeting using RGD-PEI conjugates for *in vitro* gene transfer. *J. Gene Med.* **5**:588–599 (2003).
71. P. Erbacher, T. Bettinger, P. Belguise-Valladier, S. M. Zou, J. L. Coll, J. P. Behr, and J. S. Remy. Transfection and physical properties of various saccharide, poly(ethylene glycol), and antibody-derivatized polyethylenimines (PEI). *J. Gene Med.* **1**:210–222 (1999).
72. C. C. Chen and E. E. Dormidontova. Architectural and structural optimization of the protective polymer layer for enhanced targeting. *Langmuir* **21**:5605–5615 (2005).
73. C. Cluzel, F. Saltel, J. Lussi, F. Paulhe, B. A. Imhof, and B. Wehrle-Haller. The mechanisms and dynamics of alpha v beta 3 integrin clustering in living cells. *J. Cell Biol.* **171**:383–392 (2005).
74. K. Engin, D. B. Leeper, J. R. Cater, A. J. Thistlethwaite, L. Tupchong, and J. D. McFarlane. Extracellular Ph distribution in human tumors. *Int. J. Hypertherm.* **11**:211–216 (1995).
75. H. S. Yoo, E. A. Lee, and T. G. Park. Doxorubicin-conjugated biodegradable polymeric micelles having acid-cleavable linkages. *J. Control. Release* **82**:17–27 (2002).
76. Y. Bae, S. Fukushima, A. Harada, and K. Kataoka. Design of environment-sensitive supramolecular assemblies for intracellular drug delivery: polymeric micelles that are responsive to intracellular pH change. *Angew. Chem. Int. Ed. Engl.* **42**:4640–4643 (2003).
77. Y. Bae, W. D. Jang, N. Nishiyama, S. Fukushima, and K. Kataoka. Multifunctional polymeric micelles with folate-mediated cancer cell targeting and pH-triggered drug releasing properties for active intracellular drug delivery. *Molecular Biosystems* **1**:242–250 (2005).
78. Y. Bae, N. Nishiyama, S. Fukushima, H. Koyama, M. Yasuhiro, and K. Kataoka. Preparation and biological characterization of polymeric micelle drug carriers with intracellular pH-triggered drug release property: tumor permeability, controlled subcellular drug distribution, and enhanced *in vivo* antitumor efficacy. *Bioconjug. Chem.* **16**:122–130 (2005).
79. E. R. Gillies and J. M. J. Frechet. A new approach towards acid sensitive copolymer micelles for drug delivery. *Chem. Commun.* 1640–1641 (2003).
80. E. R. Gillies and J. M. J. Frechet. pH-responsive copolymer assemblies for controlled release of doxorubicin. *Bioconjug. Chem.* **16**:361–368 (2005).
81. E. R. Gillies, A. P. Goodwin, and J. M. J. Frechet. Acetals as pH-sensitive linkages for drug delivery. *Bioconjug. Chem.* **15**:1254–1263 (2004).
82. H. R. Stapert, N. Nishiyama, D. L. Jiang, T. Aida, and K. Kataoka. Polyion complex micelles encapsulating light-harvesting ionic dendrimer zinc porphyrins. *Langmuir* **16**:8182–8188 (2000).
83. H. R. Stapert, N. Nishiyama, D. L. Jiang, T. Aida, and K. Kataoka. Poly-ion complex micelles encapsulating light-harvesting ionic Zn porphyrin dendrimers for PDT. *Abstr. Pap.-Am. Chem. Soc.* **219**:U226 (2000).
84. Y. Q. Tang, S. Y. Liu, S. P. Armes, and N. C. Billingham. Solubilization and controlled release of a hydrophobic drug using novel micelle-forming ABC triblock copolymers. *Biomacromolecules* **4**:1636–1645 (2003).
85. E. S. Lee, H. J. Shin, K. Na, and Y. H. Bae. Poly(L-histidine)-PEG block copolymer micelles and pH-induced destabilization. *J. Control. Release* **90**:363–374 (2003).
86. E. S. Lee, K. Na, and Y. H. Bae. Super pH-sensitive multifunctional polymeric micelle. *Nano Lett.* **5**:325–329 (2005).
87. E. S. Lee, K. Na, and Y. H. Bae. Doxorubicin loaded pH-sensitive polymeric micelles for reversal of resistant MCF-7 tumor. *J. Control. Release* **103**:405–418 (2005).
88. E. S. Lee, K. Na, and Y. H. Bae. Polymeric micelle for tumor pH and folate-mediated targeting. *J. Control. Release* **91**:103–113 (2003).
89. D. M. Lynn, M. M. Amiji, and R. Langer. pH-responsive polymer microspheres: rapid release of encapsulated material within the range of intracellular pH. *Angew. Chem. Int. Ed. Engl.* **40**:1707–1710 (2001).
90. A. Potinini, D. M. Lynn, R. Langer, and M. M. Amiji. Poly(ethylene oxide)-modified poly(beta-amino ester) nanoparticles as a pH-sensitive biodegradable system for paclitaxel delivery. *J. Control. Release* **86**:223–234 (2003).
91. D. Shenoy, S. Little, R. Langer, and M. Amiji. Poly(ethylene oxide)-modified poly(beta-amino ester) nanoparticles as a pH-sensitive system for tumor-targeted delivery of hydrophobic drugs. 1. *In vitro* evaluations. *Mol. Pharmacol.* **2**:357–366 (2005).
92. D. Shenoy, S. Little, R. Langer, and M. Amiji. Poly(ethylene oxide)-modified poly(beta-amino ester) nanoparticles as a pH-sensitive system for tumor-targeted delivery of hydrophobic drugs: part 2. *In vivo* distribution and tumor localization studies. *Pharm. Res.* **22**:2107–2114 (2005).
93. K. S. Soppimath, D. C. W. Tan, and Y. Y. Yang. pH-triggered thermally responsive polymer core-shell nanoparticles for drug delivery. *Adv. Mater.* **17**:318+ (2005).
94. J. Taillefer, M. C. Jones, N. Brasseur, J. E. Van Lier, and J. C. Leroux. Preparation and characterization of pH-responsive polymeric micelles for the delivery of photosensitizing anticancer drugs. *J. Pharm. Sci.* **89**:52–62 (2000).
95. J. Taillefer, N. Brasseur, J. E. van Lier, V. Lenaerts, D. Le Garrec, and J. C. Leroux. *In vitro* and *In vivo* evaluation of pH-responsive polymeric micelles in a photodynamic cancer therapy model. *J. Pharm. Pharmacol.* **53**:155–166 (2001).
96. D. Le Garrec, J. Taillefer, J. E. Van Lier, V. Lenaerts, and J. C. Leroux. Optimizing pH-responsive polymeric micelles for drug delivery in a cancer photodynamic therapy model. *J. Drug Target.* **10**:429–437 (2002).
97. H. Hayashi, M. Iijima, K. Kataoka, and Y. Nagasaki. pH-sensitive nanogel possessing reactive PEG tethered chains on the surface. *Macromolecules* **37**:5389–5396 (2004).

98. T. K. Bronich, P. A. Keifer, L. S. Shlyakhtenko, and A. V. Kabanov. Polymer micelle with cross-linked ionic core. *J. Am. Chem. Soc.* **127**:8236–8237 (2005).
99. J. van der Zee. Heating the patient: a promising approach? *Ann. Oncol.* **13**:1173–1184 (2002).
100. J. E. Chung, M. Yamato, T. Aoyagi, M. Yokoyama, Y. Sakurai, and T. Okano. Temperature-responsive polymeric micelles as intelligent drug carriers. *Abstr. Pap.-Am. Chem. Soc.* **216**:U5 (1998).
101. J. E. Chung, M. Yokoyama, T. Aoyagi, Y. Sakurai, and T. Okano. Effect of molecular architecture of hydrophobically modified poly(N-isopropylacrylamide) on the formation of thermoresponsive core-shell micellar drug carriers. *J. Control. Release* **53**:119–130 (1998).
102. J. E. Chung, M. Yokoyama, K. Suzuki, T. Aoyagi, Y. Sakurai, and T. Okano. Reversibly thermo-responsive alkyl-terminated poly(N-isopropylacrylamide) core-shell micellar structures. *Colloids Surf. B, Biointerfaces* **9**:37–48 (1997).
103. X. M. Liu, K. P. Pramoda, Y. Y. Yang, S. Y. Chow, and C. B. He. Cholesteryl-grafted functional amphiphilic poly(N-isopropylacrylamide-co-N-hydroxymethylacrylamide): synthesis, temperature sensitivity, self-assembly and encapsulation of a hydrophobic agent. *Biomaterials* **25**:2619–2628 (2004).
104. X. M. Liu, Y. Y. Yang, and K. W. Leong. Thermally responsive polymeric micellar nanoparticles self-assembled from cholesteryl end-capped random poly(N-isopropylacrylamide-co-N,N-dimethylacrylamide): synthesis, temperature sensitivity, and morphologies. *J. Colloid Interface Sci.* **266**:295–303 (2003).
105. F. Kohori, K. Sakai, T. Aoyagi, M. Yokoyama, Y. Sakurai, and T. Okano. Preparation and characterization of thermally responsive block copolymer micelles comprising poly(N-isopropylacrylamide-b-DL-lactide). *J. Control. Release* **55**:87–98 (1998).
106. J. E. Chung, M. Yokoyama, and T. Okano. Inner core segment design for drug delivery control of thermo-responsive polymeric micelles. *J. Control. Release* **65**:93–103 (2000).
107. M. Nakayama and T. Okano. Polymer terminal group effects on properties of thermoresponsive polymeric micelles with controlled outer-shell chain lengths. *Biomacromolecules* **6**:2320–2327 (2005).
108. S. Q. Liu, Y. W. Tong, and Y. Y. Yang. Incorporation and *In vitro* release of doxorubicin in thermally sensitive micelles made from poly(N-isopropylacrylamide-co-N,N-dimethylacrylamide)-b-poly(D,L-lactide-co-glycolide) with varying compositions. *Biomaterials* **26**:5064–5074 (2005).
109. S. Mitragotri. Innovation—Healing sound: the use of ultrasound in drug delivery and other therapeutic applications. *Nature Reviews Drug Discovery* **4**:255–260 (2005).
110. S. Miyazaki, C. Yokouchi, and M. Takada. External control of drug release—controlled release of insulin from a hydrophilic polymer implant by ultrasound irradiation in diabetic rats. *J. Pharm. Pharmacol.* **40**:716–717 (1988).
111. N. Rapoport, W. G. Pitt, H. Sun, and J. L. Nelson. Drug delivery in polymeric micelles: from *in vitro* to *in vivo*. *J. Control. Release* **91**:85–95 (2003).
112. N. Rapoport, A. I. Smirnov, A. Timoshin, A. M. Pratt, and W. G. Pitt. Factors affecting the permeability of *Pseudomonas aeruginosa* cell walls toward lipophilic compounds: Effects of ultrasound and cell age. *Arch. Biochem. Biophys.* **344**:114–124 (1997).
113. E. Ruel-Gariepy and J. C. Leroux. *In situ*-forming hydrogels—review of temperature-sensitive systems. *Eur. J. Pharm. Biopharm.* **58**:409–426 (2004).
114. A. V. Kabanov, E. V. Batrakov, and V. Y. Alakhov. Pluronic((R)) block copolymers for overcoming drug resistance in cancer. *Adv. Drug Deliv. Rev.* **54**:759–779 (2002).
115. G. A. Hussein, C. M. Runyan, and W. G. Pitt. Investigating the mechanism of acoustically activated uptake of drugs from Pluronic micelles. *BMC Cancer* **2**: (2002).
116. G. A. Hussein, N. Y. Rapoport, D. A. Christensen, J. D. Pruitt, and W. G. Pitt. Kinetics of ultrasonic release of doxorubicin from pluronic P105 micelles. *Colloids Surf., B Biointerfaces* **24**:253–264 (2002).
117. N. Munshi, N. Rapoport, and W. G. Pitt. Ultrasonic activated drug delivery from pluronic P-105 micelles. *Cancer Lett.* **118**:13–19 (1997).
118. N. Y. Rapoport, J. N. Herron, W. G. Pitt, and L. Pitina. Micellar delivery of doxorubicin and its paramagnetic analog, ruboxyl, to HL-60 cells: effect of micelle structure and ultrasound on the intracellular drug uptake. *J. Control. Release* **58**:153–162 (1999).
119. A. Marin, H. Sun, G. A. Hussein, W. G. Pitt, D. A. Christensen, and N. Y. Rapoport. Drug delivery in pluronic micelles: effect of high-frequency ultrasound on drug release from micelles and intracellular uptake. *J. Control. Release* **84**:39–47 (2002).
120. Z. G. Gao, H. D. Fain, and N. Rapoport. Controlled and targeted tumor chemotherapy by micellar-encapsulated drug and ultrasound. *J. Control. Release* **102**:203–222 (2005).
121. G. A. Hussein, D. A. Christensen, N. Y. Rapoport, and W. G. Pitt. Ultrasonic release of doxorubicin from Pluronic P105 micelles stabilized with an interpenetrating network of N,N-diethylacrylamide. *J. Control. Release* **83**:303–305 (2002).
122. J. D. Pruitt, G. Hussein, N. Rapoport, and M. G. Pitt. Stabilization of pluronic P-105 micelles with an interpenetrating network of N,N-diethylacrylamide. *Macromolecules* **33**:9306–9309 (2000).
123. J. D. Pruitt and W. G. Pitt. Sequestration and ultrasound-induced release of doxorubicin from stabilized pluronic P105 micelles. *Drug Deliv.* **9**:253–258 (2002).
124. J. L. Nelson, B. L. Roeder, J. C. Carmen, F. Roloff, and W. G. Pitt. Ultrasonically activated chemotherapeutic drug delivery in a rat model. *Cancer Res.* **62**:7280–7283 (2002).
125. Y. Katayama, T. Sonoda, and M. Maeda. A polymer micelle responding to the protein kinase A signal. *Macromolecules* **34**:8569–8573 (2001).
126. A. Napoli, M. Valentini, N. Tirelli, M. Muller, and J. A. Hubbell. Oxidation-responsive polymeric vesicles. *Nat. Mater* **3**:183–189 (2004).
127. R. M. Sawant, J. P. Hurley, S. Salmaso, A. Kale, E. Tolcheva, T. S. Levchenko, and V. P. Torchilin. “SMART” drug delivery systems: double-targeted pH-responsive pharmaceutical nano-carriers. *Bioconjug. Chem.* **17**:943–949 (2006).
128. N. Nasongkla, E. Bey, J. M. Ren, H. Ai, C. Khemtong, J. S. Guthi, S. F. Chin, A. D. Sherry, D. A. Boothman, and J. M. Gao. Multifunctional polymeric micelles as cancer-targeted, MRI-ultrasensitive drug delivery systems. *Nano Lett.* **6**:2427–2430 (2006).
129. J. C. Leroux, E. Roux, D. Le Garrec, K. L. Hong, and D. C. Drummond. N-isopropylacrylamide copolymers for the preparation of pH-sensitive liposomes and polymeric micelles. *J. Control. Release* **72**:71–84 (2001).

β -Lapachone-containing PEG–PLA polymer micelles as novel nanotherapeutics against NQO1-overexpressing tumor cells

Elvin Blanco^a, Erik A. Bey^a, Ying Dong^a, Brent D. Weinberg^b, Damon M. Sutton^a, David A. Boothman^a, Jinming Gao^{a,*}

^a Simmons Comprehensive Cancer Center, University of Texas Southwestern Medical Center at Dallas, Dallas, TX 75390, United States

^b Department of Biomedical Engineering, Case Western Reserve University, Cleveland, Ohio 44106, United States

Received 24 February 2007; accepted 19 April 2007

Available online 29 April 2007

Abstract

β -Lapachone (β -lap) is a novel anticancer agent that is bioactivated by NAD(P)H: quinone oxidoreductase 1 (NQO1), an enzyme overexpressed in a variety of tumors. Despite its therapeutic promise, the poor aqueous solubility of β -lap hinders its preclinical evaluation and clinical translation. Our objective was to develop β -lap-containing poly(ethylene glycol)-block-poly(D,L-lactide) (PEG–PLA) polymer micelles for the treatment of NQO1-overexpressing tumors. Several micelle fabrication strategies were examined to maximize drug loading. A film sonication method yielded β -lap micelles with relatively high loading density ($4.7 \pm 1.0\%$ to $6.5 \pm 1.0\%$) and optimal size (29.6 ± 1.5 nm). Release studies in phosphate-buffered saline (pH 7.4) showed the time ($t_{1/2}$) for 50% of drug release at 18 h. In vitro cytotoxicity assays were performed in NQO1-overexpressing (NQO1+) and NQO1-null (NQO1-) H596 lung, DU-145 prostate, and MDA-MB-231 breast cancer cells. Cytotoxicity data showed that after a 2 h incubation with β -lap micelles, a marked increase in toxicity was shown in NQO1+ cells over NQO1- cells, resembling free drug both in efficacy and mechanism of cell death. In summary, these data demonstrate the potential of β -lap micelles as an effective therapeutic strategy against NQO1-overexpressing tumor cells.

© 2007 Elsevier B.V. All rights reserved.

Keywords: β -Lapachone; Polymer micelles; Cancer nanomedicine; Poly(ethylene glycol)–poly(D,L-lactide) (PEG–PLA); Drug delivery

1. Introduction

Presently, the development of integrated cancer nanomedicine, which consists of drugs that exploit cancer-specific molecular targets combined with effective carriers for tumor-targeted drug delivery, has shown significant promise in expanding therapeutic indices for chemotherapy. β -Lapachone (β -lap) (Fig. 1A) is a novel, plant-derived anticancer drug whose cytotoxic effect is significantly enhanced by NAD(P)H: quinone oxidoreductase 1 (NQO1), a flavoprotein found overexpressed (up to 20-fold) in a variety of human cancers, including those of the lung [1], prostate [2], pancreas [3], and breast [4]. Upon β -lap administration, NQO1 induces a futile cycling of β -lap, wherein the compound cycles between its

hydroquinone, semiquinone, and quinone forms, depleting the cell of NAD(P)H in the process and leading to the generation of DNA damaging hydroxyl radicals [5]. Additionally, β -lap treatment leads to an NQO1-dependent rise in cytosolic Ca^{2+} that results in the loss of mitochondrial membrane potential, ATP depletion, unique substrate proteolysis, DNA fragmentation, and cell apoptosis [6]. The mechanism of action is independent of caspases, p53 status, and cell cycle stage [7]. Given its central role in β -lap-mediated lethality, NQO1 is a vital, exploitable target for the treatment of cancer cells that overexpress this enzyme.

While β -lap proves to be a very promising agent from a pharmacodynamic standpoint, several factors hinder conventional intravenous administration for preclinical evaluation and clinical translation. Firstly, its non-specific distribution can lead to low tumor concentrations and systemic toxicity [8]. Moreover, its polycyclic nature makes it highly hydrophobic,

* Corresponding author. Tel.: +1 214 648 9278; fax: +1 214 648 0264.

E-mail address: jinming.gao@utsouthwestern.edu (J. Gao).

with an aqueous solubility of 0.04 mg/mL [9]. Prior work by our laboratory focused on attempts to increase the aqueous solubility of β -lap through its complexation with hydroxypropyl- β -cyclodextrin (HP β -CD) [9]. However, the fast dissociation of β -lap and cyclodextrin makes the drug susceptible to aggregation and rapid clearance, warranting the use of an effective nanotherapeutic delivery vehicle that can efficiently solubilize the drug and deliver it to solid tumors.

Polymer micelles are spherical, nanosized (10–100 nm) supramolecular constructs that are garnering significant attention as a versatile drug delivery platform for cancer therapy [10–12]. Polymer micelles have a unique core-shell structure as a result of the self-assembly of amphiphilic block copolymers in aqueous environments (Fig. 1B). The hydrophobic core acts as a solubilizing reservoir for water insoluble drugs, such as β -lap, providing protection from enzymatic degradation and inactivation [13]. The hydrophilic micellar corona, in turn, forms a hydrating layer on the surface of the micelle that hinders plasma protein adsorption and subsequent rapid phagocytic clearance by the reticuloendothelial system (RES) [14]. Additionally, small micellar size, along with low critical micelle concentrations (CMCs), results in long-circulating, stable constructs that do not easily dissociate *in vivo* [15], and contributes to the preferential accumulation of micelles in tumor tissue through the enhanced permeability and retention (EPR) effect [16,17].

To exploit these numerous advantages of polymer micelles, our objective was to develop β -lap-containing micelles for an NQO1-specific therapy. In this study, we report the development of a film sonication method to fabricate β -lap micelles with relatively high loading of the drug, adequate micelle size, core-shell formation, and favorable release characteristics. Using three different cancer cell lines, β -lap micelle treatment showed a substantial increase in cytotoxicity in NQO1+ cells over NQO1- cells, highlighting the system as a potential treatment strategy against NQO1-overexpressing tumors.

2. Materials and methods

2.1. Materials

β -lap was synthesized following a previously reported procedure [18]. PEG5k-PLA5k block copolymer ($M_n = 10,000$ Da) was synthesized utilizing a ring-opening polymerization procedure published previously [19]. Poly(D,L-lactide) (PLA) ($M_n = 27,344$ Da) was purchased from Birmingham Polymers (Pelham, AL). All organic solvents were of analytical grade. H596 non-small cell lung carcinoma (NSCLC) cells, DU-145 prostate, and MDA-MB-231 breast cancer cells, were grown in DMEM with 10% fetal bovine serum, 2 mM L-glutamine, 100 units/mL penicillin, and 100 mg/mL streptomycin at 37 °C in a humidified incubator with a 5% CO₂-95% air atmosphere. All cells were routinely found free of mycoplasma infection.

2.2. β -Lap micelle fabrication

Three distinct micelle preparation methods (dialysis, solvent evaporation, film sonication) were used to encapsulate β -lap

within PEG-PLA micelles. For all preparation methods a 10% theoretical loading (e.g. 1 mg of β -lap and 9 mg of PEG-PLA diblock copolymer) was used unless otherwise stated. In the dialysis method, the drug and polymer were dissolved in acetone, placed within a dialysis bag (MW cutoff=2000 Da), and dialyzed against water overnight at 4 °C. The solvent evaporation method consisted of dissolving β -lap and PEG-PLA in acetone and adding the mixture dropwise to water under sonication by a Fisher Scientific Sonic Dismembrator 60 (Hampton, NH) with an output power of 0.010 W, after which the solvent was allowed to evaporate overnight. Finally, the film sonication procedure involved the dissolution of β -lap and PEG-PLA in acetone and evaporation of the solvent, yielding a solid film. Water was then added to the film and sonicated for 5 min. In each case, drug-loaded polymer micelles were filtered through 0.45 μ m nylon filters to remove non-encapsulated drug aggregates in solution, and all micelle preparations above were stored immediately at 4 °C to hinder premature drug release.

Drug loading was determined using a method previously established by Shuai et al. [19]. Briefly, 0.5 mL of micelle solution was centrifuged at a rotational speed of 2000 RPM for 30 min at 4 °C (Eppendorf Centrifuge 5804 R) using Amicon Ultra Centrifugal Filter Devices (MW cutoff=100,000 Da). Absorbance of β -lap in the resulting filtrate was measured ($\lambda_{max} = 257.2$ nm, $\epsilon = 105$ mL/(cm·mg β -lap)) using a Perkin

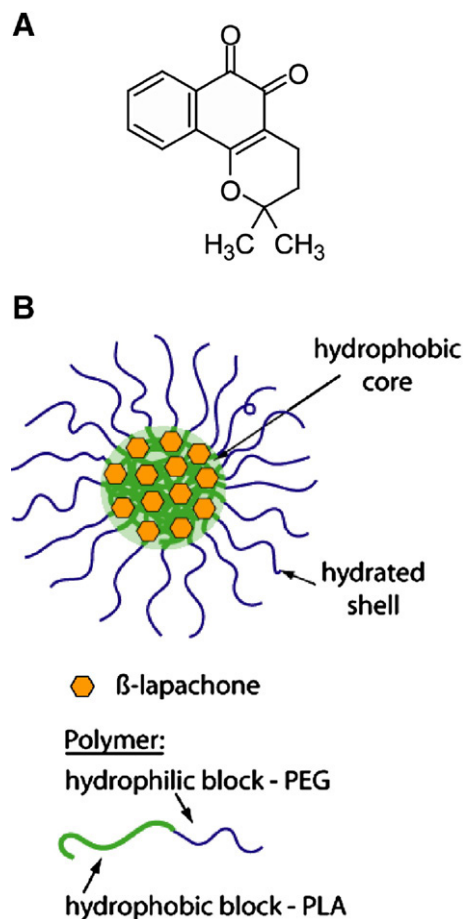


Fig. 1. (A) Chemical structure of β -lap (MW=242 Da). (B) Schematic of a β -lap-containing polymer micelle and constituent components.

Elmer Lambda 20 UV–Vis Spectrophotometer (Fremont, CA). Micelle solutions were then lyophilized overnight and the resulting freeze-dried powder was accurately weighed, dissolved in chloroform, and analyzed via UV–Vis spectrophotometry to provide the total amount of β -lap (free and micelle encapsulated). Yield, loading efficiency, and loading density of β -lap were then determined utilizing the following set of equations:

$$\% \text{ yield} = \frac{\text{total micelle amount} - \text{free } \beta\text{-lap amount}}{\text{theoretical total micelle amount}} \times 100 \quad (1)$$

$$\% \text{ drug loading efficiency} = \frac{\text{amount } \beta\text{-lap in micelles}}{\text{initial amount of } \beta\text{-lap in system}} \times 100 \quad (2)$$

$$\% \text{ drug loading density} = \frac{\text{amount } \beta\text{-lap in micelles}}{\text{amount of micelles} - \text{free } \beta\text{-lap}} \times 100 \quad (3)$$

Micelle fabrication experiments were conducted in triplicate and following data tabulation, statistical analyses between different groups were performed using a Student's two-tailed *t*-test ($P < 0.05$).

2.3. Differential scanning calorimetry (DSC) analysis

DSC measurements of the solid-state solubility of β -lap in PLA were performed using a Shimadzu Differential Scanning Calorimeter (DSC-60, Columbia, USA) with samples under a nitrogen atmosphere. The procedure was adapted from a method published by Panyam et al. [20] and previously utilized by our laboratory to determine the solid-state solubility of β -lap in poly(D,L-lactide-co-glycolide) (PLGA) [21]. Briefly, known quantities of β -lap (13 mg) and PLA (27.8 mg) were separately dissolved in acetone. Different amounts of drug were mixed with polymer, and transferred to aluminum pans. The solvent was then evaporated, and pans were crimped and weighed. Samples were heated to 180 °C at a rate of 10 °C/min. The heats of melting of β -lap were obtained using the peak integration calculation method provided by the DSC software. The solid-state solubility value of β -lap was determined by plotting enthalpy values as a function of the percentage of β -lap loading. The *X*-intercept resulting from a linear regression of the data represents the solid-state solubility value of β -lap in PLA.

2.4. β -Lap micelle characterization

Following fabrication, micelle size was determined using a Viscotek Dynamic Light Scattering (DLS) instrument (Houston, TX). Scattered light was detected at a 90° angle. Data was obtained from 10 measurements of 5 s duration and averaged utilizing the instrumental software to determine micelle size and size distribution.

Micelles were analyzed by ¹H NMR to verify core-shell architecture. β -Lap-loaded PEG–PLA micelles were prepared

using the film sonication technique at 10% w/w theoretical drug loading. Following micelle fabrication and filtration, the micelle solution was split among two Amicon Ultra Centrifugal Filter Devices (MW cutoff=100,000 Da) and concentrated by centrifugation at a speed of 2000 RPM at 4 °C to minimize premature drug loss. Micelles were then washed with water to remove free drug. Once the absorbance of both supernatants was well below a value of 0.1, micelles were freeze-dried. One batch of micelles was resuspended in D₂O, while another batch was dissolved in deuterated chloroform. The two samples were then analyzed utilizing a 400-MHz Varian NMR spectrometer (Palo Alto, CA) and the resulting spectra were compared to spectra obtained from β -lap dissolved in D₂O and PEG–PLA dissolved in chloroform.

Release studies of β -lap-containing PEG–PLA micelles were performed to examine β -lap release kinetics. Approximately 100 mg of β -lap-loaded polymer micelles were prepared utilizing the film sonication technique at a theoretical loading of 10% w/w. After micelle fabrication, the amount of loaded drug and micelles was determined, and equal amounts of micelles were aliquoted among Spectrum Float-A-Lyzer dialysis devices with a molecular weight cutoff of 100,000 Da. Release studies were conducted in triplicate in PBS at a pH of 7.4 at 37 °C. At predetermined times, the buffer solution (12 mL) was removed and replaced with an equal amount of fresh buffer solution. The amount of β -lap released from micelles was determined by measuring the absorbance of the dialysis medium at 257.2 nm via UV–Vis spectrophotometry.

2.5. Modeling of β -lap release kinetics from micelles

Theoretical models were developed to simulate the drug release profiles from polymer micelles. Previous work has shown that drug release from a micelle core occurs in two successive stages: early release that can be well described by a Higuchi dissolution model (Eqs. (4) and (5)) and late release that is well approximated by Fickian diffusion (Eq. (6)) [22]:

$$\frac{M(t)}{M(\infty)} = 1 - \left[\left(\frac{\alpha'}{\alpha_0} \right)^3 + \frac{1}{2} \frac{c_s}{c_0} \left(\left(\frac{\alpha'}{\alpha_0} \right) + \left(\frac{\alpha'}{\alpha_0} \right)^2 - 2 \left(\frac{\alpha'}{\alpha_0} \right)^3 \right) \right] \quad (4)$$

$$c_0 (\alpha_0^3 + 2\alpha'^3 - 3\alpha_0\alpha'^2) + c_s \left(4\alpha'^2\alpha_0 + \alpha_0^3 \ln \frac{\alpha_0}{\alpha'} - \alpha_0^3 - \alpha_0^2\alpha' - 2\alpha'^3 \right) = 6Dc_s a_0 t \quad (5)$$

$$\frac{M(t)}{M(\infty)} = p \left(1 - \frac{6}{\pi^2} \exp \left(\frac{-\pi^2 D t}{a_0^2} \right) \right) \quad (6)$$

where $M(t)$ is the mass of drug released at time t and $M(\infty)$ is the amount of drug released as time approaches infinity. The Higuchi model approximates drug release as a steadily moving front of dissolving drug moving inward from the periphery of the micelle core, where the drug is contained [23]. This model

has five parameters: the radius of the micelle core, a_0 ; the distance of the moving front from the center of the core at time t , a' ; the initial micelle drug loading, c_0 ; the solubility of drug in solution, c_s ; and the diffusivity of the drug in the micelle core, D_h . Later drug release was shown to be correctly approximated by Fickian diffusion out of a sphere, which has three parameters: the fraction of the drug released at infinite time, p_0 ; the radius of the micelle core, a_0 ; and the diffusivity of drug in the micelle core, D_f [24,25]. β -Lap solubility and micelle loading were known: $c_s=0.04$ mg/mL and $c_0=8.68$ mg/mL. The radius of gyration of the 5 kD PEG corona (6.16 nm) was subtracted from the hydrodynamic micelle radius (14.6 nm) to determine the size of the micelle core, $a_0=8.44$ nm, as reported previously [22]. The drug released by 360 h was used as the drug released at infinite time, p_0 . Estimates of the two remaining unknowns, the rates of β -lap diffusion, D_h and D_f , were then calculated using non-linear least squares parameter estimation (Matlab 7.1). D_h and D_f were estimated using release data from 0–18 and 18–360 h, respectively.

2.6. Cytotoxicity of β -lap micelles in vitro

Relative survival assays based on DNA content were performed in three different cancer cell lines with isogenic expression (or inhibition of enzyme activities with dicoumarol) of NQO1 as previously described [5]. H596 non-small cell lung cancer and MDA-MB-231 breast cancer cells contain homozygous *2 NQO1 polymorphisms and thereby lack NQO1 expression. Isogenic NQO1+ counterparts were generated and characterized for β -lap free drug responses as described [5,26]. In contrast, DU-145 human prostate cancer cells endogenously over-express NQO1, and its enzyme activity can be blocked by coadministration of dicoumarol, mimicking an NQO1-deficient cell. Briefly, NQO1+ or NQO1– H596 and MDA-MB-231 cells were seeded (10,000 cells/well) into each well of 48-well plates. DU-145 cells were seeded similarly. On the following day, media were removed, and media containing predetermined doses of free β -lap drug (dissolved in DMSO) or β -lap micelles (prepared via the film sonication method) were added for a duration of 2 h. For DU-145 cells, dicoumarol at a concentration of 40 μ M was coadministered to cells to inhibit NQO1. After 2 h exposures, media were then removed, control growth media added, and cells were allowed to grow for an additional 7 days. DNA content was determined by DNA fluorescence Hoescht

dye 33258, using an adaptation of the method of Labarca and Paigen [27]. Samples were read in a Perkin Elmer HTS 7000 Bio Assay Reader (Waltham, MA) and data were expressed as means \pm SE relative growth and graphed as treated/control (T/C) values from six wells per treatment.

2.7. DNA damage and cell death assays

Distinct biological assays were conducted in NQO1+ and NQO1– H596 cells to corroborate the mechanism of action of β -lap-mediated cell death via micellar drug delivery versus responses known for free drug [7,26,28,29]. The first consisted of reactive oxygen species (ROS) analyses. Following β -lap micelle exposure to cells, ROS formation was ascertained using the conversion of non-fluorescent 5, 6-Chloromethyl-2V, 7V-dichlorodihydrofluorescein diacetate (CM-H₂DCFDA) to its fluorescent derivative (DCF) by flow cytometry (FC-500 flow cytometer, Beckman Coulter Electronics, Miami, FL) as described [30].

DNA damage analyses, or alkaline comet assays, were also performed. DNA lesions, including DNA single and double strand breaks (SSBs, DSBs, respectively), as well as DNA base damage, were assessed in single cells treated with β -lap micelles using alkaline comet assays as previously described [28,31]. Slides were stained with SYBR-green and visualized using a Nikon Eclipse TE2000-E fluorescence microscope (Melville, NY), after which digital photomicrographs were taken.

Lastly, nucleotide analyses were conducted, where changes in intracellular nicotinamide adenine dinucleotide (NAD+) levels were measured in cells after β -lap micelle exposure as described [28]. Intracellular NAD+ levels were expressed as percentage of treated divided by control (%T/C).

3. Results

3.1. Effect of different micelle fabrication methods on drug loading

Several different micelle fabrication techniques were examined with the purpose of generating β -lap micelles with an adequate size, yield, and drug loading density and efficiency. Table 1 depicts the size, yield, and loading values obtained from the three different fabrication methods. As shown in the table, from an initial 10% theoretical loading, the dialysis method produced micelles with an extremely low drug loading at 0.02 \pm 0.01%, as well as a poor loading efficiency (0.08 \pm 0.04%) and micelle yield (36.3 \pm 3.40%). The solvent evaporation procedure provided a marked improvement in β -lap loading over the dialysis method, with a loading percentage of 0.39 \pm 0.05%, but with a low loading efficiency of 4.12 \pm 0.64%. Conversely, the film sonication method produced the highest β -lap loading of micelles among all three fabrication methods, with a 4.7 \pm 1.0% drug loading at a theoretical loading of 10%, a loading efficiency of 41.9 \pm 5.6%, and a high micelle yield of 85.3 \pm 6.7%. With a subsequent increase in theoretical drug loading to 20%, β -lap loading in micelles increased to 6.5 \pm 1.0%.

Table 1
 β -Lapachone micelle size, yield, and drug loading parameters from different fabrication procedures

Micelle fabrication method	Theoretical loading (%)	Micelle size (nm)	Yield (%)	Loading efficiency (%)	Loading density (%)
Dialysis	10	23.3 \pm 1.2	36.3 \pm 3.4	0.08 \pm 0.04	0.02 \pm 0.01
Solvent evaporation	10	17.3 \pm 0.2	95.0 \pm 1.8	4.1 \pm 0.6	0.4 \pm 0.1
Film sonication	5	28.4 \pm 2.7	88.6 \pm 3.7	39.8 \pm 1.0	2.2 \pm 0.1
	10	29.6 \pm 1.5	85.3 \pm 6.7	41.9 \pm 5.6	4.7 \pm 1.0
	20	26.8 \pm 3.2	85.2 \pm 3.0	32.9 \pm 5.9	6.5 \pm 1.0

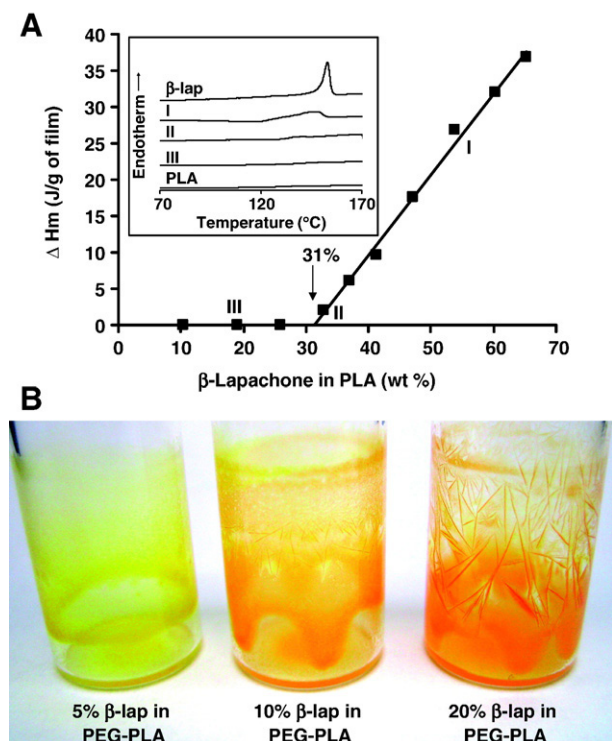


Fig. 2. Solid-state solubility studies of β -lap in PLA polymer. Fig. 2A depicts β -lap melting enthalpy (ΔH_m) as a function of β -lap loading percentage. The X -intercept indicates the solubility limit of β -lap in PLA. Fig. 2B represents images of β -lap and PLA films at different loading percentages for qualitative comparison.

Meanwhile, a lowered loading efficiency to $32.9 \pm 5.9\%$ was observed at this composition. Taken together, these data highlight the effectiveness of the film sonication method at producing higher loaded β -lap micelles over other micelle fabrication methods, with differences in loading percentage values being statistically significant ($P < 0.05$).

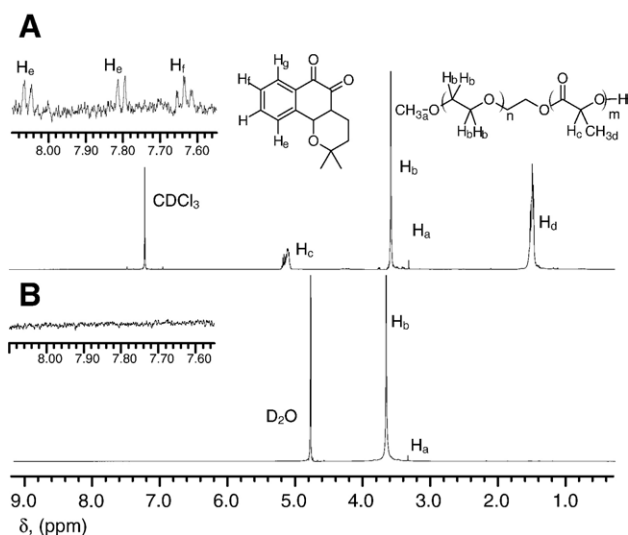


Fig. 3. ^1H NMR spectra of β -lap-loaded PEG–PLA micelles in (A) deuterated chloroform (CDCl_3) and (B) deuterated water (D_2O). Figure insets represent magnifications of the aromatic protons from β -lap.

3.2. Solubility of β -lap in PLA polymer

In order to gain insight into interactions between β -lap and the core-forming material (i.e. PLA), solid-state solubility studies were performed using DSC. Values of ΔH_m (J/g) were plotted as a function of β -lap loading percentage (Fig. 2A). The X -intercept, provided by linear regression of the data, yields the solid-state solubility of β -lap in PLA at 31%. The dissolution behavior of β -lap within PLA helps to explain discrepancies in drug loading among the different micelle fabrication procedures. Close inspection of images of β -lap/PEG5k–PLA5k films at different loading percentages illustrates the dissolution of drug within the polymer (Fig. 2B). At levels below the solid-state solubility value, the drug and polymer appear as a continuous film. However, at higher loading percentages (20%), β -lap crystals appeared in the film, indicative of drug loading above the solubility threshold of β -lap in PLA core.

3.3. β -Lap micelle characterization

Drug-loaded micelle size was determined utilizing dynamic light scattering (DLS) for each of the fabrication methods examined (Table 1). The three different methods all produced micelles of an adequate size (e.g. 10–100 nm), with the dialysis and solvent evaporation procedures yielding micelle sizes of 23.3 ± 1.2 nm and 17.3 ± 0.2 nm, respectively. The film sonication procedure produced micelles with a slightly greater average diameter (29.6 ± 1.5 nm), possibly due to the increased loading of the drug within the micelle core [32].

Encapsulation of β -lap inside micelle cores was demonstrated by comparing ^1H NMR spectra of micelle samples in deuterated chloroform (CDCl_3) and deuterated water (D_2O) (Fig. 3). In CDCl_3 , prominent resonance peaks of β -lap were observed in addition to those of PLA and PEG blocks, indicating that the micelle contains both copolymer and β -lap. In contrast, only the PEG resonance peaks were detected in D_2O , while both the PLA and β -lap resonance peaks were absent. The micelle shells consisting of PEG blocks were well solvated in D_2O and therefore showed clear ^1H NMR signal. In contrast, when β -lap was encapsulated inside micelle cores,

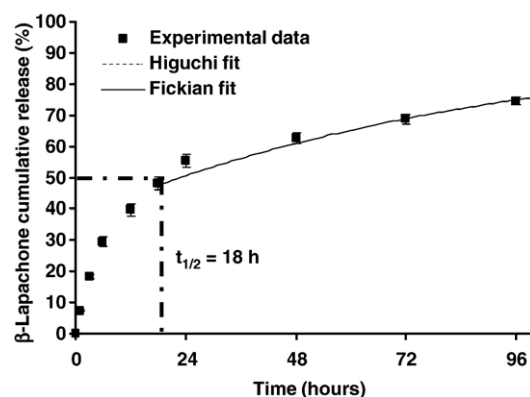


Fig. 4. In vitro β -lap release profiles from PEG–PLA polymer micelles in PBS at pH 7.4 and 37°C . The error bars were calculated as standard deviation from triplicate samples.

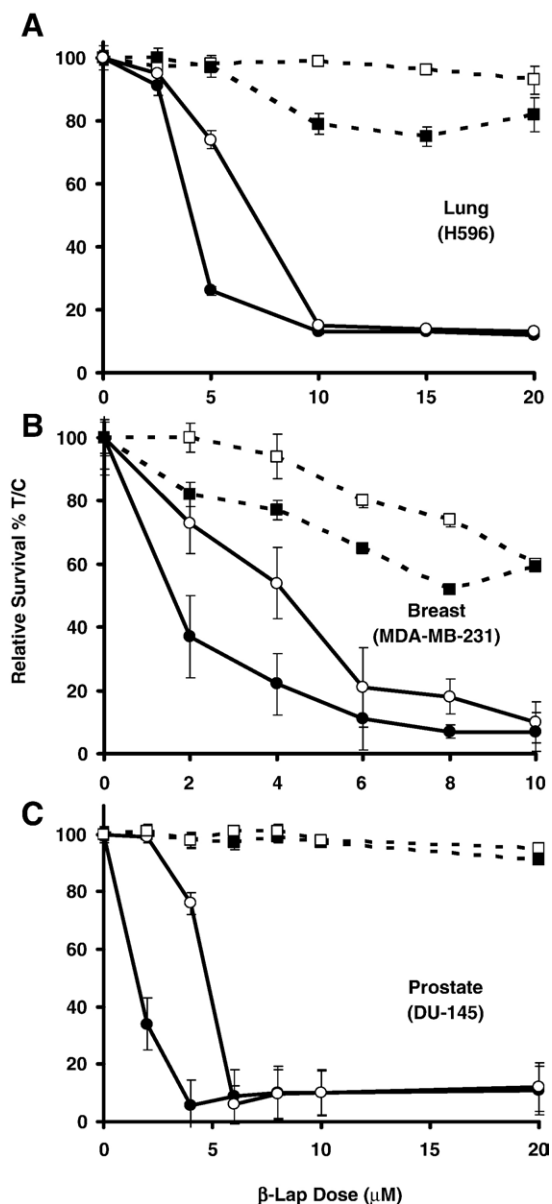


Fig. 5. Long-term, relative survival assays of (A) H596 lung, (B) DU-145 prostate, and (C) MDA-MB-231 breast cancer cells treated with β -lap at indicated doses for 2 h. In the figures, \square corresponds to NQO1 $^-$ cells treated with β -lap micelles, \blacksquare represents NQO1 $^-$ cells treated with free β -lap, \circ corresponds to NQO1 $^+$ cells treated with β -lap micelles, and \bullet represents NQO1 $^+$ cells treated with free drug.

resonance peaks of PLA blocks and β -lap were not observed due to their insufficient mobility in D_2O , consistent with the core-shell structure of polymeric micelles [33,34].

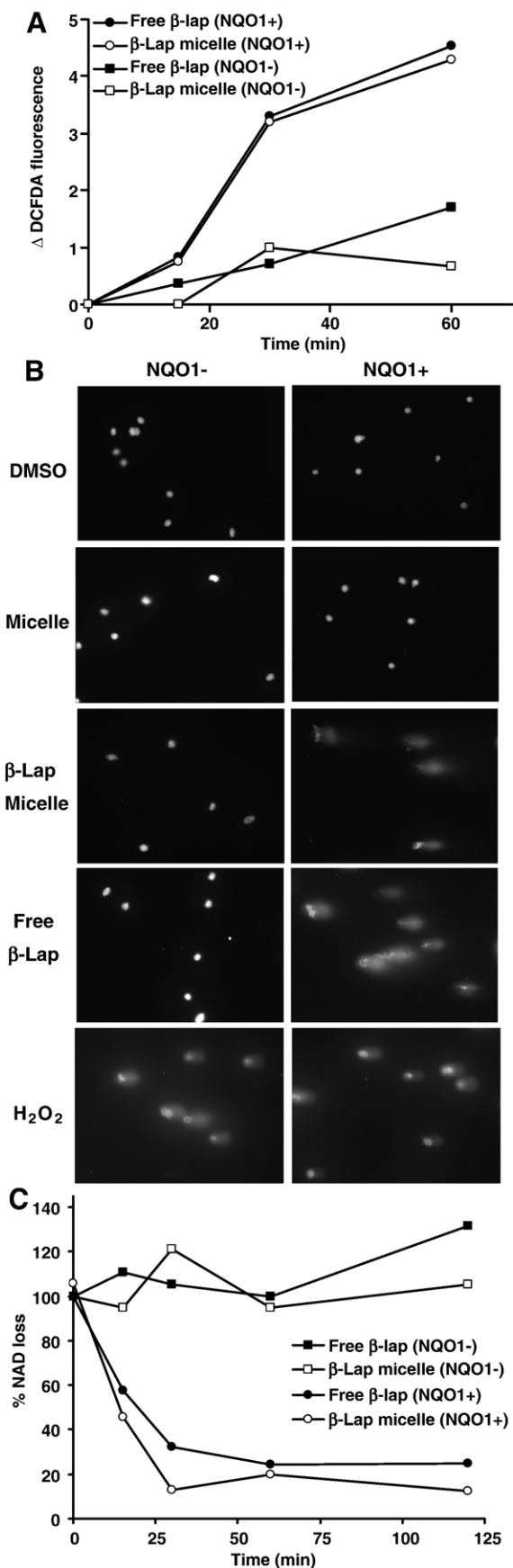
The release kinetics of β -lap from PEG-PLA polymer micelles were examined in vitro (Fig. 4). As can be seen from the figure, the time for 50% of drug release ($t_{1/2}$) is 18 h, with the majority of the drug ($\sim 75\%$) being released over the course of 4 days. Alonso and coworkers have demonstrated that PEG-PLA nanoparticles do not undergo significant degradation over two weeks incubation in PBS buffer (pH 7.4) at 37 °C [35,36]. Based on these and other findings, drug is released primarily via diffusion processes, and was modeled as such. Simulated model

drug release is shown along with experimentally measured cumulative release data. The Higuchi based model [23] output was successfully fit to the experimental measurements from 0–18 h. D_h had an estimated value of $4.2 \times 10^{-17} \text{ cm}^2/\text{s}$ (95% confidence interval: $4.0\text{--}4.4 \times 10^{-17} \text{ cm}^2/\text{s}$). After 18 h, the Fickian [24,25] diffusion approximation begins to fit the data and continues to fit the data until the end of the study. For the Fick approximation, the value of diffusion, D_f , is $2.3 \times 10^{-19} \text{ cm}^2/\text{s}$ (95% confidence interval: $2.0\text{--}2.5 \times 10^{-19} \text{ cm}^2/\text{s}$), almost 200 times slower than drug transport for the first 18 h. The quality of the model fits and low error of the parameter estimates indicate that both models well approximate the drug release data at different times of drug release. However, the diffusion rates at each stage of drug release differed considerably, suggesting that two different processes may be taking place. In the first 18 h, drug release occurs relatively quickly through a Higuchi-like mechanism. Drug released in this period of time could be precipitated in and around the micelle core but may have good access to the surrounding aqueous environment through micelle surface. However, diffusion after 18 h is dramatically slower, which may reflect drug that has less access to the surrounding hydrophilic corona. This fraction of the drug loading could be entrapped in or even dissolved in dense solid regions of the hydrophobic core, where polymer entanglement serves as a much greater impediment to drug transport.

3.4. Mechanism of action of cell death induced by β -lap micelles

Growth assays were performed to examine the mechanism of action of β -lap micelles on NQO1-overexpressing tumor cells compared to NQO1-null tumor cells. NQO1 $^-$ cells also serve to mimic normal tissues that are NQO1 deficient. Fig. 5 depicts relative survival curves (%T/C) in vitro of three different tumor cell lines (lung, prostate, and breast) treated with free β -lap and β -lap micelles at different drug doses. Results show that after a 2 h incubation with β -lap micelles, a significant increase in cytotoxicity can be observed in NQO1 $^+$ over NQO1 $^-$ cells in all three cell lines. In H596 cells, a 26% loss in survival in NQO1 $^+$ cells following 5 μM β -lap micelle administration was noted, and at 10 μM an approximate 85% loss in survival was observed. Values for β -lap micelles were consistently less cytotoxic than for free drug exposures. β -Lap micelle cytotoxicity was equal to that of free β -lap drug administration at 10 μM , with the difference in cytotoxicities at smaller doses attributed to a delay in drug release from the micelles. Finally, while free β -lap leads to an approximate 25% loss in survival in NQO1 $^-$ cells at a 15 μM dose, β -lap micelles have minimal toxicity in NQO1 $^-$ cells ($\sim 7\%$ loss in survival at 20 μM dose).

The same pattern of cell cytotoxicity for the NQO1 $^+$ cells and survival in the NQO1 $^-$ cells was evident in human prostate and breast cancer cells. In DU-145 and MDA-MB-231 cells, β -lap micelles killed more than 50% of NQO1 $^+$ cells at a dose of 6 μM . At further dose increases, β -lap micelle cytotoxicity approached that of free β -lap. NQO1 $^-$ cells were resistant to β -lap micelles. In DU-145 cells, there was less than a 10% loss in



cell survival after coadministration of dicoumarol (NQO1 inhibitor) with β -lap micelles. Similarly, NQO1⁻ MDA-MB-231 cells were resistant to β -lap micelles. Importantly drug-free micelles were shown to have no cytotoxic effect on tumor cells (data not shown).

In attempts to elucidate whether the unique mechanism of action of β -lap was preserved through micellar delivery of the drug, several key biological assays were performed in H596 cells to identify vital components of β -lap-mediated cell death in NSCLC, as reported by Bey et al. [26]. Fig. 6 shows the results of the three biological assays (ROS analysis, comet assays, and NAD loss) conducted to examine vital characteristics of β -lap-induced cell death. Administration of β -lap micelles at a dose of 10 μ M leads to oxidative stress in NQO1⁺ cells in a manner identical to that of free β -lap drug administration. In contrast, β -lap-induced oxidative stress was absent in NQO1⁻ cells. In the NQO1⁻ cells, no DNA damage was evident after exposure with free β -lap drug or β -lap micelles. However, in the NQO1⁺ cells, extensive comet tail formation can be observed, indicating DNA damage. Lastly, Fig. 6C shows NAD loss associated with β -lap micelle administration to H596 cells at the 10 μ M dose. As can be observed from the figure, no NAD loss occurs in the NQO1⁻ cells, while an exponential decrease in NAD is observed with increasing time of exposure to micelles. Taken together, these results serve to show that the unique mechanism of action of β -lap is preserved through micellar delivery.

4. Discussion

The objective of the present study was to develop polymer micelles that can effectively encapsulate β -lap with adequate loading density and minimal loss of drug and polymer. Of the three methods examined in this study, film sonication yielded micelles with the highest loading density and loading efficiency. The dialysis method has been shown to be effective in cases where the encapsulated agent is very water insoluble. Despite the low water solubility (0.04 mg/mL) of β -lap, this value is still much higher compared to agents such as paclitaxel (0.34 μ g/mL) [37]. Hence, the majority of β -lap can still be lost to the surrounding aqueous medium during dialysis, leaving only a very minimal amount ($0.02 \pm 0.01\%$) within the micelles. The solvent evaporation technique is another widely used method for micelle formation, and we have successfully formed PEG-PLA polymer micelles with high doxorubicin loading [38]. However, this method also proved inefficient at loading β -lap within micelles (loading density = $0.39 \pm 0.05\%$), mainly because of the crystallization behavior of β -lap. Both the dialysis and solvent evaporation methods have slow processes of

Fig. 6. Cell death and DNA damage assays conducted in NQO1⁺ and NQO1⁻ H596 NSCLC cells at a dose of 10 μ M of free β -lap or β -lap-containing micelles. (A) Induction of ROS in H596 cells incubated for 20 min with CM-H₂DCFDA and then treated with the dose and assessed at the times indicated. (B) Alkaline comet assays of H596 following a 2 h exposure. Vehicle alone (DMSO), micelles alone, and H₂O₂ (for NQO1 independent DNA damage) served as controls. (C) Nucleotide loss following exposure and assessed at the times indicated.

micellar formation, requiring time for organic solvent to exchange with an aqueous environment or evaporate organic solvent, respectively. In contrast, β -lap crystallization is a faster kinetic process, which can result in the loss of the majority of drug to crystal formation.

The film sonication method proved effective at achieving higher drug loading density within micelles. This increased loading can be best explained by the formation of a molecular level mixture between β -lap and PLA. During the film formation process, β -lap dissolves within the PLA core at a solid-state solubility of 31% (Fig. 2A). At values below this limit, β -lap forms a homogeneous molecular-level mixture with the PLA matrix. The dissolution of drug within the polymer matrix prevents β -lap from crystallizing during micelle formation, leading to higher drug loading density within the micelles. Similar phenomenon was observed previously by Panyam et al. where an increase in drug loading correlated with increases in solid-state solubility [20]. While the film sonication method led to a significant increase in drug loading density, the loading efficiency was only approximately 40%. We hypothesize that β -lap mixed with PEG chains in the film may not be efficiently loaded inside the micelle core upon sonication. One possible strategy to overcome this limitation is to use longer core forming blocks as demonstrated by Allen et al. [39], or the addition of PLA within the film.

The film sonication method leads to micelles with an increased amount of β -lap encapsulated within the core ($4.7 \pm 1.0\%$ to $6.5 \pm 1.0\%$). Additionally, the hydrodynamic diameter of the micelles (29.6 ± 1.5 nm) as measured by DLS also proves adequate for future in vivo delivery applications. Micelles of similar diameters (e.g. SP1049C and Genexol) have shown prolonged blood circulation times [40]. ^1H NMR studies clearly demonstrated the core-shell structure of the polymer micelles produced by the film sonication procedure. The results indicate that the drug is encapsulated within the PLA micelle core and the micelle surface is stabilized with a mobile PEG corona. Such core-shell structure has the potential advantage in the protection of the drug from enzymatic degradation while the PEG layer hinders plasma protein adsorptions and particle aggregation. Gref et al. found that reduced protein adsorption depended greatly on PEG molecular weight (~ 5000 Da) and density at the surface ($\sim 2\text{--}5\%$) [41]. In a different study, Hsiue and coworkers found that PEG–PLA micelles were stable in bovine serum albumin (BSA) for incubation timepoints of up to 25 h, as evidenced by minimal change of particle size [42]. Reduction in plasma protein interaction should translate into very stable micelles following IV injection, as shown by Kataoka and coworkers, who demonstrated that 25% of injected PEG–PLA micelles were found to be stably circulating in blood vessels 24 h after injection [43]. The aforementioned Genexol[®], a paclitaxel-containing PEG–PLA micelle formulation currently in phase I clinical trials, was shown by Bang and coworkers to have a blood elimination half-life of approximately 11 h. This same study showed that the micelle formulation had significant increase in MTD, and improved antitumor efficacy when compared to a traditional paclitaxel formulation, consistent with stable drug encapsulation in micelles in vivo [44].

In vitro growth inhibition assays demonstrate that β -lap micelles effectively kill a variety of tumor cells overexpressing NQO1 while sparing NQO1[−] cells. Close examination shows that micelle-delivered β -lap is less toxic to both NQO1⁺ and NQO1[−] cells compared to the free drug (Fig. 5). Several reasons may explain this discrepancy. Firstly, the actual intracellular concentration of β -lap may be smaller in cells incubated with β -lap micelles than those with free drug. This is possible since most anticancer agents are lipophilic (as well as hydrophobic) and can easily cross cell membranes. PEG-stabilized nanoparticles are typically internalized through fluidic phase endocytosis [14], and PEG shielding can effectively reduce cell uptake, leading to a smaller drug concentration inside the cells. Secondly, after cell internalization, micelle-delivered β -lap may not be immediately available due to micelle encapsulation. In vitro drug release studies showed the value of $t_{1/2}$ is 18 h (Fig. 4). This delayed drug availability may also contribute to a lesser cytotoxicity as shown in both NQO1⁺ and NQO1[−] cells. Despite reduced in vitro toxicity, the value of β -lap micelles will likely result in the increased drug solubility and improved pharmacokinetics over free drug during in vivo applications. In polymer–drug conjugate systems developed by Li et al. [45] and Ulbrich et al. [46] for the delivery of paclitaxel and doxorubicin respectively, the conjugated drugs showed less in vitro cytotoxicity compared to the free drugs, however, their antitumor efficacy responses were considerably higher due to increased accumulation in tumors.

Comprehensive biological studies show that the unique mechanism of action of β -lap, as shown previously by Bey et al. [26] is preserved through micellar drug delivery. In NQO1-overexpressing tumor cells incubated with β -lap micelles, reactive oxygen species (ROS) were generated (Fig. 6A) as a result of NQO1-dependent futile cycling of the β -lap and subsequent depletion of NAD(P)H from the cell (Fig. 6C). Accumulation of ROS such as hydroxyl radicals causes massive DNA damage as shown in comet assay for β -lap micelles as well as the free drug (Fig. 6B). This NQO1-specific cytotoxicity combined with micellar drug delivery bodes well for in vivo translation of the platform, where upon administration, β -lap micelles will accumulate in tumor tissue through passive targeting and release β -lap, which will only be bioactivated in the presence of high levels of NQO1. Concurrently, normal healthy tissues will be spared from the cytotoxic effect of β -lap due to lack of NQO1 expression and reduced micelle uptake.

5. Conclusions

In summary, we have successfully developed β -lap-PEG–PLA polymer micelles with adequate loading density, optimal size, core-shell structure, and diffusion-based release kinetics. Upon administration to NQO1⁺ and NQO1[−] cells, we were able to show an NQO1-dependent cytotoxicity that resembles that of free drug administration, where NQO1⁺ cells are effectively killed and NQO1[−] cells are spared. Future studies will focus on the preclinical evaluation of these micelles in NQO1-overexpressing animal tumor models.

Acknowledgements

This work was supported by an NIH grant CA90696 to JG, NIH grant CA102792 to DAB, and DOD grant W81XWH-04-1-0164 to DAB. EB is grateful for the support of a National Institutes of Health minority supplement grant. This is report CSCNP10 from the Program in Cell Stress and Cancer Nanomedicine at UT Southwestern Medical Center at Dallas.

References

- [1] M. Belinsky, A.K. Jaiswal, NAD(P)H:quinone oxidoreductase1 (DT-diaphorase) expression in normal and tumor tissues, *Cancer Metastasis Rev.* 12 (2) (1993) 103–117.
- [2] C.D. Logsdon, D.M. Simeone, C. Binkley, T. Arumugam, J.K. Greenson, T.J. Giordano, D.E. Misek, R. Kuick, S. Hanash, Molecular profiling of pancreatic adenocarcinoma and chronic pancreatitis identifies multiple genes differentially regulated in pancreatic cancer, *Cancer Res.* 63 (10) (2003) 2649–2657.
- [3] A.M. Lewis, M. Ough, J. Du, M.S. Tsao, L.W. Oberley, J.J. Cullen, Targeting NAD(P)H:Quinone oxidoreductase (NQO1) in pancreatic cancer, *Mol. Carcinog.* 43 (4) (2005) 215–224.
- [4] D. Siegel, D. Ross, Immunodetection of NAD(P)H:quinone oxidoreductase 1 (NQO1) in human tissues, *Free Radic. Biol. Med.* 29 (3–4) (2000) 246–253.
- [5] J.J. Pink, S.M. Planchon, C. Tagliarino, M.E. Varnes, D. Siegel, D.A. Boothman, NAD(P)H:Quinone oxidoreductase activity is the principal determinant of beta-lapachone cytotoxicity, *J. Biol. Chem.* 275 (8) (2000) 5416–5424.
- [6] C. Tagliarino, J.J. Pink, G.R. Dubyak, A.L. Nieminen, D.A. Boothman, Calcium is a key signaling molecule in beta-lapachone-mediated cell death, *J. Biol. Chem.* 276 (22) (2001) 19150–19159.
- [7] K.E. Reinicke, E.A. Bey, M.S. Bentle, J.J. Pink, S.T. Ingalls, C.L. Hoppel, R.I. Misico, G.M. Arzac, G. Burton, W.G. Bornmann, D. Sutton, J. Gao, D.A. Boothman, Development of beta-lapachone prodrugs for therapy against human cancer cells with elevated NAD(P)H:quinone oxidoreductase 1 levels, *Clin. Cancer Res.* 11 (8) (2005) 3055–3064.
- [8] M. Ough, A. Lewis, E.A. Bey, J. Gao, J.M. Ritchie, W. Bornmann, D.A. Boothman, L.W. Oberley, J.J. Cullen, Efficacy of beta-lapachone in pancreatic cancer treatment: exploiting the novel, therapeutic target NQO1, *Cancer Biother.* 4 (1) (2005) 95–102.
- [9] N. Nasongkla, A.F. Wiedmann, A. Bruening, M. Beman, D. Ray, W.G. Bornmann, D.A. Boothman, J. Gao, Enhancement of solubility and bioavailability of beta-lapachone using cyclodextrin inclusion complexes, *Pharm. Res.* 20 (10) (2003) 1626–1633.
- [10] G.S. Kwon, M.L. Forrest, Amphiphilic block copolymer micelles for nanoscale drug delivery, *Drug Dev. Res.* 67 (1) (2006) 15–22.
- [11] H. Otsuka, Y. Nagasaki, K. Kataoka, PEGylated nanoparticles for biological and pharmaceutical applications, *Adv. Drug Deliv. Rev.* 55 (3) (2003) 403–419.
- [12] V.P. Torchilin, Micellar nanocarriers: pharmaceutical perspectives, *Pharm. Res.* 24 (1) (2007) 1–16.
- [13] M. Jones, J. Leroux, Polymeric micelles — a new generation of colloidal drug carriers, *Eur. J. Pharm. Biopharm.* 48 (2) (1999) 101–111.
- [14] R. Savic, L. Luo, A. Eisenberg, D. Maysinger, Micellar nanocontainers distribute to defined cytoplasmic organelles, *Science* 300 (5619) (2003) 615–618.
- [15] V.P. Torchilin, A.N. Lukyanov, Z. Gao, B. Papahadjopoulos-Stenberg, Immunomicelles: targeted pharmaceutical carriers for poorly soluble drugs, *Proc. Natl. Acad. Sci. U. S. A.* 100 (10) (2003) 6039–6044.
- [16] H. Hashizume, P. Baluk, S. Morikawa, J.W. McLean, G. Thurston, S. Roberge, R.K. Jain, D.M. McDonald, Openings between defective endothelial cells explain tumor vessel leakiness, *Am. J. Pathol.* 156 (4) (2000) 1363–1380.
- [17] H. Maeda, The enhanced permeability and retention (EPR) effect in tumor vasculature: the key role of tumor-selective macromolecular drug targeting, *Adv. Enzyme Regul.* 41 (2001) 189–207.
- [18] S.M. Planchon, S. Wuerzberger, B. Frydman, D.T. Witiak, P. Hutson, D.R. Church, G. Wilding, D.A. Boothman, Beta-lapachone-mediated apoptosis in human promyelocytic leukemia (HL-60) and human prostate cancer cells: a p53-independent response, *Cancer Res.* 55 (17) (1995) 3706–3711.
- [19] X. Shuai, H. Ai, N. Nasongkla, S. Kim, J. Gao, Micellar carriers based on block copolymers of poly(epsilon-caprolactone) and poly(ethylene glycol) for doxorubicin delivery, *J. Control. Release* 98 (3) (2004) 415–426.
- [20] J. Panyam, D. Williams, A. Dash, D. Leslie-Pelecky, V. Labhasetwar, Solid-state solubility influences encapsulation and release of hydrophobic drugs from PLGA/PLA nanoparticles, *J. Pharm. Sci.-Us* 93 (7) (2004) 1804–1814.
- [21] F.J. Wang, E. Blanco, H. Ai, D.A. Boothman, J. Gao, Modulating beta-lapachone release from polymer millirods through cyclodextrin complexation, *J. Pharm. Sci.-Us* 95 (10) (2006) 2309–2319.
- [22] D. Sutton, S. Wang, N. Nasongkla, E. Dormidontova, J. Gao, Doxorubicin and beta-lapachone release and interaction with micellar core materials. *Exp. Biol. Med.* (in press).
- [23] T. Higuchi, Mechanism of sustained-action medication. Theoretical analysis of rate of release of solid drugs dispersed in solid matrices, *J. Pharm. Sci.* 52 (1963) 1145–1149.
- [24] J. Crank, *The Mathematics of Diffusion*, Oxford University Press, New York, NY, 1975.
- [25] P.L. Ritger, N.A. Peppas, A simple equation for description of solute release I. Fickian and non-fickian release from non-swelling devices in the form of slabs, spheres, cylinders or discs, *J. Control. Release* 5 (1) (1987) 23–36.
- [26] E.A. Bey, M.S. Bentle, K.E. Reinicke, Y. Dong, C.R. Yang, L. Girard, J.D. Minna, W.G. Bornmann, J. Gao, D.A. Boothman, A novel NQO1- and PARP-1-mediated cell death pathway induced in non-small cell lung cancer cells by beta-lapachone. *Proc. Natl. Acad. Sci. U. S. A.* (in press).
- [27] C. Labarca, K. Paigen, A simple, rapid, and sensitive DNA assay procedure, *Anal. Biochem.* 102 (2) (1980) 344–352.
- [28] M.S. Bentle, K.E. Reinicke, E.A. Bey, D.R. Spitz, D.A. Boothman, Calcium-dependent modulation of poly(ADP-ribose) polymerase-1 alters cellular metabolism and DNA repair, *J. Biol. Chem.* 281 (44) (2006) 33684–33696.
- [29] C. Tagliarino, J.J. Pink, K.E. Reinicke, S.M. Simmers, S.M. Wuerzberger-Davis, D.A. Boothman, Mu-calpain activation in beta-lapachone-mediated apoptosis, *Cancer Biother.* 2 (2) (2003) 141–152.
- [30] V. Panduri, S.A. Weitzman, N.S. Chandel, D.W. Kamp, Mitochondrial-derived free radicals mediate asbestos-induced alveolar epithelial cell apoptosis, *Am. J. Physiol., Lung Cell. Mol. Physiol.* 286 (6) (2004) L1220–L1227.
- [31] P.L. Olive, J.P. Banath, R.E. Durand, Heterogeneity in radiation-induced DNA damage and repair in tumor and normal cells measured using the “comet” assay, *Radiat. Res.* 122 (1) (1990) 86–94.
- [32] V.P. Torchilin, Targeted polymeric micelles for delivery of poorly soluble drugs, *Cell. Mol. Life Sci.* 61 (19–20) (2004) 2549–2559.
- [33] C.R. Heald, S. Stolnik, K.S. Kujawinski, C. De Matteis, M.C. Garnett, L. Illum, S.S. Davis, S.C. Purkiss, R.J. Barlow, P.R. Gellert, Poly(lactic acid)-poly(ethylene oxide) (PLA-PEG) nanoparticles: NMR studies of the central solidlike PLA core and the liquid PEG corona, *Langmuir* 18 (9) (2002) 3669–3675.
- [34] J.S. Hrkach, M.T. Peracchia, A. Domb, N. Lotan, R. Langer, Nanotechnology for biomaterials engineering: structural characterization of amphiphilic polymeric nanoparticles by H-1 NMR spectroscopy, *Biomaterials* 18 (1) (1997) 27–30.
- [35] R. Gref, P. Quellec, A. Sanchez, P. Calvo, E. Dellacherie, M.J. Alonso, Development and characterization of CyA-loaded poly(lactic acid)-poly(ethylene glycol)PEG micro- and nanoparticles. Comparison with conventional PLA particulate carriers, *Eur. J. Pharm. Biopharm.* 51 (2) (2001) 111–118.
- [36] P. Quellec, R. Gref, E. Dellacherie, F. Sommer, M.D. Tran, M.J. Alonso, Protein encapsulation within poly(ethylene glycol)-coated nanospheres. II.

- Controlled release properties, *J. Biomed. Mater. Res.* 47 (3) (1999) 388–395.
- [37] W. Bouquet, W. Ceelen, B. Fritzinger, P. Pattyn, M. Peeters, J.P. Remon, C. Vervaet, Paclitaxel/beta-cyclodextrin complexes for hyperthermic peritoneal perfusion — formulation and stability, *Eur. J. Pharm. Biopharm.* (in press), doi:10.1016/j.ejpb.2006.11.025.
- [38] N. Nasongkla, E. Bey, J. Ren, H. Ai, C. Khemtong, J.S. Guthi, S.F. Chin, A.D. Sherry, D.A. Boothman, J. Gao, Multifunctional polymeric micelles as cancer-targeted, MRI-ultrasensitive drug delivery systems, *Nano Lett.* 6 (11) (2006) 2427–2430.
- [39] C. Allen, D. Maysinger, A. Eisenberg, Nano-engineering block copolymer aggregates for drug delivery, *Colloids Surf., B Biointerfaces* 16 (1–4) (1999) 3–27.
- [40] D. Sutton, N. Nasongkla, E. Blanco, J. Gao, Functionalized micellar systems for cancer targeted drug delivery. *Pharm. Res.* (in press), doi:10.1007/S11095-006-9223-y.
- [41] R. Gref, M. Luck, P. Quellec, M. Marchand, E. Dellacherie, S. Harnisch, T. Blunk, R.H. Muller, ‘Stealth’ corona-core nanoparticles surface modified by polyethylene glycol (PEG): influences of the corona (PEG chain length and surface density) and of the core composition on phagocytic uptake and plasma protein adsorption, *Colloids Surf., B Biointerfaces* 18 (3–4) (2000) 301–313.
- [42] C.L. Lo, C.K. Huang, K.M. Lin, G.H. Hsiue, Mixed micelles formed from graft and diblock copolymers for application in intracellular drug delivery, *Biomaterials* 28 (6) (2007) 1225–1235.
- [43] Y. Yamamoto, Y. Nagasaki, Y. Kato, Y. Sugiyama, K. Kataoka, Long-circulating poly(ethylene glycol)–poly(D,L-lactide) block copolymer micelles with modulated surface charge, *J. Control. Release* 77 (1–2) (2001) 27–38.
- [44] T.Y. Kim, D.W. Kim, J.Y. Chung, S.G. Shin, S.C. Kim, D.S. Heo, N.K. Kim, Y.J. Bang, Phase I and pharmacokinetic study of Genexol-PM, a cremophor-free, polymeric micelle-formulated paclitaxel, in patients with advanced malignancies, *Clin. Cancer Res.* 10 (11) (2004) 3708–3716.
- [45] C. Li, D.F. Yu, R.A. Newman, F. Cabral, L.C. Stephens, N. Hunter, L. Milas, S. Wallace, Complete regression of well-established tumors using a novel water-soluble poly(L-glutamic acid) paclitaxel conjugate, *Cancer Res.* 58 (11) (1998) 2404–2409.
- [46] K. Ulbrich, T. Etrych, P. Chytil, M. Jelinkova, B. Rihova, HEMA copolymers with pH-controlled release of doxorubicin — in vitro cytotoxicity and in vivo antitumor activity, *J. Control. Release* 87 (1–3) (2003) 33–47.

Combined radiofrequency ablation and doxorubicin-eluting polymer implants for liver cancer treatment

Brent D. Weinberg,¹ Elvin Blanco,² Scott F. Lempka,¹ James M. Anderson,³ Agata A. Exner,⁴ Jinming Gao²

¹Department of Biomedical Engineering, Case Western Reserve University, Cleveland, Ohio 44106

²Simmons Comprehensive Cancer Center, University of Texas Southwestern Medical Center, Dallas, Texas 75390

³Institute of Pathology, Case Western Reserve University, Cleveland, Ohio 44106

⁴Department of Radiology, Case Western Reserve University, Cleveland, Ohio 44106

Received 15 May 2006; accepted 19 May 2006

Published online 21 November 2006 in Wiley InterScience (www.interscience.wiley.com). DOI: 10.1002/jbm.a.30926

Abstract: Previously, biodegradable polymer implants (polymer millirods) to release chemotherapeutic agents directly into tumors have been developed. The purpose of this study is to evaluate local drug distribution from these implants in liver tumors treated with radiofrequency (RF) ablation and determine if the implants provide a therapeutic improvement over RF ablation alone. Cylindrical implants were fabricated using 65% poly(D,L-lactide-co-glycolide) (PLGA), 21.5% NaCl, and 13.5% doxorubicin. Control or drug-containing millirods were implanted inside VX2 liver tumors (11 mm diameter) in rabbits after RF ablation. Therapeutic efficacy was assessed 4 and 8 days after treatment using tumor size, histology, and fluorescence measurement of drug distribution. Tumors in both test groups recurred at the boundary of the ablated region. Therapeutic doxorubicin concentrations were found in

more than 80% of the ablated area, but concentrations declined rapidly at the boundary between normal and ablated tissue. This region was characterized by a developing fibrous capsule with resolving inflammation, which restricted drug transport out of the ablated zone. The intratumoral doxorubicin implants delivered high concentrations of drug within the ablated region but only limited amounts outside the ablation zone. Future studies will focus on overcoming the fibrotic transport barrier and enhancing drug delivery to the periphery of the ablation region to prevent tumor progression. © 2006 Wiley Periodicals, Inc. *J Biomed Mater Res* 81A: 205–213, 2007

Key words: biodegradable polymer; polymer implants; intratumoral drug delivery; VX2 tumor; minimally invasive therapy

INTRODUCTION

Minimally invasive cancer treatments have been a topic of much investigation in recent years. Many types of cancer, such as hepatocellular carcinoma, are difficult to treat surgically because of limited anatomical access or poor overall patient health.¹ Additionally, these cancers do not respond well to systemically administered chemotherapy, with patient response rates less than 30%.² With significant advances in image-guided technology, the ability to percutaneously administer treatments locally to tumors has improved dramatically. These percutaneous treatments have used a variety of ablative methods including ethanol³ or acetic acid injection⁴; heating

with radiofrequency (RF),⁵ laser,⁶ or microwave⁷ energy; and cryoablation.⁸ Among these, RF ablation has shown particular promise in treating liver disease because of high response rates and relatively low incidence of major side effects.⁹ However, tumor recurrence, particularly at the boundary of RF ablation, has been found as a major limitation of this treatment.¹⁰

Much research has attempted to improve the outcome of RF ablation for cancer treatment. One frequently employed strategy has been through technological improvement of ablation techniques aimed at achieving larger and more consistent treatment regions. These improvements, such as water-cooled tips, multitined electrodes, and saline injections prior to the procedure^{11,12} have led to overall increases in the size of tumors that can be successfully treated. An alternative adjuvant strategy used in animal and human trials has been the combination of RF ablation with chemotherapy. Several studies have shown increases in the size of treatment regions when combined with intravenous administration of liposomal doxorubicin.^{13,14} Furthermore, direct intratumoral

Correspondence to: J. Gao; e-mail: jinming.gao@utsouthwestern.edu

Contract grant sponsor: NIH; contract grant numbers: R01 CA090696, T32 GM07250

injections of liposomal doxorubicin have also shown benefit in the size and extent of ablation-treated tissue.¹⁰ A recent study demonstrated improved tumor treatment response from RF ablation followed by 5-FU impregnated polyanhydride implants compared to RF alone.¹⁵ These results underscore the potential for improving RF ablation by supplementing it with systemically or locally administered drugs.

As a means of providing locally controlled delivery of drugs to tumors after RF ablation, we have previously reported on the development of cylindrical polymer implants (polymer millirods) designed for use in conjunction with the ablation procedure.^{16–18} These implants were fabricated using poly(D,L-lactide-co-glycolide) (PLGA) and were manufactured to deliver several different chemotherapeutic agents, including 5-fluorouracil,¹⁹ carboplatin,²⁰ and doxorubicin.²¹ Their cylindrical design (diameter 1.6 mm; length 8–10 mm) was specifically tailored such that the implants could be delivered in a image-guided, minimally invasive fashion through the bore of a modified 14-gauge biopsy needle, which is already commonly used in image-guided biopsy procedures.²² Polymer millirods with different drug release kinetics have been developed, including rapid release (several days),¹⁸ sustained release (as many as 21 days),¹⁹ and dual-release (burst release followed by sustained release).²¹ Most recently, we demonstrated the antitumor effect of rapid release doxorubicin implants alone in treating small (8 mm diameter) VX2 liver tumors in rabbits.²³ Data showed that doxorubicin implants led to significant tumor shrinkage over drug-free implants; however, limited drug penetration distance (~2 mm) was not sufficient to adequately eliminate all VX2 tumor cells.

The goal of the current study is to determine whether combined treatment with RF ablation and drug implants improves treatment outcome over RF ablation alone. We chose a VX2 liver carcinoma model in New Zealand White rabbits for these studies. The tumors were first treated with purposely insufficient RF ablation to simulate incomplete treatment followed by the implantation of a doxorubicin-impregnated implant. Doxorubicin was used in the implants because of its previously reported success in combination with RF ablation^{13,14} and clinical use in liver cancer therapy.²⁴ The drug also has natural fluorescence, which allows for characterization of local drug distribution in tumor/liver tissues. In this study, we assessed tumor treatment four and eight days after the procedure by measuring gross tumor size, local drug distribution, and histology. Our hypothesis was that the doxorubicin-containing implants with RF ablation would facilitate drug retention and penetration inside tumor tissues, thereby increasing treatment efficacy over RF ablation or millirod therapy alone.

MATERIALS AND METHODS

Materials

Poly(D,L-lactide-co-glycolide) (PLGA, 1:1 lactide:glycolide, inherent viscosity 0.65 dL/g) was obtained from Birmingham Polymers (Birmingham, AL). Tris-buffered saline (TBS, pH 7.4), hydrochloric acid, sodium hydroxide, *N,N*-dimethylformamide (DMF), and dimethyl sulfoxide (DMSO) were purchased from Fisher Scientific (Pittsburg, PA). Methylene chloride, poly(vinyl alcohol) (MW 13,000–23,000 Da, 87–89% hydrolyzed), and Hank's balanced salt solution (HBSS) were acquired from Sigma-Aldrich (St. Louis, MO). Doxorubicin HCl (DOX) (2 mg/mL) in saline (9 mg/mL) was acquired from Bedford Laboratories (Bedford, OH). Teflon tubes (i.d. 1.6 mm) and stainless steel plungers (o.d. 1.6 mm) were purchased from McMaster-Carr Supply Company (Cleveland, OH). Fetal bovine serum (FBS) was obtained from Cambrex (East Rutherford, NJ).

Implant fabrication

Implants were produced by a compression molding procedure described previously.^{18,23} Briefly, PLGA microspheres (~4 μ m in diameter) were produced using a single-emulsion procedure. DOX in solution was concentrated by raising the pH to 9.0 with sodium hydroxide, washing with water, resuspending, and returning the solution pH to 3.0 with hydrochloric acid. The resulting concentrated solution was combined with doxorubicin in saline and lyophilized to yield a final powder containing 38.5% doxorubicin and 61.5% NaCl (w/w). To produce the implants, 65% PLGA microspheres, 21.5% NaCl, and 13.5% doxorubicin (w/w) were mixed with a mortar and pestle, packed into a Teflon tube, and compressed with steel plungers at 90°C for 2 h. Previous studies have shown that these implants release the majority of their doxorubicin loading *in vitro* within 24 h.²³ Control implants were produced using a similar procedure with 100% PLGA.

Animals and tumor model

Adult New Zealand White rabbits ($n = 16$; Covance, Princeton, NJ) weighing 2.8–3.2 kg were used. Studies with these animals were approved by the Institutional Animal Care and Use Committee at Case Western Reserve University and carried out according to its guidelines. All surgical procedures were performed under intramuscular anesthesia with ketamine (40 mg/kg), acetylpromazine (5 mg/kg), and xylazine (5 mg/kg).

The tumor model used in this study was the VX2 carcinoma in rabbit liver, which has been widely used in studies of minimally-invasive and image-guided procedures.^{25,26} VX2 cells were first grown for 4 weeks in the thigh muscle of a donor rabbit. This tumor was harvested, cut into small pieces 1.5 mm on each side, and frozen in FBS containing 10% DMSO in a liquid nitrogen storage tank. Before implantation, the tumor pieces were thawed and washed three times in HBSS. Liver tumors were generated in the livers of

the study rabbits by implanting a small piece of frozen tumor tissue in the rabbit liver. The abdomen of the recipient rabbit was shaved and a midline incision just distal to the sternum was made. The anterior surface of the middle liver lobe was perforated to a depth of 5 mm with the outer cannula of a 22-gauge angiocatheter, and a piece of tumor measuring approximately 1 mm³ was placed into the puncture. The tumor piece was secured in place with a small piece of gelatin foam and a single biodegradable suture. The tumors were then allowed to grow in the liver for 18 days until they reached an approximate diameter of 11 mm.

Tumor treatment procedure

All tumors were treated with RF ablation, and rabbits were randomly assigned to two groups. Control group subjects ($n = 8$) received a drug-free implant, and treatment group subjects ($n = 8$) received a doxorubicin-containing implant after RF ablation was performed. For treatment, the abdomen was opened and the liver tumor located by palpation. A 17-gauge, 1 cm exposed tip ablation probe (Radionics, Burlington, MA) was inserted into the center of the tumor perpendicular to the surface of the liver. The tumor tissue was then ablated to a temperature of 80°C for 2 min, a condition sufficient to create an ablated region approximately 8 mm in diameter. Following ablation, a control or doxorubicin-containing millirod was placed into the electrode tract and secured again using a small piece of gelatin foam and a single suture. Half of the animals in each group were euthanized with a barbiturate overdose at 4 and 8 days after the treatment. Doxorubicin content remaining in the implants was measured by dissolving the implant in 2 mL DMF and extracting the remaining doxorubicin.¹⁷ The solution was diluted to 20 mL with TBS and centrifuged to remove precipitated polymer. Doxorubicin concentration of the solution was then determined by measuring the absorption at 480 nm on a spectrophotometer (Perkin Elmer Lambda 20).

Tumor analysis

Tumors were removed from the surrounding liver tissue and sliced in half at an orientation perpendicular to the implant track. The halves of the tumor were photographed, and one half of the tumor was placed in 10% buffered formalin solution, while the other half of the tumor was frozen at -20°C. The fixed tissue was embedded in paraffin, sliced, and stained with hematoxylin and eosin (H&E), or Masson's trichrome (MTC). Unstained sections were analyzed qualitatively with fluorescence microscopy. Maps of the entire stained histology slices at 40× magnification were generated at using a video microscopy system consisting of a light microscope (Olympus BX60), video camera (Sony DXC-390), position encoded motorized stage (Prior Scientific ProScan), and software (Media Cybernetics Image-Pro).²⁷ Ablated tissue, viable tumor, and inflammatory regions on these image maps were identified and manually segmented using the ImageJ (NIH) software.

Quantitative fluorescence analysis

We modified a previously established fluorescent imaging technique for measuring the fluorescent doxorubicin in tissue slices²⁸ to include subtraction of an ablated tissue background. Frozen tissue samples were sliced to 100- μ m thick sections on a cryostat microtome (Microm 505E) and scanned with a fluorescent imager (Molecular Dynamics Fluorimager SI) with the following conditions: pixel size, 100 μ m; bit depth, 16; photomultiplier gain, 850; and high sensitivity mode. An average ablation background was generated from slices of the control-treated tumors because the fluorescence of the ablated tissue varied with distance from the ablation probe. Each point within the ablated region was assigned a location between 0 and 1, according to its relative distance between the ablation center and the ablated/normal tissue interface. Fluorescence values were binned and averaged by their location to obtain a curve of background fluorescence as a function of distance from the ablation center. For each treated tissue slice, every point within the ablation was similarly assigned a location based on the fractional distance between the ablation center and ablation boundary, and the net fluorescence intensity (NFI) was calculated by subtracting the background value that corresponded to that location. NFI was converted to doxorubicin concentration using a previously published equation, $NFI = 194 \cdot [Dox]^{0.67}$, where [Dox] is the doxorubicin concentration in μ g/g.²³ This empirical equation was acquired by imaging weighed slices of liver containing known quantities of doxorubicin. Average drug distribution profiles were calculated by finding the mean of 4 profiles evenly spaced by 90° around the fluorescence image. Values were binned in increments of 0.2 mm to decrease noise. The drug penetration distance was calculated as the average distance between the implant boundary and the point where the drug concentration dropped below 64 μ g/g, which is 10 times the therapeutic drug concentration.^{29,30} To estimate the total mass of drug remaining in the tumor, we determined the average drug concentration within 4 mm of the implant surface (the approximate size of the ablated area) and multiplied this value by the tissue volume.

RESULTS

Tumor treatment results

VX2 tumors were implanted in the middle liver lobe of 16 rabbits, 8 each in the control and treatment categories. At the time of treatment, one animal in the day 4 control group did not appear to have a tumor. In a second animal in the day 8 treatment group, the tumor was significantly adhered to the lateral peritoneal wall such that the tumor could not be safely ablated. These subjects were excluded from further study. The remaining 14 rabbits had tumors in the middle lobe that were treated with RF ablation followed by the implantation of a drug-free or doxorubicin-containing implant. A summary of the treatment outcomes is shown in Table I. Livers

TABLE I
Summary of Tumor Treatment Outcome after RF Ablation and Implantation
of a Drug-Free or Doxorubicin-Containing Millirod

		Livers with Viable Tumor	Ablation Area (cm ²)	Inflammatory Area (cm ²)	Residual Tumor Area (cm ²)
Day 4	Control	1/3	0.89 ± 0.54	0.29 ± 0.04	0.89
	Treatment	2/4	0.71 ± 0.30	0.15 ± 0.14	2.11, 0.75
Day 8	Control	1/4	0.81 ± 0.31	0.23 ± 0.10	0.57
	Treatment	0/3	0.82 ± 0.28	0.21 ± 0.07	n/a

All values are shown as ± Standard Deviation.

with viable tumor were found in 3 out of the 4 treatment groups. The presence of residual tumor cells in these livers was confirmed by histology. Viable tumor was not detected in any of the rabbits in the day 8 treatment group. Grossly, the treated tissues were all characterized by a single, spherical region of ablated tissue. Livers with residual cancer contained tumor nodules outside the region of ablation-induced necrosis.

Tumor histology

Tissue histology was used to further assess the outcome of different treatment groups. Typical images of H&E-stained tissue section from an RF ablated liver on day 8 are shown in Figure 1. Figure 1(A) is a low magnification overview of the entire treated region, showing the ablation-treated region (dashed line), outside of which are two nodes of recurrent tumor (asterisks). A lighter staining region characterized by a moderate inflammatory response, infiltrating fibroblasts, and mild collagen deposition was found to circumscribe the ablation-treated region. The ablated region shows typical coagulative necrosis from RF ablation, and a greater magnification of this region is illustrated in Figure 1(B). The outlines of pretreated cells are somewhat visible, but most cytoplasmic and nuclear details are lost. Necrotic debris and partially staining cells are contained throughout the area. In contrast, the tumor region outside the ablated zone shown in Figure 1(C) is filled with viable tumor cells, which appear relatively unaffected by the nearby ablation 8 days before. The cells in this region have all of the common characteristics of VX2 cells: dense packing, low differentiation, high nuclear to cytoplasm ratio, and the presence of mitotic figures. This pattern of recurrence, a treated region bounded by untreated areas of tumor, was found in all of the liver samples with incompletely treated tumors.

Closer inspection of the doxorubicin-treated slides is shown in Figure 2. MTC-stained images are shown alongside fluorescent microscopy images from the same region. In the MTC stain on day 4 [Fig. 2(A)], the boundary between ablated and normal tissue is subtle and characterized by the presence of

inflammatory cells. Fluorescence from that region [Fig. 2(B)] shows doxorubicin fluorescence that gradually tapers across the ablation boundary. In contrast, by day 8 [Fig. 2(C)], the boundary has become much more evident and is clearly demarcated by a blue-staining boundary approximately 200 μm thick, showing moderate collagen deposition. The corresponding fluorescent image [Fig. 2(D)] shows doxorubicin in the ablated region that drops off abruptly at the ablation boundary.

Region quantification

To further quantify the effects of ablation alone and the combined treatment, areas of ablation necrosis, inflammatory tissue, and, when present, viable tumor, were calculated using regions of interest manually segmented on histology. The results are shown in Table I. The mean sizes of all 14 ablated regions and inflammatory regions were 0.80 ± 0.32 and 0.22 ± 0.10 cm², respectively. There were no statistically significant differences found between any of the groups. The individual areas of recurrent tumors are also shown in the table, but again, no major differences between groups are readily apparent. From the tumor images, it was also possible to calculate distances from the ablation center. In the day 4 tumors receiving RF ablation followed by doxorubicin-containing implants, the two residual tumors began on average 4.1 mm from the ablation electrode location, 50% of tumor was found within 7.9 mm, and 100% of the tumor area was within 12.0 mm. These distances provide valuable information about what drug distribution would be necessary to limit tumor regrowth.

Drug release in vivo

Several values quantifying drug release *in vivo* are shown in Table II. Doxorubicin masses in the original implant, the extracted implant, and in the surrounding tissue as measured by fluorescence are shown along with the values as a percentage of the original doxorubicin loading. After 4 and 8 days, an insignificant amount of drug remained in the im-

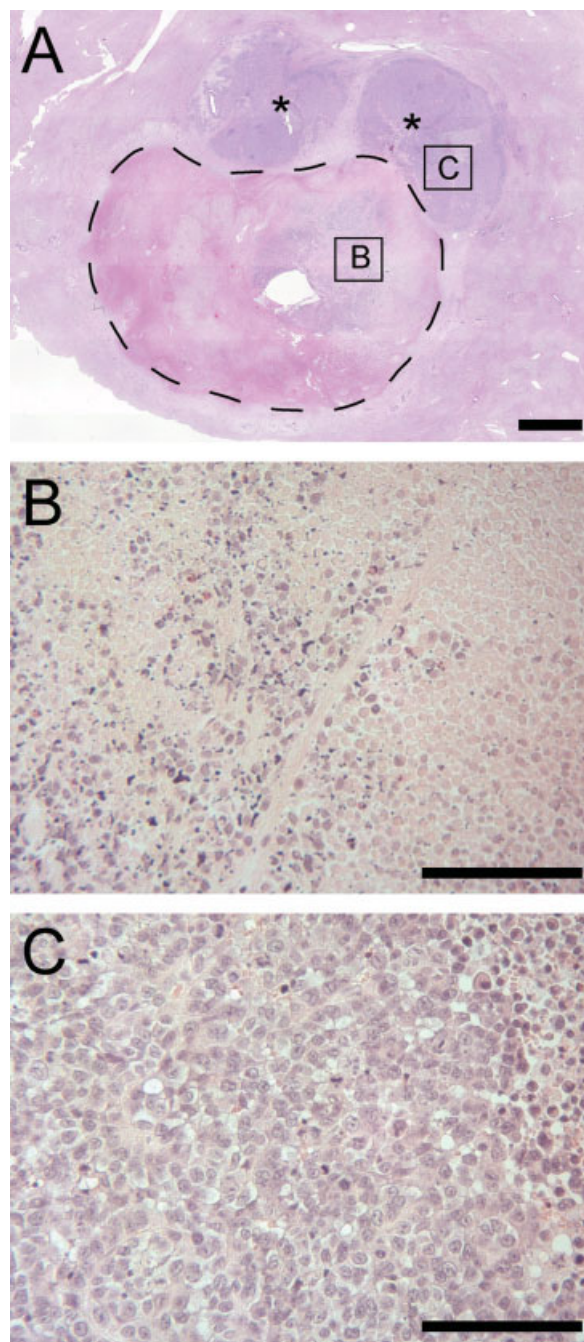


Figure 1. Representative H&E histology of tumor progression after RF ablation in a day 8 control subject. A: Overview of tumor region showing ablation treatment boundary (dashed line), two nodules of viable tumor (*), and regions magnified below. B: High magnification image of ablation-treated necrotic region. C: High magnification region of viable tumor cells untreated by the ablation. Scale bars are 2 mm in (A) and 200 μm in (B) and (C). [Color figure can be viewed in the online issue, which is available at www.interscience.wiley.com.]

plants. The drug penetration distances, defined as the average distance from the implant at which the drug concentration dropped below 64 $\mu\text{g/g}$, were 3.7 mm on day 4 and 2.1 mm on day 8. In addition

to critical drug concentrations being found 1.6 mm further from the implant on day 4, the tissue on day 4 retained significantly more of the original drug (20.4% of loading) than tissue on day 8 (3.8%). Apparent elimination rate from the tumor tissue and local half life were determined by fitting a decaying exponential of the form $D(t) = D_0 \exp(-kt)$ to the known drug masses in tissue. The elimination rate from the tumor area was $k = 0.35 \pm 0.02 \text{ day}^{-1}$ and apparent elimination half-time from tumor was of $t_{1/2} = 2.0 \pm 0.1 \text{ days}$.

Local drug distribution

Fluorescent imaging of tissue slices from the tumors revealed local drug concentrations in the extracted tissue. Two-dimensional doxorubicin distribution maps from these tissue sections are shown in Figure 3. Slices perpendicular to the long axis of the implant as well as parallel to the implant are shown for day 4 and day 8. Drug concentrations on day 4 exceed 2,000 $\mu\text{g/g}$ and extend completely to the ablation boundary [Fig. 3(A)]. Day 8 tissue drug concentrations are characterized by lower drug concentrations ($\sim 1,000 \mu\text{g/g}$) and a different distribution pattern [Fig. 3(C)]. This pattern consists of two regions of high drug concentration, within 2 mm of the implant boundary and a ring at the periphery of the ablated region, separated by a cleared zone containing much less drug. Slices parallel to the long axis of the implant show drug concentrations radiating from the flat end of the cylindrical implant on day 4 [Fig. 3(B)] and day 8 [Fig. 3(D)]. These distributions have similar properties but feature slightly lower drug concentrations and a less conspicuous clearing between the implant and the ablation boundary. The drug does not accumulate substantially beyond the ablation boundary.

Drug distribution profiles

To quantitatively display the drug distribution data, drug concentrations were binned and averaged in 0.2 mm increments for all animals from each time point. The resulting radial distribution profiles are shown as a function of the implant boundary in Figure 4. The figure numerically corroborates the observations from the 2D drug distributions. Drug concentrations are significantly higher on day 4, where significant amounts of drug extend roughly to the ablation boundary found at approximately 4 mm. On day 8, average concentrations dip to near 0 by 2 mm, but rise again slightly from drug observed at the ablation boundary. On average, significant

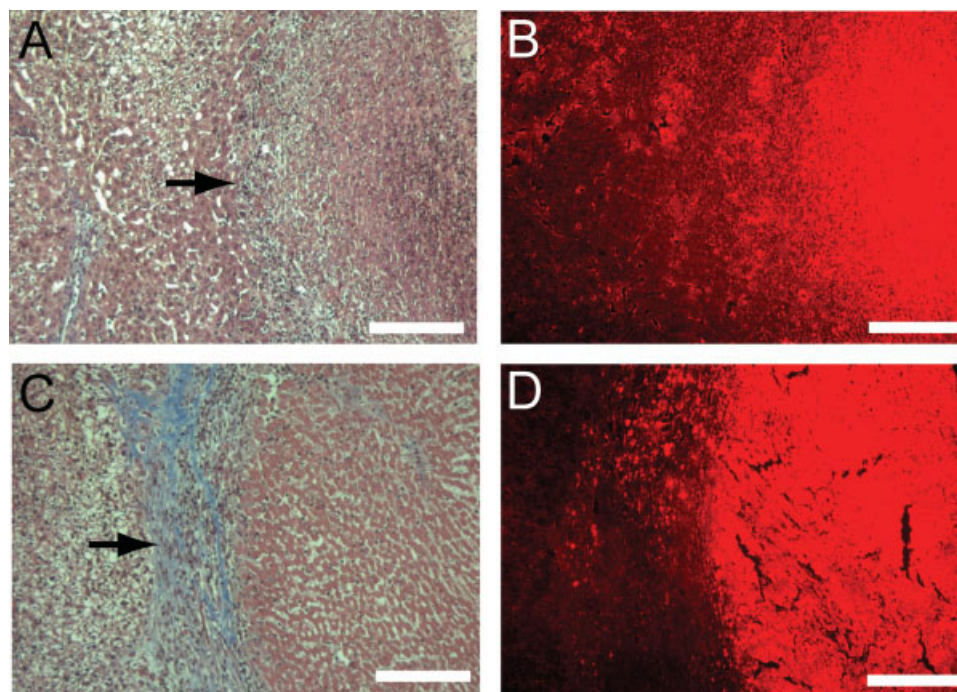


Figure 2. MTC-stained images of the ablation boundary on day 4 (A) and day 8 (C). Fluorescent microscopy images of the matching regions on day 4 (B) and day 8 (D). Ablated tissue is on the right and normal tissue on the left of each slide, with the boundary marked by the black arrows. Scale bars are 200 μm . [Color figure can be viewed in the online issue, which is available at www.interscience.wiley.com.]

amounts of doxorubicin do not extend beyond the ablation boundary.

DISCUSSION

In this study, tumors were treated by RF ablation supplemented with doxorubicin-containing PLGA implants. Local drug distributions were monitored, and therapeutic efficacy was compared against tumor treatment with RF ablation alone. Previous studies have shown that intratumorally administered drugs have a maximum effect on enlarging the treatment area when administered within 30 min after ablation,

with much of the effect lost after 48 h.¹⁰ The rapid-releasing implants used in this study seek to maximize tumor drug exposure during the narrow time window of drug sensitivity while minimizing the risk of drug resistance, which could occur if tumor cells were treated with drug concentrations below the therapeutic level for long periods of time. To simulate a clinical situation in which ablation incompletely treats cells at the tumor periphery, VX2 tumors in rabbit liver were treated with an ablation intensity not expected to completely eradicate the tumors.

Measurements of local doxorubicin concentrations around the implants revealed elevated drug concentrations in the ablation-treated region throughout the study. On day 4, more than 80% of the ablation coa-

TABLE II
Summary of Millirod Implant and Drug Release Properties

Drug Release Characteristics	Day 4	Day 8
Original drug loading (μg)	2990 \pm 200	3080 \pm 120
Drug remaining in extracted implant (μg)	190 \pm 50	200 \pm 30
Drug released (μg)	2800 \pm 200	2880 \pm 90
Drug released (% of original loading)	93.7 \pm 1.6	93.6 \pm 0.8
Drug in tissue (μg)*	590 \pm 300	120 \pm 100
Drug in tissue (% of original loading)*	20.4 \pm 11.6	3.8 \pm 3.0
Drug penetration distance (mm)*	3.7 \pm 1.3	2.1 \pm 0.3
Ablation region with [DOX] > 64 $\mu\text{g/g}$ (% of area)	81.4 \pm 13.8	39.9 \pm 28.1

Percentages shown are based on the original drug loading. All values are shown as \pm Standard Deviation.

* p -value of <0.1.

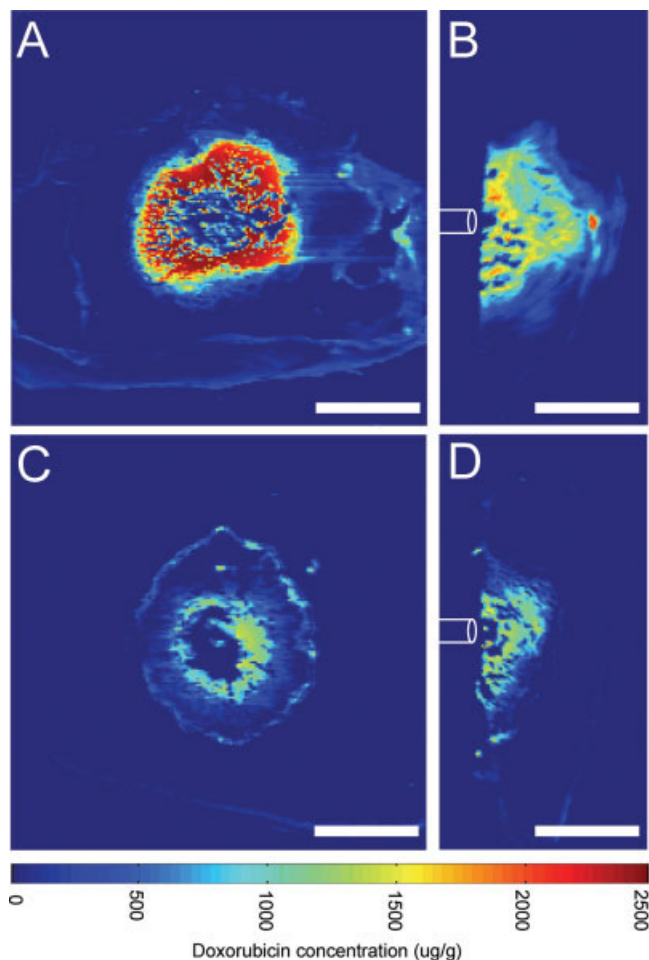


Figure 3. Doxorubicin concentration distribution maps from fluorescent imaging. Day 4 slices through the tumor center perpendicular to the implant axis (A) and slices through the end of the tumor parallel to the implant (B). Corresponding slices through the center of the tumor (C) and the end of the tumor (D) on day 8. The white cylindrical outlines indicate the approximate orientation of the implants in the parallel slices before removal. Scale bars are 5 mm. [Color figure can be viewed in the online issue, which is available at www.interscience.wiley.com.]

gulated zone contained drug at concentrations greater than $64 \mu\text{g/g}$, or 10 times higher than the accepted therapeutic concentration. Although this coverage dropped to 40% by day 8, drug concentrations as high as $1,000 \mu\text{g/g}$ were still seen adjacent to the implant and just inside the ablation boundary. Ablation of the tumor tissue facilitated the spread of drug from the implants, as the doxorubicin penetration distance (3.7 mm) and total doxorubicin contained in the tumor (20.4%) at day 4 were substantially higher than values previously reported for nonablated tumors (2.8 mm, 6.3%).²³ Furthermore, the apparent elimination half-life from ablated tumor (2.0 ± 0.1 days) is longer than previously found in nonablated tumors (1.6 ± 0.2 days), indicating that drug is eliminated more slowly from ablated tumor

than from normal tumor.²³ This may arise because ablation destroys tumor vasculature, halts mechanisms for drug metabolism, and increases drug binding to macromolecules.¹⁶ These data demonstrate the advantage of using RF ablation to improve drug delivery efficiency from millirod implants inside VX2 tumors. Meanwhile, despite high drug concentrations within the ablated area, concentrations dropped steeply to undetectable levels outside the ablation boundary. Viable tumor cells were found beyond the ablation boundary in both groups on day 4 (1/3 control vs. 2/4 treatment) but only in the control group on day 8 (1/4 control vs. 0/3 treatment). While the results represent a possible improvement in the day 8 treatment group, concluding that the treatment is better than the control is limited by small group sizes and experimental variability among rabbits.

Detailed results from histological analysis of the treated tissue sections provide insight about possible limitations of this treatment strategy. Tumors recurred outside the ablation area, where doxorubicin was not seen in substantial amounts at either time point. Doxorubicin transport to the cells outside the ablated region was limited by the formation of an inflammatory region around the ablated tissue. At day 4 this boundary consisted largely of neutrophils and monocytes typical of the chronic stages of inflammation, but by day 8 the boundary contained predominantly fibroblasts and moderate collagen deposition characteristic of fibrous capsule formation. Formation of this boundary has been previously noted in ablated normal liver tissue, where it was noted as a potential barrier to drug transport.³¹ The inflammatory tissue may act as a transport barrier in two ways. First, fibrous capsule formation with collagen deposition may create a boundary that is denser and more tortuous than ablated tumor or normal liver, which

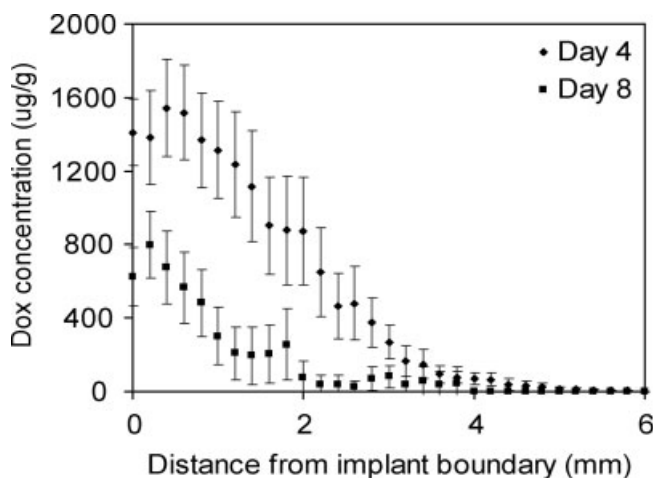


Figure 4. Average doxorubicin concentration plotted against distance from the implant boundary for day 4 and day 8. Error bars represent the 95% confidence interval.

may result in slower diffusion through this area. Second, the boundary may have a higher rate of drug clearance and metabolism due to a high fraction of vascular tissue and large number of cells that may take up and metabolize drugs and debris. A combination of these two effects limited drug exposure outside the ablation boundary, where tumor cells were found at distances ranging from 3.5 to 10.9 mm away from the implant location.

Overall, the potential benefit of combined therapy using RF ablation and chemotherapeutic implants is high despite some challenges. Doxorubicin infiltrated the tumor tissue to a greater distance and was retained in the tissue to a greater extent than when these implants were used in tumors without ablation.²³ Drug concentrations throughout the ablated region exceeded therapeutic values throughout the 8-day study period. On the other hand, untreated tumor cells persisted outside the ablated area, where drug was not found in substantial quantities. Identifying the role of fibrous capsule development in restricting doxorubicin delivery to tumor cells beyond the periphery of the ablated region is a key finding of this study. Future attempts at combining RF ablation with drug releasing implants must consider this challenge in their design.

Several improvements to the combined treatment strategy could maximize the therapeutic efficacy of these implants. Previous work has found that implants that sustain their drug release over several days provide greater drug coverage and penetration distances.¹⁷ However, since the fibrous boundary becomes progressively denser and less permeable to drug released at a later time, sustained drug release might not improve the treatment outcomes. Three other alternative strategies could overcome the fibrous boundary and improve treatment effectiveness. First, incorporation of an anti-inflammatory drug such as dexamethasone has been shown to markedly reduce the formation of the fibrous capsule after ablation³² and could be incorporated along with an anticancer drug such as doxorubicin. Second, alternative implant placements closer to the periphery of the ablated zone could reduce the drug transport distance to the viable tumor cells. Third, concurrent administration of systemic therapy targeted to the tumor periphery, such as nanoparticles targeted to tumor vasculature, may more effectively deliver drugs to the tumor cells most likely to survive ablation. Each of these approaches could maximize the therapeutic impact of local implants for tumor treatment in future studies.

CONCLUSIONS

This paper describes the use of RF ablation followed by doxorubicin-containing PLGA implants to

treat liver tumors. Despite the presence of therapeutic doxorubicin concentrations in the majority of the ablated region, tumors recurred around the boundary of the ablated zone where little drug was found. The distance of residual tumor from the implant and the extensive transport barrier posed by fibrous capsule formation after ablation restricted drug transport beyond the ablated region, thereby limiting treatment effectiveness. Nonetheless, the potential clinical benefits of implants for use in combined treatments are significant and future improvements to implant design and treatment strategies could lead to more ideal treatment.

BW is supported in part by DOD predoctoral fellowship BC043453.

References

1. Leung TW, Johnson PJ. Systemic therapy for hepatocellular carcinoma. *Semin Oncol* 2001;28:514–520.
2. Little SA, Fong Y. Hepatocellular carcinoma: Current surgical management. *Semin Oncol* 2001;28:474–486.
3. Livraghi T, Benedini V, Lazzaroni S, Meloni F, Torzilli G, Vettori C. Long term results of single session percutaneous ethanol injection in patients with large hepatocellular carcinoma. *Cancer* 1998;83:48–57.
4. Shah SS, Jacobs DL, Krasinkas AM, Furth EE, Itkin M, Clark TW. Percutaneous ablation of VX2 carcinoma-induced liver tumors with use of ethanol versus acetic acid: Pilot study in a rabbit model. *J Vasc Interv Radiol* 2004;15:63–67.
5. Goldberg SN. Radiofrequency tumor ablation: Principles and techniques. *Eur J Ultrasound* 2001;13:129–147.
6. Vogl TJ, Mack MG, Muller PK, Straub R, Engelmann K, Eichler K. Interventional MR: Interstitial therapy. *Eur Radiol* 1999;9:1479–1487.
7. Ohmoto K, Tsuduki M, Shibata N, Takesue M, Kunieda T, Yamamoto S. Percutaneous microwave coagulation therapy for hepatocellular carcinoma located on the surface of the liver. *AJR Am J Roentgenol* 1999;173:1231–1233.
8. Garcea G, Lloyd TD, Aylott C, Maddern G, Berry DP. The emergent role of focal liver ablation techniques in the treatment of primary and secondary liver tumours. *Eur J Cancer* 2003;39:2150–2164.
9. Barnett CC Jr, Curley SA. Ablative techniques for hepatocellular carcinoma. *Semin Oncol* 2001;28:487–496.
10. Goldberg SN, Saldinger PF, Gazelle GS, Huertas JC, Stuart KE, Jacobs T, Kruskal JB. Percutaneous tumor ablation: Increased necrosis with combined radio-frequency ablation and intratumoral doxorubicin injection in a rat breast tumor model. *Radiology* 2001;220:420–427.
11. Buscarini E, Buscarini L. Radiofrequency thermal ablation with expandable needle of focal liver malignancies: complication report. *Eur Radiol* 2004;14:31–37.
12. Livraghi T, Goldberg SN, Monti F, Bizzini A, Lazzaroni S, Meloni F, Pellicano S, Solbiati L, Gazelle GS. Saline-enhanced radio-frequency tissue ablation in the treatment of liver metastases. *Radiology* 1997;202:205–210.
13. Ahmed M, Liu Z, Lukyanov AN, Signoretti S, Horkan C, Monsky WL, Torchilin VP, Goldberg SN. Combination radio-frequency ablation with intratumoral liposomal doxorubicin: Effect on drug accumulation and coagulation in multiple tissues and tumor types in animals. *Radiology* 2005;235:469–477.

14. Ahmed M, Monsky WE, Girmun G, Lukyanov A, D'Ippolito G, Kruskal JB, Stuart KE, Torchilin VP, Goldberg SN. Radiofrequency thermal ablation sharply increases intratumoral liposomal doxorubicin accumulation and tumor coagulation. *Cancer Res* 2003;63:6327–6333.
15. Haaga JR, Exner AA, Wang Y, Stowe NT, Tarcha PJ. Combined tumor therapy by using radiofrequency ablation and 5-FU-laden polymer implants: Evaluation in rats and rabbits. *Radiology* 2005;237:911–918.
16. Qian F, Stowe N, Liu EH, Saidel GM, Gao J. Quantification of in vivo doxorubicin transport from PLGA millirods in thermoablated rat livers. *J Control Release* 2003;91:157–166.
17. Qian F, Stowe N, Saidel GM, Gao J. Comparison of doxorubicin concentration profiles in radiofrequency-ablated rat livers from sustained- and dual-release PLGA millirods. *Pharm Res* 2004;21:394–399.
18. Qian F, Szymanski A, Gao JM. Fabrication and characterization of controlled release poly(D,L-lactide-co-glycolide) millirods. *J Biomed Mater Res* 2001;55:512–522.
19. Qian F, Nasongkla N, Gao JM. Membrane-encased polymer millirods for sustained release of 5-fluorouracil. *J Biomed Mater Res* 2002;61:203–211.
20. Szymanski-Exner A, Gallacher A, Stowe NT, Weinberg B, Haaga JR, Gao J. Local carboplatin delivery and tissue distribution in livers after radiofrequency ablation. *J Biomed Mater Res A* 2003;67:510–516.
21. Qian F, Saidel GM, Sutton DM, Exner A, Gao JM. Combined modeling and experimental approach for the development of dual-release polymer millirods. *J Control Release* 2002;83:427–435.
22. Daniel BL, Birdwell RL, Butts K, Nowels KW, Ikeda DM, Heiss SG, Cooper CR, Jeffrey SS, Dirbas FM, Herfkens RJ. Freehand iMRI-guided large-gauge core needle biopsy: A new minimally invasive technique for diagnosis of enhancing breast lesions. *J Magn Reson Imaging* 2001;13:896–902.
23. Weinberg BD, Ai H, Blanco E, Anderson JM, Gao J. Antitumor efficacy and local distribution of doxorubicin via intratumoral delivery from polymer millirods. *J Biomed Mater Res A*. Forthcoming.
24. Leung TW, Patt YZ, Lau WY, Ho SK, Yu SC, Chan AT, Mok TS, Yeo W, Liew CT, Leung NW, Tang AM, Johnson PJ. Complete pathological remission is possible with systemic combination chemotherapy for inoperable hepatocellular carcinoma. *Clin Cancer Res* 1999;5:1676–1681.
25. Hazle JD, Stafford RJ, Price RE. Magnetic resonance imaging-guided focused ultrasound thermal therapy in experimental animal models: correlation of ablation volumes with pathology in rabbit muscle and VX2 tumors. *J Magn Reson Imaging* 2002;15:185–194.
26. Miao Y, Ni Y, Mulier S, Yu J, De Wever I, Penninckx F, Baert AL, Marchal G. Treatment of VX2 liver tumor in rabbits with “wet” electrode mediated radio-frequency ablation. *Eur Radiol* 2000;10:188–194.
27. Breen MS, Lazebnik RS, Wilson DL. Three-dimensional registration of magnetic resonance image data to histological sections with model-based evaluation. *Ann Biomed Eng* 2005;33:1100–1112.
28. Gao JM, Qian F, Szymanski-Exner A, Stowe N, Haaga J. In vivo drug distribution dynamics in thermoablated and normal rabbit livers from biodegradable polymers. *J Biomed Mater Res* 2002;62:308–314.
29. Ridge JA, Collin C, Bading JR, Hancock C, Conti PS, Daly JM, Raaf JH. Increased adriamycin levels in hepatic implants of rabbit Vx-2 carcinoma from regional infusion. *Cancer Res* 1988;48:4584–4587.
30. Swistel AJ, Bading JR, Raaf JH. Intraarterial versus intravenous adriamycin in the rabbit Vx-2 tumor system. *Cancer* 1984;53:1397–1404.
31. Blanco E, Qian F, Weinberg B, Stowe N, Anderson JM, Gao J. Effect of fibrous capsule formation on doxorubicin distribution in radiofrequency ablated rat livers. *J Biomed Mater Res A* 2004;69:398–406.
32. Blanco E, Weinberg BD, Stowe NT, Anderson JM, Gao J. Local release of dexamethasone from polymer millirods effectively prevents fibrosis after radiofrequency ablation. *J Biomed Mater Res A* 2006;76:174–182.

Antitumor efficacy and local distribution of doxorubicin via intratumoral delivery from polymer millirods

Brent D. Weinberg,¹ Hua Ai,² Elvin Blanco,³ James M. Anderson,⁴ Jinming Gao³

¹Department of Biomedical Engineering, Case Western Reserve University, Cleveland, Ohio 44106

²National Engineering Research Center for Biomaterials, Sichuan University, Chengdu, China

³Simmons Comprehensive Cancer Center, University of Texas Southwestern Medical Center, Dallas, Texas 75390

⁴Institute of Pathology, Case Western Reserve University, Cleveland, Ohio 44106

Received 22 March 2006; revised 13 April 2006; accepted 28 April 2006

Published online 21 November 2006 in Wiley InterScience (www.interscience.wiley.com). DOI: 10.1002/jbm.a.30914

Abstract: The purpose of this study was to evaluate the antitumor efficacy and local drug distribution from doxorubicin-containing poly(D,L-lactide-co-glycolide) (PLGA) implants for intratumoral treatment of liver cancer in a rabbit model. Cylindrical polymer millirods (length 8 mm, diameter 1.5 mm) were produced using 65% PLGA, 21.5% NaCl, and 13.5% doxorubicin. These implants were placed in the center of VX2 liver tumors ($n = 16$, ~8 mm in diameter) in rabbits. Tumors were removed 4 and 8 days after millirod implantation, and antitumor efficacy was assessed using tumor size measurements, tumor histology, and fluorescent measurement of drug distribution. The treated tumors were smaller than the untreated controls on both day 4 (0.17 ± 0.06 vs. 0.31 ± 0.08 cm², $p = 0.048$) and day

8 (0.14 ± 0.04 vs. 1.8 ± 0.8 cm², $p = 0.025$). Drug distribution profiles demonstrated high doxorubicin concentrations (>1000 µg/g) at the tumor core at both time points and drug penetration distances of 2.8 and 1.3 mm on day 4 and 8, respectively. Histological examination confirmed necrosis throughout the tumor tissue. Biodegradable polymer millirods successfully treated the primary tumor mass by providing high doxorubicin concentrations to the tumor tissue over an eight day period. © 2006 Wiley Periodicals, Inc. *J Biomed Mater Res* 81A: 161–170, 2007

Key words: biodegradable polymer; polymer implants; intratumoral drug delivery; VX2 tumor; minimally invasive therapy

INTRODUCTION

Minimally invasive, intratumoral strategies for the treatment of solid tumors promise to substantially improve the therapeutic outcomes for many cancers. Systemic chemotherapy is often limited by severe toxicity and patient morbidity,^{1,2} and local cancer therapy can overcome this limitation by maximizing drug delivery to malignant tissues while minimizing systemic exposure to chemotherapeutic drugs.³ Recent progress in imaging technology has created an unprecedented opportunity for minimally invasive treatment of solid tumors.⁴ With image guidance, radiologists can pinpoint the spatial location of solid tumors and use percutaneous procedures to administer local treatments.^{5–7} Combining minimally-invasive treatment

with controlled release technology provides opportunities for treating cancers in a safe and effective manner by placing drug-loaded implants directly into solid tumors.⁸ However, many studies are still needed to understand the local distribution of drugs released from intratumoral implants as well as their efficacy in treating the desired volume of tumor.

Several strategies for local chemotherapy of tumors have been developed as reviewed recently by Goldberg et al.⁹ Regionally administered chemotherapy schemes, such as intrahepatic artery infusion for liver cancer³ or intrapleural infusion for lung cancer,^{10,11} have improved clinical patient outcomes by changing drug pharmacokinetics to provide increased drug concentrations to tumor tissues while minimizing toxicity associated with treatments. To further increase the specificity of chemotherapy, other studies have implemented direct injections of anticancer agents into tumors.^{12,13} Irregular distribution of the drug and rapid clearance from the tumor site results in treatments that are highly dependent on the timing and frequency of the drug injections, which must be chosen to maximize tumor exposure to drug. These studies point to the utility of a controlled release device,

Correspondence to: J. Gao; e-mail: jinming.gao@utsouthwestern.edu

Contract grant sponsor: NIH; contract grant numbers: R01 CA090696, T32 GM07250, R01 CA090696

which can ensure the drug is properly localized and can release drug in a desired amount of time, maximizing the effect of drug on the tumor tissue.¹⁴

Drug-containing devices such as polymer implants,^{15,16} hydrogels,^{17,18} and injectable microparticles^{19,20} provide additional options for controlling drug release to tumors. Polyanhydride wafers have been studied extensively for the delivery of anticancer agents and are clinically approved (Gliadel[®]) for the delivery of BCNU to malignant gliomas.²¹ Multiple formulations of drug-containing microspheres have been shown to have antitumor effects both in animal studies and preliminary clinical trials.^{14,22} Despite these successes, drug distribution from these devices is often limited to only a few millimeters away from the device.^{23,24} Moreover, these implant strategies have only been attempted in a small subset of tumor types, and further studies are necessary to understand their drug release and its effects on treated tumor cells.

With the goal of developing a minimally invasive treatment strategy for liver cancer, we have designed doxorubicin-containing, biodegradable polymer implants for intratumoral drug delivery. These polymer implants were designed as cylindrical rods, or millirods (diameter 1.6 mm, length 8.0 mm), composed of poly(D,L-lactide-co-glycolide) (PLGA), which can be administered with image-guidance through the bore of a 14-gauge biopsy needle. Previous studies have established the release properties of these implants in both normal and radiofrequency (RF) ablated liver tissues,^{25–27} modeled the transport of drug through these tissues,²⁸ and established techniques for customizing the release rate of these millirods.^{29,30} However, the drug distribution from and efficacy of these implants in tumor tissue, which is considerably different from normal tissue in vascularity and transport properties,³¹ is currently unknown. In this study, we chose doxorubicin as the therapeutic agent because of its wide use in the treatment of primary and metastatic liver cancers.^{32,33} In addition, its natural fluorescence permits quantitative measurement of drug concentration in tissue slices from the tumor.

While other studies have established the initial proof of concept for minimally invasive, intratumoral chemotherapy,³⁴ few studies of intratumoral therapies have simultaneously measured local drug concentration and tumor histology to correlate tumor response to drug exposure. Targeting this goal, we selected an aggressive, realistic model of hepatic cancer (rabbit VX2 tumor) that has been widely used in studies of minimally invasive tumor treatments.^{35,36} A rapid delivery implant was chosen to provide the highest possible drug concentrations early in the study to maximize the initial tumor kill from the treatment and minimize the amount of time in which tumor cells might become doxorubicin resistant. Treatment effects were gauged by monitoring tumor size

through gross tissue measurements, drug distribution through fluorescent imaging of tissue slices, and cell morphology through histology. Using adjacent tumor sections for histology and fluorescent drug measurement allowed for direct correlation of drug concentrations with drug effects. Results from this study provide considerable insights for the future development of intratumoral implants as part of clinical cancer therapy.

MATERIALS AND METHODS

Materials

Poly(D,L-lactide-co-glycolide) (PLGA; 1:1 lactide/glycolide; inherent viscosity 0.65 dL/g) was obtained from Birmingham Polymers (Birmingham, AL). Tris-buffered saline (TBS, pH 7.4), hydrochloric acid, sodium hydroxide, acetonitrile, and dimethyl sulfoxide (DMSO) were purchased from Fisher Scientific (Pittsburg, PA). Ammonium formate, methylene chloride, poly(vinyl alcohol) (PVA, MW 13,000–23,000 Da, 87–89% hydrolyzed), and Hank's balanced salt solution (HBSS) were acquired from Sigma-Aldrich (St. Louis, MO). Doxorubicin HCl (DOX) (2 mg/mL) in saline (9 mg/mL) was acquired from Bedford Laboratories (Bedford, OH). Teflon tubes (i.d. 1.6 mm) and stainless steel plungers (o.d. 1.6 mm) were purchased from McMaster-Carr Supply Company (Cleveland, OH). Fetal bovine serum was obtained from Cambrex (East Rutherford, NJ).

Implant fabrication

Polymer millirod implants were produced as reported previously³⁷ and described briefly below. PLGA microspheres (~4 μ m in diameter) were produced using a single-emulsion procedure. Doxorubicin/NaCl powder mixture was prepared as follows. The acidic doxorubicin solution (pH 3.0) was basified to pH 9.0 by adding sodium hydroxide, leading to doxorubicin precipitation. The precipitated drug was washed, resuspended, and lowered to pH 3.0 using hydrochloric acid. The resulting concentrated solution was combined with doxorubicin in saline and lyophilized to yield a final powder containing 38.5% doxorubicin and 61.5% NaCl (w/w). To produce the implants, 65% PLGA microspheres and 35% doxorubicin/NaCl powder were mixed with a mortar and pestle, packed into a Teflon tube, and compressed with steel plungers at 90°C for 2 h. The resulting millirods had a composition of 65% PLGA, 21.5% NaCl, and 13.5% doxorubicin (w/w). Control implants were produced using a similar procedure with 100% PLGA microspheres.

Drug release measurement

An *in vitro* release study was performed in TBS (pH 7.4) at 37°C. Millirods ($n = 3$) were placed in vials containing 5 mL of TBS in an incubator/shaker rotating at 100 rpm.

To maintain sink conditions, the implants were moved into a fresh vial of TBS at each sampling point, and the doxorubicin concentration of the solutions was determined by measuring the absorbance at 480 nm (Perkin Elmer Lambda 20 Spectrophotometer) and determining doxorubicin concentration using an extinction coefficient of 17.62 mL/(cm mg). Explanted rods were dissolved in acetonitrile to extract the remaining doxorubicin, and the concentrations of the resulting solutions were measured using HPLC on a C-18 column (150 × 4.6 mm, 5.0 μm particle size) with a mobile phase consisting of 35% acetonitrile and 65% ammonium formate buffer (0.1% w/w) at pH 4.0.

Animals and tumor model

Adult New Zealand White rabbits ($n = 16$; Covance, Princeton, NJ) weighing 2.8–3.2 kg were used. All animal studies were approved by the Institutional Animal Care and Use Committee at Case Western Reserve University and carried out according to its guidelines. For surgical procedures, animals were anesthetized with intramuscular ketamine (40 mg/kg), acetylpromazine (5 mg/kg), and xylazine (5 mg/kg).

The tumor model used in this study was the VX2 carcinoma in rabbit liver. To implant the VX2 cells into the liver, the tumor was first grown for 4 weeks on the hind limb of a donor rabbit. The donor rabbit was euthanized, and the tumor was removed and dissected into small pieces of ~2–3 mm³. Tumor pieces were stored in fetal bovine serum with 10% DMSO in a liquid nitrogen storage tank. Prior to liver tumor implantation, the tumor pieces were rapidly thawed and washed three times with HBSS.

The implantation surgery was modified from a published procedure³⁸ and was performed on day -12. The abdomens of the recipient rabbits were shaved and prepped with betadine, after which a midline subxyphoid incision was made. The anterior surface of the middle liver lobe was perforated to a depth of 5 mm with the outer cannula of a 22-gauge angiocatheter, and a piece of tumor measuring ~1 mm³ was placed into the puncture. Small pieces of cotton and abdominal fat were secured over the puncture site using a single biodegradable suture. This method allows for the growth of a single, well demarcated tumor in the liver of each rabbit. The tumors were then allowed to grow in the liver for 12 days until day 0, when they reached an approximate diameter of 8 mm.

Tumor treatment procedure

For tumor treatment, the rabbits were randomly divided into two groups, a treatment group ($n = 8$) and a control group ($n = 8$), receiving 13.5% and 0% (w/w) doxorubicin implants, respectively. On day 0, the rabbits' abdomens were reopened as described before, and the tumor was located by palpation. The tumor was punctured through the center and perpendicular to the liver surface with an 18-gauge needle. The implant was inserted into the center of the tumor and sutured in place with a piece of cotton and fat on top of the liver. Using sodium pentobarbital euthanasia, half of the animals from each group were then euthanized on day 4, and the remaining half were euthanized on day 8.

Tumor analysis

After tissue removal, tumors were hemisected perpendicular to the implant track and photographed. One half of the tumor was placed in 10% buffered formalin solution and subsequently embedded in paraffin. Alternating slices of paraffin embedded tissue were stained with hematoxylin and eosin (H&E) or left unstained and observed qualitatively with fluorescence microscopy. The other half of the tumor was frozen at -20°C for use in fluorescent imaging analysis. The size of the tumors was evaluated by computing the area of the elliptical cross section through the center of the tumor, which is given by the equation $A = \pi R_1 R_2$, where R_1 and R_2 are the long and short radii of the ellipse, respectively. Statistical comparison was performed using a two-tailed, unpaired *t*-test with a significance level of 0.05.

Quantitative fluorescence analysis

To determine the amount of drug present in the tissue surrounding the implant, we used a previously established fluorescence imaging technique that takes advantage of doxorubicin's natural fluorescence.³⁹ Frozen liver sections of 100 μm thick were sliced from each tumor using a cryostat microtome (Microm 505E) and then scanned with a fluorescent imager (Molecular Dynamics Fluorimager SI) using the following conditions: pixel size, 100 μm; bit depth, 16; photomultiplier gain, 850; and sensitivity, high. A calibration between net fluorescence intensity (NFI), the fluorescence minus the liver background fluorescence, and doxorubicin concentration was established by imaging weighed slices of normal liver to which known amounts of doxorubicin were added. This empirical relationship, $NFI = 194[\text{Dox}]^{0.67}$, where [Dox] is the doxorubicin concentration in μg/g, was then used to convert fluorescence intensities to doxorubicin concentrations. Mean drug distribution profiles were calculated by averaging 8 profiles evenly spaced by 45° around a fluorescence image. The drug penetration distance was calculated as the average distance between the implant boundary and the point where the drug concentration dropped below 64 μg/g, which is 10 times the therapeutic drug concentration.^{40,41} To estimate the total mass of drug remaining in the tumor, we determined the average drug concentration within 4 mm of the implant surface (the approximate size of the original tumor) and multiplied this value by the tissue volume.

RESULTS

Implant properties

The implants used in this study had an average length of 8.0 ± 0.3 mm and an average diameter of 1.49 ± 0.04 mm. *In vitro* the doxorubicin-containing implants were found to release a total of 2.07 ± 0.05 mg of drug over the 8 day period, corresponding to (71.3 ± 1.7)% of the total drug loading. The release half-time was ~4 h, and the vast majority of doxorubicin, 1.98 ± 0.03 mg, was released in the first 24 h.

Tumor size

After tumor removal and sectioning, the VX2 tumors were observed qualitatively and photographed. The tumors were largely spherical, but most of the cross sections were found to be slightly elliptical. Photographs of control and treatment tumors taken on day 8 are shown in Figure 1(A,B), respectively. The control tumor seen in Figure 1(A) is a large and well-circumscribed tumor. The boundary of the tumor is a solid mass of dense tumor tissue, while the center of the tumor is necrotic and consists of a mixture of necrotic cells, inflammatory debris, red blood cells, and edema. Because the center of the tumor was liquid filled, the original location of the implant which was placed in the center of the tumor is not visible in the photograph. The treated tumor seen in Figure 1(B) is also well-circumscribed but considerably smaller than the untreated tumor. The doxorubicin containing millirod was removed from the cavity seen in the center of the tumor, and the remaining tumor is seen as a small, hard shell only a few millimeters in thickness surrounding the implant location.

Tumor measurements taken from the photographs were used to assess the effect of the implant on the growth of the tumor. An example of how the measurements were taken is seen from the measurements in Figure 1(A). The resulting measurements of cross sectional area were then averaged for all the animals in each group, and the resulting data is shown in Figure 1(C). On day 4, the treatment tumors ($0.17 \pm 0.06 \text{ cm}^2$) were approximately half the size ($p = 0.048$) of the comparable controls ($0.31 \pm 0.08 \text{ cm}^2$). The control tumors were also slightly smaller than the 8 mm diameter on day 0, which may be attributed to a response to placement of the drug free implant. By day 8, the size difference was significant, as the treatment tumors ($0.14 \pm 0.04 \text{ cm}^2$) were more than 10 times smaller ($p = 0.025$) than the controls ($1.77 \pm 0.78 \text{ cm}^2$). Notable variation in tumor size, especially in the untreated tumors on day 8, is evident, but there is a statistically significant difference in treated and control tumors on both day 4 and day 8.

Drug release *in vivo*

A summary of the drug release properties of the implants *in vivo* is shown in Table I. Doxorubicin masses in the original implant, the extracted implant, and in the surrounding tissue as measured by fluorescence are shown along with the values as a percentage of the original doxorubicin loading. For implants extracted on both day 4 and day 8, ~87% of the original drug was released, suggesting that little additional drug was released after day 4. A greater fraction of the drug was released *in vivo* than *in vitro*. Two notable differences are

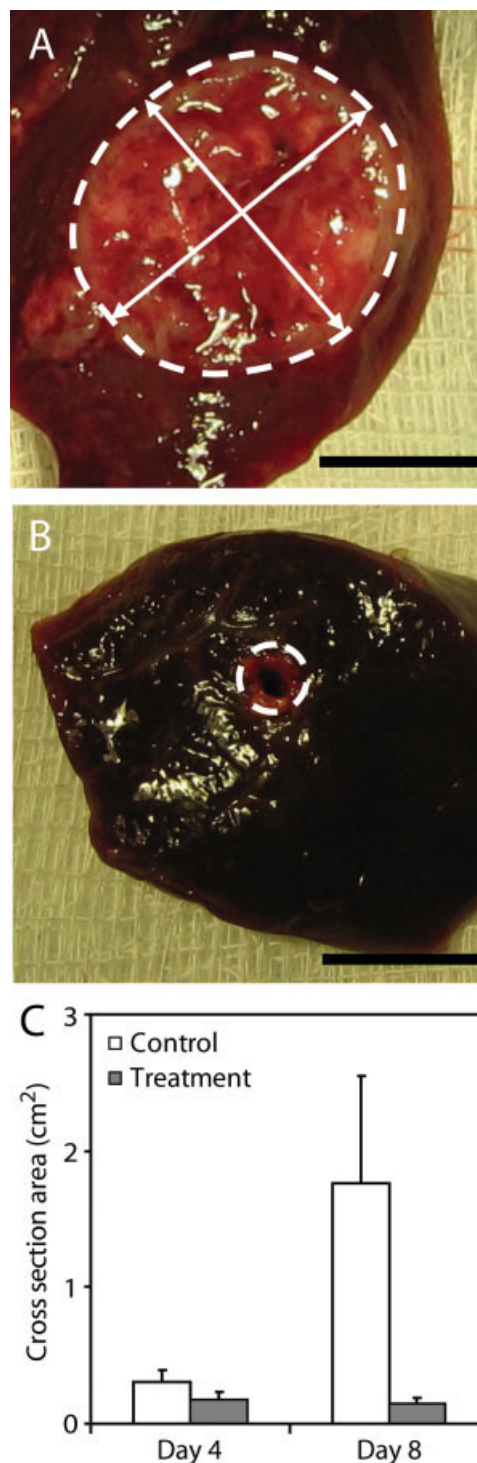


Figure 1. Photographs of a control (A) and a treated (B) tumor cross section on day 8. The boundary between the tumor and normal liver tissue is indicated with a white dotted outline, and the arrows indicate two directions along which the tumor dimensions would be measured to calculate the cross sectional area. The scale bars are 1 cm. Bar graph showing the mean cross sectional area of the treated and control tumors after 4 and 8 days (C). The error bars indicate the standard deviation of each measurement ($n = 4$). [Color figure can be viewed in the online issue, which is available at www.interscience.wiley.com.]

TABLE I
Summary of Drug Quantities *In Vivo*

	Day 4	Day 8
Original drug loading (μg)	3150 ± 110	3000 ± 190
Drug remaining in extracted implant (μg)	400 ± 40	390 ± 90
Drug released (μg)	2750 ± 130	2610 ± 120
Drug released (%)	87.2 ± 1.5	87.2 ± 2.3
Drug in tissue (μg)	210 ± 120	160 ± 70
Drug in tissue (%)	6.7 ± 3.7	5.5 ± 2.8
Drug penetration distance (mm)*	2.8 ± 0.5	1.3 ± 0.4

Percentages shown are based on the original drug loading. All values are shown \pm standard deviation.

*Statistically significant difference between days.

present between the two time points: the tissue at day 4 retains $50 \mu\text{g}$ more doxorubicin and the doxorubicin penetration distance at day 4 is 1.5 mm further from the implant boundary. Of these differences, however, only the increase in the drug penetration distance is statistically significant ($p = 0.004$). From these measurements, it is also possible to estimate the apparent elimination rate from the tumor tissue by fitting a decaying exponential of the form $D(t) = D_0 \exp(-kt)$ to the known concentrations of drug present in tissue at each time. Using this method, the elimination rate constant from the tumor area was calculated to be $k = 0.42 \pm 0.06 \text{ day}^{-1}$, which corresponds to an apparent elimination half time from tumor of $t_{1/2} = 1.6 \pm 0.2 \text{ days}$.

Fluorescent doxorubicin distribution

Local drug distributions from the treated tumors on both day 4 and day 8 were used to evaluate the overall drug exposure to each tumor region. Representative doxorubicin distributions from tumor sections on day 4 and day 8 are shown in Figure 2(A,B), respectively. At both 4 days and 8 days after the millirod implantation, concentrations of drug higher than $1000 \mu\text{g/g}$ were found in a band surrounding the implant location. These concentrations are considerably higher than the previously reported effective concentration for doxorubicin, $6.4 \mu\text{g/g}$.^{40,41} Additionally, it can be observed that the band of drug around the implant location appears to be both more intense and thicker in the day 4 distribution as compared to the day 8 distribution. Another characteristic of interest is the large degree of asymmetry in the distributions, which is more pronounced than in previous studies in normal and RF ablated liver tissues.²⁵ This asymmetry likely reflects the inhomogeneity of the doxorubicin transport properties inside VX2 tumor tissues. Average drug concentration profiles for the distributions in Figure 2(A,B) are shown in Figure 2(C). These profiles quantitatively reaffirm that average concentrations

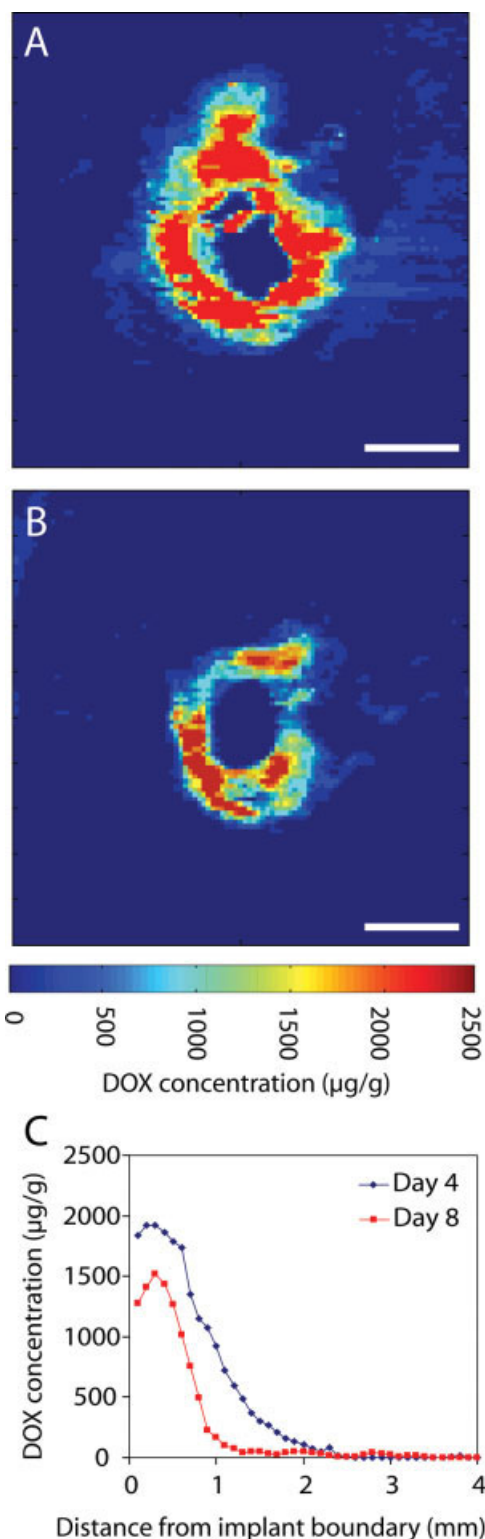


Figure 2. Doxorubicin concentration distribution maps derived from fluorescent imaging of representative tumor sections from the treated group on day 4 (A) and day 8 (B). Before removal, the implant was located in the small clearing found in the center of the image, and the scale bars are 2 mm . From these two distributions, concentration profiles plotting the average doxorubicin concentration against the distance from the implant boundary are shown for both times (C). [Color figure can be viewed in the online issue, which is available at www.interscience.wiley.com.]

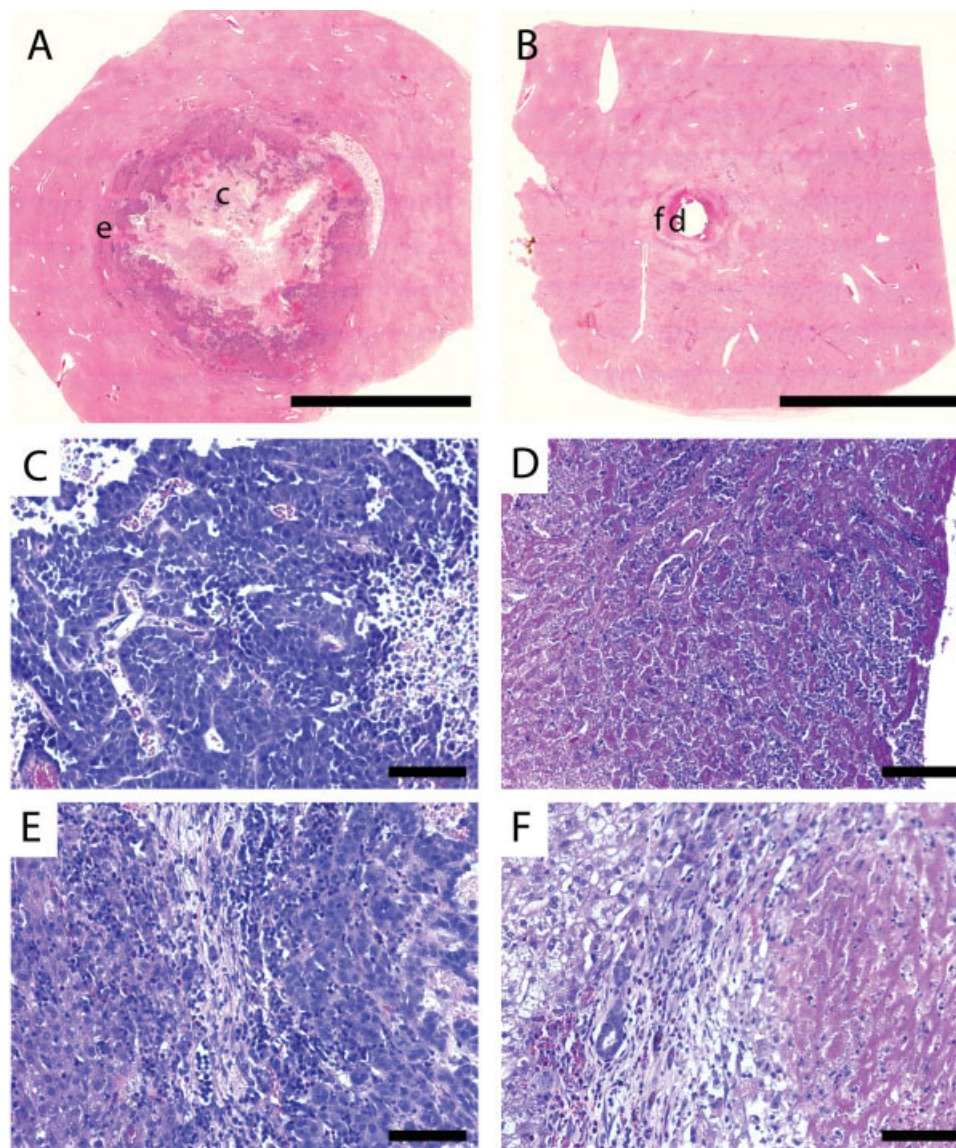


Figure 3. H&E stained sections of control (A, C, E) and treated (B, D, F) tumor sections on day 8. Low magnification images of the control (A) and treated (B) tumors indicate with lower case letters the regions from which the high magnification images are taken. The scale bars are 1 cm. High magnification images of the tumor core for control (C) and treated (D) tumors as well as the tumor/normal liver interface for control (E) and treated (F) tumors are also shown. The clearing on the right side of slide (D) is the original implant location. In (E) and (F), normal liver is found to the left of the panel while tumor is found to the right. All high magnification images (C–F) have scale bars of 100 μm . [Color figure can be viewed in the online issue, which is available at www.interscience.wiley.com.]

near the implant are higher and the drug penetrates to a greater distance in the day 4 distribution. The average doxorubicin concentration within 0.5 mm of the implant boundary in these slices is 1870 ± 60 and $1380 \pm 110 \mu\text{g/g}$ for day 4 and day 8, respectively. In contrast, little to no fluorescence was seen in the control tissue (data not shown).

Histological comparison of tumors

Representative H&E sections of a control and treated tumor on day 8 are shown in Figure 3. The

control tumor [Fig. 3(A)] is large and has a boundary of darkly staining viable tumor cells surrounding a core comprised of viable tumor cells mixed with necrotic debris, while the treated tumor [Fig. 3(B)] has a smaller boundary of largely necrotic tumor cells. The higher magnification image from the core of the control tumor [Fig. 3(C)] reveals clusters of large, irregularly shaped tumor cells with darkly staining nuclei interspersed with lighter regions of necrosis and cellular debris. In contrast, the treated tumor core [Fig. 3(D)] is heavily necrotic and contains few viable cells. Cells lack discernible boundaries and have no distinct nuclei, and basophilic remains

have aggregated. Similar differences are visible in the high magnification images of the tumor boundaries [Fig. 3(E,F)]. Again, the control tumor is filled with viable tumor cells while the treated tumor is largely necrotic. Both tumors are separated from normal tissue by a lighter staining fibrous region containing a mixture of tumor and inflammatory cells. Histological comparison of the tumors reveals marked differences between the regions exposed to doxorubicin from the implant and the untreated controls.

H&E histology [Fig. 4(A)] and fluorescent microscopy [Fig. 4(B)] from the same tissue area after 8 days allow for explicit localization of the doxorubicin into three main regions of the treated tumor. Region 1, closest to the implant location, contains dense basophilic and eosinophilic necrotic debris accompanied by high doxorubicin concentrations. Region 2 is filled with less dense necrotic debris characterized by a lack of nuclei and has detectable but considerably smaller amounts of fluorescence. Finally, Region 3 contains the fibrous band separating tumor from normal tissue, which is marked by a dotted band of fluorescent cells skirting the outer tumor boundary. Enlargement of this region [Fig. 4(C)] shows an area of enhanced cellular uptake of doxorubicin. Particularly, the nuclear detail visible in the image indicates the presence of drug in cell nuclei, the primary location of action for doxorubicin. These images indicate that even those cells at the tumor/normal tissue interface have significant doxorubicin exposure over the 8 day period of treatment. Fluorescence in this region was not observed in drug-free controls (data not shown).

While the main tumor mass in the treated animals is necrotic and exposed to high drug concentrations, there is histological evidence that residual viable tumor cells still exist on day 8. An H&E stained section shows cords of tumor cells extending ~1–2 mm from the tumor/normal tissue boundary (Fig. 5). These cells appear to be viable and are far enough from the implant location that they are unlikely to be exposed to therapeutic drug concentrations.

DISCUSSION

In this study, doxorubicin-containing PLGA implants were used to treat VX2 carcinomas in rabbit liver, and the response to treatment was simultaneously evaluated using tumor size, fluorescence drug distribution, and histology. The treated tumors were significantly smaller than the untreated controls at both day 4 and day 8. Histological analysis confirmed the tumor response to drug treatment at cellular level, where regions of viable tumor cells in untreated tumor were replaced by broad regions of necrosis in tumor implanted with doxorubicin millirods. Both macro-

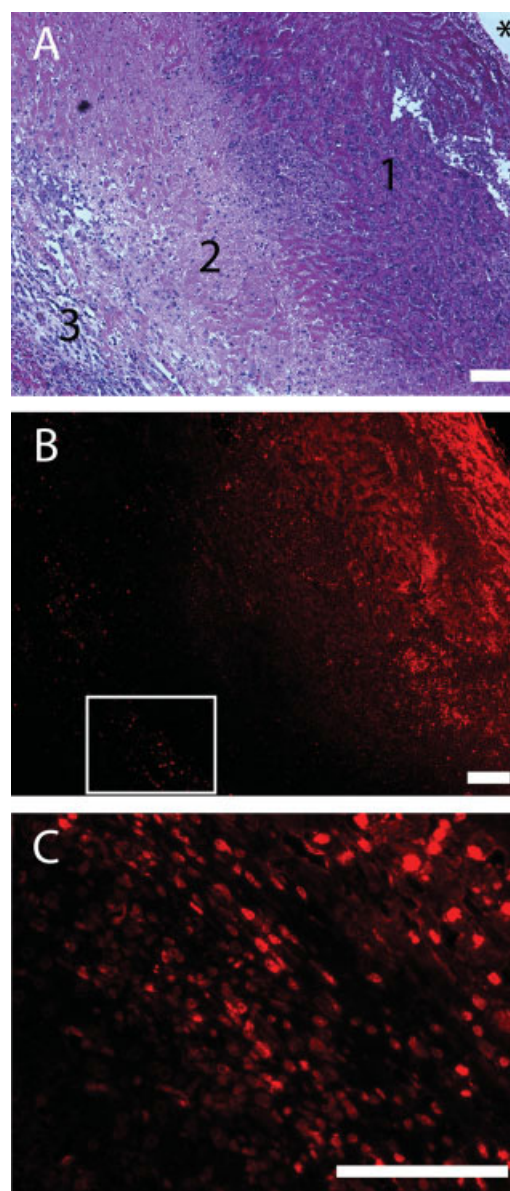


Figure 4. H&E stained and fluorescent micrographs of a treated tumor on day 8. The H&E section (A) illustrates the different tissue regions moving outward from the implant location (*): (1) a dense necrotic region, (2) a sparse necrotic region, and (3) the inflammatory boundary of the tumor. An aligned fluorescence micrograph (B) illustrates the pattern of doxorubicin distribution throughout the tumor regions. A higher magnification image (C) of the area indicated with a white box in (B) shows significant cellular uptake of doxorubicin in the inflammatory boundary of the tumor. All scale bars are 100 μm . [Color figure can be viewed in the online issue, which is available at www.interscience.wiley.com.]

scopic and microscopic analyses indicate the overall success of the implant for tumor treatment.

A rapidly releasing implant was chosen in this study to maximize drug effect immediately after implantation while still preventing the immediate drug clearance that occurs after direct injection of drug solutions.^{14,42} Doxorubicin concentrations greater

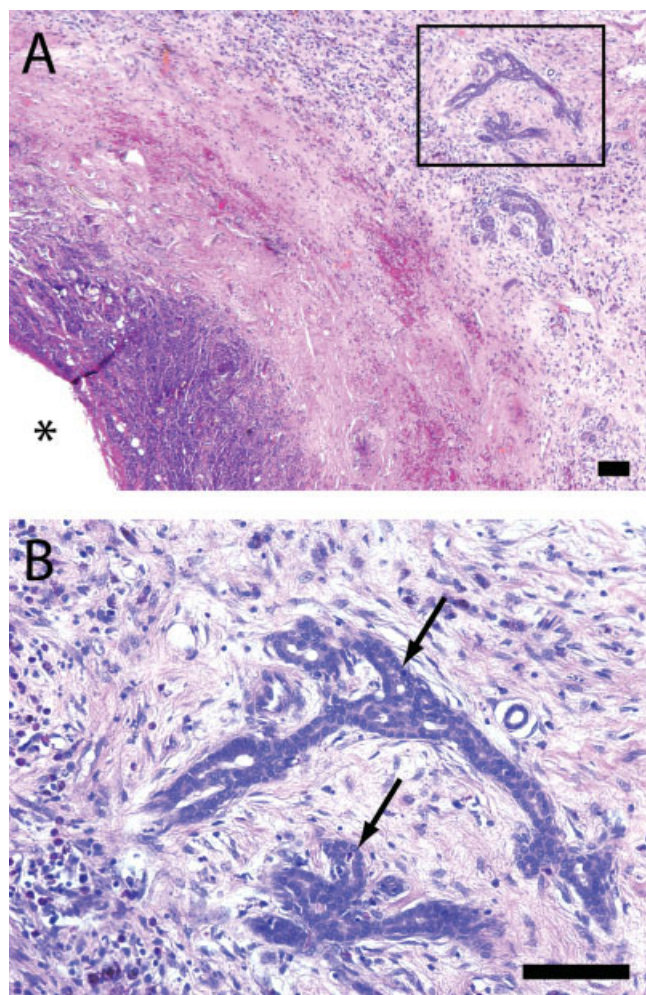


Figure 5. H&E stained micrograph of a treated day 8 tumor showing potential spread of the tumor beyond its circumscribed boundary. A low magnification image (A) indicates the implant location (*) and viable tumor cells (black box), which are magnified in (B). The two arrows indicate cords of viable tumor cells that appear to be spreading beyond the treated zone. The scale bars are 100 μm . [Color figure can be viewed in the online issue, which is available at www.interscience.wiley.com.]

than 100 times the therapeutic level were observed in tumor tissues surrounding the implant even after 8 days. In comparison, intravenously administered doxorubicin is typically eliminated from the plasma with a half-life of ~ 10 min.⁴³ Cellular uptake, drug binding to extracellular proteins, and limited perfusion in the necrotic tumor core may each contribute to prolonged drug retention from these intratumoral implants. Qualitatively, the pattern of distributions revealed a greater degree of asymmetry than previously observed in either normal or ablated liver.²⁸ The irregular drug distribution patterns may be attributed to the inhomogeneity of tumor vasculature³¹ and greater drug clearance in highly perfused areas. Overall, the doxorubicin-containing implants provided high drug concentrations for a prolonged

exposure time, albeit to only a limited region surrounding the implant.

The most surprising aspect of this study is that necrosis extends to the tumor boundary despite the limited drug penetration distance. While the initial tumors had a radius of ~ 4 mm, the maximum drug penetration distance was less than 3 mm on both day 4 and day 8. These data would suggest that the tumor periphery would not receive adequate doxorubicin to kill the VX2 cells. To the contrary, microscopic examination of histology slides showed that doxorubicin was present at the tumor boundary and necrotic tumor abutted the surrounding normal liver tissue, demonstrating the treatment of entire tumor volume. Two plausible mechanisms could explain this contradiction. In one scenario, doxorubicin may successfully treat the tumor mass without reaching 4 mm from the implant. Rapid release of high drug concentrations eliminates the VX2 cells closest to the implant, causing the tumor shrinkage observed in the study. The collapse of the tumor core subsequently brings the outer tumor boundary closer to the implant interface. Continued diffusion of drug away from the implant simultaneously moves the front of drug penetration outward, where it eventually meets the inwardly moving tumor boundary by day 4. Alternatively, doxorubicin may reach the therapeutic level at 4 mm but be undetected by this study for various reasons. First, the time points in this study were chosen to maximize the information available from drug distribution, tumor pathology, and histology. Peak drug concentrations likely occur earlier, as soon as 24 h after implantation, when doxorubicin may reach the 4 mm tumor boundary.²⁸ By day 4, drug penetration distances decrease through clearance and tumor shrinkage as described earlier. Second, doxorubicin may be present at undetectable and yet therapeutic levels beyond the measured penetration distances in this study. While previous studies have established an effective doxorubicin concentration at 6.4 $\mu\text{g/g}$,^{40,41} this number was calculated for a transient exposure to a systemically administered treatment. For a prolonged exposure such as that provided by this implant, the effective drug concentration is expected to be even lower. Future studies that differentiate the above two mechanisms will provide significant insights to fundamentally understand drug transport in tumor tissues and their effects on tumor treatment.

Although this study illustrates considerable promise of polymer millirods for local treatment of VX2 tumors, these implants are not without limitations. Viable tumor cells were observed advancing beyond the main front of the tumor (Fig. 5), potentially by lymphatic spread, which is a known mode of metastasis for the VX2 tumor cells⁴⁴ as well as many human tumors.^{45–47} Although it cannot be assured that these cells would have developed into a recurrent

tumor, future development of intratumoral treatments should actively focus on successfully delivering drug to a margin of safety beyond the main tumor mass to minimize the risk of recurrence.⁴⁸

On the other hand, combined treatment strategies with these implants offer a number of opportunities for complete tumor eradication. For example, radiofrequency (RF) ablation has been shown to facilitate drug distribution and retention in normal tissues through destruction of the tumor vasculature,²⁸ which makes it a particularly attractive candidate for use with these implants. In a combined therapy, RF ablation could destroy the vast majority of the tumor volume and surrounding vasculature, allowing greater delivery of doxorubicin to the tumor periphery. Other strategies such as systemically administered targeted nanoparticles^{49–51} that have demonstrated effective targeting to the well perfused tumor periphery⁵² may also prove synergistic to the millirod therapy. Alternatively, these implants could also be used as a neoadjuvant treatment prior to resection. Tissue conserving surgical removal of the smaller, post-treatment tumor could then be performed, minimizing the risk of local recurrence from residual cancer cells. Irrespective of the combined methods, the described polymer implants provide a versatile platform for minimally invasive, intratumoral chemotherapy, and this study provides detailed insight about drug distribution and antitumor efficacy that can be used in their further development.

CONCLUSIONS

In conclusion, doxorubicin-containing millirods have shown considerable success in treating small but aggressive liver tumors in rabbits. The treated tumors were significantly smaller than the control tumors after both 4 and 8 days, and areas adjacent to the implant contained high concentrations of doxorubicin throughout the study. Although the implants were capable of treating larger tumors than expected, the exact mechanism for this success remains incompletely understood. These promising results will open a variety of opportunities to investigate several combined treatment approaches to achieve complete tumor eradication.

BW is supported by DOD predoctoral fellowship BC043453.

References

- Nabholtz JM, Reese D, Lindsay MA, Riva A. Evidence for the use of chemotherapy in breast cancer. *Int J Clin Oncol* 2002; 7:254–264.
- Leung TW, Johnson PJ. Systemic therapy for hepatocellular carcinoma. *Semin Oncol* 2001;28:514–520.
- Aguayo A, Patt YZ. Nonsurgical treatment of hepatocellular carcinoma. *Semin Oncol* 2001;28:503–513.
- Apisarnthanarax S, Chao KS. Current imaging paradigms in radiation oncology. *Radiat Res* 2005;163:1–25.
- Goldberg SN. Radiofrequency tumor ablation: Principles and techniques. *Eur J Ultrasound* 2001;13:129–147.
- Dale PS, Souza JW, Brewer DA. Cryosurgical ablation of unresectable hepatic metastases. *J Surg Oncol* 1998;68:242–245.
- Vogl TJ, Mack MG, Muller PK, Straub R, Engelmann K, Eichler K. Interventional MR: Interstitial therapy. *Eur Radiol* 1999;9: 1479–1487.
- Guerin C, Olivi A, Weingart JD, Lawson HC, Brem H. Recent advances in brain tumor therapy: Local intracerebral drug delivery by polymers. *Invest New Drugs* 2004;22:27–37.
- Goldberg EP, Hadba AR, Almond BA, Marotta JS. Intratumoral cancer chemotherapy and immunotherapy: Opportunities for nonsystemic preoperative drug delivery. *J Pharm Pharmacol* 2002;54:159–180.
- Su WC, Lai WW, Chen HH, Hsiue TR, Chen CW, Huang WT, Chen TY, Tsao CJ, Wang NS. Combined intrapleural and intravenous chemotherapy, and pulmonary irradiation, for treatment of patients with lung cancer presenting with malignant pleural effusion. A pilot study. *Oncology* 2003;64:18–24.
- Tohda Y, Iwanaga T, Takada M, Yana T, Kawahara M, Negoro S, Okishio K, Kudoh S, Fukuoka M, Furuse K. Intrapleural administration of cisplatin and etoposide to treat malignant pleural effusions in patients with non-small cell lung cancer. *Chemotherapy* 1999;45:197–204.
- Duvillard C, Benoit L, Moretto P, Beltramo JL, Brunet-Lecomte P, Correia M, Sergent C, Chauffert B. Epinephrine enhances penetration and anti-cancer activity of local cisplatin on rat sub-cutaneous and peritoneal tumors. *Int J Cancer* 1999;81:779–784.
- Duvillard C, Romanet P, Cosmidis A, Beaudouin N, Chauffert B. Phase 2 study of intratumoral cisplatin and epinephrine treatment for locally recurrent head and neck tumors. *Ann Otol Rhinol Laryngol* 2004;113(3 Part 1):229–233.
- Emerich DF, Snodgrass P, Lafreniere D, Dean RL, Salzberg H, Marsh J, Perdomo B, Arastu M, Winn SR, Bartus RT. Sustained release chemotherapeutic microspheres provide superior efficacy over systemic therapy and local bolus infusions. *Pharm Res* 2002;19:1052–1060.
- Brem H, Piantadosi S, Burger PC, Walker M, Selker R, Vick NA, Black K, Sisti M, Brem S, Mohr G, Muller P, Morawetz R, Schold SC. Placebo-controlled trial of safety and efficacy of intraoperative controlled delivery by biodegradable polymers of chemotherapy for recurrent gliomas. *Lancet* 1995;345:1008–1012.
- Li Y, Owusu A, Lehnert S. Treatment of intracranial rat glioma model with implant of radiosensitizer and biomodulator drug combined with external beam radiotherapy. *Int J Radiat Oncol Biol Phys* 2004;58:519–527.
- Ruel-Gariepy E, Shive M, Bichara A, Berrada M, Le Garrec D, Chenite A, Leroux JC. A thermosensitive chitosan-based hydrogel for the local delivery of paclitaxel. *Eur J Pharm Biopharm* 2004;57:53–63.
- Chen FA, Kuriakose MA, Zhou MX, DeLacure MD, Dunn RL. Biodegradable polymer-mediated intratumoral delivery of cisplatin for treatment of human head and neck squamous cell carcinoma in a chimeric mouse model. *Head Neck* 2003;25:554–560.
- Almond BA, Hadba AR, Freeman ST, Cuevas BJ, York AM, Detrisac CJ, Goldberg EP. Efficacy of mitoxantrone-loaded albumin microspheres for intratumoral chemotherapy of breast cancer. *J Controlled Release* 2003;91:147–155.
- Menei P, Jadaud E, Faisant N, Boisdron-Celle M, Michalak S, Fournier D, Delhaye M, Benoit JP. Stereotaxic implantation of 5-fluorouracil-releasing microspheres in malignant glioma. *Cancer* 2004;100:405–410.

21. Brem H, Gabikian P. Biodegradable polymer implants to treat brain tumors. *J Controlled Release* 2001;74:63–67.
22. Berrada M, Yang Z, Lehnert S. Tumor treatment by sustained intratumoral release of 5-fluorouracil: Effects of drug alone and in combined treatments. *Int J Radiat Oncol Biol Phys* 2002;54:1550–1557.
23. Strasser JF, Fung LK, Eller S, Grossman SA, Saltzman WM. Distribution of 1,3-bis(2-chloroethyl)-1-nitrosourea and tracers in the rabbit brain after interstitial delivery by biodegradable polymer implants. *J Pharmacol Exp Ther* 1995;275:1647–1655.
24. Fleming AB, Saltzman WM. Pharmacokinetics of the carmustine implant. *Clin Pharmacokinet* 2002;41:403–419.
25. Qian F, Stowe N, Saidel GM, Gao J. Comparison of doxorubicin concentration profiles in radiofrequency-ablated rat livers from sustained- and dual-release PLGA millirods. *Pharm Res* 2004;21:394–399.
26. Szymanski-Exner A, Gallacher A, Stowe NT, Weinberg B, Haaga JR, Gao J. Local carboplatin delivery and tissue distribution in livers after radiofrequency ablation. *J Biomed Mater Res A* 2003;67:510–516.
27. Szymanski-Exner A, Stowe NT, Lazebnik RS, Salem K, Wilson DL, Haaga JR, Gao JM. Noninvasive monitoring of local drug release in a rabbit radiofrequency (RF) ablation model using X-ray computed tomography. *J Controlled Release* 2002;83:415–425.
28. Qian F, Stowe N, Liu EH, Saidel GM, Gao JM. Quantification of in vivo doxorubicin transport from PLGA millirods in thermoablated rat livers. *J Controlled Release* 2003;91:157–166.
29. Qian F, Saidel GM, Sutton DM, Exner A, Gao JM. Combined modeling and experimental approach for the development of dual-release polymer millirods. *J Controlled Release* 2002;83:427–435.
30. Qian F, Nasongkla N, Gao JM. Membrane-encased polymer millirods for sustained release of 5-fluorouracil. *J Biomed Mater Res* 2002;61:203–211.
31. Jain RK. Delivery of molecular and cellular medicine to solid tumors. *Adv Drug Deliv Rev* 2001;46:149–168.
32. Clavien PA, Selzner N, Morse M, Selzner M, Paulson E. Downstaging of hepatocellular carcinoma and liver metastases from colorectal cancer by selective intra-arterial chemotherapy. *Surgery* 2002;131:433–442.
33. Leung TW, Patt YZ, Lau WY, Ho SK, Yu SC, Chan AT, Mok TS, Yeo W, Liew CT, Leung NW, Tang AM, Johnson PJ. Complete pathological remission is possible with systemic combination chemotherapy for inoperable hepatocellular carcinoma. *Clin Cancer Res* 1999;5:1676–1681.
34. Jackson JK, Gleave ME, Yago V, Beraldi E, Hunter WL, Burt HM. The suppression of human prostate tumor growth in mice by the intratumoral injection of a slow-release polymeric paste formulation of paclitaxel. *Cancer Res* 2000;60:4146–4151.
35. Ramirez LH, Zhao Z, Rougier P, Bognel C, Dzodic R, Vassal G, Ardouin P, Gouyette A, Munck JN. Pharmacokinetics and antitumor effects of mitoxantrone after intratumoral or intra-arterial hepatic administration in rabbits. *Cancer Chemother Pharmacol* 1996;37:371–376.
36. Yoon CJ, Chung JW, Park JH, Yoon YH, Lee JW, Jeong SY, Chung H. Transcatheter arterial chemoembolization with paclitaxel-lipiodol solution in rabbit VX2 liver tumor. *Radiology* 2003;229:126–131.
37. Qian F, Szymanski A, Gao JM. Fabrication and characterization of controlled release poly(D,L-lactide-co-glycolide) millirods. *J Biomed Mater Res* 2001;55:512–522.
38. Geschwind JF, Ko YH, Torbenson MS, Magee C, Pedersen PL. Novel therapy for liver cancer: Direct intraarterial injection of a potent inhibitor of ATP production. *Cancer Res* 2002;62:3909–3913.
39. Gao JM, Qian F, Szymanski-Exner A, Stowe N, Haaga J. In vivo drug distribution dynamics in thermoablated and normal rabbit livers from biodegradable polymers. *J Biomed Mater Res* 2002;62:308–314.
40. Ridge JA, Collin C, Bading JR, Hancock C, Conti PS, Daly JM, Raaf JH. Increased adriamycin levels in hepatic implants of rabbit Vx-2 carcinoma from regional infusion. *Cancer Res* 1988;48:4584–4587.
41. Swistel AJ, Bading JR, Raaf JH. Intraarterial versus intravenous adriamycin in the rabbit Vx-2 tumor system. *Cancer* 1984;53:1397–1404.
42. Buahin KG, Brem H. Interstitial chemotherapy of experimental brain tumors: Comparison of intratumoral injection versus polymeric controlled release. *J Neurooncol* 1995;26:103–110.
43. Gabizon A, Shmeeda H, Barenholz Y. Pharmacokinetics of pegylated liposomal Doxorubicin: Review of animal and human studies. *Clin Pharmacokinet* 2003;42:419–436.
44. Dunne AA, Mandic R, Ramaswamy A, Plehn S, Schulz S, Lippert BM, Moll R, Werner JA. Lymphogenic metastatic spread of auricular VX2 carcinoma in New Zealand white rabbits. *Anticancer Res* 2002;22:3273–3279.
45. Hida J, Yasutomi M, Maruyama T, Fujimoto K, Uchida T, Okuno K. The extent of lymph node dissection for colon carcinoma: The potential impact on laparoscopic surgery. *Cancer* 1997;80:188–192.
46. Trocha SD, Giuliano AE. Sentinel node in the era of neoadjuvant therapy and locally advanced breast cancer. *Surg Oncol* 2003;12:271–276.
47. Yuki K, Hirohashi S, Sakamoto M, Kanai T, Shimosato Y. Growth and spread of hepatocellular carcinoma. A review of 240 consecutive autopsy cases. *Cancer* 1990;66:2174–2179.
48. Pawlik TM, Scoggins CR, Zorzi D, Abdalla EK, Andres A, Eng C, Curley SA, Loyer EM, Muratore A, Mentha G, Capussotti L, Vauthey JN. Effect of surgical margin status on survival and site of recurrence after hepatic resection for colorectal metastases. *Ann Surg* 2005;241:715–722, discussion 722–724.
49. Straubinger RM, Arnold RD, Zhou R, Mazurchuk R, Slack JE. Antivasular and antitumor activities of liposome-associated drugs. *Anticancer Res* 2004;24:397–404.
50. Torchilin VP. Targeted polymeric micelles for delivery of poorly soluble drugs. *Cell Mol Life Sci* 2004;61:2549–2559.
51. Nasongkla N, Shuai X, Ai H, Weinberg BD, Pink J, Boothman DA, Gao J. cRGD-Functionalized polymer micelles for targeted doxorubicin delivery. *Angew Chem Int Ed Engl* 2004;43:6323–6327.
52. Jain RK. Transport of molecules, particles, and cells in solid tumors. *Annu Rev Biomed Eng* 1999;1:241–263.

Modulating β -Lapachone Release from Polymer Millirods through Cyclodextrin Complexation

FANGJING WANG,¹ ELVIN BLANCO,² HUA AI,³ DAVID A. BOOTHMAN,² JINMING GAO²

¹Department of Biomedical Engineering, Case Western Reserve University, Cleveland, Ohio 44106-7207

²Simmons Comprehensive Cancer Center, University of Texas Southwestern Medical Center at Dallas, Dallas, Texas 75390-8590

³National Engineering Research Center for Biomaterials, Sichuan University, Chengdu, China

Received 3 March 2006; revised 24 May 2006; accepted 6 June 2006

Published online in Wiley InterScience (www.interscience.wiley.com). DOI 10.1002/jps.20721

ABSTRACT: β -Lapachone (β -lap) is a novel anticancer agent that kills tumors over-expressing the NADP(H): quinone oxidoreductase enzyme. However, poor aqueous solubility and low bioavailability hinder its therapeutic applications. Herein we describe the development of poly(D,L-lactide-co-glycolide) (PLGA) polymer millirods for local delivery of β -lap. The objective was to investigate the use of β -lap inclusion complexes with cyclodextrins (CDs) to control β -lap release kinetics from PLGA millirods. Differential scanning calorimetry was performed to measure drug/polymer interactions, complexation efficiency with different CDs, and complex/polymer interactions. β -Lap was found to have a solid-state solubility of 13% in PLGA. β -Lap dissolution in PLGA matrix lowered the glass transition temperature of PLGA from 44 to 31°C, and led to a slow release of β -lap (8.8 \pm 1.2% release after 22 days). For β -lap and CD interactions, increasing complexation efficiency was observed in the order of α -CD, γ -CD, and β -CD. β -Lap complexation with hydroxypropyl- β -cyclodextrin (HP β -CD) prevented drug dissolution in PLGA, and led to fast release (79.6 \pm 2.1% after 2 days). Sustained drug release was achieved when β -lap was complexed with α -CD or γ -CD. These data demonstrate the ability to tailor β -lap release kinetics via CD complexation, providing exciting opportunities for the use of β -lap-millirods for intratumoral drug delivery.

© 2006 Wiley-Liss, Inc. and the American Pharmacists Association J Pharm Sci 95:2309–2319, 2006

Keywords: cyclodextrin inclusion complexation; β -lapachone; drug-polymer interactions; poly(lactic/glycolic) acid (PLGA); drug delivery

INTRODUCTION

A rising trend in cancer chemotherapy involves site-specific, controlled release of cytotoxic agents from biodegradable polymer depots. This strategy often proves advantageous when compared to traditional administration regimens, such as

intravenous injection of drugs, where low water solubility of many anticancer drugs limits their bioavailability and anticancer efficacy *in vivo*. Controlled release strategies are superior since tumors are exposed to therapeutic levels of drug for a prolonged time period, all the while reducing toxicity to healthy cells.¹ Drug inclusion in a polymer depot also allows for potential tailoring of release kinetics, adding the benefit of being able to design the most efficacious delivery regimen. Taking these advantages into consideration, our laboratory developed a polymeric drug depot in the form of a cylindrical millirod composed of poly(D,L-lactide-co-glycolide) (PLGA), designed

Fangjing Wang and Elvin Blanco contributed equally to this work.

Correspondence to: Jinming Gao (Telephone: 1-214-648-9278; Fax: 1-214-648-0264; E-mail: jinming.gao@utsouthwestern.edu)

Journal of Pharmaceutical Sciences, Vol. 95, 2309–2319 (2006)
© 2006 Wiley-Liss, Inc. and the American Pharmacists Association

specifically for intratumoral delivery of anticancer agents. Research efforts have been devoted to the fabrication and mechanical characterization of drug-loaded polymer millirods,² as well as the control of drug release characteristics from these devices.^{3,4} Direct implantation of doxorubicin-millirods has shown successful antitumor efficacy in rabbit VX-2 liver tumors *in vivo*.⁵ In addition, local delivery of dexamethasone through millirod implants considerably improved drug effectiveness in decreasing fibrous capsule formation in ablated liver tissues compared to a systemic delivery of the drug.⁶

β -Lapachone (β -lap) is a novel antitumor agent with specific anticancer activity against human lung, prostate, and breast tumors.⁷ β -Lap has a unique mechanism of action, which relies on bioactivation by the cytosolic enzyme, NAD(P)H:quinone oxidoreductase-1 (NQO1).⁸ This enzyme is endogenously elevated in tumor cells (up to 20-fold) compared to adjacent normal cells.⁹ Furthermore, β -lap has distinct advantages over other chemotherapeutic agents in that it kills tumors independent of p53 status, cell cycle state, caspases, all the while inducing a novel μ -calpain-mediated apoptotic response.^{8,10,11} In spite of the therapeutic potential of β -lap, its low solubility (0.04 mg/mL¹²) severely limits its applications *in vivo*. Moreover, our initial work with β -lap and other hydrophobic agents (e.g. dexamethasone⁶) have shown that direct incorporation of hydrophobic drugs into PLGA matrices leads to an extremely slow release of small quantities of drugs that may limit drug availability throughout the tumor treatment.

Research from many groups has shown that drug complexation with cyclodextrins (CDs) can effectively enhance the solubility and bioavailability of otherwise water insoluble drugs.^{13,14} CDs are cyclic oligosaccharides in the form of truncated cones consisting of a hydrophobic core and a hydrophilic outer surface.^{15,16} These oligosaccharides have the ability to form inclusion complexes with drug molecules (Fig. 1), which subsequently increase the apparent water solubility of the drug. CDs are differentiated mainly in the number of glucopyranose units (6, 7, and 8 for α , β , and γ -CD, respectively).¹⁵⁻¹⁷ Hydroxypropyl- β -cyclodextrin (HP β -CD) is obtained by treating a base-solubilized solution of β -CD with propylene oxide, resulting in a CD with greater solubility (~500 mg/mL vs. 18.5 mg/mL for β -CD). Our laboratory recently utilized CDs to solubilize β -lap in aqueous solutions, and we were able to

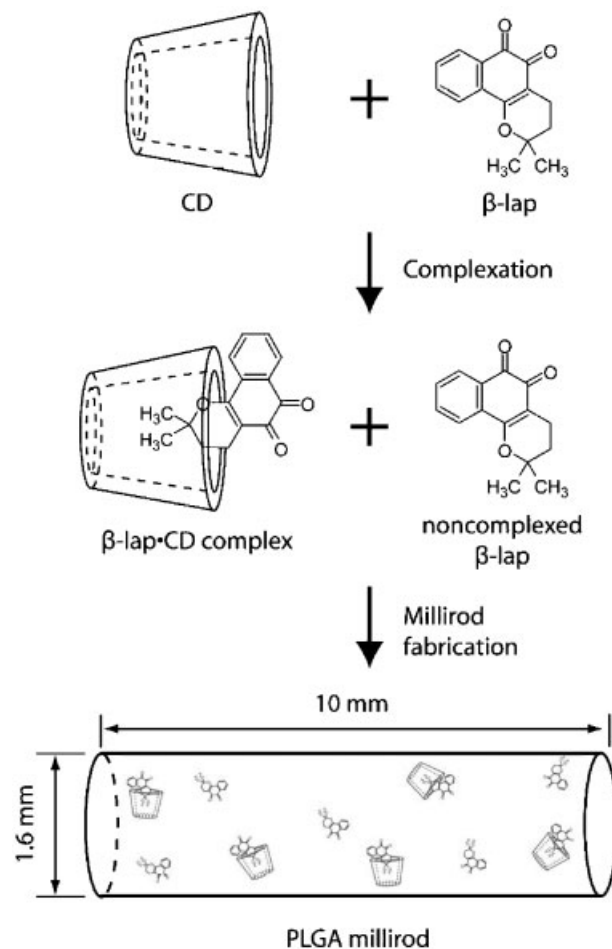


Figure 1. Schematic of β -lap · CD complexation, and incorporation of β -lap and β -lap · CD complex into the polymer millirod.

determine the binding affinities of the drug with the different CDs.¹² HP β -CD and β -CD had the highest binding affinity to β -lap ($K_c = 1.1 \times 10^3/M$), followed by γ -CD and α -CD (160/M and 20/M, respectively). In the case of β -lap complexed with HP β -CD, a 400-fold increase in drug solubility was observed (16.0 mg/mL compared to 0.04 mg/mL), with increased β -lap solubility also arising through complexation with γ -, β -, and α -CD.¹²

In the present work, we formed solid-state inclusion complexes of β -lap with different CDs and examined the interaction of free drug (as well as complexed β -lap) with PLGA. We hypothesized that CDs with different complexation affinities toward β -lap would provide an effective strategy to modulate the release kinetics of β -lap from PLGA millirods. To test this hypothesis, differential scanning calorimetry (DSC) experiments were

performed to determine the degree of interaction between the polymer and drug in the presence and absence of different types of CDs. Release studies of various β -lap·CD complex formulations were then conducted to examine the influence of different polymer-drug interactions on release kinetics. Data from this study show that drug incorporation within the CD core prevents the drug from molecular dissolution within the PLGA matrix, which in turn, results in a dramatic increase in release from the polymer depot.

MATERIALS AND METHODS

Materials

PLGA (lactide:glycolide = 50/50, MW 50000 Da, inherent viscosity 0.65 dL/g) was purchased from Birmingham Polymers, Inc. (Birmingham, AL). β -Lap was synthesized following a previously reported procedure.¹⁰ α -CD, β -CD, γ CD, and HP β -CD were obtained from Cyclodextrin Technologies Development, Inc. (CTD, High Springs, FL) with >98% purity. Glucose anhydrous was obtained from Fisher Scientific (Pittsburgh, PA).

Preparation of β -lap·D Inclusion Complexes

Accurately weighed quantities of CDs (α -CD, γ -CD, and HP β -CD) and β -lap were dissolved in a methanol/water mixture (3/1 v/v). The β -lap· β -CD complex was prepared by dissolving the drug and β -CD in a 1/2 methanol/water mixture (v/v). Following solvent evaporation, the mixture was resuspended in deionized water, stirred for 24 h, and lyophilized. The drug·CD complex was then ground to produce a fine powder and filtered through a 100 mesh sieve.

Preparation of β -Lap-Loaded PLGA Millirods

β -Lap-containing millirods were prepared by means of a compression-heat molding procedure previously described.² Briefly, the β -lap·CD complex powder and PLGA microspheres (5 μ m) were accurately weighed and mixed with a mortar and pestle. The contents were then inserted into a Teflon tube with an inner diameter of 1.6 mm. The Teflon tube was placed inside a stainless steel mold, which was placed in an iso-temp oven at 90°C \pm 2°C (Fisher Model 282A) for 2 h to allow for PLGA polymer annealing. A compression pres-

sure of 4.6 MPa was applied by means of a copper weight during the annealing process. After 2 h, the polymer millirod was removed from the Teflon tubing and cut to a length of 10 mm for subsequent analyses. A schematic diagram of the complex formation and millirod preparation is shown (Fig. 1).

To examine the effect of formation of inclusion complex on β -lap release kinetics, millirods of four different formulations were fabricated. Formulation 1 consisted of a millirod composed of 40% β -lap·HP β -CD complex (1.2% β -lap) and 60% PLGA with a molar ratio of β -lap and HP β -CD of 1:5.5. Formulation 2 consisted of 1.2% β -lap mixed with 38.8% HP β -CD (physical mixture from β -lap particles and HP β -CD powder) and 60% PLGA, while Formulation 3 consisted of 1.2% β -lap mixed with 38.8% glucose and 60% PLGA. The final formulation, Formulation 4, consisted of millirods composed of 1.2% β -lap and 98.8% PLGA. To examine the effect of different CDs on release kinetics, millirods that consisted of β -lap complexed with α -CD, β -CD, γ -CD, and HP β -CD were produced. All millirods share the same composition of 40% β -lap·CD complex (1.8% β -lap) and 60% PLGA. The molar ratios of β -lap and CD are 1:5, 1:4.5, 1:4, and 1:3.5 for α -CD, β -CD, γ -CD, and HP β -CD, respectively.

Differential Scanning Calorimetry (DSC) Analysis

DSC measurements of the solid-state solubility of β -lap in PLGA were performed using a Shimadzu Differential Scanning Calorimeter (DSC-60, Columbia, MD) with samples under a nitrogen atmosphere. The procedure was adapted from a method previously published by Panyam et al.¹⁸ to determine the solid-state solubility of dexamethasone in PLGA. Briefly, known quantities of β -lap (10.8 mg) and PLGA (19.5 mg) were separately dissolved in methylene chloride. Different amounts of drug were mixed with polymer, and transferred to aluminum pans. The solvent was then allowed to evaporate, and the pans were crimped and weighed. Samples were heated to 180°C at a heating rate of 10°C/min. The heats of melting of β -lap were obtained using the peak integration calculation method provided by the DSC software. The solid-state solubility value of β -lap was determined by plotting enthalpy values as a function of β -lap loading percentage. The X-intercept resulting from a linear regression of the data represents the percentage solubility value of β -lap in PLGA.

DSC analyses of CD · drug complex or physical mixture, as well as drug or drug · complex powder with PLGA microspheres, were carried out using a Perkin Elmer Differential Scanning Calorimeter (DSC-7, Boston, MA) with samples under a nitrogen atmosphere. Contents were weighed (approximately 10 mg) and placed in an aluminum pan. For analysis of the CD/drug complex or physical mixture, data was recorded from 20°C to 180°C at a rate of 10°C/min. In drug or drug · complex powder mixed with PLGA microspheres, the samples were pretreated at 90°C for 2 h before DSC analyses to mimic the millirod fabrication process. The sample was cooled to 20°C before a subsequent heating run from 20 to 180°C at a rate of 10°C/min. Values for glass transition temperature (T_g) and melting enthalpy were obtained using a half C_p extrapolation method and peak integration calculation method, respectively.

In vitro Release Characterization of β -lap from Polymer Millirods

Millirods were placed in glass scintillation vials that contained 10 mL phosphate buffered saline (PBS) at 37°C. The sample vials were placed in an orbital shaker (C24 model, New Brunswick Scientific, Edison, NJ) with a rotating speed of 100 rpm. At different times, the millirod was removed from the solution and placed into a new scintillation vial containing 10 mL of fresh PBS at 37°C. The concentration of released β -lap was measured using a UV-Vis spectrophotometer (PerkinElmer, Lambda 20 model, Boston, MA) at the maximum adsorption wavelength of the drug ($\lambda_{max} = 258.0$ nm). The percentage of cumulative β -lap released was obtained by normalizing the released amount to the total amount loaded in the millirods. All experiments were performed in triplicate ($n = 3$).

SEM Analysis of Millirod Microstructure

Scanning electron microscopy (SEM) was used to characterize β -lap-loaded millirod morphology. Millirods pertaining to all three previously mentioned formulations were placed in 10 mL of distilled water at 37°C for 12 h, after which time they were freeze-dried overnight. Millirods were then cut into two sections for both lateral and cross-sectional analyses. A thin film of palladium (Pd, ~ 2 nm in thickness) was sputter-coated to minimize electron charging on the sample surface. A voltage of 5 kV was used during sample

examination with a Hitachi S-4500 scanning electron microscope (Hitachi, Ltd., Tokyo, Japan).

RESULTS

DSC Characterization of β -lap · CD Complexes

Figure 2A shows the DSC thermograms of β -lap complexed with HP β -CD. Pure β -lap had a melting point of 159.7°C, with a melting enthalpy (ΔH_m°) of 94.1 J/g. When β -lap was complexed with HP β -CD at molar fractions of β -lap ranging from 67% to 33%, a decrease in melting enthalpy was observed (Fig. 2B). At 67% and 50% molar fraction, lower melting points were also observed at 156.3°C and 155.5°C, respectively. The values

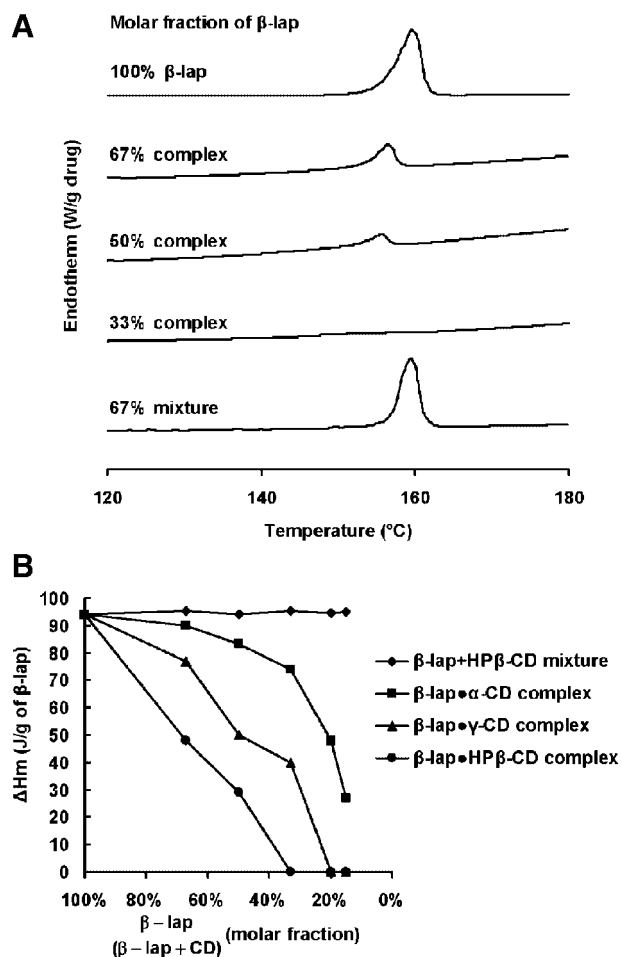


Figure 2. DSC thermograms of β -lap complexed or physically mixed with CDs. Figure A depicts DSC thermograms of β -lap complexed or mixed with HP β -CD at various molar fractions of β -lap. Figure B shows β -lap melting enthalpy (ΔH_m), when complexed or mixed with CDs, as a function of drug molar fraction.

of ΔH_m for β -lap recorded at these two molar fractions were 48.1 and 29.2 J/g, respectively, and were used to determine the percentage of β -lap in crystalline form ($\chi_{\beta\text{-lap}}$) using the following equation:

$$\chi_{\beta\text{-lap}} = \frac{\Delta H_m}{\Delta H_m^{\circ}} \times 100 \quad (1)$$

where ΔH_m is the recorded enthalpy of the β -lap when complexed with CD and ΔH_m° is the enthalpy of β -lap alone. Utilizing Eq. 1, we found that the percentage of β -lap in the crystalline form at 67% and 50% molar fractions was 51% and 31%, respectively. Also evident in Figure 2A was the disappearance of the β -lap crystalline peak at a molar fraction of 33%. In stark contrast to the β -lap \cdot HP β -CD complex, the physical mixture of the drug with HP β -CD at a β -lap molar fraction of 67% had an enthalpy similar to that of pure β -lap (Fig. 2A), with the drug melting peak occurring at the same temperature (159.2°C for the mixture compared to 159.7°C for the pure drug). In fact, the values of ΔH_m for the β -lap and HP β -CD mixture remain constant at varying molar fractions of the drug, with approximately 100% of the drug in the crystalline form (Fig. 2B).

The enthalpy data for inclusion complexes formed with α and γ -CD is shown in Figure 2B. Similar to the HP β -CD \cdot drug complex, the values of ΔH_m decreased with decreasing molar fraction of the drug, with the β -lap \cdot γ -CD complex showing a larger decline in drug crystallinity than the β -lap \cdot α -CD complex. At a molar fraction of 20%, 50% of β -lap was in crystalline form in the β -lap \cdot α -CD complex, whereas there was no drug in the crystalline form in the β -lap \cdot γ -CD complex. Taken together, at the same molar fraction, the normalized enthalpy follows the order: HP β -CD $<$ γ -CD $<$ α -CD.

Solubility of β -Lap in PLGA Polymers

In order to gain insight into interactions between β -lap and the PLGA polymer, solid-state solubility studies were carried out using DSC. Figure 3A plotted the values of ΔH_m (J/g) as a function of β -lap loading percentage. The X-intercept, provided by the linear regression of the data, yields the solid-state solubility of β -lap in PLGA, which was 13%. It should be noted that the β -lap melting temperatures were lower than that of pure drug alone (data not shown). The dissolution behavior of β -lap within the PLGA helps to explain the

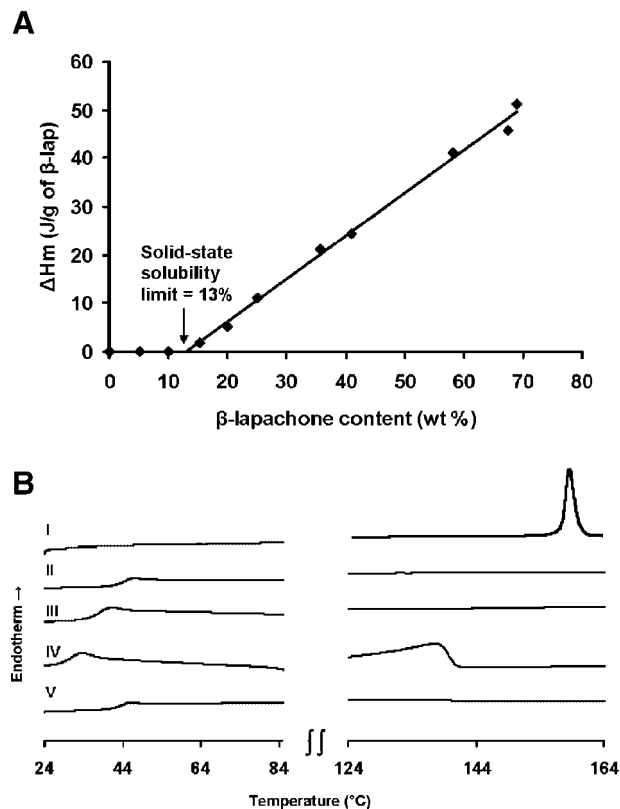


Figure 3. (A) β -Lap melting enthalpy (ΔH_m) as a function of β -lap loading percentage. The X-intercept indicates the solubility of β -lap in PLGA. (B) Effect of HP β -CD complexation on the β -lap interactions with PLGA matrix. Thermograms representing the following: (I) β -lap alone; (II) PLGA alone; (III) 10% β -lap in PLGA; (IV) 20% β -lap in PLGA; and (V) β -lap \cdot HP β -CD complex (5.7% β -lap, 34.3% HP β -CD) in PLGA.

change in thermal properties of the polymer, and more importantly, discrepancies in subsequent release studies.

DSC Characterization of β -Lap Interactions with PLGA Polymer

As previously described, the millirod fabrication process involves heat treatment in order to allow for polymer annealing. This process may lead to interactions between drug and various components of the millirod, specifically between the polymer and the drug. To determine these interactions, the millirod preparation process was mimicked and DSC analyses conducted.

The PLGA polymer has a glass transition temperature of 44°C,¹⁹ observed in thermogram II in Figure 3B. However, when 10% β -lap was

physically mixed with PLGA, the T_g of the polymer decreased to 35.4°C (III). A further decrease in glass transition occurred when drug loading was increased to 20%, yielding a T_g of 31.7°C (IV). Since a β -lap loading of 20% surpassed the solid-state solubility limit in PLGA, the drug melting peak shifted to a lower temperature ($T_m = 138^\circ\text{C}$) as observed in the endotherm. When β -lap (5.7%) was complexed with HP β -CD (34.3%), the T_g of the PLGA was not affected as shown in thermogram V, in which the glass transition of the polymer was approximately 44°C .

β -Lap Release from Polymer Millirods

Figure 4 illustrates the effect of formation of inclusion complexes on β -lap release kinetics from PLGA millirods. First, release of free β -lap from PLGA millirods was extremely slow, with only $8.8 \pm 1.2\%$ of the drug released after 22 days (Fig. 4A). When an excipient molecule, such as glucose, was added to the polymer millirod, the release of drug was faster, but the amount released was not dramatically increased ($37.0 \pm 2.0\%$ after 22 days). Significant facilitation of β -lap release was observed when the drug was either physically mixed or complexed with HP β -CD. Approximately $55 \pm 2.2\%$ of the drug was released after 2 days when HP β -CD was included in the millirod as an excipient molecule (Fig. 4A). In comparison, when β -lap was complexed with HP β -CD, $79.6 \pm 2.1\%$ of the drug was released after the first 2 days, yielding the fastest release among the different formulations. Figure 4B highlights the difference in average release rates among the different millirod formulations. In the first two time periods, the average β -lap release rate was significantly faster for millirods containing β -lap complexed with HP β -CD, with the release rate decreasing during the 12–48 h time period. Average release rates from millirods composed of β -lap mixed with HP β -CD, as well as from millirods containing glucose as an excipient, remained fairly constant throughout the time periods, demonstrating a more sustained pattern of release. The release rate of millirods with drug alone was minimal throughout the time periods, reflecting the slow release of β -lap from these millirods.

β -Lap complexation with different CDs leads to modulated differences in drug release kinetics (Fig. 5). While all the release profiles showed a noticeable improvement over free β -lap (Fig. 5A), α -CD provides the slowest release rates among all

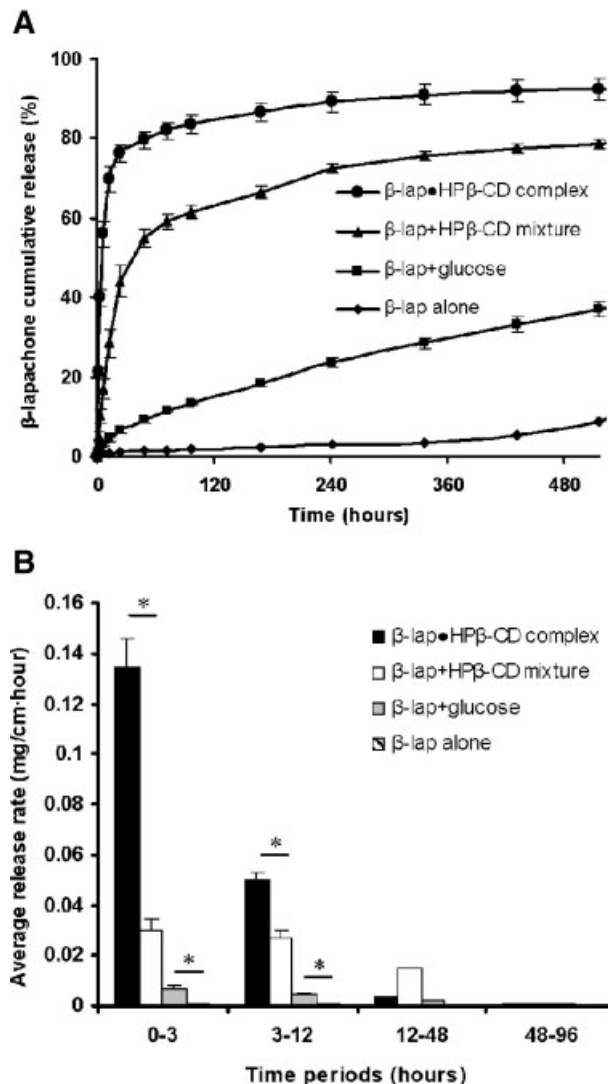


Figure 4. (A) Cumulative release of β -lap from millirods that contained β -lap (1.2%) either complexed or physically mixed with HP β -CD, and in the absence or presence of glucose. (B) Average release rates of β -lap from the millirods in (A) during various time periods. Error bars were calculated from triplicate samples. Statistical analysis between groups was performed using a Student's two-tailed t -test ($*p < 0.05$).

the CDs. After 22 days, $66 \pm 4.6\%$ of the drug was released, which was less than the amount of drug released ($\sim 90\%$ after 22 days) when β -lap was complexed with γ -, β -, or HP β -CD. Figure 5B compares average drug release rates during different initial time periods. β -Lap complexed with HP β -CD demonstrated the fastest release rate in the first 3 h. When β -lap was complexed with β -CD, drug release lacked the initial high burst with approximately half the release rate in

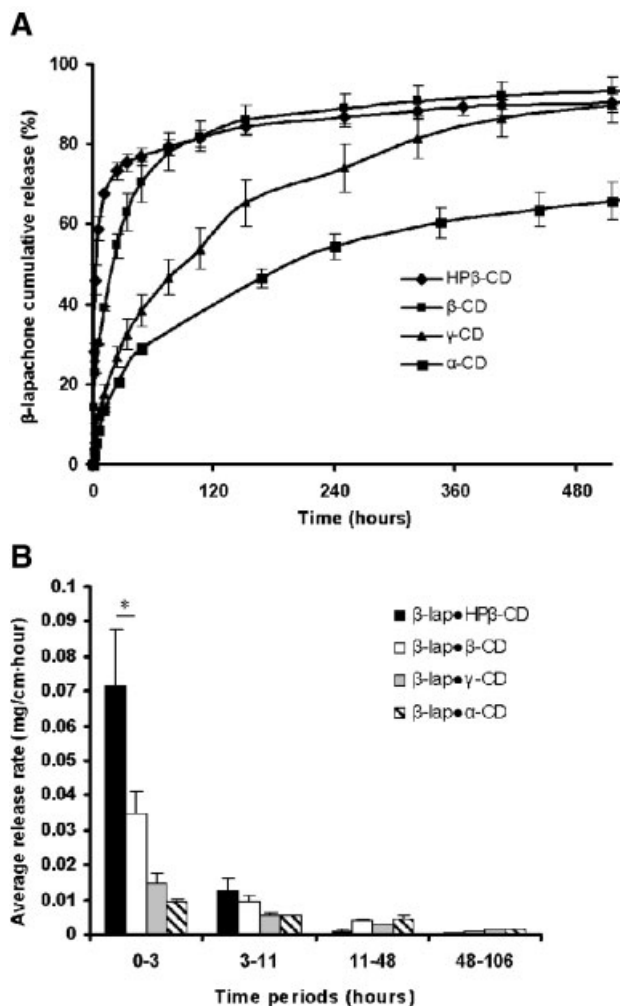


Figure 5. (A) Cumulative release of β -lap from millirods when the drug (1.8%) was complexed with different types of CDs at the same CD loading density (38.8%). (B) Average release rates of β -lap during various time periods. Error bars were calculated from triplicate samples. Statistical analysis between groups was performed using a Student's two-tailed *t*-test (**p* < 0.05).

the initial 0–3 h-period. The release kinetics from β -lap \cdot γ -CD millirods was much more sustained ($38.8 \pm 4.0\%$ of the β -lap released after 48 h) than in the previous examples.

Morphology Studies of Millirods before and after β -Lap Release

In an effort to examine the disparity in β -lap release from different millirod formulations as shown in Figure 4, SEM images were obtained from millirods that were incubated in PBS for 12 h. Following incubation in PBS, the cross-

sectional morphology of a millirod containing β -lap alone appeared very smooth (Fig. 6A). In contrast, when β -lap was complexed with HP β -CD and incubated for 12 h, there was a significant formation of pores in the millirod microstructure (Fig. 6B), a result akin to millirods containing noncomplexed β -lap, glucose, and PLGA (Fig. 6C). As observed from these figures, the latter two millirod formulations were both morphologically similar, with comparable porosity in the PLGA matrix.

DISCUSSION

Solid-State Inclusion Complex Formation Highlights Differences in Complexation Efficiency among CDs

Inclusion complexes of β -lap and four CDs (α -CD, β -CD, γ -CD, and HP β -CD) in aqueous solution were investigated previously by our laboratory. In the previous report, we demonstrated the formation of a 1:1 inclusion complexes through hydrophobic binding of the dimethyl moiety of β -lap inside the CD cavity.¹² More importantly, an enhanced water solubility of β -lap (16 mg/mL as compared to 0.04 mg/mL) was observed following HP β -CD complexation. In order to incorporate these complexes into PLGA millirods, it was necessary to form solid-state inclusion complexes of the drug with CD. In the present study, we demonstrated that β -lap and CD physical mixtures showed almost no interaction, as evidenced by the presence of a drug melting peak and near 100% crystallinity of drug (Fig. 2B), even at high molar fractions of CD. Upon formation of a solid-state complex, a decreased drug melting peak appeared, indicating a decline in melting enthalpy and loss of β -lap in its crystalline phase. This phenomenon was apparent at 67% and 50% molar fractions of β -lap (Fig. 2A). Moreover, at lower molar fractions of β -lap (33%), the drug's melting peak disappeared altogether, indicating inclusion of the drug within the CD cavity and formation of the complex. These data agreed well with previously published reports by Manosroi et al.²⁰ and Jug et al.,²¹ in which the absence of melting endothermic peaks of azelaic acid and piroxicam, respectively, indicated the incorporation of these agents within the HP β -CD cavity.

From the DSC data, a significant difference in solid-state binding affinities with β -lap was demonstrated by different CDs. These differences in interactions observed between β -lap and the

distinct CDs were previously observed,¹² and are due primarily to the cavity size of the CD. β -Lap has a low binding affinity to α -CD mainly because the drug molecule cannot fit in the small hydrophobic cavity (diameter ~ 5 Å). Increased binding affinities are observed in β - and γ -CDs because of their larger cavity size (diameter ~ 6.25 Å and 7.9 Å, respectively). HP β -CD and β -CD are better hosts than γ -CD for β -lap because their cavity size is small enough to allow for intramolecular bonding, which in turn endows the CDs with more rigidity (i.e., a more suitable host environment). γ -CD, on the other hand, has a larger cavity size and is more flexible, and binding of β -lap inside the hydrophobic cavity leads to decreased solubility of the inclusion complex.¹² In summary, HP β -CD and β -CD had a higher efficiency of forming a complex with β -lap, followed by γ -CD, which in turn was superior to α -CD.

β -Lap Complexation with CDs Led to Modulation of Release Kinetics

DSC analysis showed that β -lap had a solid-state solubility of 13% in PLGA matrix (Fig. 3A). Below this limit, β -lap forms a homogeneous molecular-level mixture inside the PLGA matrix. For β -lap and many other hydrophobic drugs, this formulation from a binary mixture typically leads to extremely slow drug release kinetics due to limited water penetration into the hydrophobic millirod (as corroborated by the limited porosity observed by SEM analyses in Figure 6A), favorable drug/polymer interactions, and low aqueous solubility of the drug (therefore a small concentration gradient across the polymer/solution interface). The above factors provide a reasonable explanation for the slow release of β -lap from PLGA millirods, where only $8.8 \pm 1.2\%$ of drug was released after 22 days.

Pore-forming hydrophilic molecules (e.g., glucose, NaCl) have been frequently used to facilitate drug release from polymer depot.^{22,23} In this study, water dissolution of glucose led to an increase in porosity inside the PLGA matrix as evidenced by SEM analysis (Fig. 6C). Increased porosity effectively enlarged the aqueous contact surface area for β -lap release from the PLGA matrix, leading to faster release kinetics over the β -lap-loaded millirods without glucose. In spite of this increased porosity, favorable hydrophobic interactions between β -lap and PLGA matrix as well as the low water solubility of β -lap are still limiting factors for a facile drug release, where only

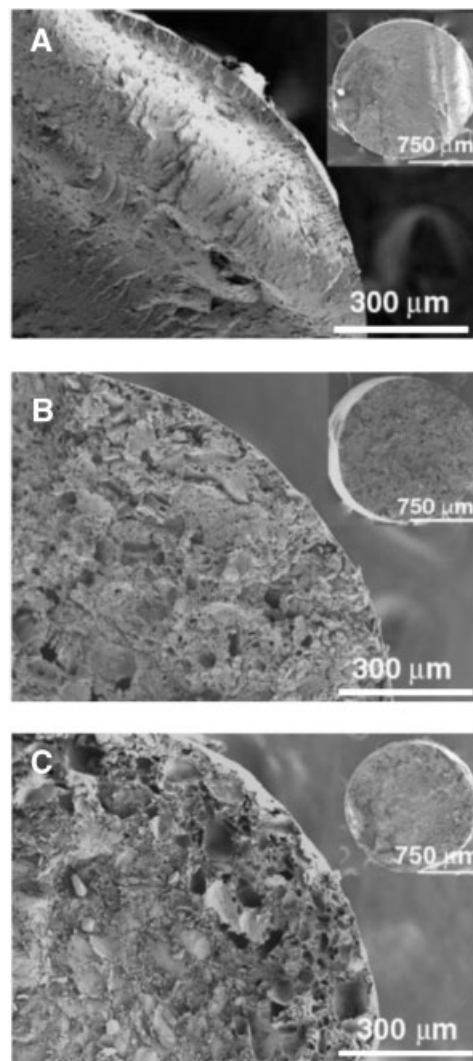


Figure 6. SEM analyses of microstructures of β -lap-loaded polymer millirods following 12 h incubation in PBS. Cross sections represent the following (A) β -lap alone (1.2% β -lap in 98.8% PLGA); (B) β -lap \cdot HP β -CD complex (1.2% β -lap, 38.8% HP β -CD, 60% PLGA); (C) 40% glucose excipient (1.2% β -lap, 38.8% glucose, 60% PLGA). Figure insets represent SEM micrographs of the entire cross section of the millirod.

$37.0 \pm 2.0\%$ of β -lap was released after 22 days. The remainder of the drug was released when the PLGA matrix was clearly degraded (data not shown), leading to a “dose dumping” of drugs that is frequently observed with polyester-based drug delivery systems.^{24–26}

Drug complexation with different CD molecules provides a useful strategy to control the release kinetics of hydrophobic drugs from a polymer depot. The faster release of the drug from

β -lap · HP β -CD millirods can best be explained by a combination of factors. Due to the lack of interactions with the PLGA, the hydrophilic CD readily dissolves in aqueous environments given its solubility of 500 mg/mL.¹² After rapid release from the millirod, the CD leaves behind pores in the matrix, which facilitates water permeation into the PLGA matrix. This increased water permeation into the millirod results in a more rapid release of β -lap from the β -lap · HP β -CD mixture millirods due to the increased porosity of the matrix. In addition to pore formation and rapid release of CD, instant *in situ* formation of drug inclusion complexes with the CD increases the water solubility of β -lap, enhancing drug release from millirods containing a mixture of β -lap and HP β -CD. This release rate is much faster than that from glucose-loaded millirods despite their similar matrix morphology. However, the fastest release is seen in millirods containing drug that is complexed with HP β -CD, due to rapid dissolution and the prevention of the formation of a molecular-level mixture between the drug and PLGA, as previously demonstrated by DSC. This solid-state solubilization of free β -lap in PLGA would otherwise hinder the drug from diffusing out of the hydrophobic environment provided by the PLGA microstructure. Panyam et al.¹⁸ showed that dexamethasone was soluble in PLGA nanoparticles, which in turn increased drug encapsulation but decreased release kinetics. Previous studies by Miyajima et al.²⁷ also showed that basic drugs interacted with PLGA by shielding the carboxyl residues of the matrix, making the millirod more rigid and less hydrophilic, affecting both polymer erosion and drug diffusion. Therefore, the rapid solubilization and diffusion of the β -lap · HP β -CD complex, as well as the absence of drug interaction with PLGA, leads to a faster release of β -lap from millirods.

It is important to note that the rate of drug release was also determined by CD complexation efficiency and the solubility of the CD. The fastest release occurred when the drug was complexed with HP β -CD, while the slowest release occurred when β -lap was complexed with α -CD, which had the lowest binding affinity with the drug. The lower drug release rate resulting from the β -CD formulation compared to the HP β -CD formulation stems primarily from its considerably lower water solubility (18 mg/mL for β -CD vs. 500 mg/mL for HP β -CD). The slower drug release kinetics observed in the γ -CD formulation is most likely caused by its lower binding constant ($\sim 160/M$),

which may lead to an increase in the molar fraction of the drug “dissolved” in the polymer matrix.

A more comprehensive understanding of the different kinetic processes during drug release is necessary to rationally design optimal millirod formulations with controllable release kinetics. Key factors may include distribution of drug among different states (e.g., “dissolution” state within PLGA matrix, complexed state with CDs, or crystalline state), drug binding constants with different types of CDs, solubility and diffusivity of drug · CD complexes, dissolution kinetics of drug and drug · CD complexes, pore formation, and water permeation rates inside the polymer. This is clearly a complex system and a mathematical model that incorporates the aforementioned processes is currently under development in order to provide a quantitative understanding of the drug release behavior from the polymer implant system.

Implications for Intratumoral Drug Delivery

The long-term goal of this research is to design β -lap-loaded polymer millirods with optimal release rates of β -lap for intratumoral drug delivery applications. Based on the results from this study, we found that an effective modulation of β -lap release rates was achieved through complexation with different CDs. For therapeutic applications where an initial “burst” release is desirable, a millirod formulation with β -lap · HP β -CD complex can be implemented to provide a maximal drug release rate in the first 3 h (Figs. 4B and 5B). In contrast, to examine the influence of prolonged drug release on therapeutic efficacy, the use of other CD molecules (e.g., γ -CD or α -CD) can provide a more moderate, sustained release of drug. In addition to their abilities in modulating drug release kinetics, CD complexation may also prove advantageous in that they it may facilitate drug penetration inside tumor tissues. A high initial drug concentration will bring about tumor cell apoptosis more rapidly, reducing the cell density and increasing subsequent drug distribution.²⁸ Additionally, β -lap is a small and hydrophobic molecule such as carmustine (BCNU) that can be easily eliminated by blood perfusion through capillaries in solid tumors.²⁹ A stable inclusion complex with a hydrophilic excipient, such as CD, may prevent this loss through an increase in molecular weight.²⁹ This would lead to longer retention times in the tumor and longer penetration distances. Current work is in

progress to evaluate the antitumor efficacy of PLGA millirods with different β -lap-CD complexes in solid tumors.

ACKNOWLEDGMENTS

This work was supported by NIH grant CA90696 to JG and DOD grant W81XWH-04-1-0164 to DAB. EB is grateful for the support of a National Institutes of Health minority supplement grant. This is report 002 from the Program in Cell Stress and Cancer Nanomedicine at UT Southwestern Medical Center at Dallas.

REFERENCES

1. LaVan DA, McGuire T, Langer R. 2003. Small-scale systems for in vivo drug delivery. *Nat Biotechnol* 21:1184–1191.
2. Qian F, Szymanski A, Gao J. 2001. Fabrication and characterization of controlled release poly(D, L-lactide-co-glycolide) millirods. *J Biomed Mater Res* 55:512–522.
3. Qian F, Nasongkla N, Gao J. 2002. Membrane-encased polymer millirods for sustained release of 5-fluorouracil. *J Biomed Mater Res* 61:203–211.
4. Qian F, Saidel GM, Sutton DM, Exner A, Gao J. 2002. Combined modeling and experimental approach for the development of dual-release polymer millirods. *J Control Release* 83:427–435.
5. Weinberg B, Ai H, Blanco E, Anderson J, Gao J. Antitumor efficacy and local pharmacokinetics of doxorubicin via intratumoral delivery from polymer millirods. *J Biomed Mater Res In Press*.
6. Blanco E, Weinberg BD, Stowe NT, Anderson JM, Gao J. 2006. Local release of dexamethasone from polymer millirods effectively prevents fibrosis after radiofrequency ablation. *J Biomed Mater Res A* 76:174–182.
7. Ough M, Lewis A, Bey EA, Gao J, Ritchie JM, Bornmann W, Boothman DA, Oberley LW, Cullen JJ. 2005. Efficacy of beta-lapachone in pancreatic cancer treatment: Exploiting the novel, therapeutic target NQO1. *Cancer Biol Ther* 4:95–102.
8. Pink JJ, Planchon SM, Tagliarino C, Varnes ME, Siegel D, Boothman DA. 2000. NAD(P)H:Quinone oxidoreductase activity is the principal determinant of beta-lapachone cytotoxicity. *J Biol Chem* 275:5416–5424.
9. Siegel D, Ross D. 2000. Immunodetection of NAD(P)H:quinone oxidoreductase 1 (NQO1) in human tissues. *Free Radic Biol Med* 29:246–253.
10. Planchon SM, Wuerzberger S, Frydman B, Witiak DT, Hutson P, Church DR, Wilding G, Boothman DA. 1995. Beta-lapachone-mediated apoptosis in human promyelocytic leukemia (HL-60) and human prostate cancer cells: A p53-independent response. *Cancer Res* 55:3706–3711.
11. Tagliarino C, Pink JJ, Reinicke KE, Simmers SM, Wuerzberger-Davis SM, Boothman DA. 2003. Mu-calpain activation in beta-lapachone-mediated apoptosis. *Cancer Biol Ther* 2:141–152.
12. Nasongkla N, Wiedmann AF, Bruening A, Beman M, Ray D, Bornmann WG, Boothman DA, Gao J. 2003. Enhancement of solubility and bioavailability of beta-lapachone using cyclodextrin inclusion complexes. *Pharm Res* 20:1626–1633.
13. Li P, Zhao L, Yalkowsky SH. 1999. Combined effect of cosolvent and cyclodextrin on solubilization of nonpolar drugs. *J Pharm Sci* 88:1107–1111.
14. Rao VM, Stella VJ. 2003. When can cyclodextrins be considered for solubilization purposes? *J Pharm Sci* 92:927–932.
15. Loftsson T. 2002. Cyclodextrins and the biopharmaceutics classification system of drugs. *J Incl Phenom Macro* 44:63–67.
16. Szejtli J. 1998. Introduction and general overview of cyclodextrin chemistry. *Chem Rev* 98:1743–1754.
17. Singh M, Sharma R, Banerjee UC. 2002. Biotechnological applications of cyclodextrins. *Biotechnol Adv* 20:341–359.
18. Panyam J, Williams D, Dash A, Leslie-Pelecky D, Labhasetwar V. 2004. Solid-state solubility influences encapsulation and release of hydrophobic drugs from PLGA/PLA nanoparticles. *J Pharm Sci* 93:1804–1814.
19. Saltzman W. 2001. Drug delivery: Engineering principles for drug therapy. New York: Oxford University Press. p 337.
20. Manosroi J, Apriyani MG, Foe K, Manosroi A. 2005. Enhancement of the release of azelaic acid through the synthetic membranes by inclusion complex formation with hydroxypropyl-beta-cyclodextrin. *Int J Pharm* 293:235–240.
21. Jug M, Becirevic-Lacan M. 2004. Influence of hydroxypropyl-beta-cyclodextrin complexation on piroxicam release from buccoadhesive tablets. *Eur J Pharm Sci* 21:251–260.
22. Qian F, Stowe N, Liu EH, Saidel GM, Gao J. 2003. Quantification of in vivo doxorubicin transport from PLGA millirods in thermoablated rat livers. *J Control Release* 91:157–166.
23. Szymanski-Exner A, Stowe NT, Salem K, Lazebnik R, Haaga JR, Wilson DL, Gao J. 2003. Noninvasive monitoring of local drug release using X-ray computed tomography: Optimization and in vitro/in vivo validation. *J Pharm Sci* 92:289–296.
24. Huang X, Brazel CS. 2001. On the importance and mechanisms of burst release in matrix-controlled drug delivery systems. *J Control Release* 73:121–136.

25. von Burkersroda F, Schedl L, Gopferich A. 2002. Why degradable polymers undergo surface erosion or bulk erosion. *Biomaterials* 23:4221–4231.
26. Wang F, Lee T, Wang CH. 2002. PEG modulated release of etanidazole from implantable PLGA/PDLA discs. *Biomaterials* 23:3555–3566.
27. Miyajima M, Koshika A, Okada J, Kusai A, Ikeda M. 1998. The effects of drug physico-chemical properties on release from copoly (lactic/glycolic acid) matrix. *Int J Pharm* 169:255–263.
28. Jang SH, Wientjes MG, Au JL. 2001. Enhancement of paclitaxel delivery to solid tumors by apoptosis-inducing pretreatment: Effect of treatment schedule. *J Pharmacol Exp Ther* 296:1035–1042.
29. Strasser JF, Fung LK, Eller S, Grossman SA, Saltzman WM. 1995. Distribution of 1,3-bis(2-chloroethyl)-1-nitrosourea and tracers in the rabbit brain after interstitial delivery by biodegradable polymer implants. *J Pharmacol Exp Ther* 275:1647–1655.

Local release of dexamethasone from polymer millirods effectively prevents fibrosis after radiofrequency ablation

Elvin Blanco,^{1*} Brent D. Weinberg,¹ Nicholas T. Stowe,² James M. Anderson,³ Jinming Gao^{1*}

¹Department of Biomedical Engineering, Case Western Reserve University, Cleveland, Ohio 44106

²Department of Surgery, Case Western Reserve University School of Medicine, Cleveland, Ohio 44106

³Institute of Pathology, Case Western Reserve University School of Medicine, Cleveland, Ohio 44106

Received 13 June 2005; accepted 20 June 2005

Published online 1 November 2005 in Wiley InterScience (www.interscience.wiley.com). DOI: 10.1002/jbm.a.30516

Abstract: Recent studies show that after radiofrequency (RF) ablation, fibrosis occurs at the ablation boundary, hindering anticancer drug transport from a locally implanted polymer depot to the ablation margin, where tumors recur. The purpose of this study is to investigate strategies that can effectively deliver dexamethasone (DEX), an anti-inflammatory agent, to prevent fibrosis. Polymer millirods consisting of poly(D,L-lactide-co-glycolide) (PLGA) were loaded with either DEX complexed with hydroxypropyl β -cyclodextrin (HP β -CD), or an NaCl and DEX mixture. *In vitro* release studies show that DEX complexed with HP β -CD released 95% of the drug after 4 days, compared to 14% from millirods containing NaCl and DEX. Rat livers underwent RF ablation and received either DEX-HP β -CD-loaded millirods,

PLGA millirods with an intraperitoneal (i.p.) DEX injection, or control PLGA millirods alone. After 8 days *in vivo*, heightened inflammation and the appearance of a well-defined fibrous capsule can be observed in both the control experiments and those receiving a DEX injection (0.29 ± 0.08 and 0.26 ± 0.07 mm in thickness, respectively), with minimal inflammation and fibrosis present in livers receiving DEX millirods (0.04 ± 0.01 mm). Results from this study show that local release of DEX prevents fibrosis more effectively than a systemic i.p. injection. © 2005 Wiley Periodicals, Inc. *J Biomed Mater Res* 76A: 174–182, 2006

Key words: dexamethasone; fibrous capsule formation; inflammation; polymer implant; radiofrequency ablation

INTRODUCTION

Presently, an immense amount of research efforts have been devoted to the development of minimally invasive strategies for the treatment of liver cancers. Chief among the techniques is radiofrequency (RF) ablation, which consists of applying a high-frequency alternating current, that results in tissue destruction by frictional heat.¹ The potential benefits of RF ablation are easily appreciated: complete destruction of the tumor within the ablation radius, short recovery times, and minimal morbidity to the patient. How-

ever, local tumor recurrence at the outer periphery of ablation limits its widespread clinical application.^{2–4} Hence, many research laboratories have suggested using RF ablation in a multimodality approach for the treatment of tumors, combining the strategy with alternative remedial options such as the systemic delivery of chemotherapeutic drugs⁵ and radiotherapy.⁶

In lieu of the above strategies, our laboratory has proposed a combination therapy involving RF ablation and the local delivery of a chemotherapeutic agent. Briefly, the combined strategy involves using RF ablation to destroy the tumor by heat, followed by the implantation of a doxorubicin-loaded polymer millirod at the site of ablation to eliminate residual malignant cells. In our laboratory, research has been carried out in the fabrication and mechanical characterization of drug-loaded polymer millirods,⁷ modulation of release characteristics of doxorubicin from the millirods,⁸ and study of doxorubicin distribution in liver tissue after RF ablation and subsequent millirod implantation.⁹ Previous research by our laboratory has also shown that postablated liver is time variant and that the inflammatory response caused by tissue charring is significant. The result is the forma-

*Present address: Simmons Comprehensive Cancer Center, University of Texas Southwestern Medical Center at Dallas, Dallas, TX 75390-8590

Correspondence to: J. Gao; e-mail: jinming.gao@utsouthwestern.edu

Contract grant sponsor: National Institutes of Health; contract grant numbers: R01-CA-90696 and T32 GM07250

Contract grant sponsor: Case Western Reserve University Medical Scientist Training Program

Contract grant sponsor: DOD predoctoral fellowship; contract grant number: BC043453

tion of a thick, well-defined fibrous capsule at the boundary of ablation.¹⁰

The appearance of a fibrous capsule is widely regarded as favorable and crucial in the walling off of an injurious site during the wound-healing process. However, fibrosis also poses a significant barrier to molecular transport, limiting the clinical acceptance of several implantable biomedical applications. Drug transport hindrance results from the avascularity of the tightly packed collagenous matrix, as well as from the lower diffusion coefficient through the fibrous capsule, arising from the decrease in fluid volume and increase in tortuosity.¹¹ Altogether, drug released from a polymer depot will reach the tissue immediately beyond the fibrous capsule only in small quantities, because most of the drug will be encapsulated within the implant site.

The local release of dexamethasone (DEX), a potent and synthetic anti-inflammatory glucocorticoid, is being investigated in attempts to prevent fibrosis surrounding devices such as implantable glucose sensors¹² and pacemaker leads.¹³ Although several mechanisms are involved in the down-regulation of inflammation after glucocorticoid administration, it is known that DEX blocks the production and secretion of various chemokines, diminishes the release of inflammatory cells to injured sites, and suppresses fibroblast proliferation, ultimately leading to reduced fibrosis.¹⁴ Although the anti-inflammatory advantages of DEX prove appealing, DEX is highly water-insoluble, which proves inconvenient in controlled release applications. Currently, DEX can be complexed with cyclodextrins, which are cyclic oligosaccharides in the form of truncated cones consisting of a hydrophobic core and a hydrophilic outer surface.^{15,16} Cyclodextrins have the ability to entrap drug molecules within the hydrophobic core, thereby increasing water solubility and bioavailability of the drug, which in turn can allow for the potentiation of the anti-inflammatory effects of DEX.

The objective of this study is to prevent fibrosis resulting from RF ablation through DEX administration. Millirods composed of poly(D,L-lactide-co-glycolide (PLGA) and containing either sodium chloride and DEX or DEX complexed with HP β -CD, were tested *in vitro* to determine release characteristics. Subsequently, millirods containing DEX complexed with HP β -CD were examined in an *in vivo* rat model. We hypothesize that the local release of DEX from polymer millirods will effectively prevent fibrous capsule formation at the ablation boundary. To test this hypothesis, RF ablated rat livers received either PLGA control millirods, PLGA control millirods and an intraperitoneal (i.p.) injection of DEX, or a DEX-loaded millirod. Results from this study show that the local release of DEX is effective at preventing fibrous capsule formation after 8 days and more effective at preventing fibrosis than a systemic administration of the drug.

MATERIALS AND METHODS

Materials

PLGA (lactide/glycolide = 1:1; MW 50,000 Da; inherent viscosity 0.65 dL/g) was purchased from Birmingham Polymers, Inc. (Birmingham, AL). Hydroxypropyl β -cyclodextrin (HP β -CD) was purchased from Cyclodextrin Technologies Development, Inc. (CTD). DEX and DEX-cyclodextrin complex (DEX-HP β -CD, 70 mg DEX per gram of complex) were purchased from Sigma (St. Louis, MO). Phosphate-buffered saline (PBS; pH 7.4) was purchased from Fisher Scientific (Pittsburgh, PA).

Polymer millirod fabrication and *in vitro* release characterization

Polymer millirods were fabricated by using a previously established compression-heat molding procedure.⁷ To summarize, millirod components were weighed separately, placed in a mortar, and well mixed by using a pestle. The contents were inserted into a Teflon tube (1.6 mm I.D.) within a stainless steel mold. The mold was then placed in an oven (Fisher Model 282A) at 90°C for 2 h with a compression pressure of 4.6 MPa. The resulting cylindrical polymer millirod, with a diameter of 1.6 mm, was cut to a length of 8 mm. Millirod Formulation 1 consisted of 24% DEX-HP β -CD complex (1.7% DEX), 16% HP β -CD, and 60% PLGA. Formulation 2 consisted of 1.7% DEX, 38.3% NaCl, and 60% PLGA, and control millirods consisted of 100% PLGA.

To characterize the *in vitro* release of DEX-loaded polymer millirods, millirods ($n = 3$) were placed in a glass scintillation vial that contained 5 mL of PBS at 37°C. A separate study of DEX release from Formulation 2 millirods was conducted in PBS solution containing 1% HP β -CD. Sample vials were placed in an orbital shaker (C24 model, New Brunswick Scientific) with a rotating speed of 100 rpm. At various time points, the millirod was removed from the solution and placed into a new scintillation vial containing 5 mL of fresh buffer at 37°C. The concentration of released DEX was measured by using a UV-Vis spectrophotometer (Perkin-Elmer Lambda 20 model) at the maximum adsorption wavelength of the drug ($\lambda_{\max} = 242$ nm). The percentage of cumulative DEX released was obtained by normalizing the released amount to the total amount loaded in the millirods.

Scanning electron microscopy analysis of millirod microstructure

Scanning electron microscopy (SEM) was used to characterize the morphology of DEX-loaded polymer millirods. Millirods were placed in 5 mL of PBS buffer at 37°C for 24 h, after which they were freeze-dried overnight. The millirods were then cut into two parts for both lateral and cross-sectional analysis. A thin film of palladium (Pd; ca. 2 nm in thickness) was sputter-coated to minimize electron charging on the sample surface. A voltage of 5 kV was used during

sample examination with a Hitachi S-4500 scanning electron microscope (Hitachi, Ltd., Japan).

RF ablation of rat livers and millirod implantation

Animal procedures adhered to the National Institutes of Health (NIH) guidelines and followed an approved protocol by the Institutional Animal Care and Use Committee (IACUC) at Case Western Reserve University. Male Sprague-Dawley rats weighing approximately 300 g were anesthetized by using an i.p. injection of sodium pentobarbital. A small midline incision was made, through which the medial lobe of the liver was exposed for RF ablation and millirod implantation. Ablation was induced by using RF-generated current (0.09–0.12 A) from a 19-gauge needle electrode (Radionics®, Burlington, MA) at $90 \pm 2^\circ\text{C}$ for 2 min. After the electrode was removed, a millirod was inserted into the electrode tract.

The *in vivo* experiments consisted of three study groups ($n = 4$). The first group received control millirods composed completely of PLGA. The second group also received a control PLGA millirod, as well as a 1-mL i.p. injection of DEX-HP β -CD complex in saline (1.25 mg of DEX-HP β -CD/kg). The third group consisted of animals that received a DEX-releasing implant (Formulation 1).

Histological analysis of ablated livers

At 4- and 8-day time points, animals were sacrificed, livers were removed, and polymer millirods were retrieved. After the liver was sectioned, it was fixed in 10% formalin solution, embedded in paraffin, and sliced to a thickness of 5 μm . Samples were stained with hematoxylin and eosin (H&E) and Masson's trichrome (MTC) stains. The H&E stain provided for appreciation of cellular detail, whereas the MTC stain facilitated the examination of collagen fibers (stained blue) and overall fibrous capsule formation. Histological images were taken by using a Nikon Eclipse TE300 microscope with a SPOT RT Slider camera. Masson's trichrome stained samples ($n = 3$) were used in quantifying the thickness of the fibrous capsule, with measurements obtained by averaging from eight radial directions around the ablation boundary. Statistical analysis between groups consisted of two-tailed *t*-tests of unequal variances, with a significance level of 0.05.

RESULTS

In vitro release of DEX from polymer millirods

The *in vitro* release characteristics of DEX from polymer millirods of two different formulations are shown in Figure 1. In Formulation 1, the DEX is complexed with HP β -CD, whereas in Formulation 2, DEX is uncomplexed in the presence of a salt excipient. Both

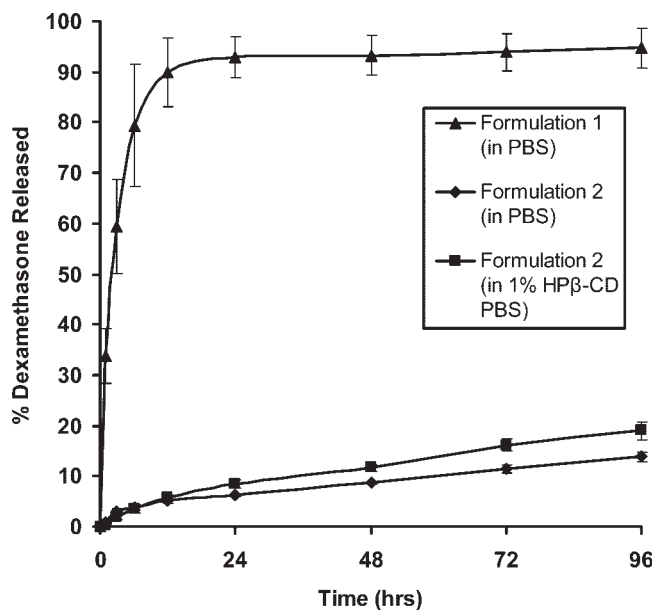


Figure 1. *In vitro* release profiles of DEX-loaded millirods of varying formulations. Formulation 1 is composed of 60% PLGA, 16% HP β -CD, and 24% DEX complexed with HP β -CD (1.7% total DEX). Formulation 2 is composed of 60% PLGA, 38.3% NaCl, and 1.7% uncomplexed DEX. The error bars were calculated from triplicate samples.

formulations contain the same loading percentage of DEX (1.7% or 0.5 mg per implant), with differences in release characteristics stemming from whether the DEX is complexed with cyclodextrin.

Data show that the release of DEX from polymer millirods pertaining to Formulation 1 is much faster than that from Formulation 2. After 6 h, approximately 80% DEX has been released when the drug is complexed with HP β -CD, whereas only 4% release was observed with millirods pertaining to Formulation 2 at the same time point. Four days into the release study, approximately 95% of the drug has been released from Formulation 1, whereas the percentage of cumulative release from Formulation 2 has only reached roughly 14%. To determine the solubilization effect of cyclodextrin on the release kinetics of dexamethasone, a release study was conducted in PBS containing 1% HP β -CD. Figure 1 shows that the release of DEX in PBS containing 1% HP β -CD is similar to that in regular PBS, with approximately 19% of the drug released after 96 h. Given the faster release of DEX from Formulation 1, millirods composed of 24% DEX-HP β -CD complex, 16% HP β -CD, and 60% PLGA were used in subsequent animal experiments.

SEM analyses of DEX-loaded millirods

To further examine the disparity in DEX release from two different formulations, SEM analyses were

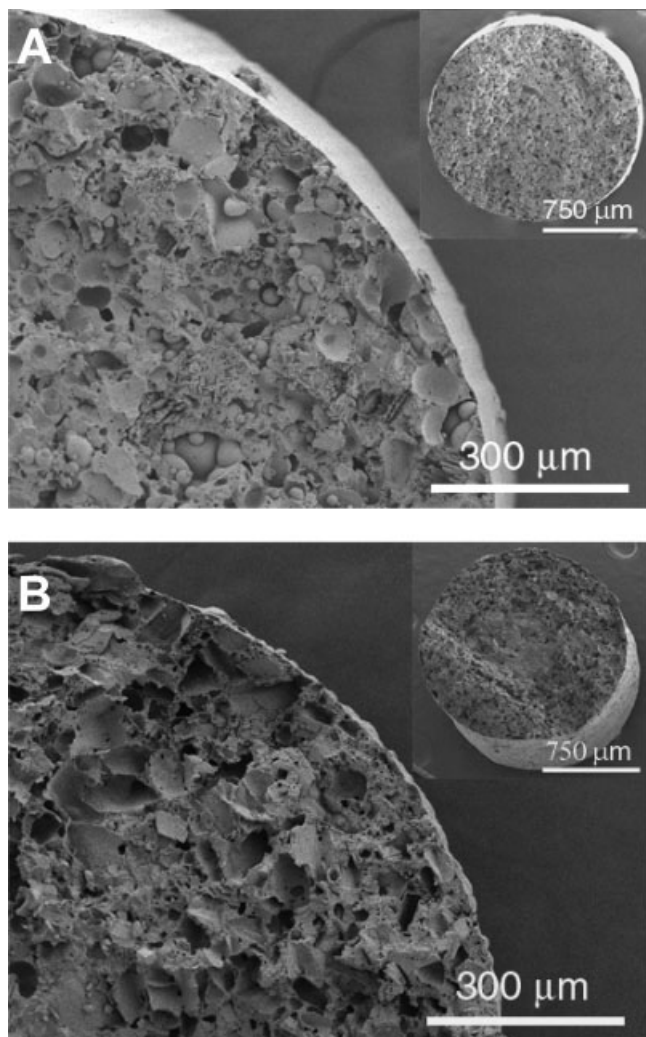


Figure 2. SEM analysis of polymer milliroad microstructure after 24-h immersion in PBS buffer. (A) A magnified image of the cross section of a milliroad pertaining to Formulation 1. (B) A cross-sectional magnification of a milliroad from Formulation 2. The insets in (A) and (B) represent low-magnification images of the cross sections of the respective milliroads.

performed on milliroads that had been immersed in PBS for 24 h. Figure 2(A,B) represents cross-sectional images of milliroad from Formulations 1 and 2, respectively. Closer examination reveals that the pores in Formulation 1 are spherical, whereas the pores in Formulation 2 are polyhedral, reflecting the original shapes of salt crystals within the polymer matrix. As can be observed from the figure insets, the two milliroad formulations are morphologically similar, with comparable porosity throughout the milliroad cross sections.

Fibrous capsule formation after RF ablation and milliroad implantation

Four days after RF ablation, the inflammatory response remains in its early stages, and although col-

lagen deposition exists at the ablation boundary, extensive fibrous capsule formation has not yet occurred. A thin layer of blue-staining collagen fibers is present to a moderate degree at the ablation boundary in livers receiving a PLGA control milliroad, heralding the initiation of fibrous capsule formation (data not shown). A similar pattern of collagen deposition can be observed in RF ablated livers that received a PLGA milliroad and an i.p. injection of DEX. Negligible amounts of collagen deposition were observed in liver samples that received DEX-loaded milliroad implants.

Eight days after RF ablation, one can observe the formation of a thick, well-defined fibrous capsule at the ablation boundary, easily discernible in Figure 3(A). A dense, collagen-rich layer exists at the ablation boundary separating the ablated and nonablated regions. The pattern of fibrous capsule formation in animals receiving a PLGA milliroad and an i.p. injection of DEX mimics that of the control experiments, and this is evident in Figure 3(B). As in the control experiment, there is a dense fibrous capsule present at the ablation boundary, evidenced by the substantial amount of blue-staining collagen fibers. These figures show that i.p. injected DEX has minimal effect on prevention of fibrosis. When liver samples undergo RF ablation and the implantation of a DEX-loaded milliroad, minimal fibrosis is present. As can be seen in Figure 3(C), only minute amounts of collagen fibers are present at the ablation boundary. A distinct boundary separates the ablated and nonablated regions.

Fibrous capsule thickness 4 and 8 days after ablation

Although histological examination of ablated liver samples provided for qualitative insight into the extent of fibrous capsule formation, a quantitative comparison displaying disparities in fibrosis among the experimental groups is shown in Figure 4. The similarity in fibrous capsule formation after 4 days between ablated livers receiving DEX as an injection and ablated livers receiving no DEX is further highlighted by the equivalent thickness measurements at the 4-day time point, with both groups containing a layer of fibrosis measuring 0.13 ± 0.01 mm. The quantitative measurement of fibrous capsule thickness in animal livers receiving DEX-loaded milliroads, 0.02 ± 0.01 mm, confirms the minimal fibrosis visible after 4 days. The calculated p -value ($p < 10^{-5}$) shows a statistical significance when comparing the DEX-loaded milliroad sample to the control sample.

Eight days after RF ablation and milliroad implantation, histological analysis shows the presence of a dense, well-formed fibrous capsule at the ablation

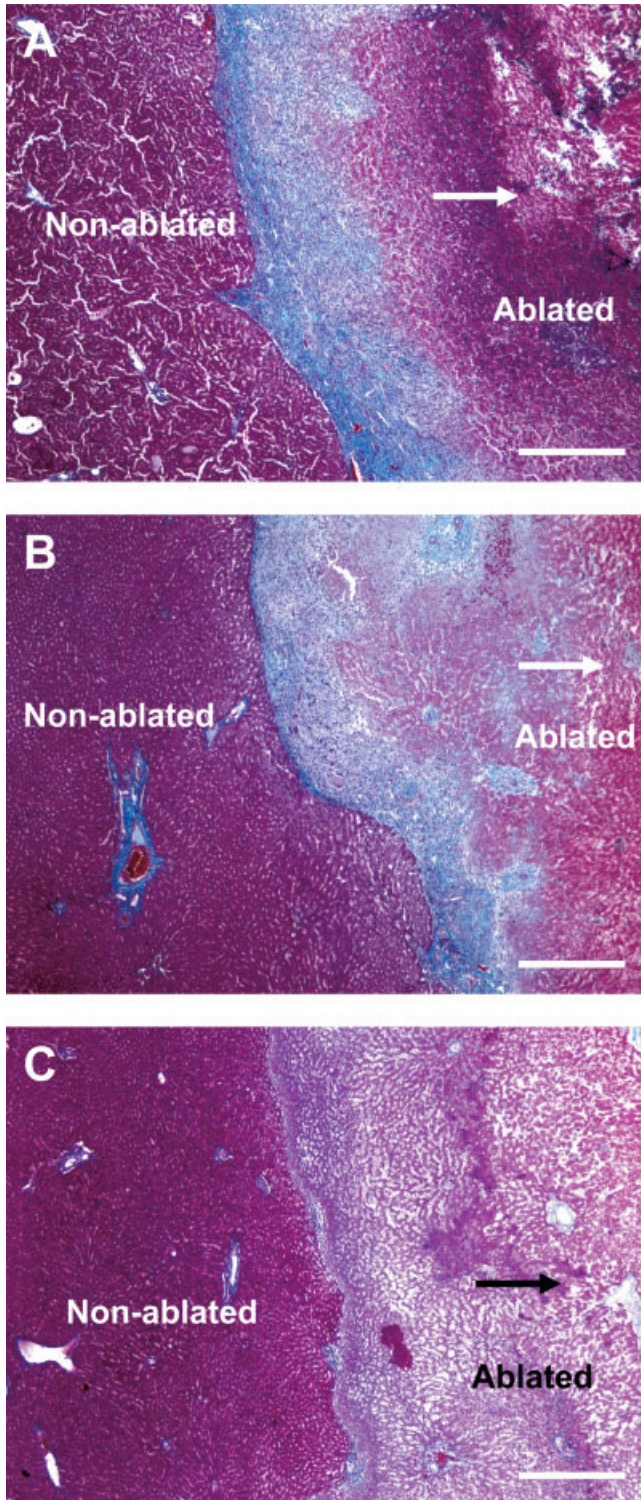


Figure 3. Histology images of liver samples 8 days after RF ablation and millirod implantation (all MTC stained; original magnification $\times 4$). (A) Postablated liver receiving a control PLGA millirod. (B) A sample that received a PLGA millirod and an i.p. injection of DEX. (C) Ablated liver that received a DEX-loaded millirod. The arrow points in the direction of the site of liver ablation/millirod implantation. The scale bars in the images = 0.5 mm. [Color figure can be viewed in the online issue, which is available at www.interscience.wiley.com.]

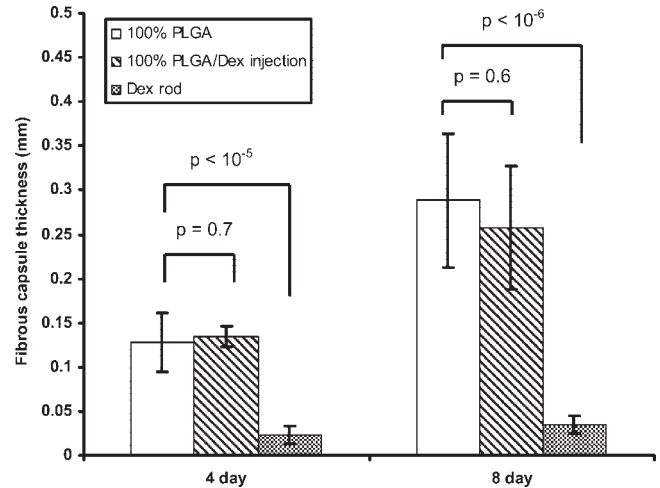


Figure 4. Measurements of fibrous capsule thickness in liver samples 4 and 8 days after RF ablation and millirod implantation in three different animal groups. The p -values are shown to highlight statistical differences between the groups.

boundary. In ablated liver samples receiving control millirods, extensive fibrosis measuring 0.29 ± 0.08 mm occurs after 8 days, which is twice the thickness measured at the 4-day time point. The average fibrous capsule thickness measurement in ablated livers receiving a PLGA millirod and an i.p. DEX injection was 0.26 ± 0.07 mm, further confirming the inefficacy of the DEX injection in preventing fibrosis. On the other hand, ablated liver samples receiving a DEX-loaded millirod had minimal collagen deposition and the absence of a fibrous capsule at the 8-day time point, with the average thickness measurement being 0.04 ± 0.01 mm. As in the 4-day time point, the p -value ($p < 10^{-6}$) shows statistical significance between control samples and livers receiving DEX-loaded millirods.

Inflammatory response at the ablation boundary after RF ablation

Fibrous capsule formation represents one of the most distinguishable characteristics of the inflammatory response, arising from processes such as leukocyte extravasation to the injured site and fibroblast migration. In an attempt to discern the prevalence of inflammatory processes that might give rise to fibrosis, H&E histology was compared for each of the animal groups at 4- and 8-day time points. The inflammatory response at the ablation boundary is in the acute phase 4 days after ablation, with most cells in the region consisting primarily of monocytes (data not shown). A similar inflammatory response was observed in RF-ablated liver samples that received an i.p. DEX injection. In sharp contrast to the acute inflam-

matory response observed in the previous animal groups, ablated livers receiving a DEX-loaded millirod showed no signs of inflammation.

By the 8-day time point, the inflammatory response has progressed and yielded the formation of a thick fibrous capsule. Now in the chronic inflammatory stage, a greater number of inflammatory cells, mainly macrophages, can be found at the ablation boundary¹⁷ [Fig. 5(A)]. Also apparent from the figure is the heightened number of fibroblasts, aligned circumferentially around the ablation tract, and the presence of new blood vessels, another hallmark of wound healing. Rat livers that received PLGA millirod implants and an i.p. injection of DEX show the same extent of inflammation as controls after 8 days, as evidenced by Figure 5(B). After DEX-loaded polymer millirod implantation, the inflammatory response at the ablation boundary is minimal after 8 days [Fig. 5(C)]. Negligible amounts of inflammatory cells and fibroblasts can be observed, explaining the lack of collagen deposition at this time point.

DISCUSSION

The objective of this study was to prevent fibrous capsule formation after RF ablation through the local release of DEX. Results from the study show that a site-specific, local release of DEX complexed with HP β -CD was effective in preventing fibrous capsule formation up to 8 days.

Complexing DEX with HP β -CD facilitates DEX delivery

The cascade of events leading to fibrous capsule formation occurs rapidly after the charring event produced by RF ablation. The rapidity of the inflammatory response warrants a fast release of DEX to counter the extravasation of neutrophils and monocytes to the site of injury, which would otherwise initiate fibroblast migration to the ablation boundary.¹² Results from this study show that DEX complexed with cyclodextrin (Formulation 1) releases much faster from polymer millirods than uncomplexed DEX (Formulation 2).

One potential explanation for the faster release of DEX from Formulation 1 could be the increased water solubility of the otherwise water-insoluble DEX when it complexes with HP β -CD. DEX has a solubility in water of 0.1 mg/mL,¹⁸ whereas DEX-HP β -CD has a solubility of 25 mg/mL, an elevated solubility that would create a higher concentration gradient for faster release. If the slow release of the drug is indeed a

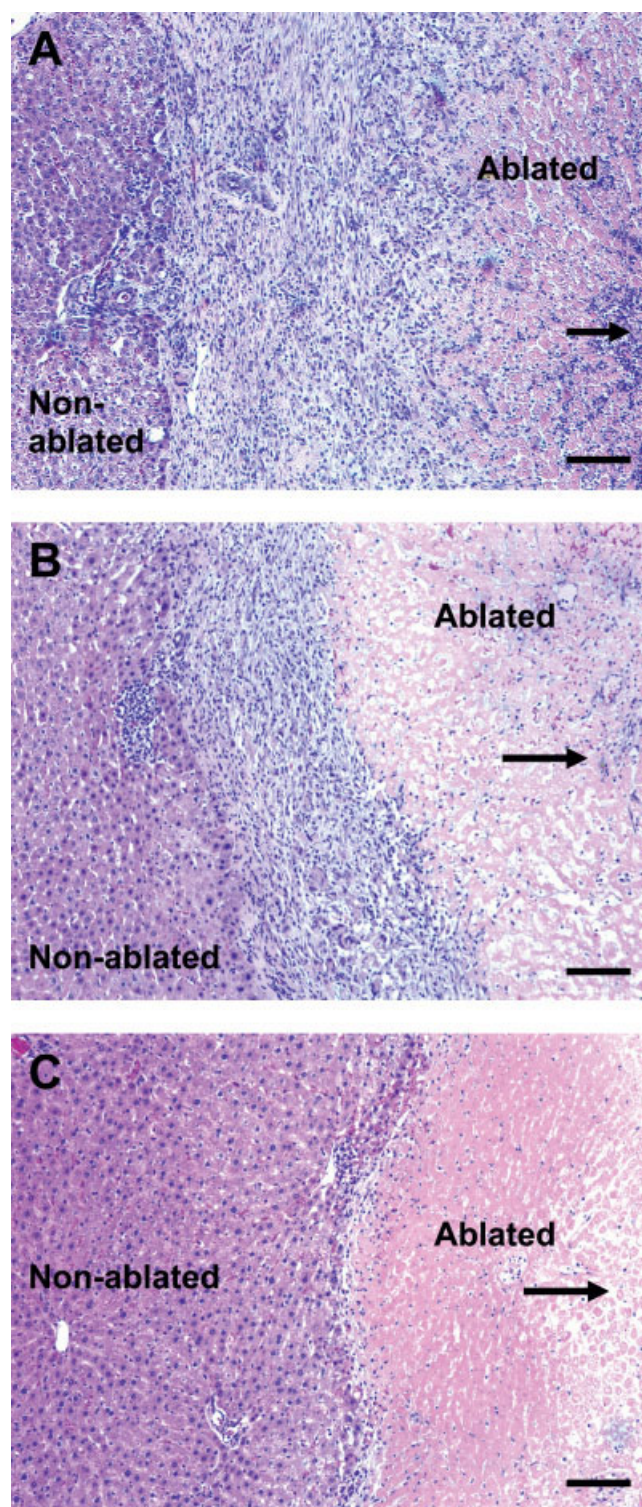


Figure 5. Histological representation of liver samples 8 days after RF ablation and millirod implantation (all H&E stained; original magnification $\times 10$). (A) A control liver sample receiving a PLGA millirod. (B) A sample that received a PLGA millirod and an i.p. injection of DEX. (C) Ablated liver that received a DEX-loaded millirod. The arrow points in the direction of the site of liver ablation/millirod implantation. The scale bars in the images = 0.1 mm. [Color figure can be viewed in the online issue, which is available at www.interscience.wiley.com.]

solubility issue, then the release of DEX from Formulation 2 in PBS solution containing 1% HP β -CD would have been much faster and would have approximated the release of millirods containing DEX-HP β -CD. However, the release of DEX is akin to that of Formulation 2 in regular PBS solution. On qualitative examination of the millirod microstructure with SEM, it was also found that the faster release of DEX was not due to an increase in the presence and size of pores in the polymer matrix. Morphologically, both formulations are comparable in terms of porosity, excluding differences in tortuosity as a cause for the discrepancies in release kinetics.

In light of these findings, the most likely explanation for the slow release of DEX from Formulation 2 millirods is the dissolution of DEX in PLGA matrix. During the annealing process at 90°C, the hydrophobic drug dissolves in the hydrophobic PLGA, leading to a molecular-level mixture with much slower release of the drug. Panyam et al.¹⁹ observed this phenomenon in DEX-releasing PLGA nanoparticles and noted that the solid-state solubility of DEX exists up to 6.7%, considerably higher than the DEX loading in these millirods. The faster release of the drug from Formulation 1 can best be explained by the fact that DEX is encapsulated within the core of the cyclodextrin, which in turn prevents drug dissolution in the polymer. The faster release and heightened bioavailability of the drug provided by millirods containing DEX complexed with HP β -CD resulted in the use of these millirods in thermoablated rat livers, in hopes of preventing the early onset of wound healing.

Locally released DEX from polymer implant prevents fibrosis

Previous studies showed that ablated liver tissue undergoes wound-healing processes, such as inflammatory cell extravasation, fibroblast migration, and collagen secretion, which eventually culminate in fibrosis. This leads to the presence of various different zones in postablated liver, composed of a zone of viable hepatocytes, a region of fibrosis, an area of cellular debris, a zone of migratory inflammatory cells, and a necrotic core. In this study, through the local delivery of water-soluble DEX from a polymer millirod implanted at the ablation site, postablated liver tissue did not undergo inflammation 8 days after ablation. Inflammatory processes, such as cellular migration and collagen deposition, were found only to a minimal degree, and no signs of fibrous capsule formation were evident. This resulted in the presence of two zones in postablated liver: an ablated, necrotic region and a nonablated region consisting of viable hepatocytes.

Systemic administration of glucocorticoids for the management of highly localized inflammatory states proves disadvantageous because of harmful side effects (e.g., hypertension, increased susceptibility to infection), as well as the failure to achieve adequately high drug concentrations at the intended site of action.²⁰ For our purposes, we want to prevent fibrous capsule formation at the boundary of ablation, with the hypothesis being that a local controlled release of DEX from a polymer millirod at the ablation site would be more effective than a systemic (intraperitoneal) injection of the drug. The results from this study show that in RF-ablated livers receiving a systemic DEX injection, fibrous capsule formation is similar to that in control-ablated livers. Inflammatory processes, including fibroblast migration and collagen deposition, can be seen to the same degree in both animal groups, yielding fibrous capsule thicknesses whose difference is not statistically significant at 4 and 8 days. Contrary to these results, DEX released locally at the site of ablation was able to prevent fibrosis up to 8 days after RF ablation, with negligible wound healing. The disparity in fibrosis between the systemic administration of DEX and the local delivery of the drug arises from the fact that the tissue immediately surrounding the injured site is exposed to higher doses of the drugs for longer periods of time when the administration is site-specific. The one-time systemic administration of DEX is rapidly cleared by the body, and the ablated region is not exposed to adequate levels of DEX.

Implications for intratumoral drug delivery

Previous work by our laboratory led to the development of a combination therapy for the treatment of liver cancer that involves destroying the tumor by RF ablation, followed by the implantation of a doxorubicin-loaded polymer millirod to eliminate recurrent malignant cells at the outer margin.⁷ Detrimental to the success of the combination therapy is the formation of a thick, well-defined fibrous capsule at the boundary of ablation that hinders drug transport past the ablated region.¹⁰ The intricate architecture of the fibrous capsule consists of tightly packed collagen fibers that give rise to a highly tortuous matrix with minimal fluid volume, which encapsulates most of the drug within the ablated region. Thus, arresting fibrous capsule formation after RF ablation through the local release of DEX should prove beneficial for intratumoral drug delivery.

Fibrous capsule formation, however, is not the only inflammatory process that can interfere with drug transport to the intended site of action. An essential component of the wound-healing process is the for-

mation of new blood vessels, occurring at later stages of inflammation, parallel with fibrosis. Several growth factors associated with wound healing contribute to angiogenesis, with vascular endothelial growth factor (VEGF) playing an important role.²¹ In the results obtained in this study, new blood vessel formation was shown to occur at the boundary of ablation (within the granulation tissue) in control livers 8 days after ablation. Contrary to these results, ablated livers receiving DEX polymer millirods showed no signs of angiogenesis at the ablation boundary. Angiogenesis at the ablation boundary can act in an unfavorable fashion, mainly because the new blood vessels increase local drug clearance. In numerous studies, DEX has been shown to exhibit antiangiogenic effects.^{22,23} Hence, the local release of DEX may enhance the effects of the intratumorally delivered chemotherapeutic agent.

Because DEX is an anti-inflammatory agent, it may also aid in preventing tumor recurrence at the ablation boundary. It is well known that an inflammatory state is critical for tumor potentiation. In and around a developing tumor, inflammatory cells secrete growth factors that in turn promote angiogenesis and remodel the extracellular matrix to facilitate metastasis.^{24,25} Fibroblasts and infiltrating inflammatory cells, such as monocytes/macrophages, granulocytes, and mast cells, produce enzymes, chemokines, and cytokines that are mitogenic for the tumor.²⁶ Postablated liver tissue exists in a highly inflammatory state, especially at the boundary of ablation, which may help explain the propensity for tumor recurrence. In light of the causal relationship between inflammation and tumor recurrence, Harrison et al.²⁷ suggested targeting the postinflammatory state as a potential follow-up to RF ablation to prevent tumor recurrence. In this study, we have shown that the local release of DEX was able to prevent inflammation at the ablation boundary. This deterrence of inflammation after RF ablation may potentially help decrease the risk of locoregional tumor recurrence.

CONCLUSIONS

Results from this study show that local delivery of DEX, complexed with HP β -CD and released from a polymer millirod after RF ablation, is capable of preventing fibrous capsule formation. Compared with ablated livers receiving a systemic DEX injection, livers receiving DEX-loaded polymer implants showed minimal inflammation and fibrosis. Future studies will focus on designing polymer millirods that release an anticancer agent concomitantly with DEX, in hopes that the anti-inflammatory effects of DEX will enhance drug transport and efficacy in tumor treatment.

The authors dedicate this work to the memory of Nicholas T. Stowe. They thank Dr. Hua Ai for SEM assistance. E. B. is grateful for the support of a National Institutes of Health minority supplement grant. B. W. is supported in part by the Case Western Reserve University Medical Scientist Training Program and NIH grant as well as DOD predoctoral fellowship.

References

1. Siperstein A, Garland A, Engle K, Rogers S, Berber E, String A, Foroutani A, Ryan T. Laparoscopic radiofrequency ablation of primary and metastatic liver tumors. *Surg Endosc* 2000;14:400–405.
2. Hori T, Nagata K, Hasuie S, Onaga M, Motoda M, Moriuchi A, et al. Risk factors for the local recurrence of hepatocellular carcinoma after a single session of percutaneous radiofrequency ablation. *J Gastroenterol* 2003;38:977–981.
3. Takada Y, Kurata M, Ohkohchi N. Rapid and aggressive recurrence accompanied by portal tumor thrombus after radiofrequency ablation for hepatocellular carcinoma. *Int J Clin Oncol* 2003;8:332–335.
4. Kosari K, Gomes M, Hunter D, Hess DJ, Greeno E, Sielaff TD. Local, intrahepatic, and systemic recurrence patterns after radiofrequency ablation of hepatic malignancies. *J Gastrointest Surg* 2002;6:255–263.
5. Bathe O, Dowden S, Sutherland F, Dixon E, Butts C, Bigam D, et al. Phase II study of neoadjuvant 5-FU + leucovorin + CPT-11 in patients with resectable liver metastases from colorectal adenocarcinoma. *BMC Cancer* 2004;4:32.
6. DiPetrillo T, Dupuy D. Radiofrequency ablation and radiotherapy: complementing treatments for solid tumors. *Semin Interv Rad* 2003;20:341–345.
7. Qian F, Szymanski A, Gao J. Fabrication and characterization of controlled release poly(D,L-lactide-co-glycolide) millirods. *J Biomed Mater Res* 2001;55:512–522.
8. Qian F, Stowe N, Saidel G, Gao J. Comparison of doxorubicin concentration profiles in radiofrequency-ablated rat livers from sustained- and dual-release PLGA Millirods. *Pharm Res* 2004;21:394–399.
9. Qian F, Stowe N, Liu E, Saidel G, Gao J. Quantification of in vivo doxorubicin transport from PLGA millirods in thermoablated rat livers. *J Control Release* 2003;91:157–166.
10. Blanco E, Qian F, Weinberg B, Stowe N, Anderson J, Gao J. Effect of fibrous capsule formation on doxorubicin distribution in radiofrequency ablated rat livers. *J Biomed Mater Res* 2004; 69:398–406.
11. Sharkawy AA, Klitzman B, Truskey GA, Reichert WM. Engineering the tissue which encapsulates subcutaneous implants. I. Diffusion properties. *J Biomed Mater Res* 1997;37:401–412.
12. Hickey T, Kreutzer D, Burgess D, Moussy F. *In vivo* evaluation of a dexamethasone/PLGA microsphere system designed to suppress the inflammatory tissue response to implantable medical devices. *J Biomed Mater Res* 2002;61:180–187.
13. Levy R, Labhasetwar V, Song C, Lerner E, Weiliam C, Vyavahare N, et al. Polymeric drug delivery systems for treatment of cardiovascular calcification, arrhythmias and restenosis. *J Control Release* 1995;36:137–147.
14. Schimmer B, Parker K. Adrenocorticotrophic hormone; adrenocortical steroids and their synthetic analogs; inhibitors of the synthesis and actions of adrenocortical hormones. In: Hardman J, Limbird L, Molinoff P, Ruddon R, Gilman A, editors. Goodman and Gilman's the pharmacological basis of therapeutics. 9th ed. New York: McGraw-Hill; 1996. p 1459–1485.
15. Vianna R, Bentley M, Ribeiro G, Carvalho F, et al. Formation of cyclodextrin inclusion complexes with corticosteroids: their characterization and stability. *Int J Pharm* 1998;167:205–213.

16. Usayapant A, Iyer B. The effect of 2-hydroxypropyl-beta-cyclodextrin on in vitro drug release of steroids from suppository bases. *Drug Dev Ind Pharm* 1999;25:387-390.
17. Anderson J. Mechanisms of inflammation and infection with implanted devices. *Cardiovasc Pathol* 1993;2:33S-41S.
18. Dilova V, Zlatarova V, Spirova N, Filcheva K, Pavlova A, Grigorova P. Study of insolubility problems of dexamethasone and digoxin: cyclodextrin complexation. *Boll Chim Farm* 2004;143:20-23.
19. Panyam J, Williams D, Dash A, Leslie-Pelecky D, Labhasetwar V. Solid-state solubility influences encapsulation and release of hydrophobic drugs from PLGA/PLA nanoparticles. *J Pharm Sci* 2004;93:1804-1814.
20. Nimmo A, Carstairs J, Patole S, Whitehall J, Davidson K, Vink R. Intratracheal administration of glucocorticoids using surfactant as a vehicle. *Clin Exp Pharmacol Physiol* 2002;29:661-665.
21. Frank S, Hubner G, Breier G, Longaker MT, Greenhalgh D, Werner S. Regulation of vascular endothelial growth factor expression in cultured keratinocytes. Implications for normal and impaired wound healing. *J Biol Chem* 1995;270:12607-12613.
22. Luo J, Shin V, Liu E, Ye Y, Wu W, So W, Chang F, Cho C. Dexamethasone delays ulcer healing by inhibition of angiogenesis in rat stomachs. *Eur J Pharmacol* 2004;485:275-281.
23. Nauck M, Karakiulakis G, Perruchoud A, Papakonstantinou E, Roth M. Corticosteroids inhibit the expression of the vascular endothelial growth factor gene in human vascular smooth muscle cells. *Eur J Pharmacol* 1998;341:309-315.
24. Wang JM, Deng X, Gong W, Su S. Chemokines and their role in tumor growth and metastasis. *J Immunol Methods* 1998;220:1-17.
25. Raz A, Levine G, Khomiak Y. Acute local inflammation potentiates tumor growth in mice. *Cancer Lett* 2000;148:115-120.
26. Coussens L, Werb Z. Inflammation and cancer. *Nature* 2002;420:860-867.
27. Harrison L, Koneru B, Baramipour P, Fisher A, Barone A, Wilson D, Dela Torre A, Cho K, Contractor D, Korogodsky M. Locoregional recurrences are frequent after radiofrequency ablation for hepatocellular carcinoma. *J Am Coll Surg* 2003;197:759-764.

Effect of fibrous capsule formation on doxorubicin distribution in radiofrequency ablated rat livers

Elvin Blanco,¹ Feng Qian,¹ Brent Weinberg,¹ Nicholas Stowe,² James M. Anderson,³ Jinming Gao¹

¹Department of Biomedical Engineering, Case Western Reserve University, Cleveland, Ohio 44106

²Department of Surgery, School of Medicine, Case Western Reserve University, Cleveland, Ohio 44106

³Institute of Pathology, University Hospitals of Cleveland, Cleveland, Ohio 44106

Received 24 October 2003; accepted 16 December 2003

Published online 22 March 2004 in Wiley InterScience (www.interscience.wiley.com). DOI: 10.1002/jbm.a.30001

Abstract: In this study, we report the histological findings of a combined therapy using radiofrequency ablation and intratumoral drug delivery in rat livers, with special attention to wound-healing processes and their effects on drug transport in post-ablated tissue. Doxorubicin-loaded millirods were implanted in rat livers that had undergone medial lobe ablation. Millirods and liver samples were retrieved upon animal sacrifice at time points ranging from 1 h to 8 days. Results demonstrate a clearly defined area of coagulative necrosis within the ablation boundary. The wound-healing response, complete with the appearance of inflammatory cells, neovascularization, and the formation of a fibrous capsule, was also observed. At the 8-day time point, fluorescence imaging analysis showed a higher concentration of doxorubicin localized within the ablation region,

with its distribution hampered primarily by fibrous capsule formation at the boundary. Given the variant nature of ablated liver, a mathematical model devised previously by our laboratory describes the data well up to 4 days, but loses reliability at 8 days. These results provide useful mechanistic insights into the wound-healing response after radiofrequency ablation and polymer millirod implantation, as well as the impact this natural corollary has on drug distribution. © 2004 Wiley Periodicals, Inc. *J Biomed Mater Res* 69A: 398–406, 2004

Key words: radiofrequency ablation; doxorubicin transport; wound-healing response; intratumoral drug delivery; polymer implants

INTRODUCTION

Although surgical excision remains the most curable option in treating hepatic cancer, only a handful of liver cancer patients are candidates for resection. Presently, several obstacles including anatomical inaccessibility of the tumor and the coexistence of various tumor nodule sites have led to a burgeoning focus on less invasive and more patient-compliant treatment modalities such as cryotherapy,^{1–3} high-intensity focused ultrasound,⁴ and radiofrequency (RF) ablation.^{5–8} The latter technique, which utilizes heat supplied by a needle electrode to eliminate tumors, has proven effective in destroying cancerous cells within the heat burst radius, but fails to eliminate remnant and viable malignant cells found at the periphery of ablation.^{9–11} In an attempt to improve this technical shortcoming, our research laboratory proposes a com-

bination therapy consisting of the following: 1) image-guided RF ablation of solid tumors, followed by 2) the implantation of a polymer millirod drug delivery device, which permits intratumoral delivery of doxorubicin, an anticancer drug, so as to eradicate any residual cancer cells.^{12–16} Hence, vital to the efficacy of the aforementioned combined strategy is the knowledge that RF ablation can drastically alter the liver tissue environment, potentially modifying the means of drug transport from the millirod implant to the surrounding liver parenchyma.

Fortunately, many recent studies have been devoted to the advancement and the establishment of RF ablation as a promising application for cancer therapy. As a result of the intense research and practice over the years, it is now well known that RF ablation causes coagulative necrosis of tissue because of the local parenchyma surpassing temperatures of up to 100°C. Destruction of tissue microvasculature accompanies the phenomenon, and peripheral small-diameter venules become thrombotic. The consequential burn wound produced by RF ablation elicits a wound-healing response from the host, brought about by the release of inflammatory mediators. Although the

Correspondence to: J. Gao; e-mail: jinming@case.edu

Contract grant sponsor: National Institutes of Health; contract grant number: R01-CA-90696

pathophysiology of the inflammatory response caused by physical injury, burns, and the implantation of foreign materials in the body has been extensively documented,^{17–20} to the best of our knowledge, the wound-healing response in liver tissues after RF ablation and its effect on drug distribution has not been reported.

Previous research conducted by our laboratory has led to the rational design of dose formulations, characterization of drug distribution, and mathematical modeling of transport within the ablated liver tissue environment.^{13,15} The mathematical model in its present form assumes that drug diffusivities and drug elimination coefficients remain constant throughout the duration of the polymer millirod implantation, as the environment is considered time-invariant. Although the model does provide acceptable approximations up to 4 days after implantation,¹⁵ the effect of the wound-healing response on drug transport at later times has not been fully examined.

The objective of this work is to histologically monitor the wound-healing response in ablated and non-ablated liver tissue with implanted polymer millirods over an 8-day period of time. We hypothesize that structural changes resulting from wound healing, especially fibrous capsule formation, will greatly affect the drug transport properties *in vivo*. Such structural changes need to be taken into consideration for the future design of polymer millirods for liver cancer treatment.

MATERIALS AND METHODS

Materials

Poly(D,L-lactide) (PLA, inherent viscosity 0.67 dL/g) and poly(D,L-lactide-co-glycolide) (PLGA, lactide/glycolide = 1:1, MW 50,000 Da, inherent viscosity 0.65 dL/g) were purchased from Birmingham Polymers, Inc. (Birmingham, AL). Poly(ethylene glycol) (PEG, M_n 4600 Da) was obtained from Aldrich (Milwaukee, WI). Doxorubicin HCl solution was purchased from Bedford Laboratories (Bedford, OH). Tris-buffered saline solution (1X) was purchased from Fisher Scientific (Pittsburgh, PA).

Animals

Male Sprague-Dawley rats (350–450 g) were obtained from Charles River Laboratories (Boston, MA). Animal procedures were adhered to the National Institutes of Health Guidelines and an approved protocol by the Institutional Animal Care and Use Committee at Case Western Reserve University.

Fabrication and *in vitro* characterization of sustained-release millirods

The doxorubicin HCl solution was desalted by dialysis in distilled water. The purified doxorubicin solution was then lyophilized to provide a fine powder. Monolithic PLGA millirods containing 5% doxorubicin, 25% NaCl, and 70% PLGA were fabricated by a compression-heat molding procedure.¹² The cylindrical millirods, measuring 1.6 mm in diameter, were cut to a length of 8 mm.

Sustained-release millirods were fabricated following a published procedure.¹⁶ First, the monolithic PLGA millirods were dipped into PEG/PLA solution in CH_2Cl_2 . The total polymer concentration was 200 mg/mL and the PEG in PLA percentage was 10%. The dipping speed was controlled by a vertically placed syringe pump at 2 mm/s. The millirods were then air-dried for 24 h followed by another round of dip-coating at the alternate end. The resulting membrane-encased millirods provide a total sustained-release phase of doxorubicin over 7 days at approximately 0.4 mg/(day · cm millirod) in Tris buffer (pH 7.4, 37°C).¹⁶

RF ablation and millirod implantation

Male Sprague-Dawley rats were anesthetized with an intraperitoneal injection of sodium pentobarbital (50 mg/kg). The abdomen was shaved and prepped with Betadine and alcohol. A local anesthetic, Marcaine, was injected subcutaneously just before skin incision. The medial lobe of the liver was then exposed through a small midline incision and exteriorized for RF ablation and millirod placement. Liver tissue ablation was produced using RF-generated current (0.09–0.12 A) from a 19-gauge needle electrode (Radionics®, Burlington, MA) at $90^\circ \pm 2^\circ \text{C}$ for a duration of 2 min. The ablated region extended approximately 4–5 mm from the electrode source. After the removal of the electrode, a millirod was inserted within the electrode tract and a small piece of cotton was sewn at the top. After the ablation procedure, 5 mL of saline solution was poured into the abdomen to assist in animal recovery, and the abdomen was then sutured. The animals were kept alive for predetermined periods of 1, 4, and 7 h, as well as 1, 2, 4, 6, and 8 days, with retrieval of polymer millirods occurring after animal sacrifice. The liver was recovered and cut perpendicular to the long axis of millirod implantation. Half was fixed in 10% formalin solution for future histological analysis, whereas the other half was preserved for doxorubicin concentration analysis.

Histology and fluorescence imaging analysis

After fixation in 10% formalin solution, the liver samples for histology analysis were embedded in paraffin, sliced to a thickness of 5 μm , and stained with hematoxylin and eosin (H&E) and Masson's trichrome (MTC) stains. Histology images were taken using a Nikon Eclipse (TE300 model) microscope.

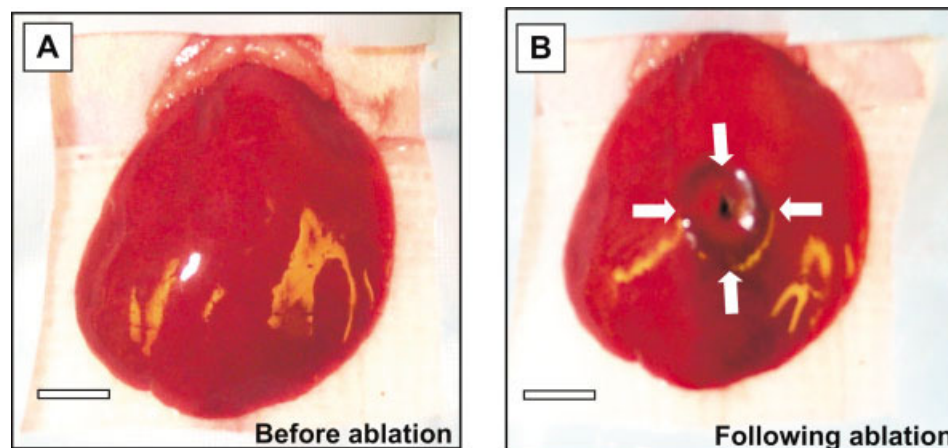


Figure 1. Medial lobe of rat liver before and immediately after RF ablation. The arrows point to the hemorrhagic rim formed as a result of ablation. The scale bars represent 5 mm. [Color figure can be viewed in the online issue, which is available at www.interscience.wiley.com.]

Frozen liver samples set aside for fluorescence microscopy analysis were mounted on a cryostat microtome with O.C.T. embedding medium (Miles Inc., Elkhart, IN), sectioned at -15°C to a thickness of $100\ \mu\text{m}$, and placed on a glass slide. Given that doxorubicin is a fluorescent molecule with excitation and emission wavelengths of 488 and 580 nm, respectively, the fluorescence microscopy images were captured using a rhodamine filter on the Nikon Eclipse microscope. For quantitative fluorescence imaging studies, the liver slices were scanned using a fluorescence imager (FluoroImagerTM SI model; Molecular Dynamics, Sunnyvale, CA). Fluorescence images were saved in TIFF format and fluorescence intensity in the images was converted to drug concentration using MatLab software (version 5.3) and a previously determined calibration curve.¹⁵ Image J software (provided free of charge by the National Institutes of Health) was used to calculate the doxorubicin concentrations spanning radially outward from the millirod implantation site. The concentration–distance profiles were then averaged from eight radial directions, with an approximate separation of 45° between each direction.

RESULTS

Gross and histological analysis of liver samples

Gross examination of rat livers

Figure 1 compares the gross images of rat livers before and immediately after RF ablation of the medial lobe of a rat liver. As depicted in Figure 1(A), the medial lobe of the liver displays a glossy, smooth, and bright red external surface before ablation, characteristics indicative of a healthy liver. However, subsequent to ablation, the liver displays a pale circular region of tissue shrinkage surrounded by a hemorrhagic rim that delineates the radius of ablation, aver-

aging 3–5 mm. The central cavity visible in Figure 1(B) corresponds to the ablation probe insertion site, serving furthermore as the site for millirod implantation.

One hour to 4 days after ablation

Within a matter of hours after RF ablation and millirod implantation, a clear distinction between ablated and nonablated zones becomes apparent in the liver samples. Figure 2(A) shows the immediate post-ablated environment, composed of a region within the radius of ablation akin to a coagulative, necrotic core—an area lacking well-defined sinusoidal and nuclear structure. The highly porous interstitial space owes itself mainly to tissue shrinkage during the charring process. The nonablated region, however, displays the characteristics of normal liver tissue morphology, including intact sinusoidal structure and undamaged hepatocytes with integral nuclear features. The results obtained are consistent with a previous short-term histological study of ablated rat livers.¹⁵ Given the short time lapse after ablation, events characteristic of the acute inflammatory response cannot yet be discerned. Inflammatory cell migration, the initial stage of the acute wound-healing process, is well underway 2 days after RF ablation and millirod implantation. A clearly defined zone of inflammatory cells, predominantly neutrophils and monocytes, is present in Figure 2(B), and the cells are shown accumulating at the ablation boundary, separating the necrotic core from the nonablated region in the process. MTC-stained images at the 2-day mark (data not shown) do not illustrate any indication of collagen deposition by fibroblasts, and no fibrous capsule formation can be seen.

Four days after RF ablation, the inflammatory re-

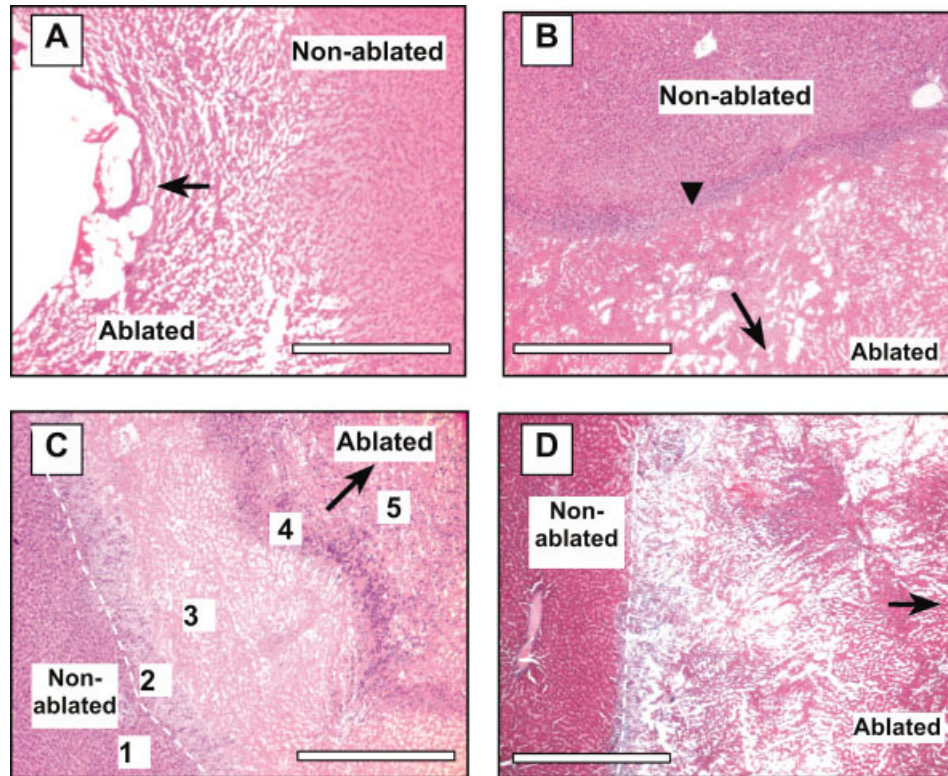


Figure 2. Histology analysis of liver samples 1 h, 2 and 4 days after RF ablation and millirod implantation. (A) One-hour H&E stained sample at original magnification of 4 \times . (B) Two-day H&E stained sample (original magnification 4 \times). The triangle in (B) points to the sharply defined zone of inflammatory cells at the ablation boundary. (C) and (D) H&E and MTC-stained samples, respectively, 4 days after RF ablation (original magnification 4 \times). Black arrows in all images point to the millirod implantation and ablation probe insertion site. The scale bars in all four images represents 1 mm. [Color figure can be viewed in the online issue, which is available at www.interscience.wiley.com.]

sponse has progressed and become quite extensive, yielding five distinct zones in the ablated and adjacent nonablated tissue, as is evident in Figure 2(C). The first zone consists of viable, nonablated hepatocytes, located well outside of the ablation radius. The second zone is characterized by fibroblast activity, whereas the third zone represents an area of cellular debris left behind by the migration of inflammatory cells, which in turn comprise the fourth zone. The fifth zone, and that closest to the ablation and millirod implantation site, represents the necrotic core.

Close observation of the distinct zones at higher magnifications yields insight into their various characteristics (data not shown). Analysis of the first zone at a higher magnification shows that this nonablated region is composed mainly of viable and healthy hepatocytes that have well-defined cytoplasm and nuclear structure. The sinusoidal morphology of normal liver tissue is also noticeable in this region. Additionally apparent in Figure 2(C) is the migratory action of inflammatory cells. At the 2-day mark, the inflammatory cells were found concentrated at the ablation boundary. However, at the 4-day mark, the inflammatory cells have moved from the ablation boundary into the necrotic zone, an event that has left an area of

cellular debris that is easily discernible by the lack of nuclei. The inflammatory zone, however, can be easily recognized by the dark stained nuclei of the monocytes, predominant cell types at this stage.¹⁹ At the ablation boundary, a fibroblast zone does exist, although an obvious and well-defined fibrous capsule is still lacking. This observation is supported by Figure 2(D), in which MTC stains show the presence of a small amount of extracellular collagen deposition arranged in a random manner.

Eight days after ablation

The inflammatory response due to tissue injury has progressed to the chronic stage 8 days after RF ablation and millirod implantation, and the formation of an extensive fibrous capsule, along with the appearance of new blood vessels, was observed. As is evident in Figure 3(A), a tight, dense layer of granulation tissue, averaging 1 mm in thickness, has formed adjacent to the ablation boundary, an event confirmed by the light blue staining region in the MTC image of Figure 3(C). Close examination of the fibrous matrix encapsulating the ablation region

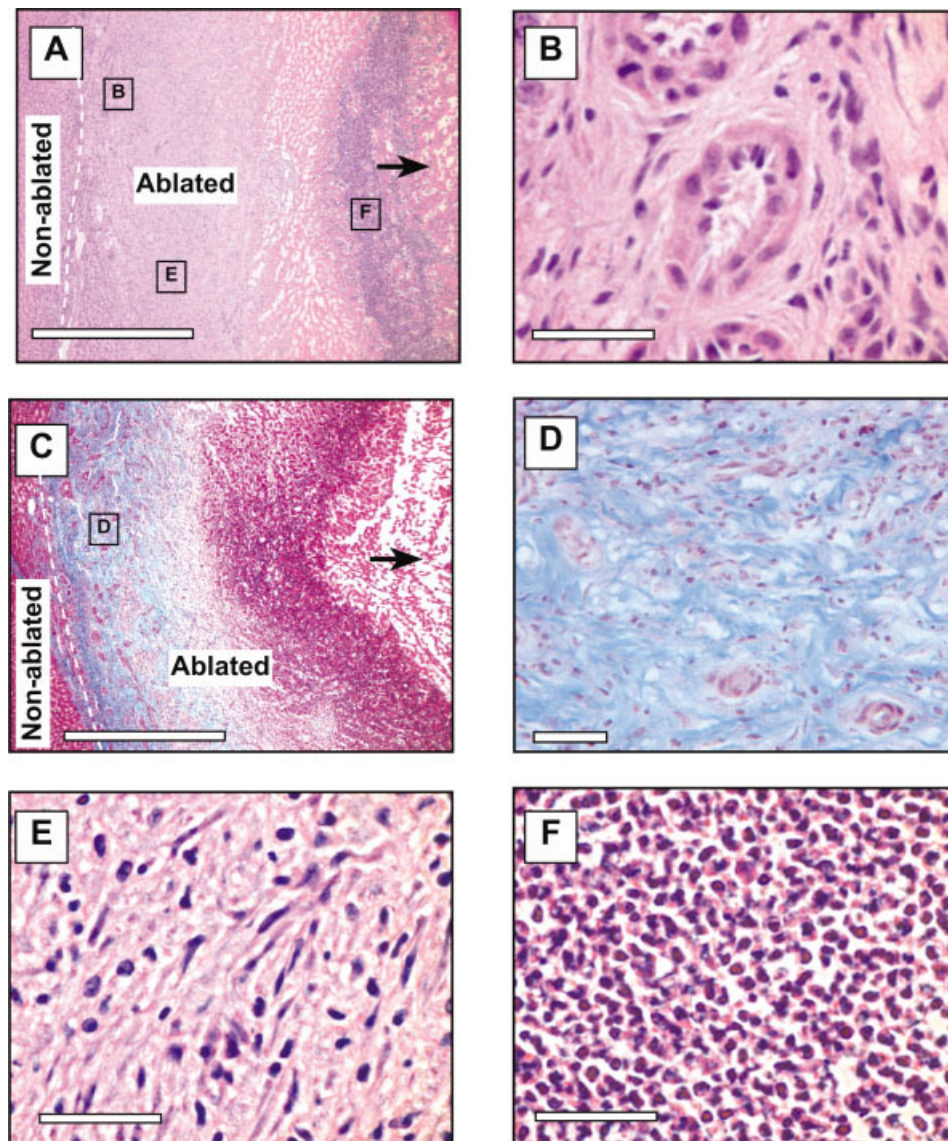


Figure 3. Liver tissue images 8 days after RF ablation and milliroad implantation. (A) H&E image showing the distinct zones of ablation (original magnification 4 \times). (B) H&E magnification of new blood vessel formation (original magnification 60 \times). (C) MTC stain highlighting fibrous capsule formation in blue (original magnification 4 \times). (D) MTC magnification of fibroblasts within the fibrous capsule layer (original magnification 40 \times). (E) and (F) H&E magnifications of fibroblasts and inflammatory cells, respectively (original magnification 60 \times). The dashed lines in (A) and (C) delineate the ablation boundary, whereas the arrows in (A) and (C) point to the site of ablation probe insertion/milliroad implantation. The scale bars in (A) and (C) represent 1 mm, whereas the scale bars in (B), (D), (E), and (F) represent 50 μ m. [Color figure can be viewed in the online issue, which is available at www.interscience.wiley.com.]

[Fig. 3(B,D,E)] yields the presence of a high density of fibroblasts and a significant amount of collagen fibril deposition. Figure 3(A) also displays the presence of the five zones seen in samples collected 4 days after ablation. At the 8-day time point, the fibrous capsule layer has become broader than in the 4-day samples, and the zone of migrating inflammatory cells, amplified in Figure 3(F), has developed into a more massive aggregation that has come to include macrophages.

Apart from showing the extent of the dense collagen fibril layer, Figure 3(B) and (D) also shows neovascu-

larization, or the formation of small new blood vessels, within the granulation tissue. As shown in the MTC-stained image [Fig. 3(D)], the endothelial tissues of the blood vessel wall are quite evident and stained red, whereas the surrounding fibrous capsule was stained light blue.

In two separate sets of control studies, the wound-healing response was examined after the implantation of doxorubicin-loaded milliroads in nonablated livers, and the implantation of drug-free milliroads in ablated livers (data not shown). In the sets of experiments conducted involving the implantation of

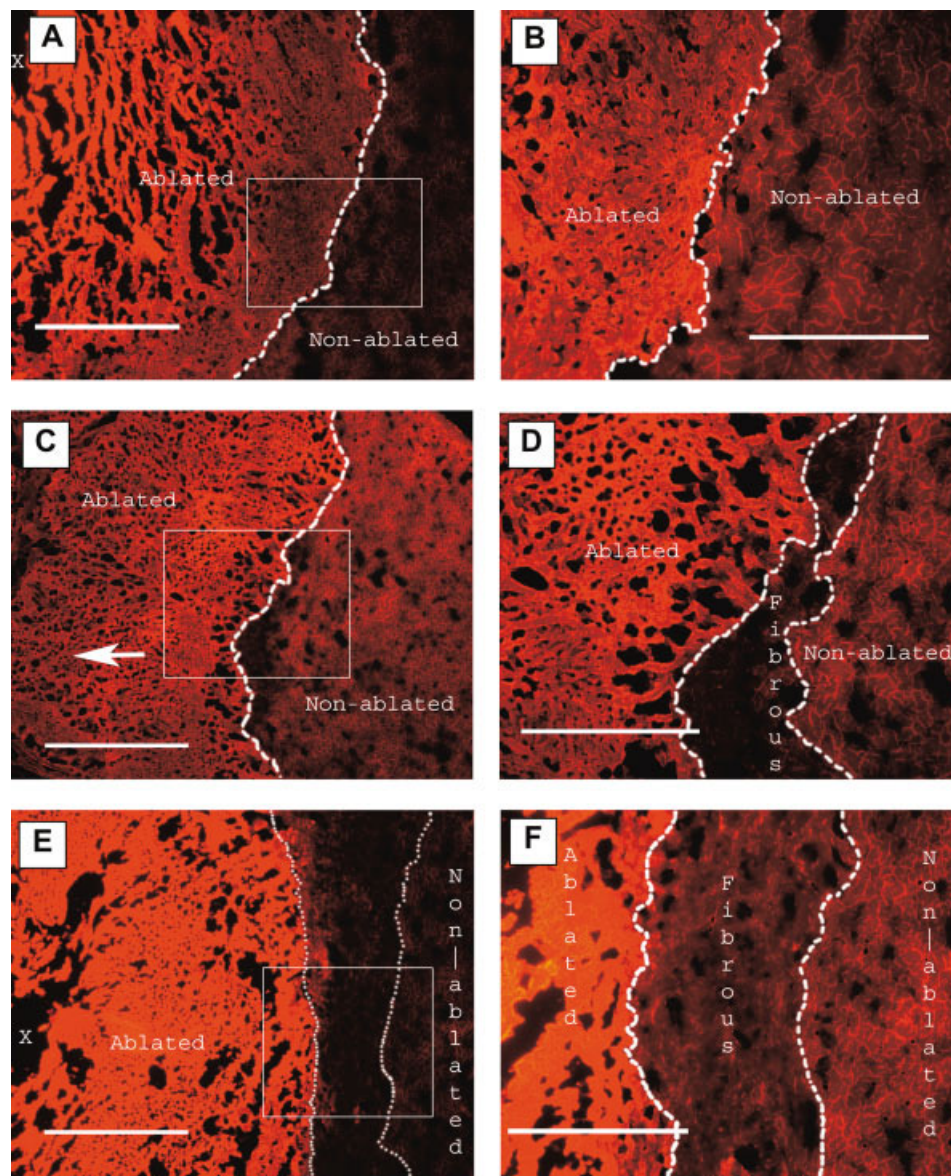


Figure 4. Fluorescence microscopy images of liver samples at various time points. (A), (C), and (E) Liver samples after RF ablation and millirod implantation at 2, 4, and 8 days, respectively (original magnification 4 \times). The boxed areas in (A), (C), and (E) are presented at higher magnifications (original magnification 10 \times) in figures (B), (D), and (F), respectively. The arrows point in the direction of the ablation probe insertion/millirod implantation site, with the letter X marking the site. The scale bars in (A), (C), and (E) are 1 mm, whereas the scale bars in (B), (D), and (F) are 0.5 mm. [Color figure can be viewed in the online issue, which is available at www.interscience.wiley.com.]

doxorubicin-loaded millirods in nonablated livers, the same wound-healing processes such as inflammatory cell migration and fibrous capsule formation were observed. However, the location of the fibrous capsule was localized around the site of implant, due mainly to the tissue injury resulting from puncturing the liver and from the presence of a foreign material. When drug-free control millirods were implanted in ablated livers, the five distinct zones presented above were readily identifiable, and a thick fibrous capsule engulfing the ablation region was observed after 8 days.

Doxorubicin distribution analysis

Fluorescence microscopy analysis: A qualitative approach

Figure 4 consists of fluorescence microscopy images obtained 2, 4, and 8 days after RF ablation, which provide insightful qualitative information on the effect of the fibrous capsule on doxorubicin distribution in RF-ablated livers. Although no morphological or nuclear detail can be discerned in these images, certain

features such as the millirod implantation site, the porous necrotic core, and the nonablated region with an intact sinusoidal network can be perceived. In Figure 4(A), a greater concentration of doxorubicin can be seen closer to the millirod implantation site 2 days after ablation, with the intensity waning throughout the necrotic core as it reaches the boundary. The magnification of the 2-day sample presented in Figure 4(B) allows for the appreciation of a sharp distinction between the ablated and nonablated regions; a higher concentration is shown to be localized within the necrotic core, with trace amounts of intensity appearing within sinusoids in the nonablated region.

Figure 4(C) and (D) shows fluorescence microscopy images of a liver sample 4 days after RF ablation. According to the histological findings presented in Figure 2(C) and (D), fibroblast activity occurs at this stage of the wound-healing response, as well as the early onset of collagen deposition, which will eventually yield a fibrous capsule adjacent to the ablation boundary. Figure 4(C) and (D) shows the presence of a dark, discontinuous region between the ablated and nonablated zones, a region with minimal to hardly any fluorescence intensity. Given its location, discontinuity, and lack of doxorubicin concentration, the zone labeled “fibrous” in Figure 4(D) is highly analogous to the fibroblast zone, and is assumed to be the early stages of fibrous capsule formation.

As shown in Figure 3, a dense and clearly defined fibrous capsule was shown to appear at the 8th day time point. Figure 4(E) shows the presence of a more extensive and well developed layer, the fibrous capsule, separating the ablated and nonablated regions, ranging from 0.5 to 1 mm in width. Of significant importance in the figure is the stark increase in doxorubicin concentration confined within the ablated region, a fluorescence intensity found to be in sharp contrast to the images obtained for the 2- and 4-day time points. The fibrous layer, better appreciated in magnification in Figure 4(F), shows low doxorubicin retention when compared with the adjacent ablated and nonablated regions.

Fluorescence imaging analysis: A quantitative approach

Fluorescence microscopy analysis provides a qualitative description of the doxorubicin distribution in a local region such as the ablation boundary. However, because of the potential photo bleaching effect, this method cannot provide reliable quantitative information on drug distribution in ablated and nonablated liver tissue. Instead, a fluorescence imaging method was used to obtain the quantitative macroscopic concentration–distance relationships for doxorubicin.

Figure 5 shows the doxorubicin concentration-ver-

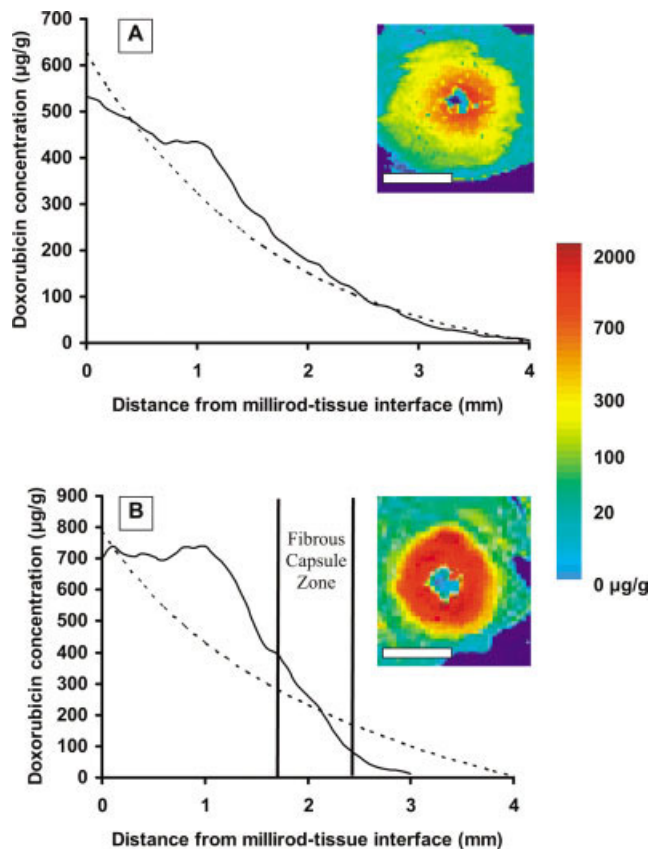


Figure 5. Doxorubicin concentration distribution in ablated liver tissues 4 days (A) and 8 days (B) after RF ablation and millirod implantation. The solid lines represent the experimental data obtained from fluorescence imaging analysis. The dashed lines represent the computer-predicted concentration–distance curves, using the following values for the constants D_a^* , D_n^* , γ^* : $1.1 \times 10^{-7} \text{ cm}^2\text{s}^{-1}$, $6.7 \times 10^{-7} \text{ cm}^2\text{s}^{-1}$, $9.6 \times 10^{-4} \text{ s}^{-1}$, respectively. The bars in (B) represent the fibrous capsule zone. The figure insets represent fluorescent images of liver samples. The scale bars in the insets represent 5 mm. The color bar represents doxorubicin concentration. [Color figure can be viewed in the online issue, which is available at www.interscience.wiley.com.]

sus-distance profiles for the 4- and 8-day time points. Although a slight increase in the doxorubicin concentration exists at the 4-day time point, the concentration is shown to decrease gradually with increasing distance from the millirod implant [Fig. 5(A)]. The figure inset in 5(A), a representative TIFF image whose fluorescence intensity has been converted to doxorubicin concentration using MatLab, qualitatively supports the general trend of the 4-day data, showing a slight accumulation of doxorubicin close to the millirod implantation site, with the concentration steadily decreasing at distances farther away from the implant. In Figure 5(B), the experimental data display a heightened doxorubicin concentration within the ablated region. The concentration remains roughly stable between 700 and 750 $\mu\text{g}/\text{g}$ for a distance of 1 mm away from the millirod tissue interface, with concentration

decreasing gradually upon the presence of the fibrous capsule and the nonablated region. The respective figure inset depicts the elevated doxorubicin concentration within the ablated region, an elevation that can best be explained by the invariant nature of ablated liver tissue, which at the 8-day time point has yielded a thicker encapsulating fibrous capsule.

Mathematical modeling of doxorubicin transport

Previously, we developed a mathematical model to quantitatively describe the drug transport processes in ablated and nonablated tissue.¹⁵ The mathematical model in its present form assumes that there is a coexistence of drug in the free and bound forms in both ablated and nonablated regions, and that free drug concentration distribution in ablated tissue changes by diffusion and drug binding, and not by perfusion or metabolism. In nonablated tissue, drug will be lost because of perfusion and/or metabolism in addition to diffusion and binding processes. Based on the above transport processes, we developed steady-state concentration distributions in both regions:

$$C_a = \frac{r_p}{D_a^*} J \cdot \ln\left(\frac{r_s}{r}\right) + C_s \quad (1)$$

$$C_n = C_s \frac{K_0(\beta r)}{K_0(\beta r_s)} \quad (2)$$

Equation 1 describes the drug concentration in ablated tissue (C_a) as a function of radius (r) from the millirod implant (radius r_p). The release flux J represents the diffusion flux at the polymer–millirod interface ($r = r_p$),

$$J = -D_a^* \frac{\partial C_a}{\partial r} \quad (3)$$

The variable r_s is the distance from the millirod to the ablation boundary, and the term D_a^* is the apparent diffusivity in ablated tissue. Equation 2 describes the drug concentration in nonablated tissue (C_n) as a function of drug concentration (C_s) at the ablation boundary, with $K_0(\beta r)$ serving as a modified Bessel function of zero order. The parameters D_n^* and γ^* , included in the Bessel functions ($\beta = \sqrt{\gamma^*/D_n^*}$), are the apparent drug diffusivity in nonablated tissue and the apparent drug elimination coefficient, respectively. The apparent diffusivities D_a^* , D_n^* , and apparent drug elimination coefficient γ^* are assumed to be invariant of time, and were previously found to be $1.1 \times 10^{-7} \text{ cm}^2\text{s}^{-1}$, $6.7 \times 10^{-7} \text{ cm}^2\text{s}^{-1}$, and $9.6 \times 10^{-4} \text{ s}^{-1}$, respectively, for doxorubicin.¹⁶

The model simulation curves for doxorubicin concentration versus distance are depicted in Figure 5. Figure 5(A) shows that the simulated model predic-

tion curve correlates well with the experimental data obtained at the 4-day time point, corroborating the gradual decrease in drug concentration. However, in Figure 5(B), the model simulation curve does not adequately fit the experimental data at the 8-day time point, due primarily to the heightened doxorubicin concentration within the ablation boundary, itself an effect of the fibrous capsule.

DISCUSSION

The main purpose of this study was to examine the wound-healing response in RF-ablated rat livers and to evaluate whether the natural healing sequelae have an effect on drug distribution from the polymer millirod implant. The results from this study demonstrate that the ablated liver tissue is a time-variant system consisting of inhomogeneous zones spanning from the millirod implantation site to the outer periphery of the ablation boundary (Figs. 2 and 3).

Previously, we developed a mathematical model to describe the drug transport processes in ablated tissues. The model simplified the ablated liver tissue as a time-invariant system with two zones of homogeneous properties, the ablated and nonablated regions.^{15,16} Within each region, the drug transport parameters (e.g., drug diffusivities and drug elimination coefficients) were assumed to be constant over time. Although this is a reasonable assumption to begin with, histology results in the current work demonstrate that the ablated liver tissue environment is much more complex, inhomogeneous in space and time. This premise is much more evident 4–8 days after ablation when extensive migration of inflammatory cells, proliferation of fibroblasts, formation of fibrous capsule, and neovascularization were observed.

Although the model predicts that the drug concentration should steadily decrease with increasing distance from the millirod at the 8-day time point, a significant deviation is observed in Figure 5(B). Fluorescence imaging analysis showed the appearance of a plateau in the drug concentration–distance curve, which demonstrates a pronounced increase in drug concentration within the ablated region. This increase in drug concentration correlates spatially with the location of the fibrous capsule [Fig. 5(B)] and is also supported by fluorescence microscopy results [Fig. 4(E,F)]. The excessive accumulation of connective tissue around the ablation boundary, consisting of highly organized and tightly packed collagen fibers, has led us to believe that this fibrous capsule acts as a barrier to drug transport. This barrier encapsulates the majority of the drug released from the millirod within the ablated region. These results agree fairly well with

the existing literature on drug transport deterrence with the emergence of collagenous tissue.^{21–24}

In parallel with the formation of the fibrous capsule, neovascularization was also observed at the 8-day time point (Fig. 3). Previous studies showed that the implantation of millirods in nonablated livers had limited drug penetration because of the drug perfusion loss through sinusoidal vasculature.¹⁵ Given that tumor recurrence was mostly observed at the ablation boundary,²⁵ neovascularization may present a challenge for local drug therapy. We hypothesize that the formation of new blood vessels may carry doxorubicin away from the ablation boundary, reducing drug exposure to residual cancer cells.

CONCLUSION

Results from this study illustrate that the wound-healing response after RF ablation has a significant impact on local drug pharmacokinetics. Perhaps the most significant finding is the obstructing nature of the fibrous capsule at the ablation boundary to drug transport. Current work is in progress to examine the incorporation of anti-inflammatory drugs (e.g., dexamethasone) within the polymer millirods with the hope of retarding the fibrous capsule formation, which in turn should facilitate drug delivery to the ablation boundary.

E. Blanco is grateful for the support of a National Institutes of Health minority supplement grant.

References

- Seifert JK, Morris DL. Indicators of recurrence following cryotherapy for hepatic metastases from colorectal cancer. *Br J Surg* 1999;86:234–240.
- Mascarenhas BA, Ravikumar TS. Experimental basis for hepatic cryotherapy. *Semin Surg Oncol* 1998;14:110–115.
- Zhou XD, Tang ZY. Cryotherapy for primary liver cancer. *Semin Surg Oncol* 1998;14:171–174.
- Malcolm AL, Ter Haar GR. Ablation of tissue volumes using high intensity focused ultrasound. *Ultrasound Med Biol* 1996;22:659–669.
- Rossi S, Garbagnati F, Rosa L, Azzaretti A, Belloni G, Quaretti P. Radiofrequency thermal ablation for treatment of hepatocellular carcinoma. *Int J Clin Oncol* 2002;7:225–235.
- Wong SL, Edwards MJ, Chao C, Simpson D, McMasters KM. Radiofrequency ablation for unresectable hepatic tumors. *Am J Surg* 2001;182:552–557.
- Wood BJ, Ramkaransingh JR, Fojo T, Walther MM, Libutti SK. Percutaneous tumor ablation with radiofrequency. *Cancer* 2002;94:443–451.
- Curley SA, Izzo F. Radiofrequency ablation of primary and metastatic hepatic malignancies. *Int J Clin Oncol* 2002;7:72–81.
- Kosari K, Gomes M, Hunter D, Hess DJ, Greeno E, Sielaff TD. Local, intrahepatic, and systemic recurrence patterns after radiofrequency ablation of hepatic malignancies. *J Gastrointest Surg* 2002;6:255–263.
- Buscarini L, Buscarini E, Di Stasi M, Vallisa D, Quaretti P, Rocca A. Percutaneous radiofrequency ablation of small hepatocellular carcinoma: long-term results. *Eur Radiol* 2001;11:914–921.
- Harrison LE, Koneru B, Baramipour P, Fisher A, Barone A, Wilson D, Dela Torre A, Cho KC, Contractor D, Korogodsky M. Locoregional recurrences are frequent after radiofrequency ablation for hepatocellular carcinoma. *J Am Coll Surg* 2003;197:759–764.
- Qian F, Szymanski A, Gao J. Fabrication and characterization of controlled release poly(D,L-lactide-co-glycolide) millirods. *J Biomed Mater Res* 2001;55:512–522.
- Qian F, Saidel G, Sutton D, Exner A, Gao J. Combined modeling and experimental approach for the development of dual-release polymer millirods. *J Control Release* 2002;83:427–435.
- Qian F, Nasongkla N, Gao J. Membrane-encased polymer millirods for sustained release of 5-fluorouracil. *J Biomed Mater Res* 2002;61:203–211.
- Qian F, Stowe N, Liu EH, Saidel GM, Gao J. Quantification of *in vivo* doxorubicin transport from PLGA millirods in thermoablated rat livers. *J Control Release* 2003;91:157–166.
- Qian F, Stowe N, Gao J. Pharmacokinetic comparison of sustained and dual-release PLGA millirods in RF ablated rat livers. *Pharm Res* 2003. Forthcoming.
- Imber G, Schwager RG, Guthrie RH, Gray GF. Fibrous capsule formation after subcutaneous implantation of synthetic materials in experimental animals. *Plast Reconstr Surg* 1974;54:183–186.
- Coleman DL, King RN, Andrade JD. The foreign body reaction: a chronic inflammatory response. *J Biomed Mater Res* 1974;8:199–211.
- Anderson J. Mechanisms of inflammation and infection with implanted devices. *Cardiovasc Pathol* 1993;2:33S–41S.
- Arturson G. Pathophysiology of the burn wound and pharmacological treatment. The Rudi Hermans lecture, 1995. *Burns* 1996;22:255–274.
- Sharkawy AA, Klitzman B, Truskey GA, Reichert WM. Engineering the tissue which encapsulates subcutaneous implants. I. Diffusion properties. *J Biomed Mater Res* 1997;37:401–412.
- Anderson JM, Niven H, Pelagalli J, Olanoff LS, Jones RD. The role of the fibrous capsule in the function of implanted drug-polymer sustained release systems. *J Biomed Mater Res* 1981;15:889–902.
- Wood RC, LeCluyse EL, Fix JA. Assessment of a model for measuring drug diffusion through implant-generated fibrous capsule membranes. *Biomaterials* 1995;16:957–959.
- Poli G. Pathogenesis of liver fibrosis: role of oxidative stress. *Mol Aspects Med* 2000;21:49–98.
- Komorizono Y, Oketani M, Sako K, Yamasaki N, Shibatou T, Maeda M, Kohara K, Shigenobu S, Ishibashi K, Arima T. Risk factors for local recurrence of small hepatocellular carcinoma tumors after a single session, single application of percutaneous radiofrequency ablation. *Cancer* 2003;97:1253–1262.

Bibliography

- (1995). "Chemotherapy in non-small cell lung cancer: a meta-analysis using updated data on individual patients from 52 randomised clinical trials. Non-small Cell Lung Cancer Collaborative Group." Bmj 311(7010): 899-909.
- Ai, H., C. Flask, et al. (2005). "Magnetite-loaded polymeric micelles as ultrasensitive magnetic-resonance probes." Advanced Materials 17(16): 1949-1952.
- Allen, C., D. Maysinger, et al. (1999). "Nano-engineering block copolymer aggregates for drug delivery." Colloids and Surfaces B-Biointerfaces 16(1-4): 3-27.
- Anni, M., L. Manna, et al. (2004). "F[o-umlaut]rster energy transfer from blue-emitting polymers to colloidal CdSe/ZnS core shell quantum dots." Applied Physics Letters 85(18): 4169-4171.
- Bae, Y., S. Fukushima, et al. (2003). "Design of environment-sensitive supramolecular assemblies for intracellular drug delivery: polymeric micelles that are responsive to intracellular pH change." Angew Chem Int Ed Engl 42(38): 4640-3.
- Bae, Y., W. D. Jang, et al. (2005). "Multifunctional polymeric micelles with folate-mediated cancer cell targeting and pH-triggered drug releasing properties for active intracellular drug delivery." Mol Biosyst 1(3): 242-50.
- Bae, Y., N. Nishiyama, et al. (2005). "Preparation and biological characterization of polymeric micelle drug carriers with intracellular pH-triggered drug release property: tumor permeability, controlled subcellular drug distribution, and enhanced in vivo antitumor efficacy." Bioconjug Chem 16(1): 122-30.
- Bailly, C. (2000). "Topoisomerase I poisons and suppressors as anticancer drugs." Curr Med Chem 7(1): 39-58.

- Ballou, B., B. C. Lagerholm, et al. (2004). "Noninvasive imaging of quantum dots in mice." Bioconjug Chem 15(1): 79-86.
- Barbone, F., M. Bovenzi, et al. (1997). "Cigarette smoking and histologic type of lung cancer in men." Chest 112(6): 1474-9.
- Belinsky, M. and A. K. Jaiswal (1993). "NAD(P)H:quinone oxidoreductase1 (DT-diaphorase) expression in normal and tumor tissues." Cancer Metastasis Rev 12(2): 103-17.
- Ben Zirar, S., A. Astier, et al. (2008). "Comparison of nanosuspensions and hydroxypropyl-beta-cyclodextrin complex of melarsoprol: Pharmacokinetics and tissue distribution in mice." Eur J Pharm Biopharm.
- Bentle, M. S., E. A. Bey, et al. (2006). "New tricks for old drugs: the anticarcinogenic potential of DNA repair inhibitors." J Mol Histol 37(5-7): 203-18.
- Bentle, M. S., K. E. Reinicke, et al. (2006). "Calcium-dependent modulation of poly(ADP-ribose) polymerase-1 alters cellular metabolism and DNA repair." J Biol Chem 281(44): 33684-96.
- Bentle, M. S., K. E. Reinicke, et al. (2007). "Nonhomologous end joining is essential for cellular resistance to the novel antitumor agent, beta-lapachone." Cancer Res 67(14): 6936-45.
- Bernstein, E. D., S. M. Herbert, et al. (2006). "Chemotherapy and radiotherapy in the treatment of resectable non-small-cell lung cancer." Ann Surg Oncol 13(3): 291-301.

- Bey, E. A., M. S. Bentle, et al. (2007). "An NQO1- and PARP-1-mediated cell death pathway induced in non-small-cell lung cancer cells by beta-lapachone." Proc Natl Acad Sci U S A 104(28): 11832-7.
- Blanco, E., E. A. Bey, et al. (2007). "Beta-lapachone-containing PEG-PLA polymer micelles as novel nanotherapeutics against NQO1-overexpressing tumor cells." J Control Release 122(3): 365-74.
- Bonner, J. A., P. M. Harari, et al. (2006). "Radiotherapy plus cetuximab for squamous-cell carcinoma of the head and neck." N Engl J Med 354(6): 567-78.
- Boothman, D. A. and A. B. Pardee (1989). "Inhibition of radiation-induced neoplastic transformation by beta-lapachone." Proc Natl Acad Sci U S A 86(13): 4963-7.
- Boothman, D. A., D. K. Trask, et al. (1989). "Inhibition of potentially lethal DNA damage repair in human tumor cells by beta-lapachone, an activator of topoisomerase I." Cancer Res 49(3): 605-12.
- Bouchard, N., F. Laberge, et al. (2008). "Adjuvant chemotherapy in resected lung cancer: two-year experience in a university hospital." Can Respir J 15(5): 270-4.
- Bouquet, W., W. Ceelen, et al. (2006). "Paclitaxel/beta-cyclodextrin complexes for hyperthermic peritoneal perfusion - Formulation and stability." Eur J Pharm Biopharm.
- Brem, H. and H. C. Lawson (1999). "The development of new brain tumor therapy utilizing the local and sustained delivery of chemotherapeutic agents from biodegradable polymers." Cancer 86(2): 197-9.
- Bucci, M. K., A. Bevan, et al. (2005). "Advances in radiation therapy: conventional to 3D, to IMRT, to 4D, and beyond." CA Cancer J Clin 55(2): 117-34.

- Canal, P., E. Gamelin, et al. (1998). "Benefits of pharmacological knowledge in the design and monitoring of cancer chemotherapy." Pathol Oncol Res 4(3): 171-8.
- Celikoglu, F., S. I. Celikoglu, et al. (2008). "Bronchoscopic intratumoral chemotherapy of lung cancer." Lung Cancer 61(1): 1-12.
- Celikoglu, F., S. I. Celikoglu, et al. (2006). "Intratumoral administration of cisplatin through a bronchoscope followed by irradiation for treatment of inoperable non-small cell obstructive lung cancer." Lung Cancer 51(2): 225-36.
- Celikoglu, S. I., F. Celikoglu, et al. (2006). "Endobronchial intratumoral chemotherapy (EITC) followed by surgery in early non-small cell lung cancer with polypoid growth causing erroneous impression of advanced disease." Lung Cancer 54(3): 339-46.
- Chen, Q., S. Tong, et al. (2004). "Targeting tumor microvessels using doxorubicin encapsulated in a novel thermosensitive liposome." Mol Cancer Ther 3(10): 1311-7.
- Chen, Y. F. and Z. Rosenzweig (2002). "Luminescent CdSe quantum dot doped stabilized micelles." Nano Letters 2(11): 1299-1302.
- Cheng, C., H. Wei, et al. (2008). "Biotinylated thermoresponsive micelle self-assembled from double-hydrophilic block copolymer for drug delivery and tumor target." Biomaterials 29(4): 497-505.
- Chung, J. E., M. Yokoyama, et al. (2000). "Inner core segment design for drug delivery control of thermo-responsive polymeric micelles." J Control Release 65(1-2): 93-103.

- Chung, J. E., M. Yokoyama, et al. (1999). "Thermo-responsive drug delivery from polymeric micelles constructed using block copolymers of poly(N-isopropylacrylamide) and poly(butylmethacrylate)." J Control Release 62(1-2): 115-27.
- Clasen, S. and P. L. Pereira (2008). "Magnetic resonance guidance for radiofrequency ablation of liver tumors." J Magn Reson Imaging 27(2): 421-33.
- Collins, L. G., C. Haines, et al. (2007). "Lung cancer: diagnosis and management." Am Fam Physician 75(1): 56-63.
- Crank, J. (1975). The Mathematics of Diffusion. New York, NY, Oxford University Press.
- Crocetti, L. and R. Lencioni (2008). "Thermal ablation of hepatocellular carcinoma." Cancer Imaging 8: 19-26.
- de Haan, L. H., G. K. Pot, et al. (2005). "In vivo relevance of two critical levels for NAD(P)H:quinone oxidoreductase (NQO1)-mediated cellular protection against electrophile toxicity found in vitro." Toxicol In Vitro.
- Dong, Y., S. F. Chin, et al. (2008). "Efficacy of Intratumoral β -Lapachone Polymer Millirod Implant for Prostate Cancer Treatment." Clin Cancer Res In press.
- Dubertret, B., P. Skourides, et al. (2002). "In vivo imaging of quantum dots encapsulated in phospholipid micelles." Science 298(5599): 1759-62.
- Duncan, R. (2003). "The dawning era of polymer therapeutics." Nat Rev Drug Discov 2(5): 347-60.
- Duncan, R. (2006). "Polymer conjugates as anticancer nanomedicines." Nat Rev Cancer 6(9): 688-701.

- Dupuy, D. E., T. DiPetrillo, et al. (2006). "Radiofrequency ablation followed by conventional radiotherapy for medically inoperable stage I non-small cell lung cancer." Chest 129(3): 738-45.
- Eliceiri, B. P. and D. A. Cheresh (1999). "The role of alphav integrins during angiogenesis: insights into potential mechanisms of action and clinical development." J Clin Invest 103(9): 1227-30.
- Elshaikh, M., M. Ljungman, et al. (2005). "Advances in Radiation Oncology." Annu Rev Med.
- Engin, K., D. B. Leeper, et al. (1995). "Extracellular Ph Distribution in Human Tumors." International Journal of Hyperthermia 11(2): 211-216.
- Etzioni, R., N. Urban, et al. (2003). "The case for early detection." Nat Rev Cancer 3(4): 243-52.
- Farokhzad, O. C., J. Cheng, et al. (2006). "Targeted nanoparticle-aptamer bioconjugates for cancer chemotherapy in vivo." Proc Natl Acad Sci U S A 103(16): 6315-20.
- Farokhzad, O. C., S. Jon, et al. (2004). "Nanoparticle-aptamer bioconjugates: a new approach for targeting prostate cancer cells." Cancer Res 64(21): 7668-72.
- Forgacs, E., S. Zochbauer-Muller, et al. (2001). "Molecular genetic abnormalities in the pathogenesis of human lung cancer." Pathol Oncol Res 7(1): 6-13.
- Frijlink, H. W., E. J. Franssen, et al. (1991). "The effects of cyclodextrins on the disposition of intravenously injected drugs in the rat." Pharm Res 8(3): 380-4.
- Frijlink, H. W., J. Visser, et al. (1990). "The pharmacokinetics of beta-cyclodextrin and hydroxypropyl-beta-cyclodextrin in the rat." Pharm Res 7(12): 1248-52.

- Gabizon, A. A. (2001). "Pegylated liposomal doxorubicin: metamorphosis of an old drug into a new form of chemotherapy." Cancer Invest 19(4): 424-36.
- Gao, J., F. Qian, et al. (2002). "In vivo drug distribution dynamics in thermoablated and normal rabbit livers from biodegradable polymers." J Biomed Mater Res 62(2): 308-14.
- Gao, X., Y. Cui, et al. (2004). "In vivo cancer targeting and imaging with semiconductor quantum dots." Nat Biotechnol 22(8): 969-76.
- Gao, X. and S. Nie (2003). "Molecular profiling of single cells and tissue specimens with quantum dots." Trends Biotechnol 21(9): 371-3.
- Gao, X., L. Yang, et al. (2005). "In vivo molecular and cellular imaging with quantum dots." Curr Opin Biotechnol 16(1): 63-72.
- Gillies, E. R. and J. M. Frechet (2005). "Dendrimers and dendritic polymers in drug delivery." Drug Discov Today 10(1): 35-43.
- Gillies, E. R. and J. M. J. Frechet (2003). "A new approach towards acid sensitive copolymer micelles for drug delivery." Chemical Communications(14): 1640-1641.
- Gillies, E. R. and J. M. J. Frechet (2005). "pH-responsive copolymer assemblies for controlled release of doxorubicin." Bioconjugate Chemistry 16(2): 361-368.
- Gillies, E. R., A. P. Goodwin, et al. (2004). "Acetals as pH-sensitive linkages for drug delivery." Bioconjugate Chemistry 15(6): 1254-1263.
- Gopal, R. (2005). "Pulmonary toxicity associated with the treatment of non-small cell lung cancer and the effects of cytoprotective strategies." Semin Oncol 32(2 Suppl 3): S55-9.

- Gopin, A., S. Ebner, et al. (2006). "Enzymatic activation of second-generation dendritic prodrugs: Conjugation of self-immolative dendrimers with poly(ethylene glycol) via click chemistry." Bioconjug Chem 17(6): 1432-40.
- Gralla, R. J., M. J. Edelman, et al. (2008). "Assessing quality of life following neoadjuvant therapy for early stage non-small cell lung cancer (NSCLC): results from a prospective analysis using the Lung Cancer Symptom Scale (LCSS)." Support Care Cancer.
- Greenwald, R. B., Y. H. Choe, et al. (2003). "Effective drug delivery by PEGylated drug conjugates." Adv Drug Deliv Rev 55(2): 217-50.
- Greish, K., J. Fang, et al. (2003). "Macromolecular therapeutics: advantages and prospects with special emphasis on solid tumour targeting." Clin Pharmacokinet 42(13): 1089-105.
- Gros, L., H. Ringsdorf, et al. (1981). "Polymeric Anti-Tumor Agents on a Molecular and on a Cellular-Level." Angewandte Chemie-International Edition in English 20(4): 305-325.
- Haag, R. (2004). "Supramolecular drug-delivery systems based on polymeric core-shell architectures." Angewandte Chemie-International Edition 43(3): 278-282.
- Hahn, I. H., R. S. Hoffman, et al. (2004). "EMLA-induced methemoglobinemia and systemic topical anesthetic toxicity." J Emerg Med 26(1): 85-8.
- Hartner, L., L. Rosen, et al. (2007). "Phase 2 dose multi-center, open-label study of ARQ 501, a checkpoint activator, in adult patients with persistent, recurrent or metastatic leiomyosarcoma (LMS)." Journal of Clinical Oncology, 2007 ASCO Annual Meeting Proceedings Part I. 25(18S): 20521.

- Hashizume, H., P. Baluk, et al. (2000). "Openings between defective endothelial cells explain tumor vessel leakiness." Am J Pathol 156(4): 1363-80.
- Higuchi, T. (1963). "Mechanism of Sustained-Action Medication. Theoretical Analysis of Rate of Release of Solid Drugs Dispersed in Solid Matrices." J Pharm Sci 52: 1145-9.
- Hirayama, F., S. Mieda, et al. (1999). "Heptakis(2,6-di-O-methyl-3-O-acetyl)-beta-cyclodextrin: A water-soluble cyclodextrin derivative with low hemolytic activity." J Pharm Sci 88(10): 970-5.
- Husseini, G. A., C. M. Runyan, et al. (2002). "Investigating the mechanism of acoustically activated uptake of drugs from Pluronic micelles." Bmc Cancer 2: -.
- Jain, R. K., E. di Tomaso, et al. (2007). "Angiogenesis in brain tumours." Nat Rev Neurosci 8(8): 610-22.
- Jemal, A., R. Siegel, et al. (2008). "Cancer statistics, 2008." CA Cancer J Clin 58(2): 71-96.
- Jeong, Y. I., H. S. Na, et al. (2008). "Antitumor activity of adriamycin-incorporated polymeric micelles of poly(gamma-benzyl l-glutamate)/poly(ethylene oxide)." Int J Pharm.
- Jeong, Y. I., S. J. Seo, et al. (2005). "Cellular recognition of paclitaxel-loaded polymeric nanoparticles composed of poly(gamma-benzyl L-glutamate) and poly(ethylene glycol) diblock copolymer endcapped with galactose moiety." Int J Pharm 296(1-2): 151-61.
- Jones, M. and J. Leroux (1999). "Polymeric micelles - a new generation of colloidal drug carriers." Eur J Pharm Biopharm 48(2): 101-11.

- Jule, E., Y. Nagasaki, et al. (2003). "Lactose-installed poly(ethylene glycol)-poly(D,L-lactide) block copolymer micelles exhibit fast-rate binding and high affinity toward a protein bed simulating a cell surface. A surface plasmon resonance study." Bioconjug Chem 14(1): 177-86.
- Kamaly, N., T. Kalber, et al. (2008). "Bimodal paramagnetic and fluorescent liposomes for cellular and tumor magnetic resonance imaging." Bioconjug Chem 19(1): 118-29.
- Kang, J., V. Kumar, et al. (2002). "Cyclodextrin complexation: influence on the solubility, stability, and cytotoxicity of camptothecin, an antineoplastic agent." Eur J Pharm Sci 15(2): 163-70.
- Kannan, T. R. and J. B. Baseman (2000). "Hemolytic and Hemoxidative Activities in *Mycoplasma penetrans*." Infect. Immun. 68(11): 6419-6422.
- Kawecki, A., D. R. Adkins, et al. (2007). "A phase II study of ARQ 501 in patients with advanced squamous cell carcinoma of the head and neck." J Clin Oncol (Meeting Abstracts) 25(18_suppl): 16509-.
- Khong, H. T., L. Dreisbach, et al. (2007). "A phase 2 study of ARQ 501 in combination with gemcitabine in adult patients with treatment naive, unresectable pancreatic adenocarcinoma." J Clin Oncol (Meeting Abstracts) 25(18_suppl): 15017-.
- Kim, T. Y., D. W. Kim, et al. (2004). "Phase I and pharmacokinetic study of Genexol-PM, a cremophor-free, polymeric micelle-formulated paclitaxel, in patients with advanced malignancies." Clin Cancer Res 10(11): 3708-16.

- Koizumi, F., M. Kitagawa, et al. (2006). "Novel SN-38-incorporating polymeric micelles, NK012, eradicate vascular endothelial growth factor-secreting bulky tumors." Cancer Res 66(20): 10048-56.
- Kukowska-Latallo, J. F., K. A. Candido, et al. (2005). "Nanoparticle targeting of anticancer drug improves therapeutic response in animal model of human epithelial cancer." Cancer Res 65(12): 5317-24.
- Kwon, G. S. and M. L. Forrest (2006). "Amphiphilic block copolymer micelles for nanoscale drug delivery." Drug Development Research 67(1): 15-22.
- Labarca, C. and K. Paigen (1980). "A simple, rapid, and sensitive DNA assay procedure." Anal Biochem 102(2): 344-52.
- Langer, R. (1998). "Drug delivery and targeting." Nature 392(6679 Suppl): 5-10.
- Langer, R. (2001). "Drug delivery. Drugs on target." Science 293(5527): 58-9.
- Langer, R. (2003). "Where a pill won't reach." Sci Am 288(4): 50-7.
- LaVan, D. A., T. McGuire, et al. (2003). "Small-scale systems for in vivo drug delivery." Nat Biotechnol 21(10): 1184-91.
- Lee, C. C., J. A. MacKay, et al. (2005). "Designing dendrimers for biological applications." Nat Biotechnol 23(12): 1517-26.
- Lee, E. S., K. Na, et al. (2005). "Doxorubicin loaded pH-sensitive polymeric micelles for reversal of resistant MCF-7 tumor." Journal of Controlled Release 103(2): 405-418.
- Lee, J., N. El-Abaddi, et al. (2006). "Noninvasive in vivo monitoring of methemoglobin formation and reduction with broadband diffuse optical spectroscopy." J Appl Physiol 100(2): 615-22.

- Lewis, A. M., M. Ough, et al. (2006). "Targeting NAD(P)H:Quinone oxidoreductase (NQO1) in pancreatic cancer." Mol Carcinog.
- Li, C., J. Nemunaitis, et al. (2006). "A phase Ib trial of ARQ 501, a selective checkpoint activator, in combination with docetaxel in patients with advanced solid tumors." J Clin Oncol (Meeting Abstracts) 24(18_suppl): 13053-.
- Li, C. and S. Wallace (2008). "Polymer-drug conjugates: Recent development in clinical oncology." Adv Drug Deliv Rev.
- Li, C. J., L. Averboukh, et al. (1993). "beta-Lapachone, a novel DNA topoisomerase I inhibitor with a mode of action different from camptothecin." J Biol Chem 268(30): 22463-8.
- Li, C. J., Y. Z. Li, et al. (1999). "Potent inhibition of tumor survival in vivo by beta-lapachone plus taxol: combining drugs imposes different artificial checkpoints." Proc Natl Acad Sci U S A 96(23): 13369-74.
- Li, P., L. Zhao, et al. (1999). "Combined effect of cosolvent and cyclodextrin on solubilization of nonpolar drugs." J Pharm Sci 88(11): 1107-11.
- Li, W., Z. Huang, et al. (2005). "Low-pH-sensitive poly(ethylene glycol) (PEG)-stabilized plasmid nanolipoparticles: effects of PEG chain length, lipid composition and assembly conditions on gene delivery." J Gene Med 7(1): 67-79.
- Lidke, D. S., P. Nagy, et al. (2004). "Quantum dot ligands provide new insights into erbB/HER receptor-mediated signal transduction." Nat Biotechnol 22(2): 198-203.

- Liu, J., H. Lee, et al. (2006). "Liposome formulation of a novel hydrophobic aryl-imidazole compound for anti-cancer therapy." Cancer Chemother Pharmacol 58(3): 306-18.
- Liu, J., L. Qiu, et al. (2006). "Preparation, characterization and in vivo evaluation of formulation of baicalein with hydroxypropyl-beta-cyclodextrin." Int J Pharm 312(1-2): 137-43.
- Liu, S. Q., Y. W. Tong, et al. (2005). "Incorporation and in vitro release of doxorubicin in thermally sensitive micelles made from poly(N-isopropylacrylamide-co-N,N-dimethylacrylamide)-b-poly(D,L-lactide-co-glycolide) with varying compositions." Biomaterials 26(24): 5064-5074.
- Liu, X. M., Y. Y. Yang, et al. (2003). "Thermally responsive polymeric micellar nanoparticles self-assembled from cholesteryl end-capped random poly(N-isopropylacrylamide-co-N,N-dimethylacrylamide): synthesis, temperature-sensitivity, and morphologies." Journal of Colloid and Interface Science 266(2): 295-303.
- Loftsson, T. (2002). "Cyclodextrins and the Biopharmaceutics Classification System of Drugs." J Incl Phenom Macro 44(1-4): 63-67.
- Logsdon, C. D., D. M. Simeone, et al. (2003). "Molecular profiling of pancreatic adenocarcinoma and chronic pancreatitis identifies multiple genes differentially regulated in pancreatic cancer." Cancer Res 63(10): 2649-57.
- Lynn, D. M., M. M. Amiji, et al. (2001). "pH-Responsive Polymer Microspheres: Rapid Release of Encapsulated Material within the Range of Intracellular pH " Angew Chem Int Ed Engl 40(9): 1707-1710.

- Maeda, H. (2001). "The enhanced permeability and retention (EPR) effect in tumor vasculature: the key role of tumor-selective macromolecular drug targeting." Adv Enzyme Regul 41: 189-207.
- Maeda, H., M. Ueda, et al. (1985). "Conjugation of poly(styrene-co-maleic acid) derivatives to the antitumor protein neocarzinostatin: pronounced improvements in pharmacological properties." J Med Chem 28(4): 455-61.
- Maeda, H., J. Wu, et al. (2000). "Tumor vascular permeability and the EPR effect in macromolecular therapeutics: a review." J Control Release 65(1-2): 271-84.
- Marin, A., H. Sun, et al. (2002). "Drug delivery in pluronic micelles: effect of high-frequency ultrasound on drug release from micelles and intracellular uptake." Journal of Controlled Release 84(1-2): 39-47.
- Matsui, M., A. Nakahara, et al. (2006). "In Situ Observation of Reduction Behavior of Hemoglobin Molecules Adsorbed on Glass Surface." IEICE Trans Electron E89-C(12): 1741-1745.
- Matsumura, Y., T. Hamaguchi, et al. (2004). "Phase I clinical trial and pharmacokinetic evaluation of NK911, a micelle-encapsulated doxorubicin." Br J Cancer 91(10): 1775-81.
- McKee, T. D., P. Grandi, et al. (2006). "Degradation of fibrillar collagen in a human melanoma xenograft improves the efficacy of an oncolytic herpes simplex virus vector." Cancer Res 66(5): 2509-13.
- Miao, X. S., P. Song, et al. (2008). "Identification of the in vitro metabolites of 3,4-dihydro-2,2-dimethyl-2H-naphthol[1,2-b]pyran-5,6-dione (ARQ 501; beta-lapachone) in whole blood." Drug Metab Dispos 36(4): 641-8.

- Michaelis, M., A. Zimmer, et al. (2005). "Increased systemic efficacy of aphidicolin encapsulated in liposomes." Oncol Rep 13(1): 157-60.
- Michalet, X., F. F. Pinaud, et al. (2005). "Quantum dots for live cells, in vivo imaging, and diagnostics." Science 307(5709): 538-44.
- Mitragotri, S. (2005). "Healing sound: the use of ultrasound in drug delivery and other therapeutic applications." Nat Rev Drug Discov 4(3): 255-60.
- Molavi, O., Z. Ma, et al. (2008). "Polymeric micelles for the solubilization and delivery of STAT3 inhibitor cucurbitacins in solid tumors." Int J Pharm 347(1-2): 118-27.
- Motoyama, K., H. Arima, et al. (2006). "Effect of 2,6-di-O-methyl-alpha-cyclodextrin on hemolysis and morphological change in rabbit's red blood cells." Eur J Pharm Sci 29(2): 111-9.
- Mukherjee, A. K., S. Basu, et al. (2001). "Advances in cancer therapy with plant based natural products." Curr Med Chem 8(12): 1467-86.
- Munro, M. H., J. W. Blunt, et al. (1999). "The discovery and development of marine compounds with pharmaceutical potential." J Biotechnol 70(1-3): 15-25.
- Munshi, N., N. Rapoport, et al. (1997). "Ultrasonic activated drug delivery from pluronic P-105 micelles." Cancer Letters 118(1): 13-19.
- Nakamura, E., K. Makino, et al. (2006). "A polymeric micelle MRI contrast agent with changeable relaxivity." J Control Release 114(3): 325-33.
- Nakanishi, T., S. Fukushima, et al. (2001). "Development of the polymer micelle carrier system for doxorubicin." J Control Release 74(1-3): 295-302.
- Nasongkla, N., E. Bey, et al. (2006). "Multifunctional polymeric micelles as cancer-targeted, MRI-ultrasensitive drug delivery systems." Nano Lett 6(11): 2427-30.

- Nasongkla, N., X. Shuai, et al. (2004). "cRGD-functionalized polymer micelles for targeted doxorubicin delivery." Angew Chem Int Ed Engl 43(46): 6323-7.
- Nasongkla, N., A. F. Wiedmann, et al. (2003). "Enhancement of solubility and bioavailability of beta-lapachone using cyclodextrin inclusion complexes." Pharm Res 20(10): 1626-33.
- Nishimura, N., R. Sugiura, et al. (2008). "Gemcitabine plus UFT combination chemotherapy as second- or third-line therapy in non-small cell lung cancer: a pilot study." J Med Invest 55(3-4): 260-6.
- Nishiyama, N. and K. Kataoka (2006). "Current state, achievements, and future prospects of polymeric micelles as nanocarriers for drug and gene delivery." Pharmacol Ther 112(3): 630-48.
- Nishiyama, N., Y. Kato, et al. (2001). "Cisplatin-loaded polymer-metal complex micelle with time-modulated decaying property as a novel drug delivery system." Pharm Res 18(7): 1035-41.
- Nishiyama, N., S. Okazaki, et al. (2003). "Novel cisplatin-incorporated polymeric micelles can eradicate solid tumors in mice." Cancer Res 63(24): 8977-83.
- O'Mahony, D., S. Kummar, et al. (2005). "Non-small-cell lung cancer vaccine therapy: a concise review." J Clin Oncol 23(35): 9022-8.
- Ohtani, Y., T. Irie, et al. (1989). "Differential effects of alpha-, beta- and gamma-cyclodextrins on human erythrocytes." Eur J Biochem 186(1-2): 17-22.
- Olive, P. L., J. P. Banath, et al. (1990). "Heterogeneity in radiation-induced DNA damage and repair in tumor and normal cells measured using the "comet" assay." Radiat Res 122(1): 86-94.

- Otsuka, H., Y. Nagasaki, et al. (2003). "PEGylated nanoparticles for biological and pharmaceutical applications." Adv Drug Deliv Rev 55(3): 403-19.
- Ough, M., A. Lewis, et al. (2005). "Efficacy of beta-lapachone in pancreatic cancer treatment: exploiting the novel, therapeutic target NQO1." Cancer Biol Ther 4(1): 95-102.
- Ozben, T. (2006). "Mechanisms and strategies to overcome multiple drug resistance in cancer." FEBS Lett.
- Panduri, V., S. A. Weitzman, et al. (2004). "Mitochondrial-derived free radicals mediate asbestos-induced alveolar epithelial cell apoptosis." Am J Physiol Lung Cell Mol Physiol 286(6): L1220-7.
- Panyam, J., Williams, D, Dash, A, Leslie-Pelecky, D, Labhasetwar, V. (2004). "Solid-state solubility influences encapsulation and release of hydrophobic drugs from PLGA/PLA nanoparticles." J Pharm Sci 93(7): 1804 - 1814.
- Pardee, A. B., Y. Z. Li, et al. (2002). "Cancer therapy with beta-lapachone." Curr Cancer Drug Targets 2(3): 227-42.
- Park, E. K., S. Y. Kim, et al. (2005). "Folate-conjugated methoxy poly(ethylene glycol)/poly(epsilon-caprolactone) amphiphilic block copolymeric micelles for tumor-targeted drug delivery." J Control Release 109(1-3): 158-68.
- Park, E. K., S. B. Lee, et al. (2005). "Preparation and characterization of methoxy poly(ethylene glycol)/poly(epsilon-caprolactone) amphiphilic block copolymeric nanospheres for tumor-specific folate-mediated targeting of anticancer drugs." Biomaterials 26(9): 1053-61.

- Park, H. J., K. J. Ahn, et al. (2005). "Susceptibility of cancer cells to beta-lapachone is enhanced by ionizing radiation." Int J Radiat Oncol Biol Phys 61(1): 212-9.
- Park, H. J., E. K. Choi, et al. (2005). "Heat-induced up-regulation of NAD(P)H:quinone oxidoreductase potentiates anticancer effects of beta-lapachone." Clin Cancer Res 11(24 Pt 1): 8866-71.
- Peer, D., J. M. Karp, et al. (2007). "Nanocarriers as an emerging platform for cancer therapy." Nat Nanotechnol 2(12): 751-60.
- Pfister, D. G., D. H. Johnson, et al. (2004). "American Society of Clinical Oncology treatment of unresectable non-small-cell lung cancer guideline: update 2003." J Clin Oncol 22(2): 330-53.
- Pink, J. J., S. M. Planchon, et al. (2000). "NAD(P)H:Quinone oxidoreductase activity is the principal determinant of beta-lapachone cytotoxicity." J Biol Chem 275(8): 5416-24.
- Pink, J. J., S. Wuerzberger-Davis, et al. (2000). "Activation of a cysteine protease in MCF-7 and T47D breast cancer cells during beta-lapachone-mediated apoptosis." Exp Cell Res 255(2): 144-55.
- Planchon, S. M., J. J. Pink, et al. (2001). "beta-Lapachone-induced apoptosis in human prostate cancer cells: involvement of NQO1/xip3." Exp Cell Res 267(1): 95-106.
- Planchon, S. M., S. Wuerzberger, et al. (1995). "Beta-lapachone-mediated apoptosis in human promyelocytic leukemia (HL-60) and human prostate cancer cells: a p53-independent response." Cancer Res 55(17): 3706-11.

- Potineni, A., D. M. Lynn, et al. (2003). "Poly(ethylene oxide)-modified poly(beta-amino ester) nanoparticles as a pH-sensitive biodegradable system for paclitaxel delivery." J Control Release 86(2-3): 223-34.
- Qian, F., G. M. Saidel, et al. (2002). "Combined modeling and experimental approach for the development of dual-release polymer millirods." J Control Release 83(3): 427-35.
- Qian, F., A. Szymanski, et al. (2001). "Fabrication and characterization of controlled release poly(D,L-lactide-co-glycolide) millirods." J Biomed Mater Res 55(4): 512-22.
- Rao, V. M. and V. J. Stella (2003). "When can cyclodextrins be considered for solubilization purposes?" J Pharm Sci 92(5): 927-32.
- Rapoport, N., Z. Gao, et al. (2007). "Multifunctional nanoparticles for combining ultrasonic tumor imaging and targeted chemotherapy." J Natl Cancer Inst 99(14): 1095-106.
- Rapoport, N., A. I. Smirnov, et al. (1997). "Factors affecting the permeability of Pseudomonas aeruginosa cell walls toward lipophilic compounds: Effects of ultrasound and cell age." Archives of Biochemistry and Biophysics 344(1): 114-124.
- Rapoport, N. Y., J. N. Herron, et al. (1999). "Micellar delivery of doxorubicin and its paramagnetic analog, ruboxyl, to HL-60 cells: effect of micelle structure and ultrasound on the intracellular drug uptake." J Control Release 58(2): 153-62.

- Reinicke, K. E., E. A. Bey, et al. (2005). "Development of beta-lapachone prodrugs for therapy against human cancer cells with elevated NAD(P)H:quinone oxidoreductase 1 levels." Clin Cancer Res 11(8): 3055-64.
- Ritger, P. L. and N. A. Peppas (1987). "A simple equation for description of solute release I. Fickian and non-fickian release from non-swellable devices in the form of slabs, spheres, cylinders or discs." Journal of Controlled Release 5(1): 23-36.
- Ross, J. F., P. K. Chaudhuri, et al. (1994). "Differential regulation of folate receptor isoforms in normal and malignant tissues in vivo and in established cell lines. Physiologic and clinical implications." Cancer 73(9): 2432-43.
- Salomon, D. S., R. Brandt, et al. (1995). "Epidermal growth factor-related peptides and their receptors in human malignancies." Crit Rev Oncol Hematol 19(3): 183-232.
- Sato, H., J. Enmi, et al. (2008). "Comparison of Gd-DTPA-induced signal enhancements in rat brain C6 glioma among different pulse sequences in 3-Tesla magnetic resonance imaging." Acta Radiol 49(2): 172-9.
- Savic, R., L. Luo, et al. (2003). "Micellar nanocontainers distribute to defined cytoplasmic organelles." Science 300(5619): 615-8.
- Sethuraman, V. A. and Y. H. Bae (2007). "TAT peptide-based micelle system for potential active targeting of anti-cancer agents to acidic solid tumors." J Control Release 118(2): 216-24.
- Shenoy, D., S. Little, et al. (2005). "Poly(ethylene oxide)-modified poly(beta-amino ester) nanoparticles as a pH-sensitive system for tumor-targeted delivery of hydrophobic drugs. 1. In vitro evaluations." Mol Pharm 2(5): 357-66.

- Shepherd, F. A., J. Dancey, et al. (2000). "Prospective randomized trial of docetaxel versus best supportive care in patients with non-small-cell lung cancer previously treated with platinum-based chemotherapy." J Clin Oncol 18(10): 2095-103.
- Shingyoji, M., D. Gerion, et al. (2005). "Quantum dots-based reverse phase protein microarray." Talanta 67(3): 472-478.
- Shiotani, K., K. Uehata, et al. (1995). "Differential effects of sulfate and sulfobutyl ether of beta-cyclodextrin on erythrocyte membranes in vitro." Pharm Res 12(1): 78-84.
- Shuai, X., H. Ai, et al. (2004). "Micellar carriers based on block copolymers of poly(epsilon-caprolactone) and poly(ethylene glycol) for doxorubicin delivery." J Control Release 98(3): 415-26.
- Siegel, D. and D. Ross (2000). "Immunodetection of NAD(P)H:quinone oxidoreductase 1 (NQO1) in human tissues." Free Radic Biol Med 29(3-4): 246-53.
- Silvestri, G. A. and M. P. Rivera (2005). "Targeted therapy for the treatment of advanced non-small cell lung cancer: a review of the epidermal growth factor receptor antagonists." Chest 128(6): 3975-84.
- Singh, M., R. Sharma, et al. (2002). "Biotechnological applications of cyclodextrins." Biotechnol Adv 20(5-6): 341-59.
- Singla, A. K., A. Garg, et al. (2002). "Paclitaxel and its formulations." Int J Pharm 235(1-2): 179-92.
- Soga, O., C. F. van Nostrum, et al. (2005). "Thermosensitive and biodegradable polymeric micelles for paclitaxel delivery." J Control Release 103(2): 341-53.

- Soppimath, K. S., D. C. W. Tan, et al. (2005). "pH-triggered thermally responsive polymer core-shell nanoparticles for drug delivery." Advanced Materials 17(3): 318-+.
- Stapert, H. R., N. Nishiyama, et al. (2000). "Poly-ion complex micelles encapsulating light-harvesting ionic Zn porphyrin dendrimers for PDT." Abstracts of Papers of the American Chemical Society 219: U226-U226.
- Stapert, H. R., N. Nishiyama, et al. (2000). "Polyion complex micelles encapsulating light-harvesting ionic dendrimer zinc porphyrins." Langmuir 16(21): 8182-8188.
- Stroh, M., J. P. Zimmer, et al. (2005). "Quantum dots spectrally distinguish multiple species within the tumor milieu in vivo." Nat Med 11(6): 678-82.
- Suh, R., K. Reckamp, et al. (2005). "Radiofrequency ablation in lung cancer: promising results in safety and efficacy." Oncology (Williston Park) 19(11 Suppl 4): 12-21.
- Sumer, B. and J. Gao (2008). "Theranostic nanomedicine for cancer." Nanomed 3(2): 137-40.
- Sutton, D., N. Nasongkla, et al. (2007). "Functionalized micellar systems for cancer targeted drug delivery." Pharm Res 24(6): 1029-46.
- Sutton, D., N. Nasongkla, et al. (2007). "Functionalized micellar systems for cancer targeted drug delivery." Pharm Res In Press.
- Sutton, D., S. Wang, et al. (2007). "Doxorubicin and beta-lapachone release and interaction with micellar core materials." Experimental Biology and Medicine Submitted.
- Suzuki, M., M. Amano, et al. (2006). "Synergistic effects of radiation and beta-lapachone in DU-145 human prostate cancer cells in vitro." Radiat Res 165(5): 525-31.

- Szejtli, J. (1998). "Introduction and General Overview of Cyclodextrin Chemistry." Chem Rev 98(5): 1743-1754.
- Tagliarino, C., J. J. Pink, et al. (2001). "Calcium is a key signaling molecule in beta-lapachone-mediated cell death." J Biol Chem 276(22): 19150-9.
- Tagliarino, C., J. J. Pink, et al. (2003). "Mu-calpain activation in beta-lapachone-mediated apoptosis." Cancer Biol Ther 2(2): 141-52.
- Tang, Y., S. Y. Liu, et al. (2003). "Solubilization and controlled release of a hydrophobic drug using novel micelle-forming ABC triblock copolymers." Biomacromolecules 4(6): 1636-45.
- Thanos, L., S. Mylona, et al. (2004). "Primary lung cancer: treatment with radio-frequency thermal ablation." Eur Radiol 14(5): 897-901.
- Torchilin, V. P. (2001). "Structure and design of polymeric surfactant-based drug delivery systems." J Control Release 73(2-3): 137-72.
- Torchilin, V. P. (2002). "PEG-based micelles as carriers of contrast agents for different imaging modalities." Adv Drug Deliv Rev 54(2): 235-52.
- Torchilin, V. P. (2004). "Targeted polymeric micelles for delivery of poorly soluble drugs." Cell Mol Life Sci 61(19-20): 2549-59.
- Torchilin, V. P. (2005). "Recent advances with liposomes as pharmaceutical carriers." Nat Rev Drug Discov 4(2): 145-60.
- Torchilin, V. P. (2007). "Micellar nanocarriers: pharmaceutical perspectives." Pharm Res 24(1): 1-16.

- Torchilin, V. P., A. N. Lukyanov, et al. (2003). "Immunomicelles: targeted pharmaceutical carriers for poorly soluble drugs." Proc Natl Acad Sci U S A 100(10): 6039-44.
- Travis, W. D., L. B. Travis, et al. (1995). "Lung cancer." Cancer 75(1 Suppl): 191-202.
- Trubetskoy, V. S., M. D. Frank-Kamenetsky, et al. (1996). "Stable polymeric micelles: lymphangiographic contrast media for gamma scintigraphy and magnetic resonance imaging." Acad Radiol 3(3): 232-8.
- Trubetskoy, V. S., G. S. Gazelle, et al. (1997). "Block-copolymer of polyethylene glycol and polylysine as a carrier of organic iodine: design of long-circulating particulate contrast medium for X-ray computed tomography." J Drug Target 4(6): 381-8.
- Ulbrich, K., T. Etrych, et al. (2003). "HPMA copolymers with pH-controlled release of doxorubicin - In vitro cytotoxicity and in vivo antitumor activity." Journal of Controlled Release 87(1-3): 33-47.
- van der Zee, J. (2002). "Heating the patient: a promising approach?" Ann Oncol 13(8): 1173-84.
- van Tilborg, G. A. F., W. J. M. Mulder, et al. (2006). "Annexin A5-conjugated quantum dots with a paramagnetic lipidic coating for the multimodal detection of apoptotic cells." Bioconjugate Chemistry 17(4): 865-868.
- Vaupel, P., F. Kallinowski, et al. (1989). "Blood flow, oxygen and nutrient supply, and metabolic microenvironment of human tumors: a review." Cancer Res 49(23): 6449-65.

- Waggoner, A. (2006). "Fluorescent labels for proteomics and genomics." Curr Opin Chem Biol 10(1): 62-6.
- Wands, J. R. and H. E. Blum (1991). "Primary hepatocellular carcinoma." N Engl J Med 325(10): 729-31.
- Wang, F., E. Blanco, et al. (2006). "Modulating beta-lapachone release from polymer millirods through cyclodextrin complexation." J Pharm Sci 95(10): 2309-19.
- Wang, Y. X., S. M. Hussain, et al. (2001). "Superparamagnetic iron oxide contrast agents: physicochemical characteristics and applications in MR imaging." Eur Radiol 11(11): 2319-31.
- Watson, A., X. Wu, et al. (2003). "Lighting up cells with quantum dots." Biotechniques 34(2): 296-300, 302-3.
- Weinberg, B. D., H. Ai, et al. (2007). "Antitumor efficacy and local distribution of doxorubicin via intratumoral delivery from polymer millirods." J Biomed Mater Res A 81(1): 161-70.
- Weller, M., S. Winter, et al. (1997). "Topoisomerase-I inhibitors for human malignant glioma: differential modulation of p53, p21, bax and bcl-2 expression and of CD95-mediated apoptosis by camptothecin and beta-lapachone." Int J Cancer 73(5): 707-14.
- Winau, F., O. Westphal, et al. (2004). "Paul Ehrlich--in search of the magic bullet." Microbes Infect 6(8): 786-9.
- Wu, X., H. Liu, et al. (2003). "Immunofluorescent labeling of cancer marker Her2 and other cellular targets with semiconductor quantum dots." Nat Biotechnol 21(1): 41-6.

- Wuerzberger, S. M., J. J. Pink, et al. (1998). "Induction of apoptosis in MCF-7:WS8 breast cancer cells by beta-lapachone." Cancer Res 58(9): 1876-85.
- Wurdeman, R. L., S. M. Mohiuddin, et al. (2000). "Benzocaine-induced methemoglobinemia during an outpatient procedure." Pharmacotherapy 20(6): 735-8.
- Yamamoto, Y., Y. Nagasaki, et al. (2001). "Long-circulating poly(ethylene glycol)-poly(D,L-lactide) block copolymer micelles with modulated surface charge." J Control Release 77(1-2): 27-38.
- Yang, D., Q. Chen, et al. (2008). "Direct and indirect immunolabelling of HeLa cells with quantum dots." Luminescence 23(3): 169-74.
- Yang, R. Y., D. Kizer, et al. (2008). "Synthetic methods for the preparation of ARQ 501 (beta-Lapachone) human blood metabolites." Bioorg Med Chem 16(10): 5635-43.
- Yoo, H. S., E. A. Lee, et al. (2002). "Doxorubicin-conjugated biodegradable polymeric micelles having acid-cleavable linkages." J Control Release 82(1): 17-27.
- Yoo, H. S. and T. G. Park (2004). "Folate receptor targeted biodegradable polymeric doxorubicin micelles." J Control Release 96(2): 273-83.
- Yuan, F., M. Leunig, et al. (1994). "Microvascular permeability and interstitial penetration of sterically stabilized (stealth) liposomes in a human tumor xenograft." Cancer Res 54(13): 3352-6.
- Zalipsky, S., M. Saad, et al. (2007). "Antitumor activity of new liposomal prodrug of mitomycin C in multidrug resistant solid tumor: insights of the mechanism of action." J Drug Target 15(7-8): 518-30.

Zhang, G., R. Zhang, et al. (2008). "Micelles based on biodegradable poly(L-glutamic acid)-b-poly lactide with paramagnetic Gd ions chelated to the shell layer as a potential nanoscale MRI-visible delivery system." Biomacromolecules 9(1): 36-42.